

Design aspects of pipe belt conveyors

Zamiralova, Maria E.

DOI

[10.4233/uuid:a989069c-54e4-4d80-a30a-a6fb9b333287](https://doi.org/10.4233/uuid:a989069c-54e4-4d80-a30a-a6fb9b333287)

Publication date

2017

Document Version

Final published version

Citation (APA)

Zamiralova, M. E. (2017). *Design aspects of pipe belt conveyors*. [Dissertation (TU Delft), Delft University of Technology]. <https://doi.org/10.4233/uuid:a989069c-54e4-4d80-a30a-a6fb9b333287>

Important note

To cite this publication, please use the final published version (if applicable).
Please check the document version above.

Copyright

Other than for strictly personal use, it is not permitted to download, forward or distribute the text or part of it, without the consent of the author(s) and/or copyright holder(s), unless the work is under an open content license such as Creative Commons.

Takedown policy

Please contact us and provide details if you believe this document breaches copyrights.
We will remove access to the work immediately and investigate your claim.

Design aspects of pipe belt conveyors

Maria Eduardovna Zamiralova

Delft University of Technology

Cover Illustration: Maria E. Zamiralova
pipe belt conveyor in EBS Terminal, the Netherlands

Design aspects of pipe belt conveyors

Proefschrift

ter verkrijging van de graad van doctor
aan de Technische Universiteit Delft,
op gezag van de Rector Magnificus prof. ir. K.C.A.M. Luyben,
voorzitter van het College voor Promoties,
in het openbaar te verdedigen op woensdag 05 juli 2017 om 10:00 uur
door

Maria Eduardovna ZAMIRALOVA

Master of Science in Mechanical Engineering,
Moscow State Mining University
geboren te Shevchenko, Kazakh SSR.

This dissertation has been approved by the promotor:
Prof. dr. ir. G. Lodewijks

Composition of the doctoral committee:

Rector Magnificus	chairperson
Prof. dr. ir. G. Lodewijks	promotor

Independent members:

Prof. dr.-ing. A. Katterfeld	Otto-von-Guericke-Universität Magdeburg (Germany)
Prof. dr.-ing. L. Overmeyer	Leibniz Universität Hanover (Germany)
Dr. C. Wheeler	The University of Newcastle (Australia)
Dr.-ing. T. Wennekamp	Phoenix Conveyor Belt Systems GmbH (Germany)
Prof. dr. A. V. Metrikine	Civil Engineering and Geosciences, TU Delft
Prof. ir. J. J. Hopman	Mechanical, Maritime and Materials, TU Delft

This dissertation is the result of research carried out at Delft University of Technology, Faculty of Mechanical, Maritime and Materials Engineering, Department of Marine and Transport Technology, Section of Transport Engineering and Logistics.



Published and distributed by: Maria Eduardovna Zamiralova
E-mail: m.zamiralova@yahoo.com

ISBN 978-94-6233-670-4

Keywords: pipe belt conveyor, belt design, bending stiffness, contact forces, FEM, troughability test, contact loss, indentation rolling resistance.

Copyright © 2017 by Maria Eduardovna Zamiralova

All rights reserved. No part of the material protected by this copyright notice may be reproduced or utilized in any form or by any means, electronic or mechanical, including photocopying, recording or by any information storage and retrieval system, without written permission of the author.

Printed in the Netherlands

To my family

"People should be beautiful in every way — in their faces, in the way they dress, in their thoughts and in their innermost selves".

— A. P. Chekhov, *Uncle Vanya*

"There is no demand for women engineers, as such, as there are for women doctors; but there's always a demand for anyone who can do a good piece of work".

— E. Clarke, the first female professor of electrical engineering in the USA, *interview 1948*

Contents

Summary	ix
Samenvatting	xiii
1 Introduction	1
1.1 An introduction to pipe belt conveyors	2
1.2 Design analysis	2
1.2.1 Advantageous aspects	2
1.2.2 Disadvantageous aspects	5
1.3 Problem statement and aim of research	7
1.4 Research questions	9
1.5 Outline of the thesis	10
2 Design Characteristics of Pipe Belt Conveyors	13
2.1 Introduction	13
2.2 Principal construction	14
2.3 Conveyor characteristics	15
2.3.1 Capacity	15
2.3.2 Belt speed	16
2.3.3 Filling degree	16
2.4 Bulk material characteristics	19
2.4.1 Bulk density	19
2.4.2 Angle of repose	19
2.4.3 Effective angle of internal friction	20
2.5 Belt characteristics	20
2.5.1 Materials and design	21
2.5.2 Belt geometry	27
2.5.3 Line mass	30
2.5.4 Nominal pipe diameter	30
2.5.5 Effective modulus of elasticity	32
2.6 Idlers and support structures	33
2.6.1 Design	33
2.6.2 Length and diameter of idler rolls	35
2.6.3 Conveyor pitch	35
2.7 Conclusions	36

3	Quantifying a Conveyor Belt Bending Stiffness	37
3.1	Introduction	37
3.2	Structural behaviour of a conveyor belt	40
3.3	Troughability test	43
3.4	Approach	45
3.4.1	Problem interpretation and assumptions	46
3.4.2	Overview of the existing models	47
3.4.3	Selected models	49
3.5	Beam models	51
3.5.1	Wang Model	51
3.5.2	Fertis Model	54
3.5.3	FEM beam model	56
3.6	Shell models	58
3.6.1	Shell-approximating analytical Wang and Fertis models	58
3.6.2	FEM shell model	58
3.6.3	Comparison Concept	59
3.7	Results	60
3.7.1	Case study	60
3.7.2	Comparison of the models and impact of an effective modulus of elasticity	62
3.7.3	Effect of a belt line mass	63
3.7.4	Impact of a belt geometry	65
3.7.5	Strain limitation	73
3.8	Guidelines for practicing engineers	74
3.9	Conclusions	76
4	Determination of Contact Forces: Experimental Approach	79
4.1	Introduction	79
4.2	Overview of existing test rigs	81
4.2.1	Static six-point stiffness devices	82
4.2.2	Static test rigs with frames and various supports	88
4.2.3	Dynamic test rigs and field measurements	100
4.2.4	Test rigs for measuring belt geometry	108
4.2.5	Analysis and design selection	111
4.3	Materials and methods	113
4.3.1	Test rig and experiment procedure	113
4.3.2	Determining belt geometry	114
4.3.3	Belt samples	114
4.4	Results	116
4.4.1	Impact of a measurement time	116
4.4.2	Influence of a pipe diameter	118
4.4.3	Belt type	121
4.4.4	Position of an overlap	123
4.5	Conclusions	126

5	Determination of Contact Forces: Analytical Solution	129
5.1	Introduction	129
5.2	Load from the belt weight	130
5.3	Load from the belt bending stiffness	131
5.3.1	Concentrated expansion moments	134
5.3.2	Evenly distributed radial load	137
5.3.3	Distributed radial load with the concentrated forces	138
5.4	Load from bulk material	142
5.4.1	Active and passive stress state theory	143
5.4.2	Bulk material stress state	145
5.4.3	Vertical stress component	146
5.4.4	Horizontal stress component	148
5.4.5	Verification with the total weight	153
5.5	Determination of the contact forces from the external loads: existing models	155
5.6	A new approach	164
5.6.1	Statically indeterminate system	164
5.6.2	Method of superposition	166
5.6.3	Unit displacements	169
5.6.4	Displacements from the external loads	172
5.6.5	Displacements from the belt weight	173
5.6.6	Displacements from the belt bending stiffness	175
5.6.7	Displacements from the bulk material load	181
5.6.8	Reaction forces from the idler rolls	187
5.7	Conclusions	189
6	Determination of Contact Forces: FEM Solution, Comparison of the Approaches	191
6.1	Introduction	192
6.2	Overview of existing PBC numerical models	193
6.2.1	Modeling a belt	193
6.2.2	Modeling idlers	195
6.2.3	Describing a contact	195
6.2.4	Boundary conditions and number of conveyor sections	195
6.2.5	Loads and load steps	197
6.3	FEM models elaborated	201
6.4	Input parameters	203
6.5	Results: case study	205
6.6	Impact analysis for empty conveyor	208
6.6.1	Derivation of the base functional dependence	208
6.6.2	Load from the belt bending stiffness	210
6.6.3	Load from the belt weight	215
6.6.4	Functional dependence for an empty pipe conveyor	218
6.7	Impact analysis for loaded conveyor	224
6.7.1	Load from the bulk material	224
6.7.2	Functional dependence for a loaded pipe conveyor	229
6.8	Conclusions	236

7 Indentation Rolling Resistance	239
7.1 Introduction	239
7.2 Overview and choice of the model	240
7.3 Indentation contact model	243
7.4 Calculation procedure	245
7.5 Determining Maxwell parameters	249
7.5.1 Loss and storage moduli	249
7.5.2 Dynamic Mechanical Test	250
7.5.3 Data interpretation	252
7.6 Results	255
7.6.1 Impact of a number of Maxwell parameters	256
7.6.2 Impact of a cross-sectional filling degree	257
7.6.3 Impact of transported bulk material	259
7.6.4 Effect of a belt mass and effective modulus of elasticity	260
7.6.5 Comparison with trough belt conveyor	262
7.7 Conclusions	263
8 Conclusions	267
8.1 Conclusions	267
8.2 Recommendations for future research	273
A Structural displacements from the vertical component of a bulk material load	277
B Structural displacements from the horizontal component of a bulk material load	283
C Development of FEM models	289
C.1 Beam Simplified Model	289
C.2 Beam Step Model	291
C.3 Shell Step Model	295
Bibliography	299
Glossary	317
Acknowledgments	325
Curriculum vitae	329

Summary

Pipe belt conveyors (PBC) are effective enclosed transport systems in bulk solids handling. They become more popular due to their advantageous design configuration. Compared to conventional open trough belt conveyors, PBCs exhibit geometrical flexibility being able to operate in tighter route curves with higher inclinations. The other beneficial design aspect is that PBCs can provide a completely enclosed system that allows them to convey so-called “difficult” materials without losses, such as dusty, contaminated bulk solids.

On other hand, PBCs exhibit a number of disadvantages, compared to the conventional trough belt conveyors, that significantly diminish the beneficial impact of a PBC design. At first, there are no recommendations developed for a conveyor belt design and selection that can ensure sufficient ability of a belt to form a stable enclosed pipe shape. Insufficient bending stiffness can cause a belt to collapse its pipe shape that can result in the losses of bulk material and increased tendency of a belt for longitudinal twisting. The other negative aspect is that a PBC system exhibits high energy consumption from the indentation rolling resistance (IRR). The high energy consumption affects the choice and costs of installation parameters of the conveyor, resulting in more strong/ heavy components that rebounds in higher capital investment to the overall system installation. In contrast with the well-standardized trough belt conveyors, there are no standards which can assist in the PBCs design.

High demand of PBCs justifies the research aiming to limit the major design disadvantages and assist in the effective design development of PBCs. For this purpose, the present thesis performs a PBC design analysis that can potentially improve conveyor system performance, aiming:

- 1) to ensure an enclosed geometry of a pipe conveyor cross section;
- 2) to reduce the IRR as a major source of PBC energy losses.

To provide the design analysis, the major PBC design characteristics that relate to an overall conveyor system, bulk material, belt design, and idler stations are reviewed. The variation range of each design parameter is established using the minimal and maximal critical values. In addition, the average values or more frequently appeared in practice are also established.

A conveyor belt bending stiffness has major influence on a conveyor belt ability to form an enclosed pipe shape. The present research quantifies a conveyor belt lateral bending stiffness using a troughability test, specified in standard ISO 703. The model selected for the troughability test represents a simply supported belt structure, subjected to a distributed self-weight, accepting a uniform belt design along the belt width. A linear-elastic material

model is assumed for a belt, using 5% small strain limitation as for normal PBC operational conditions.

The present research reviews ISO 703 and employs the following associated models for quantifying an effective modulus of elasticity: two analytical models of Wang and Fertis based on Euler-Bernoulli beam theory; their shell-approximation, corresponding to a Kirchhoff-Love theory; and two FEM models (Timoshenko beam and Mindlin-Reissner shell). The present study compares all the models, gives recommendations regarding their application and usage limitations. The impact of the varying effective modulus of elasticity, line mass and belt geometry on its troughability is investigated, establishing the functional dependence.

Insufficient pipe conveyor belt bending stiffness to form a stable pipe shape can be detected by the appearance of a contact loss, when one or more of the corresponding contact forces (CFs) become equal to zero. In this case, the CFs can be considered as a major indicator for the belt's pipe-ability. In addition, the CFs participate in the indentation phenomenon between the rigid idler rolls and the viscoelastic belt rubber that influence the IRR.

To determine PBC CFs, three approaches are proposed: experimental, analytical, and the numerical FEM. Usage of all three approaches together allows one to determine PBC CFs in a more precise way, compared to the existing studies.

For the experimental approach, the present research provides a qualitative analysis of the existing PBC test rig configurations, discuss their design advantages and disadvantages, and compares the results for CFs available. The analysis indicates that CFs measured depend on the test rig design selection. For the present analysis, a static six-point belt stiffness device is selected for measuring PBC CFs and belt's cross-sectional geometry. Using this test rig, an impact of major PBC design parameters, such as pipe diameter, belt slenderness, transverse bending stiffness, belt's mass, and position of a belt overlap, on CFs and belt's pipe-ability is investigated. The qualitative analysis of the results obtained exhibited similar load patterns with feasible values of CFs, compared to the results reported by other researchers. The results confirmed that bigger pipe diameters require higher bending stiffness and/or a larger overlap with respect to the belt width to ensure a stable pipe shape formation.

Considering the analytical approach to determine PBC CFs, the present research reviewed all the existing models and concluded that none of them can predict the CFs in a correct way. That is why a new analytical model is introduced. The analytical model is linearized around specific pipe shape configuration, by applying external loads to the pre-folded pipe shape geometry. The external loads imply the load from the belt weight, the load from the bulk material, and additional expansion load from the belt bending stiffness. The latter represents the effect of bending the belt from a flat shape into a pipe shape. Three methods of modeling the load from the belt bending stiffness are selected for the analysis: the concentrated expansion moments applied at the belt edges M_{bst} ; the radial expansion load evenly distributed along the belt's pipe q_{bst} ; and the radial distributed load q_{bst} together with the concentrated forces Q_{1bst} , Q_{2bst} . To model the load from the bulk material, a vertical and the horizontal load components are used that account for the bulk shear stresses and the load distribution along the pipe contour and along the conveyor pitch.

The linearized system of PBC CFs, statically indeterminate to a 4-th degree, is solved using the equilibrium equations and by employing the Method of Superposition (or Displacement Method). The latter implies replacing the four support restraints with the appropriate

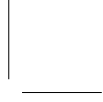
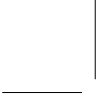
redundant forces and assuming those displacements equal to zero. The displacements are determined, considering the strain energy of the system using Maxwell-Mohr Integrals.

To determine PBC CFs using the FEM analysis, three FEM models are proposed: the Simplified Beam Model, solved within one load step, and more complex the Beam Step Model and the Shell Step Model, solved within multiple load steps. The FEM beam models support Timoshenko theory, whereas the FEM shell model is based on the theory of Mindlin-Reissner. The FEM models can closely imitate the experiment testing within the six-point stiffness device. The comparison of the results indicated that the FEM models are in close agreement with the experiment, whereas the analytical model is in agreement with the FEM. In addition, the analysis indicated that to model the load from the belt bending stiffness, only the expansion concentrated moments M_{bst} , applied at the belt edges can be used, whereas other two methods proposed do not give satisfactory results.

Using the FEM solution and the analytical model, the impact analysis is performed for the PBC CFs. The functional dependences between the CFs and input design parameters are established for an empty and loaded PBC. The impact analysis is performed considering the appearance of a contact loss in an idler station. The weakest position in the idler set for a contact loss appears for the lateral top rolls. The general design recommendations for a PBC system are established aiming to ensure belt's ability to form a stable enclosed pipe shape.

The CFs are also used in the present thesis to determine the IRR. For the IRR, a 3D generalized Maxwell model with multiple Maxwell parameters is used. The model incorporates the indentation phenomenon between the two curved surfaces (a rigid roll and viscoelastic pipe-shaped belt) using a Winkler foundation. The rheological behavior of a belt cover rubber is determined using Dynamic/Mechanical Analysis (DMA test). The experimental data for the loss and storage moduli are approximated with Prony series. The impact analysis is performed, considering how a number of Maxwell parameters, and also how the belt weight, different bulk material, cross-sectional filling degree, and belt's effective modulus of elasticity can influence the IRR friction factor. The present study indicates that the IRR friction factor, proposed in DIN 22 101 is not suitable for PBCs in the given form and proposes the alternative formulation.

The general design recommendations for PBCs are presented, aiming to diminish the energy losses from the IRR and to ensure a sufficient belt bending stiffness to form an enclosed pipe shape. The potential directions for the future research are also presented.



Samenvatting

Pijpbandtransporteurs (E. Pipe belt conveyors, PBCs) zijn effectief dichte transportsystemen voor de handling van bulkgoed. PBCs komen meer in de belangstelling door de gunstige ontwerpkenmerken ervan. In vergelijking met conventionele open, getrogde transporteurs hebben PBCs een hogere geometrische flexibiliteit doordat ze nauwere bochten kunnen maken en grotere hellingen kunnen overbruggen. Een ander ontwerpvoordeel is dat PBCs volledig gesloten zijn, waardoor zogenoemd “moeilijk” materiaal, zoals stoffig, vervuilend materiaal, zonder verliezen kan worden verplaatst.

Anderzijds hebben PBCs, vergeleken met conventionele trogtransporteurs, ook een aantal nadelen die de voordelen ervan aanzienlijk verminderen. Allereerst zijn er, in tegenstelling tot de goedgedefinieerde trogtransporteurs, voor pijpbandtransporteurs geen normen voor ontwerp en selectie op grond waarvan kan worden verzekerd dat een band een stabiele dichte pijp zal vormen. Door een te lage buigstijfheid kan de pijp inklappen, met materiaalverlies tot gevolg, of de band kan gaan draaien om de lengteas. Een ander negatief aspect is het hoge energiegebruik van een PBC-systeem tengevolge van de indrukrolweerstand (IRR). Het hogere energiegebruik heeft ook invloed op ontwerpparameters en de kosten van een systeem doordat zwaarder equipment nodig is en de investeringskosten daardoor hoger.

Door de grote vraag naar PBCs is er reden om te onderzoeken hoe de nadelen kunnen worden beperkt en hoe kan worden bijgedragen aan de effectieve ontwikkeling van het ontwerp van PBCs. In dit proefschrift is daarom een analyse gemaakt van een PBC ontwerp waarmee het mogelijk is om de prestaties van een transportsysteem te verbeteren. De analyse is gericht op:

- 1) waarborgen dat een doorsnede dwars op de band een gesloten vorm heeft;
- 2) vermindering van de indrukrolweerstand (E. Indentation Rolling Resistance, IRR) als een belangrijke bron van energieverlies in een PBC.

Ten behoeve van de ontwerpanalyse is een overzicht gemaakt van de belangrijkste kenmerken van een PBC, die verband houden met het totale transportsysteem, het bulkmateriaal, het ontwerp van de band en de rollenstellen. Voor alle ontwerpparameters worden minimale en maximale kritieke waarden vastgesteld. Daarnaast worden gemiddelde, of veel gebruikte waarden van de parameters gegeven.

De stijfheid heeft een belangrijke invloed op de mogelijkheid om de band tot een pijp om te vormen. In dit onderzoek wordt de laterale buigstijfheid van een band gekwantificeerd met behulp van een trogtest, zoals vastgelegd in de norm ISO 703. De trogtest wordt uitgevoerd met een aan de kanten opgelegde band die doorzakt onder het eigen gewicht. Er

wordt lineair-elasticiteit materiaal verondersteld, maximaal 5% vervorming en een uniforme opbouw van band in de dwarsrichting.

Er wordt in dit onderzoek een overzicht gegeven van de ISO-norm 703 en er wordt gebruik gemaakt van de volgende modellen voor het kwantificeren van een effectieve elasticiteitsmodulus: twee analytische modellen van Wang en Fertis, gebaseerd op de balkentheorie van Euler-Bernoulli; de Wang-Fertis-benadering met een plaatmodel, volgens een theorie van Kirchhoff-Love; en twee FEM-modellen (Timoshenko's balkmodel en Mindlin-Reissner's plaatmodel). De modellen worden met elkaar vergeleken en er worden aanbevelingen gedaan voor de toepassing ervan en er worden beperkingen voor het gebruik aangegeven. Onderzocht is wat de invloed op de trogbaarheid van de band is van variërende effectieve elasticiteitsmodulus en van het gewicht en de afmetingen van de band.

Een buigstijfheid van de band die te laag is om een stabiele pijp te vormen, kan worden vastgesteld door het optreden van contactverlies, als een of meer van de contactkrachten (E. Contact Forces, CFs) nul wordt. De CFs kunnen worden beschouwd als een belangrijke indicator voor de pijpbaarheid van de band. Daarnaast dragen de CFs bij aan het indeuken van de band tussen de vaste rollen en het visco-elastische rubber van de band en ze hebben invloed op de rolweerstand.

Er worden drie manieren voorgesteld voor het bepalen van de CFs van een PBC: experimenteel, analytisch en numeriek (FEM). Door gecombineerd gebruik van de drie benaderingen is het mogelijk de CFs van een PBC nauwkeuriger te bepalen dan in bestaande onderzoeken.

Het onderzoek geeft voor de experimentele benadering een kwalitatieve analyse van de bestaande PBC testbanken, de voordelen en nadelen van de ontwerpen ervan worden besproken en de beschikbare resultaten voor CFs worden vergeleken. De analyse geeft aan dat gemeten CFs afhankelijk zijn van het ontwerp van de testbank. Voor de onderhavige analyse is een statische zespuntsopstelling gekozen om de CFs van de PBC en de geometrie van de dwarsdoorsnede van de band te meten. Met behulp van deze testbank wordt de invloed van belangrijke PBC ontwerpparameters op de CFs en op de pijpbaarheid van de band onderzocht, zoals de diameter van de pijp, de slankheid van de band, de transversale buigstijfheid, de massa van de band en de positie van de overlapping. Kwalitatieve analyse van de resultaten gaf belastingspatronen met realistische waarden van de CFs, overeenkomend met resultaten welke zijn gevonden door andere onderzoekers. De resultaten bevestigen dat er bij een grotere pijpdiameter een stabiel pijpvorm te waarborgen een hogere buigstijfheid nodig is en/of een grotere overlap.

Voor de analytische methode van de bepaling van de CFS van een PCB zijn in dit onderzoek alle bestaande methoden nagegaan, en er is geconstateerd dat geen van de bestaande modellen de CFs goed kan voorspellen. Er is daarom een nieuw analytisch model ontwikkeld. Het analytische model is gelineariseerd om een gegeven pijpvorm, door het uitoefenen van externe krachten op de al gevormde pijp. De externe belastingen zijn weergaven van belastingen door het gewicht van de band, het getransporteerde materiaal, en extra belasting door de buigstijfheid van de band. Laatstgenoemde belasting geeft het effect weer van het buigen van de vlakke band tot een pijp. Voor de analyse wordt de belasting door de buigstijfheid van de band op drie manieren gemodelleerd: de uitvouwmomenten geconcentreerd uitgeoefend op de randen van de band M_{bst} , de radiale uitvouwbelasting gelijkmatig verdeeld over de pijp q_{bst} , en de radiaal verdeelde belasting q_{bst} samen met de geconcentreerde krachten Q_{1bst} en Q_{2bst} . Om de belasting voor het getransporteerde materiaal te modelleren

worden een verticale component en de horizontale componenten van de belasting gebruikt die de schuifspanningen in het materiaal en de verdeling van de last over de contour van de pijp en tussen de steunpunten van de band weergeven.

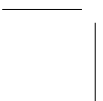
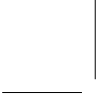
Het gelineariseerde systeem van de CFs van de PCB, statisch onbepaald van de 4-de graad, wordt opgelost met behulp van de evenwichtsvergelijkingen en door toepassing van de superpositiemethode (of verplaatsingsmethode). Dit houdt in dat de vier beperkingen voor de ondersteuning worden vervangen door passende krachten en er wordt aangenomen dat de bijbehorende verplaatsingen 0 zijn. De verplaatsingen worden bepaald door berekening van de spanningsenergie van het systeem met behulp van Maxwell-Mohr integralen.

Voor de FEM-analyse van de CFs van een PBC worden drie FEM-modellen voorgesteld: het vereenvoudigde balkmodel, en twee meer gecompliceerde meerstaps balk- en plaatmodellen. De FEM-balkmodellen zijn gebaseerd op Timoshenko's balkentheorie, het plaatmodel is gebaseerd op de theorie van Minlin-Reissner. Met de FEM-modellen kunnen de experimenten in de zespuntsbank goed worden nagebootst. Vergelijking van de resultaten geeft aan dat de FEM-modellen nauwkeurig overeenkomen met het experiment, en dat het analytische model overeenkomt met de FEM-modellen. Daarnaast is gebleken dat voor het modelleren van de belasting door de buigstijfheid van de band alleen de geconcentreerde momenten M_{bst} , uitgeoefend op de randen van de band, kunnen worden gebruikt, terwijl de andere twee voorgestelde methoden geen bevredigende resultaten geven.

Met behulp van de FEM-oplossing en het analytische model is een impactanalyse uitgevoerd voor de CFs van een PBC. De functionele afhankelijkheid tussen de CFs en ontwerpparameters is bepaald voor een lege en voor een beladen PBC. De impactanalyse is gedaan door te kijken naar het optreden van contactverlies bij een rollenstel. Voor contactverlies is het zwakste punt in het stelsel rollen bij de laterale bovenrollen. Er zijn algemene aanbevelingen voor het ontwerp van een PBC-systeem vastgesteld om te verzekeren dat de band een stabiele, gesloten pijp kan vormen.

De CFs zijn in dit proefschrift ook gebruikt voor het bepalen van de IRR. Voor de IRR is een 3D gegeneraliseerd Maxwell-model met een aantal Maxwell-parameters gebruikt. Het model omvat een weergave van de vervorming tussen twee gekromde oppervlakken (een stijve rol en een visco-elastische pijpvormige band) met behulp van een Winkler-funderingmodel. Het reologisch gedrag van de rubber deklaag van de band is bepaald met behulp van een Dynamisch/Mechanische Analyse (DMA-proef). De experimentele gegevens voor de verlies- en opslagmoduli zijn benaderd met Prony-reeksen. Er is een impactanalyse uitgevoerd om de invloed op de IRR na te gaan van een aantal Maxwell-parameters en ook van het gewicht van de band, verschillende soorten bulkmateriaal, de vullingsgraad, en de effectieve elasticiteitsmodulus van de band. Dit onderzoek geeft aan dat de IRR wrijvingsfactor die in DIN 22101 wordt voorgesteld, in de gegeven vorm voor PBCs niet bruikbaar is, en er wordt een andere formulering voorgesteld.

Er worden algemene aanbevelingen gedaan voor het ontwerp van PBCs, bedoeld om energieverlies door de IRR te verlagen, en om te waarborgen dat de band stijf genoeg is om een gesloten pijp te vormen. Er worden ook mogelijke richtingen voor verder onderzoek aangegeven.



Chapter 1

Introduction

*I keep six honest serving-men
(They taught me all I knew);
Their names are What and Why and When
And How and Where and Who.*

— R. Kipling, *Just so stories*

Pipe belt conveyors (PBCs) are an effective enclosed continuous transport systems in bulk solids handling. They are ubiquitously present worldwide in various mines, plants, factories, and marine terminals (see Figure 1.1). PBCs are utilized in a broad range of industrial sectors, such as the coal and ore mining, metallurgy, cement and construction industries, chemical production, and others.



Figure 1.1: Double pipe conveyor system operating in Tata Power Plant, Mumbai, India (Image courtesy FLSmidth Wadgassen GmbH).

1.1 An introduction to pipe belt conveyors

The current state-of-the-art of PBCs is related to the historical background of their design development. In 1940 Johns [118] patented a preliminary construction of a transport system in the USA called tubular belt conveyor. This construction implied a concept of a movable tube-shaped rubber belt used for conveying bulk material, which could be opened and closed for loading and discharging. In the 1950's, a few patents (see e.g. [204],[211]) were issued in Germany on "hose" conveyor types with a similar construction basis.

However, the founder of the major design of PBC, which is known and applied nowadays, is considered to be Hashimoto, Japan Pipe Conveyor (JPC) Company [24] [112]. Hashimoto developed the main construction of a pipe conveyor in 1964 [24, 25] and made relevant patent applications (see [96]). The first trials were not successful, as the belt was not sufficiently rigid to form a stable pipe shape. Moreover, the technologists experienced problems with belt alignment and twisting. In order to develop a suitable belt design, the JPC Company collaborated with Bridgestone Rubber Company in exchange for the manufacturing license in Japan. In 1979 the first commercial pipe conveyor system was successfully installed [24, 25, 37]. Since then a number of patents on design and technology of PBC were obtained ([97–99] etc.)

In 1988, the Bridgestone Corporation took over the JPC Company [24, 25, 112] and became the owner of all the rights on the JPC system. It started selling international licenses outside of Japan [37, 216, 230]. Having the only rights to issue the license, the company was not enough motivated for design improvements. Staples [216] reports that during that period minor attention was paid to the technological development. The installations were mostly made with insignificant adjustments, keeping the major technology of the original inception [216]. As a result, PBC started to become considered as rather costly and "difficult" transport system, in comparison to the other conveyor types, whose technologies were continually developing.

At the beginning of 1990 the original patents of JPC and Bridgestone started to expire [37, 216], which provided new companies with the opportunity to enter the market with different design solutions. That is why the research and technology on PBC is still rapidly developing and can be considered to be a rather recent exploration area.

Nowadays, many companies are involved in the pipe conveyor industry, and the number of PBC installations is rapidly growing. Geographically, the main demand for pipe conveyors is mostly concentrated in China, India, and South Africa [270]. However, according to Zhang and Steven [270], during the following few decades it is reasonable to expect market expansion in territory of South-East Asia, Australia and South America.

Growing market demand of PBCs and the rather recent history of technological development justify research aiming to improve the efficiency and reliability of this type of transport system.

1.2 Design analysis

1.2.1 Advantageous aspects

The popularity of PBCs can be explained by a number of design advantages inherent to the system.

Environmental protection

One of the most important advantages is that PBCs are environmentally friendly transport solution (see e.g. Horak [105], Zhang and Steven [270], Bahke [8], Lodewijks [139], Kessler [124], Vaka [230], Imai [112], and others). The conveyor belt, folded into a tubular shape and enclosed with overlapping edges, provides a well-sealed transport system for the bulk material. This ensures a spillage-free conveying process and prevents environmental pollution. PBCs can transport so-called “difficult” bulk solids, such as contaminated, toxic, and even radioactive materials [106], [225]).

The enclosed transport system prevents bulk material losses and provides dust-free operation (see e.g. [105], Zhang and Steven [270], Bahke [8], Lodewijks [139], Kessler [124], Vaka [230], Imai [112], and others.) As a result, the bulk material does not build-up on idler rolls and galleries, which minimizes their periodical cleaning maintenance, compared to trough conveyors [105], [112]. Imai [112] states that significant dust emission of bulk material are decisive in selection of PBCs over the other conveyor types in most of the world’s installations.

In addition, PBCs are capable to protect bulk material against undesirable impact from the environment (see e.g. Horak [105], Zhang and Steven [270], Bahke [8], Lodewijks [139], Kessler [124], Vaka [230], Imai [112], Buchanan [24, 25]). This allows companies to operate in difficult environmental and weather conditions, such as strong wind, heavy rain, high humidity and snow (see e.g., Figure 1.2).



Figure 1.2: Pipe conveyor operating in snow weather condition in Shanxi Province, China (Image courtesy of Zigong Conveying Machine Group Co. Ltd).

Geometrical flexibility

PBCs are preferred over other types of transport system due to their geometrical flexibility. PBCs negotiate tighter route curves and high inclinations (see e.g., Horak [105], Horn [106], Lodewijks [138, 139], Buchanan [25], Fletcher and du Toit [79], Hinkelmann [100], [124], CKIT [37]) The belt, folded into a pipe shape, tightly holds the bulk material transported. As a result, pipe conveyors exhibit geometrical flexibility at their route installations. They can achieve inclination angles of 27° - 30° [24, 25, 79, 138], whereas conventional open trough conveyors are limited only to 17° - 20° . If the bulk material allows the formation of plugs, then 90° inclination angle is also possible (vertical pipe conveyor, see Wesemeier [238], [239], Sisselaar [212]). In addition, while the traditional trough belt conveyors operate at horizontal route curves with small angles and large radii, pipe conveyors can make plane turns at almost 90° with a much smaller route radius [25]. Thus, in combination with inclinations, PBCs are utilized for various complex 3D route curves, which is essential for operating in difficult topographical conditions (e.g., see Figure 1.3).

The usage of a pipe conveyors can reduce the number of required transfer points in the route (see e.g., [25], CKIT [37], Horak [105], Lodewijks [139], Day [41]) Since trough conveyors can operate at horizontal curves with small angles and large radii, complex topography for transportation requires usage of more than one trough conveyor, whereas one pipe conveyor for the same route is sufficient. A decreased number of transfer points save capital investments in power stations, pulleys, chutes, control and dust collection systems needed when the traditional trough conveyors are selected instead. Moreover, it requires less



Figure 1.3: Pipe conveyor operating in complex topographical conditions in Taiyuan, Shanxi Province, China. The route passes over the rocky terrain, mountains, farms, roads and small communities (Image courtesy FLSmidth Wadgassen GmbH).



Figure 1.4: Pipe conveyors transporting bulk solids through a narrow tunnel passage during the construction of Lötschberg base tunnel in Switzerland (Image courtesy FLSmidth Wadgassen GmbH).

maintenance, as, according to Lodewijks [139], the transfer points are the biggest source of failure and damage in the transport line.

Compared to open-trough prototypes, PBCs occupy 65% less space for the installation at the same capacity (see e.g., Buchanan [24, 25], Fletcher and du Toit [79], CKIT [37], Horak [105], Vaka [230], Bahke [8]), which is very useful for underground mining or operating in indoor confined places (see Figure 1.4). Moreover, PBCs can operate in reverse order, have intermediate loading/unloading points if needed, and can convey material in both strands (CKIT [37], Wiedenroth and Staribacher [249], Wiedenroth [248]).

1.2.2 Disadvantageous aspects

Despite the design advantages mentioned, PBCs exhibit a number of drawbacks that needs to be studied and improved.

High capital costs

The major disadvantage of PBCs is related to their high capital and operating costs (see e.g., Weiss [237], Imai [112], Kessler [124], Zhang and Steven [270], Minkin *et al.* [157]). In general, Zhang and Steven [270] mention that capital investments in a PBC installation are almost two times higher than in the case of a conventional conveyor type. Imai [112] reported a 1.5 times increase of the costs for PBC, compared to a trough conveyor installation without rain cover, considering 100 m length and the same capacity of 1000 ton/hour for

both conveyors. However, Imai [112] and Lodewijks [139] mention that PBCs with longer conveying length or smaller tonnage are more cost competitive. In addition, the usage of triangular gantry, as discussed by Staples [217], also may decrease the installation cost of PBC.

High capital costs relate to the principal design of pipe conveyors, as it requires twice the number of idler rolls and more metal consumptive supportive structures. Moreover, the construction stipulates the usage of specialized components for belt turnover and transition zones, where the belt forms the required shape in the loading and the discharging phase, as well as belt's tracking and alignment systems that serve to prevent undesirable belt twisting. That is why, in general the overall capital investments are higher compared to conventional systems.

Increased energy consumption

Besides these factors, the high capital costs also relate to the fact that PBCs consume more energy than the conventional open-trough conveyors (Kessler [124], Imai [112], Zhang [269], Zhang and Steven [270], [139], Minkin *et al.* [157]). Lodewijks [139] states that energy consumption of PBCs 20% is more power per ton of the transported material compared to the traditional open-trough prototype. Energy losses appear primarily from the indentation rolling resistance (IRR) forces, which affect the tension of the overall conveyor system. The tension determines the selection of some of the conveyor components, such as motor drive power, belt strength, take-up system, idler rolls, their life/load rating bearings, etc.

The IRR constitutes the major part of the overall rolling resistance forces (see Hager and Hintz [92]). The IRR of pipe conveyors is higher than the IRR of trough belt conveyors (Zhang and Steven [270], Zhang [269]). In case of the latter, it may already form up to 61% of the overall rolling resistances [92] for horizontal systems. IRR depends on the number of physical characteristics, such as belt bending stiffness, rheological properties of the rubber, and contact forces (CFs). For pipe conveyors, the energy losses due to the indentation resistance are not well quantified.

Twisting effect

A pipe conveyor belt may twist along its conveyor length (see e.g., Zhang and Steven [270], Bahke [8], Staples and Metha [218], Day [41], Minkin *et al.* [157], Lodewijks [141], Imai [112]). When the belt rotates around its longitudinal axis, the belt overlap moves towards the bottom of the pipe. The angle of twist can be substantial, e.g., 270° during the conveyor tracking stage before commissioning (see Day [41]). Belt twisting affects the conveyor operation, as it can cause the collapse of the belt's pipe shape and spillage of the bulk material.

Most of the time, the belt twists when the conveyor route curves, but there are other factors, which can induce this undesirable effect (see Imai [112], [145]). These factors are known from practical experience, yet the actual reason of the physical phenomenon is still not well explained. This might be a reason that the practical solutions existed for conveyor belt alignment are not always effective making that process quite complex and time consuming.

Design limitations due to bulk material and belt

PBCs have special design limitations due to the bulk material transported (Lodewijks [139], Kessler [124], Vaka [230], Horak [105]). Pipe conveyors need to be designed, considering the maximum lump size of the bulk, which should generally be less than 1/3 of the pipe diameter. The maximum filling degree of the cross section is usually up till 75%. Pipe conveyors are not suitable for transporting hot bulk materials, as it does not effectively transmit heat from the inside of belt pipe out to the environment [124].

In general, PBCs can be constructed using standard trough belt conveyor components, like pulleys, power stations, take-up systems, idlers, suitable for trough conveyors (Horak [105], CKIT [37]). Though, for the belt design and its bending stiffness, pipe conveyors have special requirements (see e.g., Imai [112], Lodewijks [139], [141], CKIT [37], Buchanan [25], Vaka [230], Minkin *et al.* [157], Zhang and Steven [270], Maton [149, 150], Fletcher and du Toit [79]).

Utilization of belts designed for the traditional open-trough conveyors is not effective for the pipe systems [149]. Most of the time, a belt with a specially modified structure is employed, which rises the capital costs of the belt. In addition, the filling degree limitation for PBCs leads to the usage of approximate 50% wider belt (Lodewijks [139], Kessler [124]) in order to achieve the same volumetric capacity, compared to the trough belt conveyor with the same belt speed and 30° idler roll installation angle.

For PBCs, the bending stiffness in the lateral direction of belt has to be carefully controlled, as it is responsible for the correct formation of the enclosed pipe shape with the overlap. Moreover, it is also involved in the IRR and even influences belt tendency to twist and buckle. However, despite the significant role of the belt bending stiffness, it was not well determined and not any recommendations were developed for the industry. This draws attention to the another important disadvantage of PBCs.

Lack of standards

In contrast to the well-standardized trough belt conveyors (see e.g., DIN 22101 [45], CEMA [35]), there are no standards which can assist in the pipe conveyor's design and belting and guarantee their reliable operation in the field. Most of the time, empirical practical experience is applied in combination with the standards developed for the conventional trough systems. The rather recent history of technological development (see Section 1.1) and confidential know-how of companies active in the business of pipe conveyors nowadays result in a variety of offered products and their properties. The absence of any official design regulations cannot guarantee that products with low or questionable quality do not appear in the market. A rather limited number of companies are considered reliable in their technological expertise and consequently more frequently preferred over the other manufactures, creating a tendency to preserve a high price of pipe conveyors and their components.

1.3 Problem statement and aim of research

The previous section explained that pipe conveyors have a number of design advantages and at certain cases can be regarded as the only solution for the construction, especially when, for instance, a difficult route geometry and environment protection are required at the same

time. However, Section 1.2.2 also showed that PBCs have a number of major drawbacks that can be crucial for their selection. That is why in order to improve performance of this type of transport system, research needs to be mostly focused on diminishing or eliminating their major disadvantages. Particularly, attention needs to be paid on decreasing energy losses, ensuring ability of a belt to form a stable pipe shape, and developing design recommendations for the system and belting.

Number of studies were carried out focusing on solving these problems. However, there are several aspects that make existent research studies require further expansion, improvement or even reconsideration. Some of the existent studies lacking experimental validation and only introduce analytical and Finite Element Model (FEM) for the solution. Examples of these kind can be considered research of Wesemeier [238–242], Kulagin [126–129], Sergeeva [208–210], Dmitriev and Sergeeva [57, 58], Gładysiewicz [91] and others on CFs and rolling resistance of pipe conveyors.

Moreover, some of the existent analytical models were obtained based on the certain assumptions and simplifications that can be considered reasonably irrelevant for pipe conveyors and need further improvement or reassessment. Particularly, correction is essential for the analytical methods, determining CFs and/or belt deformations from the belt weight, belt bending stiffness and bulk material, present in studies of Dmitriev and Efimov [55], Efimov [61], Sergeeva [210], Dmitriev and Sergeeva [58], Kulagin [126–129], Dmitriev and Kulagin [56], Bazhanov [12], Gładysiewicz [91], Wesemeier [238–242], Wiedenroth [247]. The IRR, quantified in studies of Sergeeva [208, 210], Dmitriev and Sergeeva [58], Bazhanov [12] also needs to be reconsidered. This happens not only because of the improper determination of CFs, but also due to employment of the Jonkers rheological model with two-dimensional indentation profile.

On other hand, some of the studies (Hötte [107], Hötte *et al.* [108], Wiedenroth [247], Michalik *et al.* [156] [48], Molnár *et al.* [159–166], Molnár and Fedorko [158], Stehlíková *et al.* [220], Xiaoxia *et al.* [252]) were constructed only based on the empirical experimentation. It is possible to expect that the choice of the test rig design can significantly affect results of the experiment. Moreover, the unavailability of test samples with all possible combination of physical parameters together with complex experiment performance significantly limits the study of a problem behavior. Without an analytical model, they can provide just an approximate trend for the impact of various physical parameters involved. Moreover, the choice of the test rig design and the way the experiment is performed might affect the test results and the conclusions derived.

Ultimately it is possible to state that all the existing studies focused on solving negative design aspects of a PBC exhibit a number of drawbacks and need further correction and investigation. Present study takes into account all the omissions and corrects the inappropriate assumptions, accepted in previous studies, and performs a PBC design analysis that can potentially improve conveyor system performance, aiming:

- 1) to ensure an enclosed geometry of a pipe conveyor cross section;
- 2) to reduce the IRR as a major source of a PBC energy losses.

1.4 Research questions

In order to achieved research goals assigned, the following sub-questions should be answered in the present analysis:

- What are the principal design characteristics of a PBC system and its components? What is the variation range of each design parameter and its average or more frequently used value?
- How to quantify the belt's bending stiffness? Is there any way to use a standard troughability test ISO 703 for this purpose? If so, is it possible to establish a functional dependence between the belt troughability, bending stiffness, and all the influencing design parameters? How each of the design parameter can influence the belt's bending stiffness? What are the limitations of using the models that can quantify belt bending stiffness from its troughability parameter?
- How to determine the pipe conveyor CFs?
- If the CFs are measured from the experimental testing, can the selection of a test rig design influence the CFs? What test rig configuration is suitable for the present analysis, aiming to determine PBC CFs and why? Do the experimental results obtained correlate with the ones available in the existing studies?
- Aiming to determine the CFs, is it possible to represent a belt stress state that appears from folding a belt from a flat shape into a pipe shape as an additional external load, applied at the stress free belt already in a pipe shape? How to model a bulk material load for the CFs?
- Which design parameters of a PBC system influence the CFs and what is their effect? Is it possible to derive a functional dependence between the CFs and participating PBC design parameters? What is the weakest position of rolls in an idler set that can exhibit a contact loss? What is the preference for a PBC design selection aiming to avoid a contact loss and ensure sufficient belt's pipe-ability?
- How to determine the energy losses of a PBC system from the IRR and how the CFs influence the IRR friction factor? Does a number of Maxwell parameters selected to approximate the viscoelastic properties of a belt rubber influence the IRR determined? How different the IRR of a PBC system compared to the IRR of a conventional trough belt conveyor? What is the preference for a PBC design selection, aiming to limit its energy losses from the IRR?
- What are the general conclusions can be drawn from the analysis that can potentially assist for the development of an effective design of a PBC, satisfying the aim of the study?

Present study introduces a new synthesis of the analytical and (semi-) numerical models on the specified problems with the experimental validation on CFs. The CFs indicate the belt's ability to form a stable pipe shape whiteout a contact loss and also participate in the IRR. The IRR is selected for the study since it is regarded as a major source of the energy losses of PBCs. The analytical models were recognized, adapted, newly developed and employed in present study, in order to solve assigned research goals.

1.5 Outline of the thesis

The answers of the sub-questions indicated in previous section are provided in the following chapters of the thesis. Their content is organized as follows:

- **Chapter 2** presents the principal construction of a PBC system, its design characteristics and the properties of a conveyor belting. The chapter establishes the range of each design parameter variation, indicating their critical and average values.
- **Chapter 3** describes the models that can quantify the bending stiffness of the belt and its effective modulus of elasticity using the troughability test standard ISO 703. The chapter presents the review of the standard and identifies which belt's physical parameters influences its behavior in bending.
The characteristics of the PBC system and belting described in the Chapter 2 and Chapter 3 are required for determining the pipe conveyor CFs, performed in Chapters 4-6, and the IRR, reflected in Chapter 7.
- **Chapter 4** defines the role of the CFs in a structural behavior of a PBC. The chapter discusses approaches selected to determine PBC CFs and utilizes the experimental one to measure the CFs and belt deformations. It also provides an overview of the existing test rigs and gives an analysis how the test rig design influences the resultant CFs measured. The chapter selects the most appropriate test rig configuration suitable for the experimental validation of the analytical model, elaborated in Chapter 5.
- **Chapter 5** develops a new analytical model that can determine the CFs for a straight section of an empty and a loaded PBC. The analytical model investigates which loads participate in the problem and whether it is possible to use an additional expansion load from belt bending stiffness to represent the belt's behavior after its folding from a flat shape into a pipe shape. In addition, the model incorporates the impact of a bulk material load on CFs.
- **Chapter 6** presents a numerical approach to determine PBC CFs and compares the results with the experimental and analytical approaches. The chapter provides an impact analysis for the conveyor design and belting that affects the CFs. It derives the parametrized functional dependence between the CFs and participating design parameters, detects the weakest position of a CF in an idler station that can exhibit a contact loss. In addition, the pipe conveyor CFs, obtained in Chapters 4-6, determine the concentrated loads on the idler rolls that cause the IRR, studied in Chapter 7.
- **Chapter 7** presents an analytical model that determines the energy losses of a PBC due to the IRR. For the results, the rheological properties of a belt cover rubber are determined experimentally using a Dynamic Mechanical Analysis (DMA) test. The chapter analyses how the participating design parameters influence the IRR and whether the methods and models for determining the IRR used for trough belt conveyors are suitable for PBCs. It also compares the energy losses from PBC with trough belt conveyors.
- **Chapter 8** gives conclusions, developed in the Chapters 4-7, that should assist in improving PBC design, fulfilling the aim of the study.

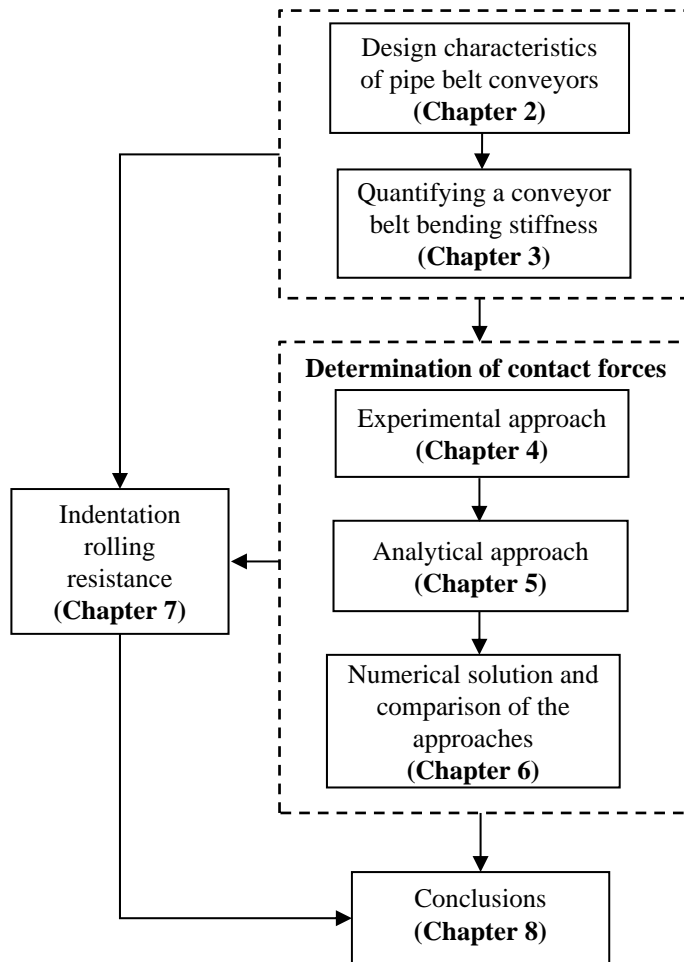
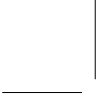


Figure 1.5: Outline of the Thesis



Chapter 2

Design Characteristics of Pipe Belt Conveyors*

"Every object is a demonstration form of infinite variety".

— Kozma Prutkov, literary pseudonym for A. K. Tolstoy and three A., V., and A. Zhemchuzhnikov brothers

This chapter discusses a principal design of a system and selection of constituent components. It provides an overview of the range of the major design characteristics of a PBC that was not made before. The range of parameters compiles all the properties and the characteristics needed for the analysis, performed in the following Chapters 3-7, as they are responsible for the load distribution between the idler rolls (i.e., for CFs), belt's pipe-ability, and also they influence on the IRR. In addition, the critical and average (or most frequently used) values of each design parameter are established.

2.1 Introduction

As stated in Chapter 1, there is no standard that can specify the design selection of a PBC system and its components. Most of the time, the decision regarding a PBC construction is made based on practical experience in combination with the standards and techniques developed specifically for conventional trough belt conveyors (e.g., DIN 22101 [45], 22102 [46, 47], ISO 15236 [170]). That is why some of the design parameters correspond to a conventional trough belt conveyor system and why some characteristics differ.

For improving a PBC performance, it is important to determine which design characteristics are responsible for the system behavior. The impact of an each design parameter must be investigated independently as well as in combination with other characteristics. Consequently, a variation range for each of the characteristics (minimum and maximum) must be established as well as its average and/or most frequent values in practice.

The major design characteristics of a PBC are inextricably linked to the principal construction of a system and its components, which is elucidated in the following section.

*This chapter is partially based on Zamiralova and Lodewijks [261], [265].

2.2 Principal construction

A principal construction of a PBC system is illustrated in Figure 2.1. It represents a naturally evolved modified design of the conventional open-trough belt conveyor. The flat belt forms an open trough, which is loaded with the bulk material. Then the belt is gradually folded into a pipe shape with the overlap on the top, enclosing the bulk material inside the pipe (see Figure 2.2). Six-roll hexagon idler stations support the belt in a pipe shape almost along the whole conveyor length. The idler stations can be designed with a single or double side idler rolls arrangement (see Figure 2.1 and also discussion in Section 2.6).

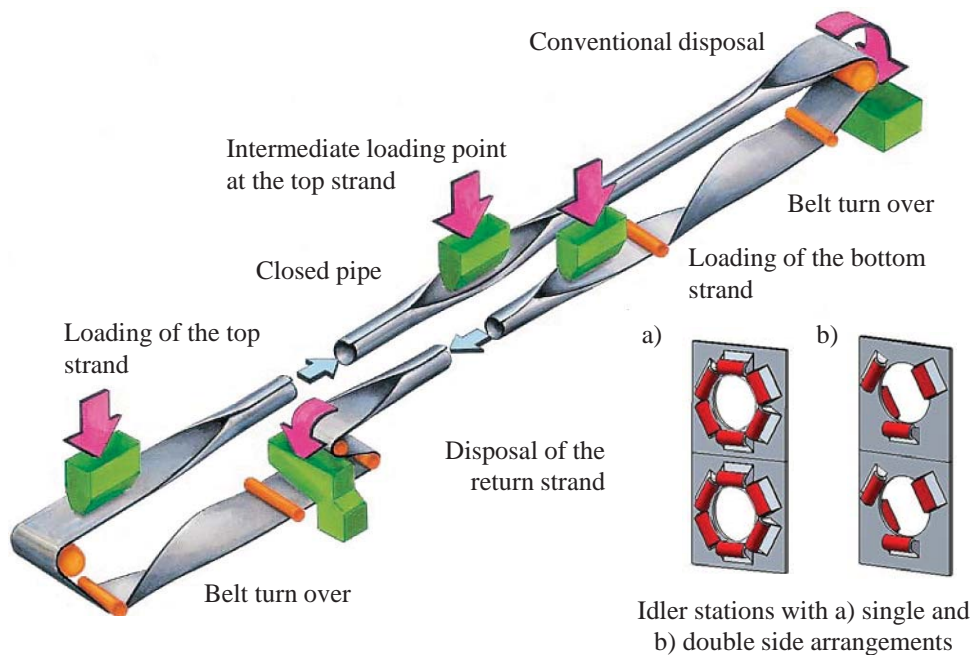


Figure 2.1: Principal construction of a PBC (Modified figure from [154])

Before the discharging phase, the belt opens back to its initial flat state. On the return strand, after passing the driven pulley, the belt can be turned over and folded into a pipe shape again with the dirty surface inside the pipe (see Figure 2.1). The return strand can also be used for transporting bulk material simultaneously with the top strand, making the design revertible. In addition, this conveyor construction allows arranging intermediate points of loading and discharging of bulk solids.

The principal construction of the system implies a number of various design characteristics, which can be classified as being related to the overall conveyor system, bulk material, belt design, idlers and support structures. This chapter is limited only to those characteristics that are decisive for the study reflected in this thesis.



Figure 2.2: Folding belt from flat shape into a pipe shape (Image courtesy of Specialty Welding & Fabricating of New York, Inc.)

2.3 Conveyor characteristics

2.3.1 Capacity

The belt capacity represents how many tons of bulk material can be conveyed by the system per hour. It is determined as follows [142]:

$$Q_c = 3.6 m'_{\text{bulk}} v = 3.6 \rho_{\text{bulk}} A_Q v, \quad (2.1)$$

where m'_{bulk} is the line mass of the bulk material transported per unit of longitudinal length, v is the belt speed, ρ_{bulk} is the density of the bulk solids, and A_Q is the cross-sectional area of the bulk material on the belt.

Theoretically, following the Eq. 2.1 and considering the maximal threshold for each of the characteristic involved established in the following sections, the maximum possible capacity can reach no more than approximately 56 000 tph (for $\rho_{\text{bulk}} = 3000 \text{ kg/m}^3$, $v = 8.4 \text{ m/s}$, belt width $B = 3200 \text{ mm}$, pipe diameter $D = 890 \text{ mm}$, and filling ratio $k_Q=1$). Taking into account the limiting recommendations for the belt speed and pipe diameter (for $D = 890 \text{ mm}$ [33]) and the fact that pipe conveyor mostly operates at 75% filling degree, it is more realistic, to expect the capacity threshold no more than 32 500 tph. In fact, the world record for the maximum capacity of a belt conveyor system in general belongs to 40 000 tph for the trough conveyor in bucket wheel excavator [26, 191].

$$Q_c = \underbrace{[0 \dots 32\,500 \dots 55\,000]}_{\text{existing extremes}} \text{ tph.} \quad (2.2)$$

2.3.2 Belt speed

Belt speed not only determines belt capacity but also determines the IRR of PBC. For open trough belt conveyors, the selection of belt speed is governed by the properties of bulk material; for fine, dusty materials with high flowability, the transportation speed is less than for raw, overburdened bulks. As for pipe conveyors, the bulk material is enclosed and slightly compressed with overlapping pipe-shaped belt, though the speed restrictions are the same as for the conventional trough conveyors due to the presence of open loading and discharging section in PBC construction. The practical experience demonstrates that the pipe diameter and conveyor capacity influence the maximum belt speed, for larger pipe diameters the maximal allowable belt speed is higher [31, 33]. For example, ContiTech® [32, 33] provides recommendations for their product specification, stating that, for instance, the belt speed for PBC with pipe diameter $D = 150$ mm should not exceed 2.3 m/s and for diameter 890 mm $v \leq 6.6$ m/s.

In general, the belt speed is in the range from 0.42 m/s to 8.4 m/s [3, 142] and has a standardized values row for the drive unit selection. According to Ramjee and Staples [194], the maximum belt speed of existing pipe conveyor constitutes 4.19 m/s, and the speed range practical for industry does not exceed approximately 6 m/s.

The results on IRR in Chapter 7, are obtained by varying the belt speed from 0 m/s to 10 m/s, giving space for advent technological solutions. Attention is paid to the more realistic range from 0.42 to 6.6 m/s, where the maximum threshold of 6.6 m/s is selected for a pipe diameter of 890 mm, according to the product recommendations [33]. In this case:

$$v = \overbrace{(0 \dots 0.42 \dots 6.6 \dots 10)}^{\text{selected/practical extremes}} \text{ m/s.} \quad (2.3)$$

existing extremes

2.3.3 Filling degree

In order to determine a cross-sectional area of the bulk material in the belt for conveyor capacity, generally, it is assumed that the belt forms a pipe shape with a contour profile close to a circle, as shown in Figure 2.3. Such an assumption is made in a number of research studies, mostly on determination of CFs [55, 58, 61, 62, 210, 256, 258, 266] and widely utilized in practice.

In this case, the area of the bulk solids A_Q can be expressed via filling degree k_Q of the cross section and radius of the pipe R :

$$A_Q = k_Q \pi R^2. \quad (2.4)$$

The parameter k_Q characterizes the filling level with respect to angle θ , according to the following dependence law:

$$\pi k_Q = \pi - 2\theta + \frac{1}{2} \sin 4\theta + \tan \lambda \sin^2 2\theta, \quad (2.5)$$

where λ is the dynamic angle of repose of the bulk material. Table 2.1 shows how the Eq.(2.5) is derived for various angles θ .

The expression (2.5) was initially presented by Gushin [89] for deep trough belt conveyors and later applied to pipe conveyors by Galkin *et al.* [80]. The graphical illustration of the

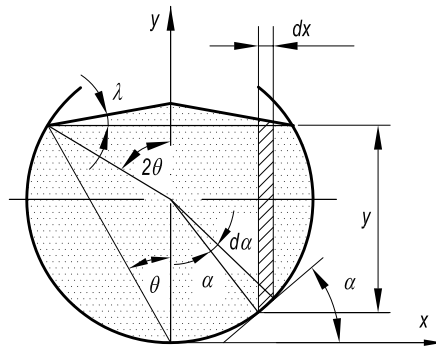


Figure 2.3: Simplified cross section of PBC (Modified figure from Gushin [89]).

dependence between filling degree k_Q and angle θ is provided in Figure 2.4 for the wood chips, coal, and iron ore selected for an example.

It is noteworthy to mention that the geometry of a pipe conveyor belt is the result of the highly nonlinear process of folding the belt from a flat shape into a pipe shape (see Figure 2.2). In fact, the assumption that the pipe cross-sectional contour is close to a circle does not take into account the impact of the belt overlap and also ignores the nonlinear structural deformations of a belt under action of all the distributed loads involved. In practice, the expression in Eq. (2.5) for the filling ratio k_Q , and angle θ requires modification.

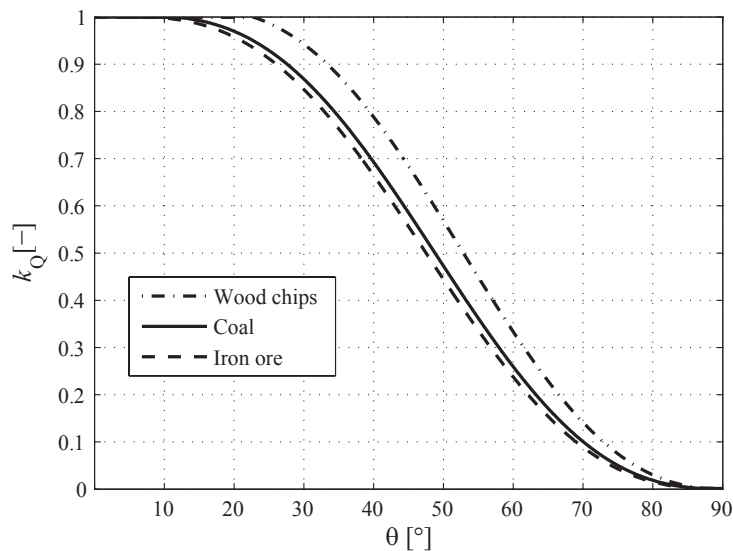
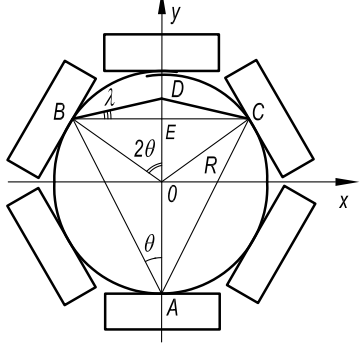
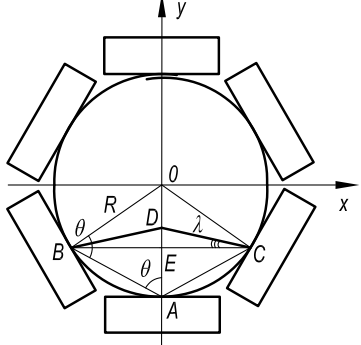


Figure 2.4: Filling degree of the cross section k_Q versus angle θ , obtained for wood chips (assuming $\lambda = 30^\circ$), coal ($\lambda = 15^\circ$) and iron ore ($\lambda = 10^\circ$), selected as an example.

Based on practical experience, the load ratio of the cross section of a PBC constitutes

Table 2.1: The derivation of Eq.(2.5) for the dependence of the filling degree k_Q and angle θ .

 <p style="text-align: center;">$0 \leq 2\theta \leq \frac{\pi}{2}$</p>	$\tan \lambda = \frac{DE}{R \sin 2\theta} \Rightarrow DE = R \sin 2\theta \tan \lambda;$ $A_{\widehat{CABO}} = R^2(\pi - 2\theta);$ $A_{\triangle BOC} = \frac{1}{2}R^2 \sin 4\theta;$ $A_{\triangle BDC} = R^2 \sin^2 2\theta \tan \lambda;$ $A_Q = A_{\widehat{CABO}} + A_{\triangle BOC} + A_{\triangle BDC} = k_Q \pi R^2;$ $\pi k_Q = \pi - 2\theta + \frac{1}{2} \sin 4\theta + \tan \lambda \sin^2 2\theta.$
 <p style="text-align: center;">$\frac{\pi}{2} \leq 2\theta \leq \pi$</p>	$BC = 2R \sin(\pi - 2\theta) = 2R \sin 2\theta;$ $DE = \frac{1}{2}R^2 BC \tan \lambda = R \sin 2\theta \tan \lambda;$ $A_{\widehat{CABO}} = R^2(\pi - 2\theta);$ $A_{\triangle BOC} = \frac{1}{2}R^2 \sin 2(\pi - 2\theta) = -\frac{1}{2}R^2 \sin 4\theta;$ $A_{\triangle BDC} = R^2 \sin^2 2\theta \tan \lambda;$ $A_Q = A_{\widehat{CABO}} - A_{\triangle BOC} + A_{\triangle BDC} = k_Q \pi R^2;$ $\pi k_Q = \pi - 2\theta + \frac{1}{2} \sin 4\theta + \tan \lambda \sin^2 2\theta.$

around 50%-60% [139] or even up to 75% [230], which corresponds to a filling degree of a conveyor $k_Q \approx 0..0.75$. A larger filling ratio is possible, though, if the loading of a belt conveyor is uneven, or the lump size of a bulk varies significantly, the large filling degree can cause the bulk material losses in the charging section of a conveyor system (see overloading of a pipe conveyor in Figure 2.5). For the study, the results are obtained for the empty pipe conveyor and also for $\frac{1}{4}$, $\frac{1}{2}$, and $\frac{3}{4}$ of the cross section, which correspond to $k_Q = 0.25, 0.5$ and also 0.75.

The conveyor capacity depends on the bulk material characteristics (bulk density, dynamic angle of repose). Moreover, the lump size of bulk identifies the requirement for a minimum pipe diameter selection. All these parameters can be classified as characteristics related to the bulk material properties.



Figure 2.5: Overloaded pipe conveyor in Kailin, Guizhou Province, China (Image courtesy Dr. Robin Steven).

2.4 Bulk material characteristics

Bulk materials exhibit different properties and characteristics, which are used as a basis for their classification (e.g., consult with DIN-ISO 3435 [51], CEMA 550 [36], FEM 2581 [69], FEM 2582 [70]). The present research is limited only to those parameters that are decisive for the study.

2.4.1 Bulk density

Bulk density ρ_{bulk} represents the weight of material per unit volume of bulk. In order to establish a variation range of bulk density, the present study focuses on $\rho_{\text{bulk}} \approx 200 \text{ kg/m}^3$ for the minimum, which is inherent to the wood chips bulk material with size 0-20 mm. This density is obtained from physical tests carried out by Wu [251]. This bulk material is selected for the lightest representative material because the biomass is becoming increasingly popular in the bulk handling industry nowadays, and pipe conveyors can be used for biomass transportation (e.g., see [231]). For the heavy bulk material representation, iron ore is selected with a bulk density of $\rho_{\text{bulk}} \approx 2500 \dots 3000 \text{ kg/m}^3$ [3]. As for the average, the coal with a bulk density of $\rho_{\text{bulk}} \approx 850 \text{ kg/m}^3$ [34, 190] is selected as the current most popular and frequently transported material in industry.

$$\rho_{\text{bulk}} = [200; 850; 2500 \dots 3000] \text{ kg/m}^3. \quad (2.6)$$

2.4.2 Angle of repose

The angle of repose is determined as an angle from the horizontal plane to a free surface of a piled bulk material subjected to critical stresses (see Schulze[205], Yokoyama [254]).

In Figure 2.3, the angle λ is a dynamic angle of repose or also named angle of surcharge of the transported bulk material. It is less than the static angle of repose λ_0 due to the action

of the dynamic loads and vibrations during transportation. The dynamic angle of repose can be determined from the static angle of repose.

Colijn [30] suggests the empirical dependence between the angle of surcharge λ and the static angle of repose λ_0 . The dependence has been obtained based on the field measurements and is governed by the troughing angle of the idlers installation β_{idl} . It equals:

$$\lambda \approx 1.1\lambda_0 - (0.1\beta_{idl} + 18^\circ). \quad (2.7)$$

Aleksandrov [1], Galkin *et al.* [80], and Gushin [88, 89] state that the dynamic angle of repose constitutes approximately 35% of the static angle of repose:

$$\lambda \approx 0.35\lambda_0. \quad (2.8)$$

CEMA [35] recommends determining an angle of surcharge as 5 to 15 degrees less than the static angle of repose:

$$\lambda \approx \lambda_0 - (5 \div 15)^\circ. \quad (2.9)$$

The value of the angle of repose is determined experimentally. Though, the selection of the experimental method influences the angle of repose measured. This makes the angle of repose to be not intrinsic property of a bulk.

For the bulk materials selected in the present study, the dynamic angles of repose are determined according to CEMA recommendations for Eq. 2.9 from the experimental data on the static angle of repose. They constitute the following values: for wood chips $\lambda = 30^\circ$ based on the experimental results of Wu [251], for coal $\lambda = 15^\circ$, and for iron ore $\lambda = 10^\circ$ based on data [3, 34, 59, 190].

2.4.3 Effective angle of internal friction

The effective angle of internal friction φ_e identifies friction that appears when bulk material slips on its own surface. This angle represents the ratio between the minor principal stress and the major principal stress in the steady-state flow [153, 205]. The effective angle of internal friction is required in the present study in order to characterize loads on a belt when the bulk material is in its active and passive stress states, while the conveyor is in motion. This bulk stress phenomenon and its impact on pipe conveyor CFs and belt deformations is revealed in Chapters 5-6.

The effective angle of internal friction is determined experimentally for particular bulk solids using Jenike shear tester.

Regarding the bulk materials selected for the study, the effective angle of internal friction of wood chips biomass (0-20 mm) is assumed to be $\varphi_e = 53^\circ$, following the experimental results obtained by Wu [251]. In the case of coal, the angle $\varphi_e = 46^\circ$ is taken from the experimental results of Moore [167] for air dried coal with a particle size of 4 mm. As for the iron ore, the internal friction angle is selected at $\varphi_e = 40^\circ$ based on the data from Look [147].

2.5 Belt characteristics

Belt characteristics are very important parameters for this research, as they are responsible for all three aspects the present study is aiming to address. Particularly, they are involved

in the load distribution between the idler rolls and, as a result, in the belt's ability to form a stable pipe shape without contact loss with idler rolls (pipe-ability) and IRR as well as and in the twisting phenomenon. The belt characteristics are inextricably linked to the belt layout design and the constituent materials selected.

2.5.1 Materials and design

Carcass

In general, a pipe conveyor belt design implies a reinforcing carcass embedded via vulcanization in covering the top, bottom, and edge layers of rubber. The carcass serves to provide certain important properties of the belt that are required for normal operation. These crucial parameters include tensile strength that identifies the belt's ability to resist tension loads

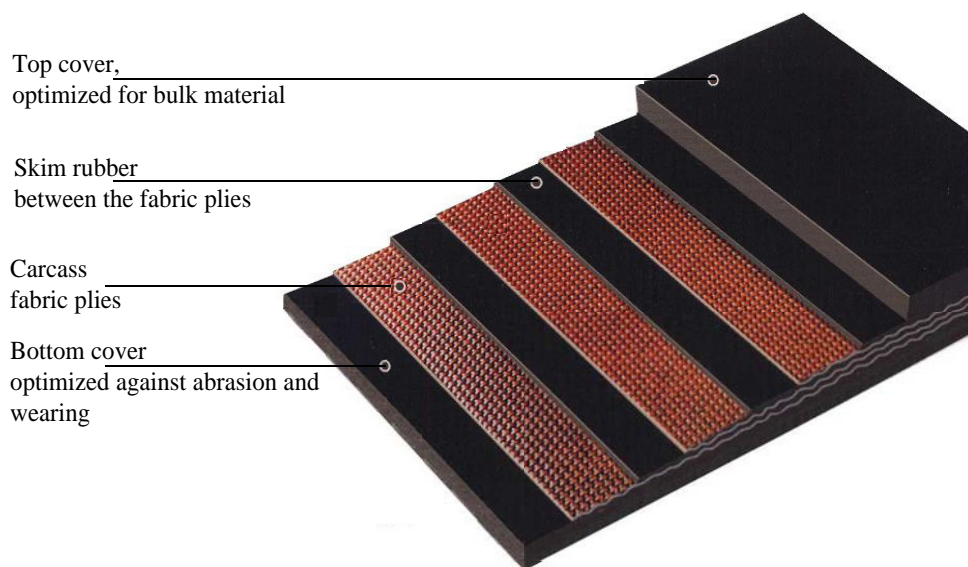


Figure 2.6: Typical structural design of multi-ply fabric conveyor belt

multi-ply. The fabric yarns in the warp direction must provide sufficient longitudinal tensile strength; whereas in the weft direction, they must provide the necessary lateral bending stiffness. Lodewijks [137] described three types of fabric carcass, classifying them based on the weave pattern as cord fabric, straight wrap, and solid woven fabric.

For long and heavy duty conveyors, it is more common to use steel cord belts, as they exhibit small elongation and are more suitable when higher tensile strength is required (starting from 1000 N/mm [3, 170]). Although for additional reinforcement and bending

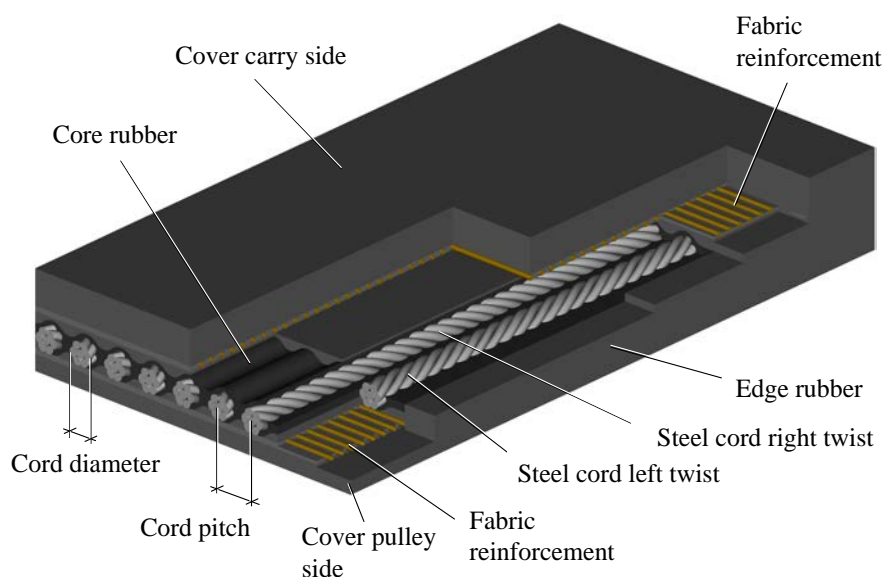


Figure 2.7: Example of a structural design of a steel cord belt with fabric reinforcement (Image courtesy of ContiTech Conveyor Belt Group, Continental AG).

stiffness, the steel cord belts can be designed in combination with extra fabric layers (see Figure 2.7).

The selection of a conveyor belt design is governed by the preference towards lower belt weight and consequently a smaller thickness when sufficient tensile and bending stiffness are provided. This principle ensures less load distribution on the idler rolls and consequently lower energy consumption of a PBC system that leads to a decrease of the capital costs of a belt and overall system components.

With recent technological development, the aramid-based carcasses are becoming more suitable for this case. The Twaron® fibre material of Teijin Aramid [143, 144, 223, 224] can be considered an example of this kind. In general, aramid material comprises the aromatic polyamide chains. It exhibits a higher tensile strength and flexibility [143], and, according to Arts [5], it is also five times lighter than steel. Moreover, the belts with an aramid-based carcass are thinner than the ST belts, as aramid cords/yarns are thinner and are embedded closer to each other than the steel cords. It is noteworthy to mention that, besides the few case studies (e.g., see Arts [5] and also mentioned in [224]), there has not been an ultimate scientific comparison specifically for PBC performance, when an EP or ST belt is replaced with a thinner, lighter and/or stiffer belt prototype with an aramid carcass.

Belt layout

Normally, for the conventional trough belt conveyors, the carcass structure is uniform along the belt width and is embedded in the rubber at a small distance from the belt rubber edges. This standard design of trough conveyor belts is not usually used for PBC systems [149].

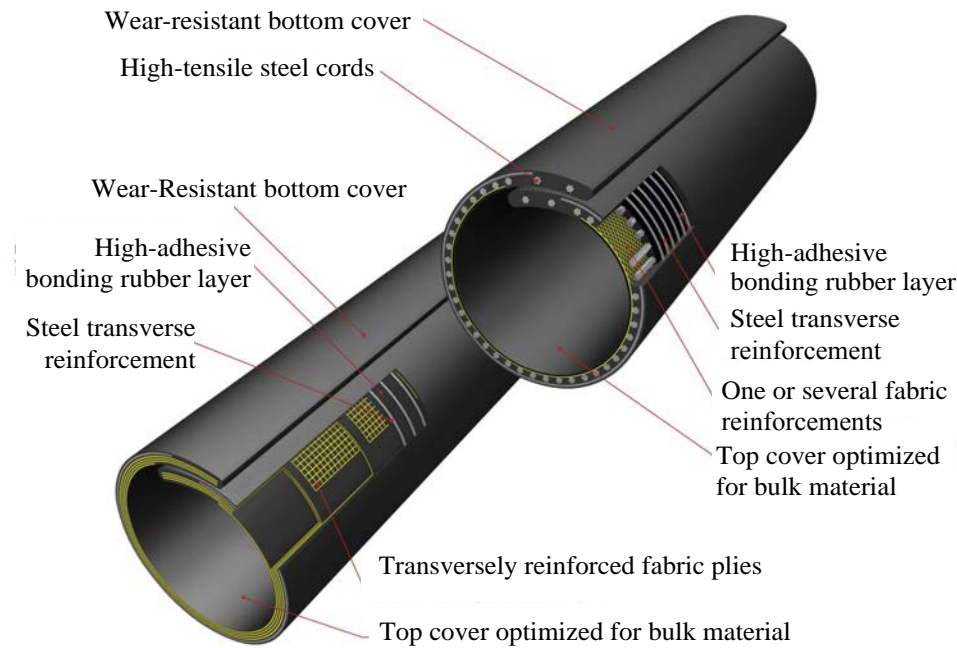


Figure 2.8: Design examples of a pipe conveyor steel cord and fabric belt. (Image courtesy of ContiTech Conveyor Belt Group, Continental AG).

The carcass of pipe conveyor belts is not uniformly designed along the width. For better maintenance of a pipe shape, the layout stipulates discrete change in the reinforcing material, arrangement of fabric layers and/or more/less frequent cord embodiment in the central part of the belt width compared to the periphery (see Figure 2.8). Discrete changes in structure imply corresponding change in the bending stiffness and line mass of the belt along the belt width, in order to provide the correct pipe shape formation.

In order to achieve a successful pipe shape formation, various patents have been developed specifically on pipe conveyor belt construction, e.g. [65, 101, 130, 193, 221, 222]. Some of the design examples are provided in Figure 2.9. In general, the belt layout is developed based on the principle of the discrete variation of belt properties along the width (*i.a.* lateral rigidity, elongation and line mass) by applying this either independently or in combination the following techniques:

1. Division of belt width into two or more zones with respect to the central mid-span. Lodewijks [139], Fletcher and du Toit [79] stated that the stable pipe shape and well-sealed overlap require that the belt zone close to the edges must be less stiff than the zone in the central part. This can be achieved with more frequent embodiment of cords or stiffer reinforcements in the belt's central zone (see Figures 2.9a, b for examples of this kind). In order to keep the overlap steadily enclosed, some of the belt designs at the edges acquire additional sub-zones with higher stiffness and also increased line mass, as illustrated in Figure 2.9e-g, m. In contrast, some of the designs imply higher bending stiffness only at the lateral idler rolls (see Figure 2.9k and l).

The alternative approach to design a pipe conveyor belt is introduced in a recent patent

[193]. It is in contrast to previously described belt constructions, suggesting that the central part of the belt as well as the parts where the belt must touch the lateral bottom idler rolls should be produced with lower bending stiffness (Figure 2.9i). Simultaneously, between the more flexible zones, the carcass exhibits excessive stiffness using more frequent embodiment of cords. This construction should ensure that the belt better conforms to the idler rolls and has a self-centering effect.

2. Asymmetry of the belt carcass due to the overlap. The examples of such designs are illustrated in Figure 2.9c, d, h, and j. Most of the time, the belt edge towards the inward coil is less flexible than the external overlapping edge. The difference in bending stiffness at the edges is realized due to the special position arrangement of the reinforcing layers not only along the belt width but also along the thickness. For example, by extending fabric layers in the corresponding belt edges and placing the reinforcement further or closer to the carrying side of the belt, shown in Figure 2.9j, allows the attainment of a higher bending rigidity for the right edge of the belt for the inward coil than for the left edge for the external coil overlap.

3. Utilisation of different materials for the zones with different bending stiffness. Some of the belt designs suggest using different reinforcing materials along the belt width, as in [10, 222] (see Figure 2.9k) or even different rubbers, as proposed by Sumino and Fujita [222] (Figure 2.9l). As an example of such a technique, Barburski[10] proposed a pipe conveyor belt design where the belt zones comprise the same fabric reinforcing yarns but with different weave patterns. It is noteworthy to emphasize that use of different materials along the belt width can cause differences in the tensile elongation of corresponding belt zones, which can generate an uneven tension distribution along the contour of the pipe. This might be a reason for the undesirable twisting effect, when the belt rotates along its longitudinal axis, as proposed by Efimov [61] and Dmitriev and Efimov [55] or in contrast, the self-centering effect, as claimed by Raaz in patent [193].

As observed, the recommendations on the effective design of a pipe conveyor belt have different and to a certain extent even contradicting requirements (e.g., the condition of increased bending stiffness in the central part of a belt, as in [65, 79, 91, 130, 139, 221], which is in contrast to the suggestions of [193, 222]). Moreover, until now, no scientific research has been carried out that can actually determine, which parts of a belt need additional stiffness as they undergo higher deformations and cause contact loss with the idler roll and which parts of belt must be more flexible in order to form a pipe shape and overlap effectively. In this case, it is important to analyze the pipe-ability of a conveyor belt with uniform belt structure and, based on these results, to develop recommendations for a more efficient design with a non-uniform structure. Based on this approach, the analysis of a pipe conveyor belt with uniform belt structure is performed in Chapters 5-6 of this study.

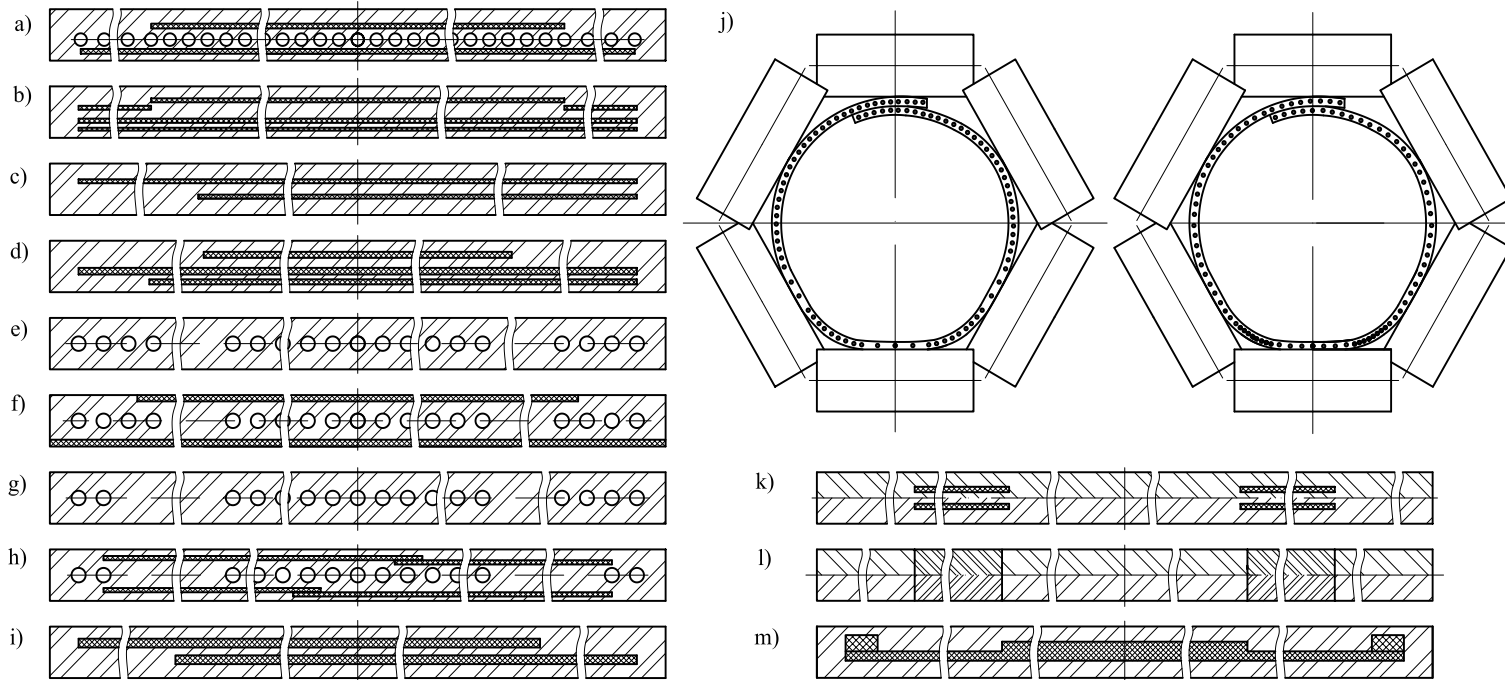


Figure 2.9: Examples of pipe conveyor belt designs. Modified from: a - Lodewijks [139, 142], Hinkelman et al. [101]; b - Lodewijks [139, 142], CKIT [37]; c, d - Kusel et al. [130]; e-g - Steven et al. [221]; h - Enshu [65]; i - Raaz [193]; j - Gładysiewicz [91]; k-m - Sumino and Fujita [222].

Belt covers

The thickness of the top and bottom covers are assigned individually. Most of the time, the top cover is thicker than the bottom one. Normally, cover rubber consists of approximately 40% styrene-butadiene-rubber (SBR) and 60% natural rubber (NR) [143]. However, the selection of constituent rubber materials can vary and depends on the operation mode and bulk handling requirements.

The selection of carrying side top cover is mostly governed by bulk handling consideration, which takes into account properties of the transporting material, its impact on the belt, abrasion and type (e.g. food, oil and grease, chemical or contaminated bulk products). Operational conditions encompass cold, heat, antistatic and fire resistance cover requirements [21, 190]. The last two are very important for underground coal mining. The mentioned recommendations categorize conveyor belt covers according to various standards (e.g. ISO 10247 [113], DIN 22102-1 [46], DIN 22100-1 [44], NEN-EN-ISO 15236 [170], etc.) by marking special code-letter in the belt nomenclature. The summarized information about cover requirements and belt marking can be found in source [190] (see Tables 2.2 and 2.3), whereas explicit descriptions for the flame-resistant and antistatic requirements are available in the publication of Brouwers [21]. Selected depths of belt covers are always assigned from a feasible range, compared to the carcass thickness.

Table 2.2: Type categories of the covers for conveyor belts [190].

Cover type letter as per		Minimum tensile strength, N/mm ²	Minimum elongation at break, %	Maximum abrasion mm ³
DIN 22131	ISO 10247			
W	(D)	18 (18)	400 (400)	90 (100)
X	(H)	25(24)	450 (450)	90(100)
Y		20	400	150
Z	(L)	15 (15)	350 (350)	250 (200)
K		20	400	200

For special cases, when the belt must operate at dramatically steep inclinations (30°~50°), as claimed in [64], the belt carrying side can be designed with rib profiles on the top cover surface in order to increase the adherence between the belt and bulk material and avoid downhill slipping of the bulk.

The selection of the bottom cover and materials is governed by the principle of minimizing the rolling resistance of the belt. The conveyor belt manufacturers apply low rolling resistance (LRR) technology, as discussed by Zhang [269]. The technology aims to select the combination of constituent cover rubber compounds that result in the reduction of rubber hysteresis and energy loss. For instance, Lodewijks and Pang [144] and Lodewijks [143] draw attention to a special aramid product from the Teijin company named Sulfron® [223, 224] that is added to the belt rubber. The researchers [143, 144] found that, on conventional trough belt conveyors, the application of the aramid carcass that reduces the belt weight in combination with the LRR rubber with Sulfron® aramid additive can substantially

Table 2.3: Categories of the covers for conveyor belts for special properties [190].

Special properties	Code letter
With antistatic covers	E
With antistatic covers and flame-resistant with covers	K
Flame resistant with and without covers and with antistatic covers	S
Heat resistant	T
Cold resistant	R
Oil and grease resistant	G
For foodstuffs	A
For chemical products	C
Safety specifications with regard to fire-engineering properties for surface use	vt
Safety specifications with regard to fire engineering, hygiene and electrical properties for underground use in German coal mining	V

diminish energy losses of a conveyor belt system.

However for PBCs, there is a lack of research that can quantify the energy consumption of a pipe conveyor system and that has investigated the influence of both technologies (LRR and aramid carcass selection) in combination. There are only case studies available on the use of technological solutions, either LRR products in constituent cover rubber (Zhang [269]) or application of an aramid carcass instead of an ST belt (Arts [5]) with respect to standard pipe conveyor belts. Moreover, the mentioned researchers reported results in terms of energy consumption or demanded torque from the drive control measured for particular installations and did not provide any dependence law between the friction factor and the input belt characteristics.

2.5.2 Belt geometry

Selection of constituent belt materials and the layout design influences belt geometry and its weight. Belt geometry is inextricably linked to the belt weight and have a significant impact on the belt's behavior. It identifies the mechanical response of the belt structure to all loads involved in the problem.

In present study, belt geometry implies the overall belt width B , belt's thickness h , and their ratio B/h that is also named as slenderness of the structure. Even though this ratio is not considered in practice as a design parameter for belt conveyors, the research study in the following chapters shows that the slenderness ratio B/h is an independent parameter that describes transverse structural behavior and is needed in order to represent a dimensionless dependence for belt's bending stiffness (Chapter 3), CFs (Chapters 5-6), and IRR (Chapter 7) with respect to other PBC input parameters.

In general, the variation range for B/h is difficult to establish even for the trough conveyor belts since the choice of the thickness and consequently the line mass are governed by many

design factors, as indicated in Section 2.5.1. Moreover, as stated in Chapter 1, the pipe conveyor belt manufacturers lack standards developed specifically for PBCs. Most of the time, they apply norms developed for conventional trough conveyors in combination with practical experience, as PBC represents a naturally evolved design of the trough belt conveyor.

That is why in order to define critical limitations for belt geometry inherent to pipe conveyor belts, it is important to analyze norms, standards, and recommendations assigned for the conventional trough conveyor belts for belt geometry and line mass and to systematize the available data from catalogs and product specifications available for both pipe and trough conveyor belts from various companies.

According to information in different standards DIN 22121 [48], DIN 22129 [49], NEN-EN-ISO 15236 [170], GOST 2085 [84], and other sources, e.g., [3, 29, 34, 59, 190], the minimum standard belt width of conventional open-trough conveyor belt equals 300 mm, whereas for the PBCs its value is assumed equal to 500 mm [154]. As for the maximum width for both types of conveyor belts, it constitutes 3200 mm [33, 182]. Taking into account the allowable production tolerance of ± 15 mm, specified in NEN-EN-ISO 15236 [170] for $B = 3200$ mm, the possible maximum belt width can reach 3215 mm value.

Regarding to the minimum critical value for the overall belt thickness, there is no any data available for pipe conveyor belts. That is why the minimum possible thickness for the trough conveyor belt equivalent to 5 mm (e.g. belt EP 200/2 2/1 [59]) is accepted. The maximum possible conveyor belt thickness of 45 mm was reported in [26, 191] for the trough conveyor world record. For pipe conveyors, Neumann and Minkin [182] describe a belt (Conti® MegaPipe 3000 ST 7400 11F/11SS DIN-X) with overall thickness of 35 mm, which becomes the maximal value from data available in catalogs and product specifications. It is noteworthy to mention though that this value might be not the greatest possible in existing PBCs operating installations.

Ultimately, for extreme values of B/h , attention needs to be paid to very wide and thin that constitutes the maximal value of B/h , and also very narrow and thick conveyor belts that yields the minimal value for B/h . Taking into account the extremes established for width and thickness, the ratios for the minimum $B/h = 300/45 = 6.67$ for trough conveyor belts, and $B/h = 500/35 = 14.29$ for pipe conveyor belts. As for the maximum threshold, the geometrical slenderness of belt structure becomes $B/h = 3215/5 = 643$.

However, realistically, conveyor belts with these combinations of belt width to thickness B/h do not exist. Approximate existing extremes are selected for the minimum - $B/h \approx 30$ (e.g., belt 800 ST 2500 10/2 according to standard NEN-EN-ISO 15236 [170] and product specification [190]) and for the maximum - $B/h \approx 300$ (selected belt 3000 EP 630/3 5/2 for product, specified in [31]). These values are chosen based on the data for conventional trough conveyor belts, since there is no information was specified for PBCs.

The difference between the realistic and non-existent geometrical extremes for B/h , makes it apparent that belt thickness (and also line mass) are implicitly regulated according to the conveyor belt width. The regulation appears via belt's minimum breaking strength that ensures belt's ability safely to resist longitudinal tensile forces. Belt's minimum breaking strength defines the type (steel cord ST or fabric EP) and also thickness of belt's carcass, which affects the overall belt's thickness h . At the same time, there are recommendations given in standard NEN-EN-ISO 15236 [170] and also in [3, 29], that assign belt width with respect to belt's minimum breaking strength and carcass type. In general, the high breaking strength needed for installations with high capacity and high belt's tensions stipulates wide

and thick belt at the same time.

After minimum and maximum geometrical and line mass extremes inherent to conveyor belts are acknowledged, it is also important to obtain research results for belt with a normal or standard combination of parameter set. This is quite challenging problem not only due to the limited data for pipe conveyor belts, but also due to the fact that the information about most frequently appearing combination of m'_{belt} and B/h for pipe conveyor belts is rather ambiguous to establish.

For this purpose, the analysis of data inherent to trough conveyor belts was carried out following special procedure. According to the recommendations of NEN-EN-ISO 15236 [170], as well as [3, 29], for each belt rating category and for each carcass type (EP and ST), all possible values of belt widths were recognized. Based on available data in product specifications [59, 190], for every size-step in belt width allowable in a given strength category and carcass type, overall belt thickness and line mass were assigned for X and Y cover grades. Collected data for all possible combinations of parameter sets was averaged to a “normal” value of geometrical ratio and line mass (see Section 2.5.3 were determined. The belt slenderness approximately amounted $B/h \approx 86$. It is important to emphasize that this value has mostly qualitative significance for the problem, as it does not reflect the most popular parameters set for physical conveyor installations, but generally shows more frequent belt design, appearing in standard recommendations, given in NEN-EN-ISO 15236 [170] and tables [3, 29].

Therefore, in order to investigate how belt geometry influences belt’s pipe-ability and load distribution between the idler rolls, the research analysis has to be performed for average $B/h \approx 86$, the minimum and maximum existent $B/h \approx 30$ and 300, and giving space for advent technological development - $B/h \approx 14.28$ and 643. In addition, the minimum threshold is enlarged starting from $B/h \approx 6.67$ in order to make apparent the dependence curves for the results on bending stiffness and CFs, provided in Chapters 3-4. Schematically, the range can be expressed as follows:

$$B/h = \overbrace{[(6.67) 14.28 \dots 30 \dots 86 \dots 300 \dots 643]}^{\text{selected extremes}} \quad (2.10)$$

$$\underbrace{\hspace{10em}}_{\text{existing extremes}}$$

average

These values are realized by varying belt’s thickness for fixed values of belt width as follows: a) $B = 300$ mm only for $B/h \approx 6.67$; b) $B = 500$ mm for $6.67 < B/h \leq 86$; c) $B = 3215$ mm for $86 \leq B/h \leq 643$.

Alles *et al.* [3] provided rough empiric geometrical recommendations for conventional trough conveyor belts with a fabric carcass, indicating that adequate behavior and troughability are achievable for belts with a ratio $B/h \leq 125$. For pipe conveyors, there is no research determining how the slenderness of a pipe conveyor belt influences its pipe-ability and what the recommendations are for the successful design development with respect to other characteristics of a PBC system. The following Chapters 3-4 of this thesis are devoted to these questions.

2.5.3 Line mass

Belt weight depends on the belt geometry and is represented by the line mass of a belt per unit longitudinal length, denoted as m'_{belt} . For the uniform belt structure without molded edges, it can be evaluated based on the following formula:

$$m'_{\text{belt}} = B (\rho_{\text{rub}}(h_{\text{top}} + h_{\text{bot}}) + \rho_{\text{carc}}h_{\text{carc}}), \quad (2.11)$$

where ρ_{rub} ($\approx 1100 \text{ kg/m}^3$), h_{top} , h_{bot} are the density and the thicknesses of the top and bottom belt rubber covers, respectively, and ρ_{carc} , h_{carc} are the density and thickness of the carcass, respectively.

In general, the variation range of a belt mass is more convenient to represent via the area related ($B \times l$) distributed weight m''_{belt} . The range is established similarly as for the belt geometry by analyzing different standards DIN 22121 [48], DIN 22129 [49], NEN-EN-ISO 15236 [170], GOST 2085 [84], and other sources.

For the possible conveyor belt mass limitations, it is reasonable to use approximate minimum belt's line mass m'_{belt} equals to area related 10 kg/m^2 (for belt EP 400/3 4/2 X according to specifications [190]) and for heavy belts - around area related 86 kg/m^2 (for belt ST 8500 14T/12T V [190]).

As for the average value, the similar procedure, as applied for finding the average belt slenderness is used. After assigning the belt line mass for every size-step in product specifications [59, 190] and following the recommendations of NEN-EN-ISO 15236 [170], and also [3, 29], the data collected is normalized, and the average belt mass constituted $m''_{\text{belt}} \approx 27 \text{ area related kg/m}^2$

In this case, the geometrical variation range of a belt distributed mass belongs to the following numerical interval:

$$m''_{\text{belt}} = [10 \dots 27 \dots 86] \text{ kg/m}^2. \quad (2.12)$$

In present study, there is a need in the belt's line mass q_{bw} transversely distributed along the belt width B . It can be expressed via the area related distributed weight of a pipe conveyor belt m''_{belt} as follows:

$$q_{\text{bw}} = m''_{\text{belt}} gl, \quad (2.13)$$

where l is longitudinal length of the belt section considered. In general for the pipe conveyor belts in plane strain state, it equals to conveyor pitch $l = l_c = l_r$, where l_c is a carry spacing in the carrying strand of a conveyor, and l_r is a carry spacing in the return strand of a conveyor.

In case of the belt samples, required in Chapter 3 for quantifying a conveyor belt lateral bending stiffness from the troughability test, and for experimental determination of CFs in Chapter 4 within the six point pipe belt stiffness device, the longitudinal sample's dimension should be equal to $b \approx (150 \pm 2) \text{ mm}$. In this case, the longitudinal length for the distributed line mass in Eq. 2.13 equals $l = b \approx (150 \pm 2) \text{ mm}$

2.5.4 Nominal pipe diameter

Standardized recommendations have not yet been developed for the pipe diameter with respect to the belt width required for the correct belt behavior in the PBC system.

The only practical recommendation for pipe diameter selection is that it needs to be verified with the lump size of the transported bulk material. Generally, the maximum lump size should be less than $1/3$ of the nominal pipe diameter [106, 139, 230]. Considering the length of the belt's overlap, it needs to be in a feasible range, as too small of an overlap cannot ensure the enclosed transportation of material in between the idler stations. At the same time, the overlap of the belt should not be too large, as it substantially increases the friction between the belt edges.

A number of researchers have provided different information on how to select a pipe diameter D with respect to belt width B . For example, Barburski [10] and Gładysiewicz [91] recommend assuming that the length of overlap equals half of the belt's pipe diameter, *i. e.*:

$$B = \left(\pi + \frac{1}{2} \right) D \approx 3.64D. \quad (2.14)$$

Similar recommendations were provided by Zaimiei *et al.*[255], slightly extending the variation range:

$$B = \left(\pi + \left(\frac{1}{2} \dots \frac{1}{3} \right) \right) D \approx (3.47 \dots 3.64)D. \quad (2.15)$$

Enshu [65] described the belt design, in which an overlap length must equal about $1/7$ of the belt width, which means approximately:

$$B \approx \frac{7\pi}{6} \approx 3.66D. \quad (2.16)$$

Alternatively, the available data from catalogs and specification brochures provided by various companies are analyzed. Table 2.4 was developed based on built projects or product specification data from [18, 32, 33, 83, 154, 182, 226], selected as examples. The data are relevant for nominal pipe diameters D_{nom} , *i. e.*, the external diameter of pipe, which identifies the hexagon dimension of idlers.

The analysis of Table 2.4 indicates that, for the same belt width, different manufacturers can produce conveyors with different nominal pipe diameters. Consequently, the selection of the pipe diameter must be made for the particular cases. It is governed by economic considerations by minimizing the capital investment in an installation, if a stable enclosed pipe shape has been ensured during operation.

For the present study, the range of variation of the ratio B/D is assumed to be equal to the following the magnitude:

$$B = (3.47 \dots 4.17)D. \quad (2.17)$$

Zhang [269] called attention to the dependency between the pipe diameter and belt stiffness. He noticed that a high belt transverse stiffness is required in order to sustain bigger pipe diameters, whereas conveyors with small pipe diameters can operate with less flexural rigidity. This general trend is drawn based on practical experience and requires further research. The research study provided in this thesis (Chapters 5-6) considers the impact of the pipe diameter as a structural curvature on the ability of the belt to form a stable enclosed pipe shape.

Table 2.4: Belt width versus pipe diameter based on product specification, catalogues and other sources [18, 32, 33, 83, 154, 182, 226].

Belt width B , mm	Nominal pipe diameter D_{nom} , mm	B/D_{nom}	Belt width B , mm	Nominal pipe diameter D_{nom} , mm	B/D_{nom}
500	120	4.17	1800	450	4.00
600	150	4.00		475	3.79
750	190	3.95	1900	500	3.80
780	200	3.90	2000		4.00
800		4.00		530	3.77
900	235	3.83	2200		585
1000	250	4.00		3.76	
1050	275	3.82	2400	600	4.00
1100	300	3.67		640	3.75
1200		4.00	2600		690
	315	3.81		4.06	
1300	350	3.71	2800	700	4.00
1350		3.86		745	3.76
1400		4.00		780	3.56
	370	3.78	3000		800
1600	400	4.00		3200	830
	420	3.81	890		3.60

2.5.5 Effective modulus of elasticity

As it will be closely discussed in Chapter 3, a conveyor belt exhibits nonlinear elastic response to the applied loads. Though, for the small strain range, it is possible to assume linear elastic behavior of a belt structure with constant Young's modulus in belt's transverse direction. Such assumption is made in the following Chapter 3 for quantifying a conveyor belt bending stiffness and also for determining pipe conveyor CFs in Chapters 5-6.

In order to perform an impact analysis, the range of the elastic modulus has to be established. For this purpose, various studies that assume orthotropic mechanical behavior of a conveyor belt are considered. Wheeler [246] suggests following approximated recommendations established by Harrison [93] for steel cord conveyor belts. These recommendations typically imply that the bending modulus of elasticity for a belt in its longitudinal direction is in the order of 40 MPa and in the lateral direction, around 20 MPa. Kulagin [128], for modeling a pipe conveyor belt in ANSYS with FEM, recommended use of an approximate transverse Young's modulus as 30% of the longitudinal modulus of elasticity. He also presented studies on FE model behavior, varying transverse bending moduli from 30 MPa to 300 MPa. Efimov [62], Dmitriev and Efimov [55] accepted the values of 50 MPa and 500 MPa for lateral and longitudinal Young's moduli, respectively. Demitriev and Sergeeva [58], as a hypothetical example, used values of 120 MPa and 300 MPa, whereas Wesemeier [242] assumed 300 and 950 MPa for moduli in the longitudinal and lateral directions, respectively.



Figure 2.10: Triangular gantry (Image courtesy of CKit Engineering (Pty) Ltd. [29]).

In the present study, the moduli of elasticity in the belt's lateral direction are accepted as varying from 1 MPa to 950 MPa. Nevertheless, as it will be shown in Chapter 3 for impact analysis of the results on bending stiffness and in Chapters 5-6 on CFs, the variation range from 1 MPa to 120 MPa is already sufficient for a clear understanding of the dependence trend of the results.

2.6 Idlers and support structures

2.6.1 Design

Structural supports and construction of idler stations for PBCs have different designs. They can be classified following the recommendations of Staples [217] as: a) box structure supports; b) a reverted U-shaped structure [105] or also named “dog house” [217] (Figure 2.12), c) a triangular gantry (Figure 2.10 [194, 217]), d) structures with light weight idler units, described by Ramjee and Staples [194]; e) different variations of the mentioned and f) special design types.

In addition, as elucidated in Section 2.2, the PBC design stipulates the presence of special idlers in transition zones, where the belt is formed into a pipe shape or is opened back a flat shape. It also requires special idlers and structural components, if the construction has intermediate loading points and belt turnover. In order to avoid an undesirable twisting effect of the belt, special training idlers can be used.

In general, the rolls can be mounted at the idler stations along the whole length of the conveyor, either at one side with a small gap between the rolls (see Figure 2.11) or with

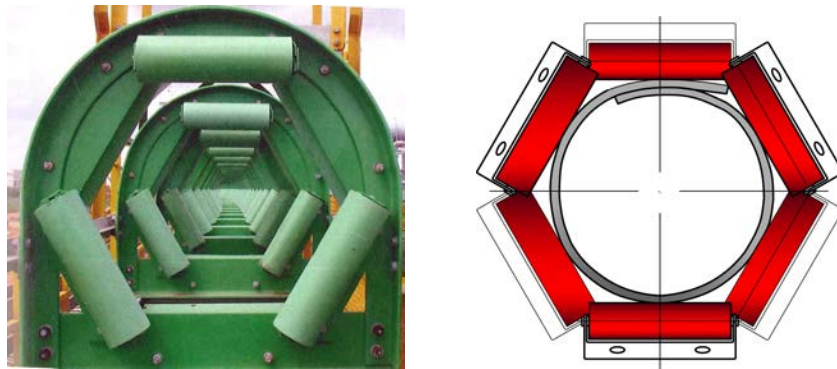


Figure 2.11: "Dog house" support structure with double side idler roll arrangement that prevents belt interference between rolls (Figure on the left shows the Sincor pipe conveyor installation in Venezuela for coal and sulfur transport. Image courtesy of Tenova TAKRAF GmbH and ContiTech Conveyor Belt Group, Continental AG).

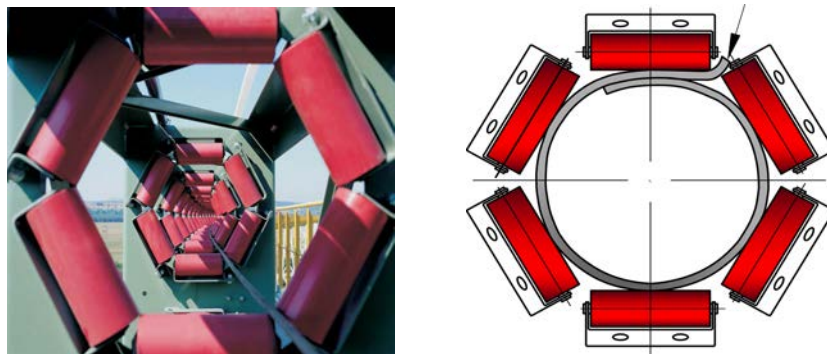


Figure 2.12: One side idler roll arrangement. If the gap between rolls is large, it can cause the belt to be pinched in between the idler rolls. (Figure on the left shows the installation in Elektrárna Melnik Power Plant, Check Republic. Image courtesy of FLSmidth Wadgassen GmbH).

three rolls at one side and three at another side of the idler panel/unit (see Figure 2.12). The arrangement of rolls on one side is less preferred, as if the gap between the rolls is rather significant, the belt edge can be pinched in the gap and be significantly damaged. The double side arrangement of rolls avoids this problem since the rolls selected have an extended length, providing an offset at the cross-sectional plane (Figure 2.12). In this case, the rolls even for the conventional trough belt conveyors can be used. However, as mentioned by Horak [105], this can increase the metal consumption of the system and the installation capital costs. That is why some companies design idlers with double side roll arrangements, using five short rolls and one top roll with an extended length at the position where the belt has an overlap.

2.6.2 Length and diameter of idler rolls

For the present study, two idler rolls characteristics are of particular interest: the length of the rolls, which can influence the CFs and contact length between the belt and the idler rolls, and the roll radius, which together with CFs affects the energy losses of a pipe conveyor due to IRR. Both of these characteristics are regulated by the pipe diameter and conveyor capacity.

In general, the length of idler rolls for a PBC is smaller than for traditional trough belt conveyors. It can be selected with respect to the idler roll arrangement at the panel, as discussed in the previous section.

The research carried out in Chapters 5-6 determines the CFs and pipe-ability using varied lengths of idler rolls in order to achieve agreement between analytical, experimental, and numerical solutions. However, in practice, the effective length of idler rolls l_{roll} of PBCs is usually no less than the side length of the regular hexagon circumscribed about the nominal pipe diameter:

$$l_{\text{roll}} \geq \frac{\sqrt{3}}{3} D_{\text{nom}}. \quad (2.18)$$

As for the idler roll radii required for quantifying IRR in the present study, they are selected based on the pipe diameter, belt speed, and loading conditions. Analysis of various catalogs, product specifications and other sources provided specifically for PBCs [194, 201, 230] shows that the roll diameter D_{roll} belongs approximately in the following range:

$$D_{\text{roll}} = [0.063 \dots 0.194] \text{ m}, \quad (2.19)$$

which coincides with the data for the trough belt conveyors [3, 190]. This range is more relevant for the critical minimum and maximum diameters, whereas the typical values equal about 0.08 m to 0.15 m (see Ramjee and Staples [194]).

2.6.3 Conveyor pitch

Conveyor pitch or idler spacing identifies the distance between the idler stations along the conveyor length. Pitch influences the load distribution between the idlers, IRR, and ability of the belt to form the desired pipe shape. The pipe conveyor belt, formed into a pipe has higher rigidity than a trough conveyor belt, as a result, the PBC can have a longer pitch without a large sag in the belt [181, 230].

The length of the carry spacing depends on the pipe diameter, loading conditions and size of the conveyor system [79, 146, 194, 230]. At the empty return strand, the carry spacing can have the same or increased length as for a loaded strand, and, as suggested by Loeffler [146], some of the idlers at the empty strand do not have to have all six rolls set for every station. The conveyor pitch may vary along the route. Vaka [230] clarified that usually the idlers are installed more frequently at the conveyor route curves.

In this thesis, the conveyor pitches at the loaded and empty return strands are denoted as l_c and l_r , respectively. Ramjee and Staples [194] reported that l_c and l_r can vary from 0.5 m to 2 m. Fletcher and de Toit [79] stated that, for maximal critical values (low load and high belt stiffness), the idler spacing can reach 3.5 m. As for the hypothetical average case

or most frequently selected length of the pitch, $l_c = l_r = 1$ m is accepted, therefore:

$$l_c = l_r = [0.5 \dots 1 \dots 3.5] \text{ m.} \quad (2.20)$$

2.7 Conclusions

This chapter introduces major PBC design characteristics that are related to the overall conveyor system, bulk material, belt design, idlers, and support structures. The variation range of each design parameter is established using the minimal and maximal critical values. In addition, the present chapter determines the average or more frequently used values for some of the most important design parameters.

Using these parameters as a basis, it becomes possible to determine the pipe conveyor belt's lateral bending stiffness (Chapter 3), pipe conveyor CFs (Chapters 5-6), ability of a belt to form stable pipe shape (Chapter 6), and the IRR (Chapter 7), and to provide an impact analysis of these characteristics.

As discussed in this chapter, one of the most fundamental characteristics for PBCs is a transverse rigidity of the belt, as it is involved in all the aspects of a PBC behavior. That is why it is important to determine belt bending stiffness in a precise way. However so far, there has been no research provided on this topic. The following Chapter 3 introduces a new methodology to quantify it based on the experimental data of the belt troughability and provides an impact analysis of all belt characteristics involved.

Chapter 3

Quantifying a Conveyor Belt Bending Stiffness*

"As far as the laws of mathematics refer to reality, they are not certain; and as far as they are certain, they do not refer to reality".

— A. Einstein, *Sidelights on Relativity*

Present chapter is focused on quantifying a pipe conveyor belt bending stiffness. A belt bending stiffness is an important parameter needed for the selection of the overall conveyor system design. Chapters 5 and 6 indicate that belt bending stiffness is responsible not only for the structural response of the belt to the external loads involved, but also it generates an additional expansion load that appears from folding a belt from a flat shape into a pipe shape. As a result, belt bending stiffness represents belt ability to form a stable pipe shape without a contact loss and determines pipe conveyor CFs, addressed in Chapters 5-6. The CFs, in turn, affect the energy losses from the IRR (Chapter 7) of an entire PBC system. A conveyor belt can be determined using the troughability test, specified in ISO 703. The impact of a belt design parameters on belt's bending stiffness needs to be investigated by varying the participating input design parameters within the range, established in Chapter 2.

3.1 Introduction

Different belt constructions e.g., steel cord and/or fabric structural reinforcements explicitly discussed in previous chapter, exhibit a different mechanical response to tensile and bending in both longitudinal and lateral directions.

The longitudinal mechanical response to tensile loads needs to be carefully controlled since the belt's minimum breaking strength is a crucial parameter for the belt's selection. For longitudinal strength of pipe conveyor belts, the standards generally developed for trough conveyors (i.a. ISO 283 [172], 7622 [176], 9856 [177], DIN 53504 [50]) are relevant and

*The Chapter is constructed generally based on the publication of Zamiralova and Lodewijks [265]

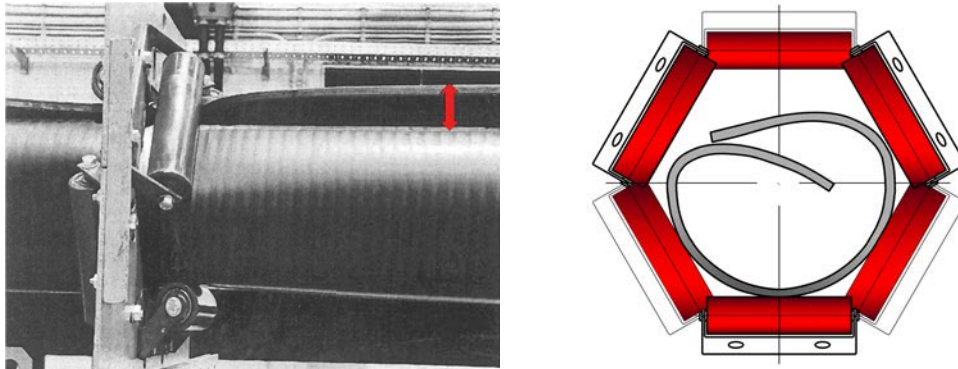


Figure 3.1: Typical problems that can be visually observed due to the incorrect selection of a belt's bending stiffness: a) excessively stiff belt causes opening of a pipe shape between the idler stations (modified figure from Wiedenroth [247]); b) too flexible belt collapses the pipe shape.

can be used in engineering practice. Such standards explicitly describe how the belt's tensile stress/strain characteristics can be quantified, including information on the measurement procedure, apparatus configuration, test samples sizes, load conditions, etc. The bending stiffness of a pipe conveyor belt in the lateral direction also has a significant impact on the conveyor operation and needs to be carefully regulated. If the belt exhibits excessive bending stiffness, it can cause an increase in the belt's IRR that results in high energy losses of the overall conveyor system. In addition, belts with high transverse rigidity can possibly experience pipe opening between the idler stations, as it is shown in Figure 3.1a.

On other hand, if a belt is too flexible in its lateral direction then its pipe shape may collapse (see Figure 3.1b) and therefore is not suitable for the correct enclosed system operation. The collapsed belt tends to exhibit a larger twist in curves along the route, which results in problematic tracking and alignment of the belt in operation. In addition, if the idlers are designed with one-side arrangement of idler rolls (see Figure 2.1) and have a significant gap in between, too flexible belt also can be pinched by the bottom idler rolls and cause idler junction failure effect of belt damage.

Despite the fact that the belt's bending stiffness is a very important parameter for the successful selection of a system design, there is no standard that can assist in this problem for pipe conveyor belting industry. As for the trough conveyor belts, there is only one standardized procedure that allows investigation of the belt's lateral bending flexibility. This procedure is described in ISO 703 [174] (analogical testing method in ASTM D378 [7]) and is named the troughability test. This test was established based on practical experience and describes the belt troughability as a ratio of the maximum deflection, produced by a belt sample under its own weight, to the belt width.

For industrial applications of pipe conveyor systems, it is convenient to express the belt's ability to form a pipe shape via the belt troughability parameter, as the latter is widely used in practice and can be measured from a simple test. Though, the current European standard ISO 703 version 2007 [174] for the troughability test has several drawbacks, which make it less effective to serve for the purpose identified.

One of the drawbacks is that the current version of ISO 703 2007 [174] stipulates only a measurement procedure. Unlike the standardized longitudinal tensile tests, the troughability test standard represents indirect measurement of the belt's transverse flexural rigidity and does not give an explicit procedure for the determination of these characteristics. The usage of the quantified bending stiffness, however, is required for the determination of the load distribution between the idler rolls, IRR and a number of other rather complex problems inherent to a PBC behavior. Moreover, the quantified bending stiffness can serve as a link between the belt's troughability performance and its ability to form a stable pipe shape (pipe-ability).

The standard does not reflect the impact of the line mass and belt geometry in the problem. Belt's pipe-ability as well as its troughability parameter are influenced by these parameters, and the recommendations for a pipe conveyor belt bending stiffness need to take them into account. For instance, the experimental results of Zamiralova and Lodewijks [261] show that thinner and wider belts need higher bending stiffness or larger overlap ratio in order to form a stable pipe shape. The effect of the belt's line mass with respect to troughability values is also considered in experiments of Wiedenroth [247].

In addition to the drawbacks mentioned, ISO 703 2007 does not provide any recommendations for the test repetition and permissible difference between obtained results, since there is no information about the sensitivity of a belt's bending behaviour and troughability values measured. Due to all mentioned aspects, the standard ISO 703 2007 applicability for the industry is limited.

As a possible alternative to ISO 703, Harrison [94, 95] proposed a different troughability test set-up with three special supports simulating a trough of a conventional three-roll idler station. The purpose of the test was to measure the length of contact between the belt sample and each of the set-up supports. The term "troughability" was redefined as a ratio between sum of the measured contact lengths and the width of the belt tested. It is important to mention that the main problems inherent to the classical troughability test were still relevant for the proposed test substitution. Moreover, the troughability test, elaborated by Harrison was not suitable for a pipe conveyor belting and [94, 95] was not officially recognized or accepted as a standard on par with ISO 703.

In order to identify, whether there is a procedure alternative to ISO 703 for testing belt bending stiffness, it is appropriate to consider a conveyor belt as a material similar to a reinforced rubber-like elastomer (see discussion in Section 3.2). Brown [22, 23] points out that while flexure tests for rigid plastics are widely used and standardized, the determination of the bending properties for flexible rubber-like materials is rarely carried out. This happens due to the fact that these materials exhibit excessive sensitivity to deformations at relatively minor loads, which affects the precision of testing. As a result, for these elastomers, there is a shortage of standards on flexural tests, unless the standard is explicitly developed for a specific product (i.e. hose, tire, seal isolation, etc.). According to Brown [22, 23], most of the time, the flexural stress/strain dependence is obtained from a cantilevered test or from a three point bending test, described in ISO 178 [171]. In the troughability standard ISO 703 [174], there is also a note reference to the mentioned ISO 178 [171], though its scope does not address rubber-like materials, limiting itself to rigid and semi-rigid plastics and thermoplastics. The extension of ISO 178 is specified in ISO 14125 [169] for fiber-reinforced plastic composites, additionally including the four point bending test procedure. The other standard ISO 1209 [178] determines bending properties for rigid cellular plastics. Only

ISO 5893 [179] deals with flexure of rubber-like materials, though it only contains general requirements for the testing equipment.

Therefore, it is possible to state that, even though the current troughability test standard ISO 703 2007 [174] has a number of drawbacks for the pipe conveyor belting industry, there is so far no alternative standardized procedure officially accepted for structures like conveyor belts. The standard ISO 703 2007 does not provide guidance for direct evaluation of the belt's flexural characteristics and does not reflect the impact of the involved parameters on belt troughability and results sensitivity.

That is why it is important to investigate whether there is a method to quantify lateral bending stiffness of a conveyor belt based on its troughability performance according to the standard ISO 703. This study then aims to identify associated calculation methods, recognize their assumptions and limitations, compare them with each other and by their means provide an impact analysis of the involved parameters on belt troughability.

The bending stiffness quantified is needed further in Thesis as it characterizes the additional expansion load on the idlers that appears from forming belt from flat shape into a pipe, and also together with the given belt line mass and geometry describes contact forces, as well as the IRR and belt's ability to form a pipe shape required. Using the model developed in this Chapter, it becomes possible to provide design recommendations for a conveyor belt simply expressed via troughability values.

3.2 Structural behaviour of a conveyor belt

In general, belt response to loads is nonlinearly elastic, which is common for rubber-like materials. Normally, besides nonlinearity, the elastomers exhibit rather excessive elasticity and extensibility with high elongation at break [11, 81]. The typical tensile stress-strain curve of rubbers is well-studied and described in a considerable amount of literature (e.g., see Bauman [11], Brown [22, 23], Gent [81], Treloar [229], etc.) In particular, the load-deformation characteristics of rubbers, comprising covers and carcass of conveyor belts, are presented in the studies of Schilling *et al.* [203], Wheeler and Munzenberger [243, 244], Nordell *et al.* [184], Mazurkiewicz [152], and others.

Various experiments conducted with conveyor belts (e.g., Lodewijks [137], Wang *al.* [236], Petrikova *et al.* [189], Schilling *et al.* [203], Keller [123], Nuttall [185], Staples and Mehta [218], etc.) show that load-deformation characteristics of overall belt structure demonstrate a similar pattern of stress-strain dependence as rubber-like elastomers. The typical curve for the fabric conveyor belt is illustrated in Figure 3.2. This curve was obtained by Lodewijks [137] for belt EP500/3 from a tensile test according to the standard DIN 22102 [47].

The stress-strain relationship depends on the mode of deformation. In the case of bending, some fibers of deformed material are stretched, and some of them are compressed at the same time. In general, the stress-strain relationship of rubber under compression is similar to the tensile mode; however, the compressive characteristic curve is slightly steeper. As a result, material behaves more stiff under compression than under tension. This observation is supported by the experiment results for rubber elastomers, given by Sommer and Yeoh [214], Treloar [229] and particularly for conveyor belt rubber – by Schilling *et al.* [203].

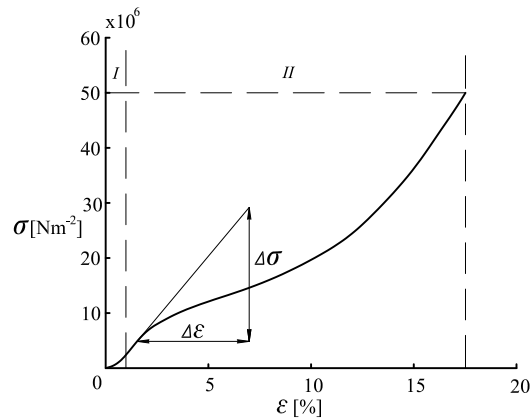


Figure 3.2: Tensile stress-strain characteristics of fabric belt EP 500/3, measured by Lodewijks [137] based on DIN 22102 [47]

The stress-strain curve deviates for belt bending and tensile tests in both longitudinal and lateral directions. In general, the belt behaves more stiff longitudinally, as its mechanical response is dominated by the steel cords and/or textile warp of fabric layers. In the lateral direction, the belt is more flexible, as it is commonly governed by the rubber compounds and, in the case of fabric belts, also by textile weft. The deviation in stress-strain characteristics for the longitudinal and transverse orthogonal direction can be observed, e.g., in the results of Petrikova *et al.* [189], Staples and Mehta [218] during the tensile tests, and in the results of Schilling *et al.* [203], during the tensile and also three point bending tests for belt position with carrying side up.

Moreover, the belt structure lay-out, implying different thicknesses of the carrying top (TS) and bottom (LS) carcass covers, also influences bending characteristics of belt in lateral direction. That is why the same belt sample generates different troughability for normal placement of belt with carrying side up and the upside down.

According to Bauman [11], the properties of reinforcement material can change the shape of the characteristic curve for overall structure, reduce or even eliminate the strain crystallization region, and also amplify the hysteresis effect due to increase of internal friction in material. In order to study explicit properties of reinforcement material, Ramos [195], Elvers *et al.* [63], Hoffman [103], Lodewijks and Pang [144], Betz [15], and a number of other researchers, conducted independent tensile and bending tests specifically for various carcass cords and fiber yarns.

The presence of rubber in the structure generates viscoelastic behavior of the conveyor belt with all consequent effects and complexity in stress-strain dependence. Besides the hysteresis effect that appears during the load retraction phase, conveyor belts also exhibit a thixotropic property, i.e. their modulus of elasticity depends on degree to which the material has been strained previously (so-called Mullins effect). The greater the previous strain and the longer the deformation was applied, the more the modulus of elasticity experiences reduction (see Bauman[11], Gent [81], Malkin and Isayev [148]). For conveyor belts, these effects can be observed in studies of Petrikova *et al.* [189], Keller [123], Lodewijks [137] and others.

Additionally, after applying a number of load cycles, the belt exhibits permanent elongation. This parameter and corresponding elastic modulus are the prime objectives of the standard ISO 9856 [177]. Notably, the static tensile characteristics of the fabric belt can also have a permanent strain (see zone (I) in Figure 3.2), which, according to Lodewijks [137], happens due to first time stretching of the woven structure of reinforcement fabric. Therefore, the described region cannot be observed during the tensile tests of used belts.

Another challenge of viscoelastic behavior manifests in its time-temperature dependence. The relaxation effect and creep of conveyor belts were tested by Czaplicka [40], Petrikova *et al.* [189], Harrison [95], Molnár *et al.* [162, 163] and other researchers. The modulus of elasticity for a dynamically loaded belt needs to be distinguished from one under static load conditions. The dynamic modulus depends on the loss and storage moduli of rubber, which can be obtained from experiment testing. Usually, the measurements are carried out by performing DMA with temperature-frequency sweep. The viscoelasticity plays an essential role in belt indentation rolling resistance and, consequently, there is a substantial amount of research available on this topic (see e.g., Lodewijks [136, 137, 140], Zamiralova and Lodewijks [266], Nuttall *et al.* [186], Nuttall [185], Rudolphi and Reicks [200] and others [184, 199, 215, 271], etc.) The effect of the belt's viscoelasticity on the system's energy consumption due to the IRR is more closely elaborated in the Chapter 7.

Taking into account the overall structural complexity, describing the behavior of the rubber-like elastomer in an analytical way is a rather a complex problem. In order to define the stress-strain curve, there were constitutive models developed based on the strain energy density function of the material, discussed by Bauman [11], Finney [78], Gent [81], Treloar [229]. The Mooney-Rivlin form that assumes isotropic incompressible material is the most common theory describing large deformations of elastomers. Its simplest approximation is a model with two coefficients, which, according to Finney [78] exhibits good agreement with tensile data with strain up to 100%. For larger strains, the high-order functions that give stresses of a square or a higher order of strain are utilized. In order to accommodate a compression and shear, for this purpose more complex alternative models were derived. Ogden, Treloar, Yeoh, Peng-Landel, Arruda-Boyce, and other material forms are examples in this category. These forms are explicitly described in the handbooks of Gent [81], Treloar [229] and others.

The studies that incorporate nonlinear elastic behavior of conveyor belts mostly provide numerical solution obtained in various software within FEM. The softwares used usually address a limited set of hyper-elastic materials. Most of the time, the Mooney-Rivlin and Ogden models are available. These materials were used by Wheeler and Munzenberger [243, 244], Petrikova *et al.* [189], Keller [123], Nordell *et al.* [184], Mazurkiewicz [152] for describing rubber in the conveyor belt structure. Additionally, in order to achieve good agreement with the experiment, Mazurkiewicz [152] also carried out finite element analysis using the Marlow model, whereas Keller [123] also employed an adaptive neo-Hook material law.

The slope of the stress-strain curve introduces the modulus of elasticity. Several researchers, for instance Bauman [11], Treloar [229], Gent [81] and others, affirm that nonlinearity in the curve of rubber-like elastomers (see Figure 3.2) implies no constant modulus of elasticity, especially for considerably high strains. This means that for these deformations, the usage of a fixed value of Young's modulus, which represents the proportionality of Hookean straight-line dependence, is not relevant anymore. It is important to mention

that the same observation is stipulated in standard DIN 53504 [50] for the tensile tests of conveyor belts.

Lodewijks [137] states that for conventional trough conveyor belts under normal operating conditions, the belt does not exhibit strain of more than 1.5%. Consequently, at this strain range for static loading mode, it is relevant to assume proportional stress-strain dependence and use constant Young's modulus of elasticity. A similar problem treatment is suggested by Schilling *et al.* [203] for pipe conveyor belts. The researchers report that the maximum pipe belt strain does not exceed 5% in tension and compression.

A constant Young's modulus was used by a number of studies in order to develop an analytical solution for rather complex problems inherent to conveyor belt behavior. Most of the time, orthotropic plate mechanics is applied, indicating different Young's moduli and Poisson ratios for a belt's longitudinal and lateral directions. Usually, the problems with such assumption are focused on investigation of load distribution between the idler rolls (e.g. see Kulagin [129], Dmitriev and Sergeeva [58], Schilling *et al.* [203]), belt deformations (see *ibid.* and also Wesemeier [238, 240]), twisting phenomenon of pipe conveyor belt (Dmitriev [54], Efimov [61]), etc. In the present study, the assumption of a constant modulus of elasticity with limitation of strains up till 5% is also considered acceptable.

3.3 Troughability test

Now that the conveyor belt structural behavior and the approximation models are described, the standard troughability test procedure, belt sample requirements and test set-up construction, needs to be acknowledged.

The apparatus for the troughability test is shown in Figure 3.3. It contains of two rigid horizontal bars, to which the belt sample is suspended by means of four steel wires. The belt sample is attached to those wires with special clamps that do not exert any bending moment that can affect the measurement of deflection. The suspension wires need to be able to move along the horizontal bars without any impediment, which can be achieved by using an assemblage with linear bearings.

The testing sample represents a cut piece of manufactured belt with a length of (150 ± 2) mm in the belt's longitudinal direction. The other two dimensions are equal to the overall width and thickness of the tested belt. In order to eliminate initial deformations, ISO 703

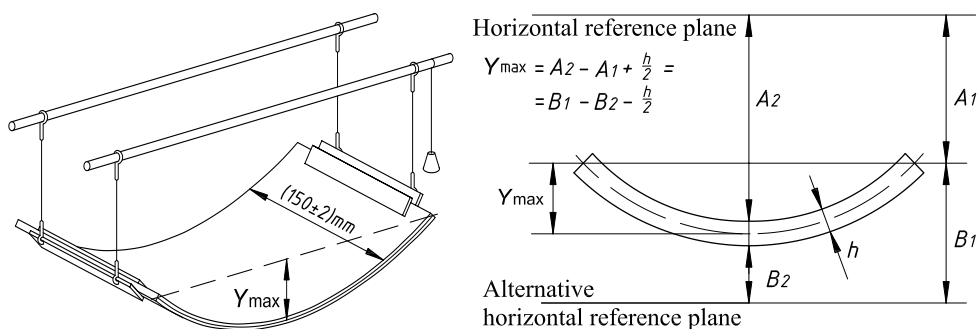


Figure 3.3: Troughability test ISO 703 [174], ASTM D378 [7].

2007 [174] recommends conditioning of the belt piece according to the standard ISO 18573 [115] under certain temperature and humidity requirements during a substantial period of time before measurement.

After conditioning, the belt sample is clamped and placed in a test rig with carrying side up. The suspended belt creates sag from its own weight. Measurement of the maximum belt deflection generated under these conditions is the purpose of the troughability test (see Figure 3.3). Due to the relaxation effect, in order to allow the belt to settle, the measurements are carried out after five minutes subsequent to the suspension of the testing piece. Results are presented as a ratio between the measured maximum deflection Y_{\max} and belt width B :

$$\text{Troughability} = \frac{Y_{\max}}{B}, \quad (3.1)$$

As it was stated in Section 3.1, the test standard does not contain recommendations for the minimum and maximum limitations of the measured troughability values with respect to the given geometry and weight of the belt. The measuring instrument, as well as its allowable absolute error, are not specified in the standards. Since for pipe conveyor belts, no guidelines ever existed and research has been performed, it is important to consider information also available for trough conveyor belts.

In the previous version of the troughability standard ISO 703 1998 [180], the minimum required troughability values were provided for the conventional trough conveyor belts with respect to trough angles. Later these recommendations were withdrawn from the current version of 2007 [174]. Though, they still can be found in a number of standards, like ISO 15236 [170], ISO 14890 [114], DIN 22102 [46], developed for conveyor belts for general use. The only recommendations that somehow consider impact of belt geometry on minimum required belt troughability can be found in standard DIN 22129 [49], provided for specific conveyor belt width values (see Table 3.1).

Table 3.1: Minimum required belt troughability for specific values of belt width according to standard DIN 22129 [49].

Belt width B , mm	Minimum troughability value
1000	0.15
1200	0.20
1400	0.25
1600	0.30

Alternatively, based on practical experience Alles *et al.* [3] report that the belt exhibits sufficient bending stiffness, when more than 35% of its width occupies the supporting idler rolls with compulsory contact between the central bottom idler roll and belt. Alles *et al.* [3] provided rough geometrical recommendations for fabric carcass belts, pointing out that adequate troughing characteristics are achievable for belts with ratio $B/h \leq 125$.

The purpose of this study is to consider the impact of the belt geometry on its troughability and establish guidelines that can assist in the pipe conveyor belt selection. Of particular interest for the minimum troughability values is to compare the results with respect to trough conveyor belts with angle of inclination of side rollers with 60° . The minimum troughability

value, specified by standard ISO 1489 [114] and recommended by Alles *et al.* [3] for this case constitutes 0.26. The motive for drawing recommendations for the maximal possible bending stiffness of a pipe conveyor belt, expressed by minimal troughability, becomes the decrease of the indentation rolling resistance and providence of the enclosed pipe shape longitudinally in between the idler stations.

In contrast to the minimum required troughability values, the recommendations for maximum possible troughability do not exist and are not specified anywhere neither for pipe conveyor belt nor even for conventional trough conveyor belts. However, as described in Section 3.1, the selection of a belt needs to be controlled in order to avoid its excessive flexibility, as for PBCs it can lead to the pipe shape collapsing. Therefore, the correct pipe shape formation should be a motive for selecting maximal possible troughability values. In present analysis the troughability range of interest is selected up till 0.5, as for the troughability exceeding that value, the bending stiffness is always unnecessary too flexible.

3.4 Approach

In order to quantify a conveyor belt bending stiffness from the troughability and provide an input analysis of the parameters involved, an analytical approach is more preferable than the empirical experimentation, though the experimental validation should be obligatorily included in the analysis. The usage of only the empirical experimentation without any analytical model is considered impractical for the problem, whereas for the analysis various belt samples having different combinations of design parameters (line mass, stiffness, and geometry) are required, which becomes problematic for the realization.

On the contrast, an analytical model that is experimentally validated allows one to quantify the belt bending stiffness directly from its troughability. By varying the involved parameters, their impact on the belt bending stiffness can be determined in terms of direct functional dependence. In addition to analytical models, the analysis can be performed using numerical approach since the numerical model, which is well-validated by the experimental data and is an agreement with the analytical solution, can be modified by increasing the order of complexity in order to reach beyond the limitation of the analytical solution.

That is why the present study aims to employ the relevant analytical and numerical models and to compare the results with the ones from the experimental testing. The solution, obtained using numerical models, can incorporate structural effects of a higher complexity than included in the analytical models.

A number of researchers propose that constant lateral bending stiffness can be derived analytically by considering independently stiffness of a belt rubber and carcass-reinforcing materials, and also their volume division in the belt structure. For fabric belts, Wheeler [246] suggested use of Lekhnitskiy's formula [133] for an orthotropic multi-layered plate with structural symmetry about its middle plane, whereas Lodewijks [137] advised the Gough-Tangorra approach [109]. For a cord-reinforced carcass, the bending stiffness can be obtained from formulas given by Huffington [110], Boyarshinov [20], and others. It is important to mention when the rubber is vulcanized together with the carcass, the overall belt structure as a combination of the constituting materials can exhibit a different modulus of elasticity than the one calculated from the formulas mentioned. Furthermore, the information about properties of the materials that comprise belt structure is not always provided by the

manufacturer of conveyor belting.

This indicates that considering the stiffness of belt constituting materials and their volume fraction in the belt structure is not relevant for the troughability problem. For the selection of relevant analytical models, a mathematical interpretation of the troughability test needs to be recognized and certain assumptions need to be accepted.

3.4.1 Problem interpretation and assumptions

First of all, the bending modulus of elasticity is assumed constant along the belt width with the condition of small strains (up till 5%), as indicated in Section 3.2. As a result, the problem becomes limited to the pipe conveyor belts with uniform belt construction. For conveyor belts with non-uniform belt structure, the standardized troughability procedure needs to be revised. It should either be supplemented with additional measurement data or completely substituted with an alternative test procedure.

It is noteworthy to mention that providing analysis in the following chapters for belts with uniform structure is very important, as it can indicate, which parts of pipe-shaped belt undergoes to larger deformations and affects formation of a well-sealed pipe shape. Based on this information, it becomes possible to design a belt with non-uniform structure, equalizing the deformations with bending stiffness using additional reinforcement. The analytical models discussed in this chapter then can be easily extended considering non-uniform belt structure with discrete change in properties (line mass and modulus of elasticity) along the belt width.

In analyzing the dimensions of a belt sample, the structure can be simplified as a prismatic beam-like or plate-like structure with width $b = (150 \pm 2)$ mm and depth h equal to the overall belt thickness. In this case, belt width B as the longest dimension of the belt sample is considered as a span of the structure.

The viscoelastic effects are not included in the analysis. Harrison [95] performed the experimental testing, measuring the troughability change due to its creep during 48 hours at certain temperature conditions. He reported that the troughability values increased very steeply up till certain value. After achieving the steady state, the troughability values did not change much exhibiting the relatively low deformation rate. In order to avoid the creep effect according to the test procedure requirements, the measurements are carried out after five minutes subsequent to the suspension of belt piece.

This means that the analytical models selected quantify an instant bending modulus of elasticity that corresponds to belt troughability at the moment of the measurement. In this case, the methods can be applied at any other measurement time for corresponding troughability value, if, of course, the 5% elastic strain limitation is fulfilled. In addition to mentioned, it is assumed that there is always sufficient time between the test repetitions, and the presence of any residual strains is completely eliminated (initial stress-free state).

Finally, the boundary conditions for the problem can be recognized from the troughability test apparatus design. The test set-up does not restrict horizontal movement of the belt piece along the bars. Also, the belt clamping provides free edges rotation without any bending moments that can affect sample deflection. Consequently, the problem with this set-up can be analytically interpreted as a simply supported a beam-like or a plate-like structure subjected to transverse uniform load from self-weight. At last, the deflections can be rather significant, so the problem is nonlinear.

3.4.2 Overview of the existing models

A substantial amount of literature on nonlinear bending of beams-like and shell/plate-like structures has been published. The analytical models available require analysis and appropriate selection for the problem.

The simplest model that can suit for the troughability test problem is a beam model. The most commonly known theory that describes nonlinear bending of beams is the Euler-Bernoulli bending theory. Based on this theory, a direct solution can be obtained for the nonlinear bending of beam structures subjected to the concentrated forces. The solution is obtained by means of elliptical integrals, as it was performed, for example, by Bisshopp and Drucker [17], and Conway [38].

In case of nonlinear bending due to distributed loads, the Euler-Bernoulli differential equations do not lead to a direct solution and can be treated only numerically with certain approximating methods and assumptions, such as, for example, power series expansion of the arc length, incorporated for instance by Rohde [198], Lee *et al.* [132], Fourier expansion of Euler-Bernoulli functions, elaborated by Seames and Conway [206], usage of approximating functions in the expression of an arc length, or replacement of the nonlinear complex problem with an equivalent pseudo-linear or simplified nonlinear system, proposed by Fertis [73, 74], Fertis and Kenee [76], Fertis and Afonta [75]. The Euler-Bernoulli governing equation for the transverse displacement w caused by the distributed load q has a following form:

$$EI \frac{d^4 w}{dx^4} = q, \quad (3.2)$$

where E is an effective modulus of elasticity, I is a moment of inertia of a beam structure. In addition to a nonlinear bending, the Euler-Bernoulli theory can accommodate the effect of axial stretch:

$$EI \frac{d^4 w}{dx^4} - EA\varepsilon \frac{d^2 w}{dx^2} = q, \quad (3.3)$$

where the cross sectional area $A = bh$, and ε is an axial extension. The axial stretching force equals then $N = EA\varepsilon$. The Eq. 3.3 reflects the beam mechanical response to a transverse load by constituting the bending term with a derivative of a fourth order and an additive term that accounts for the axial stretch.

The major drawback of the Euler-Bernoulli theory is that it does not take into account the transverse shear effects and, as a result, is applicable for thin beams and beam-like structures. In order to accommodate thick and slender structures, the Timoshenko theory is more suitable (see e.g., Timoshenko and Woinowsky-Krieger [227]). Unlike the Euler-Bernoulli structure, the Timoshenko theory allows an additional rotation between the cross section and the bending neutral axis due to the shear deformations (see e.g., Beck *et al.* [13], Timoshenko and Woinowsky-Krieger [227]). In addition to bending and stretching terms, the Timoshenko governing equation has a shear additive:

$$EI \frac{d^4 w}{dx^4} - EA\varepsilon \frac{d^2 w}{dx^2} = q - \frac{kEI}{GA} \frac{d^2 q}{dx^2}, \quad (3.4)$$

where $k = 1.2$ is a rectangular cross sectional coefficient, G is a shear modulus. For thin beams, the shear term becomes insignificant, and the Timoshenko theory converges to the Euler-Bernoulli one.

The beam models describe the structural deformations only in two planes, whereas the shell models accommodate the 3D structural behavior and can include the Poisson shear effects. The classical theory that becomes the simplest for plates and shells is the Kirchhoff-Love theory. This theory is an extension of the Euler-Bernoulli differential equations, interpreting a bending of three dimensional plate in a two dimensional form:

$$D_{\text{bend}} \left(\frac{\partial^4 w}{\partial x^4} + 2 \frac{\partial^4 w}{\partial x^2 \partial y^2} + \frac{\partial^4 w}{\partial y^4} \right) = q, \quad (3.5)$$

where a bending stiffness for the isotropic structure equals to $D_{\text{bend}} = \frac{EI}{(1-\mu^2)}$ and μ is a Poisson ratio. Introducing the Laplace operator equivalent to $\nabla^2 \equiv \frac{\partial^2}{\partial x^2} + \frac{\partial^2}{\partial y^2}$ and the biharmonic operator $\nabla^4 \equiv \frac{\partial^4}{\partial x^4} + 2 \frac{\partial^4}{\partial x^2 \partial y^2} + \frac{\partial^4}{\partial y^4}$, the governing Kirchhoff-Love differential equation for bending can be rewritten as follows:

$$D \nabla^2 \nabla^2 w = D \nabla^4 w = q. \quad (3.6)$$

One of the major assumptions of the Kirchhoff-Love theory implies that a line normal to mid-surface remains straight and perpendicular to the mid-surface after the structure is exposed to the deformations. This implies no transverse shear effect and makes the theory more applicable for thin shells and plates accommodating only bending and, if needed, axial stretching. Frequently, the solutions are obtained using Galerkin integration method (see e.g., Ivannikov *et al.* [116], Noels and Radovitzky [183], and many others). Von Karman improved the current theory expanding to the final form for large deformations (see Ventsel and Krauthammer [232], Reddy [196]).

In order to accommodate the shear effects for thick and moderately slender plate structures, the Mindlin-Reissner theory is more appropriate. This theory is a general extension of Kirchhoff-Love plate theory. Though, it additionally accounts the shear deformations assuming that the cross sections remain straight but no necessarily normal to mid-surface after loading (consult for details e.g., Ventsel and Krauthammer [232], Reddy [196]). The governing equations are expressed via the angular displacements and as follows:

$$D_{\text{bend}} \nabla^4 \left(\frac{\partial \theta_x}{\partial x} + \frac{\partial \theta_y}{\partial y} \right) = q; \quad (3.7)$$

$$\nabla^2 w^0 - \frac{\partial \theta_x}{\partial x} - \frac{\partial \theta_y}{\partial y} = \frac{kq}{Gh}; \quad (3.8)$$

$$D_{\text{bend}} \nabla^4 \left(\frac{\partial \theta_x}{\partial y} + \frac{\partial \theta_y}{\partial x} \right) = \frac{2qGh}{(1-\mu)} \left(\frac{\partial \theta_x}{\partial y} + \frac{\partial \theta_y}{\partial x} \right), \quad (3.9)$$

where w^0 is the transverse displacement of the mid-surface.

The Mindlin-Reissner theory is also called as a first-order shear-deformation theory, as it assumes the linear change of the displacements through the structural thickness. Alternatively, Levinson [134] proposed the third order theory where the transverse coordinate in the displacement field is provided as an cubical polynomial. Though, as discussed by Reddy [196], the governing equations become variationally inconsistent.

With the increased development of computer technologies, the analytical models have become semi-numerical, being capable to obtain a solution for problems with higher order

complexity and better accuracy. The most common methods are utilization of the FEM and the Finite Difference Method (FDM). In order to simplify the process of finding solution, FEM and FDM are frequently implemented with corresponding theory for beam or plate/shell structural behaviour in various commercial software applications (e.g., ANSYS, AQUAS, etc.) Most of them accommodate the generalized theories mentioned.

After the existing theories are briefly acknowledged, it is important to select the models that are more appropriate for the troughability test, accommodate all the effects needed, and select the relevant approach for the solution.

3.4.3 Selected models

One of the major purposes of this analysis is to propose the method to quantify the bending stiffness, whereas the latter is essentially affected by the choice of the analytical model.

For beams in plane stress state, the bending stiffness equals EI , where I is a structural moment of inertia that equals $I = bh^3/12$.

Baratta [9], Ashwell [6] and Wang *et al.* [234] state that the structural ratio width-to-thickness (b/h) can also influence the bending stiffness due to the anticlastic curvature effect. The effect can be significant when the width b of a rectangular structure is relatively large compared to its thickness. In this case, the bending stiffness of a beam-like structure EI needs to be accompanied by a certain correction factor that accommodates this effect. Otherwise, the model of shell/plate in the plane stress state that includes the Poisson effects becomes more relevant. In fact, the current troughability standard does not clearly specify the particular position for the measurement of the deflection. Although, if the anticlastic curvature effect is significant, the deflection at the center of the structure might essentially differ from the deflection at the edges.

In practical belt conveyor installations, the belt is supported by a number of the idlers installed with certain frequency along the whole length of the conveyor. The length of the conveyor can be substantial (e.g., tens of km long). The belt then can be considered as an orthotropic infinite shell experiencing the plane strain. Then, it becomes possible to use the bending stiffness for plate structures in the plane stress state with certain exception factor, i.e. instead of bending stiffness of a beam EI , $EI/(1 - \mu_1\mu_2)$ should be used for the orthotropic shell. Here μ_1 and μ_2 are the Poisson ratios in the belt's longitudinal and lateral directions, respectively. Consequently, as it becomes evident, the selection whether it is a beam or a shell model influences the bending stiffness quantified.

Beside of the ratio (b/h) that influences the selection of beam or shell model, the structural slenderness (B/h) determines the certain effects that need to be included in both beam and shell/plate models. In general, thin and moderately thin structures can exhibit the axial stretch in addition to the nonlinear bending. At the same time, thick and relatively slender structures are more affected by the Poisson shear effects, which become essential to be included in the model.

For the analysis, the recommendations of structural slenderness B/h developed by Steele and Balch [219] for plates are followed. The researchers classify structures as very thick with $B/h < 20$, moderately thin or slender $20 < B/h < 100$, and thin with $B/h > 100$. Ventsel and Krauthammer [232] considered thick structures with $B/h < 8 \dots 10$, thin $8 \dots 10 < B/h < 80 \dots 100$, and very thin membrane-type for $B/h > 100$. In general, for thick structures, the Timoshenko theory is appropriate, as shear stresses in the structure are significant. With the

increase in geometrical ratio, the shear effects become less influential for moderately thin members, and the Euler-Bernoulli theory can be applied. At the same time, as mentioned by Senturia [207], with increasing B/h ratio, starting from moderately thin structures the effect of axial stretch becomes more noticeable. Section 2.5.2 establishes the geometrical limits for the troughability test samples inherent specifically for conveyor belts. Considering these limits, the problem is associated with the geometry ranging from thick to very thin structures, which actually includes the theories mentioned.

Ultimately, the structural bending stiffness is affected by the selection of the model (beam or shell), and the effects that those models include (shear, bending, stretching) that are defined by the belt sample geometry. The problem can be solved using analytical and numerical approach. Moreover, as mentioned above, the numerical model that is in agreement with the analytical solution can be used in order to incorporate theories of higher complexity reaching beyond the limits of the analytical solution. As a result, the following models are selected.

For the beam models, the choice is made for the analytical models of Wang [235] and Fertis [73, 74] that describe nonlinear bending of inextensible beams using Euler-Bernoulli theory. The selection of these models is made due to their simplicity, which is very important in practical scenarios. Moreover, compared to other models, the analytical models mentioned exhibit similar trends in the results (see Section 3.7) and ultimately do not affect the conclusions about the functional dependence between the parameters involved. The Euler-Bernoulli theory is applicable for thin and moderately thin structures, which are included in geometrical range of conveyor belts.

In order to accommodate the shear effects in the beam model for thick and moderately thick belt samples, the numerical model that follows the Timoshenko theory is solved within FEM. The FEM Timoshenko beam model incorporates the nonlinear bending, stretching of the structural neutral axes, shear deformations, and the cross-sectional thinning effect due to the structural stretch. Since the Timoshenko theory transforms to the Euler-Bernoulli one, the results obtained within FEM can be validated by the analytical solution for inextensible Euler-Bernoulli based Wang and Fertis models. All the models (FEM beam, Wang, and Fertis) should generate the similar results, except for the very thick belt samples with significant shear effect and also except for the very thin structures with large troughability values when the axial stretch becomes significant.

As for the shell solution, the analytical models of Wang and Fertis are adjusted by including the Poisson ratios in the equations used for the bending stiffness $EI/(1 - \mu_1\mu_2)$. Such models approximate the structural behavior of shell in plane strain state. In this case the Euler-Bernoulli beam theory is expanded in the additional plane, and the approximating models of Wang and Fertis transform to the inextensible Kirchhoff-Love plane strain state. These shell-approximating models are suitable for thin structures.

For thick structures, in order to accommodate the Poisson shear effect, such as anticlastic curvature, the results are obtained using FEM shell model that support the Mindlin-Reissner theory. In addition to nonlinear bending and shear effect, the FEM shell model includes the axial thinning and stretching effect. This model also allows one to understand the impact of ratio (b/h) on the results comparing them with the Timoshenko-based FEM beam model. All the models used and the effects included are reflected in the Table 3.2. A brief description of the selected models is presented in the following sections.

Table 3.2: The overview of the models used in the study

	Model	Theory	Effect
Beam (2D)	Analytical Wang	Euler-Bernoulli	-bending
	Analytical Fertis		
	FEM	Timoshenko	-bending -stretching -shear
Shell (3D)	Shell-approx. analyt. Wang	Adjusted Euler-Bernoulli (Kirchhoff-Love plane strain)	-bending
	Shell-approx. analyt. Fertis		
	FEM	Mindlin-Reissner	-bending -stretching -shear

3.5 Beam models

3.5.1 Wang Model

The analytical model elaborated by Wang [235] is constructed based in the Euler-Bernoulli theory, assuming the inextensible nonlinear bending of the structure. The model considers a beam-like structure subjected to the self-weight distributed load $q = q_{bw} = m'_{belt} g b$, as illustrated in Fig. 3.4. Beam deformations are expressed via horizontal distance between the edges of the structure after deformation $2l_x$ and maximum deflection, Y_{max} , which represents the sag of belt sample measured during the troughability test.

The Euler-Bernoulli equation establishes a relation between the bending moment and curvature of the deformed structure, which for uniform beams can be written in the following

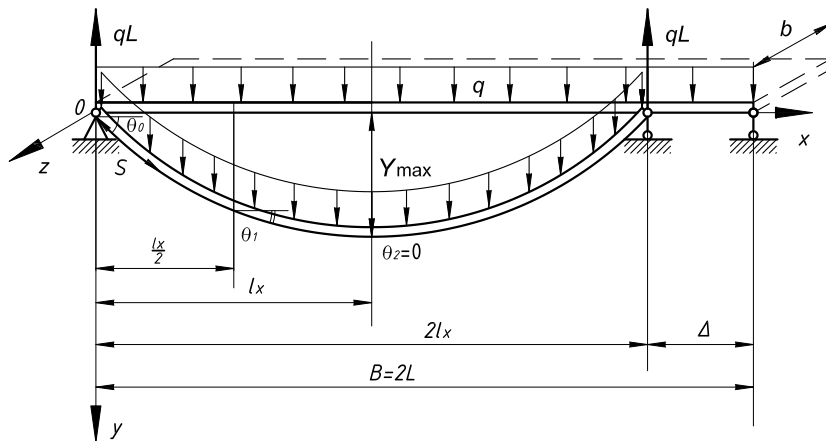


Figure 3.4: Simply supported beam subjected to the self-weight distributed load.

form:

$$\frac{d\theta}{dS} = -\frac{M(x)}{EI} = \frac{d^2y}{dx^2} \left/ \left[1 + \left(\frac{dy}{dx} \right)^2 \right]^{3/2} \right. . \quad (3.10)$$

Here θ - curvature slope; S - arc length; $M(x)$ - bending moment; x, y - horizontal and vertical positions, respectively; and EI - flexural rigidity with unknown Young's modulus E , which needs to be determined.

The Wang approach [235] is derived from the slope dependence expression of Euler-Bernoulli equation for inextensible beam structures:

$$EI \frac{d^2\theta}{dS^2} = -\frac{dM(x)}{dS} = -q(L - S) \cos \theta, \quad (3.11)$$

where L is denoted as a half-length of the beam span, which equals the overall conveyor belt width B .

Since the beam is simply supported, at $x = l_x$, the curvature slope equals to zero, and the movable hinge supports produce no moment in the structure after its deformation. Consequently, the following boundary conditions can be recognized:

$$\text{at } x = l_x, \frac{d^2\theta}{dS^2} = 0; \quad (3.12)$$

$$\text{at } x = 0, \frac{d\theta}{dS} = 0; \quad (3.13)$$

$$\text{at } x = l_x, \theta = 0. \quad (3.14)$$

According to the procedure described by Wang [235], $\cos \theta = dx/dS$ needs to be substituted into Eq. 3.11. After that, this equation is differentiated step by step with respect to S and then integrated with respect to x , where x is a horizontal projection of the arc S . As a result, Eq. 3.11 can be rewritten as follows:

$$\frac{d^2\theta}{dS^2} = \frac{q}{EI}x + C_1. \quad (3.15)$$

The constants of integrations $C_1 = -ql_x/(EI)$ is determined from the boundary condition 3.12. Taking into account that

$$\frac{d^2\theta}{dS^2} = \frac{d}{ds} \left(\cos \theta \frac{d\theta}{dx} \right) = \frac{d^2(\sin \theta)}{dS dx}, \quad (3.16)$$

Equation 3.15 can be integrated with respect to x , which yields

$$\cos \theta \frac{d\theta}{ds} = \frac{q}{2EI}x^2 - \frac{ql_x}{EI}x + C_2. \quad (3.17)$$

Considering the boundary condition in Eq.3.13, the constant equals $C_2 = 0$. Substituting the $\frac{d\theta}{dS} = \cos \theta \frac{d\theta}{dx}$ and integrating Eq. 3.17, it becomes possible to write:

$$\frac{\theta}{2} + \frac{\sin 2\theta}{4} = \frac{q}{6EI}x^3 - \frac{ql_x}{2EI}x^2 + C_3. \quad (3.18)$$

The last constant of integration $C_3 = ql_x^3/(3EI)$ is derived based on the boundary conditions 3.14. Eventually, the function reflecting the slope of the deformed structure at any x position can be computed using the form obtained by Wang [235]:

$$2\theta + \sin 2\theta = \frac{2q}{3EI} (x^3 - 3l_x x^2 + 2l_x^3). \quad (3.19)$$

On the other hand, for the inextensible beam-like structures, the maximal deflection Y_{\max} and the length of the structure span L are connected to the slope and value l_x via the following relationship:

$$L = \int_0^{l_x} \sec \theta dx; \quad (3.20)$$

$$Y_{\max} = \int_0^{l_x} \tan \theta dx. \quad (3.21)$$

Since the function $\theta(x)$ is not expressed in an explicit way, the approximation of one-third Simpson Rule is applied to the integrals in the Eqs. 3.20 and 3.21:

$$L = \int_0^{l_x} \sec \theta dx \approx \frac{l_x}{3n} \sum_{j=1}^{n/2} [\sec \theta_{2j-2} + 4 \sec \theta_{2j-1} + \sec \theta_{2j}]; \quad (3.22)$$

$$Y_{\max} = \int_0^{l_x} \tan \theta dx \approx \frac{l_x}{3n} \sum_{j=1}^{n/2} [\tan \theta_{2j-2} + 4 \tan \theta_{2j-1} + \tan \theta_{2j}]. \quad (3.23)$$

These equations are obtained by dividing the integration interval $[0; l_x]$ into an even number n of equal subsections. The slopes $\theta_0, \theta_1, \theta_2, \dots, \theta_n$ of the deformation curve correspond to dividing the interval limits at the following positions of x : $0, l_x/n, 2l_x/n, \dots, l_x$. In order to determine the modulus of elasticity, the Eqs. 3.22 and 3.23 need to be solved together with the supplementary equations for each slope that divide interval of integration. These equations are obtained by substituting corresponding x coordinates into Eq. 3.19. Taking into account that at $x = l_x$, the slope is always $\theta_n = 0$, and the number of required supplementary equations is $(n - 1)$. Solving them together with Eqs. 3.22 and 3.23, it becomes possible to determine each of the designated slope values, parameter l_x and the modulus of elasticity of the beam-like structure considered.

A higher number n of interval divisions produces more accurate results in the calculation. In order to achieve sufficient accuracy, Wang [235] used eight Simpson intervals. This study compares results, achieved for two, four and ten Simpson intervals.

It is important to mention that, according to Holden [104] and Reddy and Singh [197], the approach of Wang [235] generates certain inaccuracy due to the way commutation of the derivatives d/dS and d/dx is performed. The error appears after integration of Eq. 3.11 in respect to dS with preliminarily substituted $\cos \theta = dx/dS$, i.e.:

$$\frac{d\left(\frac{d^2\theta}{dS dx}\right)}{dS} \neq \frac{d\left(\frac{d^2\theta}{dS^2}\right)}{dx}.$$

Due to this fact an alternative solution for the problem is achieved using the approach of Fertis [73, 74].

3.5.2 Fertis Model

In general, Fertis [73, 74] elaborated an approach considering the horizontal displacement Δ , generated after the structure deformation. This displacement equals $\Delta = 2(L - l_x)$ and is illustrated in Figure 3.4. The bending moment for the structure can be written as a function of x at any position $0 \leq x \leq 2l_x$ in following form:

$$M(x) = qLx - qS\frac{x}{2}. \quad (3.24)$$

In order to reduce a problem complexity, Fertis [73, 74] proposed expression of arc length $S(x)$ in terms of the structure's horizontal displacement:

$$S(x) = x + \Delta(x). \quad (3.25)$$

Fertis [73, 74], Fertis and Lee [77], Fertis and Afonta [75] investigated various cases with different loading and boundary conditions, and proposed several approximation functions for $\Delta(x)$:

$$\Delta(x) = \Delta = \text{const}; \quad (3.26)$$

$$\Delta(x) = \Delta \frac{x}{2l_x}; \quad (3.27)$$

$$\Delta(x) = \Delta \sqrt{\frac{x}{2l_x}}; \quad (3.28)$$

$$\Delta(x) = \Delta \sin\left(\frac{\pi x}{4l_x}\right). \quad (3.29)$$

These approximation functions are mostly relevant for beams where one of the ends is permitted to move in the horizontal direction, such as a cantilever, simply supported beam, etc. Additionally, for various cases, Fertis [73, 74], Fertis and Afonta [75] achieved an alternative solution by applying the fourth-order Runge-Kutta Method. According to the authors, the comparison between results, obtained based on approximation functions in Eqs. 3.26 – 3.29), and by using the Runge-Kutta method, showed reasonably close results. Apart from this, a good match was also reported by comparing the results with data, which is available in some literature (e.g., Lau [131] for the cantilevered beams), and other solutions, which were developed using the power series method.

For simply supported beams under a distributed load and for cantilevered beams subjected to combined loading, the simplest function of $\Delta(x)$ given in Eq. 3.26 generates the most accurate results. Fertis [73, 74], Fertis and Afonta [75], Fertis and Lee [77] indicated that the error of usage in the function in Eq. 3.26 yields an error of approximately 3% or less for inextensible beams.

That is why the analysis, presented in this study, also assumes the same dependence given in Eq. 3.26. In this case, substitution of $S(x)$ into Eq. 3.24, the bending moment yields:

$$M(x) = -\frac{q}{2}(x^2 - 2l_x x). \quad (3.30)$$

For further solution development, Fertis [73, 74] introduced a function $\Lambda(x)$ into the Euler-Bernoulli Equation 3.10:

$$\Lambda(x) = \frac{d^2y}{dx^2} \left/ \left[1 + \left(\frac{dy}{dx} \right)^2 \right]^{3/2} \right. . \quad (3.31)$$

This function may be expressed in terms of the bending moment $M(x)$ as follows:

$$\Lambda(x) = \frac{d\theta}{dS} = -\frac{M(x)}{EI} = \frac{q}{2EI} (x^2 - 2l_x x). \quad (3.32)$$

On other hand, Eq. 3.31 can be utilized by making a substitution for $\tan \theta = dy/dx$. After multiplying both parts of Eq. 3.31 by dx , the left part of the equation can be integrated correspondingly in respect to x and to the right part in respect to $\tan \theta$. The result of these manipulations expresses the arc $S(x)$ of the deformation curve via function $\Delta(x)$ as follows:

$$\sin \theta = \int \Lambda(x) dx + C. \quad (3.33)$$

The integral in Eq. 3.33 can be determined by substituting the functional dependence for from Eq. 3.31 into it. The constant of integration $C = ql_x^3/(3EI)$ is computed by considering the boundary conditions 3.14, given in Section 3.5.1. Eventually, the slope of the beam deformation curve at any position $0 \leq x \leq l_x$ can be expressed as follows:

$$\sin \theta = \frac{q}{6EI} [x^3 - 3l_x x^2 + 2l_x^3]. \quad (3.34)$$

Further solution is developed by utilizing Eqs. 3.22 and 3.23 for the half-length L and the maximum deflection Y_{\max} . Integrals are obtained using one-third Simpson Rule following a similar procedure, as described in Section 3.5.1, using them in combination with the supplementary equations, generated from Eq. 3.34 for each slope according to the corresponding x values. For ensuring accuracy, Fertis [73, 74] recommends use of ten Simpson intervals. For the present study, the results are computed for Fertis model using two, four and ten Simpson intervals.

It is important to mention that Fertis [73, 74] treated only a direct problem, when the deformations are found based on the given loading and boundary conditions with known properties of the deformable beam. Consequently, for given flexural rigidity, Fertis determines the displacement Δ , satisfying Eq. 3.20 by means of trial-and-error procedure. As for the troughability test, Fertis solution is modified as described in the present study for the implicit problem, finding the bending stiffness required to produce the deflection that is measured during the troughability test.

Another important observation that is not reflected in the research of Fertis focuses on the problem, which is equivalent in terms of symmetry conditions to the original simply supported beam. Particularly, the symmetrical system, illustrated in Figure 3.5, represents the cantilevered beam with half-length L , subjected to the combined loads.

This structure generates a horizontal displacement $\Delta = L - l_x$, which is half than the one for the original simply supported beam. It is expected that for the same approximation functions of $\Delta(x)$, given in Eqs. 3.26 – 3.29, the bending moment for both equivalent systems will be the same. However, for a cantilevered system, after substituting $\Delta = L - l_x$ and $S(x)$ into Eq. 3.25, the bending moment produces greater values for given x -coordinates,

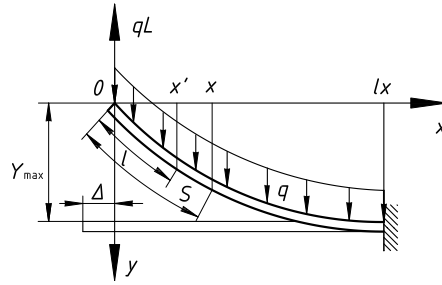


Figure 3.5: Cantilevered beam equivalent to the original simply supported system.

compared to the original simply supported structure. This consequently leads to difference in slope-dependence for both models. For instance, for the cantilevered system that assumes constant displacement approximation as in Eq. 3.26, the moment $M(x)$ and slope function give the following expressions:

$$M(x) = -\frac{q}{2} [x^2 - (L + l_x)x]; \quad (3.35)$$

$$\sin \theta = \frac{q}{12EI} [2x^3 - 3(L + l_x)x^2 + (3L + l_x)l_x^2]. \quad (3.36)$$

These expressions obviously deviate from the ones given in Eqs. 3.30 and 3.34 for the simply supported structure under the same assumption. Taking into account that both equivalent systems generate the same vertical deflection, it becomes possible to conclude that the Fertis approach produces a higher modulus of elasticity for the equivalent cantilevered problem, than the original simply supported one.

This contradiction is the result of Fertis' [73, 74] approximation of the bending moment from the distributed loads in Eq. 3.24. The expression $qSx/2$ assumes that the horizontal position of the gravity center for any arc of the deformed structure is situated in the middle of that arc projection onto the x -axis. This assumption is not always correct for the arbitrary curvilinear arcs, and the appropriate treatment needs to be carried out according to the procedure outlined, for example, by Tolstov [228], Smirnov [213], and in other mathematical handbooks. In this case, the bending moment from the distributed loads needs to be considered equal to $q \int_0^S (x - x') dl$, where l is a dummy variable of the arc S with the corresponding dummy-coordinate x' (see Figure 3.5).

Summing up, the simplicity of both Wang and Fertis methods used here make them fairly attractive in terms of their practical application. However, both methods assume certain approximations that can affect the accuracy of the solution. Moreover, these methods assume inextensible beam deflections, considering only bending term in the Euler-Bernoulli equation.

3.5.3 FEM beam model

In order to accommodate the shear and stretching, the problem is also solved using FEM beam model that supports Timoshenko theory.

The numerical FEM beam model can be solved within any commercial software that supports Timoshenko beam element type (e.g., Beam 188, Beam 189 for ANSYS, B31, B32 for ABAQUS, etc). If the models developed in different software have similar boundary conditions, meshed in a similar way, and have the similar elements types, the solutions obtained should yield similar results, as the general theory and concept behind the models are the same. As for the present study, ANSYS software is used.

For the numerical modeling, the Timoshenko two-node element Beam 188 with six degrees of freedom at each node is selected (see [4] for the reference). The element cross-section incorporates 16 integration points through the structural thickness. In addition to the nonlinear bending, axial stretch, and shear effect, this element accounts the “thinning” effect, which occurs due to the structural extension. This effect is realized by scaling the cross section of a beam as a function of axial stretch. The Poisson ratio was assumed equal to $\mu = 0.45$. The solution control is performed using the Newton-Raphson scheme. The boundary conditions mimic the simple support (see Fig. 3.4), implying the restricted displacements in y - direction at the edges with rotational allowance of the nodes, and additional x -constrain at one of the edges. The meshing of the structure in longitudinal direction is performed within 100 elements with uniform size. The beam FEM model is shown in Fig. 3.6.

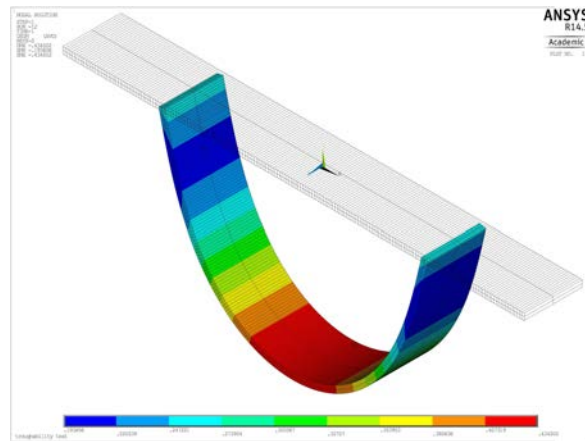


Figure 3.6: Example of a FEM model solution obtained in ANSYS within beam elements.

The FEM model includes the geometrical nonlinearity that implies finite strains (large strains that are no longer infinitesimal), and also account large rotations. Due to the assumptions made in Section 3.4.1, the material nonlinearity is not considered in the present study. However, the analysis can be extended in the future, as the elements that are eventually selected support such material complexity.

The purpose of the study is to determine a conveyor belt bending stiffness, which, for given belt sample geometry, actually means to quantify bending modulus of elasticity. The solution using FEM beam model in the software can be obtained only for direct problem, i.e. the deflection is determined based on the boundary and loading conditions with given properties of the beam. In other words, it is only possible to compute troughability of the structure based on the initially assigned modulus of elasticity.

In order to solve the implicit problem, the calculations are carried out according to the specifically developed program code using Advanced Parametric Design Language (APDL). For given deflection measured from the physical troughability test, the effective modulus of elasticity is determined via trial-and-error procedure by repeating the solution loops until the FEM model generates the same deflection of the structure as originally required with accuracy of no less than 10^{-5} . The initial guess for the modulus of elasticity is made based on the calculated result from either Wang or Fertis' analytical solution.

The FEM beam model is suitable for thick structures, though, since the Timoshenko theory converges to Euler-Bernoulli one for thin beams, the results obtained numerically for moderately thin belt samples should be comparable with the ones generated using analytical Wang and Fertis models, except for very thin structures exposed to the significant axial stretching effect.

3.6 Shell models

3.6.1 Shell-approximating analytical Wang and Fertis models

The analytical model of Wang and Fertis, described in the Sections 3.5.1 and 3.5.2, respectively, can be transformed for shell model by approximating the shell in plane strain state. The corrections of the models imply the usage of $EI/(1 - \mu_1\mu_2)$ instead of EI for the structural bending stiffness in Eqs 3.19, 3.22, and 3.23 for the Wang model, and Eqs. 3.22, 3.23, and 3.34 for the Fertis one. Since the original Wang and Fertis beam models were developed based on Euler-Bernoulli theory, the shell-approximating corrections for the bending stiffness transform the models to follow the Kirchhoff-Love plate theory for the plane strain state. These adjusted analytical models are suitable for moderately thin structures, as they include only nonlinear bending term, excluding the shear effect important for thick structures, and stretching effect, important for very thin membrane-type shells.

3.6.2 FEM shell model

In order to accommodate the shear effects for thick shells and also include the stretching effect needed for very thin belt samples, the present study introduces the FEM shell model that supports Mindlin-Reissner theory.

The solution can be obtained numerically within various commercial software applications that support the Mindlin-Reissner shell element type (e.g., Shell 181, Shell 189 for ANSYS, or S4R, S8R for ABAQUS, etc.) As mentioned in Section 3.5.3, for the similar modeling conditions (i.e., meshing, element type, interpolation method, boundary conditions, etc.), it does not matter what software is selected for the problem considered: since the theory and concept for the models are the same, the output results for the problem considered should be similar.

For the case, the FEM shell model is solved in ANSYS software within 4-node Shell181 element type with six degrees of freedom at each node (see [4] for the reference). The structure is meshed with 500 rectangular elements (100x50) with uniform size. The boundary conditions are realized similarly as for the beam throughout the whole length of the edges (simple support). The full integration procedure is implemented, and the solution control is realized with Newton-Raphson scheme. The FEM shell model supports similar effects

as for the beam (shear, bending, stretching, and also thinning effects), additionally taking into account the Poisson shear effects and impact of the geometrical ratio (b/h) of the belt sample. This allows one to investigate the appearance of the anticlastic curvature effect.

The FEM shell model accommodates the finite strains and large rotations. The material is assumed linear elastic, though the analysis can be extended in the future to include nonlinear elasticity of the material. The Poisson ratio is assumed equal to $\mu_1 = \mu_2 = 0.45$ as for the rubber in both directions. This is made in order to consider the most critical impact of a Poisson ratio, even though the belt is orthotropic and due to the longitudinal carcass reinforcement behaves stiffer along one of its dimension (in our case along b).

The FEM shell model can be used to solve the direct problem, i.e., the structural deformations (in this case troughability) are determined for given belt properties. In order to solve the implicit problem and determine the Young's modulus from the troughability parameter, the results are obtained similar to the FEM beam model by implementing the trial-and error iteration procedure until the relative difference in the deflection does not exceed 10^{-5} . The initial guess for the E -modulus value is taken from the results of Wang or Fertis models.

3.6.3 Comparison Concept

Now that all the selected beam and shell models are described, it becomes possible to compare them with each other, provide their usage limitations, and determine the impact of the physical parameters involved.

The purpose of the study is to determine the belt bending stiffness from the troughability parameter. Since the geometry of the sample is given, the problem converges to determination of the Young's modulus of elasticity E .

For the comparison, the FEM models are considered to be more precise over the analytical ones, as they provide enough fine mesh, and include all the effects needed. Moreover, they support the general theories (Timoshenko for beam and Mindlin-Reissner for shell) that cover wide range of the belt sample geometry. At the same time, the more simple analytical approaches of Wang and Fertis models can also provide enough precision for the resultant E -modulus that makes these models to be more preferable for their simplicity, compared to the FEM models. That is why, the comparison is realized for the analytical models with respect to the FEM solution.

As described in the Sections 3.5.3 and 3.6.2, the main difficulty appears from the fact that the FEM beam and shell models generate solution for the direct problem, whereas the models of Wang and Fertis (both beam and shell-approximating) are suitable for the implicit one. In order to investigate the impact of varying moduli of elasticity, the comparison is realized according to a special technique.

For the analysis, several different values of flexural moduli of elasticity are selected. For each of that value, FEM models determine corresponding values of a structural deflection. Each of that deflection is introduced as an input to Wang or Fertis models, which in turn determine bending modulus of elasticity as an output. The difference between Wang's or Fertis' elastic moduli and the ones that were initially assigned to FEM is presented as a percentile fraction as follows:

$$\frac{E_{\text{FEM}} - E_{\text{Wang or Fertis}}}{E_{\text{FEM}}} \times 100\%.$$

Similar procedure is also used for different values of the belt line mass and the belt sample geometry.

3.7 Results

3.7.1 Case study

For the experimental validation of the analytical models, a sample of a conventional trough conveyor belt with physical parameters given in Table 3.3 was selected as a case study. The troughability test was carried out for that sample according to ISO 703 2007 procedure [174].

The maximum deflection of 0.434 m was measured at the center of the belt sample with respect to the sample span (belt width B) and the sample width b . For that deflection value, the effective modulus of elasticity is determined within analytical models of Wang and Fertis with 2, 4 and 10 Simpson intervals and the results are compared. The results for the case study parameter set are given in Table 3.4 and Table 3.5.

The minimum difference in E-modulus between FEM solution and analytical models for given 0.434 m deflection is detected for the Fertis beam model (12.2%) with respect to the FEM beam solution. If the moduli of elasticity from the analytical beam models are directly

Table 3.3: Reference parameters of the physical belt sample.

Parameter	Value
Belt type	EP
Belt width B , mm	1200.67
Thickness h , mm	16.82
Geometrical ratio B/h	71.38
Longitudinal width of the sample b , mm	151.33
Moment of inertia $I = bh^3/12$, m ⁴	6.001×10^{-8}
Sample mass M_{smp1} , kg	3.672
Distributed line mass $q = q_{\text{bw}} = M_{\text{sg}}/B$, N/m	29.971

Table 3.4: Comparison of the results obtained experimentally and with FEM for the case study parameters set

FEM (trial and error)	E , MPa	Y_{max} , m (experiment)	Y_{max} , % (deviation with experiment)
Beam	9.184	0.434	10^{-5}
Shell (central position)	8.212		

Table 3.5: Comparison of the results obtained analytically and with FEM for the case study parameters set

		E , MPa	Y_{\max} , m	Y_{\max} , % (differ. with exper.)	E , % (differ. with FEM)	Y_{\max} , m	Y_{\max} , % (differ. with exper.)	E , % (differ. with FEM)	
Analytical solution for E (Y_{\max} from exper. Table 3.4)			FEM beam solut. for Y_{\max} (E from Wang or Fertis)			FEM shell solut. for Y_{\max} (E from Wang or Fertis)			
Wang	Simps.	2	6.613	0.455	4.83	27.99	0.448	3.14	19.47
		4	6.756	0.454	4.61	26.44	0.446	2.85	17.73
		6	6.817	0.453	4.38	25.77	0.446	2.72	16.99
Fertis	interv.	2	6.955	0.452	4.15	24.27	0.445	2.45	15.31
		4	7.175	0.451	3.91	21.88	0.443	2.01	12.63
		6	7.207	0.450	3.69	21.53	0.442	1.94	12.24

prescribed to FEM beam and shell models, the deviation in deflection with experiment constitutes minimum 1.9% (Fertis beam model and FEM shell solution).

Therefore, the small deviation in deflection can lead to rather large difference in modulus of elasticity. This observation demonstrates the need in sensitivity control of the modulus of elasticity and the difference in the deflection measured from the physical test. In addition, the limitations of using Wang or Fertis models that assume non-extensible structural behavior also need to be established.

In order to determine the influence of the belt slenderness, line mass and effective modulus of elasticity, the data given in Table 3.3 is used as a reference parameter set being a starting point for parameters variation. In particular, for varied effective modulus of elasticity and given geometry of the belt sample (constant B , h , b), results are also achieved using double increased and half diminished line mass, i.e. for q , $2q$ and $q/2$ (see Section 3.7.3). A similar strategy is applied to the reference parameter set by changing belt sample geometry (B , h , b) one by one for varied elastic moduli and keeping $q = \text{const}$ (see Section 3.7.4). Increasing and diminishing the reference parameter set either for geometry, or for q with the same factor of two, allows one to compare the results between each other and to identify which parameter (geometry or line mass) has a greater impact on the belt troughability.

The major goal of the case study is to show that the analytical and FEM models predict the effective E -modulus in a relevant range, since it generates the same belt's deflection and belt troughability, as observed in the experiment test. Besides of the validation purposes, it also shows the need in investigation of the models' sensitivity of E with respect to the troughability value Y_{\max}/B and how the number of Simpson intervals and also various input belt design parameters influence the results.

3.7.2 Comparison of the models and impact of an effective modulus of elasticity

Figure 3.7 illustrates the dependence graphs, obtained using Wang and Fertis analytical beam models with 10 Simpson intervals and also FEM beam and shell solution versus modulus of elasticity varied within the range established in Section 2.5.5. For the results obtained using FEM shell model, the deflection for the troughability is considered at the central position with respect to the belt sample span B and width b . Results show that the analytical models of Wang and Fertis generate a functional dependence trend similar to the FEM models.

Figure 3.8 demonstrates the difference between Wang and Fertis analytical models solved with 2, 4, and 10 Simpson intervals with respect to FEM beam and shell solution. The data shows that for large troughability values, the deviation between the FEM solution (both beam and shell) that include axial stretching becomes more noticeable, compared to the analytical beam models that assume only inextensible nonlinear bending.

The FEM shell model (Mindlin-Reissner shell) produces smaller troughability for the same E moduli, compared to the FEM beam model (Timoshenko beam). The difference appears, as the shell model takes into account impact of the shear in plane not only along the sample span (belt width B) but also along the sample width b .

The results show that increase of Simpson intervals does not significantly diminish deviation with FEM. This means that the selection of the appropriate model is more decisive in problem behavior than calculation precision, achieved with increasing number of Simpson intervals. Due to this fact, the following analytical results are determined only for 10 Simpson intervals.

For the conveyor belting industry, bending stiffness of a belt is mostly required in order to determine the structural deformations expressed as belt's ability to form a desirable shape (trough or pipe) sufficient for the application. The analysis shows that a rather significant difference in bending moduli leads to small deviation in belt deformations. The bending

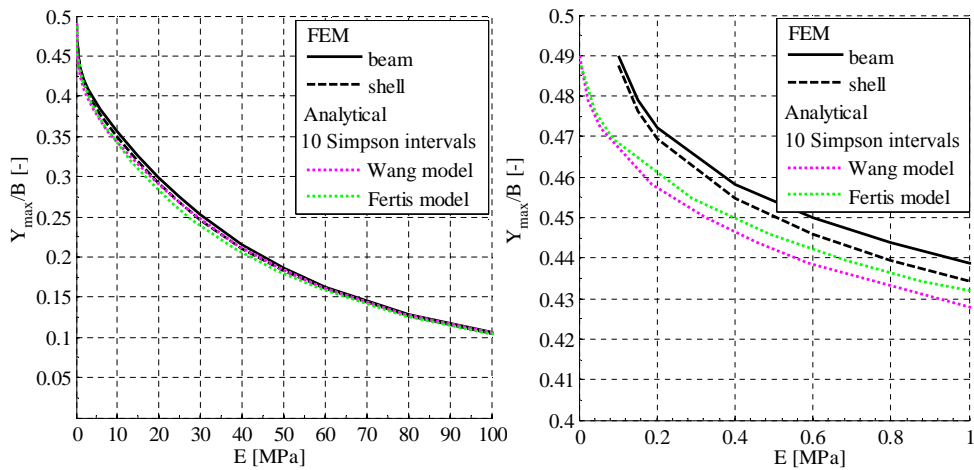


Figure 3.7: Belt troughability versus modulus of elasticity, obtained using FEM (beam and shell) and also using Wang and Fertis models with 10 Simpson intervals.

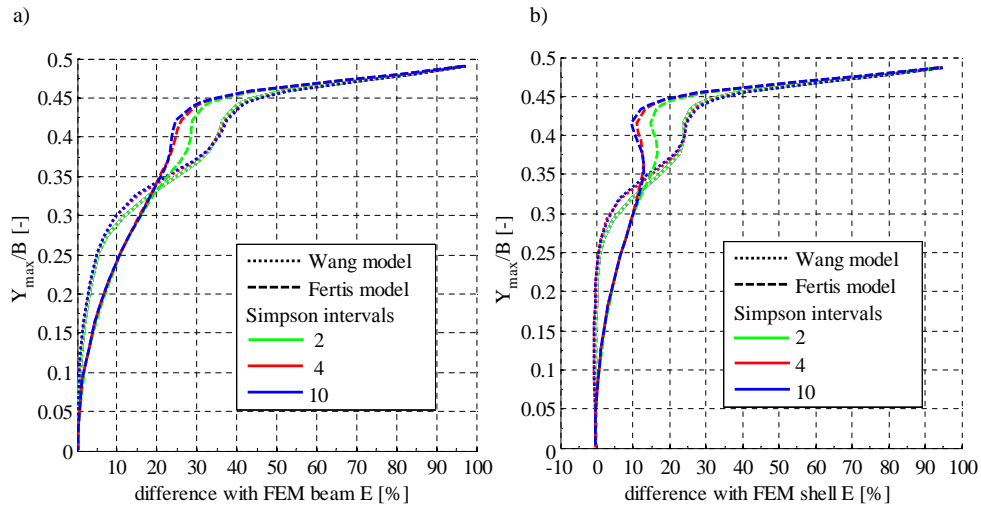


Figure 3.8: Belt troughability versus difference in elastic modulus, obtained using the analytical Wang and Fertis beam models with 2, 4 and 10 Simpson intervals, in respect to the FEM solution for a) beam and b) shell models

stiffness and belt deformation also influence the rolling resistances of the belt conveyor that in turn affect the selection of the drive power for the system. Usually, the drive power is selected within 15% margin. That is why the utilization of the Wang or Fertis models is deemed acceptable for the difference with a FEM solution of no more than 10%.

3.7.3 Effect of a belt line mass

Figure 3.9 illustrates the influence of a line mass on the belt's troughability for the case study parameter set with constant geometry (B , h , b) and line mass $q/2$, q and $2q$. The results obtained using Wang and Fertis models generate similar functional dependence trends as FEM beam and shell model at the central position of the belt sample.

For the same troughability but for the different line mass values, the resultant moduli of elasticity exhibit proportional dependence with the same factor, as the reference line mass was increased or decreased (for the particular case, see the marks on the graph for factors $\frac{1}{2}$ and 2). This means that for the same geometry of the belt sample, it is sufficient to create one dependence curve for one value of q . Other functional curves can be easily generated from the reference by simply shifting the values of elastic moduli along the abscissa with an appropriate proportional factor of the change in line mass required.

The results show that excessive line mass and or small bending stiffness increases the stretching effect of the neutral axis in the structure. The latter, as a result, causes a growth of difference between FEM beam solution and inextensible models of Wang and Fertis (see also Fig. 3.10). This difference is independent from the impact of the line mass change and significantly affected by the inclusion of the axial stretching effect. The similar effect of line mass appears also for the solution with FEM shell model.

When comparing the analytical models, for the beam solution, the Wang model is always

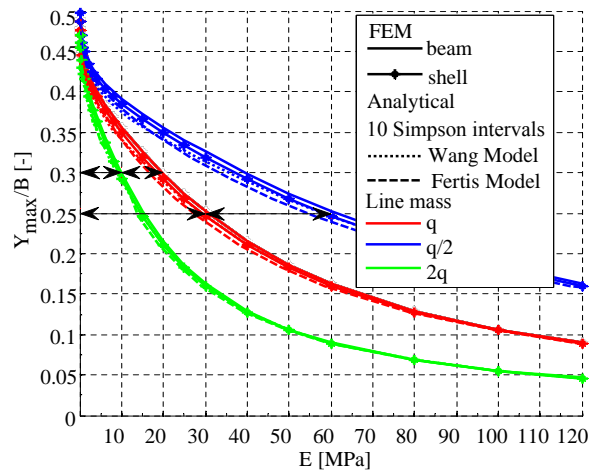


Figure 3.9: Effect of a belt's line mass on belt troughability for varied moduli of elasticity, obtained using FEM solution for beam and shell models, and using beam models of Wang and Fertis with 10 Simpson intervals.

more preferable than the Fertis one, as it predicts results for a larger deflection range with acceptable 10% difference with FEM beam model. This is also relevant for the particular input parameters, comparing the analytical results with the FEM shell solution (Fig. 3.10b). However, as it will be shown in Section 3.7.4, at certain load and geometrical parameters of a belt sample, the Fertis model can exhibit better correlation with FEM shell than the Wang solution.

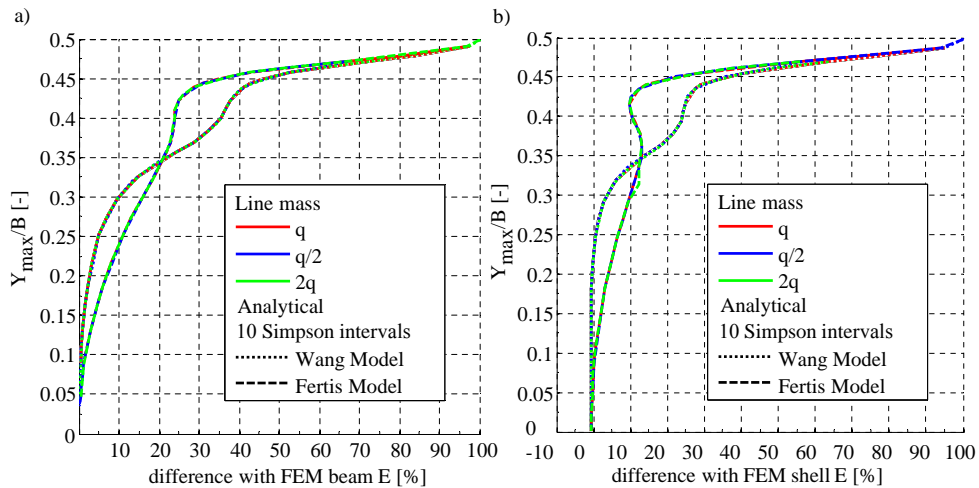


Figure 3.10: Belt troughability versus difference in elastic modulus, obtained using the analytical Wang and Fertis beam models with 10 Simpson intervals in respect to the FEM a) beam and b) shell models for line mass $q/2$, q , and $2q$.

3.7.4 Impact of a belt geometry

Belt slenderness ratio B/h

Figure 3.11 shows the impact of the belt slenderness ratio B/h on the troughability characteristics for the parameter set of the case study with constant q and b parameters. Results are obtained for geometry $B/2h$, B/h , and $2B/h$, using the analytical Wang and Fertis beam models and also the FEM beam and shell models. For the shell model, the ratio b/h is also kept constant, as its impact is considered in the next section. The deflection for FEM shell is obtained at the center (with respect to sample span B and width b) of the structure deflected.

The qualitative analysis shows that for the same modulus of elasticity, thinner and wider belts produce larger deflections than thicker and narrower ones. This observation is in agreement with Senturia [207] that states that behavior of thicker and narrower structures is dominated by the bending term, whereas thinner and wider ones are more affected by the stretching effect. This complies also with the experimental observation of Harrison [94, 95], Alles *et al.* [3] and Oehmen [187] for conveyor belts about a higher ability of thin and wide belts to conform to a trough shape.

Figure 3.12 illustrates the relative difference between the models. The stiffening effect is the reason that for larger ratio B/h , the difference between the FEM models (both beam and shell) that support the axial stretching effect and the analytical models that only assume inextensible nonlinear bending is also larger. Comparing with the FEM shell model (Fig.3.12b), the analytical beam models of Wang and Fertis can overestimate the modulus of elasticity at certain troughability parameters, represented by the negative difference between the models in the figure. This appears for thicker belt samples where the shear in both planes becomes

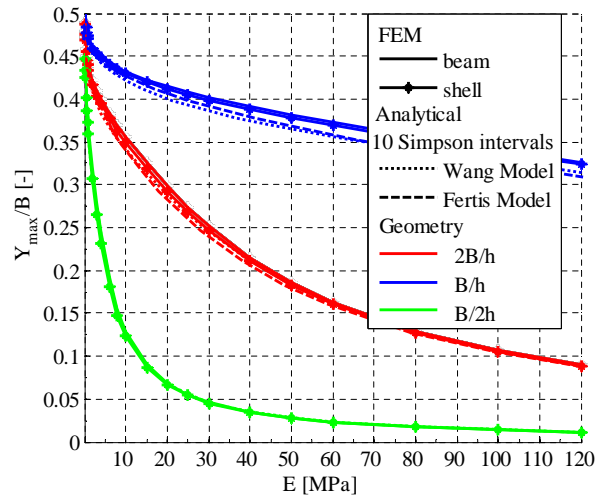


Figure 3.11: The effect of a belt geometry B/h on belt troughability, obtained using FEM beam and shell models, and also the analytical Wang and Fertis ones for beam with 10 Simpson intervals for the case study parameters set (for constant q and b , and also $b/h = \text{const}$ for the FEM shell model).

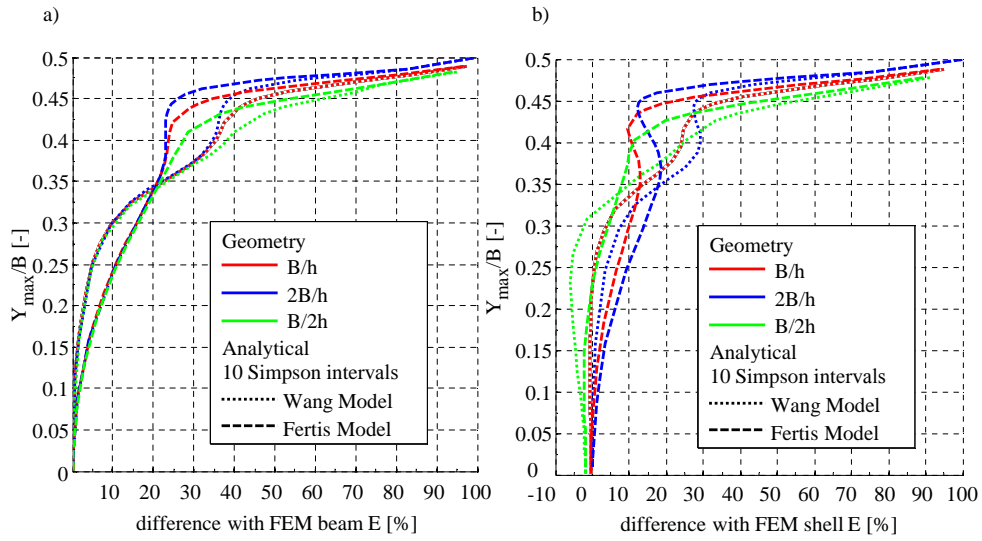


Figure 3.12: Belt troughability versus difference of elastic modulus, obtained using the analytical Wang and Fertis beam models with 10 Simpson intervals, compared to the FEM beam and shell model for the case study parameters set (keeping constant b , q , and also b/h for the FEM shell model) and geometrical ratios $B/2h$, B/h and $2B/h$.

more significant. Due to the Poisson effects incorporated by the FEM shell model within Mindlin-Reissner theory, the bending stiffness for the shell model is less, compared to the one determined using analytical beam models (no shear Euler-Bernoulli theory), and also the FEM beam model (Timoshenko theory that accommodates the shear effect only in one plane).

Considering the limits of $6.67 \leq B/h \leq 643$, established specially for conveyor belts in Section 2.5.2, the problem is associated with the geometry ranging from thick to very thin structures. Figure 3.13 represents the results, achieved for these limits for belt width $B = 3215$ mm and $B = 300$ mm and different thickness values (see Section 2.5.2). Since the influence of the line mass is proportional to the change in modulus of elasticity, the dependence curves are created for one value of $q = q_{bw} \approx 40$ N/m ($m''_{belt} = 27$ kg/m² for $l = b = 0.15$ m), selected as the average. The results are obtained using only beam models, as the shell solution and impact of b/h for each slenderness step B/h is considered in the next section.

The results show that for troughability values, starting from 0.05, with the increase of B/h the dependence curve becomes excessively flat, which explains the significant sensitivity of the results to the troughability values. Also for the same ratio $B/h \approx 86$, the resultant function for width $B = 300$ mm completely coincides with the one for $B = 3215$ mm. This fact shows that the belts' troughability does not depend on either width or thickness individually. Only their ratio B/h is necessary and sufficient to reflect the impact of a belt geometry for beam models.

Figure 3.14 shows the difference between the FEM beam and analytical Wang beam

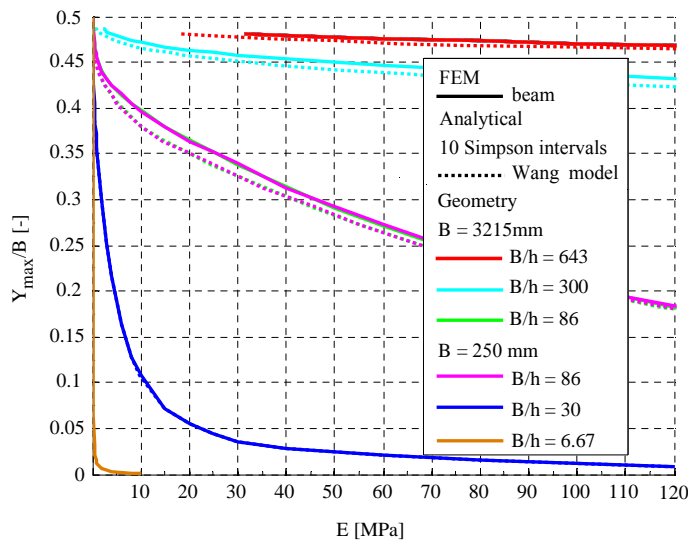


Figure 3.13: Effect of a slenderness ratio B/h change on belt troughability characteristics versus varied modulus of elasticity, within the range, established for conveyor belts and belt weight $q \approx 40 \text{ N/m}$, obtained using FEM beam model and Wang beam model with 10 Simpson intervals.

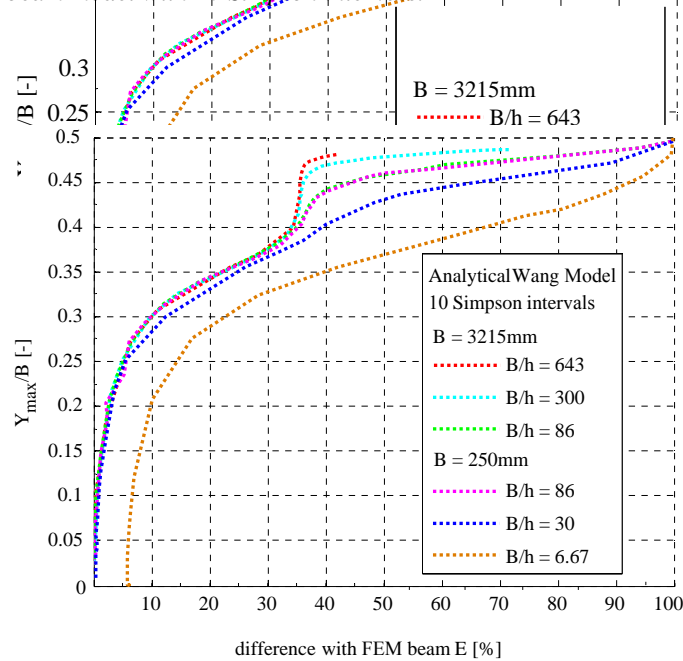
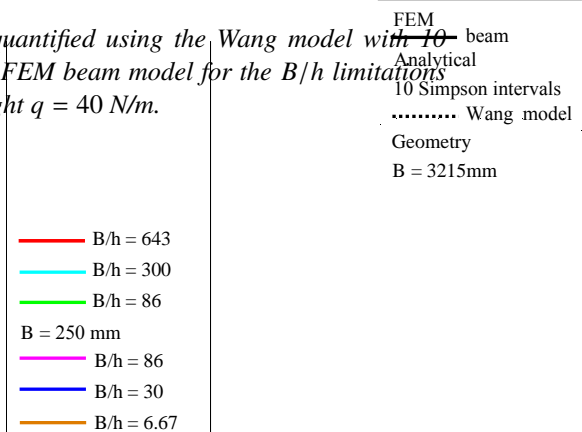


Figure 3.14: The difference in elastic moduli, quantified using the Wang model with 10 Simpson intervals in respect to the FEM beam model for the B/h limitations inherent to conveyor belts with weight $q = 40 \text{ N/m}$.



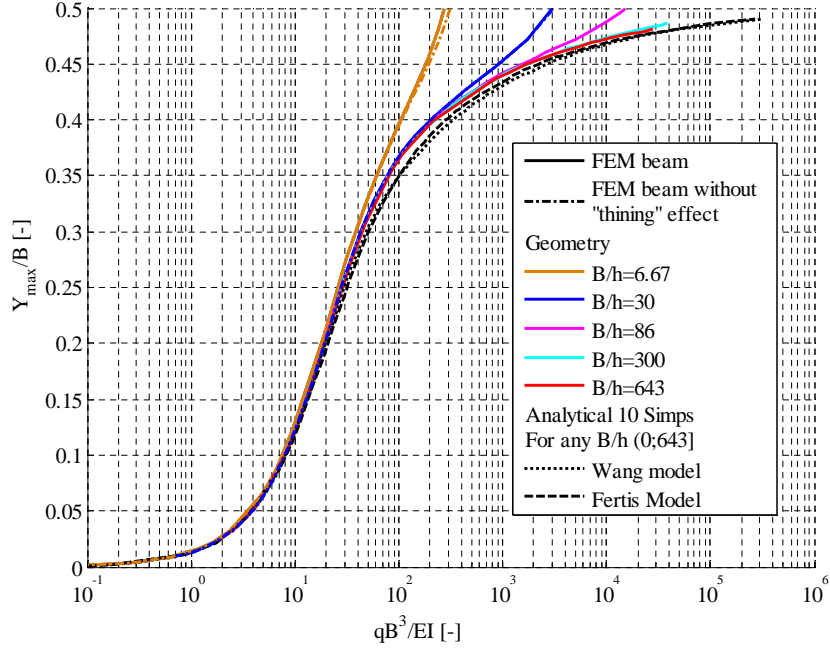


Figure 3.15: Load-deflection parametric curve for FEM beam model and using the models of Wang and Fertis with 10 Simpson intervals within specified conveyor belts' parameters range.

model. The difference increases with the increase of ratio B/h due to the geometrical stiffening effect. It appears due to the fact that the Wang model assumes only nonlinear bending, whereas the FEM shell incorporates also the axial stretching effect. Though, for a very thick structure with $B/h = 6.67$, the difference is also high even for the very small troughability values. This is a result of shear effects, which are included in the FEM model that follows the Timoshenko beam theory, but not in the model of Wang that follows the Euler-Bernoulli theory, not suitable for thick beams.

Establishing the dimensionless dependence between the input parameters of belt geometry, weight and the troughability value, the following load-deflection function for beam models can be derived:

$$\frac{Y_{\max}}{B} = f_{\text{T}}^{\text{beam}} \left(\frac{qB^3}{EI}; \frac{B}{h} \right). \quad (3.37)$$

Figure 3.15 illustrates that parametric load-deflection curve in relative scale for numerical results using the FEM beam solution, and analytical results from the Wang and Fertis approaches with 10 Simpson intervals. It is possible to observe that the inextensible analytical beam models of Wang and Fertis exhibit rather similar results and show mechanical behavior dependent only on the selected load factor, which is necessary and sufficient for these models. However, for the FEM beam, the stiffening effect takes place, as for the same modulus of elasticity, thinner and wider belts produce larger deflections than thicker and narrower ones. In addition, if the FEM beam models are obtained without scaling the beam cross section

as a function of an axial stretch, the so-called “thinning” effect, is only influential for very thick and narrow belt samples (see dash-dot line for ratio $B/h = 6.67$). As for $B/h = 30$, this effect is very small and can already be ignored due to its minor role.

As it can be seen, within the certain limitations of belt design input parameters, the analytical inextensible beam models of Wang and Fertis exhibit a satisfactory correlation with the more precise FEM beam model that in addition of the nonlinear bending includes axial stretching and shear effects. This is especially important, since the analytical models solve an implicit problem directly and is more simple and attractive for the application in practice. At the same time, more precise FEM model cannot solve indirect problem and the effective E -modulus is determined from the more complex iterative procedure of solutions that is not attractive for the practical use.

Belt sample width-to-thickness ratio b/h

Besides of the belt slenderness (B/h), the ratio (b/h) influences the solution for the shell model. Figures 3.16 illustrates the results for the case study set (see Table 3.3 for given B , h and q) and varied Young’s modulus. The results are obtained for $2b/h$, b/h , and $b/2h$ geometrical ratios. The troughability, obtained using FEM shell, corresponds to the deflection measured at the central position of the belt sample with respect to sample span B and also width b . The results in Fig. 3.16 indicate that the model produce qualitatively similar results.

Figure 3.17 shows the difference between the analytical beam models and the FEM (beam and shell). Figure 3.17a shows that for the beam models, the difference between the analytical models and FEM is independent from the change in ratio b/h . As for the shell solution (Figure 3.17b), both analytical models of Wang and Fertis overestimate the

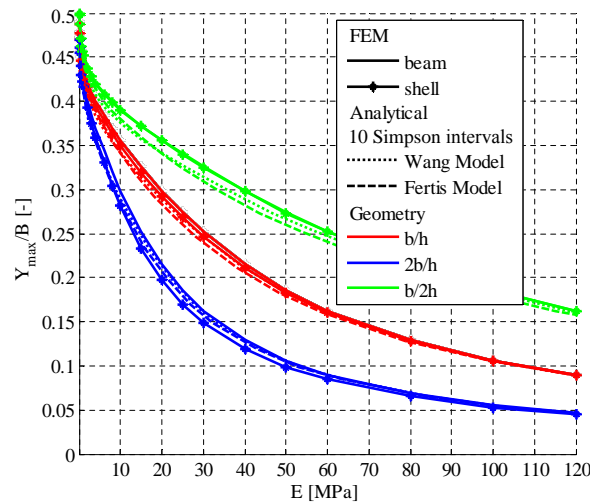


Figure 3.16: Effect of ratio b/h on belt troughability, obtained for the case study using FEM (beam and shell) models and analytical beam models of Wang and Fertis with 10 Simpson intervals. The results are obtained for $B/h = \text{const.}$

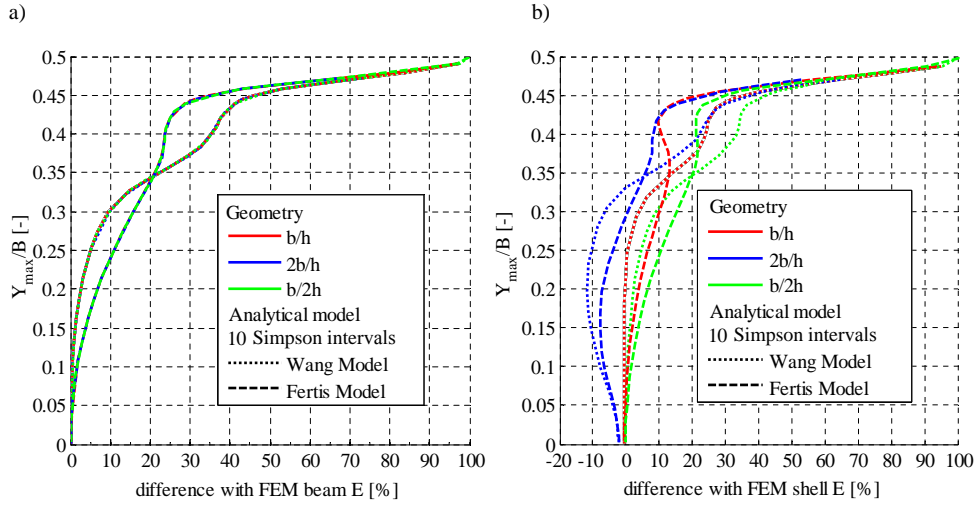


Figure 3.17: Relative difference between the FEM shell and beam models with respect to the analytical beam models of Wang and Fertis, obtained with 10 Simpson intervals and belt geometry b/h , $2b/h$, and $b/2h$. The results are obtained for $B/h = \text{const.}$

E -modulus, compared to the FEM shell solution for larger ratio b/h . This appears due to the additional Poisson effect included in the FEM shell model following Mindlin-Reissner theory that decreases the bending stiffness of the structure. Since the Wang and Fertis beam models do not take shear effect into account, they interpret the smaller deflection with higher modulus of elasticity.

Considering the anticlastic curvature effect according to the Lamb's theory, if the relatively thin and flat rectangular structure is bent around an axis parallel to one of its edges, the structure can exhibit additional transverse curvature in the direction parallel to the bending axis. Wang *et al.* [234] state that the shape of the curvature depends on the dimensionless parameter $\zeta = b^2/(rh)$ that takes into account the radius of the initially intended curvature of bending. Wang *et al.* [234] elucidates that if ζ is around the unity and less, the structure behaves like a beam in plane stress. If $\zeta \geq 20 \dots 25$, the anticlastic curvature is developed mostly close to the edges, whereas the central part remains relatively flat. This effect better replicates the shell-like behavior with plane-strain limiting approximation. Bellow *et al.* [14] mention that the shape can be considered cylindrical when $\zeta > 1000$.

The radius of the curvature R depends on the shape of the belt sample deformed. It can be characterized by deflection Y_{\max} and the horizontal distance between the edges of the structure after deformation $2l_x$ (see Figure 3.4). Both these parameters represent the functional dependence of the ratio B/h with respect to $(qB^3/(EI))$. If the maximal deflection is excessively large, as it happens when the neutral axes are stretched, the radius of curvature decreases and the parameter ζ also reduces. In this case the beam-like approximation becomes relevant.

Ultimately, the functional dependence between the troughability parameter, and belt

sample input parameters, can be expressed as following generalized function:

$$\frac{Y_{\max}}{B} = f_T^{\text{shell}} \left(\frac{qB^3}{EI}; \frac{B}{h}; \frac{b}{h} \right). \quad (3.38)$$

Taking into account the troughability requirement of $b = (150 \pm 2)$ mm and also considering the limitations established in Section 2.5.2 for B and h , inherent to conveyor belts, it becomes possible to determine the minimum and maximum possible ratios b/h with respect to each geometrical step B/h . These extreme values of b/h and their geometrical realization for modeling within B and h , are provided in Table 3.6. As it can be seen, the variation of b/h is different for each of the ratio B/h , and the largest variation appears for the average $B/h = 86$.

Table 3.6: The extreme values for b/h inherent to conveyor belt and its extreme realization for each of the geometrical step B/h .

B/h	Minimal b/h , $b = 148$ mm			Maximal b/h , $b = 152$ mm		
	b/h	B , mm	h , mm	b/h	B , mm	h , mm
6.67	3.289	300	45	3.378	300	45
30	3.289	1350	45	15.2	300	10
86	3.959	3215	37.38	30.4	430	5
300	13.81	3215	10.717	30.4	1500	5
643	29.6	3215	5	30.4	3215	5

For these geometrical input parameters, the results are obtained for the minimum and maximum ratio b/h for each geometrical step B/h using FEM beam and shell FEM models, and the analytical Wang beam model (beam in plane stress state with bending stiffness EI) and the Wang shell-approximating model (plate in plane strain state with bending stiffness $\frac{EI}{(1-\mu_1\mu_2)}$).

The analysis for the geometrical range established for conveyor belts (see Section 2.5.2 and Table 3.6) reveals that the maximal possible difference of 10.9% in deflection at the center and at the edges of the belt sample appears for the extreme maximal value $b/h = 3.378$ and $B/h = 6.67$. As for the more frequently appeared $B/h \approx 86$, the maximal possible $b/h = 30.4$ generates the difference of no more than 6.5% for $Y_{\max}/B < 0.165$. For $0.165 \leq Y_{\max}/B \leq 0.212$, the difference decreases until no more than 1% and stays at that value for $Y_{\max}/B > 0.212$. Then it is possible to state that belt with given geometrical parameters conforms a cylindrical shape, for the beam-like plane stress state ($Y_{\max}/B \geq 0.212$) and plate-like approximating plane strain state ($Y_{\max}/B \geq 0.212$), respectively.

Taking into account the sensitivity of the models for quantifying E -modulus with respect to the deflection determined from the experiment test, the position of the troughability measurement needs to be carefully controlled during the test. The authors recommend performing the measurements at the center of the belt sample, as closer to the edges the anticlastic curvature effect can influence the results.

Figure 3.18 shows the load-deflection parametric curve for the normalized belt geometry $B/h = 86$ that appears more frequently in industry. The results, obtained for the FEM beam and shell models and the analytical Wang beam and Wang shell-approximating models,

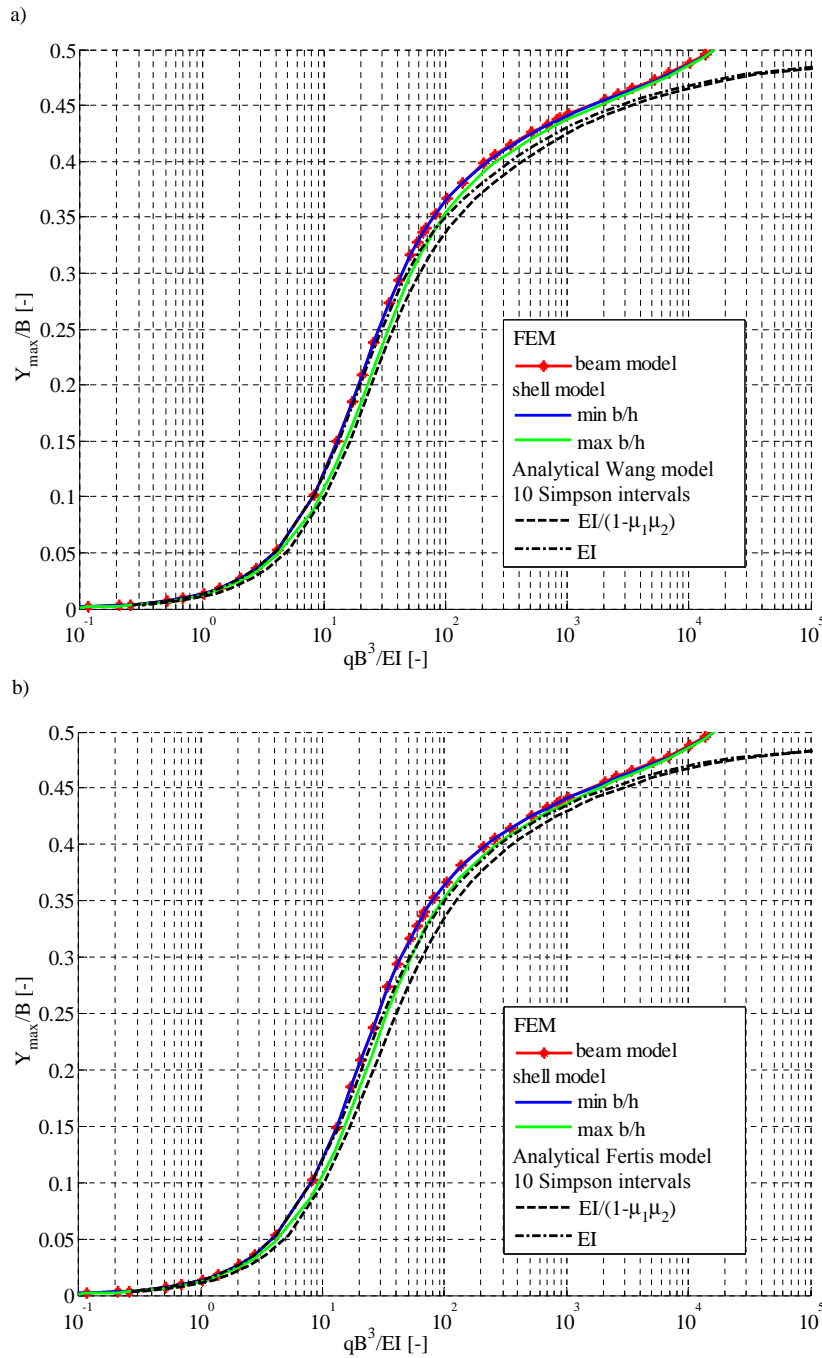


Figure 3.18: Load-deflection parametric curve $B/h = 86$ for the FEM solution of beam and shell models at the structural center and also using the analytical models of a) Wang and b) Fertis with 10-Simpson intervals within specified minimal and maximal ratio of b/h .

produce the similar dependence. For the shell models, the troughability corresponds to the central position of the sample.

Comparing the FEM beam and FEM shell solution with each other, it is possible to see that for minimal ratio b/h the models produce close results, whereas for the maximal b/h , the difference between FEM beam and FEM shell increases. This is due to the fact that the Timoshenko theory incorporated in the FEM beam model does not take into account the Poisson effects in additional plane, whereas the FEM shell model following the Mindlin-Reissner theory does. That is why, for larger ratio b/h , the difference between FEM shell and beam becomes more noticeable.

In comparison to the analytical model for smaller ratio b/h and also in the case of insignificant troughability values, the FEM solution (both beam and shell) behaves beam likewise and better conforms to the inextensible Wang beam model, as the structural stretching effect is not that significant. As for the maximum value b/h , and also when the troughability values are not that large, the FEM shell model better conforms to the shell-approximating Wang model representing the shell in plane strain state. This happens due to the fact that the structure behaves like a shell in plane strain state and also the impact of axial stretch is minimal. These observations are also relevant if the Fertis beam and shell-approximating models are used.

3.7.5 Strain limitation

The usage of the models, described for quantifying the belt's bending stiffness from the troughability test, is limited by the assumption of constant modulus of elasticity (see Section 3.2), which stipulates small strains (up till 5%) inherent to conveyor belts under normal operational conditions.

The maximum strain is detected using FEM shell model, which appears at the compressed side of the belt sag right at the edges of the deflection (with respect to the sample width b). As for the beam models (either Wang or Fertis or FEM), the maximal strain occurs at the compressed side of the structure at the central position of the sag with respect to the belt sample width b and sample span B . Figure 3.19 illustrates this maximum strain at the central position, determined by Wang model and FEM for beam and shell elements for minimum and maximum b/h ratios.

The figure shows the limitation for small strains that is $\varepsilon \leq 5\%$ for the models. For the analytical models, the strain is determined for beam in plane stress state as:

$$\varepsilon = \frac{ql_x^2 h}{4EI}, \quad (3.39)$$

whereas for the shell-like approximation in plane strain state, it equals:

$$\varepsilon = \frac{ql_x^2 h}{4EI} (1 - \mu_1 \mu_2). \quad (3.40)$$

The analytical results exhibit similar trend as the FEM solution. The graphs show that the ratio b/h does not affect the strain determined; only the selection of the approach has an influence on the results. Moreover, the shell-like approximation for the analytical models (Wang or Fertis) coincides with the corresponding solution obtained using the same model but for the beam in plane stress state.

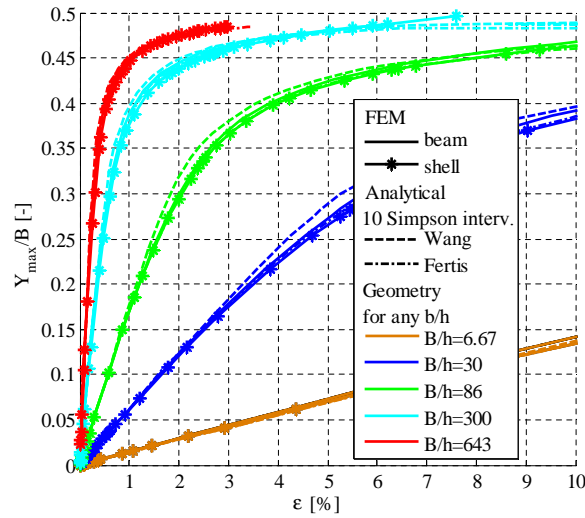


Figure 3.19: Belt troughability, obtained with FEM beam and shell model in ANSYS and using the Wang and Fertis models with 10 Simpson intervals versus maximum strain appeared in the central point of the belt sag in the compressed side of the structure.

The recommendations for using each of the model including 5% strain limitation and satisfying also 10% difference between the analytical model of Wang and numerical ANSYS solution for beam and shell models are reflected in Tables 3.8 and 3.7. A set of the guidelines is provided at the end of this Chapter that summarize the analysis and the results obtained. These guidelines can be useful for the practicing engineers aiming to utilize the analysis in industry.

3.8 Guidelines for practicing engineers

The following guidelines can be used in order to determine a conveyor belt bending stiffness based on the troughability test.

- 1). Store a testing belt sample horizontally in a flat surface following the recommendations for conditioning ISO 703 [174], ISO 18573 [115].
- 2). Measure the belt's troughability from the experimental test according to the standard ISO 703 [174] at the center of a belt sample with respect to its span (width of a belt B) and the sample width b .
- 3). Measure the average thickness h , a belt width B (sample span), and the longitudinal length b of the belt sample (see recommendations e.g., ISO 583 [173], 7590 [175], 15236 [170] and also DIN 22129 [49]). Determine the moment of inertia of the structure $I = bh^3/12$.

Table 3.7: Troughability values for geometrical slenderness B/h and the critical ratio b/h that specify limitation of using the model of Wang and Fertis with respect to the FEM shell model.

Belt geometry			Troughability value				
B/h	b/h		FEM shell 5% Strain limit.	Analytical model 5% Strain limit. (up till 10% diff. with the shell FEM)			
				Wang		Fertis	
				EI	$\frac{EI}{(1 - \mu_1 \mu_2)}$	EI	$\frac{EI}{(1 - \mu_1 \mu_2)}$
6.67	min	3.289	≤ 0.067	≤ 0.069	-	≤ 0.069	-
	max	3.378	≤ 0.066	≤ 0.069	-	≤ 0.069	-
30	min	3.289	≤ 0.258	≤ 0.289	-	≤ 0.245	-
	max	15.20	≤ 0.223	$\leq 0.050, 0.271 \dots 0.285$	0.090...0.268	$\leq 0.050, 0.195 \dots 0.268$	-
86	min	3.959	≤ 0.416	≤ 0.305	-	≤ 0.245	-
	max	30.40	≤ 0.402	$\leq 0.045, 0.285 \dots 0.360$	0.050...0.255	$\leq 0.048, 0.208 \dots 0.430$	0.080...0.160
300	min	13.810	≤ 0.473	≤ 0.315	-	≤ 0.251	-
	max	30.40	≤ 0.473	≤ 0.355	-	≤ 465	-
643	min	29.60	≤ 0.485	≤ 0.340	-	$\leq 0.320, 0.390 \dots 0.475$	-
	max	30.40	≤ 0.482	≤ 0.340	-	$\leq 0.325, 0.385 \dots 0.475$	-

- 4). Measure the sample's mass M_{bw} on a weight scale and determine distributed belt weight $q = q_{bw} = M_{sg}/B$.
- 5). Based on the troughability value and geometrical ratio of the belt sample B/h and also b/h , select the appropriate method for quantifying the belt's bending stiffness. Analytical Wang or Fertis models are selected, if they yield no more than 10% difference with the FEM solution. The usage recommendations for the troughability values with respect to the belt's geometry are provided in Table 3.7 and Table 3.8.
- 6). Determine an effective modulus of elasticity E . In case of the analytical models: for the Wang model, use Eqs. 3.19, 3.22 and 3.23, and for the Fertis model, use Eqs 3.34, 3.22 and 3.23. No more than 8 Simpson intervals need to be incorporated. In case of the FEM solution, for $B/h > 30$ the thinning effect of the structural cross section can be neglected.
- 7). Check, if the maximum strain *varepsilon* does not exceed the requirement of up till 5%. For the Wang and Fertis models, the strain equals to a percentile ratio, given in Eq. 3.39 for a beam-like plane stress-state and Eq. 3.40 for a plate-like plane strain state approximation for the structural behavior, respectively.

Table 3.8: Troughability values for geometrical slenderness B/h that specify limitation of using the model of Wang and Fertis with respect to the FEM beam model.

Belt geometry Ratio B/h (for any ratio b/h)	Troughability value	
	FEM beam 5% Strain limitation	Wang model 5% Strain limitation (up till 10% diff. with the FEM beam)
6.67	≤ 0.072	≤ 0.070
30	≤ 0.270	≤ 0.285
86	≤ 0.425	≤ 0.300
300	≤ 0.480	≤ 0.300
643	≤ 0.500	≤ 0.307

3.9 Conclusions

The following conclusions can be drawn from this chapter. The chapter shows that it is possible to determine a conveyor belt bending stiffness from the troughability test ISO 703, assuming a linear-elastic behavior of a conveyor belt for small strains (up till 5%) as a simply supported beam-like or a shell-like structure, subjected to the distributed self-weight.

To quantify a conveyor belt bending stiffness from the troughability parameter, five models were proposed: two analytical beam models of Wang and Fertis that assume inextensible Euler-Bernoulli structural bending, FEM beam model that takes into account axial stretching and shear (Timoshko beam); shell-approximating analytical models on the basis of Wang and Fertis; and FEM shell model that accounts all the effects using Mindlin-Reissner theory.

The results, obtained using the analytical and FEM models (both beam and shell) are in agreement with the experiment and exhibit the similar resultant trend.

The troughability parameter can be represented by the load-deflection parametric function of a belt bending stiffness EI , belt weight q , belt width B , and belt geometry, represented by the ratio B/h and b/h , as follows:

$$\frac{Y_{\max}}{B} = f_T^{\text{shell}} \left(\frac{qB^3}{EI}; \frac{B}{h}; \frac{b}{h} \right).$$

Results show that for the same troughability value, an impact of a belt line mass change q has a proportional effect on change in effective modulus of elasticity E for the same belt sample geometry. The effect of a belt line mass is less significant for the problem behavior than the influence of a belt geometry.

Considering the effect of a belt slenderness B/h , thin and wide conveyor belts with significant ratio B/h exhibit larger troughability for the same E -modulus, compared to more thick and narrow belts with smaller ratio B/h . This stiffening effect appears due to extension of structural neutral axes in addition to the nonlinear bending and becomes dominative when thin and wide belt samples exhibit very large troughability. At the same time, thick or narrow conveyor belts are affected by shear deformations, which are not trivial for belts with minor B/h .

For the shell numerical models, the influence of the belt sample geometry on the results needs to be represented not only by the structural slenderness B/h , but also by the ratio b/h . The latter characterizes an additional shear effect that appears in other two planes, orthogonal to the plane of the initial structural bending.

In addition, the ratio b/h represents the appearance of the anticlastic curvature effect. This effect causes the difference in the deflection measured at the center of the belt sample along the sample width b , compared to the edges of the anticlastic “saddle” shape. It can generate 10% difference in deflection at the center and at the edges of a belt sample for $B/h = 6.67$, whereas for the normalized and most frequently appeared belt slenderness $B/h = 86$, it constitutes no more than 6.5% difference. Due to this fact, the present chapter concludes that it is preferable to perform measurements at the center of the belt sample, as, close to the edges, the deflection can be significantly influenced by the anticlastic curvature effect by obtaining the “saddle” shape.

Considering the usage limitation of the models proposed, it was found that the Wang beam model is more preferable for the analysis instead of the Fertis model, as it gives a better correlation with the FEM beam model for larger range of the troughability values with the difference up till 10%. As for the shell solution, the impact of b/h influences the selection. In particular, for larger ratio b/h , the Fertis model generates better correlation with the FEM shell solution, whereas for the smaller b/h , the Wang model is more preferable. All the models proposed are limited to the small strain range (up till 5%). The usage limitation of all the models proposed are provided in Table 3.8 and Table 3.7 for the full range of a belt slenderness B/h variation.

Present chapter concludes, within the certain limitations of a belt design, the analytical models of Wang and Fertis (both beam and shell) predict a conveyor belt bending stiffness with satisfactory precision with respect to the more precise and complex FEM beam and shell models. The more simple analytical models that solve the problem directly are attractive

for the practical use, compared to the more complex FEM models that require iterative solution procedure. Within the usage limitation established in Table 3.8 and Table 3.7, it is possible to use a more simple and practically attractive analytical models, and, for the certain parameters beyond those limitations, the FEM approach is recommended to be used.

Based on the analysis made, the future research needs to focus on incorporating the non-uniform belt design structure with discrete change in properties along the belt width. In addition, the further studies have to investigate the impact of the belt's viscoelasticity (time and temperature) on the belt's troughability and bending stiffness quantified. The analysis can also integrate the nonlinear elastic models (e.g., the Mooney-Rivlin, Ogden models) for the comprising rubber-like elastomeric materials of a conveyor belt, expanding the solution for larger rate of strains (more than 5%).

A conveyor belt bending stiffness, quantified from the troughability test according to the procedure described, is a fundamental parameter needed in this thesis. In particular, belt bending stiffness is not only responsible to a belt's mechanical response towards all the loads involved, but also it represents an additional expansion load that appears from folding a pipe conveyor belt from a flat shape into a pipe shape. Both these issues influence a PBC CFs and ability of a conveyor belt to form a stable pipe shape without a contact loss, investigated in the next Chapter 5.

Chapter 4

Determination of Contact Forces: Experimental Approach*

"Interpretation of experiment is a matter of taste".

— P. Kapitsa, a Soviet physicist and Nobel laureate

A conveyor belt lateral bending stiffness, studied in previous Chapter 3, determines PBC CFs and belt transverse deformations. The CFs are important for the system design, as they link the mechanical behavior of a belt structure and impact of the all loads involved. The CFs influence the energy losses from the IRR, investigated in Chapter 7, and are also needed to represent the belts' ability to form a stable pipe shape (see Chapter 6).

This chapter is a first part of three subsequent chapters (Chapters 4, 5, and 6) devoted to the determination of PBC CFs. The division into three parts is made based on the approaches used. In particular, this chapter focuses on the experimental approach that determines CFs, whereas Chapter 5 uses an analytical approach, and Chapter 6 applies FEM and presents comparison of all three approaches together.

Since the CFs can be determined experimentally, the test rig configuration has to be properly selected. This chapter provides a qualitative analysis of the existing PBC test rig configurations, and selects the most appropriate test rig design that can closely replicate the analytical and FEM models for the validation purposes. In addition, using the experimental testing within the test rig selected, the present chapter aims to investigate the impact of major PBC design parameters, such as pipe diameter, belt width, transverse bending stiffness, belt's mass, and position of the belt overlap, on the load distribution between the individual idler rolls, as well as the ability of the belt to form a stable pipe shape.

4.1 Introduction

Installation, exploitation and operation of PBCs essentially depends on how the carried load is distributed between the idler rolls, as it identifies the contact forces from the each roll,

*The chapter is written partially based on the publications of Zamiralova and Lodewijks [259–262].

applied to the external belt surface. The significant effect of the load distribution between the idler rolls can be traced in various aspects, inherent to the running behavior of this type of continuous transport systems.

For instance, the CFs determine the IRR, studied in Chapter 7 of this thesis. The IRR, in turn, affects the tension calculation of an overall PBC system, which in turn leads to a higher energy losses of the conveyor. The high energy consumption relates to the choice and costs of installation parameters of the PBC, such as the motor power, take up system, life/ load rating of idler roll bearings, etc.

Another example is that the impact from the reaction forces can be observed in the twisting effect of a pipe conveyor belt. Reaction forces define a stabilizing moment from the friction forces between the external surface of the belt and the idler rolls, which counteracts the undesirable rotation of the belt.

The CFs can also indicate the large deformations of the cross-sectional geometry and belt disability to keep a stable pipe shape geometry or a belt collapse. This can be detected when one or more of the CFs become equal to zero. As stated by Zhang and Steven [270], Imai [112], the belt collapsed can cause spillage of a bulk material and tends to exhibit a larger twist in curves along the route, affecting tracking and alignment of a belt in operation. Therefore, the CFs relate to the cross sectional deformations and significantly contribute to the operation behavior of PBCs. It is thus evident that it is essential to have a precise method that can quantify the CFs in the most accurate way and detect which parameters have the most influence on them.

For this purpose, three methodologies exist: an empirical experimentation within existing PBC installations or using the test rigs that imitate the pipe conveyor belt behavior; an analytical approach that develops a mathematical model and directly calculates the CFs; a numerical solution (e.g., FEM, FDM), mostly achieved within various software. Each approach inherits both positive and negative aspects. Using all three approaches together allows them to complement each other, providing a reliable method to determine the CFs. The positive and negative aspects of each of the approach will be discussed further in this chapter and also in the subsequent Chapter 5 and Chapter 6.

Present chapter is focused on the experimental approach that can determine PBC CFs. The experimental testing can be used as an independent method for obtaining the CFs and providing an impact analysis of the system design parameters on the results. In addition, the experimental results are obligatory needed for validating the analytical model, developed in Chapter 5, and FEM models, created and described in Chapter 6.

The experiment measurements allow one to test the influence of the parameters, which are not included in the analytical models. For instance, the analytical model that will be described in following Chapter 5, is limited to the conveyor belt with a uniform layout along the belt width, i.e., evenly distributed belt bending stiffness and line mass. In addition, the impact of an overlap and pipe diameter selection with respect to the overall belt width is also ignored in the analytical model for the simplification purposes. In the contrast, the experimental approach can incorporate impact of those parameters together, including, for instance, an impact of belt tension, belt viscoelasticity, position of overlap, etc.

Number of the researchers, such as Hötte [107], Hötte *et al.* [108], Wiedenroth [247], Michalik *et al.* [156], Molnár *et al.* [159–166], Molnár and Fedorko [158], Stehlíková *et al.* [220], Xiaoxia *et al.* [252], Barburski [10] determine the PBC CFs only based on the empirical experimentation without any analytical solution. However, it is important to

emphasize that the experimental study has to be obligatorily accompanied with the analytical model. It can appear that the test rig design selection can influence the CFs measured. The differences can be due to the mistakes that might appear during the performance of some of the experiments and the abilities of a test rig configuration. In addition, the more parameters involved in the experiment, the higher the possibility of the appearance of a measurement error.

At the same time, the more complex configuration of a test rig allows one to test more different cases and perform an impact analysis of various design parameters on the CFs and belt deformations measured. For instance, the test rig design can offer a function of simple replacement of belt samples and change of a pipe diameter. This design function allows one to test impact of different belt types, length of overlap and belt's slenderness on CFs. Alternatively, the design configuration can have ability to include presence of a bulk material or simulate dynamic effects that also give more options for testing cases.

That is why it is important to analyze the design of the existing test rigs, examine their advantages and disadvantages with respect to the CFs and ability for testing different cases when the input parameters are varied. In addition, the attention has to be paid to the methods and test set-ups used for detecting the geometry of the belt deformed under the action of all the loads involved. Based on this analysis, the study selects the most appropriate design configuration for determining the CFs and belt geometry, also suitable for developing an analytical and numerical models. The choice has to be made keeping in mind that the more complex test rig design provides larger variety of the parameters for testing. At the same time, a high complexity of the test rig can cause the uncontrolled appearance of the measurement errors.

4.2 Overview of existing test rigs

Existing test rigs are analyzed by comparing the CFs measured with various test rig configurations. The results selected represent the case of an empty conveyor operation without a bulk material, with the overlap on the top (Fig. 4.1a) and at the bottom (Fig. 4.1b), as not all the test rigs allow one to model the presence of a bulk material. The bottom overlap position commonly implies the return strand of a PBC.

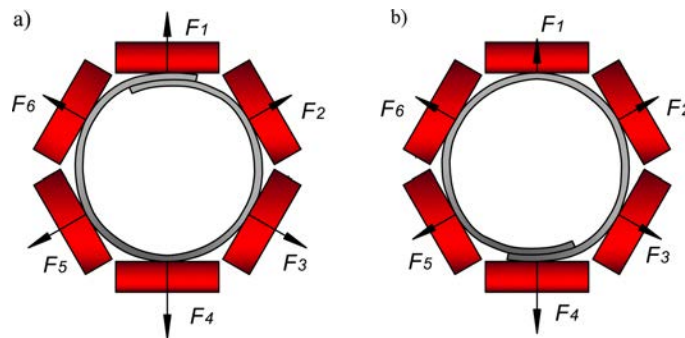


Figure 4.1: Reference pipe conveyor cross sections with CFs numerated for belt's overlap position: a) at the top; b) at the bottom.

Each of the CFs presented is given as its percentile ratio to the absolute values of all six contact forces for each test case ($F_n / \sum |F_n|$). The length of overlap of the pipe belt is presented as a ratio of the belt width to the nominal pipe diameter (B/D_{nom}). For simplification the understanding of the data from different sources, the CFs are adjusted to the belt position, forming clockwise coil, and numerated, as illustrated in Fig. 4.1. Since the belt design plays a decisive role in the PBC cross-sectional geometry and CFs, the results are supplemented with the information on the belt properties, whatsoever was provided in the source.

Due to the unavailability of detailed information on conveyor belts tested and the limited number of existing test rigs, the results selected are used only for a qualitative analysis. The test results are sensitive to errors, like an improper choice and calibration of sensors, incorrect data acquisition and processing, and human factor. Therefore, the accuracy and statistical significance of test results, obtained with various test rigs as published in different sources cannot be guaranteed.

In general, the existing test rig configurations can be classified based on their ability to perform static and/or dynamic tests, and also ability to determine the cross-sectional geometry of the belt deformed. The current overview classifies the test rigs as following:

- 1) static six point stiffness devices;
- 2) static test rigs with various frames and supports;
- 3) dynamic test rigs and field measurements;
- 4) the test rigs with inherent experimental methods used to determine belt geometry deformed.

Present section analyzes each type of test rig configuration independently.

4.2.1 Static six-point stiffness devices

A number of the researchers perform their experimental studies using six-point pipe belt stiffness device. One of the prototype of that kind, shown in Fig. 4.2, was assembled at the laboratory of **Delft University of Technology, Section of Transport Engineering and Logistics** [42]. It consisted of a wooden frame with six plates, situated hexagonally. Twelve sensors were mounted in between the frame and the plates, wherein two sensors were used for the each plate. For the measurements, three samples of the same type of a pipe conveyor

Table 4.1: Belt properties and experiment details, used for the measurements used in laboratory in Delft University of Technology, Section of Transport Engineering and Logistics [42].

Sample	Belt Type	B , mm	B/D_{nom}	Troughability	Overlap	Tension
1				0.334		
2	ST 3500	≈ 1800	≈ 4	0.341	top	no
3				0.341		



Figure 4.2: Test prototype of a static six-point stiffness device, assembled at Delft University of Technology, Section of Transport Engineering and Logistics, the Netherlands (Figure from [42]).

steel cord belt were used with an approximate length of 150 mm. The belt properties and ratio between the belt width and pipe diameter are shown in Table 4.1.

The sensors measured the load in radial direction for approximate 10 seconds with sample rate of 5 Hz for each case. The average sum of the results, obtained from both sensors, represented the CF, acting on the corresponding plate. The experiment was performed two times for each sample (Test 1 and Test 2). The test results are presented in Fig.4.3.

Analysis of the data shows that the results for the same belt type, same length of overlap and belt width can differ between the tests significantly. This can be explained by the fact that the friction between the external surface of the belt and wooden hexagon plates was not controlled during the tests. The sensors measured only loads in radial direction, consequently the force components from the friction that can be significant, were not detected by the measuring equipment. Moreover, the friction between the belt edges was not eliminated as

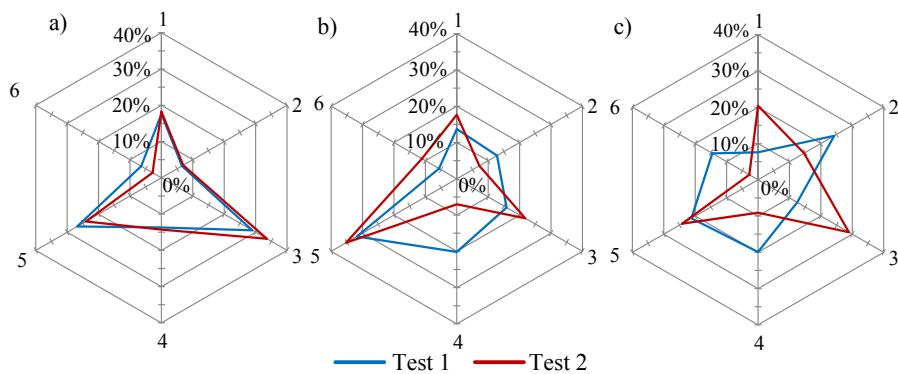


Figure 4.3: The CFs $F_n / \sum |F_n|$ (%), obtained from the test set-up at Delft University of Technology, Section of Transport Engineering and Logistics [42], measured two times (Test 1 and Test 2) for each of the belt sample: a) 1, b) 2, and c) 3. The results are adjusted according to the reference numeration and overlap position, provided in Fig. 4.1a.

well, and the belt tended to “stick” on itself at the overlap. As a result, the measurement data was very sensitive to the way the belt samples were placed in the test rig.

As for the advantageous aspects of this test configuration, it can be mentioned that the test rig is light, compact and cheap. The experiment is easy to perform and requires belt samples with the short length, which makes it possible to use the same samples as used for the troughability test. The assembly of two sensors per plate provided additional information about which side of the supporting plate had a greater load, reflecting the load distribution along the belt coil. Moreover, the impact of friction on the test results could be reduced by means of the special material sheets with low friction coefficient that can be inserted between the belt and the plates and also the overlapping edges of the belt. The relaxation effect due to the viscoelastic properties of the belt rubber compounds originally was not considered in the results. However, this can be corrected by extending the experiment time performance for each of the case.

The major disadvantage of the test rig is that it was designed only for the specific width of the samples available in the laboratory. This implies that the construction of the test rig could not be adjusted for different belt samples, length of overlap, and length of the supporting hexagon plates.

Based on the same design concept, the PBC six-point stiffness devices are elaborated being equipped with a mechanism for forming different pipe diameters for the various

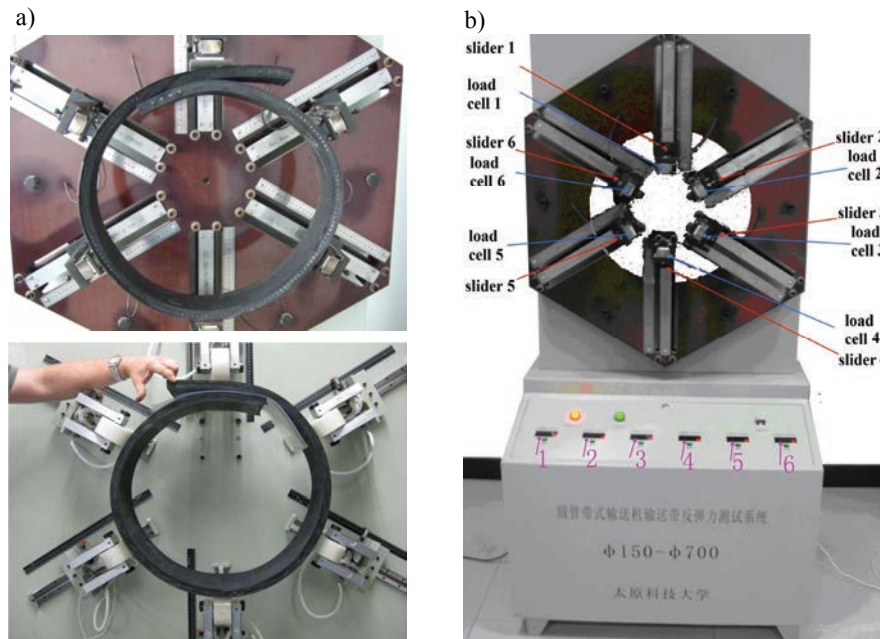


Figure 4.4: Six-point stiffness testing devices, elaborated by: a) Conveyor Dynamics Inc. together with Goodyear Engineered Products, Veyance Technologies Inc. [270] (Images courtesy of Conveyor Dynamics Inc. and Goodyear Engineered Products, Veyance Technologies Inc.); b) Taiyuan University of Science and Technology, China (Image from Xiaoxia et al. [252]).

belt widths and required length of the overlap. One of the test rig developed by **Conveyor Dynamics Inc.** together with **Goodyear Engineered Products, Veyance Technologies Inc.**, was mentioned by Zhang and Steven [270] (see Fig. 4.4a). Similar test rig configuration was introduced by Xiaoxia *et al.* [252], **Taiyuan University of Science and Technology, China** and illustrated in Fig. 4.4b. The six-point test devices presented also can perform experiments with belt samples with length, similar as it is required for the troughability test. However, for the particular test rig configurations, there are no quantitative test results available in the sources mentioned [252, 270].

Besides the studies mentioned, the results on PBC CFs were presented by Hötte [107] using six-point stiffness device, designed by the **Institute of Transport and Automation Technology (ITA) at Leibniz University of Hannover**. The construction became a main basis for the device prototype of **Phoenix Conveyor Belt Systems GmbH**. Hötte [107] described the set-up that also consisted of six hexagon plates, attached to the load cells that serve for measuring the radial normal forces. The design incorporated the usage of replaceable plates of various lengths and assemblage for modeling different pipe diameters. The sampling rate of 1 Hz was achieved together with storing data option throughout 24 hours. Impact of friction was eliminated by using talcum and two layers of Teflon® foil paper inserted between the plates and external surface of a belt sample. The measurements were controlled by fulfilling the condition that the vertical projection of CFs gave the total weight of the sample, and the projection of the CFs in lateral direction had to coincide with the theoretically calculated value.

The Hannover six-point stiffness device was also used for imitating lateral loads that appear at curves of a conveyor route due to the belt tension. Hötte [107] proposed a design solution to apply eight concentrated lateral forces on a pipe-shaped belt circumference (see Fig. 4.5). The way these forces were applied to a belt (either directly at the steel cords,

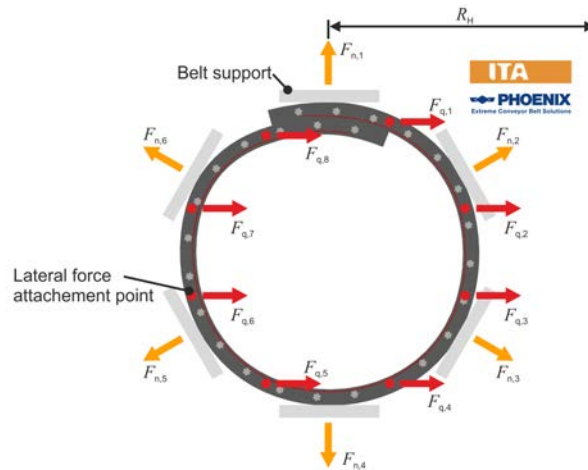


Figure 4.5: Approximate sketch of the static six-point stiffness device, assembled in Institute of Transport and Automation Technology (ITA) at Leibniz University of Hannover [107] (Image courtesy of Institute of Transport and Automation Technology (ITA) at Leibniz University of Hannover and Phoenix Conveyor Belt Systems GmbH).

Table 4.2: Properties of belt samples, used in experiment in Institute of Transport and Automation Technology (ITA) at Leibniz University of Hannover [107].

Sample	Belt Type	B , mm	B/D_{nom}	Overlap
A, B, C	ST 3150	1925	3.63	top

remained after the belt sample was stripped from the rubber at the edges prior the test, or by means of another clamping mechanism) was not specified in the source for the confidentiality reasons. The position of forces application had to be approximately equidistant along the belt contour. The values of loads were calculated based on each point's circumferential position, hypothetical radius of conveyor route curve in horizontal plane R_h , shown in Fig. 4.5, and also the desired theoretical belt tension and conveyor pitch. The lateral forces were applied symmetrically from both sides of the sample. The way the position of the selected points was measured on the belt contour was not clarified in the source. Hötte presented the results for CFs between the hexagon plates for loading conditions equivalent to the straight section and by means of eight concentrated forces simulating route curves in horizontal plane from 300 till 1000 m with a hypothetical conveyor pitch of 1 m and a tension of 300kN.

For the experiment, Hötte [107] used three samples of different pipe conveyor belt types with 150 mm length, named Sample A, B and C. These samples were attained from belts with the same minimal tensile strength and nomenclature type, but different in structural design, in particular different transverse reinforcing materials and also rubber compounds present in belt core and covers. Some of the belt samples properties are given in Table 4.2.

Furthermore, the measurements were carried out for complete 24 hour time period. The researcher reported that during the first two hours results decreased dramatically due to the relaxation effect. After 16 hours, they asymptotically reached a certain value. For the analysis, Hötte [107] recommended to use averaged results, obtained after 22 hours of the experiment. Figure 4.6 illustrates the load distribution between the idler rolls.

The researcher reported that during the overall 24-hour test, the sample C with a higher stiffness showed a larger relaxation percentage decrease of CFs compared to the Sample A with lower stiffness. Nevertheless, in absolute values, the CFs of Sample C still remain larger than generated results of other samples. This observation indicates that the viscoelastic properties of rubber compounds has an important significance for a PBC belt behavior.

To study the influence of temperature on the CFs due to the viscoelastic properties of a belt, Hötte performed tests in an environmental chamber, varying the ambient temperature from -20°C till 40°C with 20°C step of increase. The temperature effect on the CFs was characterized by considering the change of the sum of the CFs in absolute values $|F_n|$ for each of the samples. The influence of the temperature on the CFs load diagram was not present in the source.

With the six-point stiffness device, Hötte also carried out tests, qualitatively modeling load from bulk material. For this purpose, he used an over-sized compliant plastic bag as a container filled with water. The hydrostatic pressure was selected aiming eliminate the effect of the internal friction normally apparent in the bulk material. For supporting the container with water placed in the test rig, the cross section of the pipe-shaped belt was sealed with Plexiglas, attached to the test rig frame from both sides with no contact to the belt sample.

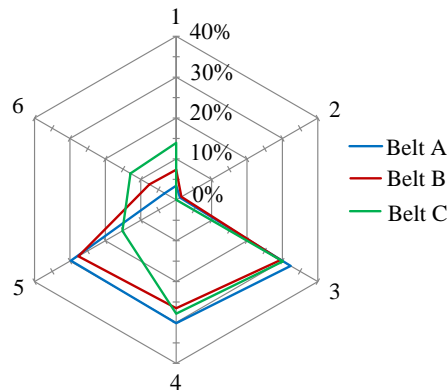


Figure 4.6: The CFs $F_n / \sum |F_n|$ (%), averaged from the data acquired from 22 till 24 hours of the experiment from the PBC six-point stiffness device, assembled in Institute of Transport and Automation Technology (ITA) at Leibniz University of Hannover [107] for three types of the belt samples, denoted as A, B and C at a straight section of a PBC (adjusted to the reference Fig.4.1a).

Additionally, performance of this test required elimination of the friction between the water container, belt surface and Plexiglas seals. Noteworthy to mention that usage of water in compliant plastic bag does not realistically imitate the impact of a bulk material pressure on the belt surface inside the pipe of PBC.

In addition, the method of imitating tension induced lateral loads from the horizontal route curve, described by Hötte, does not provide information about twisting tendency of a pipe conveyor belt. Due to the reduced length of belt samples, the problem does not reflect the effect of the shear stress flow in belt's lateral cross section, which can be influential in the phenomenon. Moreover, it needs to be carefully investigated, whether eight concentrated forces in respect to rather large belt width is sufficient to replicate similar loading condition as it happens in practice. Even though the test rig, described by Hötte [107], reflects the hypothetical tension induced by lateral loads, it was not capable to replicate the physical structural behavior and deformations under the action of tensile forces. This observation is relevant for all existent six-point stiffness devices.

Summing up, it is important to emphasize that all the six-point stiffness testing devices described have a number of significant advantages. Due to low manufacture, installation and assemblage costs, mobility and simple test performance, this type of the test rig design together with the troughability test can be considered sufficient for defying a belt's ability to form a stable pipe shape of conveyor belts with different transverse bending stiffness, pipe diameter and length of an overlap.

As a central disadvantage, six-point belt stiffness testing devices are not suitable for studying the belt behavior and deformation under the tensile force, except to the 2D case when the forces artificially are applied to the contour for imitating the lateral forces at curves, as described by Hötte [107]. In addition, the belt longitudinal tendency to twist is not possible to detect within this test rig configuration. Positive and negative aspects inherent to the test rigs of this kind are highlighted in a list below.

Pipe conveyor six-point stiffness testing device

Advantages

- Cheap, compact, mobile, light;
- Simple installation and test performance;
- Possible to form various pipe diameters;
- Easy for belt samples replacement;
- Suitable for the same belt samples as for the troughability test;
- Together with the belt troughability, can be sufficient for predicting the conveyor belt's ability to form a stable pipe shape;
- Suitable for study the relaxation effect of the viscoelastic belt rubber compounds;
- Control of the accuracy and monitoring of the friction forces impact.

Disadvantages

- No information about the belt's buckling and twisting tendency at spatial curves;
- Impossible to apply and change belt tension, except for the artificially applied pre-calculated lateral forces to imitate the 2D belt deformations at route curves (as proposed by Hötte [107]);
- Inability for proper testing the impact of the bulk material without using an additional container;
- No option to study dynamic effects and influence of conveyor pitch.

4.2.2 Static test rigs with frames and various supports

For considering impact of longitudinal effects on belt CFs and deformations, the static test rigs with frames are used.

Generally, static test rigs with frames and supports represent a section of a PBC of an actual size with the required pitch between the idler stations under the action of the tensile forces. Xiaoxia *et al.* [252] introduced one of the simplest set-up prototype, assembled in **Taiyuan University of Science and Technology, China**. The researchers described the test rig consisted of the three six-point belt stiffness devices. These devices supported the

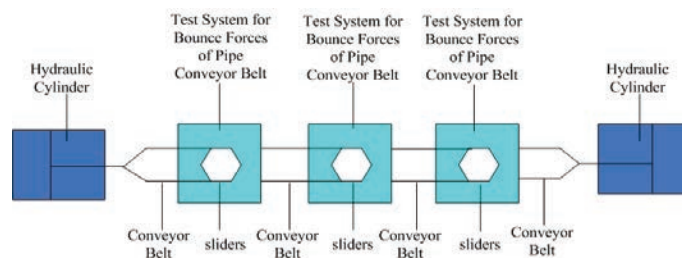


Figure 4.7: An approximate sketch of the static test rig, assembled in Taiyuan University of Science and Technology, China (Figure from Xiaoxia *et al.* [252]).

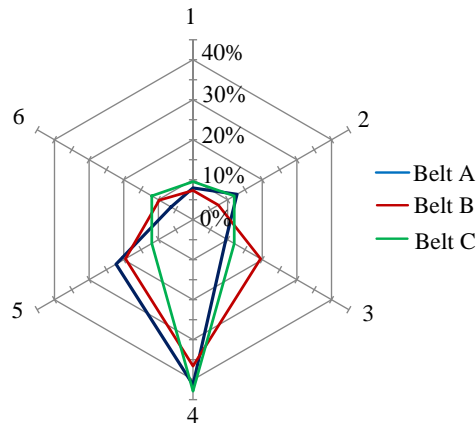


Figure 4.8: The CFs $F_n / \sum |F_n|$ (%) modeling straight section of a PBC, obtained from the test rig assembled in Taiyuan University of Science and Technology, China [252] for three types of the belt construction, denoted as A, B, and C and belt tension 300 kN.

conveyor belt formed in a pipe shape (see Fig. 4.7). The tension was applied to the belt by means of the hydraulic cylinders, positioned at the edges of the belt. The modeling of the horizontal route curves and variation of the conveyor pitch was carried out by moving the six-point testing devices in a corresponding longitudinal or lateral direction. It is important to emphasize that the procedure to achieve the correct route alignment can be quite challenging for a such testing method.

Xiaoxia *et al.* [252] tested three constructions of a conveyor belt (denoted as A, B and C) for various belt tensions and curve radii. The CFs (shown in Fig. 4.8) were presented with the similar numeration, as it was assumed in Fig. 4.1a. However, the information about the overlap coil direction with respect to the numbers of the CFs was not provided in the source. In addition, the width of the belts tested, length of the overlap, belt stiffness, position of the measuring equipment, and conveyor pitch were not reported by the researchers. Moreover, the data was presented as rounded numbers, and the accuracy of the measurements was not acknowledged.

Similar to the test rig construction described by Xiaoxia *et al.* [252], Barburski [10] introduced an experimental set-up built in **Technical University of Lodz, Poland**, that also consisted of the three six-point stiffness devices, as shown in Fig. 4.9. These six-roll sets are equipped with the load sensors that measure the forces in radial direction (see Fig. 4.9b). These idler stations are mounted to the frame that allows one to change the length of spacing between the stations. The length of rolls and their diameters was fixed. In addition, the frame provides the possibility to move the central idler set with respect to the rest two stations. By changing the position of the central idler set, the researcher can model the conveyor route in range from 50 till 400 m radius of curve in horizontal plane.

The main difference with the other test rigs designed with various frames and supports is that Barburski [10] did not apply the tensile forces at the edges of the belt in order to imitate the belt tension. The belt, already formed in a pipe shape, was dragged through the idler stations. The belt edges were left free for resting on the idler stations. In such belt

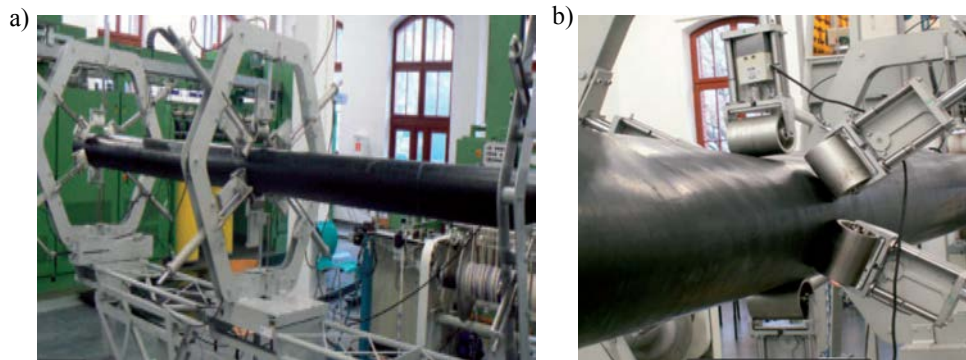


Figure 4.9: Static test rig with frames, assembled in Technical University of Lodz, Poland, and described by Barburski [10]: a) an overall view of the test rig with belt placed inside; b) a belt sample formed into a pipe shape and supported by the measuring idler set (Images from Barburski [10]).

position, the radial CFs were measured, repeating the test three times. Such manner of a belt placement inside the test rig and the uncontrolled friction forces affect the resultant CFs measured. The researcher reported the observation that the belt tended to rest more on the lateral bottom rolls exhibiting larger CFs, compared to the bottom idler rolls.

For the experiment, the researchers used nine samples (A, B, C, D, E, F, G, H, K) of different fabric belts, altered in reinforcing materials and weave patterns of weft. The difference in reinforcement implied that all the belt samples vary in belt's line mass and lateral bending stiffness. However, the resultant CFs were provided in the source only for belts A, C, and D. The data on properties and testing conditions whatsoever was given in the source for those belt samples is provided in Table 4.3. All the belt samples exhibited a tendency of a belt to collapse, indicating the contact loss between the belt and rolls by forces equal to zero, as illustrated in Fig. 4.10.

In order to improve performance of a pipe conveyor belt, the researcher elaborated a new belt design, which implied the discrete change in reinforcing material and weave patterns of the weft along the belt width. The properties of the belt with the new construction, denoted as sample N, are also provided in Table 4.3. The resultant CFs obtained using the sample N are illustrated in diagram in Fig. 4.10 As it can be seen, belt sample N generates the CFs on

Table 4.3: Details of experiment and available properties of the belt samples used by Barburski [10] for measuring the CFs, given in Fig. 4.10.

Sample	Belt Type	B , mm	B/D_{nom}	Troughability	Length l , m	Tension
A	EP	1000	3.65	Not provided	4.5	no
C				Not provided		
D				0.392 ± 0.003		
N				0.388 ± 0.003		

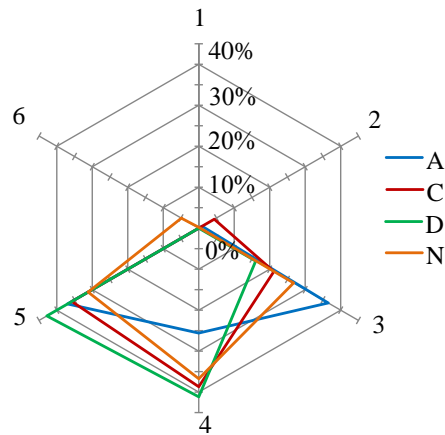


Figure 4.10: The CFs $F_n / \sum |F_n|$ (%), obtained from the test rig elaborated by Barburski [10] in Technical University of Lodz, Poland for the belt samples with different construction, denoted as A, C, D, and N available in the source. The results are adjusted to the reference Fig. 4.1.

all six rolls of an idler sets, however, the values for the top forces are insignificantly small, and the shape of a belt with a new construction formed into a pipe shape with overlap has still tendency to collapse and is insufficiently rigid for reliable operation of a PBC.

The configuration of the test rig, described by Barburski [10] did not allow the researcher to model belt tension and vertical route curves of a conveyor in the experiment. To include those effects, **Delft University of Technology, Section of Transport Engineering and Logistics** performed the experiment measurements on the test rig, built in **2005** by **Conveyor Knowledge Information Technology Pty. Ltd (CKIT) in South Africa, Johannesburg** [85] (see Fig. 4.11). The purpose of the measurements was to investigate belt deformations at curves, deflection in between the idler stations, and the CFs on the bottom idler roll at various testing conditions. The experiment was repeated in **2010** for a different belt type on



Figure 4.11: Static test rig with frames, assembled by Conveyor Knowledge Information Technology Pty. Ltd (CKIT) in Johannesburg, South Africa, 2005 (Image from [85]).



Figure 4.12: Static test rig with frames, assembled by Conveyor Knowledge Information Technology Pty. Ltd (CKIT) in Johannesburg, South Africa, 2010 (Image from Lodewijks and Pang [188]).

the test rig with a similar design construction, explicitly described by Pang and Lodewijks [188] and shown in Fig. 4.12.

The test rigs used in both experiments consisted of five special frame sections supporting a 12 m long steel cord belt, already formed in a pipe shape. Each section was 2.5 m long and equipped with the hexagon six-roll idler station with double-side arrangement (Fig. 4.13a). Before placing the belt in the test rig, the belt was stripped at the edges from the rubber, gum, and reinforcing layers. The remaining steel cords were fixed by means of rivets, or conical clamps, into disks at both belt sides (Fig. 4.13b). The disk at one edge was fixed to the rig frame, whereas another disk was attached to the hydraulic cylinder (Fig. 4.13c), served for modeling the required tension to the tested belt. The tension tested was in a range

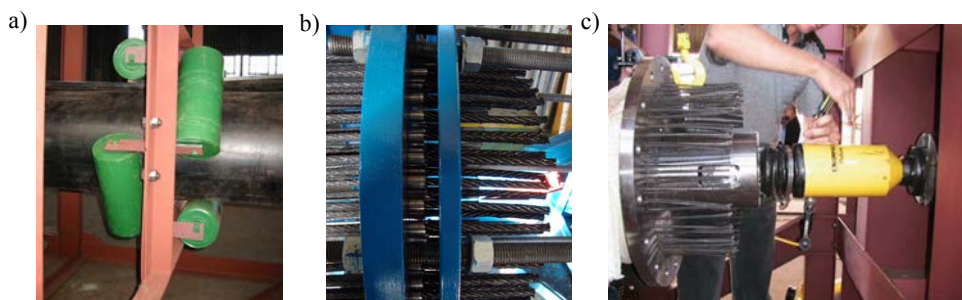


Figure 4.13: Design details of the static test rigs with frames, assembled by Conveyor Knowledge Information Technology Pty. Ltd (CKIT) in Johannesburg, South Africa in 2005 and 2010 [85, 188]: a) a six-roll idler station with double side arrangement; b) steel cords clamped to the disk with the conical tubes; c) fixation of the disk with a hydraulic jack (Images from [85, 188]).

each other with shafts at the bottom (see Fig. 4.14a). Additional elements were inserted on the topside and were connected with bolts (Fig. 4.14b). The curves were modeled in vertical plane by lifting the frames upward with hydraulic jacks. In order to fix the curve, small steel plates were inserted in the gaps between the section on the top. The size of these elements corresponds to the vertical test rig curves required (see Fig. 4.14c).

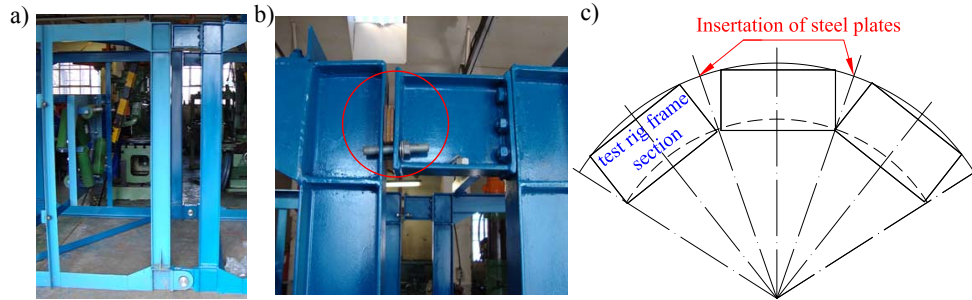


Figure 4.14: Static test rigs with frames, assembled by Conveyor Knowledge Information Technology Pty. Ltd (CKIT) in Johannesburg, South Africa in 2010 [188]: a) shaft connection of the frame sections at the bottom side; b) steel plate inserted between the section frames (Modified figures from Lodewijks and Pang [188]); c) schematic front view of the three sections of the test rig.

A steel cord belt ST3500 with 1800mm width was used for the experiment. The properties and some corresponding experiment details are presented in Table 4.4.

The measurements were performed at the central idler station, equidistant to the rig edges. Two load cells per each of the idler roll were installed between the frame and the bracket to detect the CFs in radial directions. The influence of the overlap position on the CFs' behavior was carried out by rotating the disks with clamped steel cords clockwise at appropriate angles at both belt edges. Figure 4.15 displays the results of the CFs, measured for the straight section of the test rig with overlap on the top and on the bottom. Results are adjusted to the belt coil and forces numeration, given in Fig. 4.1. In general, the analysis of the results shows that the increase of the belt tension causes an increase in the CFs №1, 2, and 3 in both relative and absolute values.

The researchers mentioned number of the issues that could affect the CFs measured. The results could be influenced by the uneven tension in the steel cords that appear at clamps during individual fixation of the cords. In addition, the belt exhibited rather high

Table 4.4: Belt properties and test details used in the experiment by Lodewijks and Pang [188].

Belt type	B , mm	B/D_{nom}	Troughab.	Length l , m	Pitch l_c , m	Overlap position	Tension, MPa
ST 3500	1800	≈ 4	≈ 0.33	12	2.25	top, bottom	0, 10, 20, 30, ..., 60

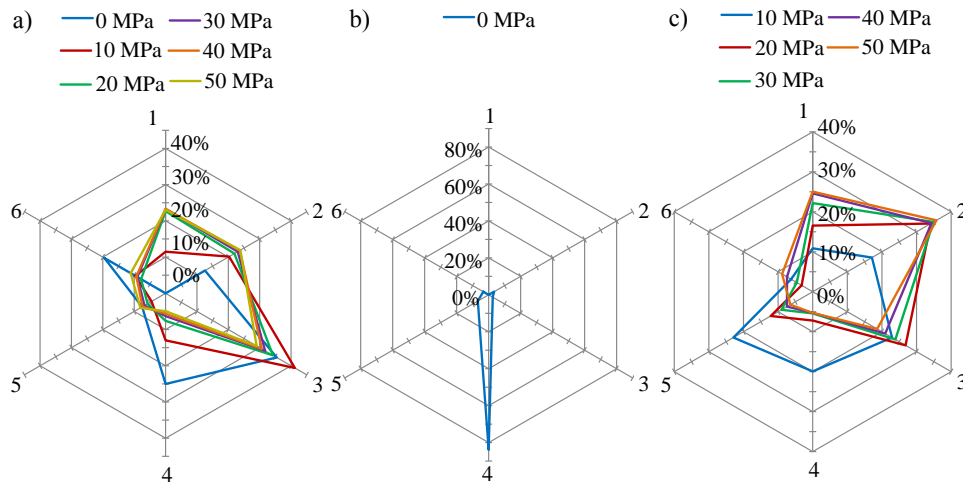


Figure 4.15: The CFs $F_n / \sum |F_n|$ (%), obtained from the test set-up assembled by Conveyor Knowledge Information Technology Pty. Ltd (CKIT) in Johannesburg, South Africa in 2010 [7] for the belt: a) with overlap on the top and varied tension; b) with the overlap at the bottom and no tension; c) overlap at the bottom with tension varied. The results are adjusted according to the reference numeration and overlap position, provided in Fig. 4.1.

transverse rigidity, thus when the belt was placed in the test rig by dragging it through the idler stations, it tended to rest more on the lateral bottom idler rolls than on the bottom rolls. Noteworthy to mention that similar tendency was reported in the test rig of Barburiski [10] previously described. In addition, since the measuring cells sensed the loads only in the radial direction, the impact of the friction forces was not considered and controlled during the test performance.

For this type of the test rig design, it is important to take into account the relaxation effect for the belt tested, as the viscoelasticity of the belt has a great influence on the results, especially in the static tests. During the experiment, the researchers reported that, over certain time period, the belt had greater sag between the idler stations. It even exhibited dents in some places in direct contact with the idler rolls. This phenomenon implies another significant disadvantage of the test rig: due to its voluminous configuration and excessive time required for placing the belt in the test rig, it becomes almost impossible to eliminate belt deformations, attained from the previous test cases.

Another drawback of the rig design implies the difficulties inherent to modeling the vertical route curve of the rig by lifting the frame sections with hydraulic jacks and inserting the steel plates at the top parts of the frames. The radii of the vertical route curves modeled could potentially be affected by the vertical sag of the central part of the test rig due to its excessive weight. Moreover, the test set-up was restricted to the curves only at the vertical plane due to its frame connections. The horizontal curves could be arranged if the frames had shaft connections between the sections at the internal periphery of the plane route curve intended. In addition, the steel plates should be inserted in the frame elements at the external periphery of the curve.

However, this approach to model the test rig route could not provide the option of testing the curvatures in both horizontal and vertical plane within the same rig design. In addition to the route curves, the test rig configuration had a lack of variation in testing pipe diameters, lengths of carry spacing, and option to change the idler stations from a double-side to one-side arrangement.

The test rig, assembled in the **Technical University of Košice in Slovak Republic**, and described by Michalik and Zajac [155], Molnar *et al.* [158–160, 162, 163, 165], Michalick *et al.* [156] needs to be considered independently from the other static test rigs designed with frames. The particular test rig was assembled to model the transition section of a PBC, where the belt gradually forms a pipe shape with an overlap.

The test rig, illustrated in Fig. 4.16, consisted of the special frames, forming the belt from a flat shape into a pipe shape at one side of the test rig. At the opposite side, the test rig had three hexagon idler stations (№1, 2, and 3) that support belt fully formed into a pipe shape. For muddling a pipe diameter required, each idler station was equipped with special six static rolls attached to the frames with the adjustable screw rails (see Fig. 4.17a and Fig. 4.17b).

In order to apply tension, the belt was fixed in the test rig with the large flat plate from one side and four plates from another side (Fig. 4.17c) using tightening bolts. Each plate was attached to the strain gage with the ball-pin for controlling tension values. The strain gages were also installed at the hexagon idler stations for measuring CFs of the full pipe-shaped belt. A fabric belt with 500N/mm minimum braking strength and total length of 8m was selected for the experiment. Properties of the tested belt are presented in Table 4.5.

Belt tension was modeled by adjusting two tension screws with ball pins at the large fixating plate. The overall tension varied from 0 to 30 kN, ascending to the maximum value and descending back to zero stepwise. After each tension step-change, the data was stored at time intervals to study the relaxation effect in belt rubber compounds. This phenomenon was observed within each interval in gradual decrease of the certain CFs (see Molnar *et al.* [162]). The maximum time step recorded was around 3.5 minutes [159].

Noteworthy to mention the fact that in the mentioned sources [155, 156, 158–160,

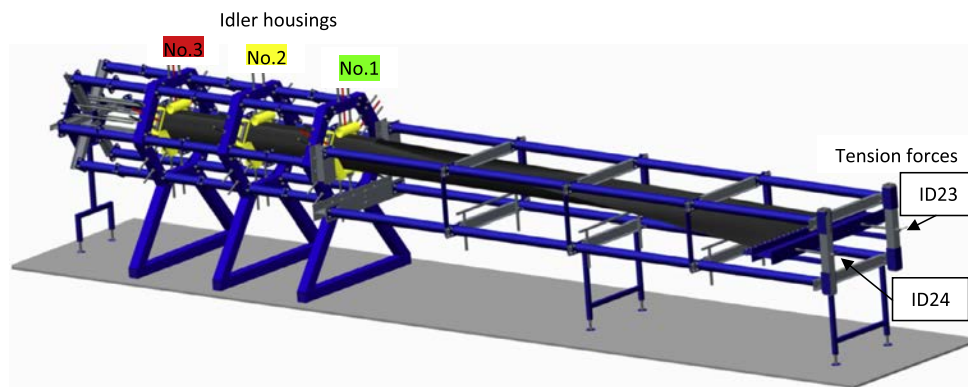


Figure 4.16: Model of the static test rig representing a PBC transition section, designed in Technical University of Košice in Slovak Republic (Figure from Molnar *et al.* [162]).



Figure 4.17: Design details of the static test rig, installed in Technical University of Košice in Slovak Republic [155, 162]: a, b) static idler rolls with screw rails (Figures from Michalik and Zajac [155]); c) fixation of a pipe-shaped belt to four plates with the bolt connection (Figure from Molnar et al. [159]).

162, 163, 165], the numeration of the CFs and their positive radial directions were clearly specified. It was expected that the values of the CFs would be positive or equal to zero in case of a contact loss between belt and idler rolls occurred. However, for certain load conditions, negative values were reported at one of the idler stations, while the same roll position at a different idler station yielded a positive result. For example, based on the average data provided by Molnar et al. [159] for the case when tension force was 2 kN, load of -12.89 N for lateral bottom roll (CFs №3 in Fig. 4.1a) was detected at idler station №2. At the same time, the same roll position reported the average force of +50.25 N at idler station №3. Negative values were even observed at all three idler stations for tension force from 0 to 4 kN [162]. It is possible to suggest that this phenomenon could be reasoned by either improper sensors calibration, or their plastic deformation, or by errors in the measurement procedure (i.e., some of the rolls were accidentally pressed against the belt due to the incorrect adjustments of their screw-rails).

Results only with positive or zero values of the CFs were selected for the comparison (see Fig. 4.18), which implied that the data were only obtained for idler station №1 with tension starting from 4 kN and for idler station №2 with tension started from 12 kN. Growth of CFs in absolute values was reported with the increased tension. In relative values, the increase moved towards to the CFs №5, 2 and 6. The results, illustrated in Fig. 4.18, are adjusted to the reference Fig. 4.1a, however the overlap coil orientation was not clearly specified in the source.

It is possible that the results obtained within this test rig could also be influenced by

Table 4.5: Belt properties and test details used in the experiment by Lodewijks and Pang [188].

Belt type	B , mm	B/D_{nom}	Trough.	Young's mod., kN/m		Overl. posit.	Tension, MPa
				E_1	E_2		
EP 500/3 4/3D	800	3.2	0.333	5567	453	top	0, 2, 4, 6, ...30

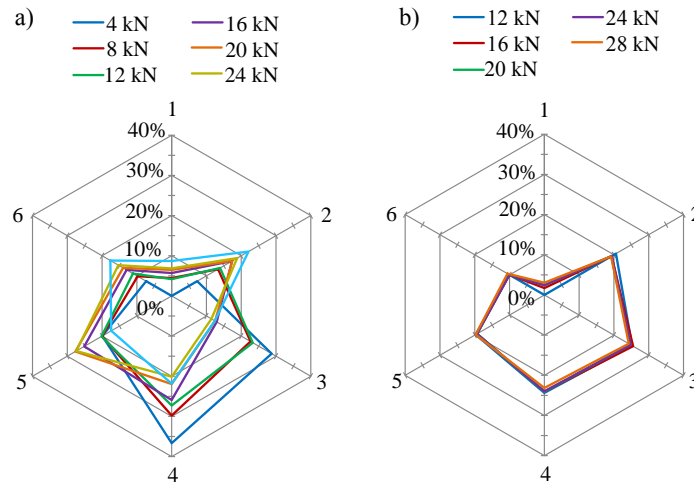


Figure 4.18: The CFs $F_n / \sum |F_n|$ (%) versus various tension forces, obtained from the test set-up assembled in the Technical University of Košice, Slovak Republic for the idler stations a) №1 and b) №2, shown in Fig. 4.16. The data is taken from [160, 162] and adjusted to the reference CFs orientation, given in Fig. 4.1a.

uneven tension distribution along the pipe belt contour. The fixation of the belt with four plates, shown on Fig. 4.17c, could cause higher tensile stresses in longitudinal parts of the belt, representing their attachments to the clamps, compared to the parts in between the plates. This phenomenon would not be critical for the results, if the measuring equipment was installed far enough from the test rig edges with the belt fixed. Otherwise, the load from the idler stations nearby to the edge would be partially carried out by the frames, diminishing the loads measured. This proposal is supported by the fact (see the data in [156, 159, 162]) that the absolute values of the CFs at idler station №2 are lower compared to station №1, and higher with respect to station №3, which is closest to the edge (see Fig. 4.16). Moreover, the loads measured at idler station №1 are additionally affected by the close proximity to the transition section that forms a flat belt into a pipe shape. This test rig configuration is a well-illustrative example how the asymmetry of the test rig design and selection of the position of the measuring equipment can affect the experiment results.

Most of the test rigs described are relatively limited in the design in terms of the variation of a pipe diameter, pitch, idler station arrangement, etc. To offer more options for the testing cases within the same experiment set-up design, an upgraded test rig configuration, illustrated in Fig. 4.19 was elaborated in **Institute of Transport and Automation Technology (ITA) at Leibniz University of Hannover** [107, 108] with the cooperation between the **Phoenix Conveyor Belt Systems GmbH**.

The test rig consisted of the special modular and telescopic frames with five idler stations, which allowed the variation of belt tension, the idler spacing between 1 and 2 m, curves in vertical and horizontal planes with the minimum radii of 50m, and idler rolls arrangement from one side to double side. The tension was provided by the hydraulic cylinders, attached to the mounting disks at both edges of the test rig. The cords were clamped to those disks. The discs had hole patterns for each cord exactly matching a PBC cross section, designed

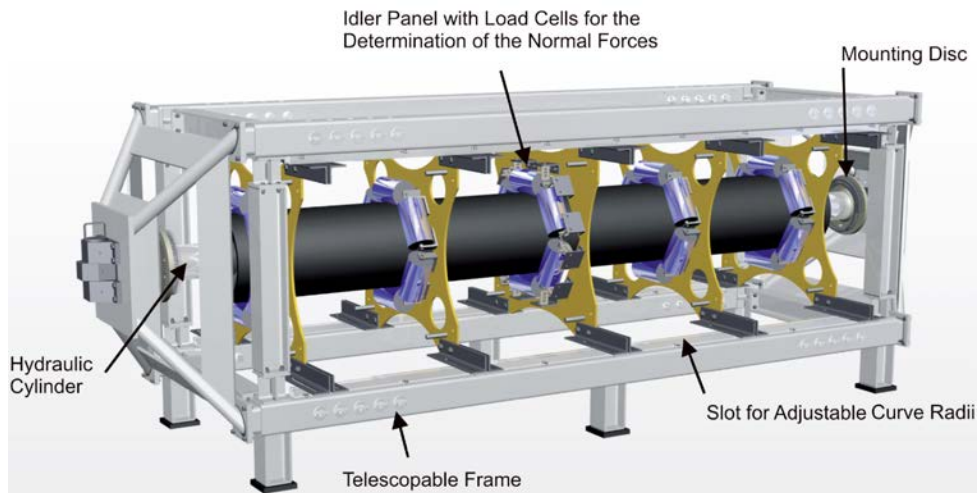


Figure 4.19: Model of the static test rig with frames, designed in cooperation with the Phoenix Conveyor Belt Systems GmbH and Institute of Transport and Automation Technology (ITA) at Leibniz University of Hannover [108] (Figure courtesy of Phoenix Conveyor Belt Systems GmbH and Institute of Transport and Automation Technology (ITA) at Leibniz University of Hannover).

for a specific belt with particular pipe diameter, belt width and even a cord pitch. Testing belt samples with different design required also replacement of the cord fixating disks with patterns matching particular belt structural lay-out. The researchers asserted that the test rig provided the option to control and apply various tension for each steel cord. Teflon® foil was used at the belt overlap in order to reduce the friction between the belt edges.

The CFs were detected by the load sensors installed at the central idler station. The results, preliminarily adjusted to Fig. 4.1a and distributed in Fig. 4.20, represent the load case of 300kN belt tension. The experiments were performed within three samples A, B, and C of the same belt types, as used in six-point testing device (see Table 4.2). The tension varied from 0 to 500kN and route curve radii - from infinity (straight section) to 200m.

Hötte [107] reported that this test rig was also used for testing the impact of a bulk materials. For this purpose, the researcher used a custom made 3m long tank filled with water. That tank consisted of the flexible and light-weight rubber tube sealed at both sides with the aluminum disks. The external diameter of disks coincided with the internal diameter of belt pipe. For the experiments with such water container, it is important to carefully control membrane stiffness of rubber tube, weight of the disks, friction between the tank and belt internal surface. Moreover, usage of water does not reflect impact of the internal friction, which participates in lateral load component. As it will be shown in Chapter 5, compared to the liquids, a bulk material transmits shear stresses, and the walls of the container can carry part of a bulk weight. In practice, while belt undergoes lateral curves in the route, parts of the bulk material are squeezed and causes higher pressure on the belt surface (passive state), whereas the parts close to periphery of the curve generate lower pressures from the active stress state. However, a usage of water eliminates possibility to study these effects.

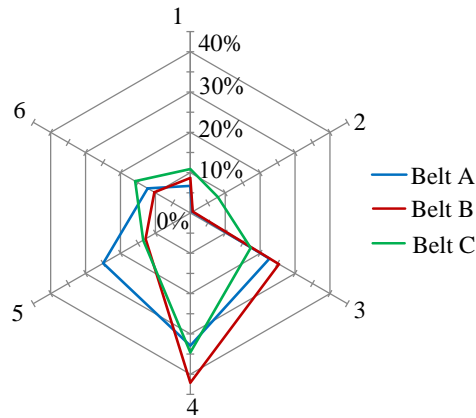


Figure 4.20: The CFs $F_n / \sum |F_n|$ (%) for the belt construction a) A, b) B, and c) C with the overlap position on the top, obtained from the test set-up, designed in cooperation with the Phoenix Conveyor Belt Systems GmbH and Institute of Transport and Automation Technology (ITA) at Leibniz University of Hannover [107, 108]. The results are adjusted to the reference Fig. 4.1a.

Despite of these issues, this test rig described occupies more privilege position compared to the other set-up configurations with frames, as it offers a larger variety of the testing conditions for the pipe conveyor belts.

Summing up for the static test rigs with various frames and supports, the configurations of these test rigs can be used to investigate behavior of a belt section of an actual size with various route curves and belt tensions. In addition, it becomes possible to observe, whether the belt has a tendency to twist at route curves, while it is formed into a pipe shape and supported by the hexagon six-roll idler stations. In addition, the test rigs allow one to study the belt relaxation response due to the applied tensile forces.

The main disadvantages of this type of a test rig design imply a voluminous set-up construction, which ultimately results in high installation costs and an excessive time requirement for a replacement of different belt samples. Moreover, despite the fact that the static test rigs with frames and supports can be used for investigating an impact of the belt viscoelasticity on the belt deformations and CFs, the studies used this type of a test rig design (mentioned in this section) paid limited attention to the viscoelastic belt's "memory" in the lateral direction due to its static fixation in a pre-folded shape over extensive time. Before repeating the tests, the belt has to be stored flat for a substantial amount of time in order to exclude the deformations from the previous measurements. This becomes impractical due to the voluminous design and problematic process of placing the belt in the test rig.

For the comparison with other test rig design types, the major positive and negative aspects of the PBC static test rigs with frames are listed below.

Pipe conveyor static test rigs with frames and supports

Advantages

- Possible to test different cases, varying route curves, pipe diameter, length of carry spacing, and rolls arrangement (one-/double-side);
- Predicts the buckling and twisting tendency of a belt in a PBC of an actual size at spatial curves;
- Suitable for modeling various belt tensions;
- Appropriate to control tension for each of the steel cords individually;
- Applicable for studying time effect and viscoelastic properties of the belt on its performance.

Disadvantages

- Massive, voluminous, expensive;
- Requires extensive time to replace the belt samples and conduct test rig adjustments for modeling various cases;
- Impractical to eliminate the effect of the initial belt deformation from the previous tests;
- For modeling belt tension, mostly excluded for the steel cord belts due to the fixation technique of the belt in a test rig;
- Requires excessive rig length in order to eliminate vicinity impact of the fixed edges that can partially carry the loads;
- Sensitive to the position of the measuring equipment regarding the fixed frame edges (especially for asymmetrical test rigs)
- No option to study the influence of dynamic effects in belt and bulk behavior.

4.2.3 Dynamic test rigs and field measurements

The problem of a belt relaxation with appearances of belt dents where belt is in contact with idler rolls for a substantial time is inherent to all static test rigs designed with frames. The solution to the challenge is to perform dynamic measurements, investigating how the dynamic effects influence a PBC behavior. In addition, dynamic measurements can provide the most close information regarding belt behavior during the system operation. Together with all possible effects that appear at various belt speeds, dynamic measurements can also reflect twisting and buckling of a belt at route curves and also its mechanical response to the tension forces applied. Dynamic tests can allow one to study how bulk materials with different properties can influence the CFs. The other static test rig configurations described are not as successful in this regard.

Dynamic tests can be obtained through the use of dynamic test rigs, or by performing field measurements. The results obtained using both options need to be discussed.

It is reasonable to expect that the dynamic test set-up modeling a pipe conveyor section of an actual size or even with reduced length, must be very voluminous and excessively expensive. As such, there is not much published information available regarding the results

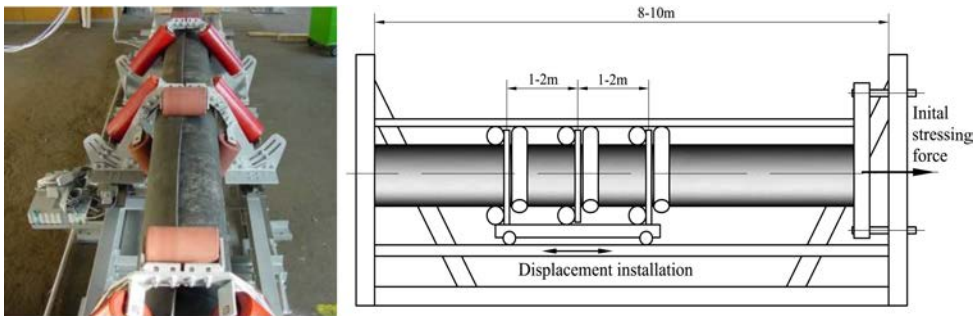


Figure 4.21: Dynamic test rig, modeling a PBC with a new belt guidance, University of Leoben, Department of Conveying Technology and Design Methods, Austria [102] (Figure 4.21 modified from Hinterholzer *et al.* [102]).

obtained within the dynamic test rig.

One of the simplest dynamic test rig was described by Kessler [124] and Hinterholzer *et al.* [102]. That test rig was installed at the **University of Leoben, Department of Conveying Technology and Design Methods, Austria**. It represented a PBC with a new belt guidance, where the belt on the return strand was transported on top of the pipe-shaped belt. The purpose of the measurement was to ascertain rolling resistance at the moving rolls. As a result, the researchers did not provide any information regarding the CFs at the idler rolls. However, it is important to note the option of modeling dynamics of a conveyor using such test rig configuration.

The test set-up described by Kessler [124] and Hinterholzer *et al.* [102] was designed to be static with a fixed belt at both edges with the required tensile load applied. The dynamics was simulated by using a movable unit with three idler stations (see Fig. 4.21). Measurements were performed at the central idler station of the unit, with pitch varied between 1 and 2m. The trolley accelerated gradually by the rack-and-pinion gear until the required speed was achieved. After that, the unit continued moving steadily almost along the entire length of the rig. Close to the test rig edge, the unit was slowly stopped.

Some dynamic results were obtained by Wiedenroth [247] at the **Institute for Materials-Handling Technology and Mining Machinery of the University of Hannover in 1995**, by means of a unique dynamic pipe conveyor test rig, illustrated in Fig.4.22. That test rig imitated the actual PBC with overall length reduced. It consisted of four sections: a 1.6m long fixation section with a take-up system and hydraulic cylinder; a 6m transition zone, forming the belt from a flat shape into a pipe; a 12m central region with hexagon six-roll idler stations, and a 7m transition discharging zone with driven pulley and the motor station.

The idler stations were designed with double side roll arrangements. The measurements were performed at the central idler station, where the belt was fully formed into a pipe shape. The researcher detected the radial and longitudinal CFs at each of the idler rolls. For control, the vector sum of all the normal forces at the six rolls and the total longitudinal force had to match the overall loads at the idler station, measured simultaneously by independent sensing equipment. In order to make this possible, the central idler station was designed with the three small supporting rolls, shown in Fig. 4.22. Those rolls were equipped with sensors that measured loads in longitudinal and radial directions. In addition, each of the bottom

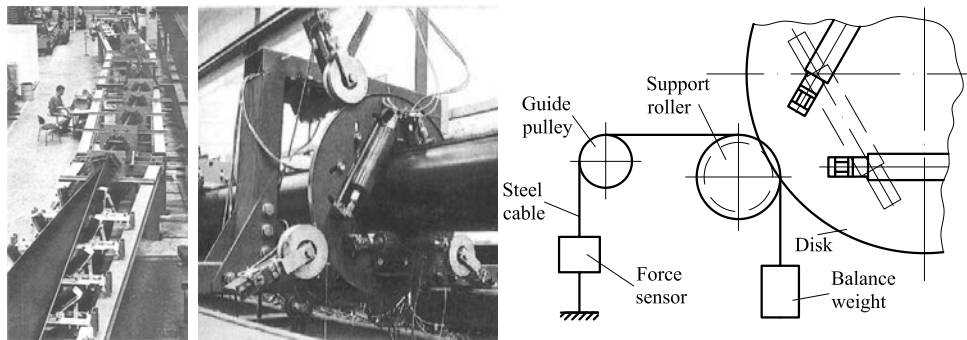


Figure 4.22: Dynamic test rig, installed at the Institute for Materials-Handling Technology and Mining Machinery of the University of Hannover in 1995 [247] (Figures modified from Wiedenroth [247]).

rolls had grooves with a wound-up thin steel cable. One side of the cable was fixed with a balance weight, and the another side was attached to the guide pulley and the force sensor (see details in Fig. 4.22). This steel cable arrangement was needed to measure a twisting torque in the belt when the route had a curve.

The route curves were simulated in the horizontal plane by adjusting the position of the idler stations with respect to their supporting frames, situated in the central zone of the conveyor (see Fig. 4.22). In between the frames of the transition and central zone, angular connecting elements were inserted for aligning the route. The transition test rig zones with pulleys, motor and take-up system were lifted by the overhead crane and placed at the required angle from both sides. This test rig configuration enabled the researcher to vary curve radii, conveyor speed, idler spacing, belt tension, and pipe diameter in a range, as presented in Table 4.6.

For the experiment, five pipe conveyor belts with different construction were used (named as A, B, C, D, and E). These belts originated from different manufacturers. Belt A had a steel cord structure; belt B, C and D – were fabric belts, and belt E was a steel cord belt with fabric layers. The properties of the belts can be found in Table 4.7. Before performing the measurements, each brand-new belt was placed in the test rig with conveyor pitch of 1 m and run at high speed for 24 hours (at least 200 full belt revolutions) with stepwise variation of the belt tension, starting from 20kN. Subsequently, the resultant belt elongation was adjusted by the take-up system, and measurements were obtained.

The researchers reported that the total vector sum of the radial CFs was affected by the variation in belt speed, idler spacing, and belt tension. They also stated that those parameters

Table 4.6: Details of the experiment, performed using the dynamic test rig installed at the Institute for Materials-Handling Technology and Mining Machinery of the University of Hannover 4.22.

Pitch $l_c = l_r$, m	Tension, kN	Belt speed v , m/s	Radii of a route curve, m
1, 1.5, 2, 3, 4	20, 30, 40, 60, 80	0.5, 1, 1.5, 2	25, 35, 50, 60, 75, ∞

Table 4.7: Properties of the belts tested in the experiment of Wiedenroth 4.22.

Sample	Belt type	B , mm	B/D_{nom}	Troughability	m'_{belt} , kg/m
A	ST 560	730	3.47	0.323	11.1
B	EP 500	800	3.48	0.319	10.3
C	EP 630	800	3.48	0.274	9.4
D	EP 500	770	3.67	0.239	9.6
E	ST1000	1000	3.58	0.344	20.8

did not influence the load distribution between the idler rolls in relative values with respect to the total sum of the CFs. Wiedenroth [247] provided the CFs in relative values, for all belt types at belt speed 2 m/s. Figures 4.23a and 4.23b were created based on that data. The results mentioned were not supported by any information regarding the corresponding pitch and belt tension, standard deviation of the measurements. Figure 4.24 represents the load distribution between the idler rolls for an empty PBC with straight route for belts C and E that was also available in the source in absolute values [247]. Noteworthy to mention that after calculating the relative values, the results for belt C, shown in Fig. 4.23 and Fig. 4.24, do not deviate significantly, whereas for the steel cord belt E, the difference in load distribution, obtained at belt speeds of 2 m/s and 0.25 m/s is more noticeable.

Comparison of the results between the fabric belt samples B and C that had the same belt width and length of overlap, showed that the bottom rolls with respect to the top rolls than the belt E.

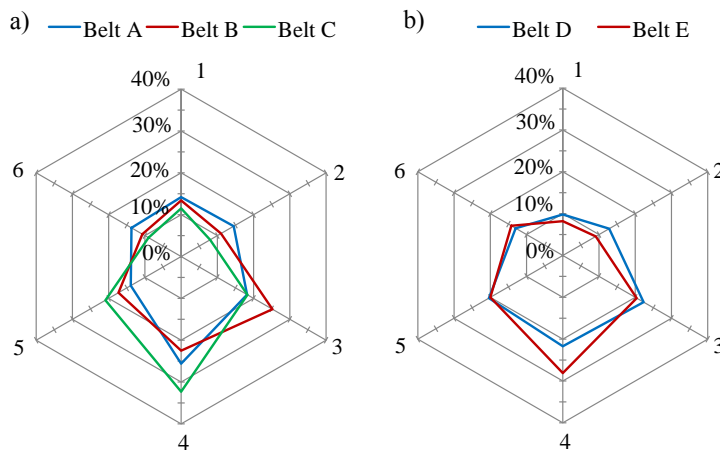


Figure 4.23: The CFs $F_n / \sum |F_n|$ (%), obtained at the dynamic test rig at the Institute for Materials-Handling Technology and Mining Machinery of the University of Hannover in 1995 [247] for a straight section of the route without the bulk material, belt speed $v = 2\text{ m/s}$ and various belt samples. Results are adjusted to the reference Fig. 4.1a.

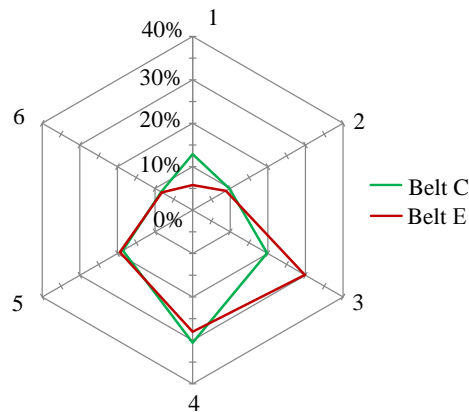


Figure 4.24: The CFs $F_n / \sum |F_n|$ (%), obtained at the dynamic test rig at the Institute for Materials-Handling Technology and Mining Machinery of the University of Hannover in 1995 [247] for 2m conveyor pitch and belt construction C (tension 40kN, $v = 2\text{m/s}$), and belt E (tension 20kN, $v = 0.25\text{m/s}$). The results are adjusted to the reference Fig. 4.1a.

was more flexible and slightly heavier. The opposite tendency could be observed for steel cord belt E, which was also heavier and rather flexible than steel cord belt A. A higher load quotient in lateral rolls was detected for the fabric belt structure D, compared to the fabric belt C with similar line mass. This was due to the fact that belt D was stiffer and had larger overlap than construction C. It is important to emphasize that those load patterns with respect to belt construction could be considered only from a qualitative point of view, as pipe conveyor belts exhibit uneven line mass and uniform transverse stiffness along their width (consult with Section 2.5.1).

Besides the experimental test rigs, dynamic measurements of contact forces can be performed using the existing PBC installations.

Bahke [8] carried out field measurements at a **“Rollgurt”-Conveyor in the lime and cement plant Alsen Breitenburg in Germany**. That PBC had a straight and an S-curve sections in its route. The aim of the tests was to measure power and torque occurring at the drive system, as well as radial and longitudinal CFs for individual idler rolls and for overall idler stations tested. The measurements were performed at four different route locations for belt width $B = 730\text{ mm}$ and ratio $B/D_{\text{nom}} = 3.65$. The information regarding other belt properties and their construction was not provided in the source. The resultant CFs, obtained by Bahke [8] for empty PBC with carry spacing of 1.5m and belt's overlap on the top and also at the bottom are presented in Fig. 4.25.

Field measurements were also carried out by Hötte [107], **Institute of Transport and Automation Technology (ITA) at Leibniz University of Hannover**. The researcher performed the experiment at the PBC in **cement plant Hugo Miebach Söhne, Portland-Zementwerk Wittekind, Germany**. This conveyor was installed with the idler stations with the double side rolls arrangement. It had inclined straight route sections as well as sections with horizontal and vertical curves.

For the measurements, four positions of the idler stations along the conveyor route were

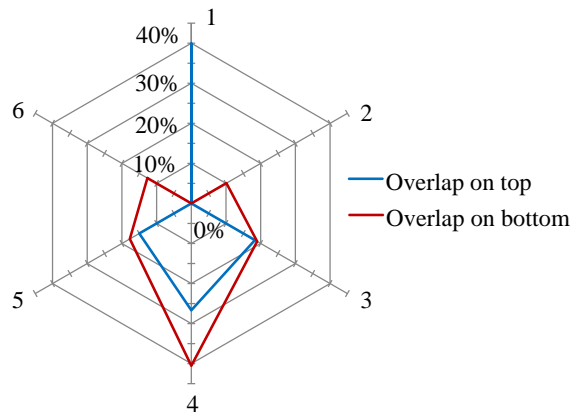


Figure 4.25: The CFs $F_n / \sum |F_n|$ (%), obtained by Bahke [8] during dynamic field measurements at a “Rollgurt”-Conveyor in the lime and cement plant Alsen Breitenburg in Germany, for overlap on the top and also at the bottom. Results are adjusted to the reference Fig. 4.1.

selected. At these locations, the idler rolls were dismantled from the panels and replaced with units, equipped with the measuring system of twelve load sensors. For each idler roll, two calibrated force transducers were placed in the brackets at both sides of the roll shaft. Therefore, the sum of data obtained by the two sensors represented the total CF for the corresponding idler roll. The belt speed was controlled during the experiment by a measuring rotary wheel encoder. The position of the rolls at the measuring idler panel was aligned using cords over two idler panels in front and two idler panels behind.

For the comparison of the results, the CFs inherent to the idler station in straight section of a conveyor route are selected. The section had a slight inclination of -0.4° , though the impact of it on CFs is considered rather insignificant. Hötte [107] also pointed out that at this location, the cross section of pipe conveyor belt had an oval shape geometry. The available details on PBC parameters at this route section are provided in Table 4.8.

The experiment was performed when the PBC operated without bulk material. That is why the results were affected only by the belt tension, conveyor route, and belt properties, some of which are given in Table 4.8. The conveyor belt consisted of the segments that had

Table 4.8: Available parameters of pipe conveyor for the conveyor section with straight route, provided by Hötte [107].

Belt type	Belt segment	Exploitation time of belt segment, years	B , mm	B/D_{nom}	Pitch l_c , m	Belt speed v , m/s
EP 1250	a	11	1350	3.86	2.4	3
	b	5				
	c	3				

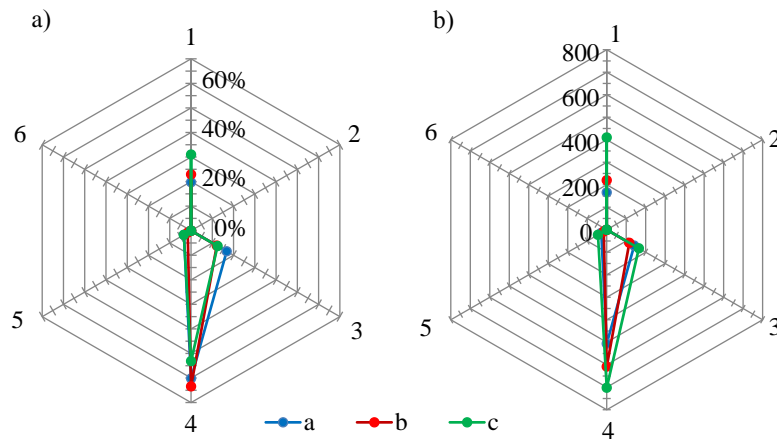


Figure 4.26: The CFs, given in: a) absolute values F_n (N); b) in relative scale $F_n / \sum |F_n|$ (%), obtained by Hötte [107], Institute of Transport and Automation Technology (ITA) at Leibniz University of Hannover, during dynamic field measurements at the pipe conveyor in cement plant Hugo Miebach Söhne, Portland-Zementwerk Wittekindin Germany. The results represent straight conveyor route section for various belt segment types (a, b and c), indicating the exploitation time. The orientation of CFs is adjusted to the reference Fig. 4.1a.

the same belt type, nomenclature, and structural design, but differed in their exploitation time. Those belt segments were denoted as (a, b and c) in the study.

The researcher detected and stored results for approximately 2 hours for each position with a sample rate of 10 Hz. Fluctuating lines represent each of the CFs of the measuring idler station over the experiment time. Hötte [107] made an interesting observation that the force lines had repeatable patterns in the results. The patterns appear in accordance to the belt segment type (a, b, or c), which were running through the idler station at the moment of the measurement.

Hötte [107] averaged the fluctuating results of CFs over the certain value for each of the belt segment type independently. In general, the belt segment type (b) showed higher CFs in absolute values than the segment type (c) and smaller CFs than the segment type (a). The researcher showed that the exploitation time of the belt significantly affects the results. Particularly, the longer the belt is in use, the smaller the CFs it generates in absolute values.

The effect of the belt exploitation time on the CFs can be explained by the viscoelasticity and the Mullins effect in the conveyor belt behavior, discussed in Section 3.2. The periodic loading and deformation of the belt during an extensive amount of time affects its stress-strain characteristics. The latter identifies the belt's bending stiffness at the moment of measurement. For the particular case, a long exploitation time of the belt leads to a decrease of the effective modulus of elasticity.

The results of the CFs for different belt segment types are provided in Fig. 4.26 in absolute values and also in relative scale. The results show a similar pattern, as the CF diagram, obtained by Bahke [8] for an empty PBC with the overlap on the top. The load distributions between the idler rolls from the both sources [8, 107] exhibit a significant force

on the top roll 1, contact loss with the lateral top rolls 2 and 6, and a higher CF at roll 3 with respect to roll 5 and overlap coil.

Summing up, it is possible to state that in general, dynamic test rigs or field measurements have their own benefits and drawbacks, compared to the static test rig configurations. They are beneficial in studying dynamic effects during a conveyor's operation, and are suitable for testing impact of various bulk materials conveyed. A main drawback, though, is the large volume and high costs of the test rig installation. Moreover, the performance of different cases by changing idler rolls, pipe diameter, and belt replacement require substantial time for the test rig adjustment.

In case of field measurements, results are limited to the case variations tested. They are also restricted to the particular belt, pipe diameter, pitch, route, etc. of the installation. As a result, the information over conveyor performance obtained from the field measurements occur post-factum, i.e., when the opportunity for optimization and change in the PBC design are generally lost. Additionally, the field experiment are affected by performance restrictions due to the requirements of a production line in a mine or a plant, where the measurement are performed. The negative and positive aspects inherent to dynamic measurements are listed below.

Pipe conveyor dynamic test rig/ field measurements

Advantages

- As close as possible for replication of a PBC behavior in industrial installations;
- Possible to test various route curves, pipe diameters, lengths of overlap, carry spacing, belt tensions and speed (for the test rig);
- Prediction of a belt buckling and twisting tendency at spatial curves;
- Provision of an even tension distribution along the belt width;
- Appropriate for studying dynamic effects in operation;
- Suitable for testing the impact of different bulk material properties, capacity, and filling ratio of the cross section;
- Complete elimination of the belt viscoelastic "solidification" in one position inherent to the static test rigs.

Disadvantages

- Massive, voluminous, excessively expensive (for the test rig);
- Requires extensive time to replace a belt and conduct test rig adjustments for modeling various cases (test rig);
- Restricted to specific conveyor parameters (for field measurements);
- Post-factum to inform for improving changes in belt design and conveyor parameters (for field measurements);
- Additional restriction due to the requirements for a PBC as a part of a production/transport line (for field measurements);
- Sensitive to the position of measuring equipment;
- Very complex for tracking the impact of the parameters involved on the results;
- Difficulties related to sensor vibration, calibration, distortion, replacement.

4.2.4 Test rigs for measuring belt geometry

As it was mentioned in Section 4.1, belt deformations and cross-sectional geometry (length of a belt overlap and its position) are inextricably linked to the PBC CFs indicating the appearance of a contact loss between the belt and idler rolls and belt tendency to collapse. However, only two researchers focused their studies on experimental determination of a geometry of a belt deformed.

Hötte [107] determined belt geometry using an optical system specially built in **Institute of Transport and Automation Technology (ITA) at Leibniz University of Hannover**. The test rig was developed on the basis of a six-point stiffness device and utilized the same belt samples, as described in Table 4.2.

The measuring system was situated at the center of a six-point stiffness device assemblage. The system consisted of a position sensor, mounted on a cantilever arm. The length of the arm could be adjusted with respect to a diameter of a pipe. The stepper motor generated the motion of the arm with the sensor. At the each angular step of a motor, the sensor detected the position of a point on internal contour of a pipe-shape belt, and an angular encoder assigned the polar coordinates of the point. As a result, such optical system could determine only internal contour of a belt geometry.

The speed of a rotary motion implied that one full revolution of the cantilever with the sensor was completed during 20 min. The researcher indicated that the experiment test could be automated repeating the revolutions for 24 hours. As a result, it became possible to track how the viscoelastic properties of a belt influenced its cross-sectional deformations.

The results obtained showed that belts with lower lateral bending stiffness exhibit larger geometrical deformations compared to the stiffer belts. In addition, Hötte carried out number of experiments, investigating which direction of overlap coil generated the largest deformations. The tests were performed for both directions of a belt coil, detecting that the largest deformations for all belt samples tested appeared when the external overlapping edge of a belt coil corresponded to the internal radius of a route curve in horizontal plane.

The test rig, used by Hötte [107] exhibits a number of significant advantages, including simple test performance ability to perform tests simultaneously using six-point stiffness device, detecting cross-sectional deformations together with the contact forces; ability to use the same belt samples as for the troughability test, linking belt deformations with the lateral bending stiffness; ability to test impact of belt's viscoelasticity on the cross-sectional geometry.

At the same time, such test rig construction implies number of disadvantages. The major drawback of the design is that the test rig described measures only the internal contour of a pipe-shaped belt. However, as it will be shown in Chapter 5, belt geometry and CFs are defined by the open structure of a cross-section. Open thin-walled structure under the action of lateral bending loads generates the additional shear flow, which, in turn, can cause appearance of a twisting moment (see Zamiralova and Lodewijks [257], Lodewijks *et al.* [145]). That is why, the test rig described by Hötte provides incomplete information needed, being limited only to the internal contour of a cross section.

Another disadvantage belongs to the rather slow revolution speed for detecting the belt contour. The experimental results for CFs provided by the researcher (see Section 4.2.1 and Section 4.2.2) exhibited rather significant change especially after first 10 minutes of the experiment. This is due to the belt's viscoelasticity effect. In case of the belt deformations,

the position of points detected at the beginning of the sensor's cycle at first minute are already different due to the relaxation effects, compared to the position of the same points at 20th minute of the cycle. In this case, the contour of all set of points detected changes, while the sensor has not yet finished the cycle. This indicates that the measurement of a cross-sectional geometry has to be performed instantly in order to eliminate the discrepancy from the viscoelasticity. In addition, the test rig described by Hötte, does not allow one to investigate the impact of a belt tension on the belt deformations at the straight route curves. In order to include a belt's tensile effect, a static test rig with the special frames was developed.

Kulagin [128] from **Moscow State Mining University, Department of Mining Mechanics and Transport** determined geometry of a belt cross section using a special static test rig that represented the section of a fabric conveyor belt of 650 mm width under an action of tensile forces and supported by the special frames, as illustrated in Fig. 4.27. The researcher formed a central 2m long section of a belt from initially flat shape into a pipe shape with $B/D_{\text{nom}} \approx 4.063$. To preserve the belt in that form, the researcher fixated the pipe-shaped belt with special straps, imitating the idler supports at both edges of the section.

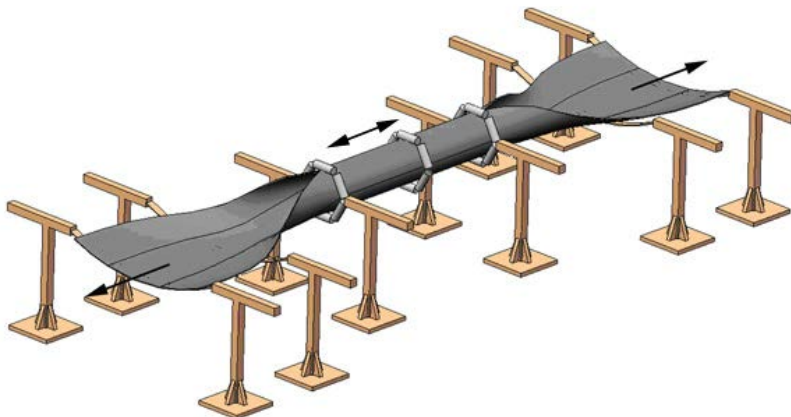


Figure 4.27: Schematic design sketch of a test rig used by Kulagin, Moscow State mining University, for determining a pipe conveyor belt deformations. Bulk material, measuring equipment, and the pulleys that provides belt tension are not shown illustrated (Figure from Kulagin [128]).

At the central position of the test rig, the researcher installed a movable idler set with measuring equipment. The sensors determined the linear displacements of the belt in radial direction. Three positions on a circumference of a belt lateral cross section were selected for the measurements. One point was situated at the bottom of a pipe-shaped cross section, whereas the other two at 45° symmetrically with respect to the bottom point (see Fig. 4.28).

Before the experiment, the belt placed in the test rig was dragged back and forth several times in order to imitate the belt passing the idler stations as it appeared in practice. After that, the belt was pre-tented by means of two pulleys, situated at both edges. At the section

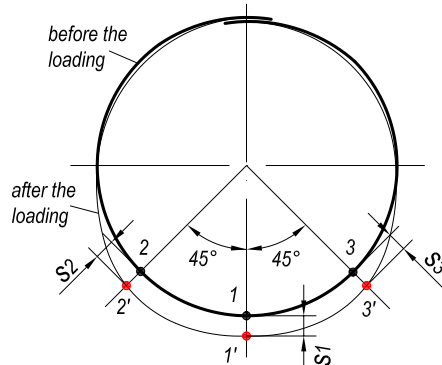


Figure 4.28: Position of three points on the cross-sectional circumference of a pipe belt and their radial displacements, determined by Kulagin in his experiment (Figure modified from Kulagin [128]).

where the belt had a trough shape, the belt was loaded with a sand, and then the bulk material was distributed with special scraper along the whole length of a belt, achieving 90% cross-sectional filling degree of a pipe. The researcher mentioned that such loading condition corresponded to the filling angle of $\theta = 30^\circ$.

At the belt tension of 1 kN, the researcher determined geometrical position of three points selected. The results are used as starting reference parameters. Gradually ascending the belt tension from 5 till 30kN with five intermediate steps, the researcher detected displacements of the same points with respect to their initial geometrical position at 1 kN tension. The belt troughability, its's bending stiffness, line mass, and other parameters of the belt tested were not specified in the source.

The researcher used these displacements aiming to validate the numerical model developed and solved using FEM in ANSYS. The numerical model closely replicated the experiment. Noteworthy to emphasize that Kulagin [128] reported the maximum difference of 23.6% in the results obtained from the numerical solution compared to the experiment. This difference can be considered relatively large, taking into account that the researcher obtained the displacements just for three points on the cross-sectional circumference for each case.

For the comparison, the maximal difference between the experiment and analytical solution for the troughability test, achieved in Chapter 3 for the case study, constitutes no more than 5%. In addition, as it was evident in Chapter 3, the belt deformations are quite insensitive to the change in effective modulus of elasticity. In this case 23.6% difference reported by Kulagin [128] can actually mean very large error in the Young's moduli of a conveyor belt and the load distribution. In addition, the researcher did not specified the sample rate and the precision of the sensors.

The static test rig described of Kulagin [128] exhibits the same disadvantages similar to all static test rigs with various frames and supports, discussed in Section 4.2.2. In particular, due to the belt's viscoelastic properties, the belt tends to solidify at one shape after a substantial period of time. This shape memory affects the resultant belt geometry and CFs as well as ability of a belt to rest more on the lateral idler rolls due to the placement

of a belt inside the test rig.

As it can be seen, Hötte [107], Kulgain [128] utilized the test rigs and the corresponding measuring procedures that do not provide fully reliable or sufficient information on a PBC cross-sectional geometry. In addition, the researchers studied impact of limited number of PBC design parameters on belt deformations. At the same time, besides the studies mentioned, there is no any published source focused on determining a PBC cross-section deformation via experimentation.

Since PBC CFs inextricably linked with the belt deformations, an alternative method for measuring a belt geometry should be introduced, aiming to improve the negative aspects and incorporate the positive aspects of the test rigs described.

4.2.5 Analysis and design selection

Such explicit analysis of the existing test rigs and test procedures presented in previous sections shows that each type of a test rig inherits a number of design advantages with inevitable presence of certain disadvantages. A qualitative analysis of the data from the experiments described indicates that the results obtained from the different sources and different configurations of the test rig deviate quite significantly. This shows how important the choice of a test rig configuration becomes for the experiment.

Nevertheless, there are some similarities in the results presented that can be used for a qualitative comparison of the experimental measurements, performed and described in this chapter (see Section 4.4). With regard to the CFs, considered as an indicator of a PBC test rig performance, it was found that for the case with overlap on the top, the loads at individual rolls were around 40% ~ 45% of the sum of all CFs (except for the results of the field measurements carried out by Hötte [107], which yielded up till 70%). For the overlap at the bottom, these forces did not exceed 80% of the sum. In general, the CF at the top roll was quite significant, compared to the other rolls. In addition, for the case with overlap on top, following the belt coil, lateral roll 2 (see reference Fig. 4.1a) was in a more loaded position, and the following lateral roll 3 was in the less loaded position.

For the qualitative analysis, the most repeatable load patterns represented the following diagrams for the case with the overlap on the top: a) all the rolls are in contact with the belt, and forces at the bottom rolls 3, 4 and 5 are more significant (see Xiaoxia *et al.* [252], Wiedenroth [247]); b) the contact loss appears at one of the top lateral rolls, most frequently for the roll 2 at the beginning of the belt coil, considering the reference Fig. 4.1a (see Hötte *et al.* [108], Hötte [107]); c) both top lateral rolls 2 and 6 have a contact loss, whereas the force at top roll 1 is significant (Bahke [8], Hötte [107]). For the overlap on the bottom, the most frequent load diagram shows a dramatic increase at the bottom roll, with minor CFs at the lateral rolls (see Pang and Lodewijks [188], Bahke [8]).

A test rig configuration implies number of PBC design parameters that can be incorporated in the test. For the perfect case, the test rig has to be adjustable for modeling all possible combinations of PBC design parameters closely replicating behavior of a conveyor in practice. However at the same time, the results obtained on very complex test rigs can be affected by the measurement errors. Some of the possible causes of error are: the wrong choice of the test rig configuration, uneven tension distribution along the belt contour, incorrect calibration of the measuring equipment, the improper choice of the sensors and their position, etc.

Furthermore, the more parameters involved in the experiment, the higher the possibility of the appearance of errors. In this case, it is hard to eliminate the impact of one parameter in the problem, whereas the presence of other parameters might be crucial for the results. That is why, it is important to perform simple experiments that reduce a number of the variables involved. After fully understanding their role in the problem for simple tests, the influence of the other additional parameters can be taken into consideration by upgrading the test rig. The present analysis shows that, except for the general trend in the results, none of the existing studies could clearly explain the influence of even major design parameters of a conveyor on CFs and belt geometry.

Taking all these issues in account, in the present research, the test rig on the basis of a static six-point stiffness device was selected for the experimental determination of PBC CFs and corresponding geometry of a belt deformed. By means of this test rig, the major design parameters (pipe diameter, belt mass, bending stiffness, and the position of the belt's overlap) are tested. The choice for this configuration of a test rig is made because of the following reasons:

- As mentioned above, the test rig is cheap to install, and the experiments are simple to perform and repeat;
- The test rig allows one to test and control the impact of belt viscoelastic properties, detecting and storing the data for the substantial period of time;
- The effect of friction forces can be minimized and controlled;
- Only limited number of major design parameters is involved, as a result, the appearance of a measurement error is also minimal;
- The experiment, performed by means of a static six-point stiffness device is more suitable to be replicated in an analytical model allowing certain assumptions (e.g., linear elasticity, statics, describing behavior of a 3D structure in a 2D form) with further impact analysis, compared to a more complex dynamic mechanical problem of an actual PBC.
- The physical experiment within the static six-point stiffness device can be easily imitated within numerical FEM analysis, realized in various software. The experimental results obtained can be utilized for the validation of FEM models;
- The test rig design allows one to use the same belt samples as for the troughability test and accommodate the same belt's bending stiffness needed in analytical and FEM models. The bending stiffness quantified, as proposed in Chapter 3 can become a link between belt's troughability with its pipe-ability.

After the type of a test rig is selected, the CFs and cross-sectional geometry of a belt deformed are determined experimentally. The details regarding the belt samples properties, test rig configuration, experiment procedure, and testing cases, are explicitly described in the following section.

4.3 Materials and methods

4.3.1 Test rig and experiment procedure

In the present study, the experiment measurements were performed by means of the static six-point belt testing device owned by **Phoenix Conveyor Belt Systems GmbH**. The approximate sketch of a test rig utilized is illustrated in Fig. 4.29. It had a similar conceptual configuration, as shown in Fig. 4.4.

The testing device was represented by the hexagon frame with six load sensors. Those sensors were connected to the plates, which could be easily dismantled. The length of the plates depended on the pipe diameter. The sensors measured the load generated from the conveyor belt sample placed into a test rig. The measurements were conducted for varying pipe diameters and positions of the belt overlap for three different belt samples. To achieve a desirable pipe diameter, the plates with the sensors could move in the radial direction by means of the special screw rails. To ensure a correct positioning of the belt formed into a pipe shape and its overlap location inside the test rig, the central mark, labeled on the belt beforehand, had to coincide with the center of the bottom plate (see Fig. 4.29). To test different positions of the belt overlap, the belt sample was rotated counter clockwise until the belt's central mark formed the required angle in respect to the central mark of the bottom plate.

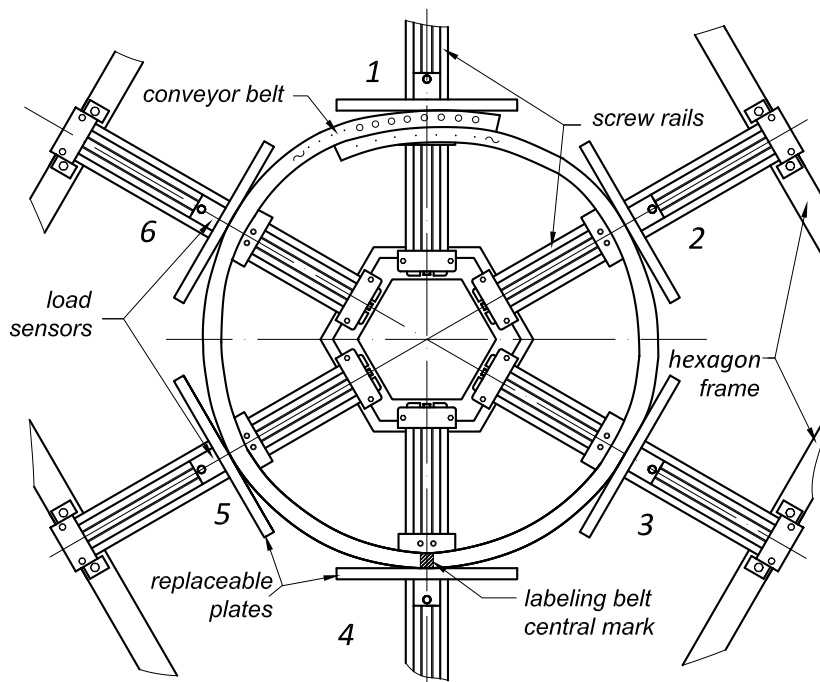


Figure 4.29: Approximate sketch of the static six-point pipe belt stiffness testing device owned by the Phoenix Conveyor Belt Systems GmbH and utilized in the experiment measuring the CFs for the steel cord belt sample.

At first, to investigate the impact of belt's rheology on CFs, one set of the measurements was attained and stored every second throughout 16 hours continuously. Prior the experiment, a belt sample had to be stored flat to eliminate the relaxation effect from the previous deformations. A substantial period of continuous measurements stipulates also an extensive time for the full belt recovery to its initial stress-free state. Aiming to test different cases with the same belt samples from the practical reasons, the rest of the measurements were detected and stored every second throughout approximately five minutes for each case.

To prevent the impact of the friction between the plates and the belt outer cover on the CFs, sheets of foil paper with low friction properties were placed in between the belt and the plates. For the control of an accurate experiment performance, the total scalar projection of a vertical load-vector from all the sensors, had to yield the total belt weight, and the total scalar projection of the horizontal force-vector, defined by the friction forces, should be close to zero.

The sensors load threshold was as low as 0.05 N. The maximum error that was detected for the total vertical force was 6.12% of the total sample weight. The maximum horizontal vector force recorded constituted 3.35 N, which implied 4.85% of the sum of the CFs values for the case.

4.3.2 Determining belt geometry

To measure a geometrical deformation of the cross section that occurred in each case, digital photographs, focused on the center of the test rig with a ruler as a dimension reference, were used. The aim of these measurements was to determine the position of the points of the belt in respect to the reference central point of the bottom plate. For this purpose, fabric belt samples were equidistantly labeled with marks along their contour. In the case of the steel cord belt, the points were used at the belt edges and also on the external belt contour with respect to the corresponding steel cords embedded in the carcass. The pixel-positions of all the points, which were determined based on their color in the photographs, were converted into a real length scale in respect to the central point of the bottom plate.

Noteworthy to emphasize that such approach allows one to determine the full contour of a belt geometry with overlap at once for each case together with the corresponding CFs. This approach is more beneficial, compared to the approach of Hötte [108], as the latter is limited to measure only internal contour of a cross section. In addition, as discussed in Section 4.2.4, the results obtained by Hötte are affected by the viscoelastic properties of a belt, as a full contour of a cross section is obtained during 20 minutes by the optical system. In contrast, the approach presented here determines instant geometry of a belt contour at the moment the CFs are measured.

4.3.3 Belt samples

In total, three belt samples were used in the experiment. All the sample properties are presented in Table 4.9. Two types of belt were used in the experiment: a steel cord and fabric belt samples.

The steel cord belt sample was relatively heavy and had a moderately high bending stiffness. Designed for PBCs, the structure of this belt type implied a more frequent number of steel cords embedded in the central zone of the belt, compared to the edge zones (see

Table 4.9: Properties of the belt samples used in the experiment. The data for the fabric belt Sample 3 is taken from Tables 3.3.

Parameter	Value		
	1	2	3
Sample№	1	2	3
Belt type	ST	EP	EP
Belt width B , mm	1793.67	1596.33	1200.67
Thickness h , mm	22.22	16.78	16.82
Slenderness B/h	80.72	95.13	71.38
Sample longitudinal length b , mm	152.00	146.67	151.33
Moment of inertia $I - bh^3/12$, m ⁴	1.39×10^{-7}	5.775×10^{-8}	6.001×10^{-8}
Sample mass M_{smp} , kg	10.431	4.902	3.672
Line mass $q_{\text{bw}} = M_{\text{smp}}g/B$, N/m	56.989	30.094	29.971
Troughability Y_{max}/B	0.354	0.398	0.434
Effective modulus of elasticity E , MPa (from FEM shell model see Chapter 3)	26.965	7.783	8.212
Bending stiffness EI , Nm ²	3.748	0.449	0.435

Section 2.5.1). As a result, the sample demonstrated an uneven line mass and stiffness distribution along its contour.

The fabric belt, on the contrary, was designed for trough belt conveyors and exhibited a constant line mass and stiffness along its belt width. Compared to the steel cord belt type, it was more flexible and lighter. The selection of this type of a belt was made aiming to compare the experimental results and CFs determined from the analytical approach. As it will be shown in Chapter 5, most of the analytical models that determine PBC CFs assume an evenly distributed belt structure along the belt width. In addition, the method introduced in Chapter 3 for determining belt's transverse flexural rigidity using the troughability test, was also established based on the same assumptions.

From the fabric belt type, two belt samples with different belt widths were used. Initially, the fabric belt sample denoted in Table 4.9 as Sample 2 was selected. It had original belt width of around 1600 mm. During the test, this sample exhibited insufficient lateral bending stiffness for given slenderness ratio B/h , which led to the collapse of a pipe belt geometry even with the substantial length of the overlap (see Section 4.4.2).

To achieve a better formation of a pipe shape, the belt Sample 2 was cut diminishing its width up till $B \approx 1200$ mm. The belt sample obtained was denoted as Sample 3 in Table 4.9. As it will be discussed in Chapter 6, similarly to the troughability parameter, the slenderness ratio B/h significantly affects the load distribution between the idler rolls in PBCs. As it will be shown in Section 4.4, the belt Sample 3 with smaller ratio B/h exhibited better tendency to form an enclosed pipe shape.

Table 4.9 shows that both Sample 2 and Sample 3 exhibited somewhat difference in linear dimensions and some parameters. This deviation appears from the inevitable production imprecision appeared during the belt manufacturing process. As a result, the belt's linear

dimensions as well as bending stiffness and line mass vary along the belt width and length. Taking into account that the slenderness ratio B/h plays significant role in the pipe conveyor belt behavior, this shows that allowable tolerance for the variation in linear dimensions along the belt width and length have to be strictly established and controlled by the manufacturers.

In Table 4.9, the lateral effective moduli of elasticity of the belt samples selected were evaluated from the troughability test using the procedure introduced in Chapter 3. In particular, the numerical solution for shell within trial-and error procedure was used for the sufficient precision. For the fabric belt Sample 3, the data is taken from Table 3.3 and Table 3.4 as a case study, establishing the link between the troughability of a belt and its ability to form a stable pipe shape. The bending stiffness of the steel cord belt sample was also determined using the similar method as for the fabric belt type, keeping in mind that the approach, presented in Chapter 3 is limited to the belts with a uniform structure along the belt width, whereas the steel cord belt sample does not exhibit such property. This assumption was made only for the qualitative analysis of the belt's bending stiffness and its influence on the CFs and belt deformations measured.

The results for CFs and corresponding geometry of all belt samples tested for various cases are presented in the next section.

4.4 Results

The CFs and geometry of a PBC cross section depend on the design input parameters of the conveyor system. A number of parameters tested is limited to the configuration of a test rig selected. In the present study, the following influencing parameters are investigated: impact of a belt's theology with respect to a measurement time, belt type, pipe diameter with respect to the length of the overlap selected, and the orientation of the overlap position. In the present study, the belt type implies impact of belt line mass, lateral bending stiffness, and design of a belt structure along the belt's width and thickness. With respect to the influencing parameters varied during the test, the results are presented.

4.4.1 Impact of a measurement time

At first, the experiment was performed aiming to investigate the impact of the belt's viscoelastic properties on the CFs measured. The measurements of CFs were performed every second during 16 hours continuously using steel cord belt Sample 1 with properties described in Table 4.9. The sample was formed in a pipe shape with a nominal pipe diameter $D_{\text{nom}} = 450$ mm and top orientation of an overlap.

Figure 4.30 illustrates the results obtained for each CF in a set versus an instant time of measurement. In general, the CFs exhibit a general decreasing trend in their absolute values with respect to a measurement time. This phenomenon is governed by the viscoelastic properties of the belt rubber compounds. The relaxation effect diminishes the expansion load from belt bending stiffness that appears from forming a belt from a flat shape into a pipe shape that results in decrease of CFs.

Figure 4.31 shows that the change in CFs during the first 5 minutes of the first experiment is not that significant. As mentioned above, in order to perform the testing of different cases with the same belt samples and also have sufficient time to eliminate the presence of a

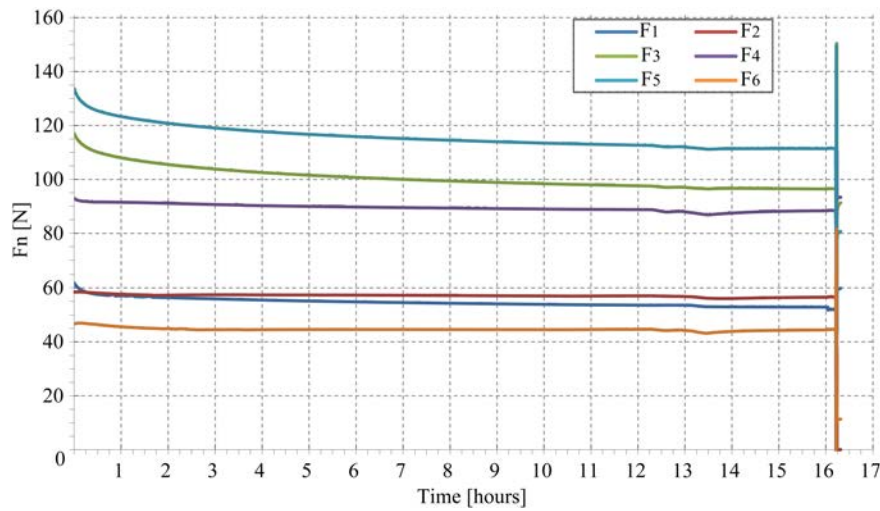


Figure 4.30: Experimental results of CFs, measured during 16 hours continuously for steel cord belt Sample 1 formed in a pipe shape with nominal pipe diameter $D_{nom} = 450$ mm and top orientation of an overlap.

residual stresses in a belt sample, for the rest of tests, the measurements were performed only during 5 minutes continuously, storing the data every second. That is why for each of the CF value, the results were average during this short period of a measurement time.

Besides the practical reasons, the time of 5 minutes was also selected since the troug-

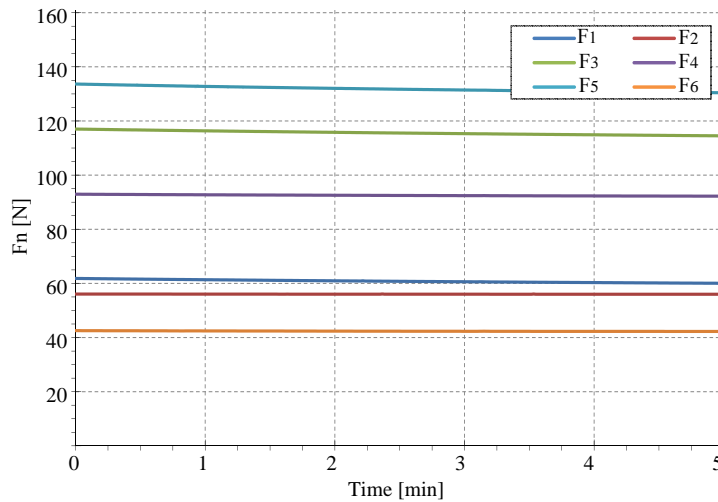


Figure 4.31: Experimental results of CFs, measured during the first 5 minutes continuously for steel cord belt Sample 1 formed in a pipe shape with nominal pipe diameter $D_{nom} = 450$ mm and top orientation of an overlap.

bility test, used for quantifying belt bending stiffness implies also the measurement after 5 minutes of a sample suspension. The belt bending stiffness quantified will be used in Chapter 5 and Chapter 6 in analytical and FEM models that determine PBC CFs, aiming to compare and validate with the experiment case study results.

4.4.2 Influence of a pipe diameter

The results were obtained varying the pipe diameter for the each of the belt type and sample with a 0° overlap position on the top of the pipe. The pipe diameters for the test were selected based on the range given in Eq. 2.17 of Chapter 2, taking into account Table 2.4 for the nominal pipe diameter that defines the hexagon dimensional position of the plates in the test rig. The impact of the pipe diameter and length of the overlap was represented by the ratio of the belt width with respect to the nominal pipe diameter B/D_{nom} . A summary of the details of the tested pipe diameters for the each sample are reported in Table 4.10.

In addition to the cases with varied length of overlap and equivalent pipe diameter, the measurements were performed for the critical case “no overlap”, which corresponded to the nominal pipe diameter 590 mm for Sample 1 and 400 mm for Sample 3, respectively. These critical cases did not have a practical significance in terms of an industrial application. Nevertheless, the purpose of such test was to validate the analytical model that will be developed in Chapter 5 for the CFs. The results for the case “no overlap” especially obtained for the fabric belt type with uniform structure, and consequently uniform line mass, geometry, and bending stiffness along the belt width, are the most important, as they are in agreement with the assumptions made in the analytical models presented in Chapter 3 and Chapter 5.

As mentioned, the results were detected and stored every second for 5 minutes, and the resultant CFs were evaluated as the arithmetic mean for the each force obtained during the test period. The quantitative results of the CFs and position of the cross-sectional points are summarized in Fig. 4.32, 4.33, and 4.34 for Samples 1, 2, and 3, respectively. The points provided in figures correspond to the external contour of a belt formed in a pipe shape. Figure 4.33 illustrates the cross section of a belt Sample 2, collapsed due to the insufficient

Table 4.10: Different pipe diameters tested for the each of the belt sample and corresponding ratios for B/D_{nom} .

Sampl №	Nominal pipe diameter D_{nom} , mm	B/D_{nom}
1	450	3.99
	500	3.59
	530	3.38
	590	3.04
2	450	3.55
3	350	3.43
	380	3.16
	400	3.00

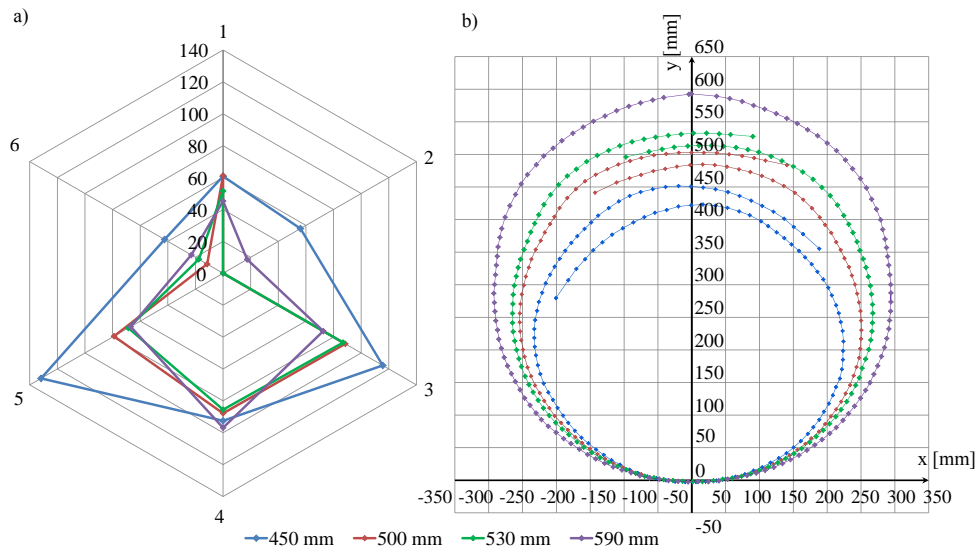


Figure 4.32: a) The CFs [N] and b) cross sectional geometry for steel cord belt type Sample 1 at various pipe diameters.

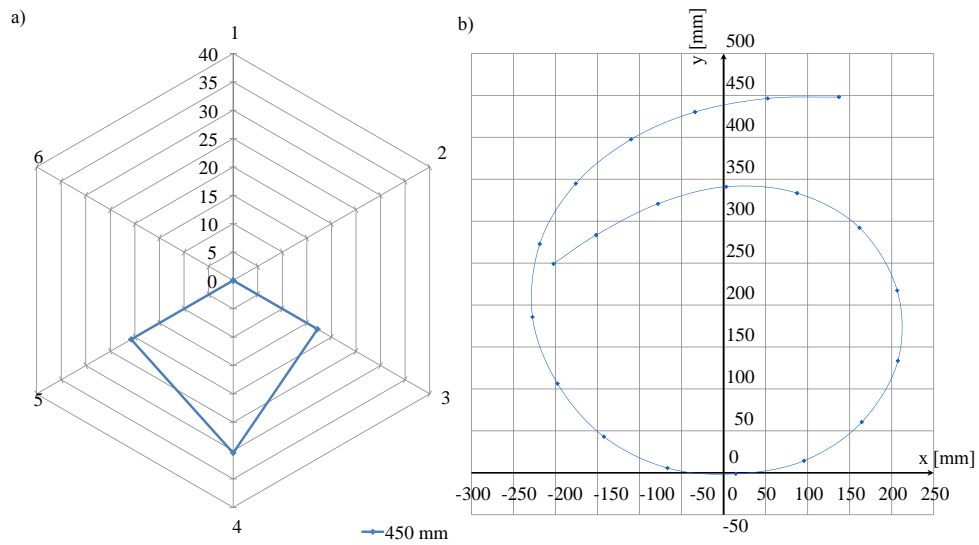


Figure 4.33: a) The CFs [N] and b) cross sectional geometry for fabric belt type Sample 2 and nominal pipe diameter 450 mm.

lateral bending stiffness.

Generally, the increase of the pipe diameter causes a decrease in CFs due to the decrease of the expansion load from the belt bending stiffness. This can be observed for the steel cord belt Sample 1 from Fig. 4.32 for pipe diameters 450, 500, 530 mm and for fabric belt

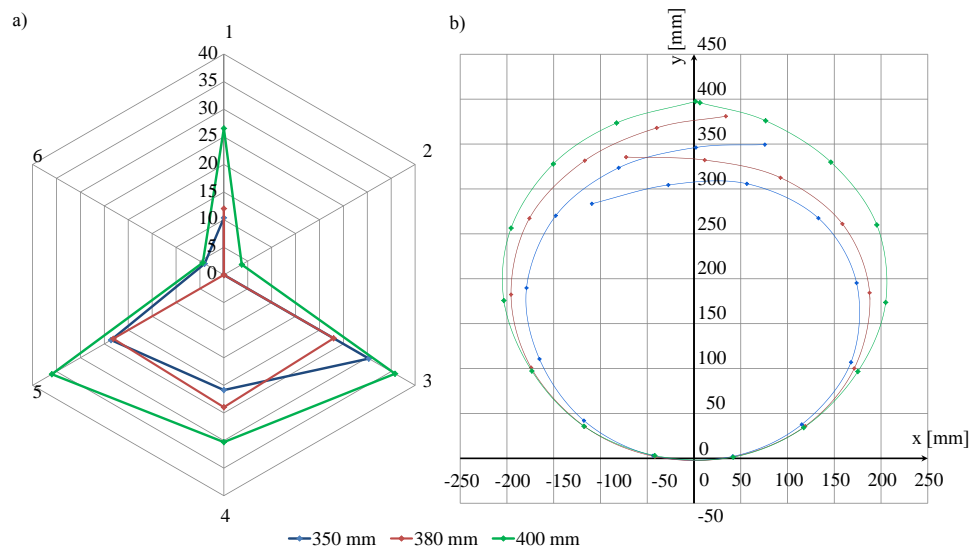


Figure 4.34: a) The CFs [N] and b) cross sectional geometry for fabric belt type Sample 3 at various pipe diameters.

Sample 3 from Fig. 4.34 for pipe diameters 350 mm and 380 mm.

The case “no overlap” for fabric belt Sample 3 produces a sudden growth of CFs. An explanation for this phenomenon is that the abutting belt edges repulse each other, generating an additional load. The repulsion force depends on the resultant from the belt weight and counteracting expansion load from the belt stiffness. If the impact of the bending stiffness is not that high, compared to the belt weight, as it appears for the fabric belt, then the repulsion effect for CFs can become more obvious. The similar observation will appear in Chapter 6 for the impact analysis, using the analytical model, developed in Chapter 5. The analytical model will incorporate additional restraint at the belt edges to trace the repulsion forces at the edges and integrates the load from the belt bending stiffness and load from the belt weight.

The load distribution between the supporting hexagon plates exhibits symmetry for the cross section without belt overlap, with a slight deviation for the steel cord Sample 1 for plates 2 and 6. The numbering of plates is illustrated in Fig. 4.1. However, if there is an overlap, the total picture of load distribution changes dramatically. Based on the results observed, following the belt contour coil with overlap on the top of the pipe, in the beginning of the belt coil, the lateral top plate 2 is in the least loaded position and the lateral bottom plate 3 - in the most loaded position, compared to the other supporting plates. Providing the qualitative analyses with existing studies, similar tendency was reported by Hötte [107], Hötte *et al.* [108], Wiedenroth [247], as described in Section 4.2. The exception for the tendency observed in the present results appears only for the steel cord belt with a pipe diameter of 450 mm and a ratio of $B/D_{\text{nom}} = 3.99$, which leads to a considerably large overlap (see Fig. 4.32).

As mentioned, the fabric belt samples exhibited poor properties to form a stable pipe shape due to low transverse rigidity. As can be noticed from Figs. 4.33 and Fig. 4.34,

Sample 3 did not form enough sealed overlap on the top, whereas Sample 2 collapsed its pipe shape. It is noteworthy to compare these two fabric samples with the considerably same line mass, structure and bending stiffness along their width.

Sample 2 for belt width $B \approx 1600$ mm with nominal diameter 450 mm and ratio $B/D_{\text{nom}} = 3.55$, is not capable to keep the pipe shape and collapses. As the pipe diameter increases, the collapsing tendency of this sample will increase. So in this case, to keep the pipe shape stable and to keep contact with all 6 plates, the sample has to have a smaller pipe diameter, i.e., $D_{\text{nom}} < 450$ mm, and the ratio B/D_{nom} should be greater than 3.55.

At the same time, Sample 3 from the same belt type but with smaller belt width, exhibited a relative stability for the nominal ratio $B/D_{\text{nom}} = 3.43$. A decrease of the pipe diameter to the ratio $B/D_{\text{nom}} = 3.55$ will lead to a larger overlap and an even more stable pipe shape of the fabric belt Sample 3. This means that for the same ratio B/D_{nom} , the same line mass, stiffness and belt structure, the belt sample with a shorter width forms a better pipe shape without collapsing. In other words, in order to maintain a stable pipe shape for the same belt type, but for different belt widths, the ratio B/D_{nom} needs to be selected in such a way, that for wider widths, higher values of ratio B/D_{nom} become necessary. The B/D_{nom} ratio selected for stability is mainly governed by the belt's bending stiffness and belt slenderness.

Although, for significantly flexible belts, it can appear that the belt is capable to maintain a stable enclosed pipe shape with large values of ratio $B/D_{\text{nom}} > 3.5 \dots 4$. This can lead to very large overlaps, and becomes impractical for PBC industrial installations.

4.4.3 Belt type

The belt type is also of particular interest, as it implies different design of belt layout and corresponding belt's bending stiffness, and line mass, distributed along the belt width.

Since the belt's bending stiffness has a great importance in the problem, the results generated by the flexible fabric belt versus the stiff steel cord belt were compared. The data measured for relatively close ratios B/D_{nom} between the belt width and pipe diameter were selected for the comparison. The results for each belt type were transferred into relative values. For load distribution between the hexagon plates, each force was given in relative value to the sum of absolute values of all the six contact forces $F_n / \sum |F_n|$, as carried out in Section 4.2 for the analysis of the existing studies and test rigs. For belt geometry, position of each point of an external belt contour was also transferred in relative value with respect to the corresponding radius of nominal pipe diameter and axes origin in the middle of a pipe. Results that can be used for comparison, were selected based on the approximate ratios $B/D_{\text{nom}} \approx 3.6, 3.4$, and 3.0 , and are presented in Figs. 4.35-4.37.

In general for CFs, some similarities between the data for fabric and steel cord belt samples for the same ratios of B/D_{nom} are noticeable, except for the case when the fabric belt Sample 2 is completely collapsed.

The central part of Sample 1 is specially designed for conveying bulk material, with more frequent installations of steel cords. It thus implies a heavier line mass and higher bending stiffness in the central part of the belt than for the rest of the belt width. Consequently, the bottom plate 4 is more loaded than the lateral bottom plates 3 and 5. In the case of the fabric belt Sample 3, the values of the CFs at lateral bottom plate 3 and 5 are higher or comparable to the CF at the bottom of plate 4.

An analysis of the data for ratio $B/D_{\text{nom}} \approx 4$ revealed that the fabric belt Sample 3 with

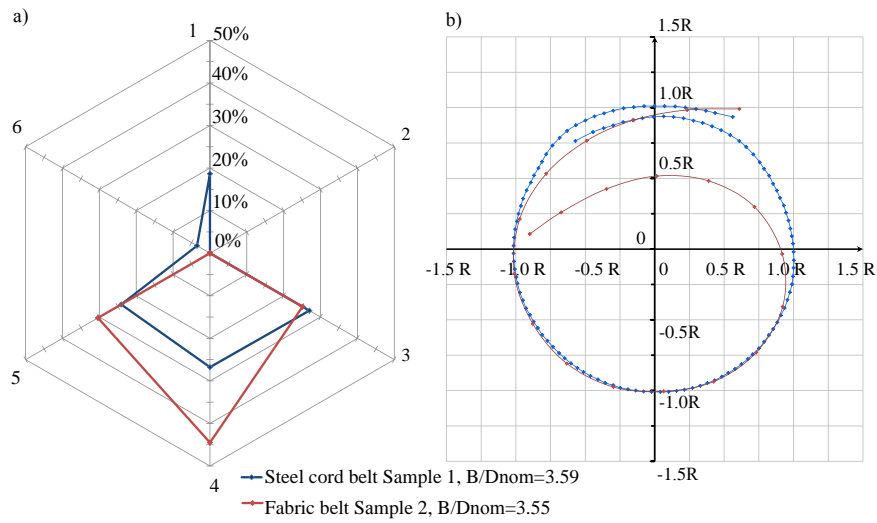


Figure 4.35: a) The CFs [%] and b) the cross sectional geometry for the steel cord belt Sample 1 and the fabric belt Sample 3 in relative values, obtained for the ratio $B/D_{nom} \approx 3.6$.

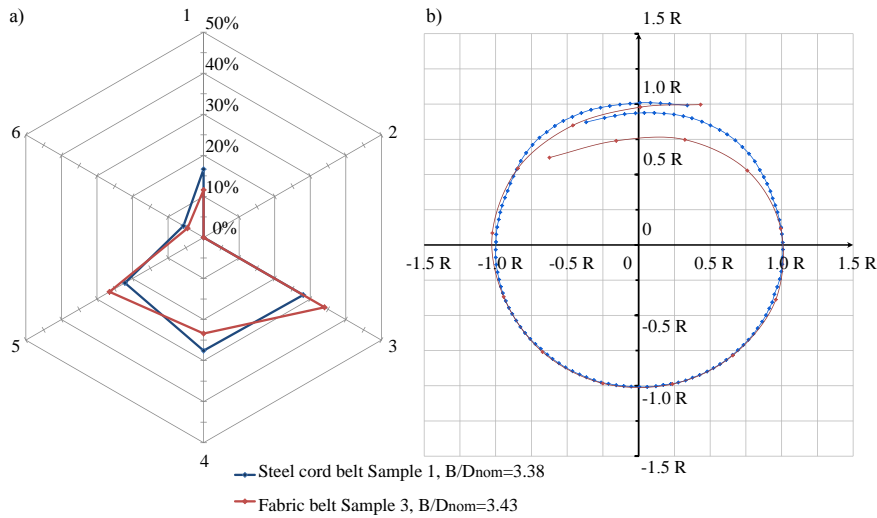


Figure 4.36: a) The CFs [%] and b) the cross sectional geometry for the steel cord belt Sample 1 and the fabric belt Sample 2 in relative values, obtained for the ratio $B/D_{nom} \approx 3.4$.

width $B \approx 1200$ mm and nominal pipe diameter 350 mm did not form enough of a sealed overlap (see Fig. 4.36) due to its minor bending stiffness. The same belt type for Sample 2 with wider belt width $B \approx 1600$ mm and nominal pipe diameter 450 mm completely collapses with ratio $B/D_{nom} \approx 3.6$ (see Fig.4.35). To achieve ratio $B/D_{nom} \approx 3.4$, the pipe

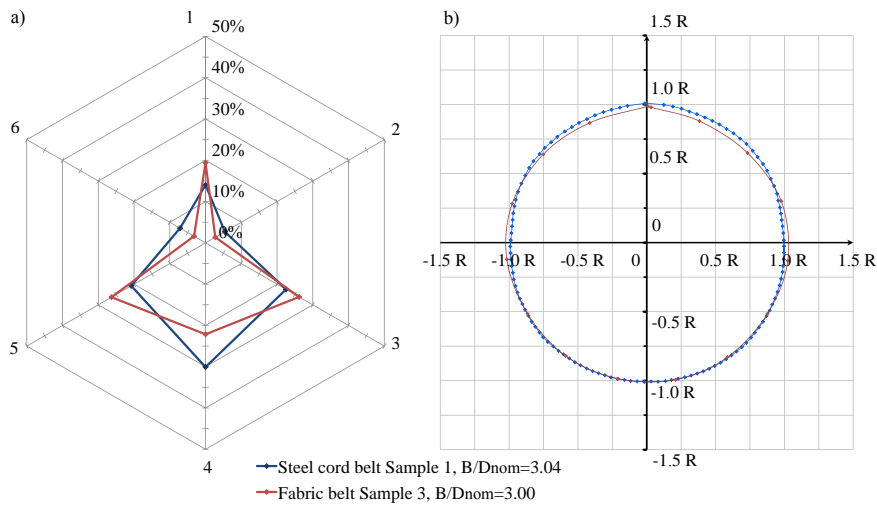


Figure 4.37: a) The CFs [%] and b) the cross sectional geometry for the steel cord belt Sample 1 and the fabric belt Sample 3 in relative values, obtained for the ratio $B/D_{nom} \approx 3.0$.

diameter of Sample 2 has to be increased, which will cause even worse collapsing response of the belt. Obviously, a further increase of a pipe diameter makes the collapsing behavior for the same fabric belt type to exacerbate. Meanwhile, the steel cord belt Sample 1, with a width $B \approx 1800$ mm and high transverse bending stiffness, easily maintains the pipe shape and is completely sealed for the same ratio $B/D_{nom} \approx 3.4$.

Ultimately, this means that in order to provide a stable pipe with a constant B/D_{nom} ratio, which is in the range of $3.5 \leq B/D_{nom} \leq 4$ for all the belt widths offered in a product line, the manufacturer has to guarantee a higher transverse bending stiffness for wider belt widths. Since the ratio between the belt width and pipe diameter $B/D_{nom} = \text{const}$, this observation correlates to the statement of Zhang [269] that larger pipe diameters require a higher transverse bending stiffness.

The present observations drawn about impact analysis of the input design parameters will be analyzed and further discussed in Chapter 6.

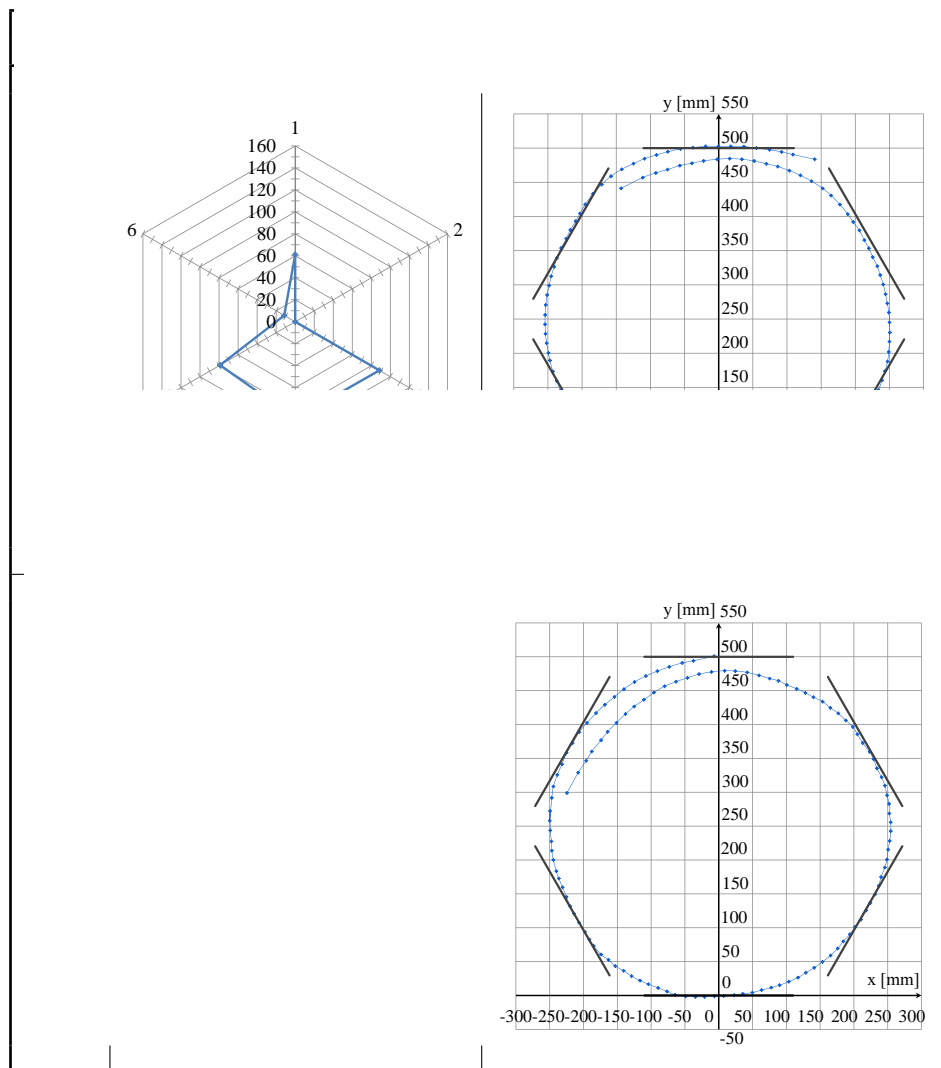
4.4.4 Position of an overlap

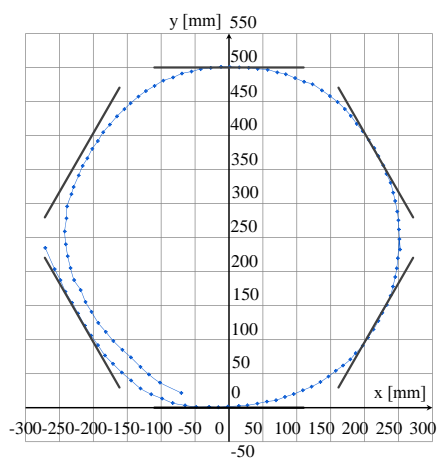
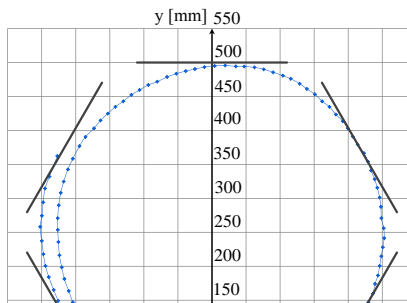
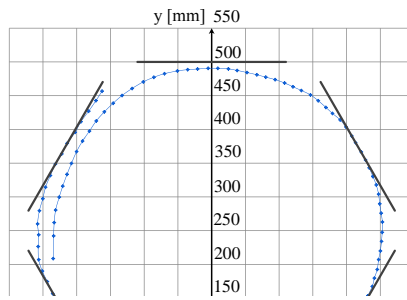
Position of overlap influences the CFs and also cross-sectional geometry of a belt deformed. Due to the twisting effect, the belt overlap position can vary with respect to the initial 0° top position. Practical experience shows that the angle of twist can be substantial, reaching up till 270° according to Day [41], and attaining $\sim 30^\circ \dots 45^\circ$ even after tracking and commissioning of a PBC (see Staples and Mehta [218]). Furthermore, on the return empty strand of a conveyor, the belt usually is transported with overlap placed at the bottom with angle of 180° with respect to the initial 0° top position. Taking this into account, the experimental results were obtained for the overlap position, varying it from initial 0° top position and ending at the bottom position of 180° . The measurements were performed

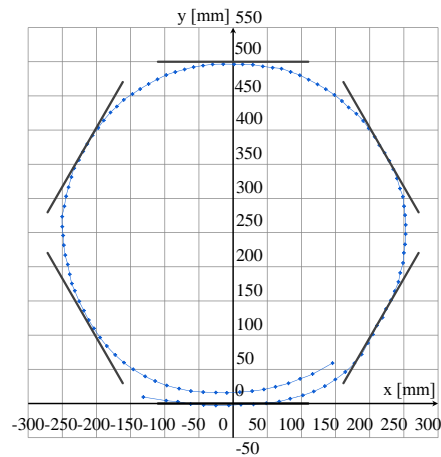
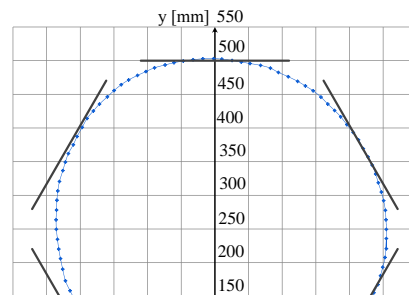
every 30° , rotating the sample counter clockwise.

Since the fabric belt did not exhibit sufficient bending stiffness to form an enclosed pipe shape with an overlap, the test steel cord belt Sample 1 with a high transverse rigidity was used for the of experiments that investigate the influence of the overlap position on the CFs and belt deformations. The ratio between the belt width B and nominal pipe diameter was kept constantly equal $B/D_{\text{nom}} = 3.59$, which corresponded to a pipe diameter of 500 mm. T:

T:







Analyses of the results shows that the position of an overlap significantly affects the load distribution between six hexagon supporting plates. If the overlap is in the position that directly presses against the plate, which corresponds to 0° , 60° , 120° , and 180° , it causes an increase of the CF on that particular plate, and the plate next to it, following counter clockwise along the coil. At the same time, following the coil clockwise, the plate situated next to the plate of overlap has a loss of the CF.

A similar situation appears at the position when the overlap presses against two of the supporting plates, as it happens at overlap rotation angles of 30° , 90° , and 150° . In this case, however, both overlap plates have an increase of the CFs and plate before has a contact loss.

4.5 Conclusions

The present chapter answers the research question on how to determine PBC CFs. For this purpose, an experimental approach is used. Aiming to select the most suitable test rig

configuration, the analysis of all the possible PBC test rig designs was performed in Section 4.2 with respect to CFs measured.

The analysis shows that the results obtained using different test rigs and described in different sources deviate quite significantly and essentially depend on the rig configuration. Taking into account all the design advantages and disadvantages from the analysis of the existing test rigs, the choice is made for the static six-point stiffness device.

A number of reasons justify the selection, prioritizing the advantage of the sufficient accuracy of the results, provided by a full control of the friction forces and a limited number of the design parameters involved that can cause a measurement error. In addition, the choice is made, since the experiment test is simple and static and can be easily replicated using analytical approach and FEM, developed in the following Chapter 5 and Chapter 6, respectively. The present experimental results can be used for the validation purposes. Another reason is that the same belt samples used for the six-point stiffness device can be used for the troughability test. The bending stiffness quantified from the troughability parameter, as recommended in Chapter 3, is needed in the analytical and FEM models for determining the CFs and can serve as a link between belt's troughability to its pipe-ability.

Despite the fact that in general, the CFs measured vary with respect to the selection of the test rig design, the qualitative analysis of the results obtained in the present chapter within the six-point stiffness device and presented in Section 4.4 shows similar load patterns, compared to the CFs attained by the different researchers by means of the different test rigs. In addition, the load at the individual plate for the each experiment case with the 0° overlap position is in range (40 ~ 48)% of the sum of all CFs (see Figs. 4.35-4.37), similarly as observed in other studies [8, 42, 107, 107, 159–166, 247, 252]. As for the 180° overlap position at the bottom of the pipe, the load on the individual plate did not exceed 80% of the sum of all CF. This observation coincides with the experimental results [8, 188].

The impact analysis is performed aiming to answer the research questions about which design parameters influence the CFs and what is their effect. The results from different test cases shows that belt geometry, bending stiffness, length of an overlap and its orientation dramatically affect the load distribution between the idler rolls. The position of the overlap causes an increase in the CFs at the plates in direct contact with the belt overlap.

As for the belt geometry, the experiments revealed that a higher transverse bending stiffness is required for the larger pipe diameters to form a pipe shape without a contact loss. The pipe diameter can be changed by either varying the length of the overlap, represented by the ratio B/D_{nom} , or selecting different belt width B (changing belt's slenderness B/h) and keeping the ratio B/D_{nom} constant. Compared to the stiffer belts with the same width, more flexible belts need higher ratio of B/D_{nom} .

Further research for the experimental approach should be focused in performing more tests with various belt structural designs, considering impact of a belt geometry, in particular the ratio of a belt slenderness B/h , ratio characterizing the length of an overlap B/D_{nom} for each belt type. In addition, the experiment tests can be performed for more design parameters, such as belt tension, presence of bulk material, belt speed, length of carry spacing, using more complex test rigs and studying their influence on contact forces and belt's pipe-ability.

The present chapter has described how PBC CFs can be determined using experimental testing. As closely discussed in Section 4.1, besides the experimental measurements, the CFs can be evaluated using analytical and FEM models. Usage of all three approaches in

complex provides a reliable strategy for determining PBC CFs, option to perform an impact analysis for design parameters involved, and to detect belt's ability to form a stable pipe shape without a contact loss.

The analysis of the test results presented in Section 4.4 showed that it is difficult to extract a functional dependence of PBC CFs with respect to the input design parameters only based on the experimental testing. That is why, next Chapter 5 develops a new analytical model that quantifies PBC CFs that can be used as a reference base to derive a functional dependence between the CFs and participating design parameters. The comparison of the results with the experiment and also the functional dependence of CFs derived are provided in Chapter 6.

Chapter 5

Determination of Contact Forces: Analytical Solution*

"Bulk handling is not rocket science - it's harder".

— Prof. dr. Mark Jones, the Head of the School of Engineering
at the University of Newcastle (Australia)

As indicated in previous chapter, CFs significantly contribute in a PBC system performance. They are needed to evaluate the energy losses from the IRR that is a prime focus of Chapter 7. In addition, they can assist when belt's ability to form a stable pipe shape is investigated (see Chapter 6). Therefore, it is important to determine the CFs in the most accurate way. The previous chapter indicated that using of an experimental approach (Chapter 4), analytical approach (this chapter), and the FEM (Chapter 6) together can provide a reliable solution when the positive and negative aspects of each of the approach are complemented.

The present chapter determines PBC CFs using an analytical approach. For developing an analytical model, a conveyor belt bending stiffness, quantified in Chapter 3 from the troughability test is used. Belt bending stiffness is needed, as it indicates not only the belt deformations as a mechanical response to the external loads from belt and bulk material, but also causes an additional expansion load that appears from folding the belt from a flat shape into a pipe shape. These aspects are investigated in the present chapter.

5.1 Introduction

Previous chapter indicated that CFs and belt deformations influence PBC system performance signifying the need to determine these parameters in the most accurate way. The CFs can be evaluated using experimental, analytical, and FEM approaches. As stated in Chapter 4, all three approaches has positive and negative aspects and used together can provide an optimal way to reflect the contact phenomenon between the belt and idler rolls and predict the CFs.

*This chapter is written partially based on the publications of Zamiralova *et al.* [267], Zamiralova and Lodewijks [263, 264].

The previous Chapter 4 used the experimental approach to determine PBC CFs, whereas the present chapter is focused on developing an analytical approach.

It is important to emphasize the significance of the analytical model, compared to the experimental and computational FEM approaches. The analytical model provides a direct function that can predict the CFs and also show directly the impact of the input design parameters involved. On the contrast, the research conducted only based on experiments without any analytical solution provides only an approximate trend reflecting impact of various physical parameters on PBC CFs. Moreover, the factors in empirical approximating formulas, which are derived specifically for certain test rig configurations, are not always relevant for other conveyor installations.

Furthermore, there is a number of experiment conditions that can generate errors in the output results. As shown in Chapter 4, the experiment results essentially depend on the selection of the test rig design, and the CFs attained from various test rigs significantly deviate. In addition, the higher complexity of the test rig design increases the possibility of the appearance of uncontrolled measurement errors, such as incorrect position and misalignment of the measuring equipment, uncontrolled friction forces, etc. Without any analytical knowledge, it becomes impossible to distinguish which test measurements gave reliable results, and which test results were compromised by the errors made during the testing. All these issues mentioned show the need that the experimental results has to be accompanied by an analytical solution.

In order to construct an accurate analytical approach, it is important to review the existing analytical models, employ the relevant theories, or newly introduce, if needed. In general, the present analysis considers the existing analytical models in two aspects: a) how the external loads are analytically introduced to the problem; b) how the resultant reaction forces are determined from those external loads.

The existing analytical models as well as the new approach developed here linearize the problem around a pre-formed pipe shape geometry under the action of all the external loads. The problem follows the Superposition Principle. The additivity property of this principle implies that the resultant action of all the loads involved in the problem can be considered as a sum of the actions caused by those loads independently. That is why, the modeling of the each of the load can be analyzed separately.

For determining pipe conveyor CFs, illustrated in Fig.4.1, the participating external loads include:

- the load from the belt weight;
- the load from the belt bending stiffness that appears from folding the belt from a flat shape into a pipe shape;
- the load caused by the bulk material.

Each of the load is considered independently in the next sections.

5.2 Load from the belt weight

The load from the belt weight q_{bw} is a vertical load, evenly distributed along the pipe cross-sectional contour (see Fig. 5.1). It can be expressed via the belt's area-related distributed

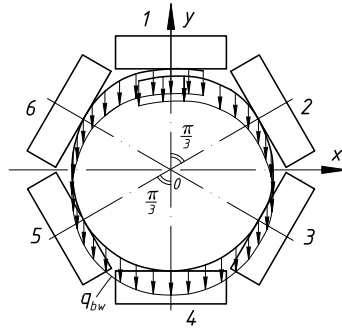


Figure 5.1: Pipe conveyor cross section under the action of the distributed load from the belt weight.

mass $q_{bw} = m''_{bw}gl$, following Eq. 2.13, discussed in Section 2.5.3. The longitudinal length l can be equal to the pitch between the idler stations $l = l_c$ or $l = l_r$. Alternatively, it can be equal to a length of a belt sample $l = b = (150 \pm 2)$ mm, used for the troughability test for quantifying an effective modulus of elasticity, as discussed in Chapter 3, and also for the experimental validation of CFs, determined within six-point stiffness device, provided in Chapter 4.

Dmitriev and Sergeeva [58], Dmitriev and Efimov [55], Sergeeva [210], Efimov [61], Gładysiewicz [91], Kalidien [120] considered the impact of the belt weight on pipe conveyor CFs.

5.3 Load from the belt bending stiffness

The load from the belt's bending stiffness represents the additional expansion load from bending the belt from the initially flat shape to a pipe shape. This load applied to the already pre-folded pipe-shaped belt geometry is a key step that allows the problem's linearization and avoids the complex, nonlinear process of forming the belt from a flat shape into a pipe shape. A number of the researchers use such approach in their analytical models, however, so far, there is no unified opinion how this load needs to be prescribed in the problem.

Wiedenroth [247] provides the general dependence trend that indicates the impact of the load from the belt's bending stiffness on CFs. According to the researcher, the total form force abides by the following rule:

$$F_{bst} = \sum_{n=1}^6 |F_n| - 1.4F_v = 2 \sum |F_n^{top}|, \quad (5.1)$$

where F_v is a total vertical vector force from all the loads involved; $|F_n^{top}| = |F_1| + |F_2| + |F_6|$ is a sum of the CFs at the top rolls in absolute values (see Fig. 4.1). For the support of this rule, Wiedenroth [247] did not provide any quantifying method neither for CFs, nor for the total form force from belt bending stiffness F_{bst} . Moreover, the experimental data in the next Chapter 6 shows that such dependence trend in most of the cases is not justified.

Gładysiewicz [91] carried out a number of the experiments for the belt in a four-roll pipe conveyor. He approximated the results into an empirical dependence and adjusted it for the

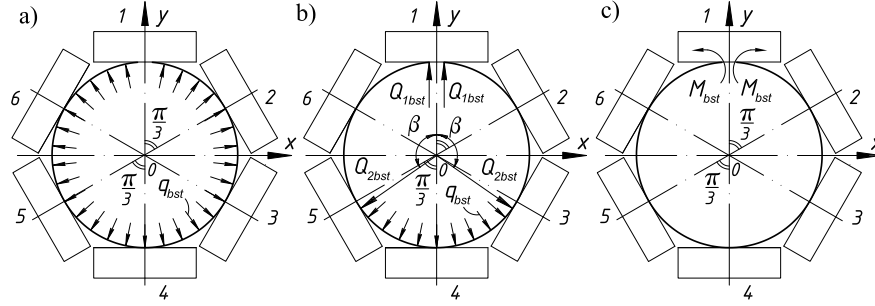


Figure 5.2: Modeling the load from the belt's bending stiffness as an additional loading condition, represented by: a) distributed radial load q_{bst} , according to Chernenko approach [27, 28]; b) distributed radial load q_{bst} in combination with two expansion concentrated forces Q_{1bst} , Q_{2bst} , situated at angle β , based on the model of Dmitriev [52]; c) a newly introduced in this thesis concentrated expansion moments M_{bst} , applied at the belt edges.

six-roll pipe conveyor. The load from the belt's bending stiffness was accounted by applying the same concentrated radial expansion forces F_{bst} from the belt at the each roll. That force equaled:

$$F_{bst} = \frac{2}{3} m''_{belt} g B l \left[2.205 + 0.915 \cos \left(2\pi \frac{h}{B} \right) \right]. \quad (5.2)$$

Another approach was introduced by Chernenko [27, 28]. The approach describes the load from the belt bending stiffness as an expansion radial load q_{bst} , evenly distributed along the pipe conveyor cross section (see Fig. 5.2a) that equals:

$$q_{bst} = \frac{E_2}{(1 - \mu_1 \mu_2)} \frac{h^3 l}{24 R^3} = \frac{EI}{2(1 - \mu_1 \mu_2) R^3}, \quad (5.3)$$

where E_2 is Young's bending modulus of elasticity of the belt in lateral direction.

This Young's modulus can be quantified from the troughability test, as described in the previous Chapter 3. μ_1 , μ_2 are the Poisson ratios of the belt in longitudinal and lateral direction, respectively; R is a radius of the pipe; h is a thickness of the belt; $I = \frac{lh^3}{12}$ is the moment of inertia of a rectangular cross section. The derivation of this load is discussed in Section 5.3.2.

The radial load defined by Chernenko was also used in the studies of Dmitriev and Sergeeva [58], Dmitriev and Efimov [55], Sergeeva [210], Efimov [61] for quantifying pipe conveyor CFs. Wesemeier [238–242] also utilized such load in his studies for four-roll vertical pipe conveyor. In addition, the researcher also suggested to include the effect of forming the belt from a flat shape into a pipe as an external concentrated force applied radially only to the belt edge right at the top roll [238]. This force has a similar to the Chernenko formula in Eq. 5.3, additionally accounting the impact of the belt's overlap in the coefficient:

$$F_{bst} = \frac{E_2}{(1 - \mu_1 \mu_2)} \frac{h^3 l}{24 R \Delta_{ov}}, \quad (5.4)$$

where Δ_{ov} is a length of the overlap of a pipe conveyor belt, folded into a pipe shape. The approach of Wesemeier [238] was also used by Kalidien [120] for a six-roll pipe conveyor.

Chernenko [27, 28] derived Eq 5.3 by describing the belt as an orthotropic shell in a plane strain state that is bent to a cylindrical shape. The approach was also expanded by Dmitriev [52], Dmitriev and Solodovnikova [53], resulting in an analytical solution on contact loads that are produced by a thin plate, formed into a pipe shape and placed inside the cylindrical chamber. The approach of Dmitriev implies the distributed Chernenko-like load q_{bst} together with the concentrated forces Q_{1bst} , Q_{2bst} , applied to the belt structure (see Fig. 5.2b). The approach of Dmitriev [52] will be discussed in the Section 5.3.3.

Summing up, it is possible to state that all the existing research studies that linearize the problem of PBC CFs and introduce the additional load from belt bending stiffness, model that load in different ways and none of the studies carried out the reliable experimental validation. As a result, up till now there is no unified and proven approach that can recommend how to prescribe such load to a problem linearized. That is why, this study aims to compare the relevant approaches in this chapter, provide experimental validation in the following Chapter 4, and make recommendations for using it in industry and for further research.

The analysis for the relevant approaches among existing studies shows that the approach of Wiedenroth [247] provides only the general influence of that load on CFs, but does not describe and quantify that load. Approach of Gładysiewicz [91] is based on the partially empirical dependence that might be valid for the particular experiment test, used for the approximation, but not appropriate for other input design parameters. Other existing studies Dmitriev and Sergeeva [58], Dmitriev and Efimov [55], Sergeeva [210], Efimov [61] utilize or modify (Wesemeier [238–242]) the approach of Chernenko [27, 28] that implies the radial load, evenly distributed along the PBC cross-sectional contour.

Present chapter also selects the approach of Chernenko [27, 28] for the further investigation and comparison, since it does not contain any empirical formulation and seems relevant for the problem. In addition, the approach of Dmitriev [52] is also selected for the comparison, as it represents the further expansion of the Chernenko approach with higher level of complexity. In addition, a new and more simple approach is introduced in this thesis for representing the load from the belt bending stiffness. This new approach implies concentrated expansion moments M_{bst} , applied at the edges of a belt, already formed in a pipe shape (see Fig. 5.2c).

Noteworthy to mention that similar idea of using the bending moments was used by Fedorko *et al.* [67, 68], Fedorko and Molnár [66] for FEM analysis (see Fig. 6.4 in Section 6.2.5). However, the researcher, used the bending moments in a direct problem to fold a belt from a stress-free flat shape into a pipe shape, whereas in present research, the bending moment is proposed for inverse problem as an additional external load, applied on linearized stress-free pipe-shaped belt. In addition, Fedorko *et al.* [67, 68], Fedorko and Molnár [66] did not propose any quantified values of the moments, determining them using a combination of an explicit and an implicit FEM analysis in software with defined finite geometrical shape of a belt. In contrast, the present analysis gives a definite expression to the moments and determines the resultant CFs analytically from them.

The analysis of the analytical results and their comparison with the experiment will be performed in Chapter 6. It will indicate, which method of modeling the load from belt bending stiffness among the selected ones predicts the correct results and which methods are not relevant and should not be applied for determining the CFs for PBCs.

Ultimately, three methods of modeling the load from the belt bending stiffness that are illustrated in Fig. 5.2, are selected for the analytical model:

- 1) a newly introduced concentrated expansion moments M_{bst} , applied at the belt edges;
- 2) the distributed radial load q_{bst} (Chernenko approach);
- 2) the distributed radial load q_{bst} in combination with the concentrated forces Q_{1bst} , Q_{2bst} (Dmitriev approach).

Each of the loading conditions is briefly described in the next sections, organizing them from a simple to complex.

5.3.1 Concentrated expansion moments

The method with concentrated expansion moment is the simplest among others, though it has not been used to determine pipe conveyor CFs. For the simplicity, the problem implies the beam structure in a Cartesian xyz coordinate system, which is formed from a stress-free flat shape into a stressed circular shape, as illustrated in Fig. 5.3.

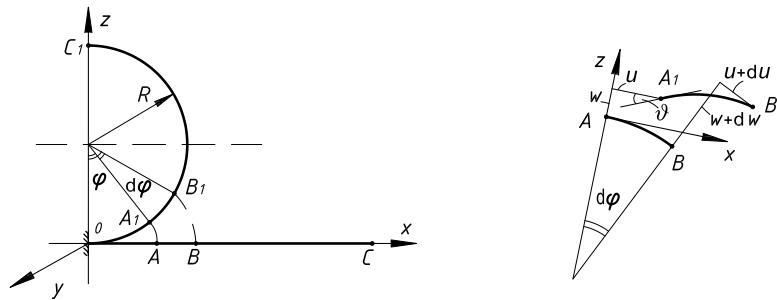


Figure 5.3: The system to determine displacements of a beam-like structure formed from flat shape into a pipe shape (the figure on the right modified from Alfutov [2]).

In this first approximation, the impact of the overlap is not considered in the problem. That is made similarly, as assumed in other approaches of Chernenko [27, 28] and Dmitriev [52], selected for the comparison. Noteworthy to mention that it is expected that the load on the top roll will be less for a belt formed into a pipe shape with overlap, compared to the case without overlap.

When the structure is folded to a pipe shape, the position of any point of that structure before the deformation in the xyz system expressed via cylindrical φ and R coordinates as follows:

$$\begin{cases} x_0 = \varphi R; \\ z_0 = 0. \end{cases} \quad (5.5)$$

After deformation, the coordinates transform to the following:

$$\begin{cases} x = R \sin \varphi; \\ z = R - R \cos \varphi. \end{cases} \quad (5.6)$$

Then the axial displacement along the deformed contour, denoted as u , and radial displacement, denoted as w can be determined as follows:

$$\begin{cases} u = x_0 - x = R \sin \varphi - R\varphi \\ w = z_0 - z = R - R \cos \varphi \end{cases} \quad (5.7)$$

According to the formulas of Alfutov [2], the strains expressed via the displacements equal:

$$\varepsilon_x = \frac{du}{dx} = \varepsilon_{0x} + \kappa_y z, \quad \varepsilon_z = \frac{dw}{dz} = 0, \quad \text{and} \quad \gamma_{xz} = \frac{du}{dz} = 0.$$

In the formula for the strain ε_x , ε_{0x} is the circumferential elongation, and κ_y is the curvature of a structure in plane xz around y -axis. Considering the small element AB , illustrated in Fig. 5.3 with length $Rd\varphi$ before deformation and A_1B_1 after deformation and following the recommendations of Alfutov [2], the axial elongation equals:

$$\varepsilon_{0x} = \frac{A_1B_1 - AB}{AB} \approx \frac{1}{R} \left(w + \frac{du}{d\varphi} \right) = 0, \quad \text{and the curvature becomes } \kappa_y = \frac{d\vartheta}{Rd\varphi} = \frac{d\varphi}{Rd\varphi} = \frac{1}{R},$$

where angle $\vartheta = \frac{1}{R} \left(\frac{dw}{d\varphi} - u \right) = \varphi$. In this case the total strain amounts to $\varepsilon_x = \varepsilon_{0x} + \kappa_y z = 0 + \frac{z}{R}$.

The material model implies the stress-strain relationship, expressed as follows (see Alfutov [2]): $\sigma_x = E\varepsilon_x = E\frac{z}{R}$, $\sigma_z = E\varepsilon_z = 0$, $\tau_{xz} = G\gamma_{xz} = 0$, where G is the shear modulus in plane xz .

Taking into account that the cross-sectional area of a small element along the structural thickness $dA = l dz$ (see Fig. 5.4), it becomes possible to determine the forces acting on the element AB . They equal:

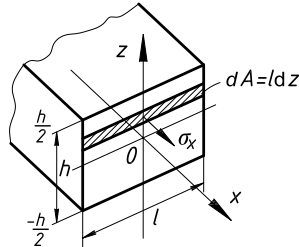


Figure 5.4: An element with cross-sectional area dA considered.

$$\begin{aligned} N &= \int_{-h/2}^{h/2} \sigma_x dA = \int_{-h/2}^{h/2} E \frac{z}{R} l dz = 0; \\ M &= \int_{-h/2}^{h/2} \sigma_x z dA = \int_{-h/2}^{h/2} E \frac{z}{R} l z dz = \frac{Elh^3}{12R} = \frac{EI}{R}; \\ Q &= \int_{-h/2}^{h/2} \tau_{xz} dA = 0. \end{aligned} \quad (5.8)$$

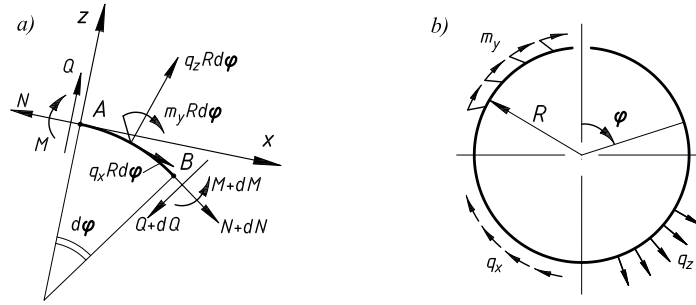


Figure 5.5: a) Loading condition needed for the element equilibrium; b) distributed loads acting on the structure (modified figures from Alfutov [2]).

Eventually, the equilibrium equations for the element AB can be written using the distributed bending moment m_y , tangential load q_x , and radial load q_z (see Fig. 5.5):

$$\begin{cases} Q - \frac{dN}{d\varphi} = Rq_x; \\ \frac{dQ}{d\varphi} + N = Rq_z; \\ -QR + \frac{dM}{d\varphi} = Rm_y; \end{cases} \Rightarrow m_y = q_x = q_z = 0. \quad (5.9)$$

The system is in the state of pure bending, and the constant moment $M = \frac{EI}{R}$, applied symmetrically at the edges of the structure is sufficient to form a circular shape.

In the analytical model, developed in the present chapter for determining the CFs, this moment is applied as an expansion load (in opposite direction) at the edges of a pipe-shaped belt, as shown in Fig.5.2c, representing in the problem linearized the effect of a preliminary bending of a belt from a flat shape into a pipe:

$$M_{bst} = \frac{EI}{R}. \quad (5.10)$$

As for the orthotropic plate in the plane strain state, the moment from the belt bending stiffness can be adjusted accounting for the Poisson ratio:

$$M_{bst} = \frac{E_2 I}{(1 - \mu_1 \mu_2) R}. \quad (5.11)$$

Noteworthy to mention is that the moment M_{bst} is derived considering the direct problem: here the flat structure (belt) in the stress-free state is formed into a pipe/circular shape with resultant stresses distribution along the contour and structural thickness. The linearized problem, in contrast, is an inverse problem: the load from the belt bending stiffness that is applied to a stress-free belt structure in a pipe shape, has to keep the belt in that pipe shape still (no displacements), but generate the stresses along the structural thickness that coincide with the finite stress state of a direct problem.

The concentrated expansion bending moments M_{bst} , applied at the edges of a stress-free pipe-shaped belt (linearized inverse problem) open the structure to the flat position. As a

result, the stress distribution will be the same as in the direct problem after deformation, but with an opposite sign. In this case, the loading condition of applied expansion moments at the edges M_{bst} of a pipe-shaped belt is still only an approximating model. Despite this fact, using this M_{bst} can be sufficient for the approach that determines PBC CFs, since the forces depend on the displacements (see Section 5.6), which are actually equivalent to the direct problem.

5.3.2 Evenly distributed radial load

The derivation of the distributed load was achieved by Chernenko [27, 28] by using the direct problem of forming the plate from a flat shape into a pipe shape, similar as discussed in the previous section. For the simplicity, it is sufficient to consider the beam model and then adjust it to the plate model in a plain strain state.

The formulas for the displacements and strains are the same as provided in the previous section, except the strain ε_x that is determined as follows:

$$\varepsilon_x = \frac{du}{dx} = \varepsilon_{0x} + \kappa_y z + \frac{1}{2}(\kappa_y z)^2.$$

The additional nonlinear summand (or also called von Karman strain) is determined via the angle ϑ as $\frac{1}{2}(\kappa_y z)^2 = \frac{1}{2} \left(\frac{d\vartheta}{Rd\varphi} \right)^2 = \frac{1}{2R^2}$. Consequently the strain equals $\varepsilon_x = \frac{1}{R}z + \frac{1}{2R^2}z^2$.

The stress-strain relationship implies: $\sigma_z = \tau_{xz} = 0$, $\sigma_x = E\varepsilon_x = E \left(\frac{1}{R}z + \frac{1}{2R^2}z^2 \right)$, and the forces then equal:

$$\begin{aligned} N &= \int_{-h/2}^{h/2} \sigma_x dA = \int_{-h/2}^{h/2} E \left(\frac{1}{R}z + \frac{1}{2R^2}z^2 \right) l dz = \frac{EI}{2R^2}; \\ M &= \int_{-h/2}^{h/2} \sigma_x z dA = \int_{-h/2}^{h/2} E \left(\frac{1}{R}z + \frac{1}{2R^2}z^2 \right) l z dz = \frac{Elh^3}{12R} = \frac{EI}{R}; \\ Q &= \int_{-h/2}^{h/2} \tau_{xz} dA = 0. \end{aligned} \quad (5.12)$$

In order to keep the system in the equilibrium, the following distributed loads need to be applied onto the structure:

$$\begin{cases} Q - \frac{dN}{d\varphi} = Rq_x \\ \frac{dQ}{d\varphi} + N = Rq_z \\ -QR + \frac{dM}{d\varphi} = Rm_y \end{cases} \Rightarrow \begin{cases} q_x = -\frac{1}{R} \frac{dN}{d\varphi} = 0; \\ q_z = \frac{N}{R} = \frac{EI}{2R^3}; \\ m_y = 0. \end{cases} \quad (5.13)$$

These formulas can be adjusted for the orthotropic plate in a plane strain state by using the additional coefficient $1/(1 - \mu_1\mu_2)$ for bending stiffness. In this case the formulas coincide with the ones proposed by Chernenko [27, 28] for the plate (see Table 5.1).

Table 5.1: Comparison of the loads, derived in this section for a beam model and by Chernenko for the plate model in [27, 28]

Beam	Shell (from Chernenko [27, 28])
$M = \frac{EI}{R}$	$M = \frac{EI}{(1 - \mu_1\mu_2)R}$
$N = \frac{EI}{2R^2}$	$N = \frac{EI}{2(1 - \mu_1\mu_2)R^2}$
$q_z = \frac{EI}{2R^3}$	$q_{bst} = q_z = \frac{EI}{2(1 - \mu_1\mu_2)R^3}$

For modeling the effect of forming belt from a flat shape into a pipe, Chernenko used the distributed radial load q_{bst} . Dmitriev and Sergeeva [58], Dmitriev and Efimov [55], Sergeeva [210], Efimov [61] also used that Chernenko-load for the linearized problem to calculate the PBC CFs.

5.3.3 Distributed radial load with the concentrated forces

The third method of modeling the load from the belt bending stiffness is the Dmitriev [52] approach. As it was mentioned before, Dmitriev [52] expanded approach of Chernenko [27, 28], considering the plate structure, formed from a flat shape into a pipe shape and then placed into the cylindrical chamber. The purpose of the study was to determine the loads that the stressed plate generates onto the chamber.

The plate, placed inside the chamber is not in contact with the latter along the whole circumference, as illustrated in Fig. 5.6a. Dmitriev assumed certain loading conditions that keep the plate in equilibrium. They imply the distributed expansion load q_{bst} , where the structure touches the chamber, and the concentrated forces Q_{1bst} , Q_{2bst} , situated at angle β , as shown in Fig. 5.6b. The researcher mentions that originally similar loads were proposed by Feodosyev [71], considering the problem of an elastic open ring placed around the stiff cylinder with slightly larger diameter than the internal diameter of a ring.

The researcher [52] states that selection for such load depiction in the problem can be considered acceptable, if there is a determinable angle β that fulfills the equilibrium requirements. For the section AB in Fig. 5.6b, the equations of equilibrium for any point can be written as follows:

$$\begin{cases} N = -Q_{1bst} \sin \varphi; \\ Q = Q_{1bst} \cos \varphi; \\ M = Q_{1bst} R \sin \varphi; \end{cases} \quad (5.14)$$

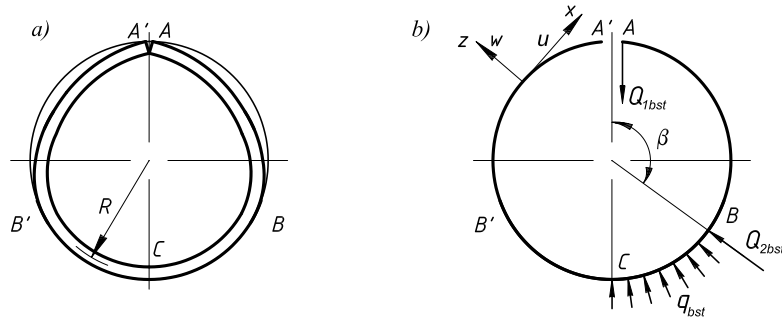


Figure 5.6: a) the deformations of a plate that was initially formed from a flat shape into a pipe shape and then placed inside the cylindrical chamber; b) the depiction of the reaction contact loads acting onto the plate from the chamber. The figure from Dmitriev [52].

and for the section BC , they equal:

$$\begin{cases} N = -Q_{1bst} \sin \varphi - Q_{2bst} \sin(\varphi - \beta) + q_{bst} R (\cos(\varphi - \beta) - 1); \\ Q = Q_{1bst} \cos \varphi + Q_{2bst} \cos(\varphi - \beta) + q_{bst} R \sin(\varphi - \beta); \\ M = Q_{1bst} R \sin \varphi + Q_{2bst} R \sin(\varphi - \beta) + q_{bst} R^2 (1 - \cos(\varphi - \beta)). \end{cases} \quad (5.15)$$

In these equations, the direction of bending moment M , the axial force N , and shear hoop force Q are shown in Fig. 5.6b.

At the section BC , the plate is in a circular shape and is in a contact with the chamber. In this case, the bending moment on this section has to be constant: $M = \text{const}$. The expression for the moment, provided in Eq. 5.15), can be transformed in the following:

$$\begin{aligned} M &= Q_{1bst} R \sin \varphi + Q_{2bst} R \sin(\varphi - \beta) + q_{bst} R^2 (1 - \cos(\varphi - \beta)) = \\ &= \sin \varphi (Q_{1bst} R + Q_{2bst} R \cos \beta - q_{bst} R^2 \sin \beta) - \\ &- \cos \varphi (Q_{2bst} R \sin \beta + q_{bst} R^2 \cos \beta) + q_{bst} R^2 \end{aligned} \quad (5.16)$$

The moment is constant in any position defined by the angle φ along the structural contour, if the following is fulfilled for Eq. 5.16:

$$\begin{cases} Q_{1bst} R + Q_{2bst} R \cos \beta - q_{bst} R^2 \sin \beta = 0 \\ Q_{2bst} R \sin \beta + q_{bst} R^2 \cos \beta = 0 \\ M = q_{bst} R^2 \end{cases} \Rightarrow \begin{cases} Q_{1bst} = \frac{q_{bst} R}{\sin \beta} \\ Q_{2bst} = -q_{bst} R \cot \beta \\ M = q_{bst} R^2 \end{cases} \quad (5.17)$$

The constant moment along the section BC implies that the structure experiences the pure bending, in the case, for the isotropic material model at the section BC , the moment equals: $M_{bst} = \frac{EI}{(1 - \mu^2)} \kappa_y$, and the curvature $\kappa_y = \frac{1}{R}$. This expression coincides with the ones proposed for M_{bst} in the previous sections for the bending moment. Taking into account the expression in Eq. 5.17 for the moment, the distributed expansion load equals

$$q_{\text{bst}} = \frac{EI}{(1 - \mu^2)R^3}.$$

Substituting the expression q_{bst} for isotropic body into system of Eq. 5.17 for the section BC , the latter can be written as follows:

$$\begin{cases} Q_{1\text{bst}} = \frac{EI}{(1 - \mu^2)R^2} \frac{1}{\sin \beta} \\ Q_{2\text{bst}} = -\frac{EI}{(1 - \mu^2)R^2} \cot \beta \\ M = \frac{EI}{(1 - \mu^2)R} \end{cases} \quad (5.18)$$

If the equations for $Q_{1\text{bst}}$ and $Q_{2\text{bst}}$ are substituted into the system of Eq. 5.14, subjected to the section AB of a structure, the following loads are obtained:

$$\begin{cases} N = -\frac{EI}{(1 - \mu^2)R^2} \frac{\sin \varphi}{\sin \beta} \\ Q = \frac{EI}{(1 - \mu^2)R^2} \frac{\cos \varphi}{\sin \beta} \\ M = \frac{EI}{(1 - \mu^2)R} \frac{\sin \varphi}{\sin \beta} \end{cases} \quad (5.19)$$

On the other hand, from the continuity considerations for the sector AB , the strain can be expressed via structural displacement as $\varepsilon_x = \varepsilon_{0x} + \kappa_y z$, where elongation ε_{0x} is equivalent to $\varepsilon_{0x} = \frac{1}{R}(w + \frac{du}{d\varphi})$, and the curvature $\kappa_y = \frac{1}{R} - \frac{d\vartheta}{Rd\varphi}$. Taking into account that the angle equals to $\vartheta = \frac{1}{R}(\frac{dw}{d\varphi} - u)$, the curvature can be written as follows:

$$\kappa_y = \frac{1}{R} \left[1 - \frac{1}{R} \left(\frac{d^2w}{d\varphi^2} - \frac{du}{d\varphi} \right) \right]. \quad (5.20)$$

The stress-strain relationship implies $\sigma_z = \tau_{xz} = 0$, $\sigma_x = \frac{E}{(1 - \mu^2)} \varepsilon_y$, then the axial force N and the moment M for the cross-section area $dA = ldz$ transform to the following expressions:

$$\begin{aligned} N &= \int_{-h/2}^{h/2} \sigma_x dA = \frac{Elh}{(1 - \mu^2)} \frac{1}{R} \left(w + \frac{du}{d\varphi} \right); \\ M &= \int_{-h/2}^{h/2} \sigma_x z dA = \frac{Elh^3}{12(1 - \mu^2)} \frac{1}{R} \left[1 - \frac{1}{R} \left(\frac{d^2w}{d\varphi^2} - \frac{du}{d\varphi} \right) \right]. \end{aligned} \quad (5.21)$$

The expressions for N and M previously found in system of Eq. 5.19 for the section AB are substituted into Eqs. 5.21. This yields the following:

$$\begin{cases} -\frac{h^2 \sin \varphi}{12R \sin \beta} = \frac{du}{d\varphi} + w; \\ \frac{\sin \varphi}{\sin \beta} = 1 - \frac{1}{R} \left(\frac{d^2w}{d\varphi^2} - \frac{du}{d\varphi} \right). \end{cases} \quad (5.22)$$

With these equations, it becomes possible to comprise the differential equation for the radial displacement w at the structural section AB , detached from the cylindrical chamber. It constitutes:

$$\frac{d^2 w}{d\varphi^2} + w = R - R \left(1 + \frac{h^2}{12R^2} \right) \frac{\sin \varphi}{\sin \beta}. \quad (5.23)$$

This is a 2-nd order linear ordinary differential equation that can be solved in the following form:

$$w(\varphi) = C_{w1} \sin \varphi + C_{w2} \cos \varphi + \frac{R}{2 \sin \beta} \left(1 + \frac{h^2}{12R^2} \right) \varphi \cos \varphi + R. \quad (5.24)$$

The constants of integration C_{w1} , C_{w2} , and the angle β are determined from the boundary conditions. At point A , there is no radial displacement, i.e., $w(0) = 0$. At point B of the structure, there is no radial displacement $w(\beta) = 0$, and also no angular rotations $\frac{dw}{d\varphi}(\beta) = 0$.

The angle β that characterizes a detachment of a plate formed into a pipe shape from the cylindrical chamber, can be obtained from the transcendental equation:

$$\left(1 - \frac{h^2}{12R^2} \right) \cos \beta + \left(1 + \frac{h^2}{12R^2} \right) \frac{\beta}{\sin \beta} = 2. \quad (5.25)$$

The findings can be applied to the linearized inverse problem for a pipe conveyor, aiming to determine the CFs. If the presence of an overlap is not taken into account, $B = 2\pi R$, and the effect of a forming a belt from a flat shape into a pipe shape (load from belt bending stiffness) can be represented by the following expansion loads, adjusted for the orthotropic body:

$$\begin{cases} Q_{1bst} = \frac{q_{bst} R}{\sin \beta} = \frac{EI}{(1 - \mu_1 \mu_2) R^2} \frac{1}{\sin \beta}; \\ Q_{2bst} = -q_{bst} R \cot \beta = -\frac{EI}{(1 - \mu_1 \mu_2) R^2} \cot \beta; \\ q_{bst} = \frac{EI}{(1 - \mu_1 \mu_2) R^3}. \end{cases} \quad (5.26)$$

These loads are applied at the structure, as shown in Fig. 5.2a. The angle β that determines the position of the load q_{bst} and Q_{1bst} , Q_{2bst} , is evaluated from Eq.5.27:

$$\left(1 - \frac{\pi^2}{3} \left(\frac{B}{h} \right)^{-2} \right) \cos \beta + \left(1 + \frac{\pi^2}{3} \left(\frac{B}{h} \right)^{-2} \right) \frac{\beta}{\sin \beta} = 2. \quad (5.27)$$

As it can be seen, the angle β in Eq. 5.27 only depends on the belt slenderness. If the presence of an overlap is not taken into account, the geometrical range for the belt slenderness B/h , established in Section 2.5.2 of Chapter 2 constitutes $6.67 \leq B/h \leq 643$. The angle β then exhibits a quite limited variation range: $\beta \approx 115.5^\circ \dots 122^\circ$.

Similar to the previous approaches, discussed in Sections 5.3.1 and 5.3.2 for modeling the load from belt bending stiffness, the problem studied by Dmitriev and discussed in this Section 5.3.3 is a direct problem. Application of the loads onto the stress-free belt already in

a pipe shape (implicit problem), needs to be considered only as an approximating approach, as it does not generate the absolutely equivalent stress field in the structure, as it would become in the finite state of nonlinear process of forming belt from flat shape into a pipe. However, the approach might generate the correct CFs, since the displacements in the direct and implicit problems are equivalent.

The results for the PBC CFs, obtained using all three approaches of modeling the load from belt bending stiffness will be compared between each other and also with the experiment in Chapter 6. This comparison will indicate whether it is possible to describe the effect of actual folding the belt from a flat shape into a pipe shape as an external load, applied to the stress-free belt in a pipe shape, and which of the methods, selected and described in Sections 5.3.1, 5.3.2, and 5.3.3 predicts the correct CFs.

Now the load from the belt weight and load from the belt bending stiffness are described for empty PBC. The next section considers the load from the bulk material needed for determining the CFs for a PBC transporting bulk solids.

5.4 Load from bulk material

Load from the bulk material is an important parameter that needs to be taken into account when the conveyor design is selected. At certain loading conditions, it can generate a positive effect on the belt ability to form a stable pipe shape, whereas the same belt without a bulk material might exhibit a contact loss between the belt and the top idler rolls.

In general, the load generated by the bulk material inside the pipe conveyor belt is a result of a highly nonlinear complex process. The loading happens when the belt is already formed from a flat shape into a trough. Next, the belt with the bulk material is gradually formed into a pipe shape by special forming idlers. During this process, the bulk material is compressed inside the pipe, resulting in a load varied not only along the pipe circumference, but also longitudinally between the idler sections. Dyachenko [60] conducted an experimental research on the displacements of bulk material layers during the formation of a belt into a pipe shape. The resultant load from the bulk material is also affected by the vibration during the transportation process, properties of a bulk, the lump size, and how evenly the feeder loads the bulk solids along the belt width.

Obviously, describing the load from the bulk material as an additional external load applied onto a belt already in a pipe shape (linearized problem) significantly reduces the complexity of a problem, aiming to determine pipe conveyor CFs. Since the design of a PBC is an evolved prototype of the conventional trough belt conveyor, number of researchers applies the methods developed specifically for trough conveyors also to a PBCs.

The simplest method (see Kalidien [120]) for modeling the load from the bulk material uses the approach, based on the area A_C , A_L of the cross section that rests onto the each of bottom idler rolls (the central idler roll denoted as C, and lateral roll indicated by L, correspondingly). The load from the bulk material is represented by the forces shown in Fig.5.7 that equal to:

$$\begin{aligned} F_L &= A_L \rho_{\text{bulk}} g l; \\ F_C &= A_C \rho_{\text{bulk}} g l. \end{aligned} \tag{5.28}$$

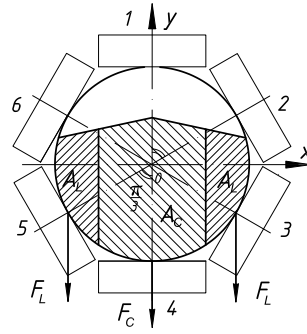


Figure 5.7: Load from the bulk material in a PBC system, represented by the area-related gravity forces (Kalidien [120]) or the forces, determined by Wiedenroth [247], following the recommendations of Grimmer and Grabner [86] for the conventional trough conveyor with with $\beta_{\text{idl}} = 60^\circ$ installation angle of the wing idler rolls.

The other similar approach was proposed by Wiedenroth [247]. The researcher assumes that the impact of the bulk material on the rolls is the same as for the conventional trough conveyor with $\beta_{\text{idl}} = 60^\circ$ installation of the wing idler rolls. The researcher refers to work of Grimmer and Grabner [86] on trough conveyors, describing the load as the vertical forces, acting on the lateral (L) and the central (C) rolls equivalent to the follows:

$$\begin{aligned} F_L &= 0.2F_{\text{bulk}}^v = 0.2k_Q\pi R^2\rho_{\text{bulk}}gl; \\ F_C &= 0.6F_{\text{bulk}}^v = 0.6k_Q\pi R^2\rho_{\text{bulk}}gl. \end{aligned} \quad (5.29)$$

In these equations, F_{bulk}^v is a total vertical load-vector from the bulk material weight. It depends on the cross-sectional filling degree k_Q (see Section 2.3.3) as follows:

$$F_{\text{bulk}}^v = k_Q\pi R^2\rho_{\text{bulk}}gl. \quad (5.30)$$

Such representations of the bulk material load are considered incomplete and do not show the correct results. As it will be shown further, the load from the bulk material does not act only at the bottom rolls, as it is assumed in the studies mentioned, but also it can generate the CFs at the top rolls, depending on the conveyor filling degree. In addition, the loading conditions, developed based on the area-related bulk gravity do not take into account the lateral expansion component from the active and passive stressed state of the compressed bulk material inside the pipe and also its longitudinal variation.

5.4.1 Active and passive stress state theory

In general, the nature of the load from the bulk material is defined by the active and passive stress state theory of a bulk solids. When the belt passes through the idler assembly, the belt is in the process of unfolding and opening outwards. During this time period, the loaded material causes a distributed active pressure on the belt surface, due to the bulk material stress state (see Fig. 5.8). Before the belt passes through the next idler station, there is

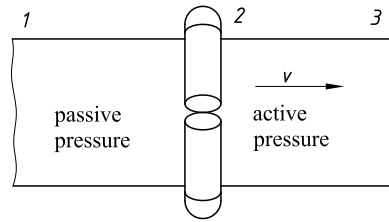


Figure 5.8: Active and passive stress state of the bulk material transported in a PBC (Image from [58]).

a certain position between the stations along the carry spacing where the belt begins to compress the material, which in turn generates the passive material pressure.

In order to accommodate the active/passive stress state theory for a PBC, a number of the researchers (Gushchin [88], Kulagin [126–129], Dmitriev and Kulagin [56], Efimov [61], Dmitriev and Efimov [55], Sergeeva [208, 210], Dmitriev and Sergeeva [58], Galkin *et al.* [80], Guo *et al.* [87], and Gładysiewicz [91]) proposed an alternative way to prescribe the load from the bulk material in a linearized problem aiming to determine the PBC CFs.

Gushchin [88] in 1972 (see also [89, 90]) developed an approach for describing the load from bulk material in a deep trough belt conveyor. The approach implied the division of the bulk material cross section into elementary layers and determination of the vertical σ_v and horizontal σ_h stress components acting onto the belt surface (see details in the next Section 5.4.2). From the equilibrium considerations, the stresses were expressed via the radial σ_φ and tangential τ_φ components distributed onto the pipe circumference. A number of researchers from the Moscow State Mining University, such as Kulagin [126–129], Dmitriev and Kulagin [56], Efimov [61], Dmitriev and Efimov [55], Sergeeva [208, 210], Dmitriev and Sergeeva [58], Galkin *et al.* [80] used approach of Gushchin applying it to a PBC system. These researchers assumed that the load from the bulk material could be represented by the pressure load, resultant only from the radial component σ_φ of bulk material stresses, ignoring the presence of the tangential constituent τ_φ . As it will come in Section 5.4.5, such approach decreases the total vertical load that leads to underestimation of the overall bulk material weight. Thus, the CFs calculated do not accurately account the actual loading in the resultant forces determined.

The same approach of accounting the load from the bulk material for PBCs was utilized by Guo *et al.* [87] and Gładysiewicz [91]. The researchers also determine the bulk material stress state similar to Gushchin, and also accommodated in CFs only the radial component from the bulk material, ignoring the tangential stresses. The only difference is that [87] included an additional effect from the angle of repose λ in the expression of height h_{bulk} for each bulk material layer, which determines the bulk material vertical stresses, (see details in Section 5.4.3), whereas the rest of the studies [55, 56, 58, 61, 80, 87, 91, 126–129, 208, 210] including also Gushchin [88], considered this effect negligible.

The analytical model, developed in this thesis, also uses the Gushchin approach to determine the load from the bulk material, although the model takes into account all the stresses components involved, preserving them as vertical and horizontal distributed loads. In addition, the present study includes the effect of an angle of repose λ (see Section 2.4.2) in the expressions for bulk stresses. The next section describes the bulk material stress state

for a better understanding of the approach used and its difference, compared to the other methods.

5.4.2 Bulk material stress state

In order to determine the loads that are generated from the bulk material, it is assumed that bulk solids is homogeneous with very small lump size, compared to the pipe diameter. The circumference of the pipe conveyor belt is divided into the elementary sections, with a length equal to $Rd\varphi$, as it was originally proposed by Gushchin [88, 89]. The bulk material cross section is split into the rectangular layers with respect to the angle φ , as illustrated in Fig. 5.9.

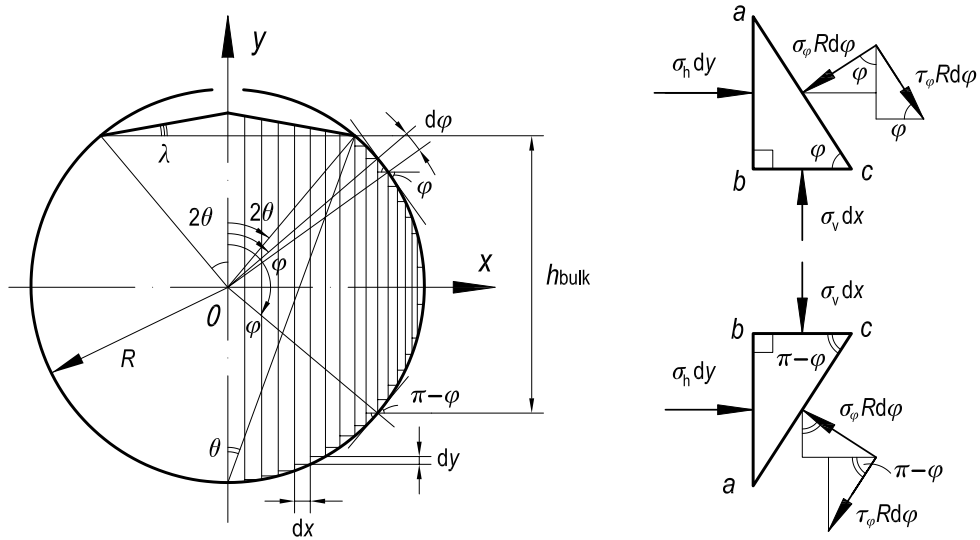


Figure 5.9: A cross section of a PBC, filled with a bulk material with the filling angle $0 \leq 2\theta \leq \frac{\pi}{2}$ and divided into the layers with respect to angle φ .

The triangular prism (abc) of the bulk material, (see Fig. 5.9) is in a stress state under the action of vertical stress σ_v , applied on its horizontal side (bc), and horizontal stress σ_h , applied on its vertical side (ab). The radial stress σ_φ and shear stress τ_φ , acting on the prism side (ac) determine the Mohr stress circle, and can be evaluated from the equilibrium consideration (see the mathematical derivation in Schulze [205], Zenkov [268], Gushchin [89]):

$$\begin{aligned} \sigma_\varphi &= \sigma_v \cos^2 \varphi + \sigma_h \sin^2 \varphi = \frac{1}{2}(\sigma_v + \sigma_h) + \frac{1}{2}(\sigma_v - \sigma_h) \cos 2\varphi; \\ \tau_\varphi &= \frac{1}{2}(\sigma_v - \sigma_h) \sin 2\varphi. \end{aligned} \tag{5.31}$$

The ratio between the radial stress and shear stress $\sigma_\varphi/\tau_\varphi$ refers to the wall friction angle between the bulk material and the belt surface. For an operational steady state of the PBCs, installed without inclination, there should not be any relative motion between the bulk material and the belt surface in transverse direction. In this case, the wall friction angle

is not fully mobilized, and the radial stress σ_φ can be considered to be perpendicular to the shear stress τ_φ . As it was mentioned above, in the studies [55, 56, 58, 61, 80, 87, 88, 91, 126–129, 208, 210], only the radial component was considered σ_φ , assuming the impact of the tangential component τ_φ to be negligible. As it will be shown in Section 5.4.5, such approach does not provide accurate results, as it decreases the overall total vector force from the bulk material weight and overestimates the lateral loads.

Since there is no relative motion between the bulk material and the belt, it is unnecessary to represent the stress state of a bulk material using radial σ_φ and tangential τ_φ stresses. Therefore, in the present study, the applied load from the bulk material can be sufficiently formulated using vertical σ_v and horizontal σ_h load components. The next sections describe each of these components accepted.

5.4.3 Vertical stress component

The bulk solid materials exhibit different behavior than the Newton fluids. Newton fluids cannot transmit shear stresses, and the pressure in a container filled with the fluid, increases linearly with the depth of the container. Contrary to Newton fluids or liquids, the bulk material does transmit the shear stresses, and the walls of the container can carry part of the bulk weight. In this case, the pressure in the container with the bulk material is less in the downward direction (see Fig. 5.10). However, for the PBC cross section, the overall dimensions in the horizontal and vertical directions are comparable. In this case, the behavior of the bulk material can be assumed similar to liquids (see the top of the graph of Fig. 5.10 for small depths).

Therefore, the vertical stress component for a PBC can be assumed to be equivalent to the hydrostatic pressure, i.e. proportional to the height h_{bulk} of the bulk material layer:

$$\sigma_v = \rho_{\text{bulk}} g h_{\text{bulk}}. \quad (5.32)$$

The vertical stress component depends on the cross sectional filling angle θ and the angular position at the structural contour φ .

If the filling angle of the cross section is in the range of $0 \leq 2\theta \leq \frac{\pi}{2}$, i.e., $0 \leq \theta \leq \frac{\pi}{4}$, for angle $2\theta \leq \varphi \leq \frac{\pi}{2}$, the vertical stress is directed upward, as illustrated in Fig. 5.11, and equals:

$$\sigma_v = \rho_{\text{bulk}} g R (\cos 2\theta - \cos \varphi). \quad (5.33)$$

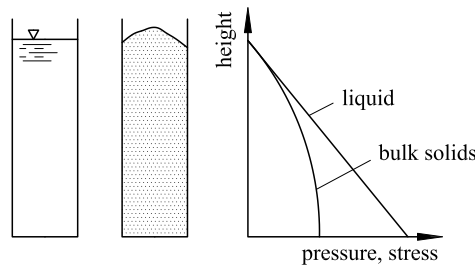


Figure 5.10: Pressure and stress, respectively, in liquids and bulk solids (Figure from Schulze [205]).

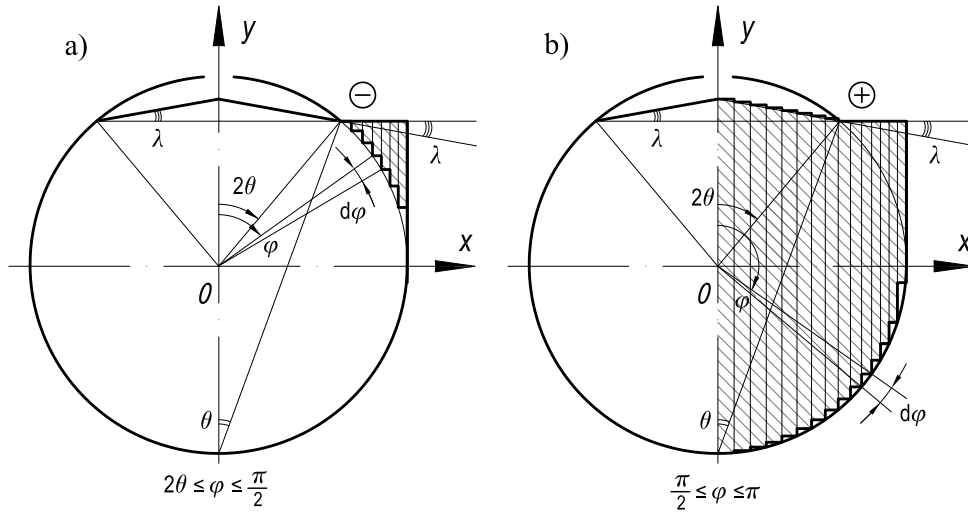


Figure 5.11: The vertical stress distribution diagram with respect to angle φ , provided for the filling angle $0 \leq 2\theta \leq \frac{\pi}{2}$ and angular position: a) $2\theta \leq \varphi \leq \frac{\pi}{2}$, and b) for $\frac{\pi}{2} \leq \varphi \leq \pi$.

For angle $\frac{\pi}{2} \leq \varphi \leq \pi - 2\theta$, the vertical stress is directed downward and equals:

$$\sigma_v = \rho_{\text{bulk}} g R (\cos 2\theta + \cos(\pi - \varphi)) = \rho_{\text{bulk}} g R (\cos 2\theta - \cos \varphi). \quad (5.34)$$

For angle $\pi - 2\theta \leq \varphi \leq \pi$, the vertical stress is directed downward and is affected by the angle of repose in motion (surcharge angle λ):

$$\begin{aligned} \sigma_v &= \rho_{\text{bulk}} g R [\cos 2\theta + \cos(\pi - \varphi) + \tan \lambda (\sin 2\theta - \sin(\pi - \varphi))] = \\ &= \rho_{\text{bulk}} g R [\cos 2\theta - \cos \varphi + \tan \lambda (\sin 2\theta - \sin \varphi)]. \end{aligned} \quad (5.35)$$

If the filling angle of the cross section is within $\frac{\pi}{2} \leq 2\theta \leq \pi$ ($\frac{\pi}{4} \leq \theta \leq \frac{\pi}{2}$), the vertical stress component can be found for any angular position $2\theta \leq \varphi \leq \pi$ using the resultant expression given in Eq. 5.35.

Noteworthy to mention that Gushchin [88], Kulagin [126–129], Dmitriev and Kulagin [56], Efimov [61], Dmitriev and Efimov [55], Sergeeva [208, 210], Dmitriev and Sergeeva [58], Galkin *et al.* [80], Gładysiewicz [91] in their studies ignored the effect of the angle of repose when the vertical stress component σ_v is determined. They assume the expression in Eq. 5.34 for angle $\pi - 2\theta \leq \varphi \leq \pi$ is the same as for the angle $2\theta \leq \varphi \leq \pi - 2\theta$ (Eqs. 5.33-5.34).

In the present research analysis, the vertical stress distribution of σ_v along the circumference of a PBC cross section is shown in Fig. 5.11. The vertical stress component remains the same in the longitudinal direction of the pipe conveyor between the idler stations. In terms of the carry spacing of a PBC for $l = l_c$ or $l = l_r$, the vertical load component developed from the bulk material for the filling angle becomes the following:

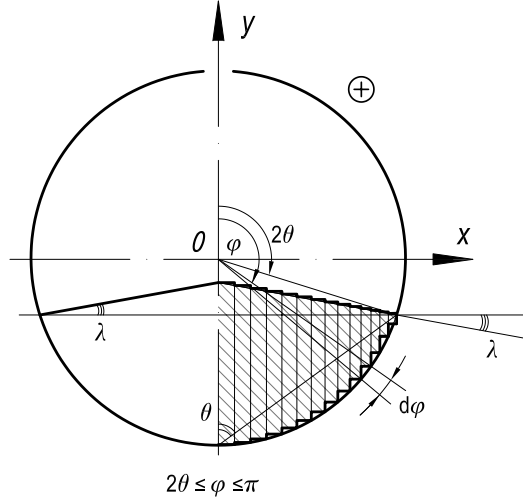


Figure 5.12: The vertical stress distribution diagram for the cross-sectional filling angle $\frac{\pi}{2} \leq 2\theta \leq \pi$ with respect to the angular position φ , $2\theta \leq \varphi \leq \pi$.

$$\begin{aligned}
 q_{\text{bulk}}^{\text{v}} &= \int_0^l \sigma_{\text{v}} dz = \sigma_{\text{v}} \int_0^l dz = \\
 &= \begin{cases} \rho_{\text{bulk}} g l R (\cos 2\theta - \cos \varphi), & \text{for } 2\theta \leq \varphi \leq \pi - 2\theta; \\ \rho_{\text{bulk}} g l R [\cos 2\theta - \cos \varphi + \tan \lambda (\sin 2\theta - \sin \varphi)], & \text{for } \pi - 2\theta \leq \varphi \leq \pi. \end{cases} \quad (5.36)
 \end{aligned}$$

In the lateral cross section of a PBC, this vertical load component $q_{\text{bulk}}^{\text{v}}$ is exerted onto the horizontal side of the prism (bc) with length dx . It can be expressed along the circumference via the angle φ :

$$dx = \begin{cases} R \cos \varphi d\varphi, & 2\theta \leq \varphi \leq \frac{\pi}{2}; \\ -R \cos \varphi d\varphi, & \frac{\pi}{2} \leq \varphi \leq \pi. \end{cases} \quad (5.37)$$

If the filling angle is in the range of $\frac{\pi}{2} \leq 2\theta \leq \pi$, the vertical component from the bulk material load, illustrated in Fig. 5.12, is defined by:

$$q_{\text{bulk}}^{\text{v}} = \rho_{\text{bulk}} g l R [\cos 2\theta - \cos \varphi + \tan \lambda (\sin 2\theta - \sin \varphi)], \quad (5.38)$$

being distributed for any angular position $2\theta \leq \varphi \leq \pi$ onto the length dx :

$$dx = -R \cos \varphi d\varphi. \quad (5.39)$$

5.4.4 Horizontal stress component

According to the Coulomb Pressure Theory, the horizontal component generated by the bulk material, is proportional to the vertical stress component (see Schulze [205]). Thus the horizontal stress σ_{h} , acting on the vertical side (ab) of the prism (abc) for each bulk material layer, can be evaluated as follows:

$$\sigma_{\text{h}} = K(z) \sigma_{\text{v}}, \quad (5.40)$$

where $K(z)$ is a bulk material lateral stress ratio, which varies along the longitudinal length and also is governed by the effective angle of internal friction φ_e (see Section 2.4.3). The internal friction angle can be determined experimentally via the Jenike shear test as a slope of the linearized effective yield locus in a Mohr stress circle constructed, as for instance described by Schulze [205]).

By taking into account the variation of the bulk lateral stress ratio $K(z)$ in the conveyor's longitudinal direction ($l = l_c$ and $l = l_r$ in case the conveyor is also loaded on the return strand), the distributed load q_{bulk}^h from the horizontal component of the transported bulk material can be evaluated as follows:

$$q_{\text{bulk}}^h = \int_0^l K(z) \sigma_v dz = \sigma_v \int_0^{l_c} K(z) dz. \quad (5.41)$$

For the critical stress states, the coefficient $K(z)$ equals:

$$K_{\min} = K_a = \frac{1 - \sin \varphi_e}{1 + \sin \varphi_e} = \tan^2 \left(\frac{\pi}{4} - \frac{\varphi_e}{2} \right) \text{ for active stress state;} \quad (5.42)$$

$$K_{\max} = K_p = \frac{1 + \sin \varphi_e}{1 - \sin \varphi_e} = \tan^2 \left(\frac{\pi}{4} + \frac{\varphi_e}{2} \right) \text{ for passive stress state.}$$

The active stress state represents the lateral expansion of the bulk material, and corresponds to the minimum value of σ_h . The passive stress state is associated with the lateral compression of the bulk material and generates a maximum value of σ_h . Both active and passive stress states are the limit stress forms of the transported bulk material. The intermediate condition between the both limit states in the longitudinal direction is unknown, and, according to Craig [39], Verruijt [233], only can be determined experimentally. Craig [39] and Verruijt [233] state that the relationship between the lateral stress coefficient, $K(z)$, and the lateral strain can be approximated by the sinusoidal curve, presented in Fig. 5.13.

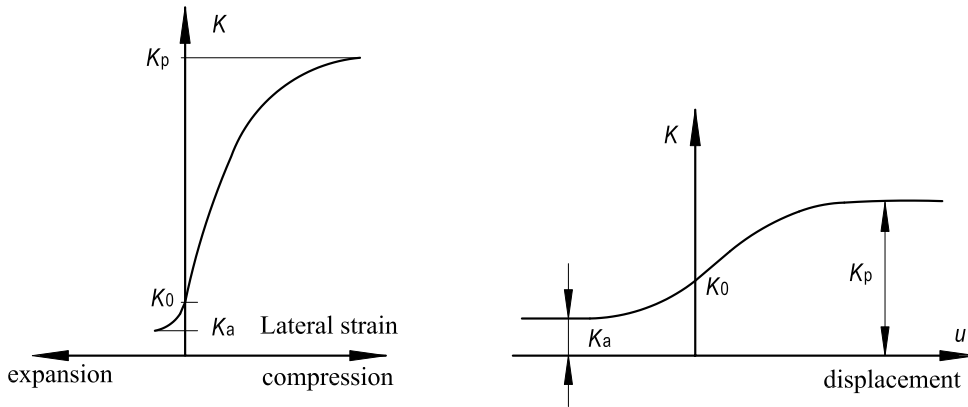


Figure 5.13: The intermediate behavior between active and passive stress states in bulk solids: a) lateral pressure coefficient versus bulk solids lateral strain (Figure from Craig [39]); b) horizontal stress as a function of a displacement (Figure from Verruijt [233]).

The exact switch from the active stress state to the passive stress state depends on the coefficient K_0 , which characterizes the earth pressure at rest when there is no lateral strain (see Craig [39]). For normally consolidated soils, it can be approximately determined from Jaky's formula [117]: $K_0 \approx 1 - \sin \varphi_e$.

According to Craig [39], in order to fully mobilize the passive stress state, the strain causing this stress state needs to be much greater than the strain, required for the full realization of the active stress state. For instance, Craig [39] reported based on the experimental data, obtained within retaining walls, the full mobilization of a passive stress state for dense sands requires 2-4% of strain, and in case of loose sands – 10-15% of strain. For comparison, the full mobilization of active stress state requires 0.25% of strain for dense sands and 1% - for loose sands.

Available literature on belt conveyor in general is analyzed, especially considering how the active/ passive stresses are distributed between the idlers. Most of the researchers for simplification purposes assume that both limit states are fully mobilized, and the switch between the active and passive stress state happens discretely and approximately in the middle of the conveyor pitch (see Fig. 5.14). Such assumption was made for open trough belt conveyors by Krause and Hettler [125], Wheeler [245], Lodewijks [137], Spaans [215], and others, and for PBCs – by Guo *et al.* [87] and Gładysiewicz [91], Kulagin [126–129], Dmitriev and Kulagin [56], Efimov [61], and others [55, 58, 208, 210]. In this case, the coefficient $K(z)$ and the horizontally distributed load equal:

$$K(z) = \begin{cases} K_a = \text{const}, & 0 \leq z \leq l/2; \\ K_p = \text{const}, & l/2 \leq z \leq l. \end{cases} \quad (5.43)$$

$$q_{\text{bulk}}^h = \frac{1}{2} \sigma_v (K_a + K_p) l.$$

Gushchin [88, 89], Galkin *et al.* [80] assume for deep trough belt conveyors that the active stress state is also fully developed and is constant along the first half of the conveyor pitch. Precisely in the middle of the carry spacing, the stresses gradually increase until the full passive stress state is reached exactly at the next idler station (see Fig. 5.15). Gushchin [88, 89] established such assumption based on the experimental data, carried out for deep trough belt conveyors. He proposed that the transition between active and passive stress state follows the curve close to a parabola function, although the researcher considered a linear approximation to be sufficient to simplify the problem, as illustrated in the Fig. 5.14 and Fig. 5.15 [88, 89], i.e.:

$$K(z) = \begin{cases} K_a = \text{const}, & 0 \leq z \leq l/2; \\ 2K_a - K_p + \frac{2}{l} (K_p - K_a) z, & l/2 \leq z \leq l. \end{cases} \quad (5.44)$$

$$q_{\text{bulk}}^h = \frac{1}{4} \sigma_v (3K_a + K_p) l.$$

Wheeler [246] used Mulani's recommendations [168], established empirically based on the practical experience for trough belt conveyors. The researchers assume that the active stress state acts over 2/3 of the idler spacing and is discretely switched to the passive stress state for the rest 1/3 of the conveyor pitch. Furthermore, the passive stress state is not fully

mobilized, as there is not sufficient deflection for open trough belt conveyors. The realization of the passive stress state according to Mulani is about 85% of the full stress state (see Fig. 5.14), thus:

$$K(z) = \begin{cases} K_a = \text{const}, & 0 \leq z \leq 2l/3; \\ 0.85K_p = \text{const}, & 2l/3 \leq z \leq l. \end{cases} \quad (5.45)$$

$$q_{\text{bulk}}^h = \frac{1}{3} \sigma_v (2K_a + 0.85K_p) l.$$

It is important to emphasize that the deformation of a pipe conveyor belt with bulk material is significantly less than the deformations at the conventional open trough conveyors. This appears due to the higher rigidity of the system of a pipe-shaped belt with bulk material. As it was mentioned above, the full realization of the passive stress state requires much higher deformation than for the active stress state, and PBCs designed with feasible parameters cannot always provide this amount of deformation. Therefore, it becomes possible that the ratio $K(z)$ for the bulk material lateral stress state does not deviate much from the critical one at the active stress state, i.e.:

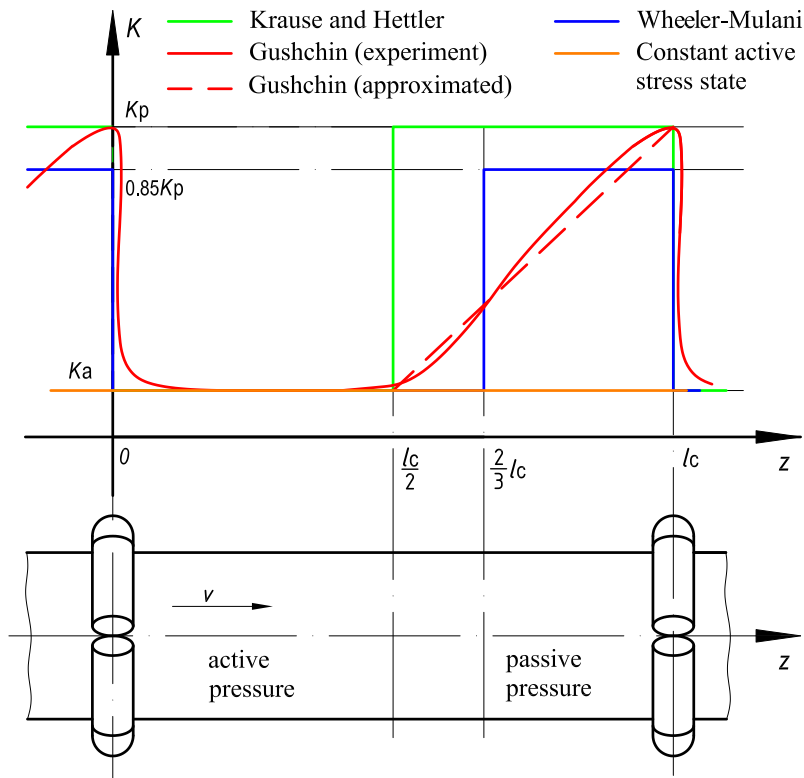


Figure 5.14: Dependence of $K(z)$ that characterizes the lateral stress state of a bulk material along the conveyor pitch.

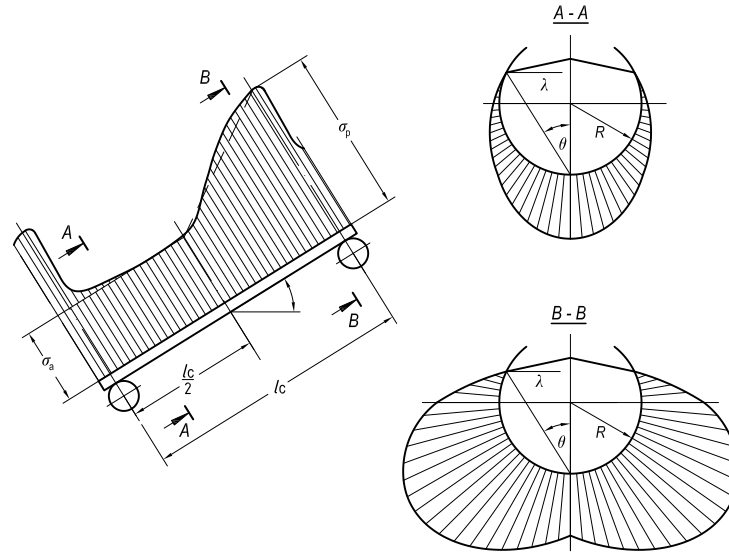


Figure 5.15: The active/passive stress state distribution of the radial stress component σ_φ of a bulk material in longitudinal direction, proposed by Gushchin [88, 89] for the deep trough belt conveyors (Modified figure from Galkin *et al.* [80]).

$$K(z) \approx K_a = \text{const.} \quad (5.46)$$

$$q_{\text{bulk}}^h = \sigma_v K_a l.$$

The experimental study of Liu *et al.* [135] performed on the conventional trough belt conveyors shows that the pressure distribution from the bulk material in longitudinal direction of the conveyor, while the belt is in motion, has a sinusoidal shape for the largest part of the carry spacing (as also mentioned by Craig [39], Verruijt [233], and also illustrated by Gushchin [88, 89]). In this case, it is possible to assume that the switch between the active and passive stress state for PBCs has also a periodical sinusoidal dependence. This dependence might have negative skew, as the development of the active and passive stress states can appear at the certain delay, and not exactly when the belt passes half of the carry spacing and goes through the idler station, respectively (as assumed in most of the studies following Karuse and Hettler Eq. 5.43 and Gushchin Eq. 5.44). In addition, due to the small strain development inherent to PBC systems, the passive stress state is not fully mobilized, i.e., it becomes equivalent to $c_K K_p$, where the coefficient $c_K \in (0 : 1]$.

The actual stress distribution inherent to PBC systems is possible to obtain only experimentally. As discussed in Chapter 4, the option of measuring the bulk material behavior inside the belt's pipe is possible only at the dynamic test rigs or at the existing installations, which becomes problematic in terms of the practical realization and costs. Even the experimental data obtained within the conventional trough belt conveyors (see study of Liu *et al.* [135]), shows that the measurement performance is a very complex dynamic process, and the results can be affected by the number of measurement errors, such as the buckling of the tactile pressure pads due to its poor contact with the belt surface, misalignment of the belt

during the conveying process, the sensitivity of the measuring equipment, etc.

Until now, such experimental testing is not available for the PBC system, the present study accommodates the existing approaches for q_{bulk}^h , given in Eqs. 5.43 - 5.46, and provides a theoretical comparison of the results. The general Eq. 5.40 needs to be used, when the experimental data becomes available and approximated with an appropriate functional dependence.

For the simplicity in this thesis, a special coefficient C^K is introduced. It characterizes the longitudinal development of the active and passive stress states along the conveyor's carry spacing. This coefficient incorporates the Eqs. 5.43 - 5.46 as following:

$$\begin{aligned}
 C^K &= \frac{1}{2} (K_a + K_p) \text{ - Krause - Hettler;} \\
 C^K &= \frac{1}{4} (3K_a + K_p) \text{ - Gushchin;} \\
 C^K &= \frac{1}{3} (2K_a + 0.85K_p) \text{ - Wheeler-Mulani;} \\
 C^K &= K_a \text{ - Constant active stress state.}
 \end{aligned} \tag{5.47}$$

Ultimately, if the filling angle $0 \leq 2\theta \leq \frac{\pi}{2}$, the distributed load, from the horizontal component of the bulk material stress state equals q_{bulk}^h :

$$\begin{aligned}
 q_{\text{bulk}}^h &= \sigma_v \int_0^l K(z) dz = \\
 &= \begin{cases} C^K \rho_{\text{bulk}} g l R (\cos 2\theta - \cos \varphi), & 2\theta \leq \varphi \leq \pi - 2\theta; \\ C^K \rho_{\text{bulk}} g l R [\cos 2\theta - \cos \varphi + \tan \lambda (\sin 2\theta - \sin \varphi)], & \pi - 2\theta \leq \varphi \leq \pi. \end{cases}
 \end{aligned} \tag{5.48}$$

If the cross-sectional filling angle is in the range of $\frac{\pi}{2} \leq 2\theta \leq \pi$, the horizontal component of the bulk material load is the same for any angular position at the structural contour $2\theta \leq \varphi \leq \pi$:

$$q_{\text{bulk}}^h = C^K \rho_{\text{bulk}} g l R [\cos 2\theta - \cos \varphi + \tan \lambda (\sin 2\theta - \sin \varphi)]. \tag{5.49}$$

This distributed load q_{bulk}^h is exerted onto the vertical side of the prism (ab) with a length dy along the circumference of the cross section (see Fig. 5.11). For any filling degree, characterized by the angle θ , dy can be expressed via the angle φ as follows:

$$dy = R d\varphi \sin \varphi, \quad 2\theta \leq \varphi \leq \pi. \tag{5.50}$$

5.4.5 Verification with the total weight

After the vertical and horizontal load components are determined, the radial stress component σ_φ and the tangential one τ_φ can be transformed by substituting the Eq. 5.33 - Eq. 5.35 for σ_v and Eq. 5.40 for σ_h into Eqs. 5.31 for σ_φ and τ_φ , respectively.

This yields for $2\theta \leq \varphi \leq \pi - 2\theta$:

$$\begin{cases} \sigma_\varphi = \rho_{\text{bulk}} g R (\cos 2\theta - \cos \varphi) (\cos^2 \varphi + K(z) \sin^2 \varphi); \\ \tau_\varphi = \frac{1}{2} \rho_{\text{bulk}} g R \sin 2\varphi (\cos 2\theta - \cos \varphi) (1 - K(z)). \end{cases} \quad (5.51)$$

As for the angle $\pi - 2\theta \leq \varphi \leq \pi$, the stresses become:

$$\begin{cases} \sigma_\varphi = \rho_{\text{bulk}} g R (\cos 2\theta - \cos \varphi + \tan \lambda (\sin 2\theta - \sin \varphi)) (\cos^2 \varphi + K(z) \sin^2 \varphi); \\ \tau_\varphi = \frac{1}{2} \rho_{\text{bulk}} g R (\cos 2\theta - \cos \varphi + \tan \lambda (\sin 2\theta - \sin \varphi)) (1 - K(z)). \end{cases} \quad (5.52)$$

It is important to mention that using only the radial load component σ_φ without the tangential one τ_φ , as it was made in the studies of Gushchin [88], Kulagin [126–129], Dmitriev and Kulagin [56], Efimov [61], Dmitriev and Efimov [55], Sergeeva [208, 210], Dmitriev and Sergeeva [58], Galkin *et al.* [80], Guo *et al.* [87], and Gładysiewicz [91]), leads to the underestimation of the resultant total vertical force and does not yield the overall bulk material weight F_{bulk}^v . Indeed, using the expression $-\sigma_\varphi \cos \varphi R d\varphi$ for the vertical projection of the σ_φ , acting on the side of the prism (*ac*) with length $R d\varphi$ (see Fig. 5.9), the total vertical force becomes the following:

$$\begin{aligned} F_{\text{bulk}}^v &= -2 \int_{2\theta}^{\pi} \int_0^l \sigma_\varphi \cos \varphi dz R d\varphi = \\ &= -2R^2 \rho_{\text{bulk}} g l \left[\int_{2\theta}^{\pi} \int_0^l \cos \varphi (\cos 2\theta - \cos \varphi) (\cos^2 \varphi + K(z) \sin^2 \varphi) dz d\varphi + \right. \\ &\quad \left. + \int_{\pi-2\theta}^{\pi} \int_0^l \cos \varphi \tan \lambda (\sin 2\theta - \sin \varphi) (\cos^2 \varphi + K(z) \sin^2 \varphi) dz d\varphi \right] \neq k_Q \pi R^2 \rho_{\text{bulk}} g l, \end{aligned} \quad (5.53)$$

which does not coincide with the total bulk weight (see Eq. 5.30), where k_Q is a filling degree of the pipe conveyor cross section.

On the contrast, if both radial σ_φ and tangential components τ_φ are preserved, their vertical projection $-(\sigma_\varphi \cos \varphi + \tau_\varphi \sin \varphi)$ yields the total vertical force, equivalent to the overall bulk weight (see Eq. 5.30 and also Eq. 2.5):

$$\begin{aligned} F_{\text{bulk}}^v &= -2R \int_{2\theta}^{\pi} \int_0^l (\sigma_\varphi \cos \varphi + \tau_\varphi \sin \varphi) dz d\varphi = \\ &= -2R^2 \rho_{\text{bulk}} g l \left[\int_{2\theta}^{\pi} \int_0^l \cos \varphi (\cos 2\theta - \cos \varphi) dz d\varphi + \right. \\ &\quad \left. + \int_{\pi-2\theta}^{\pi} \int_0^l \tan \lambda \cos \varphi (\sin 2\theta - \sin \varphi) dz d\varphi \right] = \\ &= R^2 \rho_{\text{bulk}} g l (\pi - 2\theta + \frac{1}{2} \sin 4\theta + \tan \lambda \sin^2 2\theta) = k_Q \pi R^2 \rho_{\text{bulk}} g l. \end{aligned} \quad (5.54)$$

This shows that for modeling the distributed load from the bulk material, the impact of all the load components needs to be preserved. The selection of the original vertical and horizontal components of the bulk material stress state is also sufficient, as it can be also

verified with the overall bulk weight:

$$\begin{aligned}
 F_{\text{bulk}}^v &= 2 \int_0^{\pi R} q_{\text{bulk}}^v dx = -2R^2 \rho_{\text{bulk}} g l \left[\int_{2\theta}^{\pi} \int_0^l \cos \varphi (\cos 2\theta - \cos \varphi) dz d\varphi + \right. \\
 &+ \left. \int_{\pi-2\theta}^{\pi} \int_0^l \tan \lambda \cos \varphi (\sin 2\theta - \sin \varphi) dz d\varphi \right] = k_Q \pi R^2 \rho_{\text{bulk}} g l.
 \end{aligned} \tag{5.55}$$

Following analogical manipulations of using both the vertical and horizontal stress components, the total horizontal vector-force, generated by the bulk material load, equals to zero: $F_{\text{bulk}}^h = 0$.

Noteworthy to mention that the verification with the total vertical force-vector equaled to the overall weight of the structure and the horizontal force-vector equaled to zero is also used in the experimental studies of Hötte [107], Hötte *et al.* [108], and also here in Chapter 4 that also determines the PBC CFs using experimental measurements.

Summing up for the section, the load from the bulk material required for determining of the PBC CFs can be sufficiently represented by the vertical q_{bulk}^v and horizontal q_{bulk}^h distributed load components, applied simultaneously to the belt structure along the cross-sectional circumference. Due to the Principle of Superposition, the impact of each of the load component can be considered independently and then can be added to the action of the load from the belt weight and bending stiffness. The load diagrams caused by the distributed $q_{\text{bulk}}^v dx$ and $q_{\text{bulk}}^h dy$ are shown in Fig. 5.16. These loads are also utilized in the new approach that determines the PBC CFs, developed in this chapter.

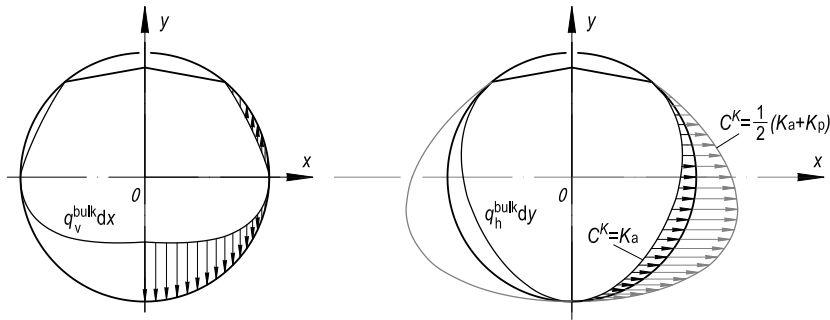


Figure 5.16: The vertical $q_{\text{bulk}}^v dx$ and horizontal $q_{\text{bulk}}^h dy$ load components that represent the load from the bulk material. The horizontal load distribution q_{bulk}^h is shown, if it is determined from Eq.5.46 and also from Eq.5.43.

5.5 Determination of the contact forces from the external loads: existing models

After the external loads are defined for a PBC system, it is important to select the approach that can determine the resultant CFs caused by those loads. For this purpose, the existing studies on this topic need to be reviewed. As it will be shown in the section, none of the studies available determines the resultant CFs in an accurate way, even if the external loads

prescribed to the models are accurate. For the unification and better understanding, all the local formulas, provided in the studies are expressed using the global parameters, used in this thesis.

As it was mentioned before, the PBC CFs are caused by the load from the belt weight, load from the belt bending stiffness, and load from the bulk material load. In general due to the linearization of the problem, the existing studies define the resultant CFs based on the Principal of Superposition, assuming that the total force produced by the sum of the external loads equals to the sum of the resultant forces, caused by those forces independently, i.e., the CF F_n at the n -th idler roll equal:

$$F_n = F_{nbw} + F_{nbs} + F_{nbulk}, \quad (5.56)$$

where F_{nbw} is the resultant force, caused by the belt weight, F_{nbs} is caused by the load from the belt bending stiffness, and F_{nbulk} corresponds to the bulk material. The majority of the existing studies focused on determination of CFs for PBCs take into account only one or two of the loads mentioned.

For instance, Wiedenroth [247] determines the CFs from the bulk material for a PBC, using the formulas, derived by Grimmer and Grabner [86] for open trough belt conveyors with idler rolls $\beta_{idl} = 60^\circ$ installation angle. The forces are shown in Fig. 5.7 and equal:

$$\begin{aligned} F_{1bulk} = F_{2bulk} = F_{6bulk} &= 0; \\ F_{3bulk} = F_{5bulk} &= F_L \cos \frac{\pi}{3}; \\ F_{4bulk} &= F_C, \end{aligned} \quad (5.57)$$

where F_L and F_C are the forces from bulk material, acting on the later (L) and central (C) bottom idler rolls, determined by Eqs. 5.29, and shown in Fig. 5.7.

Similar to Wiedenroth, Kalidien [120] determines the forces from the belt weight F_{nbw} also using the same approach as for the conventional open trough belt conveyors, i.e., the forces are defined by:

$$\begin{aligned} F_{1bw} = F_{2bw} = F_{6bw} &= 0; \\ F_{3bw} = F_{5bw} &= \frac{l_{roll}}{2R} q_{bw} B \left(1 + \frac{8}{3} K_s \right) \cos \frac{\pi}{3}; \\ F_{4bw} &= \frac{l_{roll}}{2R} q_{bw} B \left(1 + \frac{8}{3} K_s \right), \end{aligned} \quad (5.58)$$

where l_{roll} is the length of a roll (see Section 2.6.2), and the factor K_s is the static belt sag ratio that assumes the belt bending stiffness to be insignificant (see Lodewijks [137]). However, as it was shown in Chapter 3, this is not the case for the PBC systems, since they have rather significant bending stiffness. Consequently such approach does not lead to a correct solution.

In addition, Kalidien [120] determines the load from the bulk material as the vertical concentrated gravity forces based on the cross-sectional area, occupied by the bulk material at the corresponding idler rolls (see Section 5.4 and Fig. 5.7). The resultant CFs are defined considering that the projections of the gravity forces should yield in total the overall bulk

weight. The forces equal to the following:

$$\begin{aligned}
 F_{1\text{bulk}} &= F_{2\text{bulk}} = F_{6\text{bulk}} = 0; \\
 F_{3\text{bulk}} &= F_{5\text{bulk}} = F_L \cos \frac{\pi}{3}; \\
 F_{4\text{bulk}} &= F_C + 2F_L \sin^2 \frac{\pi}{3},
 \end{aligned} \tag{5.59}$$

where F_L and F_C are area-related forces, determined by Eqs. 5.28.

As it was discussed in previous sections, the approaches that determine the PBC CFs based on the area-related loads from the bulk material or usage the same loads as for the trough belt conveyors, are not relevant for the PBC system and do not generate the correct CFs.

Wesemeier [238, 240, 241] introduced an alternative approach for determining the CFs from the belt bending stiffness at the vertical 4-roll pipe conveyor. The researcher used the Displacement method in the studies [238, 240, 241].

In one of his study [238], the researcher considers the load from the belt bending stiffness as a concentrated force F_{bst} , applied vertically at one of the belt edge right at the top idler roll. Its value is given in Eq. 5.4. The researcher assumed that the CF at the top roll fully equals to $F_1 = F_{\text{bst}}$, the forces F_2 and F_4 are determined actually by the Displacement method, considering a half of the cross section (see Fig. 5.17b) as a statically indeterminate system, and the force F_3 is evaluated from the equilibrium equations taking into account the coefficient of friction f_r between the belt and rolls, as shown in Fig.5.17a, i.e.:

$$\begin{aligned}
 F_1 &= F_{\text{bst}}; \\
 F_2 &= F_4 = \left(\frac{4}{\pi} - 1 \right) F_1; \\
 F_3 &= F_1 - 2f_r F_2.
 \end{aligned} \tag{5.60}$$

Such solution of the problem is not correct, as the external force F_{bst} , applied at the top of the structure influences all the resultant CFs and not fully equal to the $F_1 = F_{\text{bst}}$.

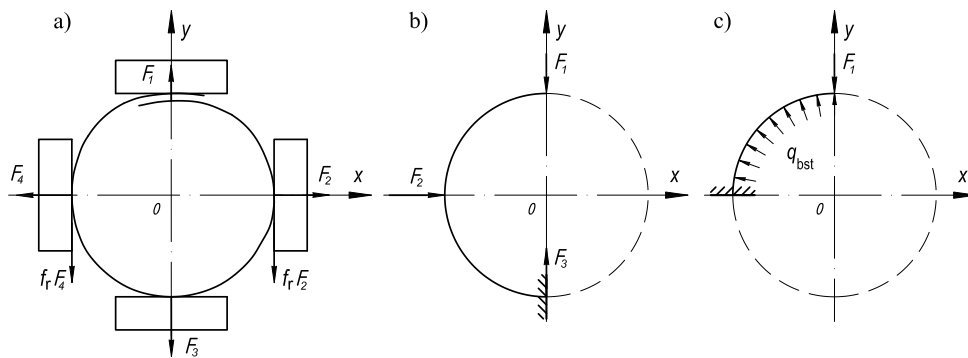


Figure 5.17: a) Pipe conveyor CFs at the 4-roll vertical PBC, caused by the load from the belt bending stiffness based on Wesemeier approach, represented by b) the concentrated force $F_1 = F_{\text{bst}}$; c) the distributed load q_{bst} .

In addition, the friction coefficient corresponds to the static friction, which needs to be determined experimentally or defines the critical case when the belt starts to rotate relatively with respect to the idler rolls.

In other studies [240, 241], Wesemeier suggest to determine the CF at the top roll, considering the quarter of the pipe (see Fig.5.17c), subjected to the radial Chernenko load q_{bst} , defined by Eq. 5.3. The researcher suggested to use also the Displacement Method, proposing only the general trend, i.e. stating that the force is a function of that load q_{bst} and the angle φ .

Despite the fact that the studies of Wesemeier [238, 240, 241] need adjustment for the 6-roll PBC, the solutions described do not correctly predict the resultant CFs even for the 4-roll PBC. However, it is important to mention that the Displacement Method used is a well-known method of treating the statically indeterminate systems and will be used in the new approach introduced in this chapter. In addition, the studies of Wesemeier [238, 240, 241] are relevant for the vertical pipe conveyor, so the impact of the belt weight and load from the bulk material are not included in the analysis of the researcher.

The researchers Dmitriev and Efimov [55], Efimov [61, 62], Dmitriev and Sergeeva [58], Sergeeva [210] determine the PBC CFs, illustrated in Fig. 5.18. They include all the loads involved (load from the belt weight, load from the belt bending stiffness, and load from the bulk material), as given in Eq. 5.56:

$$\begin{aligned}
 F_1 &= -\frac{1}{3}q_{bw}\pi R + \frac{1}{3}q_{bst}\pi R + F_{1bulk}; \\
 F_2 = F_6 &= -\frac{1}{3}q_{bw}\pi R \cos \frac{\pi}{3} + \frac{1}{3}q_{bst}\pi R + F_{2bulk}; \\
 F_3 = F_5 &= \frac{1}{3}q_{bw}\pi R \cos \frac{\pi}{3} + \frac{1}{3}q_{bst}\pi R + F_{3bulk}; \\
 F_4 &= \underbrace{\frac{1}{3}q_{bw}\pi R}_{F_{nbw}} + \underbrace{\frac{1}{3}q_{bst}\pi R}_{F_{nbst}} + \underbrace{F_{4bulk}}_{F_{nbulk}}. \\
 F_n &= F_{nbw} + F_{nbst} + F_{nbulk}.
 \end{aligned} \tag{5.61}$$

In these equations, the forces from the belt weight F_{nbw} are defined by applying at the idler rolls the vertical concentrated loads equaled to the one sixth of the weight of the pipe $F_{bw} = q_{bw} \frac{2\pi R}{6} = \frac{1}{3}q_{bw}\pi R$. The projections of those loads on the corresponding radial directions (see Fig. 5.18) define the actual forces F_{nbw} . Such approach of substituting the distributed load q_{bw} from the belt weight within the concentrated forces F_{bw} , applied vertically at the idler rolls does not produce the correct CFs F_{nbw} , caused by the actual loading q_{bw} .

For describing the forces due to the belt bending stiffness F_{nbst} , the researchers used an evenly distributed radial load defined by Chernenko [27, 28]. This load is explicitly described in Section 5.3.2 together with the other two approaches that imitate the expansion load from belt bending stiffness. However, it is important to emphasize that the researchers [55, 58, 61, 62, 210] determine the resultant CFs F_{nbst} from that load in Eqs. 5.61, assuming that they are the same for all six idler rolls and equal $F_{nbst} = q_{bst} \frac{2\pi R}{6}$. Such assumption implies the fully enclosed ring-like cross section and ignores the open structural behavior inherent to a belt formed into a pipe shape with overlap (or with small opening at the top in case the impact of the overlap is neglected).

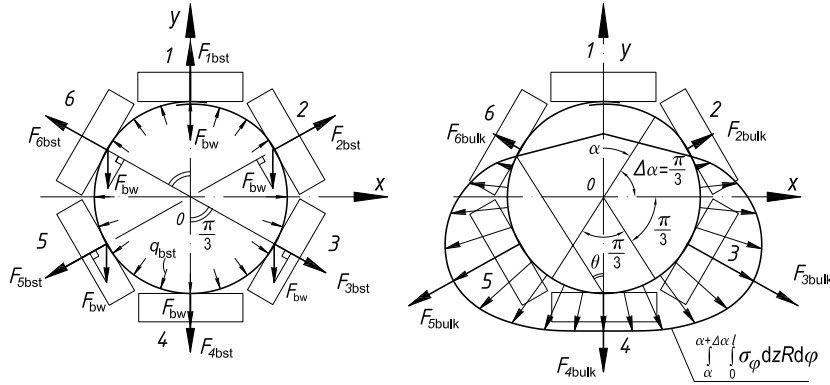


Figure 5.18: Pipe conveyor cross section with the CFs, determined based on the approach of Dmitriev and Efimov [55], Efimov [61, 62], Dmitriev and Sergeeva [58], Sergeeva [210] (Modified figure from Dmitriev and Sergeeva [58]).

As for the bulk material, the researchers [55, 58, 61, 62, 210] described the bulk material stress state using Gushchin [88, 89] approach. However, the resultant CFs are evaluated, accommodating only the radial stress component σ_φ , ignoring the presence of the tangential one τ_φ . The impact of the angle of repose was also assumed negligible, assuming ($\tan \lambda = 0$), and the expression of σ_φ for $2\theta \leq \varphi \leq \pi - 2\theta$ to be the same as for any $2\theta \leq \varphi \leq \pi$. In addition, as it was mentioned above, it was assumed that the active and passive stress states of a bulk material are fully mobilized, and the switch between these two states is discreet and appears exactly at the half of the conveyor pitch, i.e., Eq. 5.43 for $K(z)$ was relevant.

The researchers determine the forces from the bulk material at the n -th idler roll $F_{n\text{bulk}}$, using the radial load $\int_\alpha^{\alpha+\Delta\alpha} \int_0^l \sigma_\varphi dz R d\varphi$, multiplied by the length of the corresponding arc $R\Delta\alpha$ the load is distributed on. The integration limiting angles α and $\Delta\alpha$ are shown in Fig. 5.18b. The CFs are evaluated as follows:

$$F_{n\text{bulk}} = R\Delta\alpha \int_\alpha^{\alpha+\Delta\alpha} \int_0^l \sigma_\varphi dz d\varphi. \quad (5.62)$$

Ultimately, the CFs $F_{n\text{bulk}}$ in Eqs. 5.61 caused by the bulk material were provided in the studies [55, 58, 61, 62, 210] for the cross-sectional filling interval $2\theta \leq \varphi \leq \pi$, where the angle of filling equals $2\theta = \frac{\pi}{6}$, are defined as follows:

$$\begin{aligned} F_{1\text{bulk}} &= 0; \\ F_{2\text{bulk}}=F_{6\text{bulk}} &= \frac{\pi}{3} \rho_{\text{bulk}} g R^2 \frac{l}{2} \int_{\pi/6}^{\pi/2} (\cos 2\theta - \cos \varphi) (2\cos^2 \varphi + \sin^2 \varphi (K_a + K_p)) d\varphi; \\ F_{3\text{bulk}}=F_{5\text{bulk}} &= \frac{\pi}{3} \rho_{\text{bulk}} g R^2 \frac{l}{2} \int_{\pi/2}^{5\pi/6} (\cos 2\theta - \cos \varphi) (2\cos^2 \varphi + \sin^2 \varphi (K_a + K_p)) d\varphi; \\ F_{4\text{bulk}} &= 2 \frac{\pi}{6} \rho_{\text{bulk}} g R^2 \frac{l}{2} \int_{5\pi/6}^{\pi} (\cos 2\theta - \cos \varphi) (2\cos^2 \varphi + \sin^2 \varphi (K_a + K_p)) d\varphi. \end{aligned} \quad (5.63)$$

As it was mentioned above, the usage of only the radial stress component σ_φ without the tangential one τ_φ leads to the resultant sum of the vertical projections of the forces $F_{\text{bulk}}^V \neq k_Q \pi R^2 \rho_{\text{bulk}} g l$ not equivalent to the total weight of the bulk material transported. Due to this fact and also due to the drawbacks mentioned regarding the determination of the CFs from the belt weight $F_{n\text{bw}}$ and belt bending stiffness $F_{n\text{bst}}$, the approach of Dmitriev and Efimov [55], Efimov [61, 62], Dmitriev and Sergeeva [58], Sergeeva [210] cannot be used for evaluation of the CFs in a PBC system and needs to be reconsidered.

Noteworthy to mention, Guo *et al.* [87] define also the CFs $F_{n\text{bulk}}$ from the bulk material load, utilizing the similar approach as the studies [55, 58, 61, 62, 210] that account only the radial stress component σ_φ ignoring the presence of the tangential one τ_φ . The major differences from those studies [55, 58, 61, 62, 210] imply that Guo *et al.* [87] use $F_{n\text{bulk}} = \int_\alpha^{\alpha+\Delta\alpha} \int_0^l \sigma_\varphi dz R d\varphi$ without multiplying it with the arc length $R\Delta\alpha$.

In addition, the researchers take into account the angle of repose λ in expression for σ_φ , i.e., using full its expression in Eq. 5.52. Besides of using only the radial stress component σ_φ , the other drawback of the study is that it is limited to the 75% of the cross-sectional filling degree and assumes $F_{1\text{bulk}} = 0$. The limits of the integrals of CFs do not incorporate the angle of the cross sectional filling degree θ . The study of Guo *et al.* [87] accommodates only the load from the bulk material and does not provide any solution for the forces from the belt weight and bending stiffness.

An alternative approach was developed by Gładysiewicz [91], describing the PBC CFs also as a sum of the force-components, caused by the all loads involved, as given in Eq. 5.56 and illustrated in Fig. 5.19.

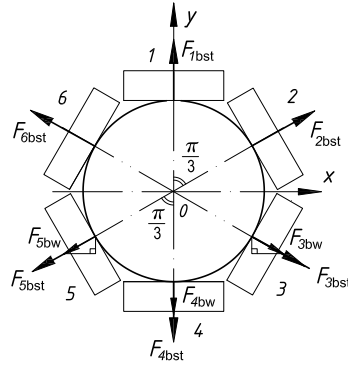


Figure 5.19: Pipe conveyor cross section with the CFs determined based on the approach of Gładysiewicz [91] without a bulk material.

In Eq. 5.56, the researcher assumes that the force-components from the belt weight F_{bnw} equal the following:

$$\begin{aligned} F_{1\text{bw}} = F_{2\text{bw}} = F_{6\text{bw}} &= 0; \\ F_{3\text{bw}} = F_{4\text{bw}} = F_{5\text{bw}} &= \frac{1}{2} q_{\text{bw}} B = q_{\text{bw}} \pi R. \end{aligned} \quad (5.64)$$

The forces from the belt weight appear only at the bottom idler rolls. However, as it will be shown in Chapter 6, this is not always correct, as at certain input parameters (bending modulus of elasticity E , the slenderness ratio of the structure B/h , the actual belt line mass q_{bw} , the forces can appear also at the top lateral rolls.

For the forces from the belt bending stiffness $F_{n\text{bst}}$, Gładysiewicz proposed to use the same concentrated forces, applied radially at the each roll. Each of the CFs is equivalent to the empiric Eq. 5.2, i.e. $F_{1\text{bst}} = F_{2\text{bst}} = F_{3\text{bst}} = F_{4\text{bst}} = F_{5\text{bst}} = F_{6\text{bst}} = F_{\text{bst}} = \text{const.}$ As it was discussed in Section 5.3, the usage of that empiric dependence might be relevant for the particular experimental results used as a basis for the approximation, but is not applicable for the other belts. In addition, Eq. 5.2 does not depend on the E -modulus of a belt and contains the belt line mass, which is a separate load.

According to Gładysiewicz [91], the empty belt conveyor ($F_{n\text{bulk}} = 0$) exhibits the same CFs at the top rolls $F_1 = F_2 = F_6$, and also the equivalent forces at the bottom rolls $F_3 = F_4 = F_5$. The existing experimental results presented in Chapter 4 show that such dependence is not fulfilled, which indicates that the approach of Gładysiewicz [91] is not correct.

As for the forces from the bulk material $F_{n\text{bulk}}$ in Eq. 5.56, the researcher introduced more sophisticated method, however, it again was based only on using the radial stress component from the bulk material. Similar to the previous approach, Gładysiewicz [91] determines σ_φ also ignoring the impact of the angle of repose $\lambda = 0$, and assuming the discrete switch between active and passive stress states described by Eq. 5.43 for $K(z)$.

The forces $F_{n\text{bulk}}$ are evaluated by projecting the radial load $\sigma_\varphi R d\varphi$ onto the corresponding line that defines the position of the roll, i.e. using $\sigma_\varphi \cos(\varphi - (\alpha + \Delta\alpha/2)) R d\varphi$. This is one of the major differences with the Eq. 5.62 of the studies of Dmitriev and Efimov [55], Efimov [61, 62], Dmitriev and Sergeeva [58], Sergeeva [210]. Moreover, $F_{n\text{bulk}}$ of Gładysiewicz incorporates the filling angle θ (see Section 2.3.3) in the integral limits, expressed in general as following:

$$F_{n\text{bulk}} = R\Delta\alpha \int_{\alpha_1}^{\alpha_2} \int_0^l \sigma_\varphi \cos\left(\varphi - \left(\alpha + \frac{\Delta\alpha}{2}\right)\right) dz d\varphi, \quad (5.65)$$

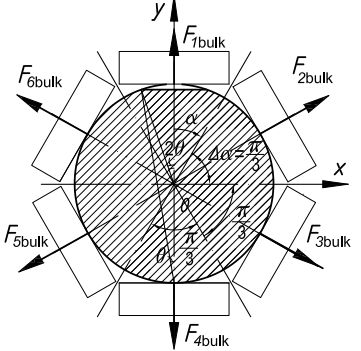
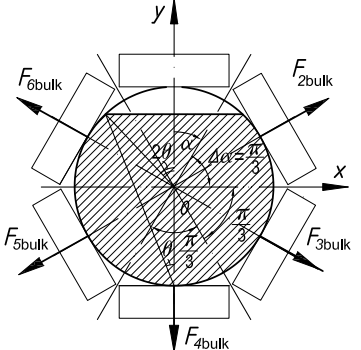
where $\alpha_1 = \alpha$, shown in Fig. 5.18b, and α_2 equals to either $\alpha + \Delta\alpha$ or $\alpha_2 = 2\theta$, depending on the idler roll position and the filling degree, as provided in Table 5.2.

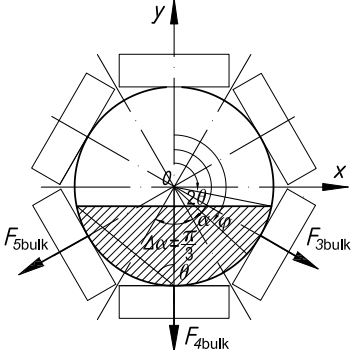
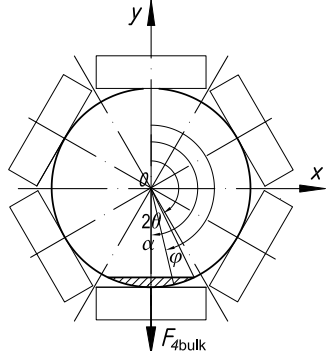
As it was shown above, the resultant vertical load, generated by only radial component of the bulk stress state σ_φ , does not give the overall weight of the bulk material, and, as a result, the approach of Gładysiewicz [91] also cannot be used in the present analysis and needs to be reconsidered.

Summing up, the existing approaches cannot determine the PBC CFs, resultant from the external loads in a correct way, even though in certain studies, some of these loads are correctly prescribed to the model.

That is why, present chapter introduces a new analytical approach that predicts the CFs at each of the six rolls and incorporates all the loads involved. The approach, constructed in the next section, is universal and can be also expanded in order to incorporate other external loads, such as the load from the belt tension that appears at the conveyor route curves.

Table 5.2: CFs from the bulk material load, determined based on Gładysiewicz [91] approach.

 <p style="text-align: center;"> $0 \leq 2\theta \leq \frac{\pi}{6}, 0 \leq \theta \leq \frac{\pi}{12}$ </p>	$F_{1\text{bulk}} = \rho_{\text{bulk}} g R^2 l \int_{2\theta}^{\pi/6} (\cos 2\theta - \cos \varphi) (2\cos^2 \varphi + \sin^2 \varphi (K_a + K_p)) \cos \varphi d\varphi;$ $F_{2\text{bulk}} = F_{6\text{bulk}} = \rho_{\text{bulk}} g R^2 \frac{l}{2} \int_{\pi/6}^{\pi/2} (\cos 2\theta - \cos \varphi) (2\cos^2 \varphi + \sin^2 \varphi (K_a + K_p)) \cos \left(\varphi - \frac{\pi}{3} \right) d\varphi;$ $F_{3\text{bulk}} = F_{5\text{bulk}} = \rho_{\text{bulk}} g R^2 \frac{l}{2} \int_{\pi/2}^{5\pi/6} (\cos 2\theta - \cos \varphi) (2\cos^2 \varphi + \sin^2 \varphi (K_a + K_p)) \cos \left(\varphi - \frac{2\pi}{3} \right) d\varphi;$ $F_{4\text{bulk}} = \rho_{\text{bulk}} g R^2 l \int_{5\pi/6}^{\pi} (\cos 2\theta - \cos \varphi) (2\cos^2 \varphi + \sin^2 \varphi (K_a + K_p)) \cos (\varphi - \pi) d\varphi.$
 <p style="text-align: center;"> $\frac{\pi}{6} \leq 2\theta \leq \frac{\pi}{2}, \frac{\pi}{12} \leq \theta \leq \frac{\pi}{4}$ </p>	$F_{1\text{bulk}} = 0;$ $F_{2\text{bulk}} = F_{6\text{bulk}} = \rho_{\text{bulk}} g R^2 \frac{l}{2} \int_{2\theta}^{\pi/2} (\cos 2\theta - \cos \varphi) (2\cos^2 \varphi + \sin^2 \varphi (K_a + K_p)) \cos \left(\varphi - \frac{\pi}{3} \right) d\varphi;$ $F_{3\text{bulk}} = F_{5\text{bulk}} = \rho_{\text{bulk}} g R^2 \frac{l}{2} \int_{\pi/2}^{5\pi/6} (\cos 2\theta - \cos \varphi) (2\cos^2 \varphi + \sin^2 \varphi (K_a + K_p)) \cos \left(\varphi - \frac{2\pi}{3} \right) d\varphi;$ $F_{4\text{bulk}} = \rho_{\text{bulk}} g R^2 l \int_{5\pi/6}^{\pi} (\cos 2\theta - \cos \varphi) (2\cos^2 \varphi + \sin^2 \varphi (K_a + K_p)) \cos (\varphi - \pi) d\varphi.$

 <p style="text-align: center;"> $\frac{\pi}{2} \leq 2\theta \leq \frac{5\pi}{6}, \frac{\pi}{4} \leq \theta \leq \frac{5\pi}{12}$ </p>	$F_{1\text{bulk}} = F_{2\text{bulk}} = F_{6\text{bulk}} = 0;$ $F_{3\text{bulk}} = F_{5\text{bulk}} = \rho_{\text{bulk}} g R^2 l \frac{1}{2} \int_{2\theta}^{5\pi/6} (\cos 2\theta - \cos \varphi)(2\cos^2 \varphi + \sin^2 \varphi (K_a + K_p)) \cos \left(\varphi - \frac{2\pi}{3} \right) d\varphi;$ $F_{4\text{bulk}} = \rho_{\text{bulk}} g R^2 l \int_{5\pi/6}^{\pi} (\cos 2\theta - \cos \varphi)(2\cos^2 \varphi + \sin^2 \varphi (K_a + K_p)) \cos (\varphi - \pi) d\varphi.$
 <p style="text-align: center;"> $\frac{5\pi}{6} \leq 2\theta \leq \pi, \frac{5\pi}{12} \leq \theta \leq \frac{\pi}{2}$ </p>	$F_{1\text{bulk}} = F_{2\text{bulk}} = F_{3\text{bulk}} = F_{5\text{bulk}} = F_{6\text{bulk}} = 0;$ $F_{4\text{bulk}} = \rho_{\text{bulk}} g R^2 l \int_{2\theta}^{\pi} (\cos 2\theta - \cos \varphi)(2\cos^2 \varphi + \sin^2 \varphi (K_a + K_p)) \cos (\varphi - \pi) d\varphi.$

5.6 A new approach

5.6.1 Statically indeterminate system

The problem is linearized around the reference geometry, which represents a circular open-structure with small opening on the top (see Fig. 5.20), i.e. the impact of the belt overlap is not considered in the approach. Similar to the Chapter 3, the belt material is assumed linear-elastic at the small strain range. The belt design implies uniform structure with constant mass and Young's bending modulus along the belt width.

The reference structure is subjected to external loads that are applied together to the structure. The loads include:

- the load from the belt weight, represented by the evenly distributed vertical load q_{bw} , discussed in Section 5.2;
- the load from the belt bending stiffness, introduced as: either a) the concentrated expansion moments applied at the belt edges; or b) the evenly distributed radial load q_{bst} (Chernenko load in Section 5.3.2); or c) the distributed radial load q_{bst} with concentrated expansion forces Q_{1bst} , Q_{2bst} (Dmitriev approach, discussed in Section 5.3.3);
- the load from the bulk material, represented by both vertical q_{bulk}^v and horizontal q_{bulk}^h load components, determined in Section 5.4.3 and Section 5.4.4, respectively.

Due to the linearization of the problem, each of the load can be considered independently. The external loads generate the resultant CFs F_1, F_2, \dots, F_6 , where the belt is in contact with the idler rolls (see Fig. 5.20). These forces are equivalent in absolute values to the reaction forces $N_{F1}, N_{F2}, \dots, N_{F6}$, respectively. Since the present approach assumes the reference cross section to be a symmetrical circle, and does not include the belt overlap, the upper roll is in contact with both edges of the belt. According to this assumption, the total reaction force at that roll equals to the sum of the reaction forces from both edges: $N_{F1} = N'_{F1} + N''_{F1}$.

The model can be simplified by substituting the contact between the rolls and the belt with a movable hinge supports in the manner, illustrated in Fig. 5.21a. This type of the

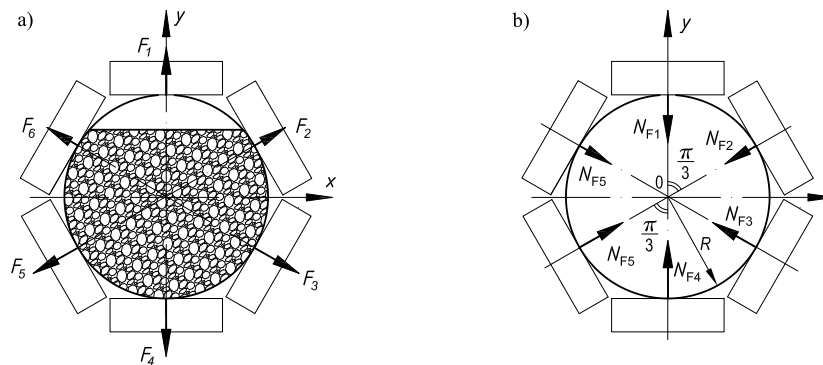


Figure 5.20: Reference cross section of a PBC assumed for the new approach with a) the CFs; b) the equivalent reaction forces.

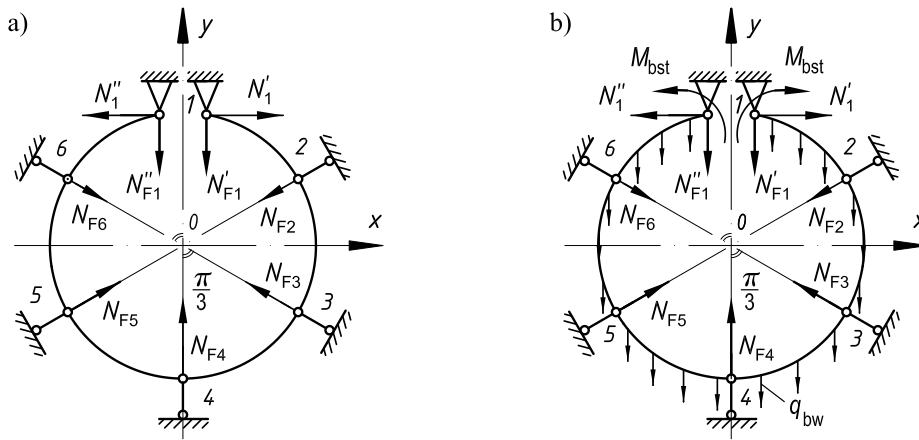


Figure 5.21: a) Simplified model for determination PBC CFs where the contact between the belt and idler roll and between the belt edges are replaced by the supports with equivalent constraints; b) statically indeterminate system, subjected to the external load from the belt weight and load from the bending stiffness represented by a constant expansion moments M_{bst} applied at the edges. The loads from the bulk material are not shown in the figure.

constrained implies the only one reaction force, directed radially from the each corresponding support. In addition, the pipe conveyor belt formed into a pipe shape without overlap might exhibit the additional repulsion forces at the edges of the structure. To imitate this, the additional reaction forces N_1' and N_1'' are incorporated within the pinned supports at the belt edges (see Fig. 5.21a). These forces are equivalent in absolute values but directed at the opposite directions, i.e. $N_1' = -N_1''$.

The constrained belt structure is subjected to all the loads involved. In case of an empty PBC, the load from the bulk material is excluded or assumed equal to zero (see Fig. 5.21b).

In order to determine the reaction forces for a symmetrical model under the symmetrical loading, it is only necessary to consider one half of the cross section with appropriate symmetry boundary conditions. As a result, an edge of the cross section at the point A can be considered to be fixed (see Fig. 5.22). The generated reaction forces N_4' and N_4'' , and the moments M_4' and M_4'' at the fixed point A are respectively equal in magnitude and are opposite in directions. For the symmetrical load and symmetrical cross section, the reaction forces then equal: $N_{F1} = 2N_{F1}'$, $N_{F2} = N_{F6}$, $N_{F3} = N_{F5}$, $N_{F4} = 2N_{F4}'$, $N_1' = -N_1''$, $N_4' = -N_4''$, $M_4' = -M_4''$.

The half of the cross section presented in Fig. 5.22 has 7 unknown reactions: N_1 , $N_{F1}' = N_{F1}/2$, N_{F2} , N_{F3} , $N_{F4}' = N_{F4}/2$, N_4' , M_4' ; and 3 equations of equilibrium: from the action of forces in the x and y direction $\sum F_x = 0$, $\sum F_y = 0$, and from the moments $\sum M_A = 0$ about the point A. The number of the unknowns exceeds the number of the equilibrium equations. The system is statically indeterminate to the 4-th degree of static indeterminacy.

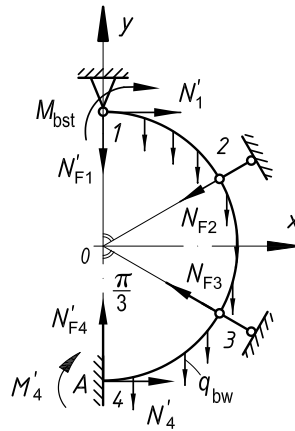


Figure 5.22: Statically indeterminate original structure of the considered symmetrical half of the PBC cross section. Loads from the bulk material are not shown in the figure.

5.6.2 Method of superposition

As previously discussed, the analytical model was linearized around the specific prescribed configuration of the conveyor belt. This consideration allows the problem to be solved, by applying the laws and methods that are inherent to the linear systems.

In order to solve the statically indeterminate system, the Method of Superposition (also called a Force-Displacement Method) is used. This method is a well-known fundamental approach of treating statically indeterminate linear systems. It was described by Gere and Timoshenko [82], Sargasyan [202], Karnovsky and Lebed [122], Karnovsky [121], Birger and Mavlyutov [16], and others.

According to the method, the reaction forces N'_1 , N'_{F1} , N_{F2} , and N_{F3} are selected as static redundants, and can be released from the structure. The redundant forces X_1 , X_2 , X_3 , X_4 are equivalent to the corresponding reaction forces N'_1 , N'_{F1} , N_{F2} , and N_{F3} , and are applied to the released structure at points 2, 3, and 4, respectively. The released structure, shown in Fig. 5.23, is enough stable to carry all the loads, and is statically determinate. Therefore, the rest force quantities (N'_{F4} , N_4 , M'_4) can be obtained from the equilibrium equations (Gere and Timoshenko [82], Sargasyan [202]).

The present approach assumes that both the original external loads and the internal redundant forces act upon the structure released. The deflections δ_1 , δ_2 , δ_3 , and δ_4 in the released structure and in the original structure should be equivalent. This means that they should be equal to zero at the points where the restrains are replaced with the redundant forces. This condition of the equivalence generates extra four compatibility equations, in addition to the equations of equilibrium.

The deflection in the released structure can be determined by superimposing the separate deflections that occur due to the external loads, as well as the deflections that occur due to the redundant forces. As a result, the equations of compatibility are then presented in the following system:

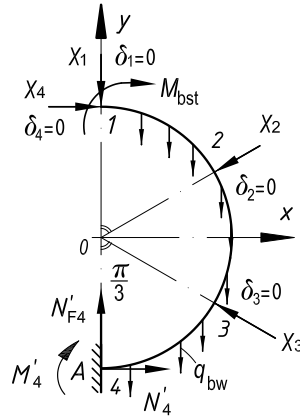


Figure 5.23: Statically determinate released system, where the redundant forces N'_1 , N'_{F1} , N'_{F2} , and N'_{F3} are replaced by the unknowns X_1 , X_2 , X_3 , and X_4 , respectively. The load from belt bending stiffness is shown as expansion concentrated forces M_{bst} , applied at the belt edges. The loads from the bulk material are not shown in the figure.

$$\begin{cases} \delta_1(X_1, X_2, X_3, X_4, P) = 0; \\ \delta_2(X_1, X_2, X_3, X_4, P) = 0; \\ \delta_3(X_1, X_2, X_3, X_4, P) = 0; \\ \delta_4(X_1, X_2, X_3, X_4, P) = 0. \end{cases} \quad (5.66)$$

In the System of Eqs. 5.66, P represents the external loads that occur due to the belt weight q_{bw} , loads from the bulk material, expressed via vertical q_{bulk}^v and horizontal q_{bulk}^h load components, and load from the belt bending stiffness, represented by either concentrated expansion moments M_{bst} , applied at the belt edges, or the evenly distributed radial load q_{bst} , or the distributed radial load q_{bst} with concentrated expansion forces Q_{1bst} , Q_{2bst} .

According to the Principle of Superposition, the System of Eqs. 5.66 can be transformed into the following form:

$$\begin{cases} \delta_1(X_1) + \delta_1(X_2) + \delta_1(X_3) + \delta_1(X_4) + \delta_1(P) = 0; \\ \delta_2(X_1) + \delta_2(X_2) + \delta_2(X_3) + \delta_2(X_4) + \delta_2(P) = 0; \\ \delta_3(X_1) + \delta_3(X_2) + \delta_3(X_3) + \delta_4(X_4) + \delta_3(P) = 0; \\ \delta_4(X_1) + \delta_4(X_2) + \delta_4(X_3) + \delta_4(X_4) + \delta_4(P) = 0. \end{cases} \quad (5.67)$$

The behavior of the belt structure is assumed to be linear-elastic. The linearity can be described within Hookean law, wherein the displacement δ_n , caused by the force X_m is linearly proportional to that force: $\delta_n = \frac{1}{E} X_m$. Where E takes the role of a stiffness of the system and value $\frac{1}{E} = \bar{\delta}_{nm}$ is a unit displacement or displacement per unit load. Analogically, the displacement $\delta_n(X_m)$ in position n , caused by the force X_m , equals to the following:

$$\delta_n(X_m) = \bar{\delta}_{nm} X_m, \quad (5.68)$$

where $\bar{\delta}_{nm}$ is a unit structural displacement at the point n , caused by the unit load $\bar{X}_m = 1$. Thus, the System of Eqs. 5.69 can be transformed:

$$\begin{cases} \bar{\delta}_{11}X_1 + \bar{\delta}_{12}X_2 + \bar{\delta}_{13}X_3 + \bar{\delta}_{14}X_4 + \delta_{1P} = 0; \\ \bar{\delta}_{21}X_1 + \bar{\delta}_{22}X_2 + \bar{\delta}_{23}X_3 + \bar{\delta}_{24}X_4 + \delta_{2P} = 0; \\ \bar{\delta}_{31}X_1 + \bar{\delta}_{32}X_2 + \bar{\delta}_{33}X_3 + \bar{\delta}_{34}X_4 + \delta_{3P} = 0; \\ \bar{\delta}_{41}X_1 + \bar{\delta}_{42}X_2 + \bar{\delta}_{43}X_3 + \bar{\delta}_{44}X_4 + \delta_{4P} = 0. \end{cases} \quad (5.69)$$

In this set of equations, the 1st index identifies the position and direction where the radial displacement occurs due to the force applied; the 2nd index refers to the force or load, caused that displacement. Thus, the displacements δ_{nP} are due to the external loads. The rule for the signs implies that the displacement is considered positive, if it is in line with the direction of the force applied.

In order to determine the displacements, the strain energy of the system needs to be considered. According to the modified Castigliano's theorem (Gere and Timoshenko [82], Karnovsky and Lebed [122]), the displacement of point n , where the force P_n is applied, depends on the bending moment M , axial force N , and shear force Q , resultant from that force P_n causing that displacement δ_n (see Fig. 5.24):

$$\delta_n = \sum \int_L \frac{M(s)}{EI} \frac{\partial M(s)}{\partial P_n} ds + \sum \int_L \frac{N(s)}{EA} \frac{\partial N(s)}{\partial P_n} ds + \sum \int_L \frac{kQ(s)}{GA} \frac{\partial Q(s)}{\partial P_n} ds. \quad (5.70)$$

This integration needs to be carried out summing all the elements in the structure over the entire contour $L = \pi R$ up to the fixed edge at the point A . In the equation, EI , EA , GA are bending, axial, and shear stiffness of the cross section, respectively. E is the Young's modulus of the belt in lateral direction, determined from the troughability test as recommended in Chapter 3. G stands for a shear modulus, which for the isotropic body equals to $G = \frac{E}{2(1 + \mu)}$, and for the orthotropic one $G = \frac{\sqrt{E_1 E_2}}{2(1 + \sqrt{\mu_1 \mu_2})}$ (see Chernenko [28]).

In Eq. 5.70, s represents the length of arc, characterizing circumferential position of any point on a pipe contour. The length of an arc element equals $ds = R d\varphi$. The area $A = lh$, and the moment of inertia I for a rectangular shape equals to $I = lh^3/12$, where l

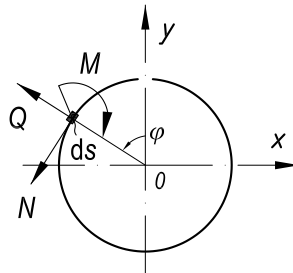


Figure 5.24: Bending moment M , axial force N , and shear force Q of the cross section (figure from Birger and Mavlyutov [16]).

is a longitudinal length of the belt that equivalent to the conveyor pitch ($l = l_c$ or $l = l_r$). Alternatively, l is equivalent to the sample width $b = (150 \pm 2)$ mm, initially used for the troughability test to determine the bending stiffness. Chapter 5 and 6 accept $l = b$, in order to compare the analytical and numerical solution for PBC CFs with the experimental results.

In Eq. 5.70, k is a dimensionless correction coefficient that also depends on the shape of the cross section. For a rectangular cross section, Boresi and Sidebottom [19], Karnovsky and Lebed [122] recommend to take $k = 1.2$.

Gere and Timoshenko [82], and Karnovsky and Lebed [122] discuss the physical meaning of the partial derivatives that appear under the integral signs in Eq. 5.70. These derivatives of bending moment M , axial force N , and shear force Q , with respect to the force P_n mean the bending moment M_{1n} , axial force N_{1n} , and shear force Q_{1n} , produced by unit dimensionless load $\bar{P}_n = 1$. Therefore, Eq. 5.70 can be written in a form, known as a Maxwell-Mohr Integral (Birger and Mavlyutov [16], Karnovsky and Lebed [122]):

$$\delta_n = \sum \int_L \frac{M_{1n}M}{EI} ds + \sum \int_L \frac{N_{1n}N}{EA} ds + \sum \int_L \frac{kQ_{1n}Q}{GA} ds, \quad (5.71)$$

where M_{1n} , N_{1n} , and Q_{1n} are the quantities, caused by the dimensionless internal unit load (or also called dummy-load (Boresi and Sidebottom [19], Karnovsky and Lebed [122], Karnovsky [121]), applied at the point n , where displacements need to be determined. The moments are considered positive in the integral if they increase the curvature of the belt structure deformed.

Karnovsky and Lebed [122], Karnovsky [121] state that, in Eq. 5.71 for structures with $B/h \geq 5$, the bending term is dominative over the axial term and the shear one. In order to achieve accurate results, the researchers recommend to use the first and the second terms for the gently sloping arched structures, and all three terms for structures with ratio of the radius of the curvature to the thickness approximately $R/h \geq 5$ (or in the present case $B/h \geq 10\pi$). Taking into account the possible limitations for the belt slenderness $6.67 \leq B/h \leq 643$, established in Section 2.5.2, the present approach also uses full expression given in Eq. 5.71 with all three terms for a sufficient precision in the results.

5.6.3 Unit displacements

In order to solve the System of Eqs. 5.69, the unit displacements $\bar{\delta}_{nm}$ as coefficients in front of the unknown reaction forces need to be determined. As discussed above, the physical meaning of Eq. 5.71 implies that the unit displacement $\bar{\delta}_{nm}$ is actually a displacement caused by the unit load $\bar{X}_m = 1$, applied at the point n .

Therefore, the unit displacements in System of Eqs. 5.69 can be obtained by applying the dimensionless dummy unit loads $\bar{X}_1 = 1$, $\bar{X}_2 = 1$, $\bar{X}_3 = 1$, $\bar{X}_4 = 1$, at the points 1, 2, 3, and 4, independently instead of the corresponding unknown redundant forces X_1 , X_2 , X_3 , X_4 , respectively. Then, the Maxwell-Mohr Integral takes the form:

$$\bar{\delta}_{nm} = \int_L \frac{M_{1n}M_{1m}}{EI} ds + \int_L \frac{N_{1n}N_{1m}}{EA} ds + \int_L \frac{kQ_{1n}Q_{1m}}{GA} ds, \quad (5.72)$$

where the bending moment M_{1m} , axial force N_{1m} , and shear force Q_{1m} are caused by unit load $\bar{X}_m = 1$.

The unit displacements according to the Maxwell-Mohr integral follow the law of reciprocal displacements, or in other words, exhibits complementary property: $\bar{\delta}_{nm} = \bar{\delta}_{mn}$. Hence, the displacements equal: $\bar{\delta}_{12} = \bar{\delta}_{21}$, $\bar{\delta}_{13} = \bar{\delta}_{31}$, \dots , $\bar{\delta}_{34} = \bar{\delta}_{43}$. As a result, the System of Eqs. 5.69 yields:

$$\begin{bmatrix} \delta_1 \\ \delta_2 \\ \delta_3 \\ \delta_4 \end{bmatrix} = \begin{bmatrix} \bar{\delta}_{11} & \bar{\delta}_{12} & \bar{\delta}_{13} & \bar{\delta}_{14} \\ \bar{\delta}_{12} & \bar{\delta}_{22} & \bar{\delta}_{23} & \bar{\delta}_{24} \\ \bar{\delta}_{13} & \bar{\delta}_{23} & \bar{\delta}_{33} & \bar{\delta}_{34} \\ \bar{\delta}_{14} & \bar{\delta}_{24} & \bar{\delta}_{34} & \bar{\delta}_{44} \end{bmatrix} \begin{bmatrix} X_1 \\ X_2 \\ X_3 \\ X_4 \end{bmatrix} + \begin{bmatrix} \delta_{1P} \\ \delta_{2P} \\ \delta_{3P} \\ \delta_{4P} \end{bmatrix} = \bar{\delta}\mathbf{X} + \delta\mathbf{P} = 0. \quad (5.73)$$

The unit load components (bending moment, axial and shear forces) in Eq. 5.72 and Eq. 5.73 are caused by the unit loads $\bar{X}_1 = 1$, $\bar{X}_2 = 1$, $\bar{X}_3 = 1$, $\bar{X}_4 = 1$, applied to the structure at points 1, 2, 3 and 4 independently. Table 5.3 presents the unit displacements and also shows the corresponding bending moment diagrams.

As a result, the formulas that determine the unit displacements equal the following:

$$\begin{aligned} \bar{\delta}_{11} &= \int_L \frac{M_{11}^2}{EI} ds + \int_L \frac{N_{11}^2}{EA} ds + \int_L \frac{kQ_{11}^2}{GA} ds = \\ &= \left(\frac{R^3}{EI} + \frac{R}{EA} \right) \int_0^\pi \sin^2 \varphi d\varphi + \frac{kR}{GA} \int_0^\pi \cos^2 \varphi d\varphi; \end{aligned} \quad (5.74)$$

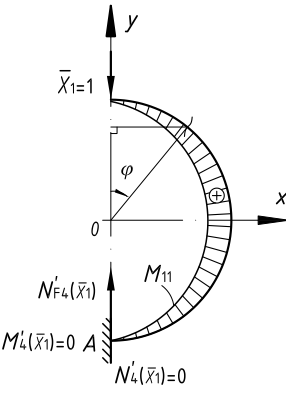
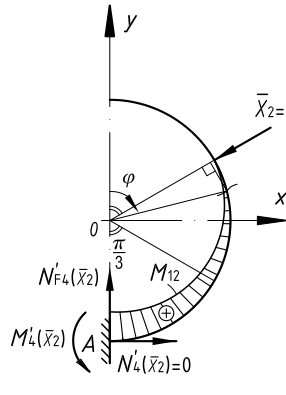
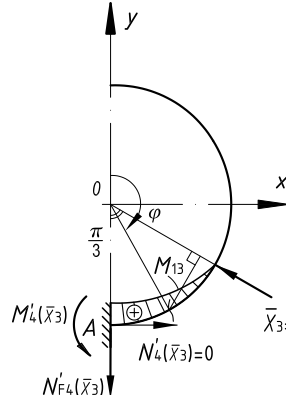
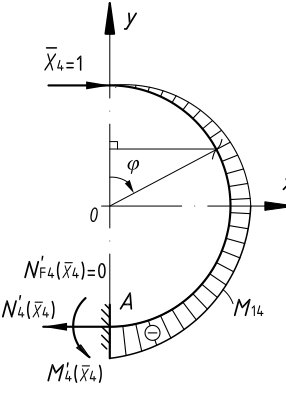
$$\begin{aligned} \bar{\delta}_{12} &= \int_L \frac{M_{11}M_{12}}{EI} ds + \int_L \frac{N_{11}N_{12}}{EA} ds + \int_L \frac{kQ_{11}Q_{12}}{GA} ds = \\ &= \left(\frac{R^3}{EI} + \frac{R}{EA} \right) \int_{\pi/3}^\pi \sin \varphi \sin \left(\varphi - \frac{\pi}{3} \right) d\varphi + \frac{kR}{GA} \int_{\pi/3}^\pi \cos \varphi \cos \left(\varphi - \frac{\pi}{3} \right) d\varphi; \end{aligned} \quad (5.75)$$

$$\begin{aligned} \bar{\delta}_{13} &= \int_L \frac{M_{11}M_{13}}{EI} ds + \int_L \frac{N_{11}N_{13}}{EA} ds + \int_L \frac{kQ_{11}Q_{13}}{GA} ds = \\ &= - \left(\frac{R^3}{EI} + \frac{R}{EA} \right) \int_{2\pi/3}^\pi \sin \varphi \sin \left(\varphi + \frac{\pi}{3} \right) d\varphi - \frac{kR}{GA} \int_{2\pi/3}^\pi \cos \varphi \cos \left(\varphi + \frac{\pi}{3} \right) d\varphi; \end{aligned} \quad (5.76)$$

$$\begin{aligned} \bar{\delta}_{14} &= \int_L \frac{M_{11}M_{14}}{EI} ds + \int_L \frac{N_{11}N_{14}}{EA} ds + \int_L \frac{kQ_{11}Q_{14}}{GA} ds = \\ &= \frac{R^3}{EI} \int_0^\pi \sin \varphi (\cos \varphi - 1) d\varphi + \left(\frac{R}{EA} - \frac{kR}{GA} \right) \int_0^\pi \sin \varphi \cos \varphi d\varphi; \end{aligned} \quad (5.77)$$

$$\begin{aligned} \bar{\delta}_{22} &= \int_L \frac{M_{12}^2}{EI} ds + \int_L \frac{N_{12}^2}{EA} ds + \int_L \frac{kQ_{12}^2}{GA} ds = \\ &= \left(\frac{R^3}{EI} + \frac{R}{EA} \right) \int_{\pi/3}^\pi \sin^2 \left(\varphi - \frac{\pi}{3} \right) d\varphi + \frac{kR}{GA} \int_{\pi/3}^\pi \cos^2 \left(\varphi - \frac{\pi}{3} \right) d\varphi; \end{aligned} \quad (5.78)$$

Table 5.3: Load components (bending moment, axial and shear forces) and corresponding bending moment diagrams, caused by the unit loads $\bar{X}_1 = 1$, $\bar{X}_2 = 1$, $\bar{X}_3 = 1$, $\bar{X}_4 = 1$, applied independently to the structure.

<p>For $\bar{X}_1 = 1$ at point 1 and $0 \leq \varphi \leq \pi$:</p> $M_{11} = R \sin \varphi;$ $N_{11} = \sin \varphi;$ $Q_{11} = -\cos \varphi.$  <p>Bending moment diagram M_{11}</p>	<p>For $\bar{X}_2 = 1$ at point 2 and $\frac{\pi}{3} \leq \varphi \leq \pi$:</p> $M_{12} = R \sin \left(\varphi - \frac{\pi}{3} \right);$ $N_{12} = \sin \left(\varphi - \frac{\pi}{3} \right);$ $Q_{12} = -\cos \left(\varphi - \frac{\pi}{3} \right).$  <p>Bending moment diagram M_{12}</p>
<p>For $\bar{X}_3 = 1$ at point 3 and $\frac{2\pi}{3} \leq \varphi \leq \pi$:</p> $M_{13} = -R \sin \left(\varphi + \frac{\pi}{3} \right);$ $N_{13} = -\sin \left(\varphi + \frac{\pi}{3} \right);$ $Q_{13} = \cos \left(\varphi + \frac{\pi}{3} \right).$  <p>Bending moment diagram M_{13}</p>	<p>For $\bar{X}_4 = 1$ at point 4 and $0 \leq \varphi \leq \pi$:</p> $M_{14} = R (\cos \varphi - 1);$ $N_{14} = \cos \varphi;$ $Q_{14} = \sin \varphi.$  <p>Bending moment diagram M_{14}</p>

$$\begin{aligned}
\bar{\delta}_{23} &= \int_L \frac{M_{12}M_{13}}{EI} ds + \int_L \frac{N_{12}N_{13}}{EA} ds + \int_L \frac{kQ_{12}Q_{13}}{GA} ds = \\
&= -\left(\frac{R^3}{EI} + \frac{R}{EA}\right) \int_{2\pi/3}^{\pi} \sin\left(\varphi - \frac{\pi}{3}\right) \sin\left(\varphi + \frac{\pi}{3}\right) d\varphi - \\
&\quad - \frac{kR}{GA} \int_{2\pi/3}^{\pi} \cos\left(\varphi - \frac{\pi}{3}\right) \cos\left(\varphi + \frac{\pi}{3}\right) d\varphi;
\end{aligned} \tag{5.79}$$

$$\begin{aligned}
\bar{\delta}_{24} &= \int_L \frac{M_{12}M_{14}}{EI} ds + \int_L \frac{N_{12}N_{14}}{EA} ds + \int_L \frac{kQ_{12}Q_{14}}{GA} ds = \\
&= \frac{R^3}{EI} \int_{\pi/3}^{\pi} \sin\left(\varphi - \frac{\pi}{3}\right) (\cos\varphi - 1) d\varphi + \frac{R}{EA} \int_{\pi/3}^{\pi} \sin\left(\varphi - \frac{\pi}{3}\right) \cos\varphi d\varphi - \\
&\quad - \frac{kR}{GA} \int_{\pi/3}^{\pi} \cos\left(\varphi - \frac{\pi}{3}\right) \sin\varphi d\varphi;
\end{aligned} \tag{5.80}$$

$$\begin{aligned}
\bar{\delta}_{33} &= \int_L \frac{M_{13}^2}{EI} ds + \int_L \frac{N_{13}^2}{EA} ds + \int_L \frac{kQ_{13}^2}{GA} ds = \\
&= \left(\frac{R^3}{EI} + \frac{R}{EA}\right) \int_{2\pi/3}^{\pi} \sin^2\left(\varphi + \frac{\pi}{3}\right) d\varphi + \frac{kR}{GA} \int_{2\pi/3}^{\pi} \cos^2\left(\varphi + \frac{\pi}{3}\right) d\varphi;
\end{aligned} \tag{5.81}$$

$$\begin{aligned}
\bar{\delta}_{34} &= \int_L \frac{M_{13}M_{14}}{EI} ds + \int_L \frac{N_{13}N_{14}}{EA} ds + \int_L \frac{kQ_{13}Q_{14}}{GA} ds = \\
&= -\frac{R^3}{EI} \int_{2\pi/3}^{\pi} \sin\left(\varphi + \frac{\pi}{3}\right) (\cos\varphi - 1) d\varphi - \frac{R}{EA} \int_{2\pi/3}^{\pi} \sin\left(\varphi + \frac{\pi}{3}\right) \cos\varphi d\varphi + \\
&\quad + \frac{kR}{GA} \int_{2\pi/3}^{\pi} \cos\left(\varphi + \frac{\pi}{3}\right) \sin\varphi d\varphi;
\end{aligned} \tag{5.82}$$

$$\begin{aligned}
\bar{\delta}_{44} &= \int_L \frac{M_{14}^2}{EI} ds + \int_L \frac{N_{14}^2}{EA} ds + \int_L \frac{kQ_{14}^2}{GA} ds = \\
&= \frac{R^3}{EI} \int_0^{\pi} (\cos\varphi - 1)^2 d\varphi + \frac{R}{EA} \int_0^{\pi} \cos^2\varphi d\varphi + \frac{kR}{GA} \int_0^{\pi} \sin^2\varphi d\varphi.
\end{aligned} \tag{5.83}$$

5.6.4 Displacements from the external loads

The displacements δ_{1P} , δ_{2P} , δ_{3P} , δ_{4P} from the external loads (load from the belt weight, load from the belt bending stiffness and load from the bulk material) can be determined from the following general form of the Maxwell-Mohr Integral:

$$\delta_{nP} = \int_L \frac{M_{1n}M_P}{EI} ds + \int_L \frac{N_{1n}N_P}{EA} ds + \int_L \frac{kQ_{1n}Q_P}{GA} ds, \tag{5.84}$$

where the bending moment M_P , axial force N_P , and shear force Q_P are caused by all these external loads.

According to the Principal of Superposition, M_P , N_P , and Q_P from all the external loads are composed of the load components from the belt weight M_{bw} , N_{bw} , Q_{bw} , from the belt bending stiffness M_{bst} , N_{bst} , Q_{bst} , and from the bulk material M_{bulk} , N_{bulk} , Q_{bulk} , respectively as follows:

$$\begin{aligned} M_P &= M_{bw} + M_{bst} + M_{bulk}; \\ N_P &= N_{bw} + N_{bst} + N_{bulk}; \\ Q_P &= Q_{bw} + Q_{bst} + Q_{bulk}; \end{aligned} \quad (5.85)$$

Consequently, the displacements from the external loads can be evaluated as a sum of the displacements from each of the external load applied to the structure independently.

$$\delta_{nP} = \delta_{nbw} + \delta_{nbst} + \delta_{nbulk}. \quad (5.86)$$

The present approach also determines each of the displacements δ_{nbw} , δ_{nbst} , δ_{nbulk} , considering the structure subjected to the action of each of the load separately.

5.6.5 Displacements from the belt weight

The structure subjected to the distributed vertical load from the belt weight is illustrated in Fig. 5.25. The system is statically determinate, so the reaction forces from the belt weight can be found from the equilibrium equations, as following:

$$\begin{aligned} \sum F_x = 0 : \quad N'_4(q_{bw}) &= 0. \\ \sum F_y = 0 : \quad N'_{F4}(q_{bw}) &= \pi q_{bw} R. \\ \sum M_A = 0 : \quad M'_4(q_{bw}) &= \int_0^{\pi/2} q_{bw} R^2 \sin \varphi d\varphi + \int_{\pi/2}^{\pi} q_{bw} R^2 \sin(\pi - \varphi) d\varphi = \\ &= \int_0^{\pi} q_{bw} R^2 \sin \varphi d\varphi = 2q_{bw} R^2. \end{aligned} \quad (5.87)$$

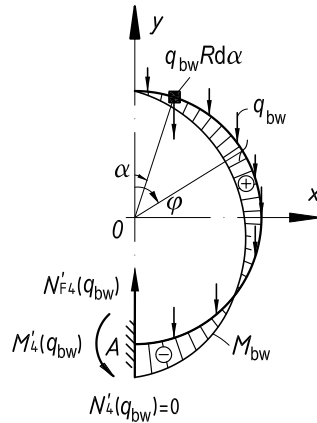


Figure 5.25: Statically determinate system subjected to the distributed vertical load from the belt weight q_{bw} and resultant bending moment diagram M_{bw} , demonstrated on the structural cross-sectional contour.

Introducing the dummy angular parameter $0 \leq \alpha \leq \varphi$, where $0 \leq \varphi \leq \pi$, the bending moment M_{bw} , the axial force N_{bw} , and the shear force Q_{bw} can be determined.

The following expressions define the bending moment M_{bw} :

$$\begin{aligned} dM_{bw}(\alpha) &= q_{bw}R^2(\sin \varphi - \sin \alpha)d\alpha; \\ M_{bw} &= \int_0^\varphi dM_{bw}(\alpha) = q_{bw}R^2 \int_0^\varphi (\sin \varphi - \sin \alpha)d\alpha = q_{bw}R^2 (\varphi \sin \varphi + \cos \varphi - 1). \end{aligned} \quad (5.88)$$

The axial force N_{bw} , generated by the belt weight, is defined by:

$$\begin{aligned} dN_{bw}(\alpha) &= q_{bw}R \sin \varphi d\alpha; \\ N_{bw} &= \int_0^\varphi dN_{bw}(\alpha) = \int_0^\varphi q_{bw}R \sin \varphi d\alpha = q_{bw}R\varphi \sin \varphi. \end{aligned} \quad (5.89)$$

The shear force component Q_{bw} equals:

$$\begin{aligned} dQ_{bw}(\alpha) &= -q_{bw}R \cos \varphi d\alpha; \\ Q_{bw} &= \int_0^\varphi dQ_{bw}(\alpha) = -\int_0^\varphi q_{bw}R \cos \varphi d\alpha = -q_{bw}R\varphi \cos \varphi. \end{aligned} \quad (5.90)$$

Substituting these load components into the Eq. 5.84 together with the corresponding unit loads, given in Table 5.3, the displacements caused by the belt weight at points 1, 2, 3, and 4 where the unknown redundant forces are applied at the original structure (Fig. 5.23), can be calculated from the following equations:

$$\begin{aligned} \delta_{1bw} &= \int_L \frac{M_{11}M_{bw}}{EI} ds + \int_L \frac{N_{11}N_{bw}}{EA} ds + \int_L \frac{kQ_{11}Q_{bw}}{GA} ds = \\ &= \frac{q_{bw}R^4}{EI} \int_0^\pi \sin \varphi (\varphi \sin \varphi + \cos \varphi - 1) d\varphi + \frac{q_{bw}R^2}{EA} \int_0^\pi \varphi \sin^2 \varphi d\varphi + \\ &+ \frac{q_{bw}kR^2}{GA} \int_0^\pi \varphi \cos^2 \varphi d\varphi; \end{aligned} \quad (5.91)$$

$$\begin{aligned} \delta_{2bw} &= \int_L \frac{M_{12}M_{bw}}{EI} ds + \int_L \frac{N_{12}N_{bw}}{EA} ds + \int_L \frac{kQ_{12}Q_{bw}}{GA} ds = \\ &= \frac{q_{bw}R^4}{EI} \int_{\pi/3}^\pi \sin \left(\varphi - \frac{\pi}{3} \right) (\varphi \sin \varphi + \cos \varphi - 1) d\varphi + \\ &+ \frac{q_{bw}R^2}{EA} \int_{\pi/3}^\pi \varphi \sin \left(\varphi - \frac{\pi}{3} \right) \sin \varphi d\varphi + \frac{q_{bw}kR^2}{GA} \int_{\pi/3}^\pi \varphi \cos \left(\varphi - \frac{\pi}{3} \right) \cos \varphi d\varphi; \end{aligned} \quad (5.92)$$

$$\begin{aligned} \delta_{3bw} &= \int_L \frac{M_{13}M_{bw}}{EI} ds + \int_L \frac{N_{13}N_{bw}}{EA} ds + \int_L \frac{kQ_{13}Q_{bw}}{GA} ds = \\ &= -\frac{q_{bw}R^4}{EI} \int_{2\pi/3}^\pi \sin \left(\varphi + \frac{\pi}{3} \right) (\varphi \sin \varphi + \cos \varphi - 1) d\varphi - \\ &- \frac{q_{bw}R^2}{EA} \int_{2\pi/3}^\pi \varphi \sin \left(\varphi + \frac{\pi}{3} \right) \sin \varphi d\varphi - \frac{q_{bw}kR^2}{GA} \int_{2\pi/3}^\pi \varphi \cos \left(\varphi + \frac{\pi}{3} \right) \cos \varphi d\varphi; \end{aligned} \quad (5.93)$$

$$\begin{aligned}
\delta_{4bw} &= \int_L \frac{M_{14}M_{bw}}{EI} ds + \int_L \frac{N_{14}N_{bw}}{EA} ds + \int_L \frac{kQ_{14}Q_{bw}}{GA} ds = \\
&= \frac{q_{bw}R^4}{EI} \int_0^\pi (\cos \varphi - 1)(\varphi \sin \varphi + \cos \varphi - 1) d\varphi + \\
&+ \left(\frac{q_{bw}R^2}{EA} - \frac{q_{bw}kR^2}{GA} \right) \int_0^\pi \varphi \sin \varphi \cos \varphi d\varphi.
\end{aligned} \tag{5.94}$$

5.6.6 Displacements from the belt bending stiffness

As indicated in Section 5.3, three approaches of modeling the load from the belt bending stiffness are selected aiming to investigate, which approach provides the correct results for the PBC CFs. That is why the displacements are determined for each of the approach selected, independently.

Concentrated expansion moments M_{bst}

If the load from forming the belt from a flat shape into a pipe shape is represented by the concentrated expansion moments M_{bst} , applied at the belt edges (see Section 5.3.1), the statically determined symmetrical half of a belt structure illustrated in Fig. 5.26, generates the following reaction forces from the equilibrium equations:

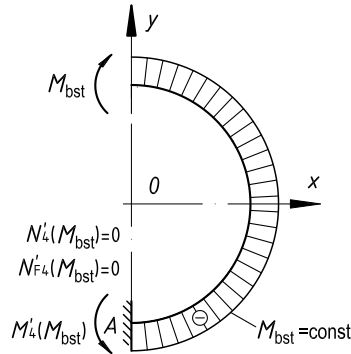


Figure 5.26: Statically determinate system subjected to the expansion concentrated moment M_{bst} that models the load from the belt bending stiffness and its resultant bending moment diagram, demonstrated on the structural cross-sectional contour.

$$\begin{aligned}
\sum F_x = 0 : \quad N'_4(M_{bst}) &= 0. \\
\sum F_y = 0 : \quad N'_{F4}(M_{bst}) &= 0. \\
\sum M_A = 0 : \quad M'_4(M_{bst}) &= -M_{bst} = \frac{EI}{R}.
\end{aligned} \tag{5.95}$$

For any $0 \leq \varphi \leq \pi$, the bending moment, the axial and the shear forces are constant:

$$\begin{aligned}
M_{bst} &= -\frac{EI}{R} = \text{const}. \\
N_{bst} &= Q_{bst} = 0.
\end{aligned} \tag{5.96}$$

This load from the belt bending stiffness generates the following displacements:

$$\delta_{1\text{bst}} = \int_L \frac{M_{11}M_{\text{bst}}}{EI} ds = -R \int_0^\pi \sin \varphi d\varphi = -2R; \quad (5.97)$$

$$\delta_{2\text{bst}} = \int_L \frac{M_{12}M_{\text{bst}}}{EI} ds = -R \int_{\pi/3}^\pi \sin \left(\varphi - \frac{\pi}{3} \right) d\varphi = -\frac{3R}{2} \quad (5.98)$$

$$\delta_{3\text{bst}} = \int_L \frac{M_{13}M_{\text{bst}}}{EI} ds = R \int_{2\pi/3}^\pi \sin \left(\varphi + \frac{\pi}{3} \right) d\varphi = -\frac{R}{2}; \quad (5.99)$$

$$\delta_{4\text{bst}} = \int_L \frac{M_{14}M_{\text{bst}}}{EI} ds = -R \int_0^\pi (\cos \varphi - 1) d\varphi = \pi R. \quad (5.100)$$

Evenly distributed radial expansion load q_{bst}

Alternatively, the other method of modeling the load from belt bending stiffness is selected for the analysis. In particular, it is investigated whether this load, represented as an expansion radial load q_{bst} evenly distributed along the cross-sectional contour and proposed by Chernenko [27, 28], generates the correct CFs. This load is defined by the Eq. 5.3 and is explicitly described in Section 5.3.2. The statically determined structure, subjected to this load and shown in Fig. 5.27, exhibits the following resultant reaction forces:

$$\begin{aligned} \sum F_x = 0 : N'_4(q_{\text{bst}}) &= q_{\text{bst}}R \int_0^{\pi/2} \sin \varphi d\varphi + q_{\text{bst}}R \int_{\pi/2}^\pi \sin(\pi - \varphi) d\varphi = 2q_{\text{bst}}R. \\ \sum F_y = 0 : N'_{F4}(q_{\text{bst}}) &= 0. \\ \sum M_A = 0 : M'_4(M_{\text{bst}}) &= q_{\text{bst}}R^2 \int_0^{\pi/2} \sin \varphi d\varphi + q_{\text{bst}}R^2 \int_{\pi/2}^\pi \sin(\pi - \varphi) d\varphi = 2q_{\text{bst}}R^2. \end{aligned} \quad (5.101)$$

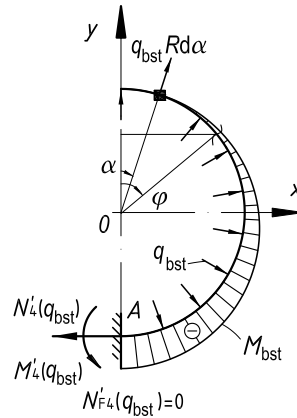


Figure 5.27: Statically determinate system subjected to the evenly distributed expansion radial load q_{bst} , given in Eq. 5.3 that reproduces the load from the belt bending stiffness and resultant bending moment diagram M_{bst} , demonstrated on the structural cross-sectional contour.

The bending moment M_{bst} , the axial force N_{bst} , and the shear force Q_{bst} can be evaluated using the dummy angular parameter $0 \leq \alpha \leq \varphi$, where $0 \leq \varphi \leq \pi$.

The bending moment M_{bst} is defined by:

$$\begin{aligned} dM_{\text{bst}}(\alpha) &= -q_{\text{bst}}R^2 \sin(\varphi - \alpha)d\alpha; \\ M_{\text{bst}} &= \int_0^\varphi dM_{\text{bst}}(\alpha) = -q_{\text{bst}}R^2 \int_0^\varphi \sin(\varphi - \alpha)d\alpha = q_{\text{bst}}R^2 (\cos \varphi - 1). \end{aligned} \quad (5.102)$$

As for N_{bst} , it equals:

$$\begin{aligned} dN_{\text{bst}}(\alpha) &= -q_{\text{bst}}R \sin(\varphi - \alpha)d\alpha; \\ N_{\text{bst}} &= \int_0^\varphi dN_{\text{bst}}(\alpha) = -q_{\text{bst}}R \int_0^\varphi \sin(\varphi - \alpha)d\alpha = q_{\text{bst}}R(\cos \varphi - 1). \end{aligned} \quad (5.103)$$

The shear force Q_{bst} can be expressed with:

$$\begin{aligned} dQ_{\text{bst}}(\alpha) &= q_{\text{bst}}R \cos \varphi d\alpha; \\ Q_{\text{bst}} &= \int_0^\varphi dQ_{\text{bst}}(\alpha) = q_{\text{bst}}R \int_0^\varphi \cos \varphi d\alpha = q_{\text{bst}}R \sin \varphi. \end{aligned} \quad (5.104)$$

Structural displacements caused by this loading condition within the distributed q_{bst} at the considering points are determined by substituting Eq. 5.102 - 5.104 into the general formula for the Maxwell-Mohr Integral in Eq. 5.84 together with the corresponding unit loads from Table 5.3. The displacements become equivalent:

$$\begin{aligned} \delta_{1\text{bst}} &= \int_L \frac{M_{11}M_{\text{bst}}}{EI} ds + \int_L \frac{N_{11}N_{\text{bst}}}{EA} ds + \int_L \frac{kQ_{11}Q_{\text{bst}}}{GA} ds = \\ &= \left(\frac{q_{\text{bst}}R^4}{EI} + \frac{q_{\text{bst}}R^2}{EA} \right) \int_0^\pi \sin \varphi (\cos \varphi - 1) d\varphi - \frac{kq_{\text{bst}}R^2}{GA} \int_0^\pi \sin \varphi \cos \varphi d\varphi; \end{aligned} \quad (5.105)$$

$$\begin{aligned} \delta_{2\text{bst}} &= \int_L \frac{M_{12}M_{\text{bst}}}{EI} ds + \int_L \frac{N_{12}N_{\text{bst}}}{EA} ds + \int_L \frac{kQ_{12}Q_{\text{bst}}}{GA} ds = \\ &= \left(\frac{q_{\text{bst}}R^4}{EI} + \frac{q_{\text{bst}}R^2}{EA} \right) \int_{\pi/3}^\pi \sin \left(\varphi - \frac{\pi}{3} \right) (\cos \varphi - 1) d\varphi - \\ &\quad - \frac{kq_{\text{bst}}R^2}{GA} \int_{\pi/3}^\pi \cos \left(\varphi - \frac{\pi}{3} \right) \sin \varphi d\varphi; \end{aligned} \quad (5.106)$$

$$\begin{aligned} \delta_{3\text{bst}} &= \int_L \frac{M_{13}M_{\text{bst}}}{EI} ds + \int_L \frac{N_{13}N_{\text{bst}}}{EA} ds + \int_L \frac{kQ_{13}Q_{\text{bst}}}{GA} ds = \\ &= - \left(\frac{q_{\text{bst}}R^4}{EI} + \frac{q_{\text{bst}}R^2}{EA} \right) \int_{2\pi/3}^\pi \sin \left(\varphi + \frac{\pi}{3} \right) (\cos \varphi - 1) d\varphi + \\ &\quad + \frac{kq_{\text{bst}}R^2}{GA} \int_{2\pi/3}^\pi \cos \left(\varphi + \frac{\pi}{3} \right) \sin \varphi d\varphi; \end{aligned} \quad (5.107)$$

$$\begin{aligned}
\delta_{4bst} &= \int_L \frac{M_{14} M_{bst}}{EI} ds + \int_L \frac{N_{14} N_{bst}}{EA} ds + \int_L \frac{k Q_{14} Q_{bst}}{GA} ds = \\
&= \frac{q_{bst} R^4}{EI} \int_0^\pi (\cos \varphi - 1)^2 d\varphi + \frac{q_{bst} R^2}{EA} \int_0^\pi (\cos \varphi - 1) \cos \varphi d\varphi + \frac{k q_{bst} R^2}{GA} \int_0^\pi \sin^2 \varphi d\varphi.
\end{aligned} \tag{5.108}$$

Evenly distributed radial load q_{bst} with concentrated forces Q_{1bst} , Q_{2bst}

In addition, the CFs for a PBC are determined, describing the load from the belt bending stiffness as a combination of the distributed radial load q_{bst} , and concentrated forces Q_{1bst} and Q_{2bst} , situated at angle β at the contour of the lateral cross section, as proposed by Dmitriev [52]. These loads are explicitly discussed in Section 5.3.3 and can be evaluated from the system of Eqs. 5.26. The angle β is found from the transcendental Eq. 5.27.

If such loads are applied to the statically determinate structure, demonstrated in Fig. 5.28, the resultant reaction forces are found from the equations of equilibrium:

$$\begin{aligned}
\sum F_x = 0 : N'_4(q_{bst}, Q_{1bst}, Q_{2bst}) &= Q_{2bst} \sin \beta + q_{bst} R \int_\beta^\pi \sin \varphi d\varphi = q_{bst} R. \\
\sum F_y = 0 : N'_{F4}(q_{bst}, Q_{1bst}, Q_{2bst}) &= -Q_{1bst} - Q_{2bst} \cos \beta - q_{bst} R \int_\beta^\pi \cos \varphi d\varphi = 0. \\
\sum M_A = 0 : M'_4(M_{bst}, Q_{1bst}, Q_{2bst}) &= Q_{2bst} R \sin \beta + q_{bst} R^2 \int_\beta^\pi \sin \varphi d\varphi = q_{bst} R^2.
\end{aligned} \tag{5.109}$$

The bending moment M_{bst} , the axial force N_{bst} , and the shear hoop force M_{bst} depend on the angular position of angle φ .

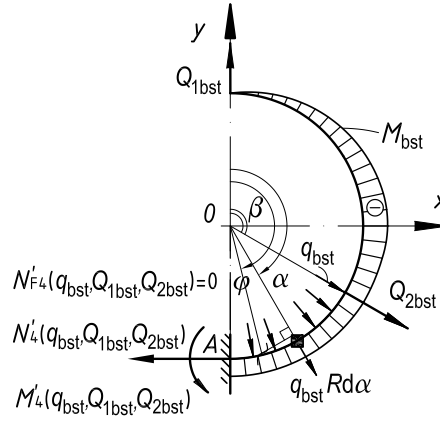


Figure 5.28: Statically determinate system subjected to the load from belt bending stiffness represented by the expansion evenly distributed radial load q_{bst} in combination with the concentrated forces Q_{1bst} , Q_{2bst} , applied at angle β and resultant bending moment diagram M_{bst} , demonstrated on the structural cross-sectional contour. The loads q_{bst} , Q_{1bst} , Q_{2bst} are defined by the System of Eqs. 5.26, and angle β is found from 5.27.

For $0 \leq \varphi \leq \beta$, they equal:

$$\begin{aligned} M_{\text{bst}} &= -Q_{1\text{bst}}R \sin \varphi = -\frac{q_{\text{bst}}R^2}{\sin \beta} \sin \varphi; \\ N_{\text{bst}} &= -Q_{1\text{bst}} \sin \varphi = -\frac{q_{\text{bst}}R}{\sin \beta} \sin \varphi; \\ Q_{\text{bst}} &= Q_{1\text{bst}} \cos \varphi = \frac{q_{\text{bst}}R}{\sin \beta} \cos \varphi. \end{aligned} \quad (5.110)$$

For $\beta \leq \varphi \leq \pi$, the impact of the distributed load q_{bst} on M_{bst} , N_{bst} , and Q_{bst} can be described using the dummy angular parameter $\beta \leq \alpha \leq \varphi$. Then the moment becomes:

$$\begin{aligned} dM_{\text{bst}}(\alpha) &= -q_{\text{bst}}R^2 \sin(\varphi - \alpha)d\alpha; \\ M_{\text{bst}} &= -Q_{1\text{bst}}R \sin \varphi - Q_{2\text{bst}}R \sin(\varphi - \beta) - q_{\text{bst}}R^2 \int_{\beta}^{\varphi} \sin(\varphi - \alpha)d\alpha = -q_{\text{bst}}R^2. \end{aligned} \quad (5.111)$$

As for the axial force, it can be defined by:

$$\begin{aligned} dN_{\text{bst}}(\alpha) &= -q_{\text{bst}}R \sin(\varphi - \alpha)d\alpha; \\ N_{\text{bst}} &= -Q_{1\text{bst}} \sin \varphi - Q_{2\text{bst}} \sin(\varphi - \beta) - q_{\text{bst}}R \int_{\beta}^{\varphi} \sin(\varphi - \alpha)d\alpha = -q_{\text{bst}}R. \end{aligned} \quad (5.112)$$

Ultimately, the shear force can be obtained from:

$$\begin{aligned} dQ_{\text{bst}}(\alpha) &= q_{\text{bst}}R \cos(\varphi - \alpha)d\alpha; \\ N_{\text{bst}} &= -Q_{1\text{bst}} \sin \varphi - Q_{2\text{bst}} \sin(\varphi - \beta) - q_{\text{bst}}R \int_{\beta}^{\varphi} \sin(\varphi - \alpha)d\alpha = -q_{\text{bst}}R. \end{aligned} \quad (5.113)$$

The displacements of the belt structure due to loads from the belt bending stiffness, expressed within q_{bst} , $Q_{1\text{bst}}$, and $Q_{2\text{bst}}$ at the points considered, can be evaluated by substituting the Eqs. 5.110 - 5.113 for M_{bst} , N_{bst} , and Q_{bst} into the Maxwell-Mohr Integral for the external loads (Eq. 5.84).

The displacements $\delta_{n\text{bst}}$ depend on the position of β , which in turn is defined by the slenderness ratio B/h according to the transcendental Eq. 5.27. Taking into account the geometrical range, established specifically for conveyor belts in Section 2.5.2, the slenderness ratio B/h of interest varies in the limits $6.67 \leq B/h \leq 643$.

If $\beta < \frac{2\pi}{3}$, as illustrated in Fig. 5.29a, which means that $B/h \leq 10.85$, the displacements then for conveyor belting $6.67 \leq B/h \leq 10.85$ become equivalent:

$$\begin{aligned} \delta_{1\text{bst}} &= \int_L \frac{M_{11}M_{\text{bst}}}{EI} ds + \int_L \frac{N_{11}N_{\text{bst}}}{EA} ds + \int_L \frac{kQ_{11}Q_{\text{bst}}}{GA} ds = \\ &= -\left(\frac{q_{\text{bst}}R^4}{EI} + \frac{q_{\text{bst}}R^2}{EA} \right) \left[\frac{1}{\sin \beta} \int_0^{\beta} \sin^2 \varphi d\varphi + \int_{\beta}^{\pi} \sin \varphi d\varphi \right] - \\ &\quad - \frac{kq_{\text{bst}}R^2}{GA} \frac{1}{\sin \beta} \int_0^{\beta} \cos^2 \varphi d\varphi; \end{aligned} \quad (5.114)$$

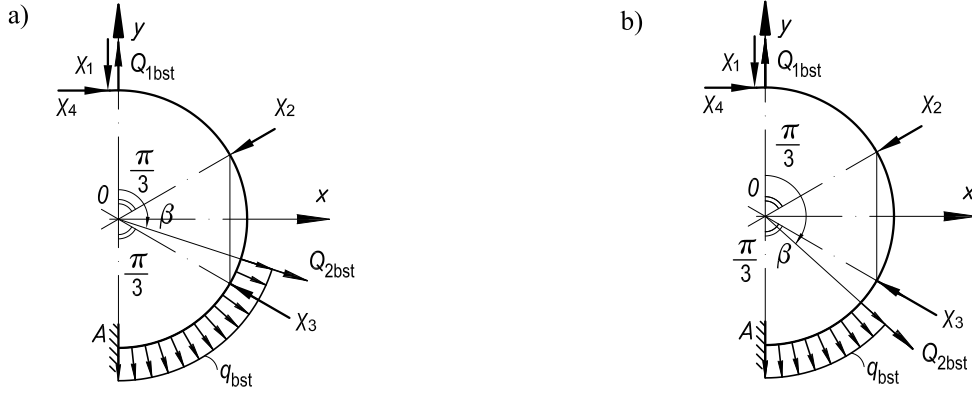


Figure 5.29: Statically determinate system subjected to the redundant forces X_1, X_2, X_3, X_4 and the load from belt bending stiffness, represented by the expansion evenly distributed radial load q_{bst} in combination with the concentrated forces Q_{1bst}, Q_{2bst} , applied at angle: a) $\beta < \frac{2\pi}{3}$; and b) $\beta \geq \frac{2\pi}{3}$.

$$\begin{aligned} \delta_{2bst} &= \int_L \frac{M_{12}M_{bst}}{EI} ds + \int_L \frac{N_{12}N_{bst}}{EA} ds + \int_L \frac{kQ_{12}Q_{bst}}{GA} ds = \\ &= - \left(\frac{q_{bst}R^4}{EI} + \frac{q_{bst}R^2}{EA} \right) \left[\frac{1}{\sin \beta} \int_{\pi/3}^{\beta} \sin \varphi \sin \left(\varphi - \frac{\pi}{3} \right) d\varphi + \int_{\beta}^{\pi} \sin \left(\varphi - \frac{\pi}{3} \right) d\varphi \right] - \\ &\quad - \frac{kq_{bst}R^2}{GA} \frac{1}{\sin \beta} \int_{\pi/3}^{\beta} \cos \varphi \cos \left(\varphi - \frac{\pi}{3} \right) d\varphi; \end{aligned} \quad (5.115)$$

$$\begin{aligned} \delta_{3bst} &= \int_L \frac{M_{13}M_{bst}}{EI} ds + \int_L \frac{N_{13}N_{bst}}{EA} ds + \int_L \frac{kQ_{13}Q_{bst}}{GA} ds = \\ &= \left(\frac{q_{bst}R^4}{EI} + \frac{q_{bst}R^2}{EA} \right) \int_{2\pi/3}^{\pi} \sin \left(\varphi + \frac{\pi}{3} \right) d\varphi; \end{aligned} \quad (5.116)$$

$$\begin{aligned} \delta_{4bst} &= \int_L \frac{M_{14}M_{bst}}{EI} ds + \int_L \frac{N_{14}N_{bst}}{EA} ds + \int_L \frac{kQ_{14}Q_{bst}}{GA} ds = \\ &= - \frac{q_{bst}R^4}{EI} \left[\frac{1}{\sin \beta} \int_0^{\beta} (\cos \varphi - 1) \sin \varphi d\varphi + \int_{\beta}^{\pi} (\cos \varphi - 1) d\varphi \right] - \\ &\quad - \frac{q_{bst}R^2}{EA} \left[\frac{1}{\sin \beta} \int_0^{\beta} \sin \varphi \cos \varphi d\varphi + \int_{\beta}^{\pi} \cos \varphi d\varphi \right] + \frac{kq_{bst}R^2}{GA} \frac{1}{\sin \beta} \int_0^{\beta} \sin \varphi \cos \varphi d\varphi. \end{aligned} \quad (5.117)$$

If $\beta \geq \frac{2\pi}{3}$ (see Fig. 5.29b) that is equivalent to the slenderness $10.85 \leq B/h \leq 643$, the displacements δ_{1bst} , δ_{2bst} , and δ_{4bst} are the same as in Eqs. 5.114, 5.115, and 5.117, respectively, except for δ_{3bst} , which equals:

$$\begin{aligned}
\delta_{3bst} &= \int_L \frac{M_{13} M_{bst}}{EI} ds + \int_L \frac{N_{13} N_{bst}}{EA} ds + \int_L \frac{k Q_{13} Q_{bst}}{GA} ds = \\
&= \left(\frac{q_{bst} R^4}{EI} + \frac{q_{bst} R^2}{EA} \right) \left[\frac{1}{\sin \beta} \int_{2\pi/3}^{\beta} \sin \varphi \sin \left(\varphi + \frac{\pi}{3} \right) d\varphi + \int_{\beta}^{\pi} \sin \left(\varphi + \frac{\pi}{3} \right) d\varphi \right] + \\
&+ \frac{k q_{bst} R^2}{GA} \frac{1}{\sin \beta} \int_{2\pi/3}^{\beta} \cos \varphi \cos \left(\varphi + \frac{\pi}{3} \right) d\varphi.
\end{aligned} \tag{5.118}$$

5.6.7 Displacements from the bulk material load

The load from the bulk material is represented by the two components: the vertical distributed load q_{bulk}^v and the horizontal one q_{bulk}^h , applied at dx and dy , respectively along the pipe conveyor cross-sectional contour. Taking into account the linear behavior of the system and the Principal of Superposition, the effect of each load component can be summed, and the bending moment, the axial force and the shear force components become:

$$\begin{aligned}
M_{bulk} &= M_{bulk}^v + M_{bulk}^h; \\
N_{bulk} &= N_{bulk}^v + N_{bulk}^h; \\
Q_{bulk} &= Q_{bulk}^v + Q_{bulk}^h;
\end{aligned} \tag{5.119}$$

As a result, the displacements from the bulk material load can be obtained by summing the displacements from each of the component from that load, i.e.:

$$\delta_{nbulk} = \delta_{nbulk}^v + \delta_{nbulk}^h, \tag{5.120}$$

where each of the displacement can be determined independently.

The displacements from the bulk material load are determined considering each of the bulk material load component independently.

The vertical component

$q_{bulk}^v dx$, defined by Eqs. 5.36 - 5.39 in Section 5.4.3 represents the vertical component of the load from bulk material. The distribution of this load depends on the filling degree k_Q of the cross section, expressed via the filling angle θ as given in Eq. 2.5, and the angular position φ ($2\theta \leq \varphi \leq \pi$) at the contour.

If the filling degree, characterized by the filling angle θ , is in the range of $0 \leq 2\theta \leq \frac{\pi}{2}$ or $0 \leq \theta \leq \frac{\pi}{4}$, the load $q_{bulk}^v dx$, applied to the statically determinate structure produces the following resultant forces and moment at the fixed edge (see Fig. 5.30):

$$\begin{aligned}
\sum F_x = 0 &: N'_4(q_{bulk}^v dx) = 0. \\
\sum F_y = 0 &: N'_{F4}(q_{bulk}^v dx) = \int_{2\theta}^{\pi} q_{bulk}^v dx = \frac{1}{2} k_Q \pi R^2 \rho_{bulk} g l = \frac{1}{2} F_{bulk}^v. \\
\sum M_A = 0 &: M'_{4}(q_{bulk}^v dx) = \int_{2\theta}^{\pi} q_{bulk}^v dx R \sin \varphi = \\
&= -\frac{1}{12} \rho_{bulk} g R^2 l (\cos^3 3\theta - 9\cos^2 \theta - 2 \tan \lambda \sin^3 2\theta).
\end{aligned} \tag{5.121}$$

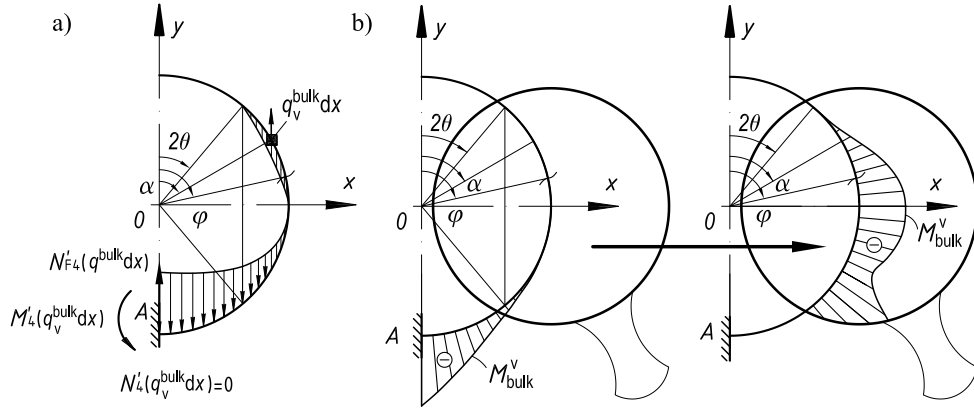


Figure 5.30: a) Statically determinate system subjected to the vertical bulk material load component $q_v^{\text{bulk}} dx$ for the cross-sectional filling angle $0 \leq 2\theta \leq \frac{\pi}{2}$, and the resultant diagrams for b) bending moment M_{bulk}^v . The load is defined by Eq. 5.36 and Eq. 5.37.

Besides of the filling degree, the bending moment M_{bulk}^v , the axial force N_{bulk}^v , and the shear force Q_{bulk}^v that occur due to the vertical load component from the bulk material, vary with respect to the angular position φ along the cross-sectional contour. In order to incorporate the effect of the distributed load, the dummy angular parameters $2\theta \leq \alpha \leq \varphi$ is introduced.

For the angular position $2\theta \leq \varphi \leq \pi - 2\theta$, the bending moment M_{bulk}^v , the axial N_{bulk}^v , and shear Q_{bulk}^v equal:

$$\begin{aligned} M_{\text{bulk}}^v &= -\rho_{\text{bulk}} g R^3 l \int_{2\theta}^{\varphi} \Phi_M^v(\theta, \varphi, \alpha) d\alpha; \\ N_{\text{bulk}}^v &= -\rho_{\text{bulk}} g R^2 l \sin \varphi \int_{2\theta}^{\varphi} \Phi_{NQ}^v(\theta, \alpha) d\alpha; \\ Q_{\text{bulk}}^v &= -\rho_{\text{bulk}} g R^2 l \cos \varphi \int_{2\theta}^{\varphi} \Phi_{NQ}^v(\theta, \alpha) d\alpha. \end{aligned} \quad (5.122)$$

As for $\pi - 2\theta \leq \varphi \leq \pi$, the bending moment M_{bulk}^v , the axial force N_{bulk}^v , and shear force Q_{bulk}^v are equivalent to the following:

$$\begin{aligned} M_{\text{bulk}}^v &= -\rho_{\text{bulk}} g R^3 l \left[\int_{2\theta}^{\varphi} \Phi_M^v(\theta, \varphi, \alpha) d\alpha + \tan \lambda \int_{\pi-2\theta}^{\varphi} \Phi_{M\lambda}^v(\theta, \varphi, \alpha) d\alpha \right]; \\ N_{\text{bulk}}^v &= -\rho_{\text{bulk}} g R^2 l \sin \varphi \left[\int_{2\theta}^{\varphi} \Phi_{NQ}^v(\theta, \alpha) d\alpha + \tan \lambda \int_{\pi-2\theta}^{\varphi} \Phi_{NQ\lambda}^v(\theta, \alpha) d\alpha \right]; \\ Q_{\text{bulk}}^v &= \rho_{\text{bulk}} g R^2 l \cos \varphi \left[\int_{2\theta}^{\varphi} \Phi_{NQ}^v(\theta, \alpha) d\alpha + \tan \lambda \int_{\pi-2\theta}^{\varphi} \Phi_{NQ\lambda}^v(\theta, \alpha) d\alpha \right]. \end{aligned} \quad (5.123)$$

Eqs. 5.122-5.123 contain the functions Φ_M^v , $\Phi_{M\lambda}^v$, Φ_{NQ}^v , and $\Phi_{NQ\lambda}^v$ that are specially introduced for the simplicity of the formulas. They substitute the following:

$$\begin{aligned}
\Phi_M^v(\theta, \varphi, \alpha) &= (\cos 2\theta - \cos \alpha) \cos \alpha (\sin \varphi - \sin \alpha); \\
\Phi_{M\lambda}^v(\theta, \varphi, \alpha) &= (\sin 2\theta - \sin \alpha) \cos \alpha (\sin \varphi - \sin \alpha); \\
\Phi_{NQ}^v(\theta, \alpha) &= (\cos 2\theta - \cos \alpha) \cos \alpha; \\
\Phi_{NQ\lambda}^v(\theta, \alpha) &= (\sin 2\theta - \sin \alpha) \cos \alpha.
\end{aligned}
\tag{5.124}$$

For the filling degree $0 \leq 2\theta \leq \frac{\pi}{2}$ considered, the diagram of bending moment M_{bulk}^v is illustrated on the cross sectional contour in Fig. 5.30 for any $2\theta \leq \varphi \leq \pi$.

If the filling degree of the cross section belongs to the interval $\frac{\pi}{2} \leq 2\theta \leq \pi$ or $\frac{\pi}{4} \leq \theta \leq \frac{\pi}{2}$ (see Fig. 5.31), the resultant reaction forces $N_4'(q_{\text{bulk}}^v dx)$, $N_{F4}'(q_{\text{bulk}}^v dx)$, and the moment $M_4'(q_{\text{bulk}}^v dx)$, produced by the statically determined system under the action of the vertical bulk material load component, have the same final resultant expressions, as Eqs. 5.121 - 5.121.

For this filling angle $\frac{\pi}{2} \leq 2\theta \leq \pi$, the bending moment M_{bulk}^v , the axial force N_{bulk}^v , and the shear force Q_{bulk}^v are the same for any angular position (see Fig. 5.31) and are defined by:

$$\begin{aligned}
M_{\text{bulk}}^v &= -\rho_{\text{bulk}} g R^3 l \int_{2\theta}^{\varphi} [\Phi_M^v(\theta, \varphi, \alpha) + \tan \lambda \Phi_{M\lambda}^v(\theta, \varphi, \alpha)] d\alpha; \\
N_{\text{bulk}}^v &= -\rho_{\text{bulk}} g R^2 l \sin \varphi \int_{2\theta}^{\varphi} [\Phi_{NQ}^v(\theta, \alpha) + \tan \lambda \Phi_{NQ\lambda}^v(\theta, \alpha)] d\alpha; \\
Q_{\text{bulk}}^v &= \rho_{\text{bulk}} g R^2 l \cos \varphi \int_{2\theta}^{\varphi} [\Phi_{NQ}^v(\theta, \alpha) + \tan \lambda \Phi_{NQ\lambda}^v(\theta, \alpha)] d\alpha.
\end{aligned}
\tag{5.125}$$

The structural displacements generated due to the bulk material vertical load component are defined by substituting M_{bulk}^v , N_{bulk}^v , and Q_{bulk}^v , given in Eqs. 5.122 - 5.123 or in Eqs. 5.125 into Eq. 5.84) for the Maxwell-Mohr Integral. The resultant displacements $\delta_{n\text{bulk}}^v$ depend on the filling angle θ of the cross section.

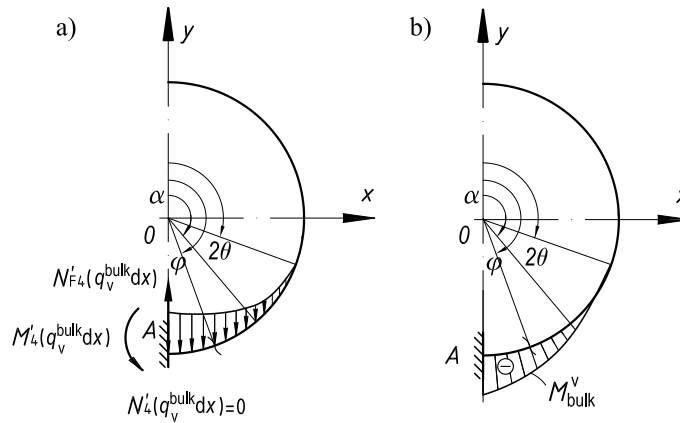


Figure 5.31: a) Statically determinate system subjected to the vertical bulk material load component $q_{\text{bulk}}^v dx$ for the filling angle $\frac{\pi}{2} \leq 2\theta \leq \pi$, and the resultant diagram for b) bending moment M_{bulk}^v . The load is defined by Eq. 5.38 and Eq. 5.39.

Table 5.4: The filling angle θ and the corresponding filling degree k_Q of a PBC cross section, found using Eq. 2.5 for the bulk materials selected in Section 2.4.

Filling angle θ	Cross sectional filling degree k_Q (Eq. 2.5)		
	Wood chips ($\lambda = 30^\circ$)	Coal ($\lambda = 15^\circ$)	Iron ore ($\lambda = 10^\circ$)
$0 \leq 2\theta \leq \frac{\pi}{3}$	$0.946 \leq k_Q \leq 1$	$0.868 \leq k_Q \leq 1$	$0.847 \leq k_Q \leq 1$
$\frac{\pi}{3} \leq 2\theta \leq \frac{\pi}{2}$	$0.684 \leq k_Q \leq 0.946$	$0.585 \leq k_Q \leq 0.868$	$0.556 \leq k_Q \leq 0.847$
$\frac{\pi}{2} \leq 2\theta \leq \frac{2\pi}{3}$	$0.333 \leq k_Q \leq 0.684$	$0.259 \leq k_Q \leq 0.585$	$0.238 \leq k_Q \leq 0.556$
$\frac{2\pi}{3} \leq 2\theta \leq \pi$	$0 \leq k_Q \leq 0.333$	$0 \leq k_Q \leq 0.259$	$0 \leq k_Q \leq 0.238$

In particular, the limiting borders that define the switch between the calculation formulas for the displacements are: 1) $0 \leq 2\theta \leq \pi/3$; 2) $\pi/3 \leq 2\theta \leq \pi/2$; 3) $\pi/2 \leq 2\theta \leq 2\pi/3$; 4) $2\pi/3 \leq 2\theta \leq \pi$. Appendix A provides the exact formulas for the each of the θ -case.

Taking into account the relationship between the angle of filling θ and the filling degree k_Q of a conveyor cross section, established in Eq. 2.5 Chapter 2, the limits for θ that characterize the switch between the calculation formulas for the displacements can be expressed via k_Q for given dynamic angle of repose λ . In Section 2.4 three bulk material types (wood chips, coal, and iron ore) are selected as examples. Table 5.4 gives the data for the cross sectional filling degree k_Q with respect to the critical limits of θ for each of the bulk material selected.

The horizontal component

The horizontal component of the bulk material load $q_{\text{bulk}}^h dy$ also depends on the filling angle θ and the angular position of φ ($2\theta \leq \varphi \leq \pi$) on the cross-sectional contour.

If the filling angle corresponds to the range $0 \leq 2\theta \leq \frac{\pi}{2}$ or $0 \leq \theta \leq \frac{\pi}{4}$, the distributed horizontal load $q_{\text{bulk}}^h dy$ applied at the structural contour of the statically determinate system, shown in Fig. 5.32, produces the following reaction forces and moment at the fixed edge:

$$\begin{aligned}
 \sum F_x = 0 : N'_4(q_{\text{bulk}}^h dy) \int_{2\theta}^{\pi} q_{\text{bulk}}^h dy &= \\
 = C^K \rho_{\text{bulk}} g R^2 l \left[\int_{2\theta}^{\pi} (\cos 2\theta - \cos \varphi) \sin \varphi d\varphi + \tan \lambda \int_{\pi-2\theta}^{\pi} (\sin 2\theta - \sin \varphi) \sin \varphi d\varphi \right] & \\
 \sum F_y = 0 : N'_{F4}(q_{\text{bulk}}^h dy) &= 0. \\
 \sum M_A = 0 : M'_4(q_{\text{bulk}}^h dy) = \int_{2\theta}^{\pi} q_{\text{bulk}}^h R(\cos \varphi + 1) dy &= \\
 = C^K \rho_{\text{bulk}} g R^3 l \int_{2\theta}^{\pi} (\cos 2\theta - \cos \varphi) \sin \varphi (\cos \varphi + 1) d\varphi + & \\
 + \tan \lambda \int_{\pi-2\theta}^{\pi} (\sin 2\theta - \sin \varphi) \sin \varphi (\cos \varphi + 1) d\varphi & \left. \right] . \tag{5.126}
 \end{aligned}$$

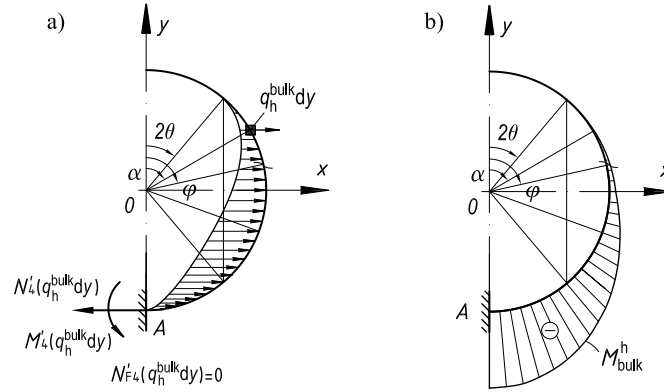


Figure 5.32: a) Statically determinate system subjected to the horizontal bulk material load component $q_h^{\text{bulk}} dy$ for the cross-sectional filling angle $0 \leq 2\theta \leq \frac{\pi}{2}$, and b) the resultant diagrams for bending moment. The load $q_h^{\text{bulk}} dy$ is defined by Eq. 5.48 and Eq. 5.50.

Introducing the dummy angular parameter $2\theta \leq \alpha \leq \varphi$, the bending moment M_{bulk}^h , the axial N_{bulk}^h force, and the shear force Q_{bulk}^h , generated for the filling angle $0 \leq 2\theta \leq \frac{\pi}{2}$ are defined with respect to the angle φ .

For $2\theta \leq \varphi \leq \pi - 2\theta$, they equal:

$$\begin{aligned} M_{\text{bulk}}^h &= C^K \rho_{\text{bulk}} g R^3 l \int_{2\theta}^{\varphi} \Phi_M^h(\theta, \varphi, \alpha) d\alpha; \\ N_{\text{bulk}}^h &= C^K \rho_{\text{bulk}} g R^2 l \cos \varphi \int_{2\theta}^{\varphi} \Phi_{NQ}^h(\theta, \alpha) d\alpha; \\ Q_{\text{bulk}}^h &= C^K \rho_{\text{bulk}} g R^2 l \sin \varphi \int_{2\theta}^{\varphi} \Phi_{NQ}^h(\theta, \alpha) d\alpha. \end{aligned} \quad (5.127)$$

Considering that angular position $\pi - 2\theta \leq \varphi \leq \pi$, the formulas transform to the following expressions:

$$\begin{aligned} M_{\text{bulk}}^h &= C^K \rho_{\text{bulk}} g R^3 l \left[\int_{2\theta}^{\varphi} \Phi_M^h(\theta, \varphi, \alpha) d\alpha + \tan \lambda \int_{\pi-2\theta}^{\varphi} \Phi_{M\lambda}^h(\theta, \varphi, \alpha) d\alpha \right]; \\ N_{\text{bulk}}^h &= C^K \rho_{\text{bulk}} g R^2 l \cos \varphi \left[\int_{2\theta}^{\varphi} \Phi_{NQ}^h(\theta, \alpha) d\alpha + \tan \lambda \int_{\pi-2\theta}^{\varphi} \Phi_{NQ\lambda}^h(\theta, \alpha) d\alpha \right]; \\ Q_{\text{bulk}}^h &= C^K \rho_{\text{bulk}} g R^2 l \sin \varphi \left[\int_{2\theta}^{\varphi} \Phi_{NQ}^h(\theta, \alpha) d\alpha + \tan \lambda \int_{\pi-2\theta}^{\varphi} \Phi_{NQ\lambda}^h(\theta, \alpha) d\alpha \right]. \end{aligned} \quad (5.128)$$

In Eqs. 5.127-5.128, $\Phi_M^h(\theta, \varphi, \alpha)$, $\Phi_{M\lambda}^h(\theta, \varphi, \alpha)$, $\Phi_{NQ}^h(\theta, \varphi, \alpha)$, and $\Phi_{NQ\lambda}^h(\theta, \varphi, \alpha)$ define the following functions:

$$\begin{aligned}
\Phi_M^h(\theta, \varphi, \alpha) &= (\cos 2\theta - \cos \alpha) \sin \alpha (\cos \varphi - \cos \alpha); \\
\Phi_{M\lambda}^h(\theta, \varphi, \alpha) &= (\sin 2\theta - \sin \alpha) \sin \alpha (\cos \varphi - \cos \alpha); \\
\Phi_{NQ}^h(\theta, \alpha) &= (\cos 2\theta - \cos \alpha) \sin \alpha; \\
\Phi_{NQ\lambda}^h(\theta, \alpha) &= (\sin 2\theta - \sin \alpha) \sin \alpha.
\end{aligned} \tag{5.129}$$

The corresponding bending moment diagram for M_{bulk}^h is presented in Fig. 5.32b.

If the filling angle of the cross section is in the range $\frac{\pi}{2} \leq 2\theta \leq \pi$ or $\frac{\pi}{4} \leq \theta \leq \frac{\pi}{2}$, as provided in Fig. 5.33a, the resultant reaction forces and the moment at fixed point A becomes the following:

$$\begin{aligned}
\sum F_x = 0 : N'_4(q_{\text{bulk}}^h dy) &= \int_{2\theta}^{\pi} q_{\text{bulk}}^h dy = \\
&= C^K \rho_{\text{bulk}} g R^2 l \int_{2\theta}^{\pi} [\cos 2\theta - \cos \varphi + \tan \lambda (\sin 2\theta - \sin \varphi)] \sin \varphi d\varphi. \\
\sum F_y = 0 : N'_{F4}(q_{\text{bulk}}^h dy) &= 0. \\
\sum M_A = 0 : M'_4(q_{\text{bulk}}^h dy) &= \int_{2\theta}^{\pi} q_{\text{bulk}}^h R (\cos \varphi + 1) dy = \\
&= C^K \rho_{\text{bulk}} g R^3 l \int_{2\theta}^{\pi} [\cos 2\theta - \cos \varphi + \tan \lambda (\sin 2\theta - \sin \varphi)] \sin \varphi (\cos \varphi + 1) d\varphi.
\end{aligned} \tag{5.130}$$

In contrast to the vertical bulk material load component, discussed in the previous section, the resultant reactions at the fixed point A, caused by the horizontal load component have different expressions for $0 \leq 2\theta \leq \frac{\pi}{2}$ and the filling $\frac{\pi}{2} \leq 2\theta \leq \pi$.

As for the bending moment M_{bulk}^h , the axial force N_{bulk}^h , and the shear force Q_{bulk}^h , the filling angle $\frac{\pi}{2} \leq 2\theta \leq \pi$ yields the same formulas at any angular position $2\theta \leq \varphi \leq \pi$ at the

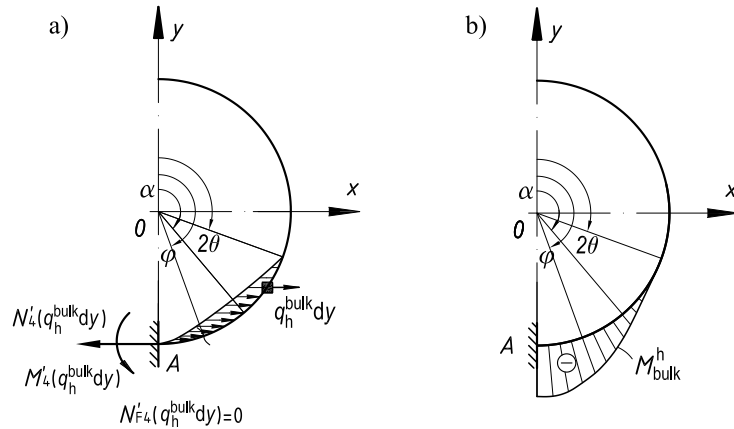


Figure 5.33: a) Statically determinate system subjected to the horizontal load component $q_{\text{bulk}}^h dy$ from the bulk material for the cross-sectional filling angle $\frac{\pi}{2} \leq 2\theta \leq \pi$, and b) the resultant diagrams for bending moment M_{bulk}^h , demonstrated at the cross-sectional contour. The load $q_{\text{bulk}}^h dy$ is defined by Eq. 5.49 and Eq. 5.50.

cross-sectional contour:

$$\begin{aligned}
 M_{\text{bulk}}^h &= C^K \rho_{\text{bulk}} g R^3 l \int_{2\theta}^{\varphi} \left[\Phi_M^h(\theta, \varphi, \alpha) + \tan \lambda \Phi_{M\lambda}^h(\theta, \varphi, \alpha) \right] d\alpha; \\
 N_{\text{bulk}}^h &= C^K \rho_{\text{bulk}} g R^2 l \cos \varphi \int_{2\theta}^{\varphi} \left[\Phi_{NQ}^h(\theta, \alpha) + \tan \lambda \Phi_{NQ\lambda}^h(\theta, \alpha) \right] d\alpha; \\
 Q_{\text{bulk}}^h &= C^K \rho_{\text{bulk}} g R^2 l \sin \varphi \int_{2\theta}^{\varphi} \left[\Phi_{NQ}^h(\theta, \alpha) + \tan \lambda \Phi_{NQ\lambda}^h(\theta, \alpha) \right] d\alpha.
 \end{aligned} \tag{5.131}$$

The bending moment diagram for M_{bulk}^h is illustrated in Fig. 5.33b.

The structural displacements where the redundant forces are applied, can be evaluated one by one by substituting M_{bulk}^h , N_{bulk}^h , and Q_{bulk}^h from Eqs. 5.127, 5.128 or Eqs. 5.131 into Eq. 5.84) for the Maxwell-Mohr Integral. The resultant displacements are presented in Appendix B of this thesis with respect to the filling angle θ limits. The latter characterize the switch between the calculation formulas of the displacements including the following cases: 1) $0 \leq 2\theta \leq \pi/3$; 2) $\pi/3 \leq 2\theta \leq \pi/2$; 3) $\pi/2 \leq 2\theta \leq 2\pi/3$; 4) $2\pi/3 \leq 2\theta \leq \pi$.

Noteworthy to mention that the approach developed in this chapter determines the CFs based on the structural displacements of a belt's pipe contour according System of Eqs. 5.73. To include the effect of a bulk solids, the problem is simplified, considering actually an empty belt, subjected to the external load from the bulk material. However, it is important to keep in mind that, in actual system "belt-bulk", the stress-strain state of a bulk inside the belt's pipe is mutually related to the stress-strain state of a belt. As a result, it is possible to expect that the displacements and CFs in analytical solution, assuming an empty belt under the action of the external equivalent bulk material load to be higher, compared to the deformations and CFs of an actual system "belt-bulk", observed in practice.

5.6.8 Reaction forces from the idler rolls

The system of Eqs. 5.73 provides the supplementary equations in addition to the equations of equilibrium for the original statically undetermined system.

The unit displacements needed for the system of Eqs. 5.73 can be calculated using the Eqs. 5.74-5.83. As for the displacements from the external loads, they are evaluated summing up all the displacements caused by a) the load from the belt weight found from Eqs. 5.91-5.94; b) the displacements from the belt bending stiffness load, defined using either Eqs. 5.97-5.100 or Eqs. 5.105-5.108 or Eqs. 5.114 - 5.118; and c) the displacements produced by the bulk material load, represented by the vertical (Appendix A Eqs. A.1-A.11) and the horizontal components (Appendix B Eqs. B.1-B.11).

Substituting all the displacements found into the system of Eqs. 5.73, the latter can be solved with respect to the unknown redundant forces X_1 , X_2 , X_3 , and X_4 . The rest of the reactions at the fixed point A of the statically determinate system subjected to all the loads, applied together at the structure (see Fig. 5.23), can be obtained by means of the equilibrium equations.

For the bending stiffness represented by the concentrated expansion moment M_{bst} , the

reaction force become:

$$\begin{aligned}
\sum F_x = 0 : N'_4 &= X_4 - (X_2 + X_3) \sin \frac{\pi}{3} + \int_{2\theta}^{\pi} q_{\text{bulk}}^h dy. \\
\sum F_y = 0 : N_{F4}' &= X_1 - (X_3 - X_2) \cos \frac{\pi}{3} + \pi q_{\text{bw}} R + \frac{1}{2} F_{\text{bulk}}^v. \\
\sum M_A = 0 : M_4' &= 2X_4 R - (X_2 + X_3) R \sin \frac{\pi}{3} + 2q_{\text{bw}} R^2 + M_{\text{bst}} + \\
&+ \int_{2\theta}^{\pi} q_{\text{bulk}}^v R \sin \varphi dx + \int_{2\theta}^{\pi} q_{\text{bulk}}^h R (\cos \varphi + 1) dy.
\end{aligned} \tag{5.132}$$

Here, the loads from the bulk material $q_{\text{bulk}}^v dx$ and $q_{\text{bulk}}^h dy$ need to be evaluated taking into account the filling angle θ , i.e. using the corresponding formulas for $0 \leq \theta \leq \frac{\pi}{2}$, and for $\frac{\pi}{2} \leq \theta \leq \pi$.

Similarly, for the bending stiffness represented by the distributed radial load q_{bst} , determined by Eq. 5.3, the equilibrium equations become:

$$\begin{aligned}
\sum F_x = 0 : N'_4 &= X_4 - (X_2 + X_3) \sin \frac{\pi}{3} + 2q_{\text{bst}} R + \int_{2\theta}^{\pi} q_{\text{bulk}}^h dy. \\
\sum F_y = 0 : N_{F4}' &= X_1 - (X_3 - X_2) \cos \frac{\pi}{3} + \pi q_{\text{bw}} R + \frac{1}{2} F_{\text{bulk}}^v. \\
\sum M_A = 0 : M_4' &= 2X_4 R - (X_2 + X_3) R \sin \frac{\pi}{3} + 2q_{\text{bw}} R^2 + 2q_{\text{bst}} R^2 + \\
&+ \int_{2\theta}^{\pi} q_{\text{bulk}}^v R \sin \varphi dx + \int_{2\theta}^{\pi} q_{\text{bulk}}^h R (\cos \varphi + 1) dy.
\end{aligned} \tag{5.133}$$

For the bending stiffness represented by the distributed radial load q_{bst} together with concentrated forces $Q_{1\text{bst}}$, $Q_{2\text{bst}}$, defined by the system of Eqs. 5.26, the equilibrium equations are the same as provided above in Eqs. 5.133.

For the full cross section of the PBC, as illustrated in Fig. 5.20 and Fig. 5.21, the reaction forces $N_4' = -N_4''$ and the bending moment $M_4' = -M_4''$ from each half of the cross section are respectively equal in magnitude, and are opposite in their directions. Therefore, the PBC reaction forces can be eventually calculated from the following system of equations:

$$\begin{cases} N_{F1} = 2N'_{F1} = 2X_1; \\ N_{F2} = N_{F6} = X_2; \\ N_{F3} = N_{F5} = X_3; \\ N_{F4} = 2N'_{F4} = 2X_1 + X_2 - X_3 + 2\pi q_{\text{bw}} R + F_{\text{bulk}}^v; \\ N_1' = -N_1'' = X_4. \end{cases} \tag{5.134}$$

If the reaction forces are being evaluated for the empty PBC system, than the load from the bulk material as well as the corresponding displacements need to be assumed equal to zero in the formulas provided.

The reaction forces, given in system of Eqs. 5.134 define the PBC CFs needed. The contact forces and the reactions are equivalent in their absolute values, but opposite in the direction (see Fig. 5.20), i.e.,

$$F_1 = -N_{F1}, F_2 = F_6 = -N_{F2} = -N_{F6}, F_3 = F_5 = -N_{F3} = -N_{F5}, F_4 = -N_{F4}.$$

Here, the CFs are presumed positive if they are directed as shown in Fig. 5.21a. It needs to be kept in mind that the reaction forces at the constrained points actually represent the contact between the belt and the idler rolls. In this case, if after the evaluation, one or more of the reaction forces in Eq. 5.134, becomes negative, i.e., having the opposite direction as assumed, this means that there is a contact loss between the belt and idler rolls at the corresponding points. In this case, the maximal negative redundant force is assumed to be equal to zero and the equivalent constraint has to be excluded from the structure. The corresponding displacement component must be removed from the systems of Eqs. 5.73 and 5.134. After that, the calculation must be repeated until all the reaction forces become positive or equal to zero.

The results for PBC CFS, obtained using the method introduced in this chapter will be presented in next Chapter 4 together with the numerical, and experimental results.

5.7 Conclusions

This chapter answers the research question on how to determine PB CFs. For this purpose, an analytical approach is used. From the analysis performed in Section 5.5 for the existing studies, it was evidenced that none of the analytical models determine the PBC CFs in a correct way, even if some of the external loads are prescribed to the model correctly. That is why, a new analytical approach is developed in this chapter.

The new approach implies the linearization of the mechanical problem, considering linear-elastic behavior of a belt and small structural displacements. The latter became possible by substituting a complex nonlinear process of forming a flat belt into a pipe shape within an additional expansion load from the belt bending stiffness, applied to the initial stress-free belt already in a pipe shape.

The analysis in Section 5.3 shows that there is no unified opinion on the method how this load can be prescribed and there is no any experimental validation of the existing methods proposed. In this chapter, three methods of modeling the load from the belt bending stiffness are selected for the further investigation: the concentrated expansion moments applied at the belt edges M_{bst} ; the radial expansion load evenly distributed along the belt's pipe q_{bst} ; and the radial distributed load q_{bst} together with the concentrated forces Q_{1bst} , Q_{2bst} .

In following Chapter 6, the analytical results obtained within all three methods are compared with the experiment and with the numerical solution, and the correct method will be selected. This will allow one to answer the research question whether it is possible to represent a belt stress state that appears from folding the belt from a flat shape into a pipe shape as an additional external load.

The analytical model developed includes the effect of a bulk material, answering the research question on how to model a bulk material load for the CFs. The load from the bulk material is presented using vertical and the horizontal load components that account the bulk shear stresses and the load distribution along the lateral pipe contour and along the conveyor pitch. The corresponding load can be transferred into the radial and tangential components. Analysis in Section 5.4.5 shows that all the existing models that determine PBC CFs from the bulk load analytically, use only the radial bulk load component, neglecting the presence of the tangential one. As concluded in Section 5.4.5, such approach underestimates the overall bulk material weight, indicating that the impact of both load components (either vertical and

the horizontal one or the radial and the tangential one) is obligatory to use.

Considering the future research using the analytical model, the following aspects can be incorporated.

As mentioned in Section 5.6.7, the present analytical model determines PBC CFs and belt deformations, simplifying behavior of a mechanical system "belt-bulk" to the system when an empty belt is subjected to the external bulk material load. As a result, the analytical solution can predict the resultant CFs higher than the ones observed in practice, since the belt's stress-strain state is mutually related to the stress-strain state of a bulk solid inside the pipe, and, at higher cross-sectional filling degrees, the displacements of a belt are less than if the ones evaluated within the analytical model presented. The future research has to investigate this effect for loaded PBC by modeling the bulk particulate solids inside the belt's pipe and their mutual stress-strain relationship.

The analytical approach developed in this chapter can be considered as a universal analytical model for various loading conditions and can be also easily expanded incorporating other effects and external loads, such as the lateral load from the belt tension that appears at the conveyor route curves, discrete change of a belt properties along its width, and presence of a belt overlap.

To accommodate even more complex effects (i.e., to include the large structural deformations, integrate the contact effects between the belt and idler rolls, to model the shear effects in both planes, etc.), Chapter 6 determines PBC CFs using FEM analysis and compares the results with the analytical solution, and the experiment. This is made for the validation purposes and also aiming to determine whether a more simple analytical model that is more attractive for the practical use predicts PBC CFs in a feasible range, compared to a FEM solution that is more complex, time consuming, and less attractive in terms of an application.

The analytical model presented is also needed in the following Chapter 6 to perform an impact analysis and to answer the research questions on which design parameters of a PBC system influence the CFs and what is their effect. In addition, the analytical model is used as a basis to derive a functional dependence between the CFs and participating PBC design parameters. Using an impact analysis, it becomes possible to determine which conveyor characteristics can cause a contact loss between the belt and the idler rolls and what is the weakest position of a roll in an idler set for that. These research questions are all answered in the next Chapter 6.

Chapter 6

Determination of Contact Forces: FEM Solution, Comparison of the Approaches

*"Grau, theurer Freund, ist alle Theorie,
Und grün des Lebens goldner Baum".* *"My friend, all theory is grey,
And green the golden tree of life".*
— J. W. Goethe, *Faust*

In addition to the experimental approach, provided in Chapter 4, and the analytical solution, developed in Chapter 5, the CFs can be determined numerically within FEM. This chapter is a concluding chapter that evaluates the CFs using FEM and compares the results with respect to analytics and experiment.

As indicated in the previous chapters, the CFs are important design parameters that need to be correctly determined and controlled. They are required as input parameters in the following Chapter 7 of this thesis aiming to determine the IRR of the entire PBC system. In addition, the CFs can diagnose the belt's ability to form a stable pipe shape with respect to the belt's lateral bending stiffness. The appearance of a contact loss between the belt and idler roll, investigated in the present chapter, can be considered as an indicator for the insufficient pipe-ability.

This chapter establishes a functional dependence of PBC CFs, parameterized with respect to all participating conveyor design parameters. A conveyor belt bending stiffness required for quantifying the CFs in the analytical and numerical approaches is determined from the troughability parameter, as proposed in Chapter 3, and becomes a link between the troughability of the belt and its pipe-ability.

*The chapter is partially constructed using publications of Zamiralova and Lodewijks [263, 264].

6.1 Introduction

As discussed in the previous chapters, for the successful selection of a PBC design, the CFs need to be accurately evaluated. In particular, the CFs influence the IRR of the system, which will be determined in Chapter 7, participate in the twisting phenomenon of the belt in the stabilizing moment from the friction forces. The CFs can indicate whether the belt has sufficient bending stiffness to form a stable pipe shape without its collapse, i.e., without generating a contact losses between the belt and the idler rolls, detected when one or more of CFs become equal to zero. The belt's bending stiffness and pipe-ability need to be carefully controlled, however, up to date, there is no design recommendations established for PBCs that can ensure a well-sealed pipe shape. A high bending stiffness can preserve belt's ability to form an enclosed pipe shape, but might be unnecessary significant in terms of the energy consumption of a conveyor. As a result, the CFs can be used to compromise between the energy consumption and belt's ability to form an enclosed pipe shape.

All the issues mentioned indicate the need to determine PBC CFs in the most accurate way. As mentioned in Chapter 4, the CFs can be evaluated using three approaches: experimental, analytical, and FEM. Each approach inherits both positive and negative aspects. Using all three approaches together allows them to complement each other, providing a reliable method to determine the CFs. Chapter 4 and Chapter 5 presented the experimental and analytical approaches for quantifying PBC CFs, respectively, whereas the present chapter evaluates the load distribution between the idler rolls using FEM.

As for the numerical FEM approach, the computational models constructed in different software can differ in their simulation procedures, numerical methods, description of belt structure, number of elements, the way the boundary conditions are prescribed, convergence criteria, etc. Obviously, these factors inevitably can reason to difference in the output results for PBC CFs. That is why, it is important to validate the FEM solution with the experiment and to accompany with the analytical solution.

The selection of FEM models in this chapter needs to closely replicate the analytical problem, solved in Chapter 5, and the experiment, described in Chapter 4, to allow the comparison of the results, also presented in this chapter. The numerical model validated with the experiment and in agreement with the analytics, can be transformed to a more complex version, incorporating the nonlinear effects, such as the nonlinear structural deformations, three-dimensional shear effects, and contact interaction between the belt external surface and the idler rolls.

It is possible to expect that a more complex FEM model that incorporates all the nonlinearities and is closer to the practical problem, predicts the CFs in a more precise way, compared to the analytical approach, limited with the assumptions and simplifications accepted. However, the FEM solution can require significant time for the convergence and is not attractive in terms of the application in the practical use. At the same time, for a certain input design parameters, a more simple analytical model that is more attractive for industrial application can provide suitable results in a feasible range. That is why the CFs determined within the FEM need to be compared with the analytical solution at various combination of input parameters. This is carried out in the present chapter.

In order to develop numerical models that determine PBC CFs in the most suitable and accurate way, it is important to analyze the studies that also used numerical approach for modeling a PBC load distribution. Such analysis will indicate, whether it is possible to use

the similar methods for the numerical models developed or if there is a need to incorporate other methods for achieving a better accuracy in the results.

6.2 Overview of existing PBC numerical models

For the simplicity of the analysis, all the existing numerical models of PBCs were developed and solved using FEM, and employed in ANSYS, ABAQUS or any other commercial software.

Usually, the process of finding a solution in software is divided into three steps: 1) preprocessor; 2) obtaining a solution itself, and 3) post-processor for finding and presenting the various results.

Major process of modeling the problem appears in the preprocessor and is mostly of a particular interest of the present study for the analysis. The preprocessor includes selection of a type of an analysis, creation of a model's geometry, assigning an element type as well as material models and corresponding properties, creation of contact pairs, establishing the boundary conditions, applying the loads with respect to load steps, and providing the solution controls. The overview of the existing studies corresponds to a number of modeling aspects inherent to a preprocessor.

6.2.1 Modeling a belt

Geometry

The initial geometry of a belt in the model can have either a pipe shape or a flat plane shape, depending on the way the load from the belt bending stiffness is assigned to the problem (see further details in Section 6.2.5)

If the belt has an initial pipe shape, the difference in belt geometry belongs to the way of modeling the belt overlap. Del Coz Diaz *et al.* [43] assumed in the numerical model that a belt had a symmetrical cylindrical shape with small opening on the top (cross section

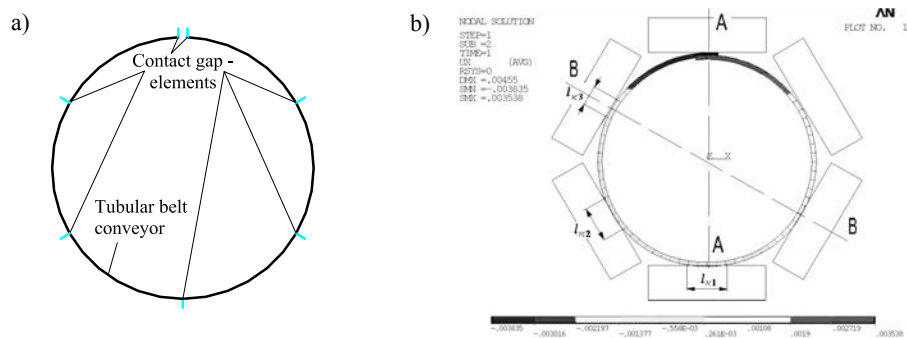


Figure 6.1: Cross section of the numerical models for simulating a section of a PBC, developed by: a) del Coz Diaz *et al.* [43] (figure reconstructed from del Coz Diaz *et al.* [43]); b) Kulagin [126–129], Dmitriev and Kulagin [56], Dmitriev and Sergeeva [58], Sergeeva [208, 210] (figure from [208]).

is shown in 6.1a. The similar shape was used by Pang and Lodewijks [188], and Yan [253]. However, the researchers [188, 253] prescribed the presence of an overlap with additional expansion load, determined very roughly and applied to one symmetrical side of belt to imitate the outer belt edge in overlap. Kulagin [126–129], Dmitriev and Kulagin [56], Dmitriev and Sergeeva [58], Sergeeva [208, 210] modeled the overlap with length that constituted $0.1B$, whereas the ratio B/h was significant (see Fig. 6.1b). For such thin belt structure, the overlap of $0.1B$ was very small with respect to a pipe diameter, consequently the presence of the overlap did not have a great influence on the results as if the belt had a symmetrical pipe shape with opening on the top.

If the initial geometry of a belt was flat plane or had a trough shape, the solution procedure incorporates an obligatory step of gradual folding the belt into a pipe shape needed. Usually at the end of this process, the belt's finite state represents a full geometry of an overlapping coil. The procedure of a belt formation was incorporated in the models of Schilling *et al.* [203], Fedorko *et al.* [67, 68], Fedorko and Molnár [66], Wesemeier [238–242] and is discussed further in Section 6.2.5, considering the load from belt bending stiffness. Using such a numerical model, Wesemeier [238] investigated the impact of belt tension on the gap that appeared between the overlapping edges of a folded belt.

Material and structural design

For the numerical modeling of a pipe conveyor belt, most of the researchers selected shell element types. The following elements were mentioned in the sources: flat 4-node Shell63 (Kulagin [126–129], Dmitriev and Kulagin [56], Dmitriev and Sergeeva [58], Sergeeva [208, 210], Wesemeier [238–242]) and double-curved 8-node Shell93 (Pang and Lodewijks [188], Yan [253], del Coz Diaz *et al.* [43]) in ANSYS; double curved 4-node SR4 in ABAQUS (Fedorko *et al.* [67, 68], Fedorko and Molnár [66]). The last two element types incorporate shear effects, being suitable for thin and thick structures, whereas the element type Shell63 is restricted to the thin shells with large ratio R/h and does not include the impact of shear. Moreover, Shell63 has to satisfy the size requirement that each flat element substitutes the curvilinear surface of no more than 15° arc, becoming less suitable for the problem. Taking into account the large geometrical variation range $6.67 \leq B/h \leq 643$ of a belt slenderness, established in Section 2.5.2 for PBCs, the element type selected in the present study for numerical modeling should support the shear effects and be suitable for the curvilinear structures with small ratio of R/h .

An isotropic behavior of a belt structure was assumed by del Coz Diaz *et al.* [43], Pang and Lodewijks [188], Yan [253], assigning constant Young's modulus in all three directions of a belt structure, which does not reflect belt's properties observed in practice. The rest of the studies [56, 58, 66–68, 126–129, 208, 210, 238–242], selected the shell elements that supported orthotropic elastic properties of belt, assigning different uniform Young's moduli and Poisson ratios in longitudinal and lateral direction of a conveyor belt.

The orthotropic properties of a belt were also achieved by Schilling *et al.* [203], modeling the belt material with shell elements with reinforcing layers. The properties of the material were found by the researchers from the experimental testing. The belt and the belt's rubber were subjected to tensile, compression and bending tests. The tests were simulated numerically with solid elements with embedded trusses and with shell elements with reinforcing layers, exhibiting the correlation between each other and with the experimental results. By

means of the shell elements with reinforcing layers, Schilling *et al.* [203] could simulate an uneven belt structure with discrete change of a belt design along the belt width, whereas the rest of the studies assumed it to be uniform.

6.2.2 Modeling idlers

For modeling the geometry of idler rolls, the researchers [56, 58, 66–68, 126–129, 188, 208, 210, 238–242, 253] usually used areas with a cylindrical shape (full cylinder or a symmetrical half of a cylinder). The material of idler rolls was selected using isotropic shell elements, assigning Young's elastic modulus inherent to steel.

Alternatively, del Coz Diaz *et al.* [43] introduced the problem, where the idler rolls were replaced with special contact gap elements, as shown in Fig. 6.1a. For this purpose, the researchers used special element type Contact52 in ANSYS, represented by the combination of a viscous Newtonian damper and a Hookean elastic springs with certain sliding and sticking stiffness. Such approach was used in order to introduce the contact between the belt and idler rolls in the problem without actual modeling the rolls themselves.

6.2.3 Describing a contact

A number of the researchers selected an alternative approach to introduce the contact between the belt and idlers in the problem. In most of the cases, either one or two contact pairs are incorporated.

One contact pair is always a contact between the belt and the idler rolls. Besides the simplifying method of del Coz Diaz *et al.* [43], a number of other researchers [56, 58, 66–68, 126–129, 188, 208, 210, 238–242, 253] introduced it as a surface-to-surface contact. Fedorko *et al.* [67, 68], Fedorko and Molnár [66] utilized a feature of a general contact, available in ABAQUS. Kulagin [126–129], Dmitriev and Kulagin [56], Dmitriev and Sergeeva [58], Sergeeva [208, 210], Wesemeier [242] as ANSYS users, assigned the pair as two coupling bodies: a more flexible contact body (belt) by using an additional element type Conta174 and a more rigid target body (idler rolls) by means of an element type Targe170. In addition, for achieving a better accuracy, the researchers used a refining feature reducing the size of elements involved in the contact and increasing their number.

Two contact pairs were incorporated in the model of Fedorko [67, 68], Fedorko and Molnár [66]. In addition to the contact pair belt-rolls, the researchers introduced a self-contact of a belt that appears in the overlap. The self-contact was prescribed between internal and external belt's surfaces for better simulation of the physical problem. In contrast, some of the models that did not include a belt's self-contact exhibited a penetration of the belt edges into each other. This indicates that contact of belt edges should be obligatory incorporated in the numerical models.

6.2.4 Boundary conditions and number of conveyor sections

The main difficulty in decision made for the boundary conditions and length of the PBC section is to sufficiently replicate the behavior of a long PBC with infinite length in a dynamic mode by a simplification with the static PBC section with reduced length.

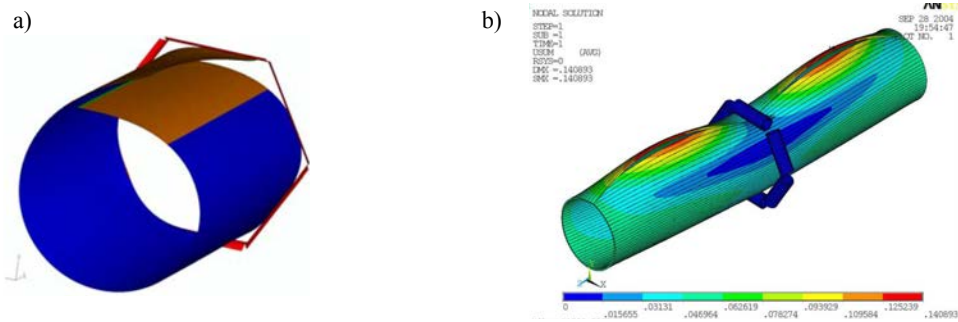


Figure 6.2: Numerical models consisted of a one idler set, developed by: a) Schilling *et al.* [203] (figure from [203]); b) Kulagin [126–129], Dmitriev and Kulagin [56] (figure from Kulagin [127]).

For the static analysis, all degrees of freedom (DOF) of the idler rolls are fixed in all the studies. As for the boundary conditions of a belt and a number of conveyor sections included in the model, the choice is made differently in various sources with respect to the aims of the study, e.g., whether the CFs, or the belt deformations are determined, or the experimental test set-up is replicated with FEM model.

The equilibrium is achieved for the FEM models by applying the tensile forces at one or both edges, supporting the belt via contact by the idler rolls fixed with all DOF, and prescribing different DOF conditions to the edges of a belt formed into a pipe shape. The belt's DOF implies the variations as such: an option of full fixation of one belt edge Kulagin [126–129], Dmitriev and Kulagin [56]; planar DOF, i.e., implying the belt cross sections remain plane at both belt edges (Schilling *et al.* [203]); and DOF of symmetry prescribed at both edges Wesemeier [242]). In addition, the displacements preliminary calculated from the conveyor route can be prescribed to the belt edges, modeling the bending of a conveyor

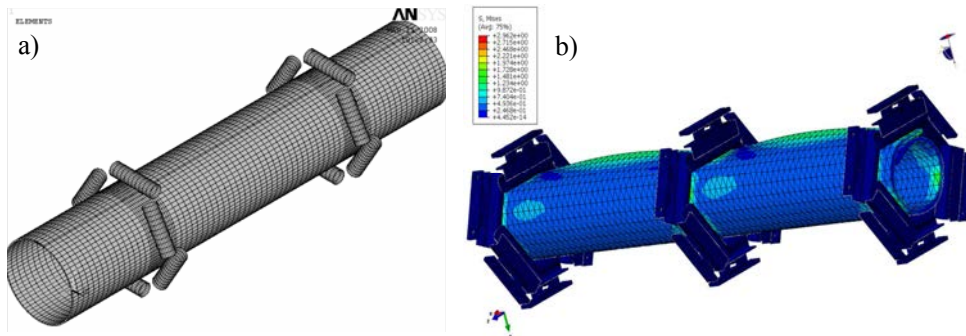


Figure 6.3: The numerical model of a belt formed in a pipe shape with a) two idlers and a length of belt section of two carry spacing, developed by Dmitriev and Sergeeva [58], Sergeeva [208, 210] (figure from Dmitriev and Sergeeva [58]); b) three idler stations and belt with length of two carry spacing, elaborated by Fedorko and Molnár [66], Fedorko *et al.* [68] (figure from Fedorko and Molnár [66]).

route in horizontal and vertical planes (Kulagin [126–129], Dmitriev and Kulagin [56]).

Besides the deviation in boundary conditions, the existing FEM models can differ in the number of PBC sections modeled. One conveyor section with idler set was the design in the numerical models developed by Schilling *et al.* [203]) for a belt of one conveyor pitch with the contact with the supporting idler rolls, situated at one edge of a belt (see Fig. 6.2a). Pang and Lodewijks [188], Yan [253] also selected the belt sample of no more than one conveyor pitch long, placing the idler set in the middle of a section. Kulagin [126–129], Dmitriev and Kulagin [56] elaborated the numerical model of a belt with length of two carry spacing with one idler set in the middle (as illustrated in Fig. 6.2b). Some numerical models included longer sections with two idlers stations (see Fig. 6.3a), like models of Dmitriev and Sergeeva [58], Sergeeva [208, 210], Kulagin [126–129], Dmitriev and Kulagin [56], Wesemeier [242] and even three idler stations see Fig. 6.3b), simulated by Fedorko and Molnár [66], Fedorko *et al.* [68]. Del Coz Diaz *et al.* [43] described the model of a 240 m long pipe conveyor belt, being interested in studying the effect of belt warping and not in evaluation of CFs and belt deformations. Such a long model was possible to solve in the software, as the idlers were replaced with special gap-elements. This significantly reduced the total number of elements in the model.

When the conveyor section and its boundary conditions are selected for FEM model, it is important to remember that the distance from the belt edges constrained, a number of the idler stations in the model, and a length of carry spacing can significantly affect the results of CFs and belt deformations measured. If the belt section does not have sufficient length, the major part of the load will be accounted at the belt edges fixed and also at the idler rolls in the close vicinity to the fixed edges, compared to the idler in the middle of the section. The analogous problem is observed for to the experimental test rigs with frames and supports, as discussed in Section 4.2.2.

As a result, the FEM model should be described by balancing between the total number of elements available in the software for the solution, time of achieving the convergence, and a number of a PBC sections and idler sets included.

6.2.5 Loads and load steps

Similar to the analytical model, introduced in Chapter 5, the external loads prescribed in the FEM models can include: load from the belt weight; load from the belt bending stiffness; load from the bulk material; belt tensile forces.

Load from the belt weight is always included in the analysis by activating the gravity function in the software. Belt tension is simulated by applying the external tensile forces distributed along the belt edges or as pre-calculated belt axial displacements. In addition, for modeling the route curves in vertical and horizontal plane/ -s, additional displacements of belt edges are subjected to the belt model. In most of the cases, load from bulk material is accounted as an external distributed load (see more details further) without actual modeling the bulk material itself.

The most difficulty for numerical modeling of a PBC appears from the load from the belt bending stiffness. With respect to the way the load from folding a belt from a flat shape into a pipe shape in simulated, all the external loads mentioned can be applied to the model all at once or be activated in steps.

Load from belt bending stiffness

The division of a solution process into load steps depend on how the load from the belt bending stiffness is simulated.

If the problem is solved with one load step, the belt is subjected to all the external loads and its initial geometry is already a pipe shape. The load from the belt bending stiffness is either not included in the problem (del Coz Diaz *et al.* [43]) or is simulated as an additional external load applied at a stress-free pipe shaped belt. Kulagin [126–129], Dmitriev and Kulagin [56], Dmitriev and Sergeeva [58], Sergeeva [208, 210] used for this case an additional radial load q_{bst} evenly distributed along the belt contour. The load q_{bst} can be evaluated using Eq. 5.3 and is explicitly discussed in Section 5.3.2.

A number of the researchers, such as Wesemeier [239], Schilling *et al.* [203], Fedorko *et al.* [67, 68], Fedorko and Molnár [66], solved the problem with more than one step. In most of the cases, at the first step the belt is formed from a flat shape (or more rarely from a trough shape) into a pipe shape. At the subsequent steps, the contact between the belt and idler rolls is activated and the rest of the external loads, like gravity, load from bulk material, tensile forces are applied.

Noteworthy to mention is the numerical model of Schilling *et al.* [203] with a four load-step procedure. At the first step, the researchers prescribed the displacement field to the belt and folded it from a flat shape into a pipe shape. After achieving the solution, the gravity was activated, DOF for belt edges were applied, and the problem was solved again. The third step included the impact of tensile forces. For modeling the route curves at fourth load step, the researchers solved the problem assigning additional pre-calculated displacements to one of the belt's edge.

A similar procedure was applied by Fedorko *et al.* [67, 68], Fedorko and Molnár [66]. At first, the belt was formed into a pipe shape using the external moments M_1 and M_2 (see Fig. 6.4) distributed along the belt edges and applied to belt one after another. At this stage, the line of belt's bottom nodes situated at the belt's axis of symmetry was fixed for all DOF. The values of the moments were determined using a combination of an explicit and an implicit analysis in ABAQUS with defined finite geometrical shape of a belt. At the next solution step, either the belt was dragged through the idlers, or the idlers were moved in such a way that the belt coil was placed inside the surrounding of the coil six-roll idler sets. After

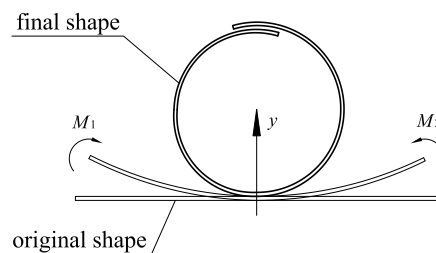


Figure 6.4: Folding a belt from a flat shape into a pipe shape with an overlap using the distributed moments M_1 and M_2 according to the modeling procedure of Fedorko *et al.* [67, 68], Fedorko and Molnár [66] (figure reconstructed from Fedorko *et al.* [67]).

that, the researchers performed the next solution step by activating the gravity. In addition, the contact between the belt and idlers and self-contact of belt edges were actuated. The fixing constraints at the central line of belt nodes were removed, and the belt was released, assigning the folding moments $M_1 = M_2 = 0$.

Load from the bulk material

Few studies included the presence of a bulk material and its impact on CFs and belt deformations in the numerical models. The way the load was simulated is discussed in present section.

Del Coz Diaz *et al.* [43] described that the load from the bulk material for 50% of the cross-sectional filling degree was described in the numerical model of a PBC as an additional pressure distributed onto the belt surface, ignoring the presence of an angle of repose. However, the researchers did not specify how the value of such load was initially calculated. Guo *et al.* [87] utilized Discrete Element Method (DEM) in EDEM software for simulating the particle behavior of a bulk material inside the pipe conveyor. For modeling the belt, the researchers used a full enclosed cylinder, ignoring its open structure with an overlap. The filling degree was fixed and constituted 75%. Performing DEM analysis, the researchers focused their attention on particles inside the pipe, ignoring the belt deformations important for the analysis, as there is a mutual relation between the belt deformations and bulk material behavior overlapped by the belt.

Noteworthy to mention is the approach of modeling the load from bulk material for FEM analysis, developed by Kulagin [126–129], Dmitriev and Kulagin [56] and later employed by Dmitriev and Sergeeva [58], Sergeeva [208, 210]. The researchers divided the cross-sectional contour of a pipe-shaped belt into 24 sections with respect to the angular position of α , $2\theta \leq \alpha \leq 0$, and the filling degree of 75%, as illustrated in Fig. 6.5. In particular, the division was made using equivalent arcs with angle $\Delta\alpha$. These arcs divide the area of a pipe shaped belt model into 24 strips. This was made in order to subject each of this strip to the corresponding radial bulk material load, imitating the distribution along the belt lateral cross section.

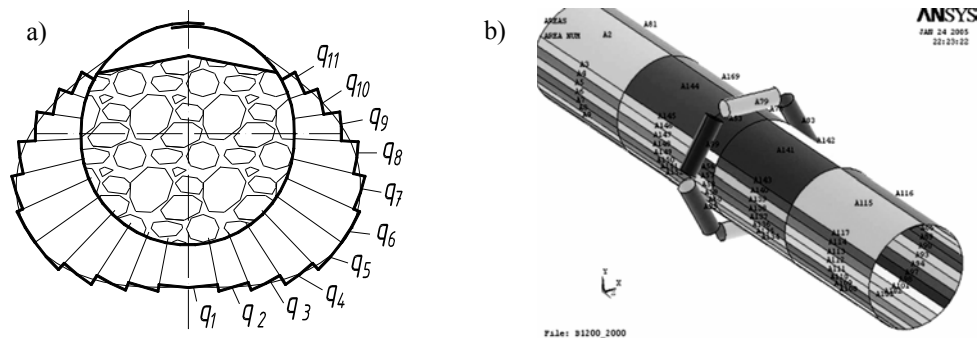


Figure 6.5: Modeling the load from bulk material using the radial load component according to the approach, developed by Kulagin [126–129], Dmitriev and Kulagin [56] and utilized later by Dmitriev and Sergeeva [58], Sergeeva [208, 210] (modified figures from Dmitriev and Sergeeva [58], Kulagin [129]).

In order to incorporate the distribution of the bulk material load in longitudinal direction, the researchers assumed that the switch between active and passive stress states appears discretely right in the middle of carry spacing (see Section 4.4.4). Each of the 24 strips of a belt area were additionally divided in two parts right at half of carry spacing, as shown in Fig. 6.5. The resultant 48 belt strips were subjected to the corresponding constant loads, evaluated for each n -th strip for active and passive parts as $q_{n\text{bulk}} = \int_{\alpha}^{\alpha+\Delta\alpha} \sigma_{\varphi} R d\varphi$. The radial stress component σ_{φ} was determined as provided in Eq. 5.51 and Eq. 5.52 and the function $K(z)$ was selected, as given in Eq. 5.43.

Such loading model implies the constant pressure within each strip. The researchers indicate that higher number of dividing strips generates smoother load distribution on the belt surface and thus a better accuracy in the results.

Noteworthy to remind that, similar to the analytical solution, the numerical models, described by Kulagin [126–129], Dmitriev and Kulagin [56], Dmitriev and Sergeeva [58], Sergeeva [208, 210], include only the radial component from the bulk material load σ_{φ} , whereas the tangential component τ_{φ} is ignored. As shown in Section 5.4.5, the usage of only the radial component does not generate the overall belt weight and leads to incorrect results. Instead, either both radial σ_{φ} and tangential load components τ_{φ} should be used, or the load from bulk material can be sufficiently represented by the vertical σ_v and horizontal σ_h load components applied together to the belt contour.

Despite the fact that only the radial load component was used in the studies [56, 58, 126–129, 208, 210], the approach of dividing the belt area into the strips and applying the load from the bulk material with respect to the lateral and longitudinal belt position can be considered as the closest method to model the impact of bulk material on PBC CFs and belt deformations.

After all the existing methods of modeling the PBC behavior with FEM approach are discussed, some of the procedures reviewed can be also employed in the FEM models, elaborated to in present chapter to determine PBC CFs. For instance, the following simulation methods and aspects are also utilized: selecting the element types that support shear effects for the belt material model; describing the contact model with two contact pairs (a contact between the belt, and the idler rolls and the belt's self-contact at the edges), option of dividing the solution into the load steps; modeling the load from the belt bending stiffness by either as an external additional load or by actually folding the belt structure from a flat shape into a pipe shape.

Some of the modeling methods are improved. For instance, the method of describing the load from the bulk material, developed by Kulagin [126–129], Dmitriev and Kulagin [56] is modified by providing a more smooth load distribution along the pipe cross-sectional contour. Some of the modeling methods are newly applied, like, for instance, how the belt is folded from a flat shape into a pipe shape or activating and deactivating some of the elements using their "birth" and "death" function.

All the modeling methods utilized in the FEM models, developed to determine PBC CF, and their mutual relation with respect to the aims of the research are explicitly described in the next section.

6.3 FEM models elaborated

As it was discussed in Chapter 4, the methodology selected to determine PBC CFs in the present analysis implies using experimental, analytical, and numerical FEM approaches together. That is why, the FEM models are elaborated persuading the following aims:

- 1) to validate the model with the experimental results;
- 2) to achieve an agreement with the analytical solution;
- 3) to determine how the load from the belt bending stiffness should be prescribed;
- 4) to perform an impact analysis.

For these aims, in total three numerical FEM models are developed: a Beam Simplified Model, a Beam Step Model, and a Shell Step Model. The reasoning for the selection of these three models is the following.

Beam Simplified Model

The major reasoning for selecting this FEM model is its simplicity, fast convergence, and its close replication of the analytical model, developed in Chapter 5.

The Beam Simplified Model represents a linearized 2D beam model for a belt already in a pipe shape and subjected to the external loads. The belt's self-contact at the edges and the contact between the belt and the plates are simplified as belt's node constraints, similarly as in the analytical model. The simulation procedure of this model is provided in Appendix C.

The load from the belt bending stiffness can be prescribed to belt using: a) M_{bst} , b) q_{bst} , and c) q_{bst} , Q_{1bst} , Q_{2bst} (see Sections 5.3.1 - 5.3.3). The load from bulk material can be also included in the analysis, if the longitudinal length of a beam section is extended to a conveyor pitch.

The Beam Simplified Model can be solved using linear and nonlinear analysis. The linear analysis makes the Beam Simplified Model entirely the same as the analytical one. It might appear that for certain design parameters, a simple analytical (or the Beam Simplified Model linear solution) that is more attractive in a practical use predicts the CFs with the satisfactory accuracy, compared to a more complex and time consuming FEM step models.

If the agreement in the results is achieved, the Beam Simplified Model can be solved within a nonlinear analysis, as a step towards an increase of the problem complexity, accommodating large displacements of a belt structure under the action of the loads involved. The comparison with the experiment and with the more complex Beam Step Model with reduced length of supporting plates (imitating the node constraint and also simulating belt stress state after folding its from a flat shape into a pipe shape) will indicate which method of modeling the load from the belt bending stiffness proposed (M_{bst} or q_{bst} or q_{bst} , Q_{1bst} , Q_{2bst}) provides the correlation in CFs.

Beam Step Model

This model occupies an intermediate position between the simplest (analytical and the Beam Simplified Model) and the most complex model (the Shell Step Model), linking these models

between each other.

The major reason for the selection is that due to the reduced number of the elements, the convergence time is significantly decreased, compared to the more complex FEM model. This becomes especially attractive for performing an impact analysis required, as it allows one to solve different cases with various design parameters with the reasonable time. The other reason is that comparison with the Beam Simplified Model (Nonlinear analysis) can indicate which method of modeling the load from the belt bending stiffness as an additional external load can predict the correct results.

The Beam Step Model is a 2D nonlinear beam model. It is solved in steps and, in the first load step, it incorporates actual formation of a belt structure from the original stress free flat shape into a stressed pipe shape. The model also includes a contact between the belt and plates and belt's self contact at the edges. The modeling procedure of the Beam Step Model is provided in Appendix C.

The model is solved using two variations: the length of the supporting plates is analogous to the experiment test case, and with the plates with the reduced length.

The first option is to make the model as close as possible to the experiment, aiming to validate with the test results for the case study and determine whether the results substantially deviate with the most precise Shell Step Model. If the difference is not that significant, the Beam Step Model can be used further fulfilling the role of a more precise but less time consuming model instead of the Shell Step Model.

The case with the reduced length of plates is used to compare the results when the belt is formed from a flat shape into a pipe shape with the nonlinear solution of the Beam Simplified Model, simulated with the reduced length of plates, indicating which method of modeling the load from belt bending stiffness predicts the correct CFs.

Shell Step Model

This model is selected, as it is the most precise model and it closely reproduces the experiment test with the six-point stiffness device, described in Chapter 4. If the physical parameters assigned to the model are the same as in the experiment, the solution from the Shell Step Model can be compared with the CFs measured at the test.

The Shell Step Model is a nonlinear 3D shell model and accommodates the shear effects in longitudinal and lateral directions. As a result, the anticlastic curvature effect is also included in the analysis.

Similar to the previous model, the Shell Step Model is solved in steps. At the first solution step, a stress-free flat belt is formed from a flat shape into a pipe shape, performing a nonlinear analysis. In the next load steps the belt is placed inside the hexagon plates and is released, whereas the rest of the loads are applied and activated. For better correlation with the experiment for the case without an overlap, this FEM model takes into account a small difference between the external pipe diameter of a belt, formed into a pipe shape, and a nominal diameter D_{nom} , characterizing the position of the hexagon plates, see further discussion in Section 6.5. All the details regarding modeling procedure of the Shell Step Model are provided in Appendix C.

The major drawback of the Shell Step Model, is that it requires an extensive time for the convergence and becomes impractical for investigating the results for different cases and input parameters. That is why, this model is used only for the case study verification. For the

impact analysis that requires running a large number of different cases, the time of achieving fast solution is in the priority, the Beam Simplified Model and the Beam Step Model are used.

The major distinctive aspects of all the FEM models elaborated are summarized in Table 6.1, organizing the models from the simple to more complex. The FEM analysis is performed using APDL programming language in ANSYS, however, any other commercial software can replicate the same models. The exact procedures for elaborating and solving the FEM models are provided in Appendix C.

6.4 Input parameters

After the FEM models elaborated to determine PBC CFs are described, it is important to specify the input parameters used for the models.

At first, the analysis is performed, aiming to validate the analytical model and also the FEM models with the experiment case study. For the validation, the physical parameters of a fabric belt Sample 3, provided in Table 4.9 are assigned for the belt model. The selection is made, as in the experiment with the six-point stiffness device, belt Sample 3 exhibited an ability to form a symmetrical pipe shape for the case “no overlap” without belt collapsing (see Chapter 4). Similarly, the analytical model and the FEM models do not include the presence of a belt’s overlap.

The fabric belt Sample 3 exhibited uniform structural design in belt transverse direction (along the belt width). This fits the assumptions made in the analytical model, developed in Chapter 5 for determining the CFs and the approach, developed in Chapter 3 for evaluating belt’s effective modulus of elasticity from the troughability test. The latter is especially important, as the Young’s modulus, extracted from the troughability parameter is assigned for the case study as a belt property to the present FEM and analytical models.

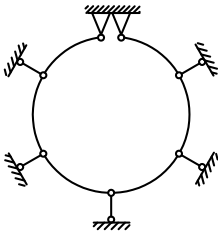
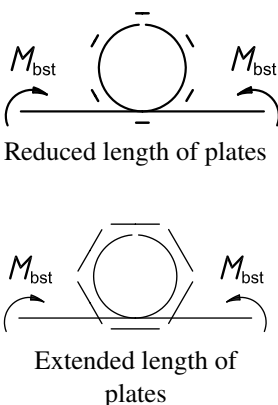
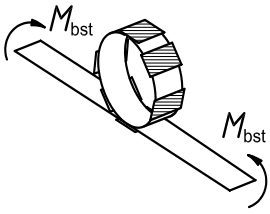
For the Beam and Shell Step Models, the supporting plates were designed using the same dimensions, as in the experiment. The isotropic properties of the plates are assigned using Young’s modulus and Poisson ratio inherent to steel ($E_{\text{steel}} \approx 2.11 \times 10^{11}$ and $\mu_{\text{steel}} \approx 0.28$, correspondingly). In order to take into account the shear effect, the belt’s Poisson ratio was assigned approximately equal to $\mu_1 = \mu_2 \approx 0.45$ as for the rubber in all belt directions.

In addition, the Beam and the Shell Step Models took into account the difference between the nominal pipe diameter of the supporting plates and the actual external diameter of a belt’s pipe. The difference appears due to the manufacturing inaccuracy of a belt Sample 3, that caused the small difference between the belt width designated and the actual width of a belt produced. If the correlation between the analytical, FEM, and the experiment case study is achieved, it becomes possible to perform the impact analysis of the various PBC design parameters on the CFs.

For the impact analysis, the properties provided in Table 4.9 for the fabric belt Sample 3 with a uniform structural design are used as a reference set for the variation.

At the beginning, the impact analysis is carried out, considering each external load independently. This means that the influence of the input parameters is analyzed for the problem of a belt, subjected to either load from belt bending stiffness, or load from belt weight, or load from bulk material. The impact analysis is performed for each of the load using similar procedure as for the troughability test in Chapter 3.

Table 6.1: The major distinctive aspects of all the FEM models elaborated to determine PBC CFs using FEM analysis

FEM Model	Model type	Analysis	Load from the belt bending stiffness	Contact and plates
<p>Beam Simplified Model</p> 	2D Beam	One step solution - Linear - Nonlinear	As an additional external load: - M_{bst} - q_{bst} - $q_{bst}, Q_{1bst}, Q_{2bst}$	- No contact Plates: only constrained nodes (as in the analytics)
<p>Beam Step Model</p> 	2D Beam	Multiple step solution (restart analysis) - Nonlinear	Belt is folded from a flat shape into a pipe	Two contact pairs: - Belt-plates - Belt's self-contact Plates: - reduced length (imitates a node constraint from the analytics) - extended length (as in the experiment)
<p>Shell Step Model</p> 	3D Shell	Multiple step solution (restart analysis) - Nonlinear	Belt is folded from a flat shape into a pipe	Two contact pairs: - Belt-plates - Belt's self-contact Plates: - extended length (as in the experiment)

In particular, for each of the participating input parameter, the results are achieved and compared with the reference set, when one of the influencing design parameter is double increased and also half reduced, whereas the rest of the parameters are assumed to be constant. This allows one to obtain the functional dependence between the CFs and the input design parameters for each of the load.

After the impact analysis is performed for each of the load independently, the general master curve is developed for an empty and loaded PBC, when the loads participate all together. The results achieved are provided in the next section.

6.5 Results: case study

The CFs obtained for the case study using all the models developed are presented as diagrams with the numeration that corresponds to Fig. 4.1a.

Figure 6.6 illustrates the comparison of the experiment and the CFs, evaluated from the analytical linear model, developed in Chapter 5, and the linear solution of the Beam Simplified Model.

The CFs are obtained using three methods of modeling the load from the belt bending stiffness, characterized by: a) expansion concentrated moment applied at the belt edges M_{bst} (see Section 5.3.1); b) evenly distributed radial load q_{bst} (Section 5.3.2); and c) distributed radial load q_{bst} with concentrated forces Q_{1bst} and Q_{2bst} , situated at angle β (see Section 5.3.3).

The first observation shows that the results from the analytical and the linear solution of the Beam Simplified Model exhibit the difference in CFs, compared to the experiment.

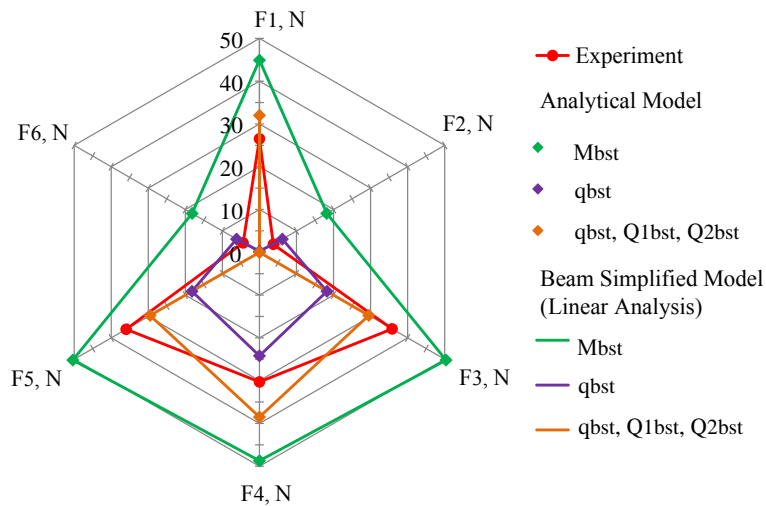


Figure 6.6: The comparison of the experiment case study results and the CFs, evaluated from the analytical linear model, developed in Chapter 5, and the linear solution of the Beam Simplified Model. The results are obtained using three methods of modeling the load from the belt bending stiffness

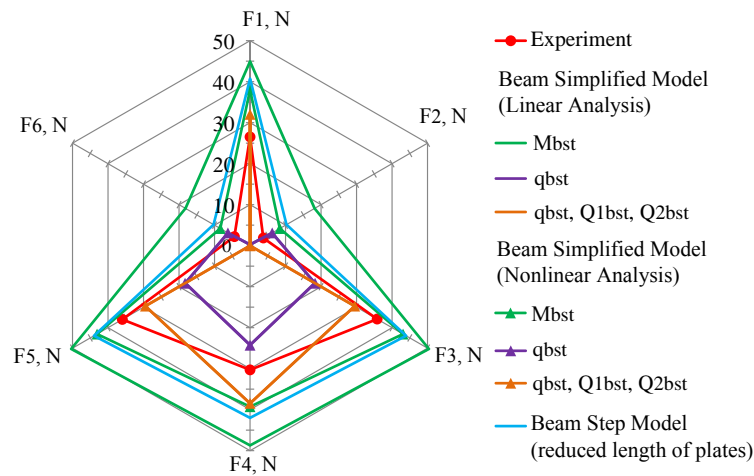


Figure 6.7: The comparison of the experiment case study results and the CFs, determined from the Beam Simplified Model (Linear and Nonlinear solution) using three methods of modeling the load from the belt bending stiffness, and the Beam Step Model, simulated with the reduced length of plates.

However all the CFs obtained are not out of the feasible range. In addition, the analytical solution is fully in agreement with the numerical results of the Beam Simplified Model regardless how the load from the belt bending stiffness is described. Moreover, it is possible to see that the using the expansion concentrated moments M_{bst} , applied at the belt edges for modeling a load from the belt bending stiffness, generates the similar load pattern as the experiment.

To clarify which method of modeling the load from the belt bending stiffness is correct, the experimental results are compared with the Beam Simplified Model for both linear and nonlinear solution and also with the Beam Step Model, converged with the reduced length of the supporting plates. Figure 6.24 shows the results obtained.

Comparing the linear and nonlinear solution of the same Beam Simplified Model, it is possible to observe that, if the load from belt bending stiffness is represented either by q_{bst} or by q_{bst} together with forces Q_{1bst} , Q_{2bst} , the difference between the linear and nonlinear solution is negligible. As for the concentrated expansion moment M_{bst} , the difference between the linear and the nonlinear analysis of the Beam Simplified Model, on the contrary, has a significant effect. Moreover, the nonlinear solution of the Beam Simplified Model with M_{bst} is closer to the experiment case study.

Comparison of the Beam Simplified Model, where the load from the belt bending stiffness is prescribed as an additional external load, and the Beam Step Model that simulates folding process of a belt from a flat shape into a pipe shape, indicates that the concentrated expansion moment M_{bst} correlates with the results of the Beam Step Model and can be used further in the analytical and the FEM models. At the same time, the other options of modeling the load from belt bending stiffness (q_{bst} and q_{bst} with Q_{1bst} , Q_{2bst}) do not produce correct CFs and even the load patterns.

The length of the plates for the Beam Simplified Model was reduced aiming to minimize

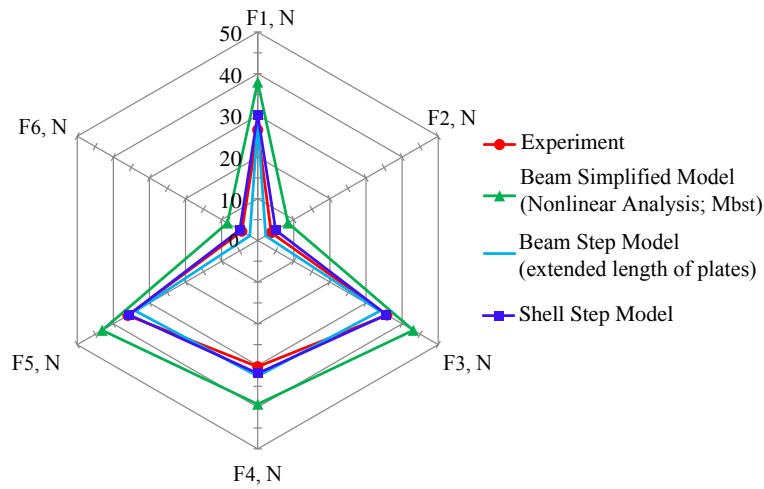


Figure 6.8: The comparison of the experiment case study results and the CFs, determined from the Beam Simplified Model (Nonlinear solution) using M_{bst} as a load from the belt bending stiffness, the Beam Step Model, simulated with the extended length of plates, and the Shell Step Model.

the impact of a contact effect between the belt and the plates, making the model as close as possible to the Beam Simplified Model. The minimal length of the plates constituted 0.015m in lateral direction. The further length reduction affects the problem convergence.

The correlation between the Beam Simplified Model and the Beam Step Model indicates that, despite the fact that the structural stress field of a belt, obtained from a direct problem (when the belt is folded from a flat shape into a pipe shape) is not equivalent to an approximating inverse problem (when a stress-free belt already in a pipe shape and is subjected to the external load from the belt bending stiffness), the CFs obtained from both direct and inverse problems are actually equivalent, if the load from the belt bending stiffness prescribed as expansion concentrated moments M_{bst} .

Now, when the correct method of modeling the load from the belt bending stiffness is selected, the Beam Simplified Model, converged using only M_{bst} , is compared with the Beam Step Model and the Shell Step Model. Both FEM step models are solved with the extended length of the supporting plates and also include a small gap between the nominal pipe diameter used for the hexagon plates and the external pipe diameter of a belt, attained from the imprecision of the belt manufacturing.

In general, as it can be seen from Fig. 6.8, all three models generate rather close results to the experiment. The CFs of the Beam Simplified Model are the highest, as the model does not incorporate the small difference between the nominal and the belt's external pipe diameters, accounted in the FEM step models. The Shell Step Model fits slightly better for the experiment case study CFs, compared to the Beam Step Model and generates slightly higher forces. The increase in CFs is due to the higher stiffness of the shell model occurred from the shear effects in both longitudinal and lateral planes, whereas the Beam Step Model incorporates the shear effect only in one plane.

Comparison of the experiment, analytical model, and all the FEM models between each

other makes it possible to state that the analytical approach, developed in Chapter 5 is in the agreement with the numerical FEM approach, whereas the FEM approach is in the agreement with the experiment.

It is important to note that the present study compares only one set of the points for the case study, since it satisfies the assumptions accepted for the analytical and the FEM models. Consequently, more experimental data is required for the further validation of the analytical and the FEM models. At the same time, the agreement achieved shows that the more simple and less time consuming models (the Beam Step Model and the Beam Simplified Model) can generate the feasible results and can be used further for the impact analysis, instead of the Shell Step Model. The latter is a more precise model, but is less attractive for the practical use due to the extensive time required for the convergence. The ability to run different cases for various input parameters within the reasonable time is in the priority for the impact analysis.

In addition, for the impact analysis, the analytical model, developed in Chapter 5 is also used as a basis for deriving a functional dependence between the input design parameters of a PBC and the CFs. At certain PBC designs, it can appear that the analytical model can also predict the PBC CFs in a feasible range. The impact analysis is carried out in the next section for an empty and loaded PBC.

6.6 Impact analysis for empty conveyor

A large number of the design parameters participate in the problem and can influence pipe. To perform an impact analysis, the functional dependence trend between the CFs and the design parameters involved need to be established. Since the FEM models are determined numerically, it becomes difficult to establish the functional dependence for all the parameters involved.

That is why, the analytical model, developed in Chapter 5 can be used as a starting point. Despite the fact that the assumptions inherent to a linearized analytical model are not relevant for the complex nonlinear models (e.g., the usage of Principle of Superposition), the linear model can be considered as a special case of a more generalized nonlinear solution and can indicate the basis for the general functional dependence.

6.6.1 Derivation of the base functional dependence

For the linearized analytical model, the CFs F_n are evaluated from the system of Eq. 5.134. These CFs depend, in turn, on the forces, denoted as X_n and determined from the system of Eq. 5.73, using method of superposition. Each equation in the system of Eq. 5.73, represents a dependence between the unit displacements $\bar{\delta}_{nm}$ and the displacements from the external loads δ_{nP} . These displacements reflect an impact of all the design parameters involved on the CFs. In addition, as stated in Section 5.6.8, if, after solving the system of Eq. 5.73, one of the forces X_n becomes negative, this means that there is a contact loss. In this case, the maximal negative force is assumed equal to zero, the corresponding displacements are also set to zero, and the equivalent equation is removed from the system. The solution procedure repeats until all the CFs remain positive or equal to zero.

In order to detect the dependence trend between the CFs and the displacements, influenced by the design parameters, the problem can be analyzed mathematically, using the analytical model as a basis. For instance, if there is only one CF in the system, which is, of course, a hypothetical example for a PBC, this CF remain can be evaluated as follows:

$$\bar{\delta}_{11}X_1 + \delta_{1P} = 0 \quad \Rightarrow X_1 = -\frac{\delta_{1P}}{\bar{\delta}_{11}} \quad \Rightarrow X_m \sim \frac{\delta_{nP}}{\bar{\delta}_{nm}}. \quad (6.1)$$

If there are only two CF in the system, the solution equals:

$$\begin{cases} \bar{\delta}_{11}X_1 + \bar{\delta}_{12}X_2 + \delta_{1P} = 0; \\ \bar{\delta}_{12}X_1 + \bar{\delta}_{22}X_2 + \delta_{2P} = 0. \end{cases} \Rightarrow \begin{cases} X_1 = \frac{\bar{\delta}_{12}\delta_{2P} - \bar{\delta}_{22}\delta_{1P}}{\bar{\delta}_{11}\bar{\delta}_{12} - \bar{\delta}_{12}^2} \\ X_2 = \frac{\bar{\delta}_{12}\delta_{1P} - \bar{\delta}_{11}\delta_{2P}}{\bar{\delta}_{11}\bar{\delta}_{12} - \bar{\delta}_{12}^2} \end{cases} \Rightarrow X_n \sim \frac{\sum \bar{\delta}_{nm}\delta_{nP}}{\sum \bar{\delta}_{nm}^2}. \quad (6.2)$$

If there are three CFs preserved in the system, the dependence can be expressed as following:

$$\begin{cases} \bar{\delta}_{11}X_1 + \bar{\delta}_{12}X_2 + \bar{\delta}_{13}X_3 + \delta_{1P} = 0; \\ \bar{\delta}_{12}X_1 + \bar{\delta}_{22}X_2 + \bar{\delta}_{23}X_3 + \delta_{2P} = 0; \\ \bar{\delta}_{13}X_1 + \bar{\delta}_{23}X_2 + \bar{\delta}_{33}X_3 + \delta_{3P} = 0. \end{cases} \Rightarrow X_n \sim \frac{\sum \bar{\delta}_{nm}^2\delta_{nP}}{\sum \bar{\delta}_{nm}^3}. \quad (6.3)$$

And finally, if all four forces take place in the system, the CFs represent the dependence as follows:

$$\begin{cases} \bar{\delta}_{11}X_1 + \bar{\delta}_{12}X_2 + \bar{\delta}_{13}X_3 + \bar{\delta}_{14}X_4 + \delta_{1P} = 0; \\ \bar{\delta}_{12}X_1 + \bar{\delta}_{22}X_2 + \bar{\delta}_{23}X_3 + \bar{\delta}_{24}X_4 + \delta_{2P} = 0; \\ \bar{\delta}_{13}X_1 + \bar{\delta}_{23}X_2 + \bar{\delta}_{33}X_3 + \bar{\delta}_{34}X_4 + \delta_{3P} = 0; \\ \bar{\delta}_{14}X_1 + \bar{\delta}_{24}X_2 + \bar{\delta}_{34}X_3 + \bar{\delta}_{44}X_4 + \delta_{4P} = 0. \end{cases} \Rightarrow X_n \sim \frac{\sum \bar{\delta}_{nm}^3\delta_{nP}}{\sum \bar{\delta}_{nm}^4}. \quad (6.4)$$

As it can be seen, after solving the system of Eq. 5.73, the dependence of the resultant CFs are in the same order of magnitude as the following ratio:

$$X_n \sim \frac{\sum \bar{\delta}_{nm}^{n-1}\delta_{nP}}{\sum \bar{\delta}_{nm}^n}, \quad (6.5)$$

where n is a total number of the non-zero CFs equivalent to m number of system equations solved.

To establish a dependence as a function of the CFs and PBC design parameters involved, the unit displacements and the displacements from the external loads need to be analyzed.

Taking into account that $I = lh^3/12$, $A = lh$, $R = B/(2\pi)$, and $G = \frac{E}{2(1+\mu)}$ as for the isotropic body assumed, the unit displacements, provided in Eqs. 5.74-5.83, can be written in the following functional form:

$$\bar{\delta}_{nm} = C_{nm1}^* \frac{R}{EA} \left(C_{nm2}^* \frac{B^2}{h^2} + C_{nm3}^*(\mu) \right), \quad (6.6)$$

where C_{nm1}^* , C_{nm2}^* , and $C_{nn3}^*(\mu)$ are the constants that are different for each of the force, participating in the system. The present analysis does not consider the effect of the varied Poisson ratio on CFs, as a result, the ratio is assumed the same and constant for any case. This means that $C_{nm3}^*(\mu) = \text{const}$ and the expression in Eq. 6.6 can be written simply as follows:

$$\bar{\delta}_{nm} = C_{nm1} \frac{R}{EA} \left(C_{nm2} \frac{B^2}{h^2} + 1 \right), \quad (6.7)$$

where $C_{nm1}, C_{nm2} \in \mathbb{R}$.

As for the displacement from external loads δ_{nP} , they represent a sum of the displacements, caused by: a) load from belt bending stiffness; b) load from the belt weight, and c) load from the bulk material. In order to establish a general functional dependence for PBC CFs, at first, the impact analysis is accomplished, considering each of the load independently using the Principle of Superposition, and then analyzing all the loads in their combination.

6.6.2 Load from the belt bending stiffness

If the CFs are caused only by the expansion load, appeared from the folding a belt from a flat shape into a pipe shape, the impact analysis is carried out only using the moments M_{bst} , applied at the belt edges of a stress free belt already in a pipe shape to model the load from the belt bending stiffness. This load is selected, since it generates correct CFs for the case study analysis, whereas the rest two loading conditions (q_{bst} , and also q_{bst} with Q_{1bst} , Q_{2bst}), led to the incorrect solution.

For the linearized analytical model, the displacements, caused by the expansion moment M_{bst} and provided in Eqs. 5.97-5.100, can be expressed simply in the following form:

$$\delta_{nP} = \delta_{nbst} = C_{nbst} R, \quad (6.8)$$

where $C_{nbst} \in \mathbb{R}$.

Substituting the expressions Eq. 6.7 and Eq. 6.8 into the functional dependence, provided in Eq. 6.5, and after the transformation, each of the CF can be expressed as following functional dependence with respect to the involved PBC design parameters:

$$\frac{F_{nbst}}{EA} = C_{n1} \frac{C_{n2} \frac{B^6}{h^6} + C_{n3} \frac{B^4}{h^4} + C_{n4} \frac{B^2}{h^2} + 1}{C_{n5} \frac{B^8}{h^8} + C_{n6} \frac{B^6}{h^6} + C_{n7} \frac{B^4}{h^4} + C_{n8} \frac{B^2}{h^2} + 1}, \quad (6.9)$$

$C_{n1}, \dots, C_{n8} \in \mathbb{R}$ are the real constants different for each of the force in the system set. For the simplicity needed in further analysis, a definite function of a belt slenderness $\Psi(B/h)$ is introduced:

$$\Psi(B/h) = \frac{C_{n2} \frac{B^6}{h^6} + C_{n3} \frac{B^4}{h^4} + C_{n4} \frac{B^2}{h^2} + 1}{C_{n5} \frac{B^8}{h^8} + C_{n6} \frac{B^6}{h^6} + C_{n7} \frac{B^4}{h^4} + C_{n8} \frac{B^2}{h^2} + 1}. \quad (6.10)$$

In this case, if the load from the belt bending stiffness is only involved, the linearized models generate the CFs that simply represent functions of a belt slenderness B/h , i.e.:

$$\frac{F_{n\text{bst}}}{EA} = C_{n1} \Psi(B/h) = f_n^{\text{bst}} \left(\frac{B}{h} \right). \quad (6.11)$$

Using this dependence as a basis, the impact analysis is performed, using the case study input parameter (fabric belt Sample 3 Table 4.9) set as for the reference.

At first, the dependence function of Eq. 6.11 is received for the analytical model and also for the Simplified Beam Model (linear and nonlinear analysis). The results are illustrated in Fig. 6.9, achieved varying the belt slenderness in a range $6.67 \leq B/h \leq 643$, preliminarily established in Section 2.5.2 of Chapter 2.

Figure 6.9a represents the CFs attained when all four constraints are preserved in the system. As it can be seen, for the slenderness ratio $B/h \leq 32$, it is possible to observe negative values for the CFs $F_2 = F_6$ and even for $N'_1 = N''_1$. In this case, the graph shows the correct CFs only for the range $B/h > 32$ (the area of the figure is denoted as **I**), whereas for $B/h \leq 32$, there is at least one contact loss.

Following the principle, described in Section 5.6.8, if there are more than one negative CF are obtained after the solution, the maximal negative one is assumed equal to zero. The corresponding displacements and equations need to be removed from the system of Eq. 5.73, and, after the modification, the system has to be solved again.

Figure 6.9b shows the recalculated CFs for the assumed contact loss $F_2 = F_6 = 0$. Again, it is possible to observe the negative values for the CFs $N'_1 = N''_1$, occurring for thick belt structures with slenderness ratio $B/h \leq 10.8$. The negative $N'_1 = N''_1$ means that the belt edges tend to expand and do not contact each other anymore (the contact loss). In this case from the graphs, attained for $F_2 = F_6 = 0$, only the area, limited by the slenderness ratio $10.8 < B/h \leq 32$ and denoted as **II** in Fig. 6.9b is needed for the resultant functional dependence.

In order to eliminate the negative values for $N'_1 = N''_1$, the system of Eq. 5.73 is transformed, assuming again the contact losses, in particular for $F_2 = F_6 = 0$ and $N'_1 = N''_1 = 0$. Figure 6.9c provides the results, achieved after solving the transformed system of Eq. 5.73. For creating the overall functional dependence, only the area, denoted as **III** in Fig. 6.9c for the slenderness ratio $6.67 \leq B/h \leq 10.8$ is used.

Finally, the resultant functional dependence for CFs, caused by the load from the belt bending stiffness is received in Fig. 6.9d for all variation range of belts slenderness $6.67 \leq B/h \leq 643$ by combining the areas **I**, **II**, and **III** at one graph.

The analysis of the graphs present in Fig. 6.9, shows that the effect of the load from the belt bending stiffness causes rather extensive top CF F_1 , compared to the other CFs. At the same time, the contact loss generally appears for the lateral top position F_2 and F_6 , and also at the edges N'_1, N''_1 .

In addition, the general resultant trend shows that CFs significantly decrease with the increase of the slenderness ratio B/h . For instance, the significant reduction appears for belt structures with $B/h > 200$ already and, for the maximal critical ratio $B/h = 643$, the absolute values of the CFs become no larger than 1N. This effect can be explained by the fact that, for thin belt structures with large ratio of N/h , the belt deformations become more local close to the edges, where the expansion moments M_{bst} are applied.

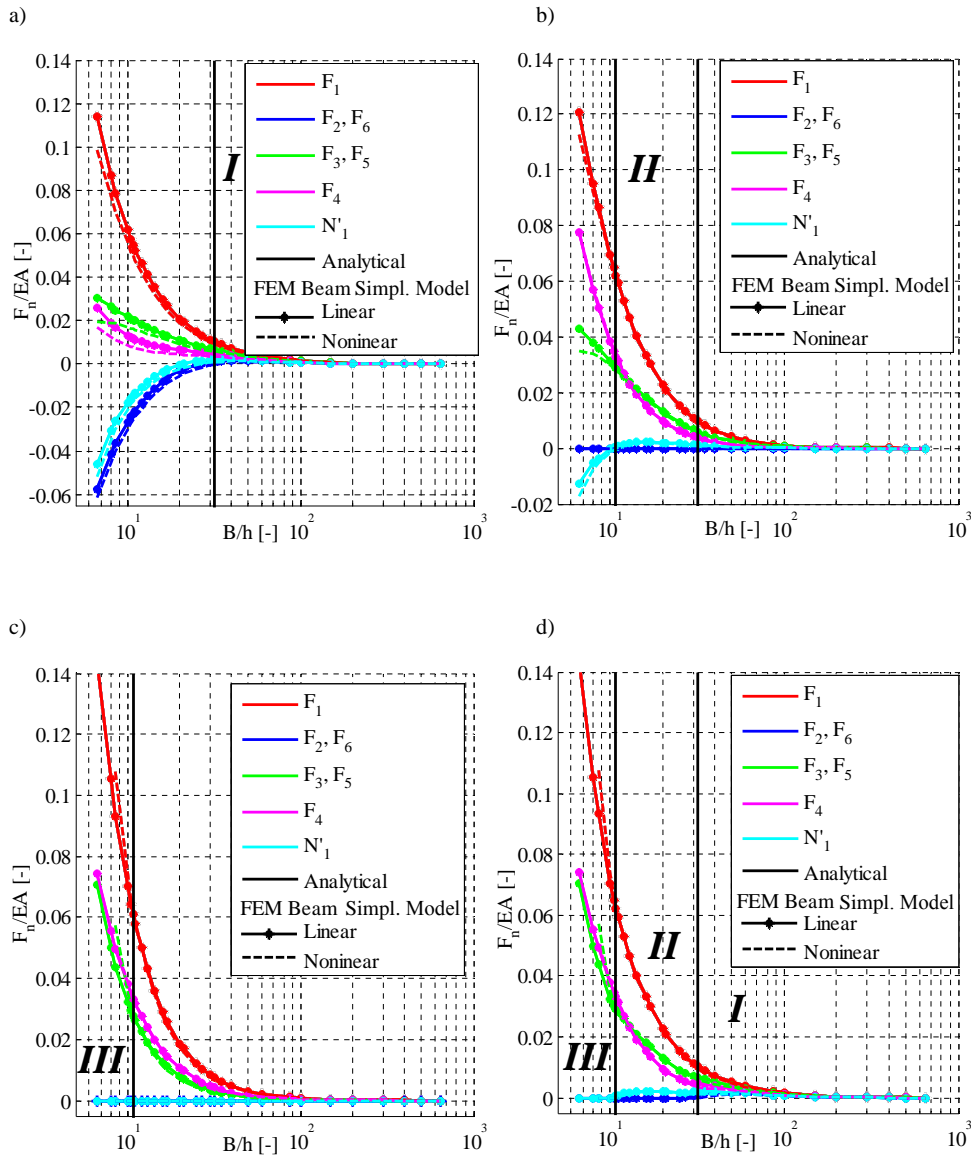


Figure 6.9: The comparison of the functional dependence given in Eq. 6.11 for CFs, determined from the analytical model and also from the numerical Beam Simplified Model, solved using the linear and nonlinear analysis. The results are provided for: a) assuming that all the constraints are preserved in the model; b) assuming the contact loss for $F_2 = F_6 = 0$; c) assuming the contact loss for $F_2 = F_6 = 0$ and $N'_1 = N''_1 = 0$; d) for the actual dependence trend, obtained by combining the areas I, II, and III at one graph. The graphs are valid for any E and l .

Comparing the analytical results with the linear and nonlinear solution of the Beam Simplified Model in Fig. 6.9, it is possible to state that all the models selected exhibit the similar resultant trend for CFs. The analytical model accurately reproduces the same results as the linear analysis of the Beam Simplified Model. If the results are attained for the nonlinear solution of the Beam Simplified Model, the larger difference in curves appears more for thicker belt structures with smaller ratio of B/h . The difference between the linear and the nonlinear analysis appears, as for the belts with small ratios B/h , more constraints are removed from the structure, and, as a result, belt exhibits larger deformations, compared to the initial pipe shape. Taking into account that the linearized models account only small structural displacements, the difference between the linear and nonlinear solution for $B/h < 10$ becomes more noticeable.

As a next step, the impact of other participating parameters on CFs is analyzed. In particular, the same analysis is performed, creating the dependence curves, as in Fig. 6.9, for the double increased and half reduced elastic modulus of elasticity, i.e., comparing the graphs for given E as in Fig. 6.9 with the dependence graphs for $E/2$ and $2E$. Similarly, the results are obtained, varying the longitudinal length of a belt structure, whereas the Young's modulus is assumed to be constant, i.e., comparing the case for $l = b$ (Fig. 6.9) with the resultant curves for $2l$, and $l/2$. And at last, in the same manner, the effect of belt's structural thickness h is studied, comparing the curves $F_{n\text{bst}}/(EA)$, received for $h/2$, h , and $2h$ for the same B/h variation and keeping $l = b = \text{const}$, $E = \text{const}$.

The analysis of the results for the varied participating parameters indicates that the general dependence trend, provided in Fig. 6.9 does not change with respect to the change in Young's modulus E , longitudinal length l of a belt sample, and the belt's structural thickness h , as soon as the belt's slenderness B/h is preserved constant. This proves that the expression for CFs in Eq. 6.11 is necessary and sufficient for the analytical solution and also the FEM Beam Simplified Model (both linear and nonlinear analysis).

As a step towards a more precise FEM model, the similar dependence graphs are attained for the Beam Step Model using the plates with reduced length for supporting the belt. As mentioned above, this is made in order to closely imitate the constraints, assumed in the analytical model and the Beam Simplified Model. The reduced length of plates is selected accepting its value as minimal as possible for the problem convergence. Figure 6.10a shows that the resultant curves, obtained for the Beam Step Model and for nonlinear solution of the Beam Simplified Model, are very close. The correlation between these models proves that the load from belt bending stiffness can be sufficiently represented for this variation range of B/h by the expansion moment M_{bst} , applied to the belt edges of a stress-free belt in a pipe shape.

In addition, the Beam Step Model is solved using the maximal length of supporting plates. In particular, the maximal length is assumed equal to a length of a side of a regular hexagon, circumscribed about the nominal pipe diameter. In other words, it has the same length as a conveyor idler roll with one side rolls arrangement, i.e., $l_{\text{pl}} = l_{\text{roll}} = (1/\sqrt{3})D_{\text{nom}}$ (see Section 2.6.2). Figure 6.10b shows that the curves, obtained from the models are very close. In order to spot the differences, the results are presented in a logarithmic scale.

As it is expected, the solution from the Beam Step Model with the reduced length of plates exhibits better agreement with the Beam Simplified Model, compared to the case of the extended length of plates. However, the largest difference between the models appears for the CFs that are relatively small (the CFs $N_1' = N_1''$ and $F_2 = F_6$), whereas the CFs with

significant values ($F_1, F_3 = F_5, F_4$) exhibit quite close correlation in the solution.

The increased length of plates provides a more stable position for the belt conformed to a pipe shape, as, at the certain B/h values, the Beam Step Model with $l_{pl} = \max$ obtains the CF, whereas for $l_{pl} = \min$, it detects the contact loss for CFs in position F_2 and F_6 . With the increase of the length of plates from minimal value to a maximum, the CFs change up till the certain value and then they remain the same, even though the length of plates continues increasing. The constant value is characterized by the size of the contacting surface of the belt deformed that does not change after the length of plates reach a certain value. In this case, the shape of a contact spot for each plate has a mutual relation with the corresponding CF and, for the case with maximal length of plates, exhibits the similar character of the functional dependence, as CFs do according to Eq. 6.11.

This statement is supported by the fact that the same graphs, given in Fig. 6.28 are reproduced for the same variation of B/h , if the input parameters for Young's modulus E , the longitudinal length of belt sample l , and the belt thickness h are varied. This indicates that, for all beam models, Eq. 6.11 is necessary and sufficient to express the CFs, caused by the load from belt bending stiffness as a function with respect to other participating design parameters.

After the functional dependence is received, reflecting the CFs caused only by the load from belt bending stiffness, the effect of the belt weight can be studied the next.

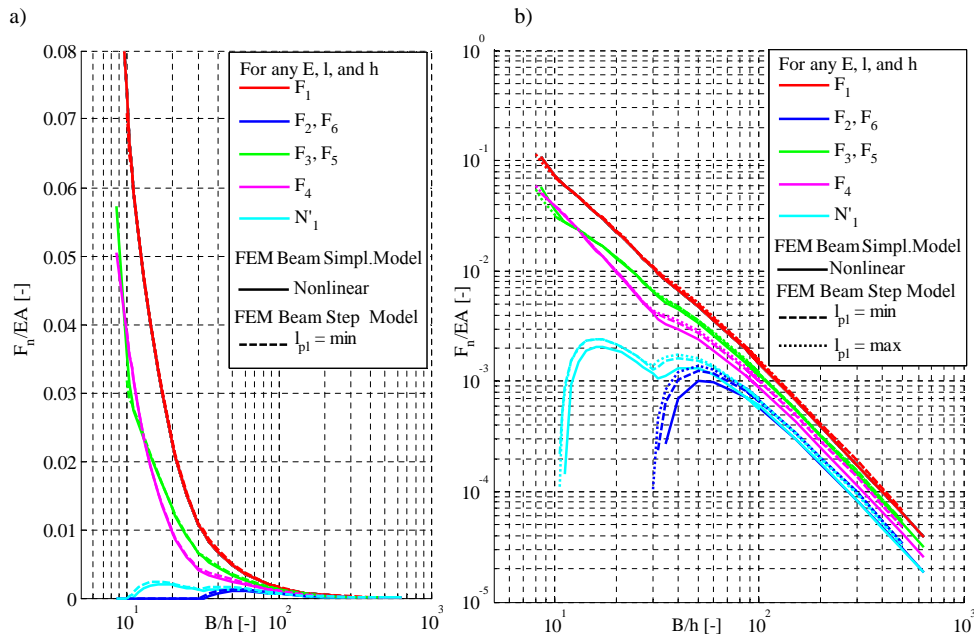


Figure 6.10: a) The functional dependence of Eq. 6.11 for CFs, determined from the nonlinear solution of the Beam Simplified Model and the Beam Step Model, converged for the plates with reduced length $l_{pl} = \min$; b) the same graphs plotted in the logarithmic scale together next to the results for the Beam Simplified Model with extended length of plates $l_{pl} = \max$.

6.6.3 Load from the belt weight

If the CFs are generated only by the load from the belt weight, the general functional dependence between the CFs and other participating design parameters can be derived again starting from the analysis of linearized analytical model.

As mentioned above, for the analytical model, the CFs represent a functional dependences on unit displacements and displacements from the external load, following the expression, given in Eq. 6.5). The unit displacements conform to the formulas, as provided in Eq. 6.6. As for the displacements from the bet weight, the Eqs. 5.91-5.94 can be transformed, taking into account that $I = lh^3/12$, $A = lh$, $R = B/(2\pi)$, and $G = \frac{E}{2(1 + \mu)}$. Similar to the unit displacements, the Poisson ratio is assumed constant for the analysis, and the Eqs. Eqs. 5.91-5.94 convert to the following expression:

$$\delta_{nbw} = C_{nbw1} \frac{q_{bw} R^2}{EA} \left(C_{nbw2} \frac{B^2}{h^2} + 1 \right), \quad (6.12)$$

where $C_{nbw1}, C_{nbw2} \in \mathbb{R}$.

If the displacements from the belt weight in Eq. 6.12 and the unit displacements from Eq. 6.7 are substituted to the general dependence formula in Eq. 6.5, after a transformation, the CFs, caused only by the load from belt weight, can be written in the following form:

$$\frac{F_{nbw}}{q_{bw} B} = C_{n9} \Psi(B/h) \left(C_{n10} \frac{B^2}{h^2} + 1 \right), \quad (6.13)$$

where the constants $C_{n9}, C_{n10} \in \mathbb{R}$, and $\Psi(B/h)$ is the same function of a belt slenderness, as provided in Eq. 6.10.

In other words, the effect of the load from the belt weight on CFs, given in Eq. 6.13 represents a functional dependence of a belt slenderness, similar as achieved in the previous section, i.e.:

$$\frac{F_{nbw}}{q_{bw} B} = f_n^{bw} \left(\frac{B}{h} \right). \quad (6.14)$$

The expression in Eq. 6.14 can be considered as a reference functional dependence for performing the impact analysis. Similar as for the load from the belt bending stiffness, the CFs are attained for the varied belt slenderness B/h within the range $6.67 \leq B/h \leq 643$, established in Section 2.5.2. As for the rest of the design parameters, the reference input is provided in Table 4.9 for the fabric belt Sample 3.

Figure 6.11 provides the resultant graphs obtained for CFs with respect to varied belt slenderness, using analytical solution, and also the numerical Beam Simplified Model (linear and nonlinear analysis). For better understanding the figure, at first, the graphs are discussed for the analytical model and the linear solution of the Beam Simplified Model (see only solid lines and solid lines with stars).

Figure 6.11a shows the results, obtained for the case, when all the constraints are preserved in the model. As it can be seen, the CFs for F_1 , $F_2 = F_6$, and $N_1' = N_1''$ are negative and remain negative for the all range of the belt slenderness. This means that, if the load from belt weight is only involved in the problem, it always causes at least one contact loss in the system.

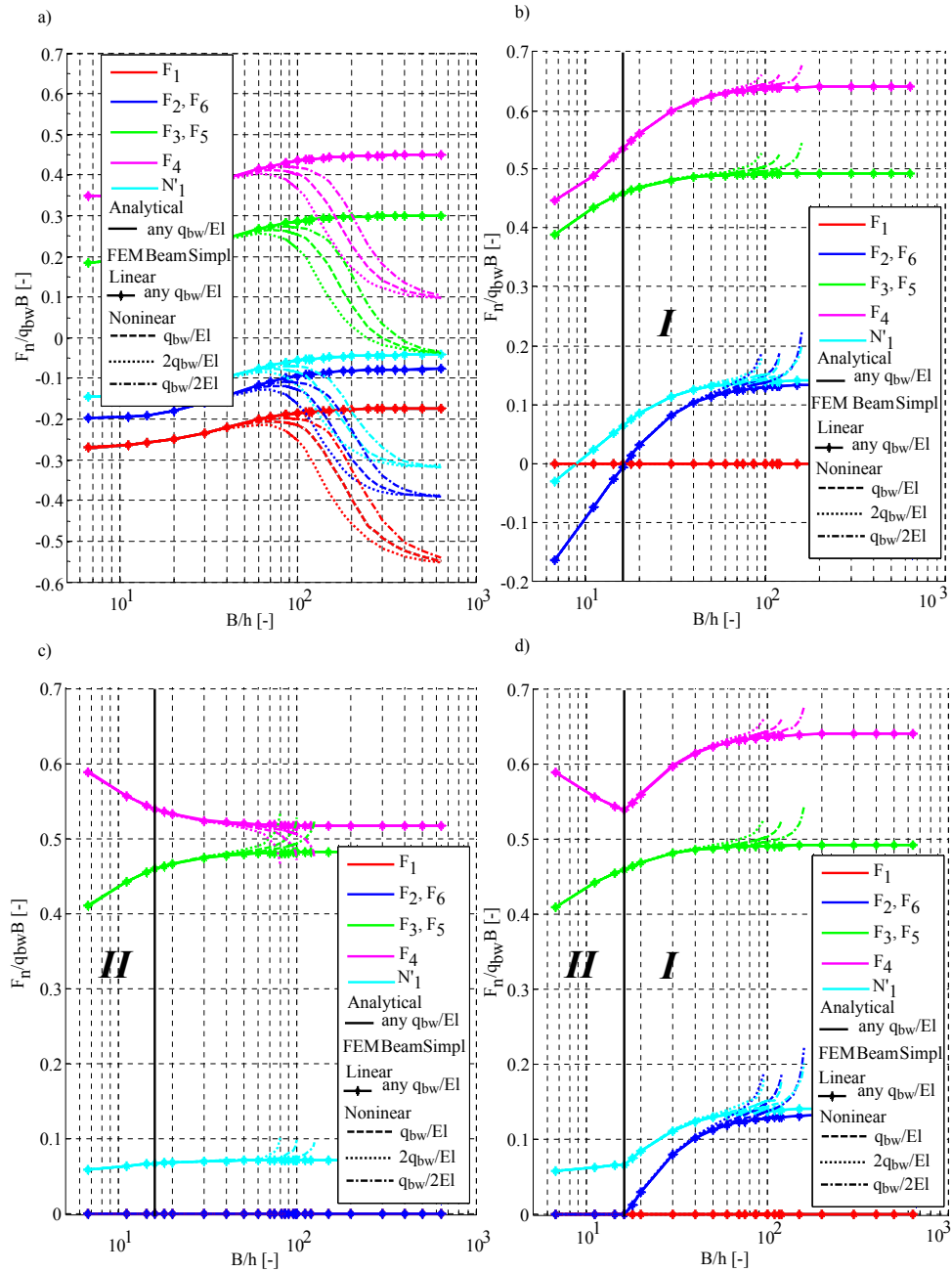


Figure 6.11: Comparison of the functional dependence, given in Eq.6.14 and Eq. 6.15 for CFs, determined from the analytical model and also from the Beam Simplified Model (linear and nonlinear analysis). The results are provided for: a) assuming that all the constraints are preserved in the model; b) assuming the contact loss for $F_1 = 0$; c) assuming the contact loss for $F_1 = 0$ and $F_2 = F_6 = 0$; d) for the actual dependence trend, obtained by combining the areas I and II at one graph. The graphs are obtained for $q_{bw}/(EI)$, $2q_{bw}/(EI)$, and $q_{bw}/(2EI)$.

Following the principal stated in Section 5.6.8, the largest negative CF needs to be assumed equal to zero, the corresponding constrain should be removed from the model, and the system of Eqs. 5.73 should be recalculated. This is repeated until all the CFs remain positive or equal to zero.

Figure 6.11d shows the resultant general functions for CFs, obtained after all the manipulations performed similarly as for the load from the belt bending stiffness. The figure is obtained by combining the areas **I** and **II** in one graph for the full variation range of B/h . The areas **I** and **II** correspond to the following cases of a contact loss: **I** for $F_1 = 0$, and **II** for $F_1 = 0, F_2 = F_6 = 0$.

The analysis of final Fig. 6.11d shows that, if the only the belt weight is taken into account, the major part of the load is distributed to the bottom plate F_4 , and also to the lateral bottom plates $F_3 = F_5$. At the same time, there is always a contact loss between the belt and the top plate (force $F_1 = 0$) and, for thick structures with slenderness ratio $B/h < 16$, the CFs $F_2 = F_6 = 0$ are also equal to zero.

Considering the nonlinear solution of the Beam Simplified Model for the reference parameter set (dashed line in Fig. 6.11), it is possible to observe that the function closely conforms to a linear solution, especially for thick structures. With the increase of a belt slenderness, the deviation between the linear and nonlinear solution becomes more noticeable. This is due to the fact that thinner belt structures with larger ratio B/h are more flexible and, as a result, tend to exhibit extensive nonlinear deformations, not accounted in the analytical models. Due to this fact, at certain ratio of B/h , the belt structure fully collapses, and the nonlinear Beam Simplified Model does not converge anymore. For the reference parameter set (dashed line in Fig. 6.11), the last convergence is achieved for $B/h \approx 120$.

At the same time, the linear analysis of belts with very large ratio B/h conforms to straight lines for each CF. Analyzing the Maxwell-Mohr Integrals, provided in Eqs. 5.91-5.94, it is possible to see that each of the displacement is comprised by the sum of the partial displacements from the bending moment M , the axial force N , and the shear hoop force Q , generated by the external load. Moreover, the displacement from the bending moment is in the fourth order of the belt slenderness $\sim (B/h)^4$, whereas the displacements from the axial N and hoop Q forces are in the second order of belt slenderness $\sim (B/h)^2$. This means that, for thin structures with large ratio of B/h , the results become more dominated by bending part, conforming to a straight line in CFs, whereas for small B/h ratios, the effect of N and Q becomes comparable to the bending effect.

For the next step, the CFs parameterized are received with respect to the belt slenderness variation by changing other participating design parameters with a factor of two. In particular, the results are obtained for double increased and half reduced Young's modulus, i.e. for $2E$ and $E/2$. Similarly, the longitudinal length of belt sample $l = b$ is varied, assuming $2l$ and $l/2$, and the belt weight is changed for $2q_{bw}$ and $q_{bw}/2$. The CFs obtained are compared for various combinations of E, l , and q_{bw} .

The analysis of the results obtained shows that, for various combinations of E, l , and q_{bw} , the linear solution of the analytical and the Beam Simplified Models conforms to the same lines, as expected in Eq. 6.14. As for the nonlinear solution of the Beam Simplified Model, the results for CFs depend on the design ratio of $q_{bw}/(EI)$. As soon as the ratio $q_{bw}/(EI)$ is constant, the corresponding resultant curves from the nonlinear solution coincide. Figure 6.11 exhibits a functional dependences obtained for the design ratios $q_{bw}/(EI)$, $2q_{bw}/(EI)$, and $q_{bw}/(2EI)$.

Taking this into account, it is possible to state that the CFs caused by the load from the belt weight are not only a function of the belt slenderness B/h , as proposed in Eq. 6.14, but also is defined by the ratio $q_{bw}/(EI)$, i.e.:

$$\frac{F_{nbw}}{q_{bw}B} = f_n^{bw} \left(\frac{B}{h}; \frac{q_{bw}}{EI} \right). \quad (6.15)$$

The analysis for CFs, caused by the belt weight is limited to the Beam Simplified Model, as the Beam Step Model accounts the actual belt formation from a flat shape into a pipe shape at first load step (see Appendix C). In this case, the presence of the load from the belt bending stiffness cannot be eliminated in the Beam Step Model.

After the load from the belt weight and the load from the belt bending stiffness are analyzed, it becomes possible to investigate an empty PBC, where both of these loads are involved.

6.6.4 Functional dependence for an empty pipe conveyor

In order to extract a functional dependence for empty PBC, the linearized analytical model is again considered as a starting reference base. For the linear model, the principal so superposition is fulfilled. In this case, the resultant CFs from two loads is equivalent to the sum of the forces, caused by those loads independently. In this case for an empty PBC, it can be written as follows:

$$F_n = F_{nbst} + F_{nbw}. \quad (6.16)$$

Substituting the functional dependences for each of the force F_{nbst} and F_{nbw} for the linear model, given in Eq. 6.11 and Eq. 6.14, respectively, the CFs can be transformed to the following expressions:

$$F_n = EA f_n^{bst} \left(\frac{B}{h} \right) + q_{bw} B f_n^{bw} \left(\frac{B}{h} \right); \quad (6.17)$$

$$\frac{F_n}{EA} = f_n^{bst} \left(\frac{B}{h} \right) + \frac{q_{bw} B}{EA} f_n^{bw} \left(\frac{B}{h} \right); \quad (6.18)$$

$$\frac{F_n}{EA} = f_n^{*empt} \left(\frac{q_{bw} B}{EA}; \frac{B}{h} \right) \quad \text{or} \quad \frac{F_n}{EA} = f_n^{empt} \left(\frac{q_{bw}}{EI}; \frac{B}{h} \right). \quad (6.19)$$

As it can be seen, the CFs depend on the belt slenderness and the ratio $\frac{q_{bw}}{EI}$. The impact of the latter has a proportional effect on CFs, if the slenderness is preserved constant. Indeed, this conclusion can be derived, since the expressions for F_{nbst} and F_{nbw} , given in Eq. 6.11 and Eq. 6.14, respectively, are substituted to the general Eq. 6.16. Figure 6.12 shows that impact of the ratio $\frac{q_{bw}}{EI}$ on CFs for the analytical linear solution, obtained for $B/h = \text{const}$ as for the reference case study. As it can be seen, the CFs represent straight lines in a form $y = ax + c$, where C_{n1}, \dots, C_{n10} for given B/h fulfill the role of the slope-intercept coefficients a and c . If there is a contact loss (at least one of the CF becomes negative), the corresponding displacements are assumed equal to zero, the equivalent equation is removed from the system of Eq. 5.73, and the CFs are recalculated. Due to this fact, after these manipulations, the straight lines in Fig. 6.12 shows a rather abrupt change due to the alteration in their slope-intercept coefficients.

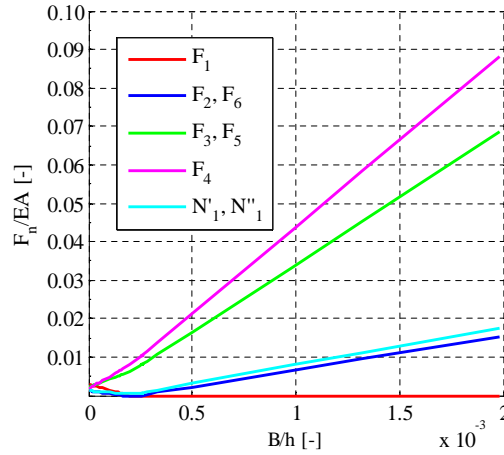


Figure 6.12: Impact of ratio $q_{bw}/(EI)$ on CFs for linear model, obtained using analytical approach for given slenderness ratio $B/h = 71.38 = \text{const}$, used as for the case study.

The impact of belt slenderness B/h has a more complex effect on CFs than the ratio $\frac{q_{bw}}{EI}$. Figure 6.13 shows the results, obtained using analytical approach and also the Beam Simplified Model (both linear and nonlinear solution). The graphs are constructed for the varied belt slenderness within the range $6.67 \leq B/h \leq 643$, established in Section 2.5.2. The rest of the parameters are used as for the reference fabric belt Sample 3, provided in Table 4.9 and keeping $q_{bw}/(EI) = \text{const}$.

The graphs in Fig.6.13 are obtained following the similar methodology as applied in the previous Section 6.6.2 and Section 6.6.2 for Fig. 6.9 and Fig. 6.11b, respectively, by combining the areas of the graph for different cases of a contact loss appearance. In particular, if after obtaining the graphs, at least one CF becomes negative for a certain range of a belt slenderness, for that range, the highest negative CF is assumed equal to zero, the corresponding displacements are removed from the System of Eq. 5.73, and the CFs are recalculated again. The procedure is repeated until all the CFs remain positive or equal to zero for all range of the parameters variation. The area-parts needed from all the graphs obtained are combined, constructing the resultant functional dependence.

Figure 6.13 shows the resultant dependence of the CFs, achieved for the full range of B/h -variation. The figure is obtained by composing the areas **I**, **II**, **III**, **IV**, and **V** that correspond to the following cases: **I** shows all the positive CFs, if all the constraints are preserved in the system; **II** represents the contact loss for $F_2 = F_6 = 0$; **III** states for the contact loss for $F_2 = F_6 = 0$ and $N'_1 = N''_1 = 0$; **IV** exhibits the contact loss for $F_2 = F_6 = 0$ and $F_1 = 0$; **V** shows the contact loss for $F_1 = 0$.

For better understanding the dependence trend, the result for CFs parameterized are shown in log-scale in Fig. 6.14. This is needed to perform a qualitative comparison with the similar graphs, obtained for different input parameters. The logarithmic scale allows one to detect the difference and analyze the effects of different input design parameters.

The analysis of the graphs in Fig. 6.13 and Fig.6.14 shows that that analytical solution

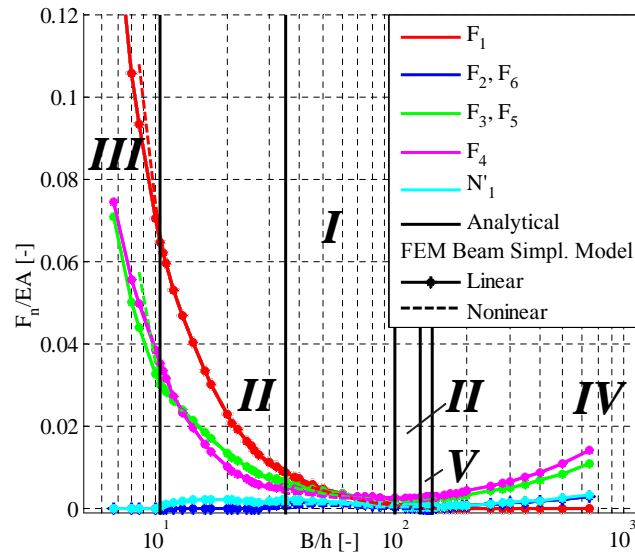


Figure 6.13: Comparison of the functional dependence given in Eq. 6.19) for an empty PBC CFs, determined from the analytical model and also from the Beam Simplified Model, solved using linear and nonlinear analysis. The results are provided for varied belt slenderness by combining the areas **I**, **II**, **III**, **IV**, and **V** at one graph. The graphs are valid for the reference ratio $q_{bw}/(EI)$.

is always in agreement with the linear analysis of the Beam Simplified FEM Model. In addition, linear and nonlinear results for the FEM model exhibit similar dependence trend in the results, which indicates that the analytical model provides quite close results at certain slenderness ratio B/h . Moreover, the logarithmic scale shows that the highest difference in the results appear to be for the CFs with smaller absolute values, whereas the highest CFs are quite in agreement.

The next step of the analysis investigates an impact of the participating design parameters. In particular, the results are obtained for double increased and half reduced bending modulus of elasticity E , distributed belt weight q_{bw} , and the longitudinal length of a belt section l . The results are achieved for different their combinations and compared between each other. As it was expected from the analysis of Eq. 6.19, the impact of the parameters variation follows the same dependence curves, as soon as the ratio $q_{bw}/(EI)$ remain constant.

Figure 6.15 illustrates the results in a logarithmic scale, obtained for $2q_{bw}/(EI)$ and $q_{bw}/(2EI)$. As it can be seen, for smaller ratio $q_{bw}/(EI)$, the curve of the linear solution better conforms to a nonlinear dependence. This is due to the fact that stiff and/or lighter belts exhibit smaller deformations that coincide with the assumption for the linear analytical and the Beam simplified Model. In addition, the smaller ratio of $q_{bw}/(EI)$ exhibits no contact loss for a wider range of the belt slenderness.

The analysis of Fig. 6.15 indicates that a conveyor belt can exhibit sufficient pipe-ability, if the belt slenderness is in the approximate range $35 \leq B/h \leq 116$. If for the given B/h -ratio it is expected to have a contact loss, the pipe-ability can be improved by selecting either a lighter belt, or more stiff belt structure, or by increasing a conveyor pitch. However, the effect

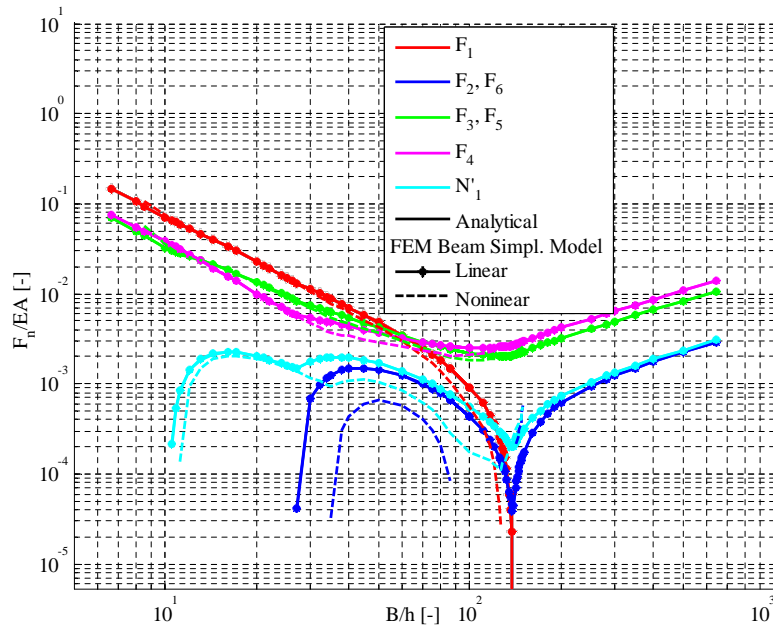


Figure 6.14: Comparison of the CFs parameterized according to Eq. 6.19, plotted in a log-scale versus belt slenderness ratio B/h and determined from the analytical approach and the Beam Simplified Model, solved using linear and nonlinear analysis. The graphs are valid for the reference ratio $q_{bw}/(EI)$.

of a carry spacing requires further investigation, as the impact of orthotropic belt properties and also the belt tension need to be taken into account.

Moving towards the more precise FEM model, the functional dependences are obtained using the Beam Step Model, converged for plates with reduced $l_{pl} = \min$ and extended length $l_{pl} = \max$. The values of the reduced length of plates are selected for each B/h -case as minimal as possible for the problem convergence.

Figure 6.16 shows the results for the reference parameter set $q_{bw}/(EI) = \text{const}$, obtained from the Beam Step Model, plotting them next to the curves from the Beam Simplified Model. As it can be seen, the general shapes of the curves resemble each other, and the solution of the Beam Step Model with $l_{pl} = \min$ better conforms to the Beam Simplified Model, compared to $l_{pl} = \max$ (as the small plates almost resemble the assumption for node-constraints). This indicates that assumptions made for the analytical and the Beam Simplified Model can give reasonable results in the feasible range. The largest deviation between the curves is detected for the least loaded CFs, in particular, for $F_2 = F_6$ and $N_1' = N_1''$.

Another important aspect is that the analytical model developed predicts high CFs than the Beam Step Model. At the same time, the Beam Step Model that incorporates the contact with plates with extended length also yields the reasonably high CFs. This makes the solution between the simple analytical model and the more complex Beam Step Model with a full contact with hexagon plates to be rather similar. In addition, even though the present impact

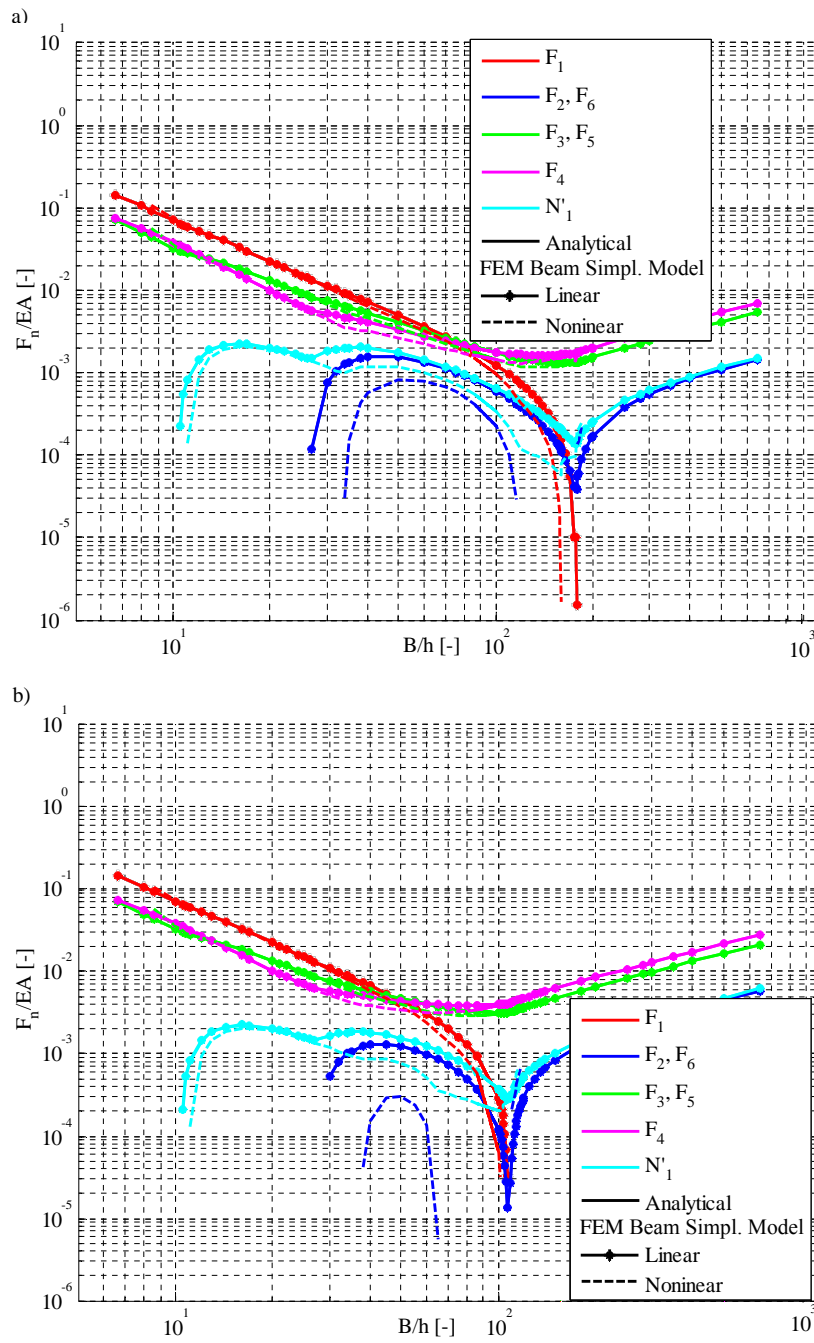


Figure 6.15: Comparison of the functional dependence given in Eq. 6.19 for empty PBC CFs, determined from the analytical model and also from the Beam Simplified Model, (both linear and nonlinear analysis). The results are provided for a) $q_{bw}/(2EI)$; b) $2q_{bw}/(EI)$.

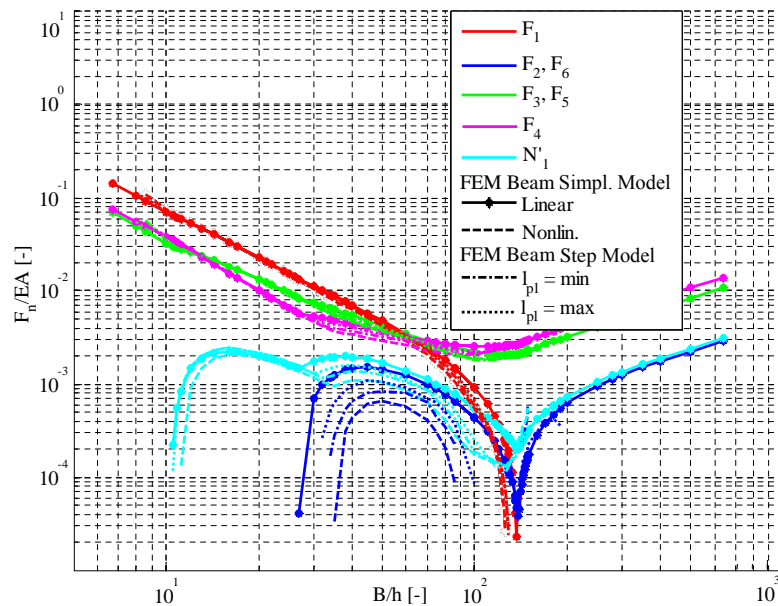


Figure 6.16: The functional dependence of CF parameterized, obtained using the Beam Simplified Model (both linear and nonlinear solution) and the Beam Step Model for reduced $l_{pl} = \min$ and extended $l_{pl} = \max$ length of the supporting plates. The curves are valid for the reference $q_{bw}/(EI) = \text{const}$.

analysis does not consider the Shell Step Model, it is reasonable to expect that shell model should give the CFs higher than the Beam Step Model moving towards the results, predicted by the analytical approach. Indeed, the results presented for the case study in Section 6.5 proves such expectation. The difference between the Beam Step Model and the Shell Step Model appears from the additional shear effect and is expected to be in order of $1/(1 - \mu^2)$ for isotropic and $1/(1 - \mu_1\mu_2)$ for the orthotropic structure.

These observations indicate that the analytical model developed in Chapter 5 gives reasonable results and can be used further in the analysis for loaded PBC. Moreover, the reasonable overestimation of the CFs ensures more safe design recommendations for the industry, giving somewhat space for the sensitivity of the model.

The analysis using the Shell Step Model and the models with the further complexity increase can be performed in future research, implementing the similar comparison procedure between the models and continue the hierarchy of the models, shown in Table. 6.1. The possible increase of the problem complexity can include the impact of a longitudinal stiffness in between the idler rolls, effect of a belt tension, a belt's overlap, belt's viscoelasticity and non-uniform belt structure along the width B .

For the more complex numerical models, the analytical approach, developed in Chapter 5 can be used as a starting reference point for their validation. Further research should be focused on development of the quantified recommendations for belt's pipe-ability and usage limitations of the models and approaches proposed.

6.7 Impact analysis for loaded conveyor

6.7.1 Load from the bulk material

In order to take into account the impact of the bulk material on CFs, at first, the analysis is performed, considering the linearized analytical model, subjected only to the bulk material load, whereas the load from the belt weight and the load from the belt bending stiffness are not included in the analysis.

For the linearized problem, a functional dependence between the CFs, caused by the bulk material load, and design parameters involved, can be derived by applying the principal of superposition, i.e., considering the impact of the vertical and horizontal load components independently, and then summing up their effects.

Analysis of the displacements, caused by the vertical bulk material load component, provided in Appendix A, shows that, in addition to other participating design parameters, $\delta_{n\text{bulk}}^v$ depends on the filling angle θ and the dynamic angle of repose λ , addressed in Section 2.3.3 and Section 2.4.2, respectively. The filling angle θ can be expressed via cross sectional filling degree k_Q according to Eq. 2.5. As for the angle of surcharge λ , its impact on CFs is not considered in the study, assuming it to be constant and equal to $\lambda = 30^\circ = \text{const}$, as for the coal (see Section 2.4.2).

Taking into account that $I = lh^3/12$, $A = lh$, $R = B/(2\pi)$, and $G = \frac{E}{2(1+\mu)}$, as for the isotropic body assumed, and that $\tan \lambda = \text{const}$, and θ is a function of k_Q , the displacements, given in Eqs. A.1-A.11, can be written in the following functional form:

$$\delta_{n\text{bulk}}^v = C_{n\text{bulk}1}^v \frac{\rho_{\text{bulk}} g l R^2}{EA} \left(C_{n\text{bulk}2}^v \frac{B^2}{h^2} f_{n1}^v(k_Q) + C_{n\text{bulk}3}^v f_{n2}^v(k_Q) + 1 \right), \quad (6.20)$$

where the constants $C_{n\text{bulk}1}^v$, $C_{n\text{bulk}2}^v$, $C_{n\text{bulk}3}^v \in \mathbb{R}$ and the functions $f_{n1}^v(k_Q)$, $f_{n2}^v(k_Q)$ of a PBC cross-sectional filling degree k_Q are derived from the trigonometric functions of a filling angle θ .

The general dependence for CFs, caused by the vertical load component can be found, by substituting the displacements $\delta_{n\text{bulk}}^v$ from the external vertical component of the bulk material load, given in Eq. 6.20, and the unit displacements $\bar{\delta}_{nm}$, provided in in Eq. 6.7 into the system of Eq. 5.73. The general solution of that system conforms to the expression, provided in Eq. 6.5. After a number of transformations, the following functional dependence for CFs can be obtained:

$$\frac{F_{n\text{bulk}}^v}{\rho_{\text{bulk}} g l R} = C_{n11} \Psi(B/h) \left(C_{n12} \frac{B^2}{h^2} f_{n1}^v(k_Q) + C_{n13} f_{n2}^v(k_Q) + 1 \right), \quad (6.21)$$

where $\Psi(B/h)$ is the same function of a belt slenderness, provided in Eq. 6.10, and the constants C_{n11} , C_{n12} , $C_{n13} \in \mathbb{R}$.

The both sides of Eq. 6.21 are divided into πk_Q . The parameter F_v^{bulk} characterizing the total weight of a bulk material load in a PBC as follows:

$$F_v^{\text{bulk}} = k_Q \pi R^2 \rho_{\text{bulk}} g l \quad (6.22)$$

can be introduced into Eq. 6.21, transforming it to the following general function:

$$\frac{F_{n\text{bulk}}^v}{F_v^{\text{bulk}}} = f_{n\text{bulk}}^v \left(\frac{B}{h}; k_Q \right). \quad (6.23)$$

In other words, the CFs from the vertical bulk material load component represent the functions of a belt slenderness B/h and the cross-sectional filling degree k_Q .

The analogical analysis of the displacements $\delta_{n\text{bulk}}^h$, given in Eq. B.1-B.11 in Appendix B, from the horizontal load component yields the resultant CFs in a similar functional form:

$$\frac{F_{n\text{bulk}}^h}{F_{n\text{bulk}}^v} = C^K f_{m\text{bulk}}^h \left(\frac{B}{h}; k_Q \right), \quad (6.24)$$

where C^K is a coefficient that implies the longitudinal development of the active and passive stress states along the conveyor pitch between the idler stations (see Section 5.4.4).

According to the principal of superposition inherent to the linear analysis, the total CFs, caused by the bulk material load can be found from the sum of the forces from the each load component. This leads to the following:

$$F_{n\text{bulk}} = F_{n\text{bulk}}^v + F_{n\text{bulk}}^h; \quad (6.25)$$

$$\frac{F_{n\text{bulk}}}{F_{n\text{bulk}}^v} = f_{n\text{bulk}}^v \left(\frac{B}{h}; k_Q \right) + C^K f_{n\text{bulk}}^h \left(\frac{B}{h}; k_Q \right). \quad (6.26)$$

The coefficient C^K is a function of K_a and K_p , as discussed in Section 5.4.4. K_a and K_p , in turn, depend on the effective angle of internal friction φ_e of a bulk material, addressed in Section 2.4.3. If φ_e is assumed constant, for instance, equal to $\varphi_e = 46^\circ = \text{const}$ as for the coal (selected in Section 2.4.3), the coefficient C^K , presented in Eqs. 5.47 convert to the following constant values:

$$\left[\begin{array}{l} C^K = \frac{1}{2} (K_a + K_p) \approx 3.145 - \text{Krause - Hettler;} \\ C^K = \frac{1}{4} (3K_a + K_p) \approx 1.654 - \text{Gushchin;} \\ C^K = \frac{1}{3} (2K_a + 0.85K_p) \approx 1.845 - \text{Wheeler-Mulani;} \\ C^K = K_a \approx 0.163 - \text{Constant active stress state.} \end{array} \right. \quad (6.27)$$

Therefore, the functional dependence for CFs, caused by the bulk material load can be simply written in a following form:

$$\frac{F_{n\text{bulk}}}{F_{n\text{bulk}}^v} = f_n^{\text{bulk}} \left(\frac{B}{h}; k_Q \right). \quad (6.28)$$

At first, the impact of the belt slenderness on CFs is considered for the PBC half-filled with the coal (filling degree $k_Q = 0.5$, the angle of internal friction $\varphi_e = 46^\circ$, and dynamic angle of repose $\lambda = 15^\circ$), selected in Section 2.4 as a hypothetical example, and with conveyor pitch of $l = l_c = 1\text{m}$. As for the coefficient C^K , the results are obtained using approach of Gushchin, i.e., for $C^K \approx 1.654$. In addition, the impact of usage of different, provided in Eq. 6.27 are compared further, when the impact of filling degree k_Q on CFs is considered.

The results for CFs parameterized as in Eq. 6.28 are obtained using the analytical model and the Beam Simplified Model (linear and nonlinear solution). At first, the assumption that all the constraints are preserved in the system is accepted. The results indicated that there

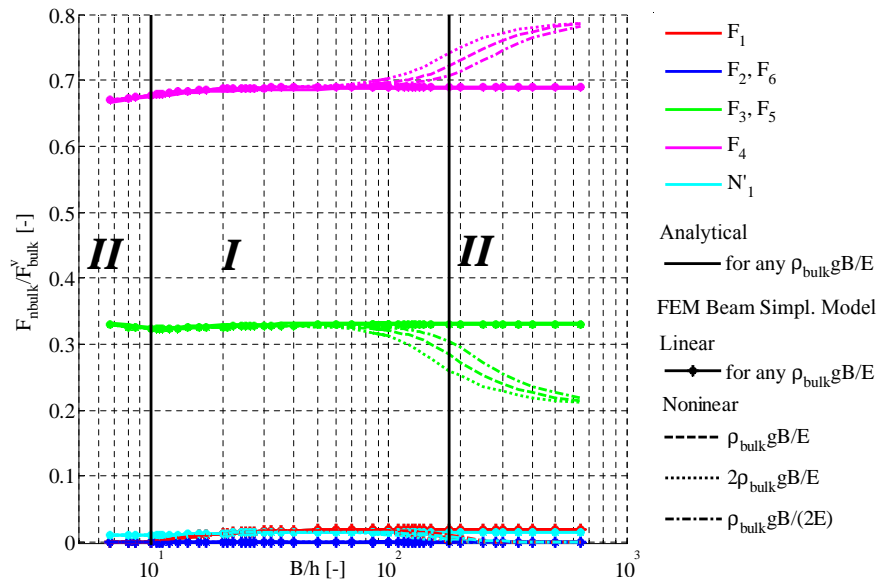


Figure 6.17: The functional dependences, given in Eq. 6.28 and Eq. 6.29 for CFs, determined from the analytical model and also from the Beam Simplified Model (linear and nonlinear analysis). The results are provided for the cross sectional filling degree $k_Q = 0.5$ and the ratios $\rho_{\text{bulk}}gB/E$, $2\rho_{\text{bulk}}gB/E$, and $\rho_{\text{bulk}}gB/(2E)$, combining the areas of a contact loss **I** and **II** at one graph.

was at least one contact loss for $F_2 = F_6 = 0$ for the full range of the B/h variation. The technique similar to the previous sections is used. It represents a repetitive procedure of assuming the largest negative CF equal to zero and recalculating all the CFs until all them remain positive or equal to zero. After that, the final graph is attained by combining the area parts of all the graphs at one for the full variation range of B/h needed.

Figure 6.17 illustrates the resultant functional dependence of CFs parameterized versus the belt slenderness B/h . The graph is obtained by combining the areas **I** and **II** for the following contact loss options: **I** - for the contact loss at $F_2 = F_6 = 0$; **II** - for the contact loss at $F_2 = F_6 = 0$, $F_1 = 0$.

In general, the linear solution of the Beam Simplified Model and the analytical model are in agreement. For thick belt structures, the linear solution (both analytics and the FEM) are in agreement with the nonlinear results. However, with the increase of the belt slenderness, the difference becomes more noticeable. This is due to the fact that, for the same loading conditions, thinner belts exhibit larger deformations than the ones allowed in the linear analysis.

Noteworthy to mention is that, similar to the effect of the load from the belt weight, the linear solution for the thin belt structures conforms to the dependence close to a straight line. This can be explained by the fact that the displacements in the linear analysis, evaluated from the Maxwell-Mohr Integral, are partially comprised by the bending moment M , the axial force N , and the shear hoop force Q from the external loads. The displacements from the bending moment M are in order $\sim (B/h)^4$ of a belt slenderness, whereas effect of the

axial N and hoop Q forces are in order $\sim (B/h)^2$. For thin belt structures with large ratios B/h , the effect of bending moment prevails the effect of axial and hoop forces, as a result, the dependence curve for very large values of B/h asymptotically conforms to a straight line, compared to the part of the graph with small B/h -ratio, where the effects of a bending moment M , axial force N , and hoop Q forces are comparable.

Figure 6.17 contains also the curves, obtained for the varied input parameters. In particular, the results are obtained for double increased and half reduced bending modulus of elasticity E , belt width B , and the density of a bulk material ρ_{bulk} . For different their combinations, the dependence graphs for CFs are obtained and compared between each other.

The results show that the functional dependence for the linear solution (both analytical and the Beam Simplified Model) follows only Eq. 6.28 and is not affected by the change of the input parameters mentioned. At the same time, the nonlinear solution appears to be dependable on the ratio $\rho_{\text{bulk}}gB/E$. In this case, the functional dependence of CFs, caused by a bulk material load, can be rewritten in the following form:

$$\frac{F_{n\text{bulk}}}{F_{n\text{bulk}}^v} = f_n^{\text{bulk}} \left(\frac{B}{h}; k_Q; \frac{\rho_{\text{bulk}}gB}{E} \right). \quad (6.29)$$

Figure 6.17 shows that for thin belts, the effect of the ratio $\rho_{\text{bulk}}gB/E$ becomes more noticeable. Heavier the bulk material is, or more flexible the belt structure is produced, the larger structural deformations appear. This becomes the reason for the larger difference between the linear and nonlinear solution.

Figure 6.17 is obtained for the cross-sectional filling degree $k_Q = 0.5$, using approach of Gushchin in Eq. 6.27 to describe the distribution of the horizontal component of a bulk material load along the conveyor pitch.

Aiming to analyze the effect k_Q of the cross-sectional filling degree, the results are obtained using analogical principal of the appearance of a contact loss, as for Fig. 6.17, whereas the other parameters in Eq. 6.28 and Eq. 6.29 are preserved constant ($B/h = \text{const}$, $\rho_{\text{bulk}}gB/E = \text{const}$). The properties of a bulk material correspond to coal, selected as an example and described in Section 2.4. As for the belt properties, the data, given in Table 4.9 for fabric belt Sample 3 was used, except to the longitudinal length of a belt that was accepted equal to a conveyor pitch $l = l_c = 1\text{m}$.

Figure 6.18 shows the results, obtained for the CFs parameterized versus the filling degree, varied within the range $k_Q = 0.05\dots 1$. In addition, Fig. 6.18 reflects the impact of the approach selected for the coefficient C^K to describe the bulk material load distribution along the conveyor pitch. In particular, the curves are plotted using not only Gushchin approach, but also approach of Krause and Hettler, Wheeler-Mulani, and the approach that assumes constant active stress state along the whole conveyor pitch (see Section 5.4.4 and Eq. 6.27 for the values).

The analysis of the graphs plotted in Fig. 6.18 shows that the approach that assumes constant active stress state ($K_a = \text{const}$) implies the minimal horizontal load component, dominated by the vertical load component. The approach of the Krause and Hettler, on opposite, implies the highest lateral load, compared to the vertical one, since it was developed for the conventional trough belt conveyor (see Section 5.4.4). The trough belt conveyors, naturally exhibit larger lateral deformations of a belt in between the carry spacing than PBCs do. Compared to the extreme approaches, the approach of Gushchin and Wheeler-Mulani

implies the intermediate lateral loads and the resultant values of the CFs. Taking into account that there is no experimental results are available for the load distribution of a bulk material inside the PBCs, the choice for the further analysis is made for the non-extreme Gushchin approach, since it was based on the experimental results, performed for deep trough belt conveyors with the cross section close to an open pipe.

Considering the effect of k_Q on the CFs parameterized, for the small filling degree, the effect of the vertical bulk material load is comparable to its horizontal load component, that is why it is possible to observe the contact loss for the top forces $F_2 = F_6 = 0$, whereas the bottom force F_4 becomes higher than the forces $F_3 = F_5$.

However, with the increase of the filling degree k_Q , the effect of horizontal load component grows and prevails the vertical load component (except for the $K_a = \text{const}$ approach). This leads to the appearance of a positive CFs ($F_2 = F_6$) > 0 and increase of the CFs $F_3 = F_5$. Since the distribution of the horizontal load component for large values k_Q implies more significant values towards the bottom of the pipe, as a result, the contact loss can be observed for the CFs $N_1' = N_1''$ and F_1 , whereas the lateral bottom forces $F_3 = F_5$ become larger than the bottom CF F_4 .

The graphs presented in Fig. 6.18 are obtained for the reference belt slenderness $B/h \approx 71.38$ and $\rho_{\text{bulk}}gB/E = \text{const}$. However, the change in B/h -ratio and the load parameter $\rho_{\text{bulk}}gB/E$ can cause different curves of the CFs parameterized than the ones provided in

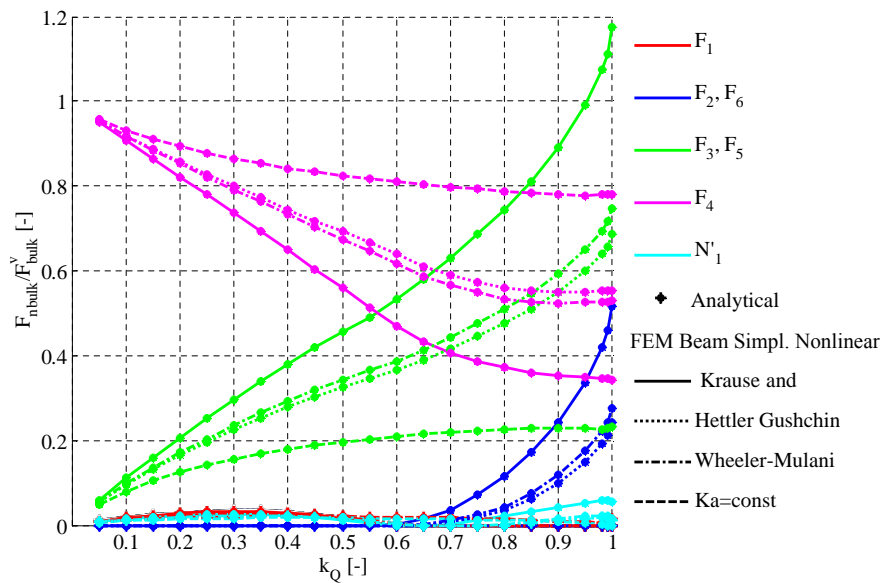


Figure 6.18: Effect of the PBC cross-sectional filling degree k_Q on the CFs parameterized, obtained for the reference $\rho_{\text{bulk}}gB/E = \text{const}$, using analytical approach and the Beam Simplified Model (nonlinear analysis). The data is presented, using four different approaches that describe the bulk material load distribution along the conveyor pitch, characterized by the coefficient C^K -values, given in Eq. 6.27.

Fig. 6.18.

After the character of a bulk material load is analyzed and the parametric dependence function is obtained, it becomes possible to consider a loaded PBC, subjected to a combination of the load from the bulk material, the load from the belt weight, and the load from the belt bending stiffness. The CFs, obtained for loaded PBC are investigated in the next section.

6.7.2 Functional dependence for a loaded pipe conveyor

In order to obtain a general functional dependence of CFs for a loaded PBC, the linearized analytical model, described in Chapter 5, is used as a starting reference. Based on the Principle of Superposition, the CF at the each idler roll can be evaluated as a sum of the CFs, determined from the each of the load, applied to a structure independently. Taking into account that the load from belt bending stiffness, the load from belt weight, and the load from bulk material are involved together in the problem, in this case:

$$F_n = F_{nbst} + F_{nbw} + F_{nbulk}. \quad (6.30)$$

Substituting the general functions for the CFs F_{nbst} , F_{nbw} , and F_{nbulk} , provided for the linear solution in Eq. 6.11, Eq. 6.14, and Eq. 6.28), respectively, the CFs for a loaded PBC can be rewritten as follows:

$$F_n = EA f_n^{bst} \left(\frac{B}{h} \right) + q_{bw} B f_n^{bw} \left(\frac{B}{h} \right) + F_{bulk}^v f_n^{bulk} \left(\frac{B}{h}; k_Q \right). \quad (6.31)$$

Both parts of the Eq. 6.31 can be divided into the axial stiffness EA . Substituting the expression for a total bulk weight F_{bulk}^v and after some transformations, Eq. 6.31 becomes the following:

$$\frac{F_n}{EA} = f_n^{bst} \left(\frac{B}{h} \right) + \frac{q_{bw} B}{EI h} f_n^{bw} \left(\frac{B}{h} \right) + \frac{1}{4\pi} \frac{\rho_{bulk} g B}{E} k_Q \frac{B}{h} f_n^{bulk} \left(\frac{B}{h}; k_Q \right). \quad (6.32)$$

This expression for CFs can be rewritten in a more laconic function dependence:

$$\frac{F_n}{EA} = f_n^{loaded} \left(\frac{B}{h}; \frac{q_{bw}}{EI}; \frac{\rho_{bulk} g B}{E}; k_Q \right). \quad (6.33)$$

As it can be seen, for a loaded PBC, the CFs become a function of a belt slenderness B/h , belt's axial stiffness EA , and the load parameters that characterize the ratios of a belt weight or a bulk weight versus the belt's stiffness, and the PBC cross-sectional filling degree k_Q .

In order to visualize the dependence in Eq. 6.33, the CFs are obtained using the analytical model and the FEM Beam Simplified Model (linear and nonlinear solution) for a PBC half-filled with the coal with carry spacing of $l = l_c = 1\text{m}$. The properties of the bulk material are described in Section 2.4, whereas the properties of a belt correspond to the reference parameters (see Sample 3 in Table 4.9). The coefficient C^K for the longitudinal development of a lateral bulk material load is determined using Gushchin approach.

The results, illustrated in Fig. 6.19, represent the parameterized CFs versus the belt slenderness varied within the range, established in Section 2.5.2 for conveyor belts. Figure

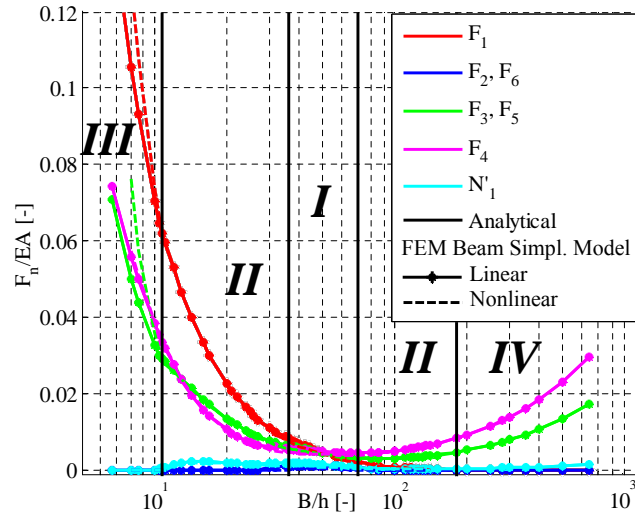


Figure 6.19: The functional dependence of CFs versus the belt slenderness according to Eq. 6.33, obtained using the analytical approach and the Beam Simplified Model, (linear and nonlinear analysis). The results are provided for $\rho_{\text{bulk}}gB/E = \text{const}$, $q_{\text{bw}}/(EI) = \text{const}$, and the cross sectional filling degree $k_Q = 0.5$.

6.19 was obtained by combining the parts of the graphs, denoted as **I**, **II**, **III**, and **IV**, characterizing the appearance of a contact loss for the full variation range of a belt slenderness B/h . Each of the area is determined independently and signifies the following possible behavior of a loaded pipe conveyor belt: **I** when all the CFs are positive, **II** when there is a contact loss for the CFs $F_2 = F_6 = 0$, **III** - when the contact loss is detected for the CFs $F_2 = F_6 = 0$ and $N_1' = N_1''$; **IV** - for the contact loss only for $F_1 = 0$.

To perform a qualitative analysis on how the change of the input design parameters reflected in Eq. 6.33 can influence the resultant dependence curves for CFs, the reference Fig.6.19 is presented in a logarithmic scale in Fig. 6.20, providing an ability to detect the difference for the smaller values $F_n/EA = 0..0.02$. This is especially important, as the contact loss for F_2 occurs exactly in this range.

The analysis of Fig. 6.20 shows that the linear analytical model and the linear solution of the Beam Simplified Model are very close and almost coincide. This close agreement with the FEM shows that the analytical approach is sufficiently precise for the linearized problem. As for the nonlinear solution, the highest with linear solution can be detected for the CFs with smaller values ($F_2 = F_6$ and $N_1' = N_1''$), whereas the CFs with larger values (F_4 , $F_3 = F_5$, and F_1) are quite close. Moreover, the increase of a belt slenderness for thinner belts deteriorate the ability to converge of the nonlinear model. This is due to the fact that thinner belts exhibit larger structural deformations and higher tendency of a belt to collapse.

The impact analysis is performed, considering the impact of $\rho_{\text{bulk}}gB/E$ and $q_{\text{bw}}/(EI)$, and the PBC cross-sectional filling degree k_Q on CFs evaluated.

The influence of the load parameter from the belt weight $q_{\text{bw}}/(EI)$ is investigated first. The CFs are obtained for $k_Q = 0.5$, using the same reference parameters for the belt and bulk, as in Fig. 6.20, but for the double increased $2q_{\text{bw}}/(EI)$ and half-reduced $q_{\text{bw}}/(2EI)$

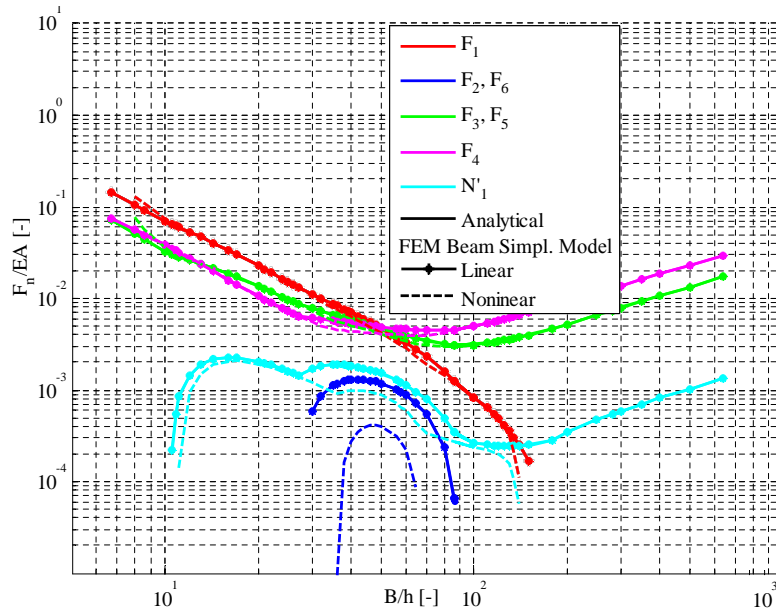


Figure 6.20: The functional dependence of CFs versus the belt slenderness according to Eq. 6.33, obtained using the analytical approach and the Beam Simplified Model, (linear and nonlinear analysis). The results are provided for $\rho_{\text{bulk}}gB/E = \text{const}$, $q_{\text{bw}}/(EI) = \text{const}$, and the cross sectional filling degree $k_Q = 0.5$. The results represent the same graph as provided in Fig. 6.19, but plotted in logarithmic scale.

the oad-parameter. At the same time the parameter from the bulk material load is preserved constant $\rho_{\text{bulk}}gB/E = \text{const}$. The load parameters needed were achieved by changing the belt line mass q_{bw} , length of a conveyor pitch l , and the Young's modulus E , one by one and in various their combinations. As soon as $q_{\text{bw}}/(EI) = \text{const}$ and $k_Q = \text{const}$, the results for CFs follow to the same corresponding curves, confirming the functional dependence, given in Eq. 6.33 for both linear and nonlinear solution.

Moreover, the comparison of the graphs, illustrated for $q_{\text{bw}}/(2EI)$ and $2q_{\text{bw}}/(EI)$ in Fig. 6.21 and for the reference $q_{\text{bw}}/(EI)$ in Fig. 6.20, indicates that the no-contact loss range of a belt slenderness is wider for a smaller ratio of $q_{\text{bw}}/(EI)$. Indeed, the largest load parameter $2q_{\text{bw}}/(EI)$ causes that all the CFs remain positive and non-equal to zero at the belt slenderness range $38 < B/h < 57$, whereas the smallest parameter $q_{\text{bw}}/(2EI)$ offers a wider range of $35 < B/h < 80$ for the nonlinear solution.

In other words, the selection of a lighter or a stiffer belt can positively influence the belt's pipe-ability. In addition, it is possible to see that the correlation between the linear solution (from both analytical model and the FEM Beam Simplified Model) and the nonlinear results (only the Beam Simplified Model) is better for smaller $q_{\text{bw}}/(EI)$. This is due to that fact that deformations of stiffer and lighter belts are smaller and closer to the ones accepted in the linear models.

The same analysis is performed, considering the impact of a bulk material load-parameter

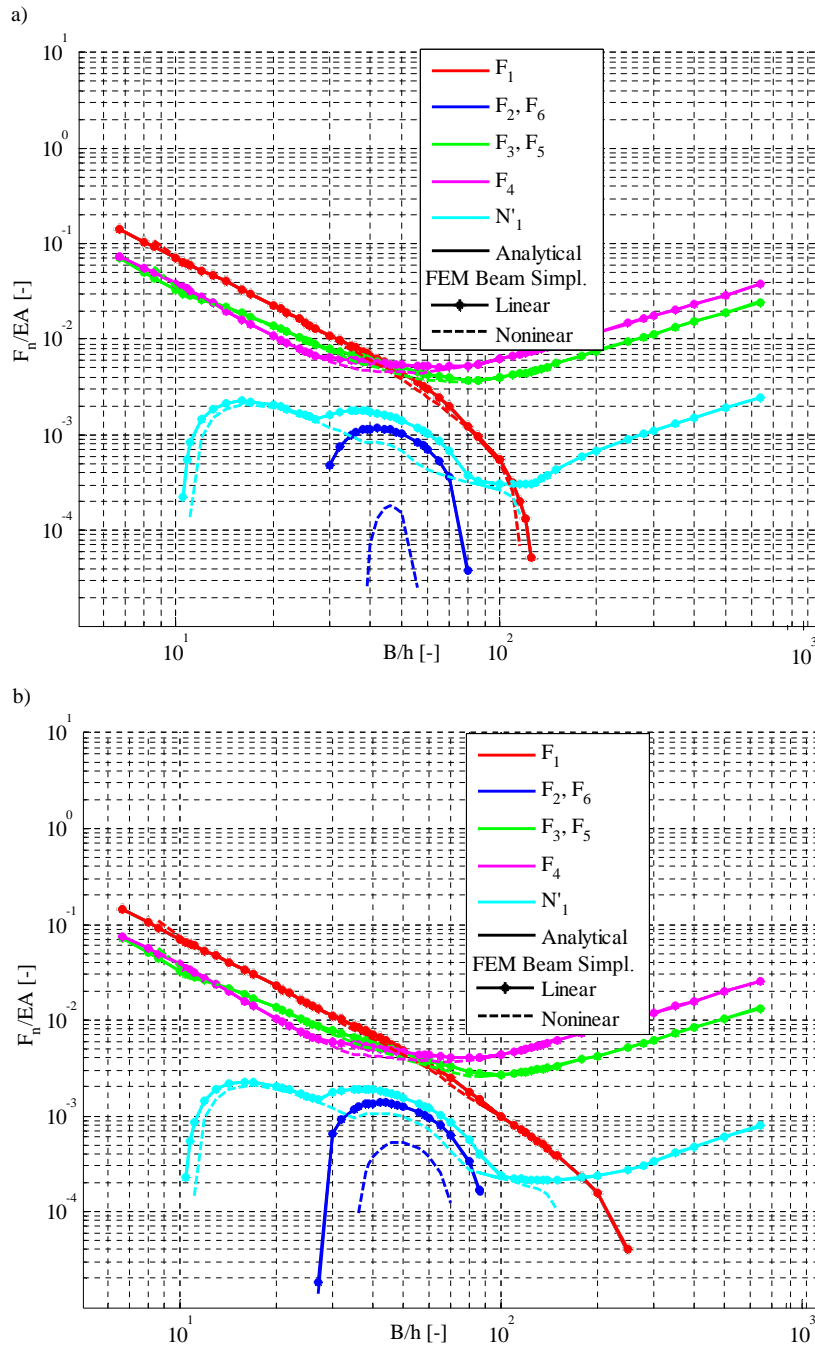


Figure 6.21: Comparison of the functional dependences for CFs parameterized according to Eq. 6.33), obtained using analytical model and also the Beam Simplified Model (linear and nonlinear analysis) for the loaded PBC, half-filled with coal ($k_Q = 0.5$). The results are provided for a) $q_{bw} / (2EI)$; b) $2q_{bw} / (EI)$, whereas $\rho_{bulk} g B / E$ is preserved constant for all the variation range of B/h .

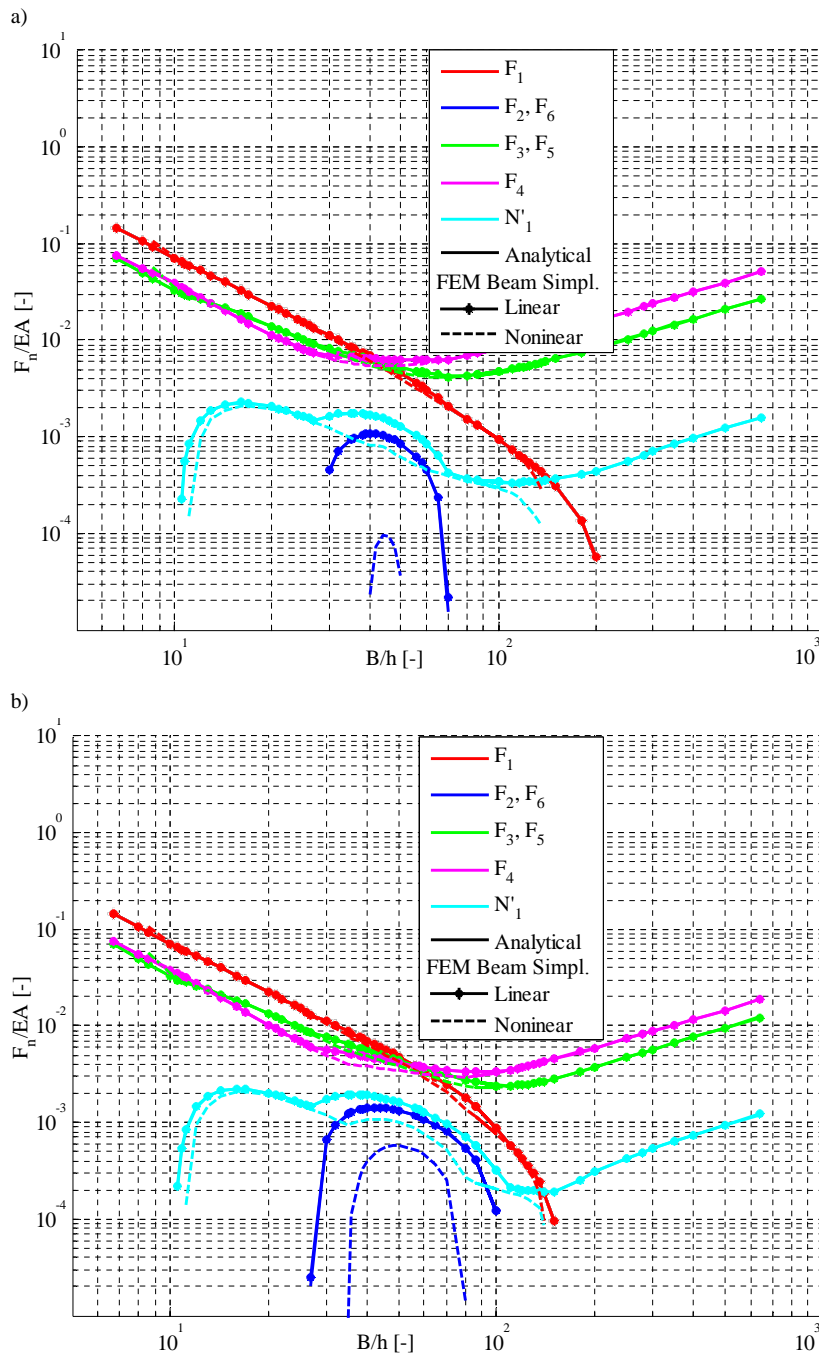


Figure 6.22: Comparison of the functional dependences for CFs parameterized according to Eq. 6.33, obtained using analytical model and also the Beam Simplified Model (linear and nonlinear analysis) for the loaded PBC, half-filled with coal ($k_Q = 0.5$). The results are provided for a) $\rho_{\text{bulk}}gB/(2E)$; b) $2\rho_{\text{bulk}}gB/E$, whereas $q_{\text{bw}}/(EI)$ is preserved constant for all the variation range of B/h .

$\rho_{\text{bulk}}gB/E$ change on CFs parameterized. For this case, on opposite, the impact of $q_{\text{bw}}/(EI)$ parameter is preserved constant as well as the filling degree $k_Q = 0.5 = \text{const}$, as for the reference case.

Similarly, the results are attained and compared for different cases, solved using double increased $2\rho_{\text{bulk}}gB/E$ and half reduced bulk material load-parameter $\rho_{\text{bulk}}gB/(2E)$. This was performed by changing a bulk material density ρ_{bulk} , the Young's modulus E of a belt, and belt width B (keeping the value of B/h needed). The change is performed for each parameter one by one and in their various combinations. The analysis shows that no matter how these design parameters are changed, as soon as $k_Q = \text{const}$, $q_{\text{bw}}/(EI) = \text{const}$, and $\rho_{\text{bulk}}gB/E = \text{const}$, the CFs yield the same dependence curves, following Eq. 6.33.

Figure 6.22 illustrates the CFs parameterized versus the belt slenderness, received for the parameters $\rho_{\text{bulk}}gB/(2E)$ and $2\rho_{\text{bulk}}gB/E$ from the bulk material load. As it can be seen, the change of the parameter $\rho_{\text{bulk}}gB/E$ with the same factor of two has a greater effect on CFs than the impact of a $q_{\text{bw}}/(EI)$ from the belt weight (compare Fig. 6.22 with Fig. 6.21).

In addition, it is possible to conclude that the increase of the parameter from the bulk material load $\rho_{\text{bulk}}gB/E$ can significantly deteriorate belt's pipe-ability by diminishing the range of a belt slenderness where the PBC exhibits all six positive CFs. In particular, a satisfactory pipe-ability can be attained using belts with slenderness of $39 < B/h < 56$ for $2\rho_{\text{bulk}}gB/E$ and with slenderness $32 < B/h < 86$ for $\rho_{\text{bulk}}gB/(2E)$.

This observation allows one to conclude that belt tends to form a more stable pipe shape, if it has sufficient belt stiffness, is not extensively wide and/or if it is designated to operate with lighter bulk material. The design recommendation would be for the preference with more stiff, lighter and/or less wide belts, if heavy bulk material has to be conveyed.

All the functional dependences of CFs, presented above were obtained only for the half-filled PBC with $k_Q = 0.5$. The next step of the impact analysis, is to account the effect of the cross-sectional filling degree change. If all the load parameters are assumed constant $q_{\text{bw}}/(EI) = \text{const}$, $\rho_{\text{bulk}}gB/E = \text{const}$, the effect of a filling degree k_Q can be considered analogical to the previous cases for the belt slenderness varies.

Figure 6.23 contains the resultant curves of CFs, obtained for the reference PBC with a conveyor pitch of 1 loaded with coal at 25% and also at 75% of a cross-sectional filling.

Comparison of the graphs, illustrated in Fig. 6.23 for $k_Q = 0.25$ and $k_Q = 0.75$ and also in Fig. 6.20 for $k_Q = 0.5$ indicates that with the increase of a filling degree, the belt's pipe-ability deteriorates. Moreover, the difference between the linear and nonlinear solution also increases for higher values of k_Q , since the belt structure exhibits larger deformations that are far more different from the linear ones. That is why, for $k_Q = 0.75$, the linear solution exhibits again the positive CFs for very thin belts with $B/h > 250$, whereas the nonlinear FEM solution has no convergence and predicts a complete collapsing of a belt's pipe.

Noteworthy to mention that the analytical model, elaborated in Chapter 5 and also the FEM models, developed in this chapter, determine the CFs for loaded PBC, considering an actually empty belt structure, subjected to the external load to reproduce the impact of a bulk material. However, the actual problem, observed in practice, implies a mutual relation of a two-component system "belt-bulk", where the stress-strain state of a bulk inside the belt's pipe inextricably linked to the stress-strain state of a belt. As a result, it might appear that for the higher filling degree, the belt filled with the bulk material exhibits smaller deformations and, as a result, the CFs, compared to the ones predicted by the analytical and the FEM

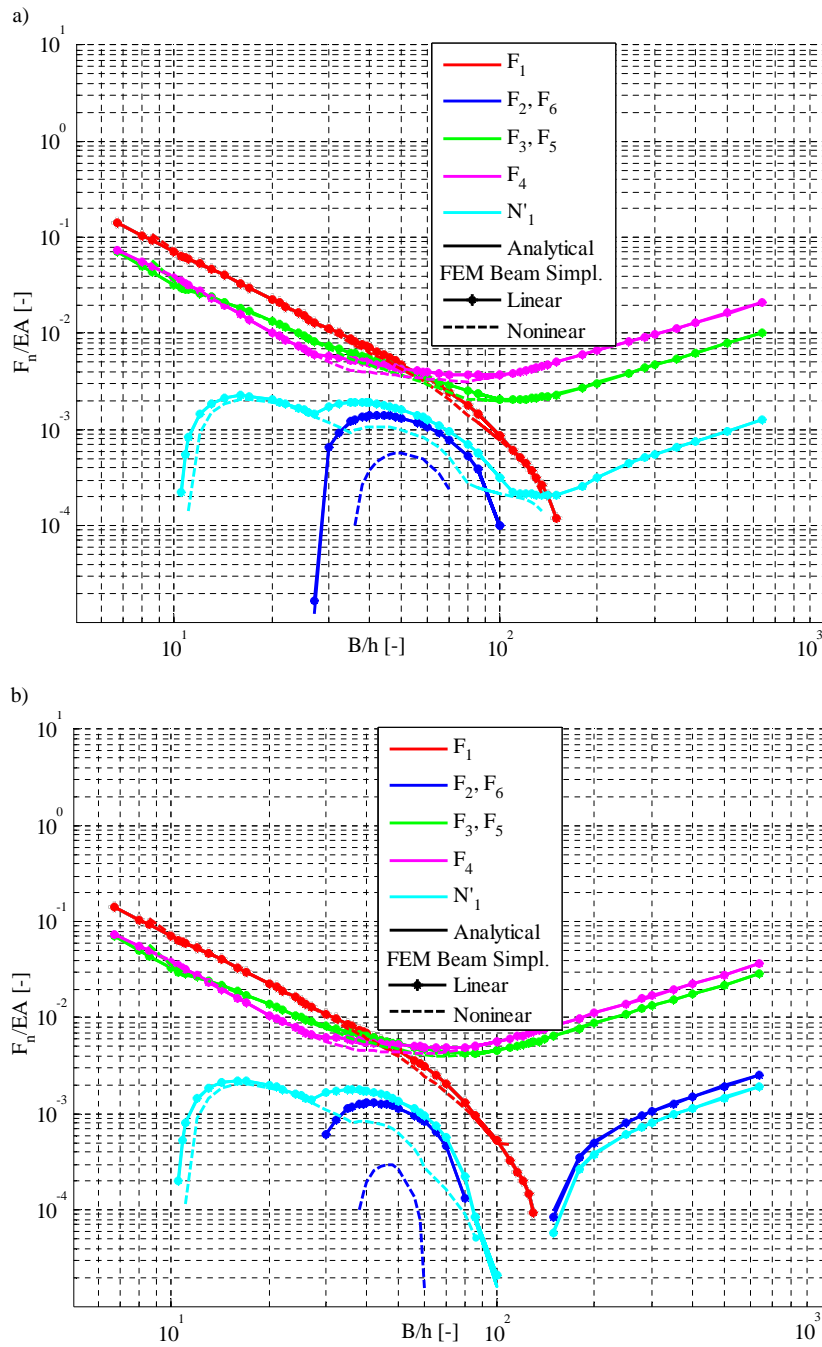


Figure 6.23: Comparison of the functional dependences for CFs parameterized according to Eq. 6.33, obtained using analytical model and also the Beam Simplified Model (linear and nonlinear analysis) for the PBC loaded with coal. The results are provided for a) $k_Q = 0.25$; b) $k_Q = 0.75$, whereas $q_{bw}/(EI) = \text{const}$ and $\rho_{\text{bulk}}gB/E = \text{const}$ are preserved constant for all the variation range of B/h .

models, as the latter actually consider only a belt itself, subjected to the external load.

Summing up for the overall Section 6.6, it is possible to state that the appearance of a PBC contact loss between the belt and the supporting idler rolls is influenced by the filling degree k_Q of a conveyor cross section and the type of a bulk material transported and also by the belt's properties and geometry selected. In order to improve belt's pipe-ability, the belt has to be selected in a such a way, aiming to minimize the value of the load ratios $\rho_{\text{bulk}}gB/E \rightarrow \min$ and $q_{\text{bw}}/(EI) \rightarrow \min$ to operate at smaller ratios of the filling degree k_Q (if possible).

Noteworthy to emphasize that the present approach of determining the CFs is limited to the linear-elastic material of a belt. This implies the small strain limitation for the belt. The present analysis does not provide the numerical recommendations for this requirement, leaving it for the future research. However, the limitation of 5% belt strain, accepted as for the troughability test approach deemed to be consistent for the analysis performed and suitable for the strain range of a pipe conveyor belt under normal operational conditions (see Section 3.2).

6.8 Conclusions

This chapter answers the research question on how to determine PB CFs. For this purpose, the FEM analysis is used. To determine the CFs, three FEM models are proposed: the Beam Simplified Model, the Beam Step Model and the Shell Step Model. In addition, the chapter provides a comparison of the results, obtained using the experimental approach, performed in Chapter 4, the analytical approach, developed in Chapter 5, and all the FEM models elaborated.

The comparison of CFs for the case study in Section 6.5 indicates that the FEM models (the Shell Step Model and the Beam Step Model) are in close agreement with the experiment. At the same time, the CFs from the Beam Step Model and the Beam Simplified Model correlate with each other and also are in agreement with the analytical model. In this case, it is possible to state that the FEM models and the analytical model are validated with the experiment for the case study.

The impact analysis performed using the analytical and the FEM models for different input parameters allows one to conclude that, at certain PBC designs, a more simple analytical model that is more attractive for the practical use determines the CFs with the feasible accuracy, compared to a FEM solution that is more complex, time consuming, and less attractive in terms of an application. In addition, the simple analytical model and also the complex FEM models predict a similar dependence trend of CFs parameterized with respect to the change in input parameters.

The case study comparison in Section 6.5 and also the impact analysis, performed in Section 6.6.2 for the load from the belt bending stiffness, conclude that it is possible to represent a belt stress state that appears from folding the belt from a flat shape into a pipe shape as an additional external load, aiming to determine PBC CFs. For this purpose, only the expansion concentrated moments M_{bst} , applied at the belt edges can be used. Other methods, proposed in Chapter 5, like using distributed expansion load q_{bst} and also distributed expansion load q_{bst} together with the concentrated forces $Q_{1\text{bst}}$, $Q_{2\text{bst}}$, do not give satisfactory results.

Present chapter provides an impact analysis, answering the research questions on which parameters of a PBC system influence the CFs and what is their effect. For this purpose, a function dependences between the CFs and the participating PBC design parameters are derived, using the analytical model as a basis.

For an empty PBC, the functional dependence of CFs parametrized with respect to the belt's axial stiffness EA represents a function of a belt slenderness B/h and the load ratio from the belt weight $q_{bw}/(EI)$:

$$\frac{F_n}{EA} = f_n^{\text{empt}} \left(\frac{q_{bw}}{EI}; \frac{B}{h} \right).$$

For a PBC loaded with a bulk material, in addition to the parameters mentioned, the functional dependence of CFs incorporates the effect of the ratio from the bulk material load $\rho_{\text{bulk}}gB/E$ and PBC cross-sectional filling degree k_Q :

$$\frac{F_n}{EA} = f_n^{\text{loaded}} \left(\frac{B}{h}; \frac{q_{bw}}{EI}; \frac{\rho_{\text{bulk}}gB}{E}; k_Q \right).$$

The function of CFs for loaded PBC converges to the dependence for an empty PBC, if the bulk density and the cross-sectional filling degree are assumed equal to zero.

In general, with the increase of the load parameters $q_{bw}/(EI)$ and $\rho_{\text{bulk}}gB/E$, the CFs increase, however at certain combinations of their values, one or more CFs can become equal to zero (a contact loss). For the linear solution, these parameters have a proportional effect on CFs parameterized.

The impact of a belt slenderness B/h , i.e. the ratio between the belt width versus the belt thickness, has a significant effect on CFs and need to be carefully controlled. Despite the fact that such ratio is a well-known parameter used in mechanics of materials to characterize the structural behavior (i.e. domination of shear, stretching or bending), conveyor belting manufacturers do not use this parameter as a criteria for the belt design selection. As a result, the belts manufactured can exhibit quite a variation for width and thickness dimensions due to the insufficient requirement for their precision in manufacturing process. The present chapter indicates that, in order to ensure sufficient pipe-ability of a conveyor belt, the slenderness ratio B/h has to be carefully controlled.

The satisfactory design of a belt has to guarantee the operation without a contact loss, when the belt is empty and also loaded with a cross-sectional filling degree desired (usually around $k_Q = 0.5...0.75$) with certain margin allowance. The results for CFs obtained in present chapter allows one to conclude that the weakest position for a contact loss occurs for a lateral top rolls for CFs F_2 , or F_6 . There, the contact loss tends to appear the first. If the belt's pipe-ability is deteriorated further, after $F_2 = F_6$ become equal to zero, it is possible to expect the next contact loss at the top roll F_1 .

The preference for a PBC design selection, aiming to avoid a contact loss and ensure sufficient belt's pipe-ability, has to minimize the values of the load ratios $\rho_{\text{bulk}}gB/E \rightarrow \min$ and $q_{bw}/(EI) \rightarrow \min$. If a conveyor does not exhibit sufficient pipe-ability, especially expected when a heavy bulk material has to be transported, the belt design can be chosen towards lighter and transversely stiffer belts with smaller belt width. Moreover, the belt slenderness has to be taken into account. The extreme values are not preferable, as significantly thick belts (with approximate $B/h < 30$) tend to exhibit a contact loss at the position force F_2 and

F_6 , whereas thin belts ($B/h > 130$) can fully collapse a pipe with the contact loss with all three top rolls. In this case, thinner belts with higher ratio of B/h requires higher stiffness to form a pipe shape. A better pipe-ability is observed for approximate slenderness ratios ($35 < B/h < 75$), however the limits can be negotiated, considering the impact of all the participating parameters together.

The future research has to be focused in performing more experiments for better validation of the analytical model for both empty PBC and loaded with a bulk material. In addition, the numerical recommendations has to be developed for the usage limitation of the present models (both analytical and the FEM), satisfying 5% small strain for the linear-elastic belt material assumed.

The present model uses a simplified analytical model and also the FEM models. The Shell Step model incorporates higher level of the problem complexity towards the one, observed in practice. The future research can be focused in investigating the impact of a more complex effects on CFs using the FEM models, by incorporating the presence of a belt overlap, belt's nonlinear elasticity, the rheological properties of a belt constituting rubber, non-uniform design of a belt along the width and also thickness, belt's orthotropic properties and effect of a belt tension with respect to the length of a conveyor pitch, actual presence of a bulk material and its behavior inside the pipe. For all these complex problems, the analytical model proposed in Chapter 5 can be used as a starting reference point for the validation and base for the impact analysis for all the numerical models used.

As stated, above, increasing the belt lateral bending stiffness can improve belt's pipe-ability. At the same time, high bending stiffness can reason an increase in PBC CFs that escalate the IRR of a PBC system. The significant IRR affects the energy consumption of entire conveyor, rebounding in its capital and maintenance costs. The next Chapter 7 determines the IRR of a PBC and investigates which parameters have an effect on the IRR and how this source of the energy losses can be diminished.

Chapter 7

Indentation Rolling Resistance *

"The Law of conservation of energy tells us we can't get something for nothing, but we refuse to believe it".

— I. Asimov, *Book of Science and Nature Quotations*

As it was mentioned in Chapter 1, one of the major disadvantages of a PBC design is that this type of a conveyor system exhibits high levels of energy consumption. The major part of PBC energy losses appears from the IRR. The present chapter provides an approach to calculate the IRR for PBCs, incorporating a three-dimensional generalized contact model with multiple Maxwell parameters. The viscoelastic properties of the belt's rubber are determined experimentally, using a DMA tests.

The IRR depends not only on rheological properties of belt rubber, but also on a number of other PBC design parameters and on the CFs, exerted on the idler rolls. The previous Chapters 4, 5, and 6 introduced a new approach to determine the PBC CFs, whereas this chapter incorporates these CFs in the indentation contact model. This allows one to trace how all the participating design parameters of a PBC affect the system's IRR energy losses.

A PBC belt needs a higher bending stiffness, compared to the conventional trough belt conveyors, to ensure a stable pipe-ability. The CFs are increased due to the presence of an additional expansion load from folding a belt from a flat shape into a pipe shape. The belt's structural stiffness and the load from the belt's bending stiffness depend on the effective modulus of elasticity, determined from the troughability test, as it is recommended in Chapter 3. This chapter discusses how to design a PBC system aiming to limit the IRR and not deteriorate the belt's pipe-ability at the same time.

7.1 Introduction

Chapter 1 indicates that high energy consumption can be considered as one of the major problems of a PBC system. This disadvantage diminishes the significance of other positive aspects of a PBC design, like geometrical flexibility of a route and ability to convey "difficult"

*The Chapter is written based on the publications of Zamiralova and Lodewijks [256, 258] Zamiralova *et al.* [266]

bulk materials sustainably in a completely enclosed transport system. The high energy consumption affects the choice and costs of installation parameters of the conveyor, resulting in more strong/ heavy/ powerful components. As a result, the overall conveyor system becomes more expensive.

The energy losses of a conveyor system significantly depends on the rolling resistance forces. The total rolling resistance force, which is distributed over each roll of the idler set, represents the sum of the resistance forces due to the rotational inertia of the idler rolls, the flexural deformation of the material and the belt, and the IRR due to the indentation of the idler rolls into the belt rubber surface.

The IRR of a PBC is higher than the IRR of a conventional open trough belt conveyor. In case of the latter, it may already form up to 61% of the total rolling resistance for a horizontal conveyor [92]. One of the major reasons is that CFs of a PBC, that influences the IRR, are higher due to the presence of additional expansion load from folding belt from a flat shape to a pipe shape.

In order to decrease the IRR for PBCs, it is important to quantify the IRR and analyze which participating PBC design parameters has the greatest influence on this source of the system's energy losses, aiming to limit their impact. This allows one to develop recommendations for more efficient design of a PBC that can have less energy consumption from the IRR being decreased, whereas other advantageous design aspects are not affected.

7.2 Overview and choice of the model

In order to evaluate the IRR for PBCs and obtain accurate results, the correct indentation model should be selected. The chosen model should be computationally friendly and should give an appropriate level of accuracy. In general, the existing indentation models, developed for belt conveyors, can be classified based on the assumptions made to describe the rheology of the rubber (material model) and the contact deformation (deformation model).

Considering the material model, the indentation phenomenon needs to be explained in terms of the viscoelastic characteristics. An absolutely elastic material recovers completely to the initial state, as soon as the stress that caused that deformation is removed. The belt's elasticity can be described analytically as a Hookean string with certain stiffness, denoted here as E_M , as shown in Fig. 7.1a. Viscous material, on the contrary, exhibits time dependence to the strain and can be represented by the dash-pot with a certain damping factor η_M (see Fig. 7.1b). The body with viscoelastic properties exhibits both viscous and elastic characteristics when undergoing the deformation. A viscoelastic body comes back to the initial state with time delay, causing the energy dissipation.

The viscoelastic properties can be represented by a combination of the elastic strings and viscous dash-pots, using, for example, the simplest Maxwell Model (see Fig. 7.1c) or equivalent Voight model (see Fig. 7.1d) as a basis. The most popular representation of a viscoelastic material used for quantifying the IRR for belt conveyors, belongs to the so-called SLS-model (standard linear solid) with three Maxwell parameters, illustrated in Fig. 7.1e. The model consists of two strings and one dash-pot, characterized by one relaxation time equivalent to $\tau = \eta_{M1}/E_{M1}$. The Maxwell model can be expanded by incorporating multiple $(2n + 1)$ Maxwell components, comprising a Generalized Maxwell Model depicted in Fig. 7.1c) or equivalent Voight model (see Fig. 7.1f).

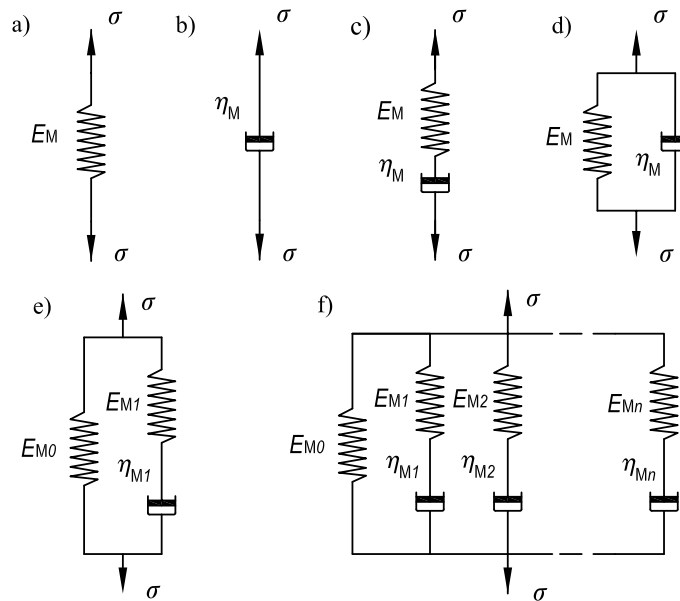


Figure 7.1: a) Hookean string representing an absolutely elastic body; b) dash-pot modeling the material's viscosity; c) a viscoelastic Maxwell model, consisted of a dash-pot and a string; d) Voigt viscoelastic model; e) three parameters viscoelastic Maxwell model (SLS-Model); f) viscoelastic Generalized Maxwell Model.

Considering the deformation model, the difference in existing approaches is the way how the stress-strain characteristics are described in the backing layer of the viscoelastic belt covers. The simplest approximation used is a Winkler foundation model (see e.g., May *et al.* [151], Lodewijks [136, 137]), schematically shown in Fig. 7.2. The model implies a number of viscoelastic strings placed on the rigid base, like a “mattress”. Each of the viscoelastic string can be represented by the three-parameter Maxwell Model for the simplest case or by the Generalized Maxwell Model with multiple Maxwell elements, if needed. The strings do not interact with each other. As a result the Winkler foundation depicts only the compression stresses and does not take into account the internal shear. The thickness of the string mattress layer corresponds to the thickness of a belt's rubber layer that is in contact with the idler rolls.

The alternative deformation model used to evaluate the IRR, is the viscoelastic half space (see Hunter[111]) that represents the material base with infinite thickness (see Fig. 7.2b). This model takes into account the impact of shear in addition to the compression stress distribution. The IRR predicted by the viscoelastic half space model appears to be higher than determined with Winkler foundation.

Using the material and deformation models described, various researchers have determined the IRR for flat-belt and a conventional open trough belt conveyor (see e.g., Jonkers [119], Spaans [215], May *et al.* [151], Lodewijks [136, 137], Rudolphi [199], Rudolphi and Reicks [200]), pouch (Nuttall [185], Nuttall *et al.* [186]) and also PBCs (Dmitriev and Sergeeva [58], Sergeeva [208, 210]).

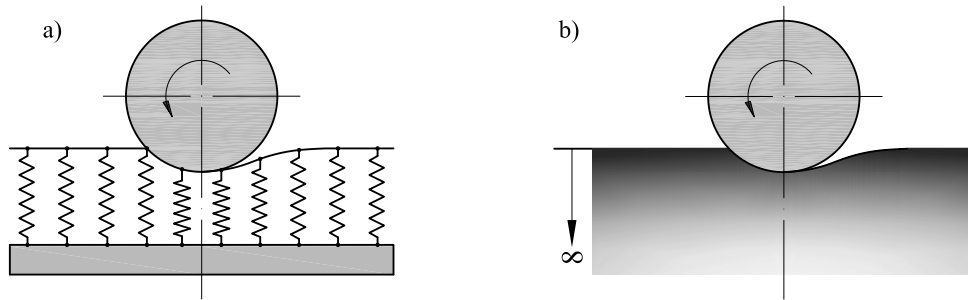


Figure 7.2: a) Winkler foundation, consisted of viscoelastic strings; b) the viscoelastic half space with infinite thickness.

Two of the most commonly used indentation models were developed by Jonkers [119] and Spaans [215] for a flat-belt and open trough belt conveyors. The researchers prescribe the indentation force in terms of the vertical load, instead of the geometrical indentation depth. Both approaches use a three-parameter Maxwell model, and assume that the indentation strain profile is symmetrical with respect to the central line of the idler and does not depend on the belt speed. As shown by Lodewijks [136, 137], these assumptions lead to the overestimation of the total IRR force and does not reflect the actual phenomenon. May *et al.* [151] also presented a model for the calculation of the IRR forces by using a 3 parameter Maxwell model with a single relaxation time using Winkler foundation for the deformation model. Hunter [111] used a half space plane approach in the description of his indentation model. This allowed for the inclusion of the creep-response viscoelastic behavior.

Lodewijks [136, 137] developed an approach similar to May *et al.* [151], and added the friction correction factor. This factor takes into account Hunter's model [111] with the shear stress between adjusted Winkler foundation "matrass" strings. Lodewijks [136, 137] also used a three-parameter Maxwell model. These three Maxwell parameters were obtained by approximating the loss and storage moduli of the rubber from the three-point bending DMA test analysis).

Rudolphi [199], Rudolphi and Reicks [200] used a two-dimensional model with an expanded generalized Maxwell model. Maxwell parameters were obtained from DMA tests, by approximating experimental results with Prony series. However, as noted by Lodewijks [136, 137], a three-parameter Maxwell model, with a single relaxation time, provides a simple and sufficient description of the contact phenomenon between the idler rolls and a flat belt.

Wheeler [246] determined the IRR factor for flat-belt conveyors by using a computational approach with a FEM. Analytical results about the energy losses of the flat belt due to the IRR were compared with experimental data by means of special recirculating belt conveyor test facility. The researcher measured the total horizontal force acting on the idler roll due to the IRR.

Another numerical approach was described by Qiu [192] for a two dimensional viscoelastic model. The researcher introduced boundary elements in the computational model and represented the solution with a set of Fourier series. Coefficients were related to the viscoelastic shear loss and storage moduli of the rubber. The disadvantage of the numerical

approach is that the solution for the IRR factor cannot be represented as a compact function of input parameters explicitly and need to be computed every time for the certain critical input parameters.

Nuttall [185], Nuttall *et al.* [186] developed a model to determine the IRR for pouch belt conveyors. The researchers indicated that the two-dimensional indentation models with one relaxation time, used to simulate the contact between the roll and flat belt, are not suitable to reflect the contact model between the curved surface of a rigid idler roll and curved surface of a viscoelastic belt rubber inherent to pouch belt conveyors. Hence, Nuttall [185], Nuttall *et al.* [186] constructed a new three-dimensional contact model with multiple relaxation times to model different deformation rate at the contact region. For this purpose, the Generalized Maxwell Model was incorporated. The researchers provided the results for 3 and 7 Maxwell parameters, which were obtained from the rheological experimental analysis of the storage modulus, loss modulus and loss factor of the pouch conveyor belt cover rubber.

For PBCs, preliminary values for the dimensionless IRR factor were presented by Dmitriev and Sergeeva [58], Sergeeva [208, 210]. The researchers used Jonker's indentation model [119] as a basic approach. As it was mentioned above, Lodewijks [136, 137] proved, that this approach comprises an assumption that overestimates the IRR factor. It assumes that the contact profile is symmetrical and does not depend on the belt speed. In addition, the Jonker's model incorporates a three-parameters Maxwell model with one relaxation time, suitable to reflect the contact between the idler roll and a flat belt. However, for PBCs, a three-dimensional indentation contact model is required, since the viscoelastic belt, formed into a pipe shape interacts with curved surface of a rigid idler roll cylinder. Despite the drawbacks mentioned of the approach of Dmitriev and Sergeeva [58], Sergeeva [208, 210], there is no any other available research study attempted to quantify the IRR of PBCs. One of the reasons can be that no any research study could appropriately evaluate the PBC CFs.

Therefore, in order to determine the IRR for PBCs in an accurate way, a three-dimensional contact model with multiple Maxwell parameters is presented in this chapter. The model is developed by Nuttall [185], Nuttall *et al.* [186] for pouch belt conveyors and is adapted here for PBCs. The CFs needed to determine the IRR are calculated using the approach, developed in Chapters 4, 5, and 6. The Maxwell parameters are obtained by approximating the experimental data with Prony series from the tension DMA tests of the pipe conveyor belt cover rubber with frequency/temperature sweep mode. The indentation contact model used is described in the next section.

7.3 Indentation contact model

The indentation contact model selected to represent the interaction between the idler roll and a belt is schematically illustrated in Fig. 7.3. The figure illustrates the idler roll as a rigid cylinder with radius $R_1 = D_{\text{roll}}/2$, rolling over the curved viscoelastic surface of the belt with radius $R_2 = R$. The variation of the idler roll diameter is provided in Section 2.6 and a pipe diameter of a belt depends on the nominal pipe diameter of the idler rolls situation in the station (see Section 2.5.4).

The contact area between a pipe belt and a roll has an elliptical shape. The geometry of the contact spot indicates, that the contact time depends on the contact width along the

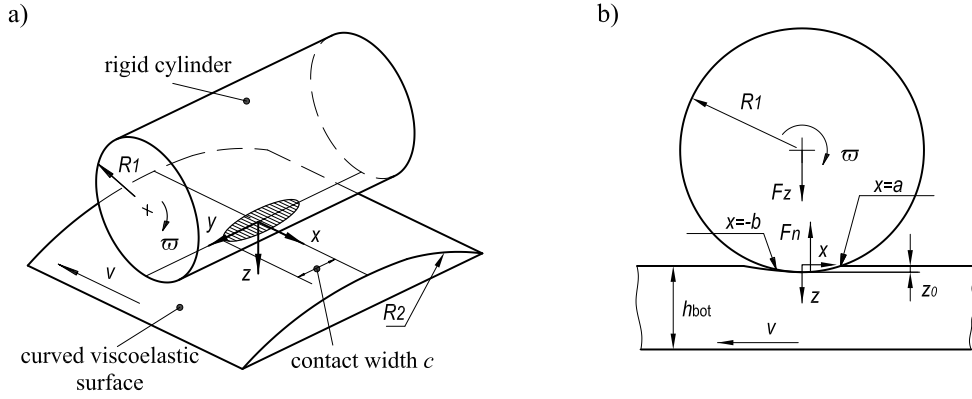


Figure 7.3: A three-dimensional indentation contact model between two curved surfaces: the rigid cylinder (idler roll) and the viscoelastic belt rubber cover (modified figure from Nuttall [185], Nuttall *et al.* [186]).

length of the idler roll. That is why the Generalized Maxwell Model with multiple relaxation time suites better, compared to the SLS-model. In case of the latter, the plane profile of a contact spot has a rectangular shape.

The belt moves with a linear speed v , and is covered with a viscoelastic layer with a thickness h_{bot} that equals to the thickness of a rubber ply of a belt bottom cover. A rigid roll with a radius R_1 , is compressed under the contact load $F_z = F_n$, and rolls over the belt cover with an angular frequency ω . The force F_n causes is determined according to the approach in Chapters 4, 5, and 6. The cylinder indents the viscoelastic base with a depth of z_0 . The first point, where the rubber and the roll come into the physical contact, is specified as $x = a$ as a leading edge. At the point $x = -b$ as a trailing edge, the physical contact between surfaces ends.

As was derived by Nuttall [185], Nuttall *et al.* [186], the deformation w of the contact viscoelastic plane with Winkler foundation in three dimensions, can be described as follows:

$$w(x, y) = z_0 - \frac{x^2}{2R_1} - \frac{y^2}{2R_2}, \quad (7.1)$$

where $-b \leq x \leq a$ and $x \ll R_1$, $y \ll R_2$. The pressure distribution in the contact plane can be expressed as:

$$\sigma(x, y) = \frac{E_{M0}}{2R_1 h_{\text{bot}}} (a^2 - x^2) + \sum_{i=1}^m \frac{E_{Mi} k_{Mi}}{h_{\text{bot}} R_1} \left[x - a + (a + k_{Mi}) \left(1 - \exp\left(\frac{x - a}{k_{Mi}}\right) \right) \right]. \quad (7.2)$$

In Eq. 7.2, parameter k_{Mi} equals to $k_{Mi} = v\tau_i = \frac{v\eta_{Mi}}{E_{Mi}}$, whereas E_{M0} and E_{Mi} denote the stiffness of springs. η_{Mi} indicates the damping factor in the spring and dash-pot assembly of the Generalized Maxwell Model, illustrated in Fig. 7.1f.

The geometrical parameters of the indentation viscoelastic contact can be found based on following considerations. Along the leading edge $x = a(y, z_0)$, there is no deformation yet, so it can be found by setting $w(a(y, z_0), y) = 0$. The function of the trailing edge of

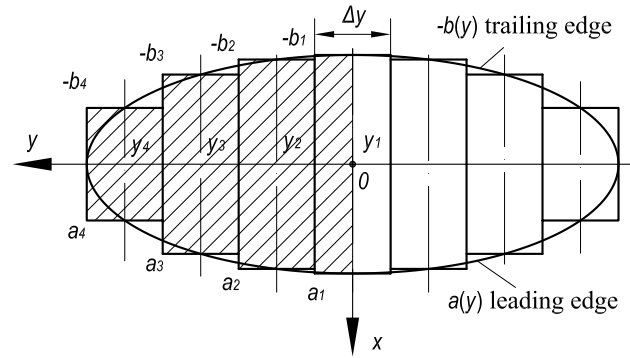


Figure 7.4: An elliptical contact region, between the belt and idler roll, divided into seven strips.

the contact spot $x = -b(y, z_0)$ can be determined considering that there is no stress after the idler roll moved away $\sigma(-b(y, z_0), y) = 0$. The half-length of the contact region c can be obtained by setting the stress distribution $\sigma(0, c) = 0$.

The indentation depth z_0 , $0 < z_0 < h_{\text{bot}}$, needs to be evaluated in terms of the normal CF, in particular, satisfying the requirement that already known CFs should be also equivalent to the contact plane pressure, integrated over the whole area of the contact profile. In other words, the indentation depth is determined from the following equation:

$$F_n = 2 \int_0^{c(z_0)} \int_{-b(y, z_0)}^{a(y, z_0)} \sigma(x, y) dx dy. \quad (7.3)$$

In the presented formula, the limit under the integral sign is a function $-b(y, z_0)$ that cannot be presented in an explicit form. In order to overcome this problem, the contact plane is divided into strips, simplifying the integration process of the stress distribution over the entire contact region (see Fig. 7.4). The step by step calculation procedure to determine the IRR factor for PBC is provided in the next section.

7.4 Calculation procedure

The following procedure can be used for quantifying the IRR for PBCs:

- 1). At first, the normal CFs for each roll of the idler set needs to be evaluated, as described in Chapters 4, 5, and 6. In order to perform the analysis, the initial guess should be set for the indentation depth value z_0 on the interval $0 < z_0 < h_{\text{bot}}$.
- 2). The half-length c of the contact region, shown in Fig. 7.3 and Fig. 7.4, needs to be determined by setting the stress distribution $\sigma(0, c) = 0$. Therefore,

$$z_0 = \frac{c^2}{2R_2} \Rightarrow c = \sqrt{2R_2 z_0}. \quad (7.4)$$

3). The contact region with length $2c$ is divided into strips, as it is illustrated in Fig. 7.4. The necessary number of divisions should be determined by balancing between the calculation time consuming and the level of accuracy desired.

Figure 7.4 shows that the number of strips was $m = 7$. As was stated by Nuttall [185], Nuttall *et al.* [186], this number of elements shows acceptable accuracy.

After dividing the contact area, the values of the y -coordinates of the centerlines of an each strip for the half-length equal:

$$y_1 = 0; \quad y_2 = \frac{2c}{m}; \quad \dots; \quad y_p = \frac{6c}{m}, \quad (7.5)$$

where $p = (m + 1)/2$ for odd number of m .

4). After the position of y -coordinates of the strips are determined, the x -coordinates of the leading edge function for the centerlines of each strip need to be evaluated. Along the edge $x = a(y, z_0)$ there is no deformation, in this case,

$$w(a(y, z_0), y) = 0 \quad \Rightarrow \quad a(y, z_0) = \sqrt{2R_1 \left(z_0 - \frac{y^2}{2R_2} \right)}. \quad (7.6)$$

Substituting the values of y_1, y_2, \dots, y_p , provided in Eqs. 7.5 into Eq. 7.6, the corresponding values of the leading contact edge $a_p(y_p, z_0)$ can be found for each strip. For the first strip, a_1 equals:

$$a_1 = \sqrt{\frac{R_1(c^2 - y_1^2)}{R_2}}. \quad (7.7)$$

Analogically, the rest a_2, a_3, \dots, a_p are determined.

5). Analogically, the calculation of the x -coordinates of the trailing edge as a function $x = -b(y)$ can be performed for the centerlines of each strip. They can be evaluated, considering that there is no contact stresses in the viscoelastic body, after the belt passed the indentation contact position with the idler roll. This means that $\sigma(-b(y), y) = 0$. From this equation, the x -coordinates of trailing edge can be found for each strip. For the first strip it equals:

$$b_1 \Leftarrow \frac{E_{M0}}{2R_1 h} (a_1^2 - b_1^2) + \sum_{i=1}^m \frac{E_{Mi} k_{Mi}}{h R_1} \left[-b_1 - a_1 + (a_1 + k_i) \left(1 - \exp\left(-\frac{b_1 + a_1}{k_{Mi}}\right) \right) \right] = 0. \quad (7.8)$$

The rest b_2, b_3, \dots, b_p are found in analogical way.

6). The normal CFs, denoted here as $F_n^{\text{calc}}(z_0)$ for each idler roll, can be evaluated by integrating the function of the contact stress over the entire contact region according to Eq. 7.3. For quantifying the value, the integration operator in Eq. 7.3 is replaced with an equivalent summation mathematical operator. For odd number of strips m , Eq. 7.3 can be transformed into the following form:

$$F_n^{\text{calc}}(z_0) = 2 \left[\frac{\Delta y}{2} \int_{-b_1}^{a_1} \sigma(x, y) dx + \Delta y \sum_{j=2}^p \int_{-b_j}^{a_j} \sigma(x, y) dx \right], \quad (7.9)$$

where $\Delta y = 2c/m$.

7). On other hand, the CF $F_n^{\text{calc}}(z_0)$ should be equivalent to the value F_n , determined using PBC design parameters following the approach, developed in Chapters 4, 5, and 6 for each corresponding idler roll. The correct value of the indentation depth z_0 , $0 < z_0 < h_{\text{bot}}$, can be found from following equation:

$$F_n - F_n^{\text{calc}}(z_0) = 0. \quad (7.10)$$

The solution of Eq. 7.10 can be obtained using a numerical method of a root-finding algorithm. The present approach utilized the secant method with the approximating function $f(z_0) = F_n - F_n^{\text{calc}}(z_0)$. However, any other analogical numerical algorithm can be employed for that purpose. The root-searching iteration of z_0 repeats, until the accuracy of the convergence reaches 10^{-4} precision.

8). After the correct value of the indentation depth is found, the x-coordinates of the leading and trailing edges $(-b_1; a_1)$, $(-b_2; a_2)$, ..., $(-b_p; a_p)$ need to be finally recalculated for each dividing strip. This operation is carried out again using Eqs. 7.6-7.8.

9). The torque M_y from the asymmetric pressure distribution about the centre of the roll in the indentation contact region can be evaluated from the following expression:

$$M_y = 2 \int_0^c \int_{-b(y, z_0)}^{a(y, z_0)} x \cdot \sigma(x, y) dx dy. \quad (7.11)$$

The rolling IRR force $F_{\text{ind}n}$ at each n -th roll of the idler set depends on that resistance torque:

$$F_{\text{ind}n} = \frac{M_y}{R_1}. \quad (7.12)$$

Replacing the integration operator with the equivalent summation with respect to the entire contact region, Eq.7.12 can be rewritten for all seven dividing strips:

$$F_{\text{ind}n} = \frac{2}{R_1} \left[\frac{\Delta y}{2} \int_{-b_1}^{a_1} x \sigma(x, y) dx + \Delta y \sum_{j=2}^p \int_{-b_j}^{a_j} x \sigma(x, y) dx \right]. \quad (7.13)$$

10). Eventually the dimensionless friction factor from the IRR f_{ind} can be quantified. In general for each idler roll, it represents the ratio between the resistance force $F_{\text{ind}n}$ and the CFs F_n , caused that indentation, i.e.:

$$f_{\text{ind}n} = F_{\text{ind}n} / F_n. \quad (7.14)$$

After a number of transformations, performed over entire step procedure using only the mathematical forms of formulas, it becomes possible to express the indentation friction factor, provided in Eq. 7.14, as a following general function:

$$f_{\text{ind}n} = \frac{F_n^{1/4} h_{\text{bot}}^{1/4}}{R_1^{5/8} R_2^{1/8}} \Upsilon_{\text{PBC}} \left(\frac{k_{\text{Mi}}}{a_p}; \frac{b_p}{a_p}; E_{\text{M}0}; E_{\text{M}i} \right), \quad (7.15)$$

where Υ_{PBC} is a certain function of Maxwell parameters and the x -coordinates of the leading and trailing edges in the contact profile.

For the entire PBC system, it is possible to expect that the overall average friction factor should represent the ratio between the sum of the resistance forces, determined for all six rolls in the idler station divided by the sum of the CFs causing that IRR:

$$f_{\text{ind}} = \left(\sum_{n=1}^6 F_{\text{ind}n} \right) / \left(\sum_{n=1}^6 F_n \right). \quad (7.16)$$

However, to understand the energy losses from the IRR of a PBC system, it is more informative to evaluate the friction factor according to DIN 22 101 [45] as a ratio between the sum of all six resistance forces, determined at the idler set, divided by the “useful” loads from the belt and bulk material weight. The “useful” loads mean the loads that the conveyor is actually developed for its transportation. The friction factor equals:

$$f_{\text{ind}}^{\text{DIN}} = \frac{\sum_{n=1}^6 F_{\text{ind}n}}{q_{\text{bw}}B + F_{\text{bulk}}^{\text{V}}}, \quad (7.17)$$

where the total belt weight is expressed via belt line mass q_{bw} , distributed along the belt width B . It can be actually expressed via the area-related belt mass m''_{belt} as given in Eq. 2.13. The total weight of a bulk material $F_{\text{bulk}}^{\text{V}}$ can be evaluated based on the Eq. 6.22 and depends not only on the bulk material density, but also on the filling degree k_{Q} of a PBC cross-section.

The analysis of the indentation contact model described indicates that it is logical to expect the IRR friction factor, determined for PBCs to be higher than the IRR of a trough and a flat-belt conveyor. The possible reasons that can potentially cause the increase of the IRR are: a) a three-dimensional contact profile between two curved surfaces of a belt and idler rolls, compared to a flat-to-flat surface indentation contact for a trough and flat-belt conveyors; b) six rolls are used in the idler assembly for a PBC instead of the conventional three-roll station or a one roll for a flat belt; c) the CFs that influence the IRR forces are higher for PBCs due to the presence of an additional load from belt bending stiffness.

Noteworthy to mention that for conventional trough belt conveyors, the load from the belt bending stiffness is insignificant, since the belt develops the deformations from bending with small curvature. In this case, the impact of the load is not included neither in the dominator of the friction factor in Eq. 7.17, nor among the “useful” loads in the denominator of Eq. 7.17.

As for PBCs, Chapter 6 shows that this load can have a significant effect on CFs and ultimately on the corresponding resistance forces, especially for belts that are very stiff in lateral direction. Since the impact of that load is not included as a “useful” load in denominator of Eq. 7.17, whereas the resistance forces encompass its effect, it is reasonable to expect that the friction factor $f_{\text{ind}}^{\text{DIN}}$, determined from Eq. 7.17 is much higher, compared to the factor f_{ind} , determined according to Eq. 7.16. Moreover, the higher the effective modulus of elasticity of a belt in lateral direction, the higher difference between these friction factors may be expected.

After the indentation model used is described and the corresponding energy losses are evaluated with the friction factors f_{ind} and $f_{\text{ind}}^{\text{DIN}}$, the Maxwell parameters need to be determined. This is done by performing the DMA experimental testing with the pipe conveyor belt cover rubber, as elucidated in the next section.

7.5 Determining Maxwell parameters

Maxwell parameters of a viscoelastic material can be determined only via experimental testing. The rheological tests need to provide a quantified physical characteristics that can reflect the material's ability to recover back to initial state with a time delay when the periodical load or deformation are applied to the material and removed.

The oscillatory experiments with varying sinusoidal stress and strains are called DMA tests. The storage modulus E' , the loss modulus E'' , and the loss factor $\tan \delta$ become the viscoelastic output characteristics measured during these tests.

7.5.1 Loss and storage moduli

When the oscillating periodical strain is applied to a sample during the DMA test, the stress developed in the material tested and its phase with respect to the strain dependence becomes the purpose of the analysis (see Lodewijks[140]). For instance, the strain applied during DMA test follows the sinusoidal law (see Fig. 7.5):

$$\varepsilon = \varepsilon_0 \sin(\varpi t), \quad (7.18)$$

where ε is an instant strain applied at the moment of the measurement, ε_0 is an initial strain, ϖ is frequency of the strain oscillation with respect to time t .

As mentioned by Lodewijks[140], Gent [81], absolutely elastic material exhibits the resultant stress response in the same phase as a strain, having similar sinusoidal characteristic (zero phase angle), as illustrated in Fig. 7.5:

$$\sigma = \sigma_0 \sin(\varpi t). \quad (7.19)$$

The stress response of the viscous material exhibits a periodical stress dependence, however with the difference in phase angle of $\delta = \pi/2$ (see Fig. 7.5), constituting the

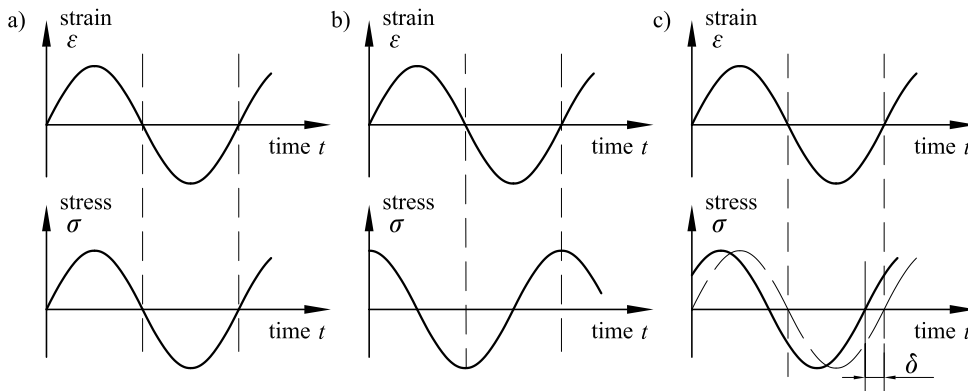


Figure 7.5: Instant stress characteristic as a response to an oscillating sinusoidal strain for: a) elastic material; b) viscous material; c) viscoelastic material, characterized by the lag in the dependences.

following:

$$\sigma = \sigma_0 \sin(\omega t + \pi/2) = \sigma_0 \cos(\omega t). \quad (7.20)$$

Taking into account that viscoelastic material exhibits both elastic and viscous properties, the resultant stress functional dependence as a response to a sinusoidal oscillating strain exhibits similar periodical function with intermediate phase angle δ , compared to the critical values of elastic and viscous materials:

$$\sigma = \sigma_0 \sin(\omega t + \delta). \quad (7.21)$$

The storage modulus E' characterizes the elastic measure of the rheological properties, whereas the loss modulus E'' signifies the viscous part. The ratio between the loss and storage moduli constitutes the loss factor (or phase factor) δ , representing the energy dissipation during each load cycle. These three rheological characteristics equal:

$$\begin{cases} E' = \frac{\sigma_0}{\varepsilon_0} \cos \delta; \\ E'' = \frac{\sigma_0}{\varepsilon_0} \sin \delta; \\ \tan \delta = \frac{E''}{E'}. \end{cases} \quad (7.22)$$

As mentioned by Lodewijks[140], the oscillating strains can be applied during the rheological DMA tests in tensile, bending (three point bending or dual cantilever), and compression modes. The selection of the loading mode and frequency range should be consistent with the physical range of the exploitation of that viscoelastic material tested.

In addition, it is important to take into account the observation, drawn by Lodewijks[140] from the analysis of the rubber data measured during the DMA tests. Lodewijks[140] showed that the viscoelastic dynamic/mechanical properties for loss and storage moduli, as well as for loss factor, obtained for the same rubber and for the same mode of DMA testing, but obtained from the different machines, could exhibit difference in the results. This could yield to the deviation in energy losses calculated as an output and the ultimate value of the IRR factor, drawing attention to the sensitivity of the rheological characteristics measured during the experiment. This could yield to the deviation in energy losses calculated as an output and the ultimate value of the IRR factor. This indicates that, despite the fact that the rheological characteristics measured during the test are intrinsic properties, they exhibit significant sensitivity to the way the DMA test is performed.

7.5.2 Dynamic Mechanical Test

In order to determine the viscoelastic Maxwell parameters of PBCs, the rheological behavior of the pipe conveyor belt cover rubber was studied via a dynamic mechanical laboratory test. The laboratory experiment was performed by using Dynamic Mechanical Analyzer DMA Q800 of TA-instruments with tensile setup equipment. The DMA apparatus set up is illustrated in Fig. 7.6.

For the experiment, a sample of a PBC cover rubber was used. The dimensions of the sample were determined by measuring them at three locations and then finding the average



Figure 7.6: Dynamic Mechanical Analyzer Q800 performing the temperature-frequency sweep for a rubber sample designated for PBC belt cover. The liquid nitrogen was used to achieve the temperature inside the testing chamber below the room temperature.

value for each sample side. Ultimately, the sample dimensions constituted $(22.58 \times 9.07 \times 2.20)$ mm.

The DMA measurements were conducted for a temperature range of -80°C to 80°C . In order to cool the sample below the room temperature, the liquid nitrogen was used to decrease the ambient temperature inside the testing chamber. An oscillating tensile strain was applied to the sample and the stress was measured in the rubber tested. At the same time, the sample was heated with $1^{\circ}\text{C}/\text{min}$ during continuous frequency sweeps between 0.32 and 60 Hz were applied. Each frequency sweep required about one minute, so one frequency sweep was achieved per one Celsius degree.

The advantage of this characterization procedure is that this type of test mode provides more data during the glass transition of the rubber and offers a more detailed master curve based on the frequency-temperature superposition principle.

The viscoelastic properties, characterized by the dependence of the storage modulus E' , the loss modulus E'' , and the loss factor δ were measured versus the strain frequency and the ambient temperature. The glass transition temperature of the rubber for certain frequencies can be detected as a sudden decrease of the storage modulus or the peak of the [81, 140]. Gent[81] states that the glass transition happens at the temperature when rubber segments move very slowly ($\sim 0.1\text{s}^{-1}$), and the material behaves like a rigid glass.

Figure 7.7a shows a plot of the storage modulus versus temperature at six different frequencies. The glass transition region is between -60°C and -20°C during which the modulus decreases by a factor of 30 to 40. At -70°C the full glassy plateau is not yet reached and storage modulus varies between 500 and 900 MPa. Figure 7.7b shows the curve of the DMA measurement as a direct measure of the energy dissipation. For instance, the dissipation pick of the loss factor, detected at the frequency of 1 Hz, appears at -53°C glass transition temperature.

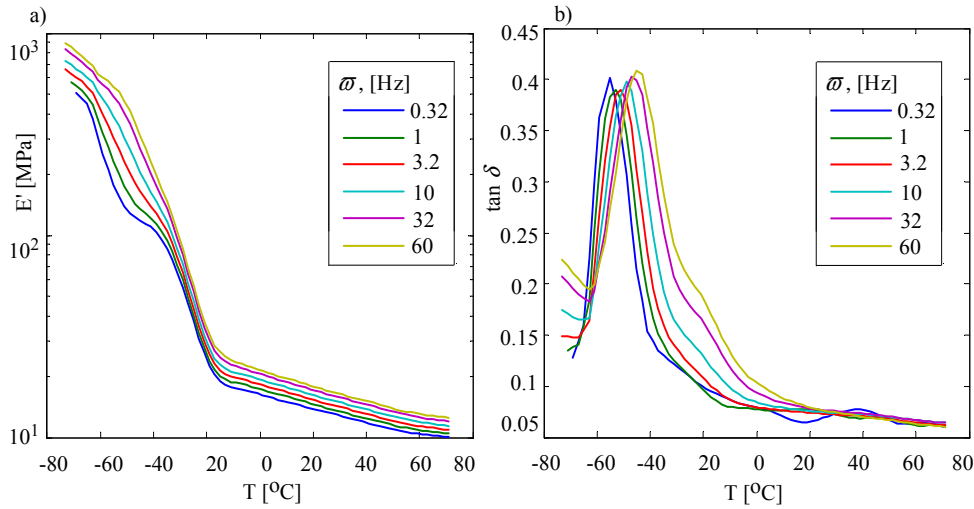


Figure 7.7: The experimental data for temperature-frequency sweep, obtained from DMA test for: a) storage modulus E' , E'' , and b) the loss factor $\tan \delta$.

7.5.3 Data interpretation

The Maxwell parameters needed for the IRR model in Section 7.3, can be found by approximating the experimental data of the viscoelastic characteristics E' , E'' , and $\tan \delta$, measured from DMA test.

For this purpose, first of all, the data analysis needs to be conducted by interpolating the measurement data to a fixed and equidistant temperature scale. The results should be plotted versus frequency, as it is shown in Fig. 7.8. The highest data points are taken at the lowest temperature and vice versa.

Based on the principle of the frequency-temperature superposition (see Williams *et al.* [250], Gent [81]), the so-called master curve can be constructed. When a logarithmic scale is used for the frequency axis, one of the curves for certain temperature needs to be selected as a reference curve. The other interpolated curves for the next temperatures are shifted along the frequency axis until the distance between the shifted points and the reference curve points are minimum. The lateral shift factor a_T depends on the temperature T and follows the Williams-Landel-Ferry (WLF) equation, described by Williams *et al.* [250]:

$$\log(a_T) = \frac{C_{1T}(T - T_{\text{ref}})}{C_{2T} + (T - T_{\text{ref}})}. \quad (7.23)$$

In Eq. 7.23, C_{1T} , C_{2T} are the WLF constants, and T_{ref} is a reference temperature, with respect to which other temperature curves are shifted.

A frequency-temperature superposition principle, as stated by Ferry [72], Gent [81], implies that frequency change is completely equivalent to a change in temperature or time. A measurement at one temperature can be applied at other temperatures, which allows the data to be inter- and extrapolated to temperature and frequency levels that were not accessed during the measurement process. The graph displayed in Fig.7.9a represents the

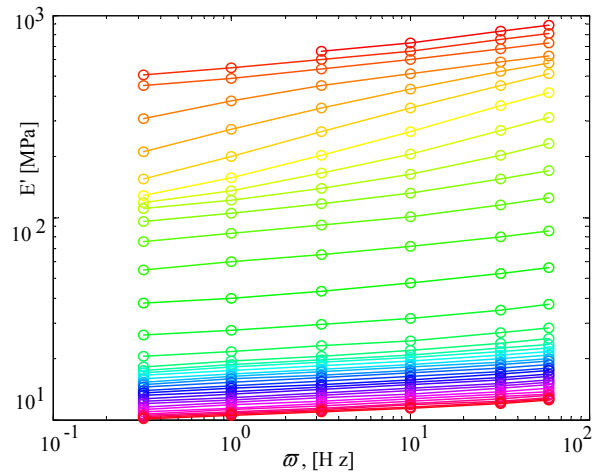


Figure 7.8: Storage modulus E' interpolated versus frequency for different temperatures.

resultant master curve, formed for the reference room temperature $T_{\text{ref}} = 20^\circ\text{C}$, whereas Fig. 7.9 illustrates the corresponding shift factor function a_T applied for the master curve interpolation.

In order to obtain the Maxwell parameters for the viscoelastic generalized Maxwell model, illustrated in Fig. 7.1e, the master curves data the storage E' and loss E'' moduli are approximated with a Prony term series, as it was recommended, for instance, by Ferry [72]:

$$E'(\omega) = E_{M0} + \sum_{i=1}^m \frac{E_{Mi} \omega^2 \tau_i^2}{1 + \omega^2 \tau_i^2}; \quad (7.24)$$

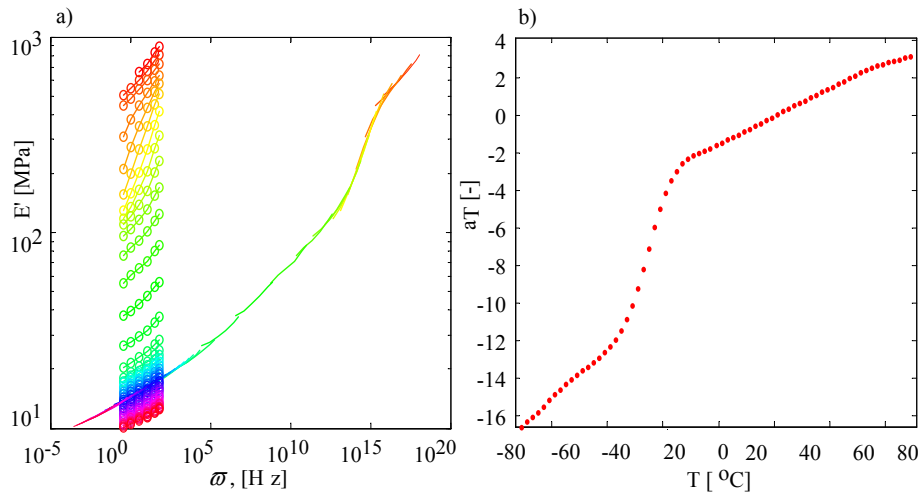


Figure 7.9: a) A master curve for storage modulus E' , constructed for the reference temperature $T_{\text{ref}} = 20^\circ\text{C}$ and b) the corresponding shift factor function a_T .

$$E''(\varpi) = \sum_{i=1}^m \frac{E_{Mi} \varpi^2 \tau_i^2}{1 + \varpi^2 \tau_i^2}, \quad (7.25)$$

where ϖ is the frequency of the strain application; E_{M0} , E_{Mi} represent the stiffness of the elastic strings of the generalized Maxwell model, shown in Fig. 7.1e; $\tau_i = \eta_{Mi}/E_{Mi}$ is the relaxation time of the viscous dampers with damping factor η_{Mi} (see Fig. 7.1e).

Figure 7.10 shows the master curve for reference temperature $T_{\text{ref}} = 20^\circ\text{C}$, approximated using 7 and 13 Maxwell parameters of the Prony series. These Maxwell parameters are used further to evaluate the IRR for PBCs. In addition, 3 Maxwell parameters, determined experimentally by Lodewijks [136, 137] for SLS-model, are also used for the comparison to evaluate the PBC IRR.

The number of the Maxwell parameters essentially determines the accuracy of the master curve approximation. The more Maxwell parameters used for the approximation, the better the data fits the master curve. However, an increase of the number of the Maxwell parameters significantly increases the computation time of the indentation depth and the total energy losses from the IRR. That is why it is important to find the optimum between the sufficient accuracy of the approximation and the computational time.

The resultant IRR friction factors, determined using 3, 7 and 13 Maxwell parameters will be compared in Section 7.6.1, indicating how the number of the Maxwell parameters selected for viscoelastic master curve approximation influences the resultant energy losses for a PBC system. In addition, the impact of PBC design parameters on the IRR is also analyzed.

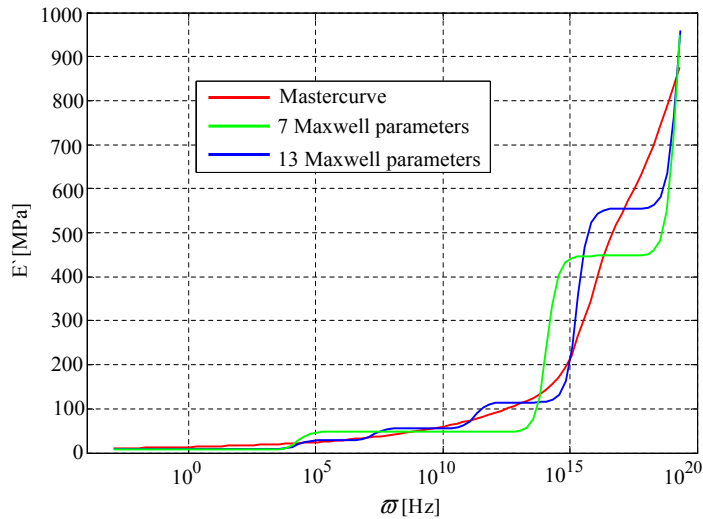


Figure 7.10: Master curve of the storage modulus E' , constructed with respect to the reference room temperature $T_{\text{ref}} = 20^\circ\text{C}$ and its Prony series approximation with 7 and 13 Maxwell parameters.

7.6 Results

In order to perform an impact analysis and to evaluate how the participating PBC design parameters influence the IRR, it is important to consider the general functional dependence, derived in Eq. 7.15 for one roll in the PBC idler set. Based on this function, it is possible to state that the IRR for one roll depends on the CF F_n , the thickness of the bottom rubber cover h_{bot} , the radii of the idler roll R_1 and the belt's pipe R_2 , and the rubber rheology, represented by the Maxwell parameters.

The present analysis investigates only how the design parameters that participate in the loads of PBC CFs, determined in Chapter 4, 5, and 6, influence the IRR. In addition, the effect of a number of Maxwell parameters selected in Section 7.5 to approximate the rubber viscoelasticity, needs to be analyzed and selected.

For this purpose, a numerical example is used to quantify the IRR friction factor. The following input data for the PBC system are assumed in the simulation. For the reference, some of the belt parameters inherent to the Sample 3, provided in Table 4.9 are accepted. The belt has width equivalent to $B = 1.20067\text{m}$ and the overall structural thickness $h = 0.01682\text{m}$. The thickness of the bottom ply of the cover rubber, participating in the IRR phenomenon, constitutes $h_{\text{bot}} = 0.003\text{m}$. The carry spacing of the PBC system is assumed equal to $l_c = l_r = 1\text{m}$. The area-related belt mass is assumed equal to $m'_{\text{belt}} = 20.209\text{kg/m}^2$, proportionally as if the belt Sample 3, described in Table 4.9 would be 1 m long.

The pipe diameter is assumed equal to a nominal pipe diameter $D = D_{\text{nom}} = 0.4\text{m}$. The diameter of the idler rolls is selected according to the product specification of an idler rolls' manufacturer [201] equivalent to 0.108 m with respect to the nominal pipe diameter. In this case, the indentation phenomenon appears between the two curved surfaces, characterized by the curvature $R_1 = D_{\text{roll}}/2$ of the rigid roll and curvature $R_2 = R = 0.2\text{m}$ of the belt viscoelastic belt, formed into a pipe shape.

At first, it is assumed that conveyor is designated for transporting coal with density $\rho_{\text{bulk}} = 850\text{kg/m}^3$. The other properties are described in Section 2.4. The conveyor is operated empty, and also loaded with bulk material with the cross-section filling degree $k_Q = 0.25, 0.5, \text{ and } 0.75$ (see for the reference Section 2.3.3). Later on, the IRR is evaluated for other types of a bulk material. The CFs were evaluated using numerical solution of the Beam Simplified Model, described in Chapter 6 and in Appendix C for the same given design parameters and loading conditions. These CFs are needed in the IRR model described in Section 7.4, to determine the indentation depth and the IRR friction factor.

In the presented simulations the number of strips dividing the elliptical contact region in plane is chosen equal to $m = 7$, as selected in the example (see Fig. 7.4). For all cases, the IRR friction factor is determined for different belt speeds v , varying it in the range from 0 to 10m/s, as defined in Section 2.3.2.

It is important to emphasize that diameter of the pipe is assigned, assuming belt geometry as an open pipe shape without an overlap. This was made consistent with the approach, developed in Chapter 4 and Chapter 5 to evaluate the PBC CFs. However, the indentation model, described in Section 7.3, does not take into account the indentation contact of belt edges, both interacting with the top roll with CFs F_1' and F_1'' . For the belt top roll only CF F_1 was used. The influence of the repulsion CFs N_1' and N_1'' of contacting viscoelastic belt edges is not included in the model either. This can cause certain difference in the IRR friction factor, and the results presented become an approximation. At the same time, the

indentation model presented in Section 7.3 is perfectly suitable for actual PBCs with the cross-sectional geometry of a belt folded into a pipe shape overlap. In this case, the radius $R_2 = D_{\text{nom}}/2$.

7.6.1 Impact of a number of Maxwell parameters

Figure 7.11 illustrates the difference of the IRR factor with 75% filling ratio of the cross section of the pipe, obtained for 3 (according to Lodewijks [136, 137]), 7 and 13 rheological Maxwell parameters versus the speed of the pipe conveyor belt.

In general, it can be observed that with the increase of a belt speed, the IRR increases. This appears due to the fact that with the increase of an oscillating frequency of a load application, the viscoelastic rubber after deformation from rigid idler rolls does not have sufficient time to recover back before the next idler station. The dependence obtained correlates with the conclusions, received by Lodewijks [136] for flat and trough belt conveyors.

The IRR friction factor f_{ind} , evaluated using Eq. 7.16, is shown in Fig. 7.11a. The factor, determined according to DIN 22 101 [45] standard by means of Eq. 7.17 is presented in Fig. 7.11b. The difference between the results due to the selection of the formula for evaluating the friction factor is explained and discussed in the next section.

A comparison of the data, presented in Fig. 7.11, shows that the increase of the number of the Maxwell parameters decreases the values of the IRR factor. This is caused by the fact that, for representation of the deformation of the elliptical surface between belt and roll, shown in Fig. 7.11, the model with 3 Maxwell parameters is not capable to sufficiently differentiate between the deformation rates varied over the ellipse contour. As a result, the model becomes stiffer and overestimates the IRR. This observation is consistent with the

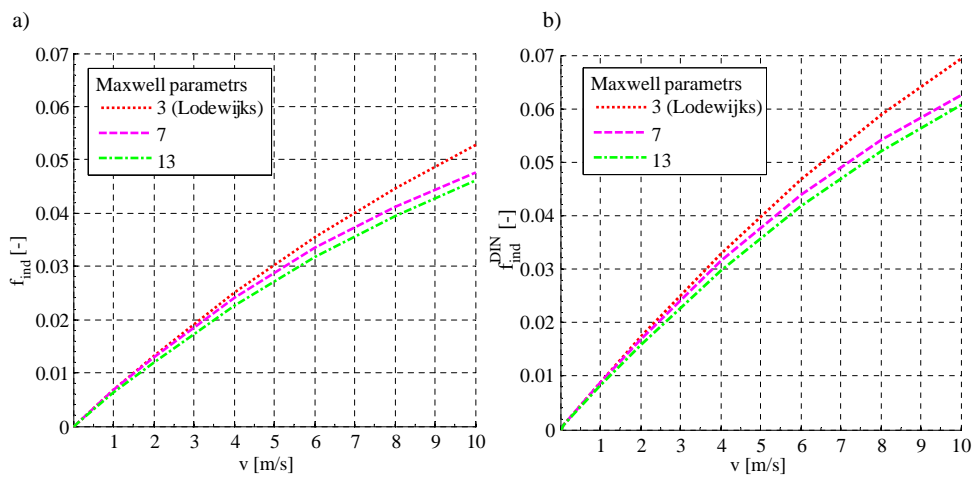


Figure 7.11: The IRR friction factor, determined for the same PBC, loaded with coal with the cross-sectional filling degree $kQ = 0.75$ and evaluated according to a) Eq. 7.16 and b) Eq. 7.17 as recommended by the DIN standard. The results are obtained using 3 (selected for the comparison from Lodewijks [136, 137]), 7, and 13 Maxwell parameters.

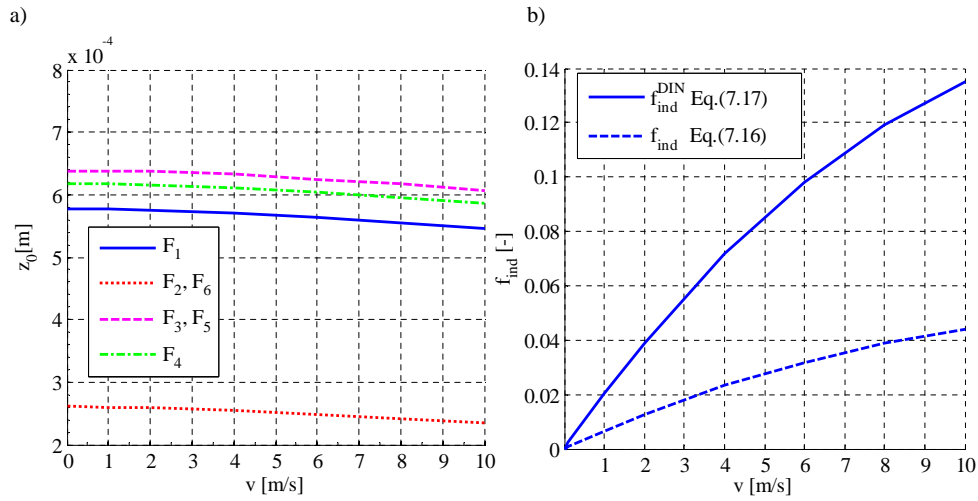


Figure 7.12: a) The indentation depth z_0 , determined for each idler roll in the set and b) the difference of the IRR friction factor, evaluated using Eq. 7.16 and Eq. 7.17. The results are obtained using seven Maxwell parameters for empty PBC versus belt speed varied.

results no matter which equation is used for evaluating the IRR friction factor.

At the same time, it is important to take into account that the increase of a number of the Maxwell parameters significantly increases the computational time. Seven Maxwell parameters seem to provide a sufficient precision of the IRR friction factor and acceptable time consumption for its computing. The rest of the graphs, presented further in the next sections are obtained using seven Maxwell parameters only.

7.6.2 Impact of a cross-sectional filling degree

At first, the results are obtained for an empty PBC without bulk material. Figure 7.12 illustrates the indentation depth and the IRR friction factor. The latter is determined using Eq. 7.16 and also Eq. 7.17 for the same input parameters. The results are obtained for seven Maxwell parameters, determined experimentally from the DMA test, as described in Section 7.5.

The indentation depth, shown in Fig. 7.12a, is evaluated from the PBC CFs by applying the numerical algorithms to solve Eq. 7.10. The results are presented for each CFs in the idler set, illustrated in Fig. 4.1 with corresponding numeration. As it can be seen, the indentation depth gradually decreases with the increase of the belt speed, as at higher speeds and thus at higher deformation rates, the belt behaves stiffer. The highest indentation depth is detected for the lateral bottom rolls, since the corresponding CFs $F_3 = F_5$ are the largest, even compared to the bottom roll F_4 . At the same time, the smallest indentation depth appears for the lateral top roll in the least loaded position, characterized by the smallest CFs $F_2 = F_6$.

Figure 7.12b shows the dependence of the IRR friction factor with respect to the belt

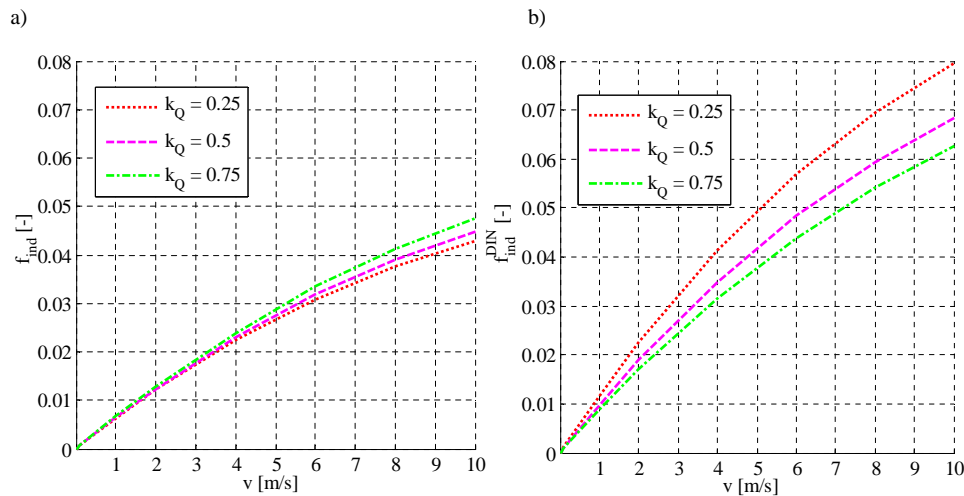


Figure 7.13: The IRR friction factor, determined for the same PBC, loaded with coal with the cross-sectional filling degree $k_Q = 0.25$, 0.5 , and 0.75 , according to a) Eq. 7.16 and b) Eq. 7.17 as recommended by the DIN standard. The results are obtained using seven Maxwell parameters.

speed varied. As it can be seen, the energy losses, determined from Eq. 7.17 according to the logic of DIN 22 101 [45] are excessively high, compared to the IRR friction factor evaluated from Eq. 7.16.

As it was proposed in Section 7.4, the DIN-standard, developed for trough belt conveyors, accounts the IRR friction factor as a sum of the resistance forces, divided into the “useful” conveying load that is weight of a belt and bulk material. This logic is suitable for trough belt conveyors, when the impact of a belt bending stiffness on CFs is insignificant. For PBCs, the impact of an additional load from folding the belt from a flat shape into a pipe shape is substantial. However, it is not incorporated in the denominator of Eq. 7.17, whereas the resistance forces in the numerator are significantly increased.

As for Eq. 7.16 that evaluates the friction factor as a sum of the resistance forces divided to the sum of the CFs, that caused the resistance, the presence of an additional load from belt bending stiffness is taken into account in both parts of the fraction. That is why Eq. 7.17 yields to very high friction factor values, whereas Eq. 7.16 gives reasonable results in the right amount of order, similar to those measured in the field.

Figure 7.13 shows the results for the rolling friction coefficient f_{ind} for the 25%, 50% and 75% filling ratio of the PBC cross section, evaluated again using Eq. 7.16 and also Eq. 7.17. If the friction factor is estimated according to Eq. 7.16 (see Fig. 7.13a), the growth of the load due to the filling degree of the PBC causes increase in the energy losses, since the CFs and corresponding resistance forces are higher. However, if the friction factor is calculated according to DIN-standard (see Fig. 7.13b), the results lead to the opposite observation. This can be explained again by the fact that the impact of the load from belt bending stiffness is ignored in the denominator of 7.17. With the increase of the filling degree, the “useful” bulk material weight increases in the denominator of the fraction, whereas the impact of the

load from belt bending stiffness on resistance forces remains the same.

In other words, Fig. 7.13b shows that operating a PBC without bulk material or with small loading conditions ($k_Q = 0.25$) is less efficient, compared to higher filling degree $k_Q = 0.5$ and $k_Q = 0.75$, due to the presence of additional energy losses from additional expansion load that appears from folding the belt from a flat shape into a pipe shape. To justify a PBC installation, the higher filling degree loading conditions are more preferable.

7.6.3 Impact of transported bulk material

All the graphs presented in the previous sections for the PBC loaded are obtained for coal as a bulk material transported. In order to analyze, how different bulk material influences the energy losses from the IRR, the results are obtained and compared, as if the same PBC is used for transporting iron ore and also wood chips. These two types of a bulk material are selected in Section 2.4 as the critical representatives for the heaviest (iron ore with $\rho_{\text{bulk}} = 3000 \text{ kg/m}^3$) and the lightest (wood chips $\rho_{\text{bulk}} = 200 \text{ kg/m}^3$) bulk solids. For these bulk materials, the CFs are evaluated using nonlinear solution of the Beam Simplified numerical model. The properties of a bulk material (dynamic angle of repose and internal friction angle), needed for CFs, can be found in Section 2.4.2 and Section 2.4.3, correspondingly.

Figure 7.14 provides the results for the IRR friction factor, obtained using Eq. 7.16 and Eq. 7.17 for the same filling degree $k_Q = 0.75$. As it can be seen, the heaviest bulk material causes higher CFs, that in turn generates higher resistance forces. This is in agreement with the results, obtained based on Eq. 7.16, shown in Fig. 7.14a. Figure 7.14b shows that heavier bulk material increases the “useful” load in denominator of Eq. 7.17, whereas the

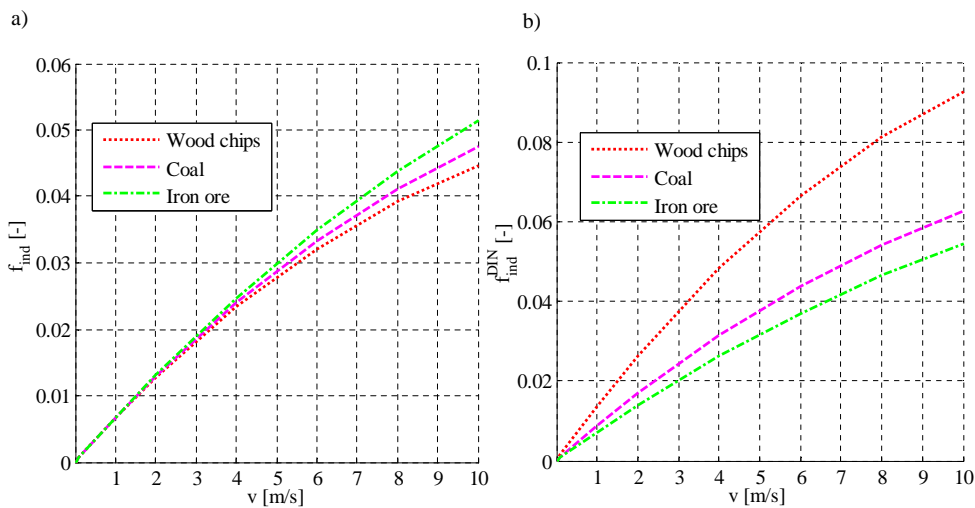


Figure 7.14: The IRR friction factor, determined for the same PBC, loaded with coal, iron ore, and wood chips with the cross-sectional filling degree $k_Q = 0.75$ and evaluated according to a) Eq. 7.16 and b) Eq. 7.17 as recommended by the DIN standard. The results are obtained using seven Maxwell parameters.

role of the belt bending stiffness becomes less influential for the resistance forces. As a result, the friction factor, estimated based on the DIN formula Eq. 7.17, is higher for the lighter bulk solids (wood chips in present case).

7.6.4 Effect of a belt mass and effective modulus of elasticity

In order to investigate the effect of a belt mass on the IRR friction factor, the results are obtained when the reference are-related distributed line mass is double-increased $2m'_{\text{belt}}$ and also half-reduced $m'_{\text{belt}}/2$. Figure 7.15 illustrates the resultant graphs for the IRR friction factor versus belt speed next to the similar reference dependence, obtained for m'_{belt} . The IRR friction factor is determined using Eq. 7.16 and also as it is recommended by the DIN-standard in Eq. 7.17. The values are received for PBC, loaded with coal with $k_Q = 0.75$ cross-sectional filling degree.

The analysis of the graphs shows the similar tendency in the results, as it was obtained in previous sections. In particular, with the increase of a belt line mass, the IRR friction factor f_{ind} , estimated according to Eq. 7.16 increases, since the CFs become higher. At the same time, if the Eq. 7.17 is used for evaluating the IRR friction factor, the same resistance forces generate an opposite dependence: with the increase of a belt mass, $f_{\text{ind}}^{\text{DIN}}$ decreases, since the denominator in Eq. 7.17 inherits higher value.

Similar trend can be observed in Fig. 7.16, if, instead of a belt's line mass, the effective modulus of elasticity is changed, in particular, the results are obtained, if the reference value of E is double increased $2E$ and half reduced $E/2$. The difference between f_{ind} and $f_{\text{ind}}^{\text{DIN}}$ significantly grows for higher values of E . This again can be explained that substantial values of effective modulus of elasticity means higher load from belt bending stiffness. The

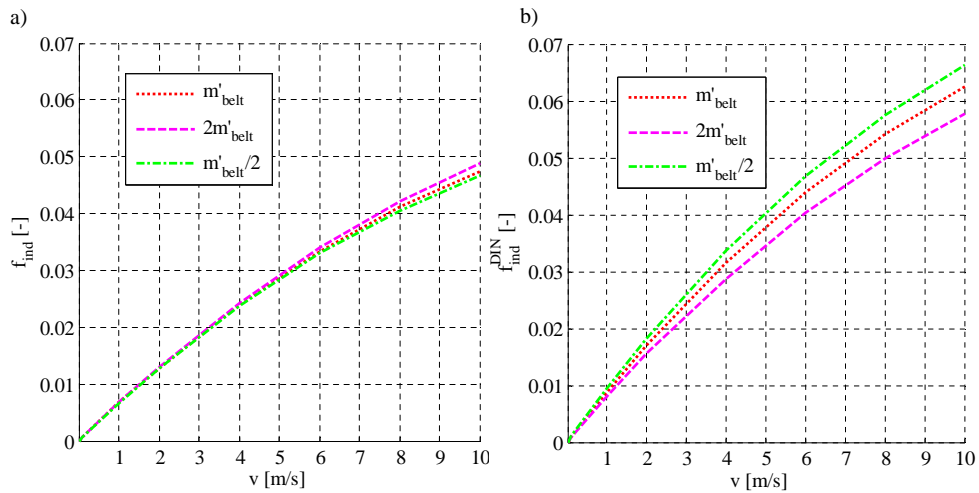


Figure 7.15: The effect of a belt line mass on the IRR friction factor, determined for PBC, loaded with coal with the cross-sectional filling degree $k_Q = 0.75$ and evaluated according to a) Eq. 7.16 and b) Eq. 7.17 as recommended by the DIN standard. The results are obtained using seven Maxwell parameters.

latter increases the CFs that in turn reasons in greater rolling resistance forces.

Since Eq. 7.17 does not include the load from belt bending stiffness as a “useful” load together with the belt and bulk material weight in the denominator of the fraction, f_{ind} exhibits dramatic increase in the results. The effect exacerbates for PBC with highest values of $f_{\text{ind}}^{\text{DIN}}$ detected for $2E$, since the denominator is minimal. Equation 7.16, on the opposite, includes the presence of a load from belt bending stiffness in both nominator and denominator of the fraction f_{ind} , and the results have reasonable values that correlates with ones observed in practice.

The analysis of the input parameters indicates that the effect of a load from belt bending stiffness has to be included among “useful” loads, if DIN formula is used. Otherwise, the friction factor evaluated inherits significant values that do not correspond to the ones used in practice. Moreover, the load from the belt bending stiffness is needed to preserve a stable enclosed pipe shape and justifies the selection of a PBC for the installation over a conventional trough belt conveyor.

In general, as it was shown in previous sections, if the IRR friction factor is determined according to Eq. 7.16, the energy losses of a PBC from the IRR will increase, if the participating load design parameters (cross-sectional filling degree, bulk density, belt weight and its effective modulus of elasticity) causes an increase of PBC CFs. In addition to CFs, based on the Eq. 7.15, derived in Section 7.4, the IRR friction factor can be also diminished by changing geometry of a belt and idler rolls, for instance, by selecting smaller thickness of the bottom rubber cover and also using larger diameters of the idler rolls and belt’s pipe.

During the design selection, it is important to balance between the low IRR and the belt’s pipe ability, as some of the design parameters can cause a decrease of the IRR, but can reason a contact loss and even collapse of a belt’s pipe. The collapsed belt can cause a

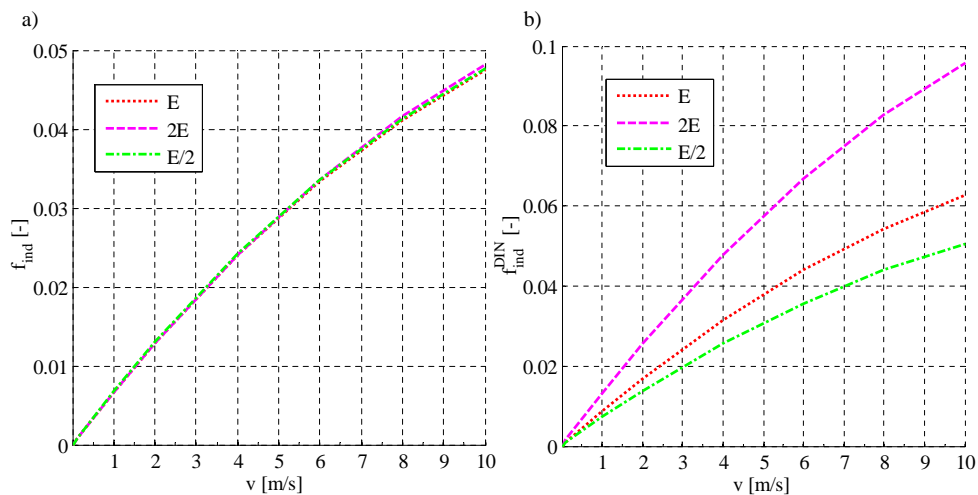


Figure 7.16: The effect of a belt line mass on the IRR friction factor, determined for PBC, loaded with coal with the cross-sectional filling degree $k_Q = 0.75$ and evaluated according to a) Eq. 7.16 and b) Eq. 7.17 as recommended by the DIN standard. The results are obtained using seven Maxwell parameters.

spillage of a bulk material and loose an ability to provide a completely enclosed transport system being a major PBC design advantage over the open trough belt conveyor.

7.6.5 Comparison with trough belt conveyor

In order to compare the energy losses of a PBC from the IRR with respect to a conventional trough belt conveyor, the condition of the same capacity is used for the reference.

Both PBC and the trough conveyor are transporting the coal. PBC is filled with 75% of a cross section and is operated with belt speed varied up till 10 m/s. The trough belt conveyor selected for the comparison has the same capacity and the same belt speed variation. The equivalence in capacity is achieved by selecting a wider belt. The belt mass and other parameters of the trough belt conveyor are selected in such a way that the total vertical load from belt weight and bulk material remain the same as for PBC, i.e., $q_{bw}B + F_{bulk}^V = \text{const}$. The values for the IRR friction factor for the open trough belt conveyor are obtained using approach of May *et al.* [151] and three Maxwell parameters, determined by Lodewijks [136, 137].

Lodewijks [136, 137] proposed a general functional dependence formula for indentation model, developed by May *et al.* [151] that characterizes the IRR friction factor for one idler roll in a flat-belt and also trough belt conveyor. The function is derived using SLS-viscoelastic model with three Maxwell parameters E_{M0} , E_{M1} , and η_{M1} (see Fig 7.1e) and can be expressed in the following form:

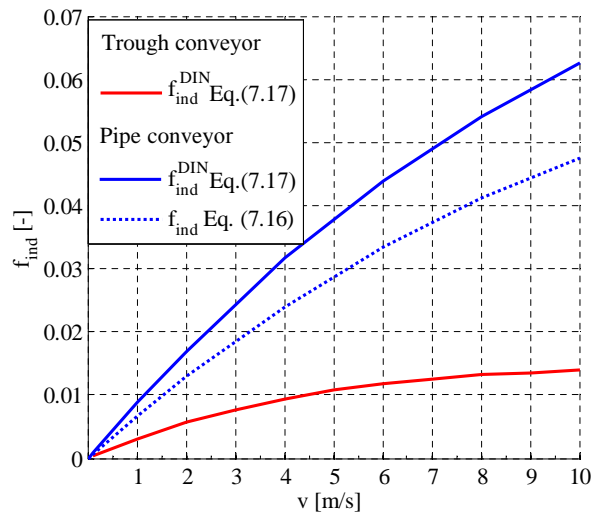


Figure 7.17: The IRR friction factor for PBC and for conventional open trough belt conveyor versus belt speed, evaluated according to DIN standard (see Eq. 7.17). The CFs for trough belt conveyor are determined for the same conveyor capacity Q_c , bulk material (coal), and the same vertical loads $q_{bw}B + F_{bulk}^V = \text{const}$, as for $k_Q = 0.75$ filling degree of a PBC.

$$f_{\text{ind}}^{\text{May}} = \frac{F_n^{1/3} h_{\text{bot}}^{1/3}}{R_1^{2/3}} \Upsilon_{\text{May}} \left(\frac{k_{\text{M1}}}{a}; \frac{b}{a}; E_{\text{M0}}; E_{\text{M1}} \right). \quad (7.26)$$

Here, Υ_{May} is a certain function of x -coordinates of the leading and trailing edges a and b in a contact square indentation contact profile, and viscoelastic Maxwell parameters.

As for PBC, Eq. 7.15, derived in Section 7.4 for one idler roll, has a similar dependence. If three Maxwell parameters are involved, it reduces to the following function:

$$f_{\text{ind}n} = \frac{F_n^{1/4} h^{1/4}}{R_1^{5/8} R_2^{1/8}} \Upsilon_{\text{PBC}} \left(\frac{k_{\text{M1}}}{a}; \frac{b}{a}; E_{\text{M0}}; E_{\text{M1}} \right). \quad (7.27)$$

Comparing the results for a PBC and a trough belt conveyor for the particular input parameters and the same values of CFs, the IRR of a PBC obtained is always larger than for trough belt conveyor.

Considering the IRR energy losses for entire conveyor systems, Fig.7.17 illustrates the results of the IRR friction factor, evaluated using the Eq. 7.16 and according DIN recommendations in Eq. 7.17. As for trough belt conveyor, only DIN $f_{\text{ind}}^{\text{DIN}}$ was used.

As it can be seen, even for three Maxwell parameters, the IRR friction factor of a PBC is much higher than the IRR of an open trough belt conveyor. The difference increases with the increase of a belt speed. Considering the practical variation range of a conveyor belt speed up till 6 m/s, established in Section 2.3.2, f_{ind} of a PBC (see Eq. 7.16) is 2.16 times higher than the indentation friction factor of a trough belt conveyor, whereas for $v = 6\text{m/s}$, it increases and becomes ≈ 2.85 times higher than for a PBC.

7.7 Conclusions

This chapter answers the research question, established in Chapter 1 on how to determine the energy losses of a PBC system from the IRR and how the load parameters in CFs influence the IRR friction factor.

To determine the IRR for a PBC, a three-dimensional generalized Maxwell model is used that incorporates multiple Maxwell parameters and Winkler foundation. In general, with the increase of a belt speed, the IRR friction factor of a PBC increases.

The IRR friction factor, evaluated using Eq. 7.17 as recommended by the DIN 22 101 standard predicts very high energy losses. The highest values belong to the case of an empty PBC. With the increase of the filling degree, belt mass or bulk weight, Eq. 7.17 exhibits a decrease of the IRR friction factor. This effect is explained by the increasing role of the load from the belt bending stiffness in indentation CFs of the nominator of Eq. 7.17, whereas the denominator for the fraction does not include that load.

Equation 7.16, on opposite, includes the effect of a load from belt bending stiffness in both nominator and denominator of the friction factor formula. As a result, the IRR friction factor values, evaluated using Eq. 7.16 correlate with ones observed in practice. With the increase of a belt mass, belt stiffness, bulk density, or conveyor cross-sectional filling degree, the IRR friction factor increases.

Present study indicates that the IRR friction factor, proposed in DIN 22 101 is not suitable for PBCs in the given form. Either Eq. 7.16 should be used, or DIN friction factor in Eq.

7.17 should be transformed, accounting the load from belt bending stiffness, added to the belt weight and bulk material in the denominator of the fraction. This can be supported, considering that load from the belt bending stiffness is also a “useful” load for a PBC, needed to form an enclosed pipe shape and justifying the selection of a PBC over any other conveyor type.

The analysis of the results, obtained using a different number of Maxwell parameters to approximate the viscoelastic properties of a belt rubber, allows one to conclude that with the increase of a number of the Maxwell parameters, the IRR of a PBC decreases. This is due to the fact that the more Maxwell parameters are used, the more accurate the indentation contact profile can be described, differentiating the deformation rates over the entire contact region. On other hand, the increase of a number of Maxwell parameters significantly affect the computation time. Balancing between the precision and the computation time, seven Maxwell parameters are selected as an optimal number.

The comparison of the IRR friction factor, obtained for PBC and a conventional open trough belt conveyor in Section 7.6.5 indicates that, for the same capacity and the vertical loads, the IRR of a PBC is $\approx (2.16...2.85)$ times higher than the IRR for a trough belt conveyor for a belt speed up till 6 m/s. With the increase of a belt speed, the difference increases.

The analysis performed in this chapter allows one to answer the research question about design preference of a PBC aiming to limit the energy losses of a PBC from the IRR. Equation 7.15, derived in Section 7.4, indicates the IRR friction factor decreases if the CFs are insignificant. In this case, the design preference of a PBC system, aiming to limit the energy consumption from the IRR, has to minimize the CFs and participating load design parameters, i.e., selecting lighter belt with lower effective modulus of elasticity and with the lower values of PBC cross-sectional filling degree for given type of a bulk material.

Based on Eq.7.15 derived, it is possible to conclude that the IRR friction factor can be also diminished by changing geometry of a belt and idler rolls, for instance, by selecting a smaller thickness of the bottom rubber cover and also using larger diameters of the idler rolls and belt’s pipe.

Finally, the IRR can be decreased, if the viscoelastic properties of the rubber, represented by Maxwell parameter, can be improved by diminishing the viscous input in a rheological rubber behavior.

The stiffer and lighter belts with smaller thickness of the belt rubber cover that at the same can have improved viscoelastic properties, can be achieved by applying new energy saving LRR technologies, discussed in Section 2.5.1. In particular, the smaller thickness of a belt with reduced weight, can be achieved by using aramid cables for the belt carcass instead of the steel cords at the belt’s tensile strength ensured. Additionally, the rubber properties can be improved by reducing the hysteresis of belt cover rubber, attained by using different constituent rubber components.

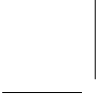
The principal of a design selection, aiming to diminish the IRR by reducing the load design parameters of CFs, should be balanced by the design requirement for sufficient belt’s pipe-ability, because some of the design parameters can cause a decrease of the IRR, but can be a reason of a contact loss and even collapse of a belt’s pipe.

For instance, as shown in Chapter 4, a large pipe diameter requires high bending stiffness to maintain a stable enclosed pipe shape. At the same time, a high bending stiffness causes an increase in CFs that in turn exacerbates the energy losses from the IRR. In this case, the

optimal design need to be established by balancing these two requirements.

That is why, the future research should determine the equilibrium between these two effects and apply mathematical methods of optimization for developing the optimum in a PBC design selection.

The model can be also improved by accounting the impact of a belt's overlap on the CFs and belt geometry that can have an influence on the pipe geometry and CFs, involved in indentation phenomenon. This can affect the IRR friction factor. In addition, the model presented in this chapter that determines the IRR for a PBC, requires experimental validation with results from the test measurements and practical PBC installations. And finally, the future research on the presented approach will be focused on the determination of the Maxwell parameters by approximating the rheological data from the dynamic/mechanic test with a reduced frequency range, inherent to the standard PBC operation mode in order to reduce the computational efforts.



Chapter 8

Conclusions

*"Vita brevis,
ars longa,
occasio praeceps,
experimentum periculosum,
iudicium difficile."*

*"Life is short,
and art long,
opportunity fleeting,
experience perilous,
and decision difficult"*

— Hippocrates, *Aphorismi*

This chapter presents the final general conclusions, drawn from this thesis, aiming to improve a PBC design and to answer the major research questions, established in Chapter 1. The findings presented can potentially be used in the future for developing a more effective design of a PBC. The recommendations for the future research are presented in Section 8.2.

8.1 Conclusions

The research presented in this thesis performs a PBC design analysis that can potentially improve a conveyor system performance, aiming:

- 1) *to ensure an enclosed geometry of a pipe conveyor cross section;*
- 2) *to reduce the IRR as a major source of a PBC energy losses.*

These major research aims are achieved by answering the auxiliary research questions in the chapters of this thesis.

Chapter 2 provides an answer to the following research questions.

- What are the principal design characteristics of a PBC system and its components?

The major PBC design characteristics are described in the chapter, relating to the overall conveyor system, bulk material, belt design, and idlers and support structures.

- What is the variation range of each design parameter and its average or more frequently used value?

The variation range of each design parameter is established using the minimal and maximal critical values. In addition, the average values or more frequently appeared in practice are provided for some of the design parameters. The research in this thesis indicated that a belt slenderness is an important design parameter for PBCs. Chapter 2 establishes a variation range for B/h inherent specifically to conveyor belts that was not made before. The range constituted $30 \leq B/h \leq 300$ and is extended to $6.67 \leq B/h \leq 643$, giving space for the future advent technologies, whereas the average value of B/h is accepted for $B/h \approx 86$.

Chapter 3 answers to the following research questions.

- How to quantify the belt's bending stiffness? Is there any way to use a standard troughability test for this purpose?

The major conclusion of the study states that it is possible to quantify a conveyor belt bending stiffness from the troughability parameter, obtained using standardized troughability test procedure, reflected in the current NEN-EN-ISO 703 [174]. To quantify a conveyor belt bending stiffness from the troughability parameter, six models are proposed: two analytical beam models of Wang and Fertis, their shell-approximation, and two FEM models (both beam and shell). The results, obtained using the analytical and the FEM models are in agreement with the experiment and exhibit a similar resultant trend.

- Is it possible to establish a functional dependence between the belt troughability, bending stiffness, and all the influencing design parameters?

The troughability parameter can be represented by the load-deflection parametric function of a belt bending stiffness EI , its width B , mass q_{bw} , and geometry, expressed by the ratio B/h and b/h . For the shell models, the troughability function can be written as follows:

$$\frac{Y_{\max}}{B} = f_T^{\text{shell}} \left(\frac{q_{bw} B^3}{EI}; \frac{B}{h}; \frac{b}{h} \right).$$

The beam models exhibit similar functional dependence to input design parameter, except to the ratio of b/h . The troughability of the beam models is independent to that parameter.

- How each of the design parameter can influence belt's bending stiffness?

Results show that for the same troughability value, an impact of a belt line mass change q has a proportional effect on change in effective modulus of elasticity E for the same belt sample geometry.

Considering the effect of a belt slenderness B/h , thin and wide conveyor belts with significant ratio B/h exhibit larger troughability for the same E -modulus, compared to more thick and narrow belts with smaller ratio B/h due to the stiffening effect. This effect appears from the structural extension in addition to the nonlinear bending and becomes dominative when thin and wide belt samples exhibit very large troughability. At the same time, thick or narrow conveyor belts are affected by shear deformations, which are not trivial for belts with minor B/h .

For the shell numerical models, the ratio b/h characterizes an additional shear effect from both structural planes of bending. In addition, it influences the appearance of the anticlastic curvature effect, especially observed for smaller ratio of b/h and B/h .

- What are the limitations of using the models that can quantify belt bending stiffness from its troughability parameter?

All the models proposed are limited to the belt's small strain range (up till 5%), satisfying the assumption of a linear elastic belt behavior under normal operational conditions. The usage of the analytical models, that are more attractive for the practical use, is limited to the 10% difference with the FEM models. The FEM models are more precise, but requires more complex iterative solution, less convenient for the practical application. The usage limitations of the models is provided in Table 3.7.

Chapter 4, **Chapter 5**, and **Chapter 6** give the answers to the following research questions.

- How to determine the pipe conveyor CFs?

To determine PBC CFs, three approaches are proposed: experimental approach in Chapter 4, analytical approach in Chapter 5, and the numerical FEM approach in Chapter 6. Usage of all three approaches together allows one to determine PBC CFs in a more precise way, compared to the existing studies.

For the analytical approach, the analysis performed in Chapter 5 for the existing studies, evidenced that none of the analytical models available determine the PBC CFs in a correct way. That is why, a new analytical approach is developed in Chapter 5. To determine the CFs with FEM, three models are elaborated: the Beam Simplified Model, the Beam Step Model and the Shell Step Model. For the experimental approach in Chapter 4, the CFs were measured for the same belt samples, as used in the troughability test, aiming to validate the analytical and the FEM models.

A comparison of CFs for the case study, obtained using the experimental, analytical, and the FEM approaches, indicated that the FEM models (the Shell Step Model and the Beam Step Model) are in close agreement with the experiment. At the same time, the CFs from the Beam Step Model and the Beam Simplified Model correlate with each other and also are in agreement with the analytical model. In this case, it is possible to state that the FEM models and the analytical model proposed to determine PBC CFs are validated with the experiment for the case study.

The analysis indicated that, at certain PBC designs, a more simple analytical model that is more attractive for the practical use determines the CFs in a feasible range, compared to the FEM models that are more complex, time consuming, and less attractive in terms of an application. In addition, the simple analytical model and also the complex FEM models predict a similar dependence trend of CFs parameterized with respect to the change in input parameters.

- If the CFs are measured from the experimental testing, can the selection of a test rig design influence the CFs?

The analysis of the existing test rigs and the CFs measured, performed in Chapter 4, indicates that the CFs measured from the experimental testing can be influenced by the test rig design selection.

- What test rig configuration is suitable for the present analysis, aiming to determine PBC CFs and why?

To determine PBC CFs and taking into account all the advantages and disadvantages of the existing test rig configuration, the selection is made in Chapter 4 for the static six-point stiffness device.

The choice is made prioritizing a sufficient accuracy of the results obtained from the test rig that was provided by a full control of the friction forces and minimizing a number of the design parameters involved that can cause a measurement error. Another reason for the rig selection is that the experiment test is simple and static, and can be easily replicated using the analytical approach (Chapter 5) and the FEM (Chapter 6). The present experimental results can be used for the validation purposes. Another reason is that the same belt samples used for the six-point stiffness device can be used for the troughability test. The bending stiffness quantified from the troughability parameter, as recommended in Chapter 3, is needed in the analytical and FEM models for determining the CFs and can serve as a link between belt's troughability to its pipe-ability.

- Do the experimental results obtained correlate with the ones available in the existing studies?

The qualitative analysis of the results obtained in Chapter 4 exhibited similar load patterns with feasible values of CFs, compared to the results attained by the different researchers and using different test rigs. Furthermore, for the each experiment case with the 0° overlap position, the load at the individual plate was in a range (40 ~ 48)% of the sum of all CFs, whereas for the 180° overlap position at the bottom, the CF on the individual plate did not exceed 80% of the sum of all CF. This observations correlate with the results available in the existing studies.

- Aiming to determine the CFs, is it possible to represent a belt stress state that appears from folding a belt from a flat shape into a pipe shape as an additional external load, applied at the stress free belt already in a pipe shape?

Chapter 5 reviewed all the existing studies that determine PBC CFs, by replacing a complex folding process of a belt from a flat shape into a pipe shape with an additional external load, applied at the stress free belt already in a pipe shape. Three methods of modeling this load from the belt bending stiffness are selected for the analysis: the concentrated expansion moments applied at the belt edges M_{bst} that was also newly introduced in Chapter 5; the radial expansion load evenly distributed along the belt's pipe q_{bst} , proposed by Chernenko [27, 28]; and the radial distributed load q_{bst} together with the concentrated forces Q_{1bst} , Q_{2bst} , presented by Dmitriev [52].

The CFs obtained from the analytical and the FEM models, using all three methods of modeling the load from the belt bending stiffness are compared in Chapter 6 with the experiment case study and also with the FEM step models, since the step models simulate an actual formation of a belt from a stress-free flat shape into a pipe shape.

The analysis indicated that it is indeed possible to represent a belt stress state that appears from folding a belt from a flat shape into a pipe shape as an additional external load, if the PBC CFs are determined. For this purpose, only the expansion concentrated moments M_{bst} , applied at the belt edges can be used. Other methods proposed in Chapter 5 do not give satisfactory results.

- How to model a bulk material load for the CFs?

Chapter 5 proposed an analytical method to model a bulk material load for the CFs using a vertical and the horizontal load components that account the bulk shear stresses. Analysis in Chapter 6 shows that all the existing models that determine PBC CFs from the bulk load analytically, use only the radial bulk load component, neglecting the presence of the tangential one. Chapter 5 proves that such approach underestimates the overall bulk material weight, indicating that the impact of both load components (either vertical and the horizontal one or the radial and the tangential one) is obligatory to use.

- Which design parameters of a PBC system influence the CFs and what is their effect? Is it possible to derive a functional dependence between the CFs and participating PBC design parameters?

In order to investigate which design parameters can influence the PBC CFs and derive a functional dependence between the CFs and the input design parameters, the analytical model is used as a basis.

For an empty PBC, the functional dependence of CFs parametrized with respect to the belt's axial stiffness EA represents a function of a belt slenderness B/h and the load ratio from the belt weight $q_{bw}/(El)$:

$$\frac{F_n}{EA} = f_n^{\text{empt}} \left(\frac{q_{bw}}{El}; \frac{B}{h} \right).$$

For a PBC loaded with a bulk material, in addition to the parameters mentioned, the functional dependence of CFs incorporates the effect of the ratio from the bulk material load $\rho_{\text{bulk}}gB/E$ and PBC cross-sectional filling degree k_Q :

$$\frac{F_n}{EA} = f_n^{\text{loaded}} \left(\frac{B}{h}; \frac{q_{bw}}{El}; \frac{\rho_{\text{bulk}}gB}{E}; k_Q \right).$$

The function of CFs for loaded PBC converges to the dependence for an empty PBC, if the bulk density and the cross-sectional filling degree are assumed equal to zero.

In general, with the increase of the load parameters $q_{bw}/(El)$ and $\rho_{\text{bulk}}gB/E$, the CFs increase, however at certain combinations of their values, one or more CFs can become equal to zero (a contact loss). For the linear solution, these parameters have a proportional effect on CFs parameterized.

The impact of a belt slenderness B/h , has a significant effect on CFs, and has a more complex dependence character as shown in Chapter 6. In order to ensure sufficient pipe-ability of a conveyor belt, the slenderness ratio B/h has to be carefully controlled, despite the fact that this parameter has never been used by the manufacturers before as a criteria for the belt design selection.

In addition, the experimental results in Chapter 4 indicates that, if the presence of an overlap is taken into account, the PBC CFs are also influenced by the length of an overlap with respect to the nominal pipe diameter, represented by the ratio B/D_{nom} , and the orientation of an overlap. The latter causes an increase for the CF that is in the position of a direct contact with the belt overlap.

- What is the weakest position of a roll in an idler set that can exhibit a contact loss? What is the preference for a PBC design selection aiming to avoid a contact loss and ensure sufficient belt's pipe-ability?

The results for CFs obtained in Chapter 6 shows that the weakest position for a contact loss occurs for a lateral top rolls for CFs F_2 , or F_6 . If the belt's pipe-ability is deteriorated further, it is possible to expect the next contact loss at the top roll F_1 in addition to the contact losses for F_2 and F_6 .

The preference for a PBC design selection, aiming to avoid a contact loss and ensure sufficient belt's pipe-ability, has to minimize the values of the load ratios $\rho_{\text{bulk}}gB/E \rightarrow \min$ and $q_{\text{bw}}/(EI) \rightarrow \min$. If a conveyor does not exhibit sufficient pipe-ability, especially expected when a heavy bulk material has to be transported, the belt design can be chosen towards lighter and transversely stiffer belts with smaller belt width. Moreover, the belt slenderness has to be taken into account. The extreme values are not preferable, as significantly thick belts (with approximate $B/h < 30$) tend to exhibit a contact loss for the CFs F_2 and F_6 , whereas thin belts ($B/h > 130$) can fully collapse a pipe with the contact loss with all three top rolls. In this case, thinner belts with higher ratio of B/h requires higher stiffness to form a pipe shape. A better pipe-ability is observed for approximate slenderness ratios ($35 < B/h < 75$), however the limits can be negotiated, considering the impact of all the participating parameters involved together.

Taking into account the conclusions drawn in Chapter 4 from the experimental testing of belts formed into a pipe shape with an overlap, an additional advice for the design preference would be to select the belts for larger pipe diameters with a higher transverse bending stiffness to form a pipe shape without a contact loss. Compared to the stiffer belts with the same width, more flexible belts need higher ratio of B/D_{nom} .

Chapter 7 answers to the following research questions.

- How to determine the energy losses of a PBC system from the IRR and how the the load parameters in CFs influence the IRR friction factor?

To determine the IRR for a PBC, a three-dimensional generalized Maxwell model is used that incorporates multiple Maxwell parameters and Winkler foundation.

The IRR friction factor, evaluated using Eq. 7.17 as recommended by the DIN 22 101 standard predicts very high energy losses. With the increase of the filling degree, belt mass or bulk weight, Eq. 7.17 exhibits a decrease of the IRR friction factor. This effect is explained by the increasing role of the load from the belt bending stiffness in indentation CFs of the nominator of Eq. 7.17, whereas the denominator does not include that load.

Equation 7.16, on opposite, includes the effect of the load from belt bending stiffness in both nominator and denominator of the friction factor formula. As a result, the IRR friction factor values, evaluated using Eq. 7.16 correlate with ones observed in practice. With the increase of a belt mass, belt stiffness, bulk density, or conveyor cross-sectional filling degree, the IRR friction factor increases.

Present study indicates that the IRR friction factor, proposed in DIN 22 101 is not suitable for PBCs in the given form. Either Eq. 7.16 should be used, or DIN friction factor in Eq. 7.17 should be transformed, accounting the load from belt bending stiffness, added to the "useful" loads from the belt weight and load from the bulk material.

- Does a number of Maxwell parameters selected to approximate the viscoelastic properties of a belt rubber influence the IRR determined?

The analysis of the results, obtained allows one to conclude that a number of Maxwell parameters selected to approximate the viscoelastic properties of a belt rubber influences the IRR determined. The more the Maxwell parameters is used, the lower IRR friction factor can be achieved. At the same time, the increase of the number of Maxwell parameters significantly affects the computation time. Balancing between the precision and the computation time, seven Maxwell parameters are selected as an optimal number.

- How different the IRR of a PBC system compared to the IRR of a conventional trough belt conveyor?

The comparison of the IRR friction factor, obtained for a PBC and a conventional open trough belt conveyor indicates that, for the same capacity and the vertical loads, the IRR of the PBC is $\approx (2.16...2.85)$ times higher than the IRR for a trough belt conveyor for a belt speed up till 6 m/s. With the increase of a belt speed, the difference increases.

- What is the preference for a PBC design selection, aiming to limit its energy losses from the IRR?

The design preference for a PBC system, aiming to limit the energy consumption from the IRR, has to minimize the CFs and participating load design parameters, i.e., selecting lighter belt with lower effective modulus of elasticity and lower values of a PBC cross-sectional filling degree for given type of a bulk material.

Based on Eq.7.15 derived, it is possible to conclude that the IRR friction factor can be also diminished by changing geometry of a belt and idler rolls, for instance, by selecting a smaller thickness of the bottom rubber cover and also using larger diameters of the idler rolls and belt's pipe.

Finally, the IRR can be decreased, if the viscoelastic properties of the rubber compounds, represented by Maxwell parameter, can be improved by diminishing the viscous input in a rheological rubber behavior.

The principal of a design selection, aiming to diminish the IRR by reducing the load design parameters of CFs, should be balanced by the design requirements for a sufficient belt's pipe-ability. The stiffer and lighter belts with smaller thickness of a belt rubber cover with better viscoelastic properties can be improved by using LRR solutions for constituent components for the belt rubber covers and for the carcass.

8.2 Recommendations for future research

The future research that can contribute and continue the findings on a more effective PBC design selection, presented in this thesis, can be developed in the following possible directions.

- **Quantifying a conveyor belt bending stiffness**

The approach of determining a conveyor belt bending stiffness from the troughability test developed in this thesis, needs further experimental validation for different belt's input parameters. The results should be also compared with the alternative procedures, like three- and four-point bending tests.

The model for the troughability test can be expanded by incorporating a non-uniform belt design structure with discrete change in properties along the belt width. In addition, the further studies have to investigate the impact of the belt's viscoelasticity (time and temperature) on the belt's troughability and bending stiffness quantified. The analysis can also integrate the nonlinear elastic models (e.g., the Mooney-Rivlin, Ogden models) for the comprising rubber-like elastomer materials of a conveyor belt, expanding the solution for larger limitation strains (more than 5%).

- **Determining PBC CFs**

Further research for the experimental approach should be focused in performing more tests with various belt structural designs. In addition, the experiment tests can be performed for more design parameters, such as belt tension, presence of bulk material, belt speed, length of carry spacing, using more complex test rigs and studying their influence on contact forces and belt's pipe-ability. In addition, the research can significantly benefit, if the experimental measurements can be performed for the bulk material load distribution inside the pipe, performed for a running PBC installation or in a dynamic test rig.

Both FEM and analytical approaches described require further experimental validation for different PBC design parameters, performed not only using a six-point stiffness device, but also for both empty PBC and loaded with bulk material. In addition, the numerical recommendations has to be developed for the usage limitation of the present models (both analytical and the FEM), satisfying 5% small strain for the linear-elastic belt material assumed.

The analytical and the FEM models, developed in this thesis to determine the PBC CFs, can be also expanded by incorporating other effects and external loads, such as the lateral load from the belt tension that appears at the conveyor route curves, discrete change of a belt properties along its width, and presence of a belt overlap.

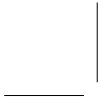
The FEM approach proposed can be expanded, by incorporating a higher lever of the problem complexity towards the one, observed in practice, i.e., by incorporating belt's nonlinear elasticity, the rheological properties of a belt constituting rubber, modeling carcass design of a belt, including belt's orthotropic properties and effect of a belt tension with respect to the length of a conveyor pitch, actual presence of a bulk material and its behavior inside the pipe, and dynamic effects. All these complex problems can be solved using numerical analysis (like FEM, FDM, DEM), incorporated in software. The analytical model proposed in this thesis can be used as a starting reference point for the validation and base for the impact analysis for all the complex numerical models used.

- **Estimating the IRR**

The model, developed in this thesis to determine PBC IRR, can benefit by accounting the impact of a belt's overlap. In addition, the model presented in this chapter that determines the IRR for a PBC, requires experimental validation with the results from the test measurements and practical PBC installations. And finally, the future research on the presented approach can benefit by using the Maxwell parameters, determined with a reduced frequency range, inherent to the standard PBC operation mode.

- **Selecting the optimal design of a PBC**

For selecting a more effective PBC design, the future research has to incorporate optimization mathematical methods for the findings presented in this thesis, aiming to achieved an optimum between ensuring a stable belt's pipe-ability and limiting the energy losses from IRR. The numerical recommendations have to be developed for the full range of input design parameters. For the sufficient belt's bending stiffness, the recommendations can be expressed, linking belt's pipe-ability via troughability parameter. Based on these findings, a more effect design for a PBC and belting can be elaborated.



Appendix A

Structural displacements from the vertical component of a bulk material load

The formulas, provided for the displacements contain the functions $\Phi_M^v(\theta, \varphi, \alpha)$, $\Phi_{M,\lambda}^v(\theta, \varphi, \alpha)$, $\Phi_{NQ}^v(\theta, \varphi, \alpha)$, and $\Phi_{NQ,\lambda}^v(\theta, \varphi, \alpha)$ that are used for the simplification purposes. These functions are defined in Chapter 5 by Eqs. 5.124, respectively.

In general, the displacements depend on the filling degree of a PBC lateral cross section, characterized by the filling angle θ . There are four critical angular positions of θ that determine the structural displacements $\delta_{n\text{bulk}}^v$ using different formulas.

1). The case when the filling degree is characterized by the angle $0 \leq 2\theta \leq \frac{\pi}{3}$, or $0 \leq \theta \leq \frac{\pi}{6}$, illustrated in Fig. A.1, the displacements in line with the corresponding redundant forces equal:

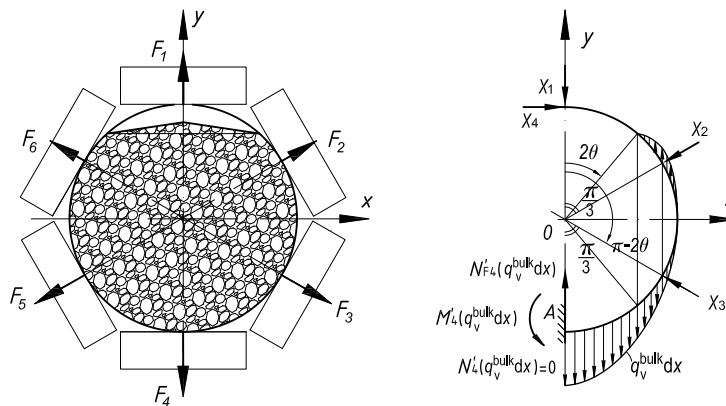


Figure A.1: The statically determinate system, subjected to the redundant forces X_1 , X_2 , X_3 , X_4 , and the vertical load component from the bulk material $q_{\text{bulk}}^v dx$, distributed along the contour with angular position $2\theta \leq \varphi \leq \pi$, where $0 \leq 2\theta \leq \frac{\pi}{3}$.

$$\begin{aligned}
\delta_{1\text{bulk}}^{\text{v}} &= \int_L \frac{M_{11}M_{\text{bulk}}^{\text{v}}}{EI} ds + \int_L \frac{N_{11}N_{\text{bulk}}^{\text{v}}}{EA} ds + \int_L \frac{kQ_{11}Q_{\text{bulk}}^{\text{v}}}{GA} ds = \\
&= -\frac{\rho_{\text{bulk}}gR^5l}{EI} \left[\int_{2\theta}^{\pi} \sin \varphi \int_{2\theta}^{\varphi} \Phi_M^{\text{v}}(\theta, \varphi, \alpha) d\alpha d\varphi + \right. \\
&+ \tan \lambda \int_{\pi-2\theta}^{\pi} \sin \varphi \int_{\pi-2\theta}^{\varphi} \Phi_{M,\lambda}^{\text{v}}(\theta, \varphi, \alpha) d\alpha d\varphi \left. \right] - \\
&- \frac{\rho_{\text{bulk}}gR^3l}{EA} \left[\int_{2\theta}^{\pi} \sin^2 \varphi \int_{2\theta}^{\varphi} \Phi_{NQ}^{\text{v}}(\theta, \alpha) d\alpha d\varphi + \tan \lambda \int_{\pi-2\theta}^{\pi} \sin^2 \varphi \int_{\pi-2\theta}^{\varphi} \Phi_{NQ,\lambda}^{\text{v}}(\theta, \alpha) d\alpha d\varphi \right] - \\
&- \frac{k\rho_{\text{bulk}}gR^3l}{GA} \left[\int_{2\theta}^{\pi} \cos^2 \varphi \int_{2\theta}^{\varphi} \Phi_{NQ}^{\text{v}}(\theta, \alpha) d\alpha d\varphi + \tan \lambda \int_{\pi-2\theta}^{\pi} \cos^2 \varphi \int_{\pi-2\theta}^{\varphi} \Phi_{NQ,\lambda}^{\text{v}}(\theta, \alpha) d\alpha d\varphi \right]; \tag{A.1}
\end{aligned}$$

$$\begin{aligned}
\delta_{2\text{bulk}}^{\text{v}} &= \int_L \frac{M_{12}M_{\text{bulk}}^{\text{v}}}{EI} ds + \int_L \frac{N_{12}N_{\text{bulk}}^{\text{v}}}{EA} ds + \int_L \frac{kQ_{12}Q_{\text{bulk}}^{\text{v}}}{GA} ds = \\
&= -\frac{\rho_{\text{bulk}}gR^5l}{EI} \left[\int_{\pi/3}^{\pi} \sin \left(\varphi - \frac{\pi}{3} \right) \int_{2\theta}^{\varphi} \Phi_M^{\text{v}}(\theta, \varphi, \alpha) d\alpha d\varphi + \right. \\
&+ \tan \lambda \int_{\pi-2\theta}^{\pi} \sin \left(\varphi - \frac{\pi}{3} \right) \int_{\pi-2\theta}^{\varphi} \Phi_{M,\lambda}^{\text{v}}(\theta, \varphi, \alpha) d\alpha d\varphi \left. \right] - \\
&- \frac{\rho_{\text{bulk}}gR^3l}{EA} \left[\int_{\pi/3}^{\pi} \sin \varphi \sin \left(\varphi - \frac{\pi}{3} \right) \int_{2\theta}^{\varphi} \Phi_{NQ}^{\text{v}}(\theta, \alpha) d\alpha d\varphi + \right. \\
&+ \tan \lambda \int_{\pi-2\theta}^{\pi} \sin \varphi \sin \left(\varphi - \frac{\pi}{3} \right) \int_{\pi-2\theta}^{\varphi} \Phi_{NQ,\lambda}^{\text{v}}(\theta, \alpha) d\alpha d\varphi \left. \right] - \\
&- \frac{k\rho_{\text{bulk}}gR^3l}{GA} \left[\int_{\pi/3}^{\pi} \cos \varphi \cos \left(\varphi - \frac{\pi}{3} \right) \int_{2\theta}^{\varphi} \Phi_{NQ}^{\text{v}}(\theta, \alpha) d\alpha d\varphi + \right. \\
&+ \tan \lambda \int_{\pi-2\theta}^{\pi} \cos \varphi \cos \left(\varphi - \frac{\pi}{3} \right) \int_{\pi-2\theta}^{\varphi} \Phi_{NQ,\lambda}^{\text{v}}(\theta, \alpha) d\alpha d\varphi \left. \right]; \tag{A.2}
\end{aligned}$$

$$\begin{aligned}
\delta_{3\text{bulk}}^{\text{v}} &= \int_L \frac{M_{13}M_{\text{bulk}}^{\text{v}}}{EI} ds + \int_L \frac{N_{13}N_{\text{bulk}}^{\text{v}}}{EA} ds + \int_L \frac{kQ_{13}Q_{\text{bulk}}^{\text{v}}}{GA} ds = \\
&= \frac{\rho_{\text{bulk}}gR^5l}{EI} \left[\int_{2\pi/3}^{\pi} \sin \left(\varphi + \frac{\pi}{3} \right) \int_{2\theta}^{\varphi} \Phi_M^{\text{v}}(\theta, \varphi, \alpha) d\alpha d\varphi + \right. \\
&+ \tan \lambda \int_{\pi-2\theta}^{\pi} \sin \left(\varphi + \frac{\pi}{3} \right) \int_{\pi-2\theta}^{\varphi} \Phi_{M,\lambda}^{\text{v}}(\theta, \varphi, \alpha) d\alpha d\varphi \left. \right] + \\
&+ \frac{\rho_{\text{bulk}}gR^3l}{EA} \left[\int_{2\pi/3}^{\pi} \sin \varphi \sin \left(\varphi + \frac{\pi}{3} \right) \int_{2\theta}^{\varphi} \Phi_{NQ}^{\text{v}}(\theta, \alpha) d\alpha d\varphi + \right. \\
&+ \tan \lambda \int_{\pi-2\theta}^{\pi} \sin \varphi \sin \left(\varphi + \frac{\pi}{3} \right) \int_{\pi-2\theta}^{\varphi} \Phi_{NQ,\lambda}^{\text{v}}(\theta, \alpha) d\alpha d\varphi \left. \right] + \\
&+ \frac{k\rho_{\text{bulk}}gR^3l}{GA} \left[\int_{2\pi/3}^{\pi} \cos \varphi \cos \left(\varphi + \frac{\pi}{3} \right) \int_{2\theta}^{\varphi} \Phi_{NQ}^{\text{v}}(\theta, \alpha) d\alpha d\varphi + \right. \\
&+ \tan \lambda \int_{\pi-2\theta}^{\pi} \cos \varphi \cos \left(\varphi + \frac{\pi}{3} \right) \int_{\pi-2\theta}^{\varphi} \Phi_{NQ,\lambda}^{\text{v}}(\theta, \alpha) d\alpha d\varphi \left. \right]; \tag{A.3}
\end{aligned}$$

$$\begin{aligned}
\delta_{4\text{bulk}}^v &= \int_L \frac{M_{14} M_{\text{bulk}}^v}{EI} ds + \int_L \frac{N_{14} N_{\text{bulk}}^v}{EA} ds + \int_L \frac{k Q_{14} Q_{\text{bulk}}^v}{GA} ds = \\
&= -\frac{\rho_{\text{bulk}} g R^5 l}{EI} \left[\int_{2\theta}^{\pi} (\cos \varphi - 1) \int_{2\theta}^{\varphi} \Phi_M^v(\theta, \varphi, \alpha) d\alpha d\varphi + \right. \\
&+ \tan \lambda \int_{\pi-2\theta}^{\pi} (\cos \varphi - 1) \int_{\pi-2\theta}^{\varphi} \Phi_{M\lambda}^v(\theta, \varphi, \alpha) d\alpha d\varphi \left. - \right. \\
&- \left(\frac{\rho_{\text{bulk}} g R^3 l}{EA} - \frac{k \rho_{\text{bulk}} g R^3 l}{GA} \right) \left[\int_{2\theta}^{\pi} \sin \varphi \cos \varphi \int_{2\theta}^{\varphi} \Phi_{NQ}^v(\theta, \alpha) d\alpha d\varphi + \right. \\
&+ \tan \lambda \int_{\pi-2\theta}^{\pi} \sin \varphi \cos \varphi \int_{\pi-2\theta}^{\varphi} \Phi_{NQ\lambda}^v(\theta, \alpha) d\alpha d\varphi \left. \right]. \tag{A.4}
\end{aligned}$$

2). The case when the filling angle is in the range $\frac{\pi}{3} \leq 2\theta \leq \frac{\pi}{2}$, or $\frac{\pi}{6} \leq \theta \leq \frac{\pi}{4}$ is shown in Fig. A.2.

The displacements for this filling angle can be evaluated as follows:

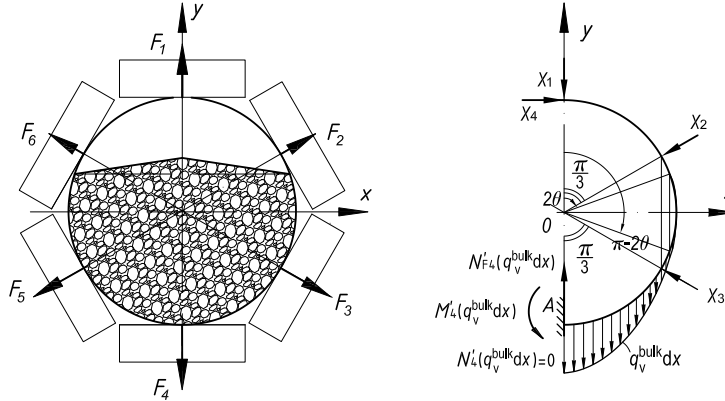


Figure A.2: The statically determinate system, subjected to the redundant forces X_1 , X_2 , X_3 , X_4 , and the vertical load component from the bulk material $q_{\text{bulk}}^v dx$, distributed along the contour with angular position $2\theta \leq \varphi \leq \pi$, where $\frac{\pi}{3} \leq 2\theta \leq \frac{\pi}{2}$.

$\delta_{1\text{bulk}}^v$ equals the same as provided in Eq. A.1;

$$\begin{aligned}
 \delta_{2\text{bulk}}^v &= \int_L \frac{M_{12}M_{\text{bulk}}^v}{EI} ds + \int_L \frac{N_{12}N_{\text{bulk}}^v}{EA} ds + \int_L \frac{kQ_{12}Q_{\text{bulk}}^v}{GA} ds = \\
 &= -\frac{\rho_{\text{bulk}}gR^5l}{EI} \left[\int_{2\theta}^{\pi} \sin\left(\varphi - \frac{\pi}{3}\right) \int_{2\theta}^{\varphi} \Phi_M^v(\theta, \varphi, \alpha) d\alpha d\varphi + \right. \\
 &+ \tan \lambda \int_{\pi-2\theta}^{\pi} \sin\left(\varphi - \frac{\pi}{3}\right) \int_{\pi-2\theta}^{\varphi} \Phi_{M\lambda}^v(\theta, \varphi, \alpha) d\alpha d\varphi \left. \right] - \\
 &- \frac{\rho_{\text{bulk}}gR^3l}{EA} \left[\int_{2\theta}^{\pi} \sin \varphi \sin\left(\varphi - \frac{\pi}{3}\right) \int_{2\theta}^{\varphi} \Phi_{NQ}^v(\theta, \alpha) d\alpha d\varphi + \right. \\
 &+ \tan \lambda \int_{\pi-2\theta}^{\pi} \sin \varphi \sin\left(\varphi - \frac{\pi}{3}\right) \int_{\pi-2\theta}^{\varphi} \Phi_{NQ\lambda}^v(\theta, \alpha) d\alpha d\varphi \left. \right] - \\
 &- \frac{k\rho_{\text{bulk}}gR^3l}{GA} \left[\int_{2\theta}^{\pi} \cos \varphi \cos\left(\varphi - \frac{\pi}{3}\right) \int_{2\theta}^{\varphi} \Phi_{NQ}^v(\theta, \alpha) d\alpha d\varphi + \right. \\
 &+ \tan \lambda \int_{\pi-2\theta}^{\pi} \cos \varphi \cos\left(\varphi - \frac{\pi}{3}\right) \int_{\pi-2\theta}^{\varphi} \Phi_{NQ\lambda}^v(\theta, \alpha) d\alpha d\varphi \left. \right]; \tag{A.5}
 \end{aligned}$$

$$\begin{aligned}
 \delta_{3\text{bulk}}^v &= \int_L \frac{M_{13}M_{\text{bulk}}^v}{EI} ds + \int_L \frac{N_{13}N_{\text{bulk}}^v}{EA} ds + \int_L \frac{kQ_{13}Q_{\text{bulk}}^v}{GA} ds = \\
 &= \frac{\rho_{\text{bulk}}gR^5l}{EI} \int_{2\pi/3}^{\pi} \sin\left(\varphi + \frac{\pi}{3}\right) \left[\int_{2\theta}^{\varphi} \Phi_M^v(\theta, \varphi, \alpha) d\alpha + \right. \\
 &+ \tan \lambda \int_{\pi-2\theta}^{\varphi} \Phi_{M\lambda}^v(\theta, \varphi, \alpha) d\alpha \left. \right] d\varphi + \\
 &+ \frac{\rho_{\text{bulk}}gR^3l}{EA} \int_{2\pi/3}^{\pi} \sin \varphi \sin\left(\varphi + \frac{\pi}{3}\right) \left[\int_{2\theta}^{\varphi} \Phi_{NQ}^v(\theta, \alpha) d\alpha + \right. \\
 &+ \tan \lambda \int_{\pi-2\theta}^{\varphi} \Phi_{NQ\lambda}^v(\theta, \alpha) d\alpha \left. \right] d\varphi + \\
 &+ \frac{k\rho_{\text{bulk}}gR^3l}{GA} \int_{2\pi/3}^{\pi} \cos \varphi \cos\left(\varphi + \frac{\pi}{3}\right) \left[\int_{2\theta}^{\varphi} \Phi_{NQ}^v(\theta, \alpha) d\alpha + \right. \\
 &+ \tan \lambda \int_{\pi-2\theta}^{\varphi} \Phi_{NQ\lambda}^v(\theta, \alpha) d\alpha \left. \right] d\varphi; \tag{A.6}
 \end{aligned}$$

$\delta_{4\text{bulk}}^v$ is equivalent to the expression given in Eq. A.4;

3). For the case when the filling angle belongs to $\frac{\pi}{2} \leq 2\theta \leq \frac{2\pi}{3}$ or $\frac{\pi}{4} \leq \theta \leq \frac{\pi}{3}$, as shown in Fig. A.3, the displacements become equivalent to the following:

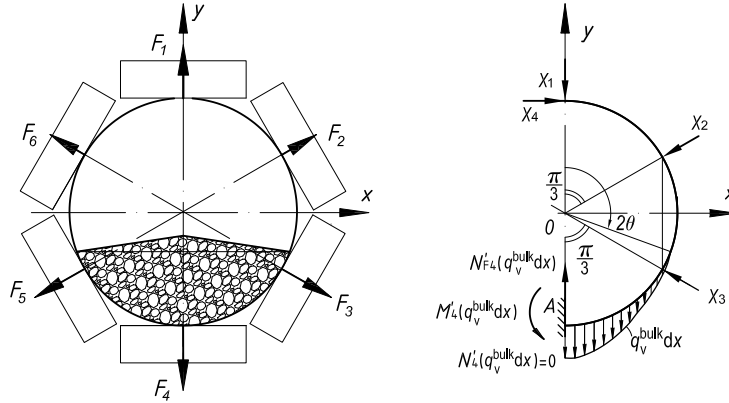


Figure A.3: The statically determinate system, subjected to the redundant forces X_1, X_2, X_3, X_4 , and the vertical load component from the bulk material $q_{\text{bulk}}^v dx$, distributed along the contour with angular position $2\theta \leq \varphi \leq \pi$, where $\frac{\pi}{2} \leq 2\theta \leq \frac{2\pi}{3}$.

$$\begin{aligned}
 \delta_{1\text{bulk}}^v &= \int_L \frac{M_{11} M_{\text{bulk}}^v}{EI} ds + \int_L \frac{N_{11} N_{\text{bulk}}^v}{EA} ds + \int_L \frac{k Q_{11} Q_{\text{bulk}}^v}{GA} ds = \\
 &= -\frac{\rho_{\text{bulk}} g R^5 l}{EI} \int_{2\theta}^{\pi} \sin \varphi \int_{2\theta}^{\varphi} [\Phi_M^v(\theta, \varphi, \alpha) + \tan \lambda \Phi_{M\lambda}^v(\theta, \varphi, \alpha)] d\alpha d\varphi - \\
 &\quad -\frac{\rho_{\text{bulk}} g R^3 l}{EA} \int_{2\theta}^{\pi} \sin^2 \varphi \int_{2\theta}^{\varphi} [\Phi_{NQ}^v(\theta, \alpha) + \tan \lambda \Phi_{NQ\lambda}^v(\theta, \alpha)] d\alpha d\varphi - \\
 &\quad -\frac{k \rho_{\text{bulk}} g R^3 l}{GA} \int_{2\theta}^{\pi} \cos^2 \varphi \int_{2\theta}^{\varphi} [\Phi_{NQ}^v(\theta, \alpha) + \tan \lambda \Phi_{NQ\lambda}^v(\theta, \alpha)] d\alpha d\varphi;
 \end{aligned} \tag{A.7}$$

$$\begin{aligned}
 \delta_{2\text{bulk}}^v &= \int_L \frac{M_{12} M_{\text{bulk}}^v}{EI} ds + \int_L \frac{N_{12} N_{\text{bulk}}^v}{EA} ds + \int_L \frac{k Q_{12} Q_{\text{bulk}}^v}{GA} ds = \\
 &= -\frac{\rho_{\text{bulk}} g R^5 l}{EI} \int_{2\theta}^{\pi} \sin \left(\varphi - \frac{\pi}{3} \right) \int_{2\theta}^{\varphi} [\Phi_M^v(\theta, \varphi, \alpha) + \tan \lambda \Phi_{M\lambda}^v(\theta, \varphi, \alpha)] d\alpha d\varphi - \\
 &\quad -\frac{\rho_{\text{bulk}} g R^3 l}{EA} \int_{2\theta}^{\pi} \sin \varphi \sin \left(\varphi - \frac{\pi}{3} \right) \int_{2\theta}^{\varphi} [\Phi_{NQ}^v(\theta, \alpha) + \tan \lambda \Phi_{NQ\lambda}^v(\theta, \alpha)] d\alpha d\varphi - \\
 &\quad -\frac{k \rho_{\text{bulk}} g R^3 l}{GA} \int_{2\theta}^{\pi} \cos \varphi \cos \left(\varphi - \frac{\pi}{3} \right) \int_{2\theta}^{\varphi} [\Phi_{NQ}^v(\theta, \alpha) + \tan \lambda \Phi_{NQ\lambda}^v(\theta, \alpha)] d\alpha d\varphi;
 \end{aligned} \tag{A.8}$$

$$\begin{aligned}
 \delta_{3\text{bulk}}^v &= \int_L \frac{M_{13} M_{\text{bulk}}^v}{EI} ds + \int_L \frac{N_{13} N_{\text{bulk}}^v}{EA} ds + \int_L \frac{k Q_{13} Q_{\text{bulk}}^v}{GA} ds = \\
 &= \frac{\rho_{\text{bulk}} g R^5 l}{EI} \int_{2\pi/3}^{\pi} \sin \left(\varphi + \frac{\pi}{3} \right) \int_{2\theta}^{\varphi} [\Phi_M^v(\theta, \varphi, \alpha) + \tan \lambda \Phi_{M\lambda}^v(\theta, \varphi, \alpha)] d\alpha d\varphi + \\
 &\quad + \frac{\rho_{\text{bulk}} g R^3 l}{EA} \int_{2\pi/3}^{\pi} \sin \varphi \sin \left(\varphi + \frac{\pi}{3} \right) \int_{2\theta}^{\varphi} [\Phi_{NQ}^v(\theta, \alpha) + \tan \lambda \Phi_{NQ\lambda}^v(\theta, \alpha)] d\alpha d\varphi + \\
 &\quad + \frac{k \rho_{\text{bulk}} g R^3 l}{GA} \int_{2\pi/3}^{\pi} \cos \varphi \cos \left(\varphi + \frac{\pi}{3} \right) \int_{2\theta}^{\varphi} [\Phi_{NQ}^v(\theta, \alpha) + \tan \lambda \Phi_{NQ\lambda}^v(\theta, \alpha)] d\alpha d\varphi;
 \end{aligned} \tag{A.9}$$

$$\begin{aligned}
 \delta_{4\text{bulk}}^v &= \int_L \frac{M_{14} M_{\text{bulk}}^v}{EI} ds + \int_L \frac{N_{14} N_{\text{bulk}}^v}{EA} ds + \int_L \frac{k Q_{14} Q_{\text{bulk}}^v}{GA} ds = \\
 &= -\frac{\rho_{\text{bulk}} g R^5 l}{EI} \int_{2\theta}^{\pi} (\cos \varphi - 1) \int_{2\theta}^{\varphi} [\Phi_M^v(\theta, \varphi, \alpha) + \tan \lambda \Phi_{M\lambda}^v(\theta, \varphi, \alpha)] d\alpha d\varphi - \\
 &\quad - \left(\frac{\rho_{\text{bulk}} g R^3 l}{EA} - \frac{k \rho_{\text{bulk}} g R^3 l}{GA} \right) \int_{2\theta}^{\pi} \sin \varphi \cos \varphi \int_{2\theta}^{\varphi} [\Phi_{NQ}^v(\theta, \alpha) + \\
 &\quad + \tan \lambda \Phi_{NQ\lambda}^v(\theta, \alpha)] d\alpha d\varphi.
 \end{aligned} \tag{A.10}$$

4). The case, shown in Fig. A.4, when the filling angle is in a range of $\frac{2\pi}{3} \leq 2\theta \leq \pi$, or $\frac{\pi}{3} \leq \theta \leq \frac{\pi}{2}$, produces the resultant displacements $\delta_{1\text{bulk}}^v$, $\delta_{2\text{bulk}}^v$, and $\delta_{4\text{bulk}}^v$, equivalent to the ones provided in Eqs. A.7, A.8, and A.10, respectively, except to the displacement $\delta_{3\text{bulk}}^v$, which equals:

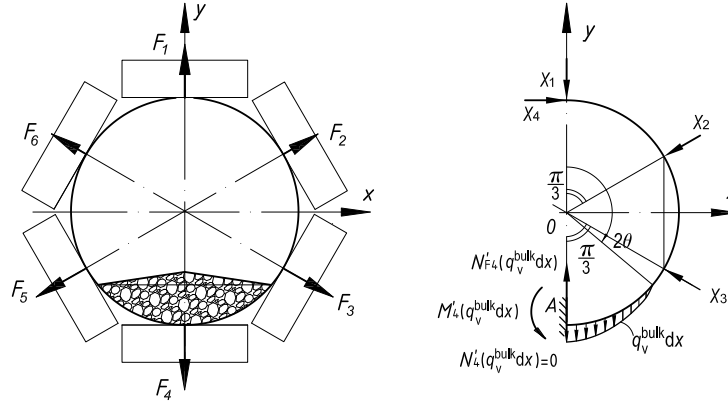


Figure A.4: The statically determinate system, subjected to the redundant forces X_1 , X_2 , X_3 , X_4 , and the vertical load component from the bulk material $q_{\text{bulk}}^v dx$, distributed along the contour with angular position $2\theta \leq \varphi \leq \pi$, where $\frac{2\pi}{3} \leq 2\theta \leq \pi$.

$$\begin{aligned}
 \delta_{3\text{bulk}}^v &= \int_L \frac{M_{13} M_{\text{bulk}}^v}{EI} ds + \int_L \frac{N_{13} N_{\text{bulk}}^v}{EA} ds + \int_L \frac{k Q_{13} Q_{\text{bulk}}^v}{GA} ds = \\
 &= \frac{\rho_{\text{bulk}} g R^5 l}{EI} \int_{2\theta}^{\pi} \sin \left(\varphi + \frac{\pi}{3} \right) \int_{2\theta}^{\varphi} [\Phi_M^v(\theta, \varphi, \alpha) + \tan \lambda \Phi_{M\lambda}^v(\theta, \varphi, \alpha)] d\alpha d\varphi + \\
 &\quad + \frac{\rho_{\text{bulk}} g R^3 l}{EA} \int_{2\theta}^{\pi} \sin \varphi \sin \left(\varphi + \frac{\pi}{3} \right) \int_{2\theta}^{\varphi} [\Phi_{NQ}^v(\theta, \alpha) + \tan \lambda \Phi_{NQ\lambda}^v(\theta, \alpha)] d\alpha d\varphi + \\
 &\quad + \frac{k \rho_{\text{bulk}} g R^3 l}{GA} \int_{2\theta}^{\pi} \cos \varphi \cos \left(\varphi + \frac{\pi}{3} \right) \int_{2\theta}^{\varphi} [\Phi_{NQ}^v(\theta, \alpha) + \tan \lambda \Phi_{NQ\lambda}^v(\theta, \alpha)] d\alpha d\varphi.
 \end{aligned} \tag{A.11}$$

Appendix B

Structural displacements from the horizontal component of a bulk material load

For the simplification, the expressions for the displacements contain the functions $\Phi_M^h(\theta, \varphi, \alpha)$, $\Phi_{M,\lambda}^h(\theta, \varphi, \alpha)$, $\Phi_{NQ}^h(\theta, \varphi, \alpha)$, and $\Phi_{NQ,\lambda}^h(\theta, \varphi, \alpha)$, being defined in Chapter 5 by Eqs. 5.129, respectively.

In general, the displacements depend on the filling degree of a PBC lateral cross section, characterized by the filling angle θ . There are four cases of filling angle θ that generates different expression for the displacements $\delta_{n\text{bulk}}^h$.

1). If the filling angle is in the range of $0 \leq 2\theta \leq \frac{\pi}{3}$, or $0 \leq \theta \leq \frac{\pi}{6}$, as shown in Fig. B.1, the displacements in line with the corresponding redundant forces equal:

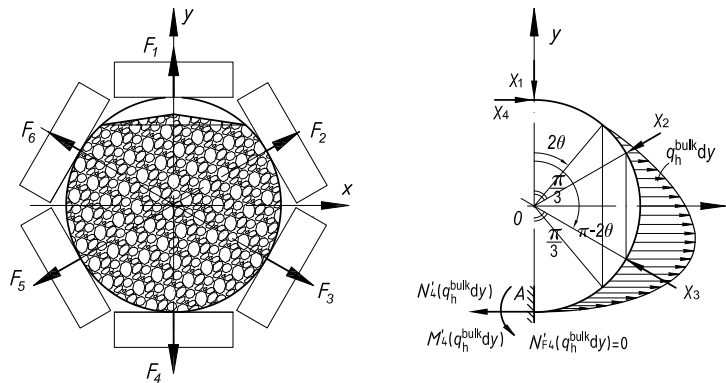


Figure B.1: The statically determinate system, subjected to the redundant forces X_1 , X_2 , X_3 , X_4 , and the horizontal load component from the bulk material $q_{\text{bulk}}^h dy$, distributed along the contour with angular position $2\theta \leq \varphi \leq \pi$, where $0 \leq 2\theta \leq \frac{\pi}{3}$.

$$\begin{aligned}
\delta_{1\text{bulk}}^h &= \int_L \frac{M_{11} M_{\text{bulk}}^h}{EI} ds + \int_L \frac{N_{11} N_{\text{bulk}}^h}{EA} ds + \int_L \frac{k Q_{11} Q_{\text{bulk}}^h}{GA} ds = \\
&= \frac{C^K \rho_{\text{bulk}} g R^5 l}{EI} \left[\int_{2\theta}^{\pi} \sin \varphi \int_{2\theta}^{\varphi} \Phi_M^h(\theta, \varphi, \alpha) d\alpha d\varphi + \right. \\
&+ \tan \lambda \int_{\pi-2\theta}^{\pi} \sin \varphi \int_{\pi-2\theta}^{\varphi} \Phi_{M\lambda}^h(\theta, \varphi, \alpha) d\alpha d\varphi \left. + \right. \\
&+ \left(\frac{C^K \rho_{\text{bulk}} g R^3 l}{EA} - \frac{C^K k \rho_{\text{bulk}} g R^3 l}{GA} \right) \left[\int_{2\theta}^{\pi} \sin \varphi \cos \varphi \int_{2\theta}^{\varphi} \Phi_{NQ}^h(\theta, \alpha) d\alpha d\varphi + \right. \\
&+ \tan \lambda \int_{\pi-2\theta}^{\pi} \sin \varphi \cos \varphi \int_{\pi-2\theta}^{\varphi} \Phi_{NQ\lambda}^h(\theta, \alpha) d\alpha d\varphi \left. \right]; \tag{B.1}
\end{aligned}$$

$$\begin{aligned}
\delta_{2\text{bulk}}^h &= \int_L \frac{M_{12} M_{\text{bulk}}^h}{EI} ds + \int_L \frac{N_{12} N_{\text{bulk}}^h}{EA} ds + \int_L \frac{k Q_{12} Q_{\text{bulk}}^h}{GA} ds = \\
&= \frac{C^K \rho_{\text{bulk}} g R^5 l}{EI} \left[\int_{\pi/3}^{\pi} \sin \left(\varphi - \frac{\pi}{3} \right) \int_{2\theta}^{\varphi} \Phi_M^h(\theta, \varphi, \alpha) d\alpha d\varphi + \right. \\
&+ \tan \lambda \int_{\pi-2\theta}^{\pi} \sin \left(\varphi - \frac{\pi}{3} \right) \int_{\pi-2\theta}^{\varphi} \Phi_{M\lambda}^h(\theta, \varphi, \alpha) d\alpha d\varphi \left. + \right. \\
&+ \frac{C^K \rho_{\text{bulk}} g R^3 l}{EA} \left[\int_{\pi/3}^{\pi} \sin \left(\varphi - \frac{\pi}{3} \right) \cos \varphi \int_{2\theta}^{\varphi} \Phi_{NQ}^h(\theta, \alpha) d\alpha d\varphi + \right. \\
&+ \tan \lambda \int_{\pi-2\theta}^{\pi} \sin \left(\varphi - \frac{\pi}{3} \right) \cos \varphi \int_{\pi-2\theta}^{\varphi} \Phi_{NQ\lambda}^h(\theta, \alpha) d\alpha d\varphi \left. \right] - \\
&- \frac{C^K k \rho_{\text{bulk}} g R^3 l}{GA} \left[\int_{\pi/3}^{\pi} \sin \varphi \cos \left(\varphi - \frac{\pi}{3} \right) \int_{2\theta}^{\varphi} \Phi_{NQ}^h(\theta, \alpha) d\alpha d\varphi + \right. \\
&+ \tan \lambda \int_{\pi-2\theta}^{\pi} \sin \varphi \cos \left(\varphi - \frac{\pi}{3} \right) \int_{\pi-2\theta}^{\varphi} \Phi_{NQ\lambda}^h(\theta, \alpha) d\alpha d\varphi \left. \right]; \tag{B.2}
\end{aligned}$$

$$\begin{aligned}
\delta_{3\text{bulk}}^h &= \int_L \frac{M_{13} M_{\text{bulk}}^h}{EI} ds + \int_L \frac{N_{13} N_{\text{bulk}}^h}{EA} ds + \int_L \frac{k Q_{13} Q_{\text{bulk}}^h}{GA} ds = \\
&= -\frac{C^K \rho_{\text{bulk}} g R^5 l}{EI} \left[\int_{2\pi/3}^{\pi} \sin \left(\varphi + \frac{\pi}{3} \right) \int_{2\theta}^{\varphi} \Phi_M^h(\theta, \varphi, \alpha) d\alpha d\varphi + \right. \\
&+ \tan \lambda \int_{\pi-2\theta}^{\pi} \sin \left(\varphi + \frac{\pi}{3} \right) \int_{\pi-2\theta}^{\varphi} \Phi_{M\lambda}^h(\theta, \varphi, \alpha) d\alpha d\varphi \left. \right] - \\
&- \frac{C^K \rho_{\text{bulk}} g R^3 l}{EA} \left[\int_{2\pi/3}^{\pi} \sin \left(\varphi + \frac{\pi}{3} \right) \cos \varphi \int_{2\theta}^{\varphi} \Phi_{NQ}^h(\theta, \alpha) d\alpha d\varphi + \right. \\
&+ \tan \lambda \int_{\pi-2\theta}^{\pi} \sin \left(\varphi + \frac{\pi}{3} \right) \cos \varphi \int_{\pi-2\theta}^{\varphi} \Phi_{NQ\lambda}^h(\theta, \alpha) d\alpha d\varphi \left. \right] + \\
&+ \frac{C^K k \rho_{\text{bulk}} g R^3 l}{GA} \left[\int_{2\pi/3}^{\pi} \sin \varphi \cos \left(\varphi + \frac{\pi}{3} \right) \int_{2\theta}^{\varphi} \Phi_{NQ}^h(\theta, \alpha) d\alpha d\varphi + \right. \\
&+ \tan \lambda \int_{\pi-2\theta}^{\pi} \sin \varphi \cos \left(\varphi + \frac{\pi}{3} \right) \int_{\pi-2\theta}^{\varphi} \Phi_{NQ\lambda}^h(\theta, \alpha) d\alpha d\varphi \left. \right]; \tag{B.3}
\end{aligned}$$

$$\begin{aligned}
\delta_{4\text{bulk}}^h &= \int_L \frac{M_{14}M_{\text{bulk}}^h}{EI} ds + \int_L \frac{N_{14}N_{\text{bulk}}^h}{EA} ds + \int_L \frac{kQ_{14}Q_{\text{bulk}}^h}{GA} ds = \\
&= \frac{C^K \rho_{\text{bulk}} g R^5 l}{EI} \left[\int_{2\theta}^{\pi} (\cos \varphi - 1) \int_{2\theta}^{\varphi} \Phi_M^h(\theta, \varphi, \alpha) d\alpha d\varphi + \right. \\
&+ \tan \lambda \int_{\pi-2\theta}^{\pi} (\cos \varphi - 1) \int_{\pi-2\theta}^{\varphi} \Phi_{M\lambda}^h(\theta, \varphi, \alpha) d\alpha d\varphi \left. + \right. \\
&+ \frac{C^K \rho_{\text{bulk}} g R^3 l}{EA} \left[\int_{2\theta}^{\pi} \cos^2 \varphi \int_{2\theta}^{\varphi} \Phi_{NQ}^h(\theta, \alpha) d\alpha d\varphi + \right. \\
&+ \tan \lambda \int_{\pi-2\theta}^{\pi} \cos^2 \varphi \int_{\pi-2\theta}^{\varphi} \Phi_{NQ\lambda}^h(\theta, \alpha) d\alpha d\varphi \left. + \right. \\
&+ \frac{C^K k \rho_{\text{bulk}} g R^3 l}{GA} \left[\int_{2\theta}^{\pi} \sin^2 \varphi \int_{2\theta}^{\varphi} \Phi_{NQ}^h(\theta, \alpha) d\alpha d\varphi + \right. \\
&+ \tan \lambda \int_{\pi-2\theta}^{\pi} \sin^2 \varphi \int_{\pi-2\theta}^{\varphi} \Phi_{NQ\lambda}^h(\theta, \alpha) d\alpha d\varphi \left. \right]. \tag{B.4}
\end{aligned}$$

2). If the filling angle belong to the values of $\frac{\pi}{3} \leq 2\theta \leq \frac{\pi}{2}$, or $\frac{\pi}{6} \leq \theta \leq \frac{\pi}{4}$, as it can be seen in Fig. B.2, the displacements are defined by:

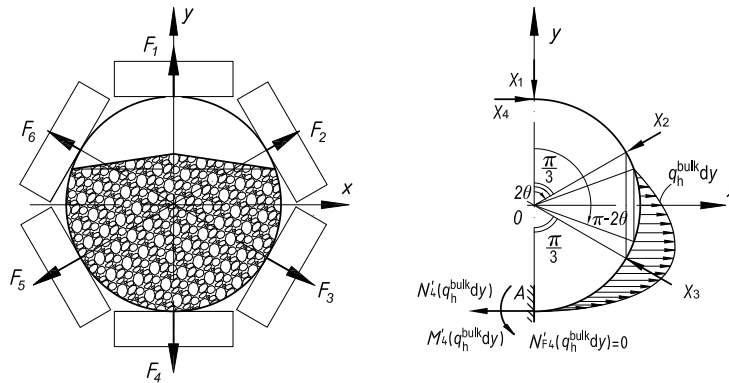


Figure B.2: The statically determinate system, subjected to the redundant forces X_1 , X_2 , X_3 , X_4 , and the horizontal load component from the bulk material $q_{\text{bulk}}^h dy$, distributed along the contour with angular position $2\theta \leq \varphi \leq \pi$, where $\frac{\pi}{3} \leq 2\theta \leq \frac{\pi}{2}$.

$\delta_{1\text{bulk}}^h$ is equivalent to the expression given in Eq. B.1;

$$\begin{aligned}
\delta_{2\text{bulk}}^h &= \int_L \frac{M_{12}M_{\text{bulk}}^h}{EI} ds + \int_L \frac{N_{12}N_{\text{bulk}}^h}{EA} ds + \int_L \frac{kQ_{12}Q_{\text{bulk}}^h}{GA} ds = \\
&= \frac{C^K \rho_{\text{bulk}} g R^5 l}{EI} \left[\int_{2\theta}^{\pi} \sin\left(\varphi - \frac{\pi}{3}\right) \int_{2\theta}^{\varphi} \Phi_M^h(\theta, \varphi, \alpha) d\alpha d\varphi + \right. \\
&+ \tan \lambda \int_{\pi-2\theta}^{\pi} \sin\left(\varphi - \frac{\pi}{3}\right) \int_{\pi-2\theta}^{\varphi} \Phi_{M\lambda}^h(\theta, \varphi, \alpha) d\alpha d\varphi \left. + \right. \\
&+ \frac{C^K \rho_{\text{bulk}} g R^3 l}{EA} \left[\int_{2\theta}^{\pi} \sin\left(\varphi - \frac{\pi}{3}\right) \cos \varphi \int_{2\theta}^{\varphi} \Phi_{NQ}^h(\theta, \alpha) d\alpha d\varphi + \right. \\
&+ \tan \lambda \int_{\pi-2\theta}^{\pi} \sin\left(\varphi - \frac{\pi}{3}\right) \cos \varphi \int_{\pi-2\theta}^{\varphi} \Phi_{NQ\lambda}^h(\theta, \alpha) d\alpha d\varphi \left. - \right. \\
&- \frac{C^K k \rho_{\text{bulk}} g R^3 l}{GA} \left[\int_{2\theta}^{\pi} \sin \varphi \cos\left(\varphi - \frac{\pi}{3}\right) \int_{2\theta}^{\varphi} \Phi_{NQ}^h(\theta, \alpha) d\alpha d\varphi + \right. \\
&+ \tan \lambda \int_{\pi-2\theta}^{\pi} \sin \varphi \cos\left(\varphi - \frac{\pi}{3}\right) \int_{\pi-2\theta}^{\varphi} \Phi_{NQ\lambda}^h(\theta, \alpha) d\alpha d\varphi \left. \right]; \tag{B.5}
\end{aligned}$$

$$\begin{aligned}
\delta_{3\text{bulk}}^h &= \int_L \frac{M_{13}M_{\text{bulk}}^h}{EI} ds + \int_L \frac{N_{13}N_{\text{bulk}}^h}{EA} ds + \int_L \frac{kQ_{13}Q_{\text{bulk}}^h}{GA} ds = \\
&= -\frac{C^K \rho_{\text{bulk}} g R^5 l}{EI} \int_{2\pi/3}^{\pi} \sin\left(\varphi + \frac{\pi}{3}\right) \left[\int_{2\theta}^{\varphi} \Phi_M^h(\theta, \varphi, \alpha) d\alpha + \right. \\
&+ \tan \lambda \int_{\pi-2\theta}^{\varphi} \Phi_{M\lambda}^h(\theta, \varphi, \alpha) d\alpha \left. \right] d\varphi - \\
&- \frac{C^K \rho_{\text{bulk}} g R^3 l}{EA} \int_{2\pi/3}^{\pi} \sin\left(\varphi + \frac{\pi}{3}\right) \cos \varphi \left[\int_{2\theta}^{\varphi} \Phi_{NQ}^h(\theta, \alpha) d\alpha + \right. \\
&+ \tan \lambda \int_{\pi-2\theta}^{\varphi} \Phi_{NQ\lambda}^h(\theta, \alpha) d\alpha \left. \right] d\varphi + \\
&+ \frac{C^K k \rho_{\text{bulk}} g R^3 l}{GA} \int_{2\pi/3}^{\pi} \sin \varphi \cos\left(\varphi + \frac{\pi}{3}\right) \left[\int_{2\theta}^{\varphi} \Phi_{NQ}^h(\theta, \alpha) d\alpha + \right. \\
&+ \tan \lambda \int_{\pi-2\theta}^{\varphi} \Phi_{NQ\lambda}^h(\theta, \alpha) d\alpha \left. \right] d\varphi; \tag{B.6}
\end{aligned}$$

$\delta_{4\text{bulk}}^h$ is equivalent to the expression given in Eq. B.4;

3). When the filling angle value is within the range $\frac{\pi}{2} \leq 2\theta \leq \frac{2\pi}{3}$, or $\frac{\pi}{4} \leq \theta \leq \frac{\pi}{3}$ (see Fig. B.3), the displacements can be evaluated using the following expressions:

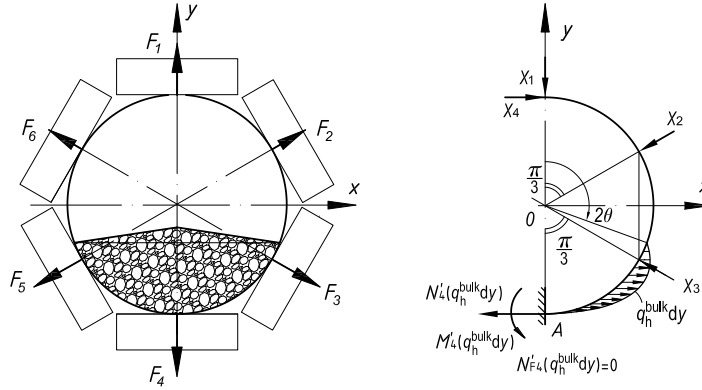


Figure B.3: The statically determinate system, subjected to the redundant forces X_1 , X_2 , X_3 , X_4 , and the horizontal load component from the bulk material $q_h^{\text{bulk}} dy$, distributed along the contour with angular position $2\theta \leq \varphi \leq \pi$, where $\frac{\pi}{2} \leq 2\theta \leq \frac{2\pi}{3}$.

$$\begin{aligned}
 \delta_{1\text{bulk}}^{\text{h}} &= \int_L \frac{M_{11} M_{\text{bulk}}^{\text{h}}}{EI} ds + \int_L \frac{N_{11} N_{\text{bulk}}^{\text{h}}}{EA} ds + \int_L \frac{k Q_{11} Q_{\text{bulk}}^{\text{h}}}{GA} ds = \\
 &= \frac{C^K \rho_{\text{bulk}} g R^5 l}{EI} \int_{2\theta}^{\pi} \sin \varphi \int_{2\theta}^{\varphi} [\Phi_M^{\text{h}}(\theta, \varphi, \alpha) + \tan \lambda \Phi_{M\lambda}^{\text{h}}(\theta, \varphi, \alpha)] d\alpha d\varphi + \\
 &+ \left(\frac{C^K \rho_{\text{bulk}} g R^3 l}{EA} - \frac{C^K k \rho_{\text{bulk}} g R^3 l}{GA} \right) \int_{2\theta}^{\pi} \sin \varphi \cos \varphi \int_{2\theta}^{\varphi} [\Phi_{NQ}^{\text{h}}(\theta, \alpha) + \\
 &+ \tan \lambda \Phi_{NQ\lambda}^{\text{h}}(\theta, \alpha)] d\alpha d\varphi;
 \end{aligned} \tag{B.7}$$

$$\begin{aligned}
 \delta_{2\text{bulk}}^{\text{h}} &= \int_L \frac{M_{12} M_{\text{bulk}}^{\text{h}}}{EI} ds + \int_L \frac{N_{12} N_{\text{bulk}}^{\text{h}}}{EA} ds + \int_L \frac{k Q_{12} Q_{\text{bulk}}^{\text{h}}}{GA} ds = \\
 &= \frac{C^K \rho_{\text{bulk}} g R^5 l}{EI} \int_{2\theta}^{\pi} \sin \left(\varphi - \frac{\pi}{3} \right) \int_{2\theta}^{\varphi} [\Phi_M^{\text{h}}(\theta, \varphi, \alpha) + \tan \lambda \Phi_{M\lambda}^{\text{h}}(\theta, \varphi, \alpha)] d\alpha d\varphi + \\
 &+ \frac{C^K \rho_{\text{bulk}} g R^3 l}{EA} \int_{2\theta}^{\pi} \sin \left(\varphi - \frac{\pi}{3} \right) \cos \varphi \int_{2\theta}^{\varphi} [\Phi_{NQ}^{\text{h}}(\theta, \alpha) + \tan \lambda \Phi_{NQ\lambda}^{\text{h}}(\theta, \alpha)] d\alpha d\varphi - \\
 &- \frac{C^K k \rho_{\text{bulk}} g R^3 l}{GA} \int_{2\theta}^{\pi} \sin \varphi \cos \left(\varphi - \frac{\pi}{3} \right) \int_{2\theta}^{\varphi} [\Phi_{NQ}^{\text{h}}(\theta, \alpha) + \tan \lambda \Phi_{NQ\lambda}^{\text{h}}(\theta, \alpha)] d\alpha d\varphi;
 \end{aligned} \tag{B.8}$$

$$\begin{aligned}
 \delta_{3\text{bulk}}^{\text{h}} &= \int_L \frac{M_{13} M_{\text{bulk}}^{\text{h}}}{EI} ds + \int_L \frac{N_{13} N_{\text{bulk}}^{\text{h}}}{EA} ds + \int_L \frac{k Q_{13} Q_{\text{bulk}}^{\text{h}}}{GA} ds = \\
 &= - \frac{C^K \rho_{\text{bulk}} g R^5 l}{EI} \int_{2\pi/3}^{\pi} \sin \left(\varphi + \frac{\pi}{3} \right) \int_{2\theta}^{\varphi} [\Phi_M^{\text{h}}(\theta, \varphi, \alpha) + \tan \lambda \Phi_{M\lambda}^{\text{h}}(\theta, \varphi, \alpha)] d\alpha d\varphi - \\
 &- \frac{C^K \rho_{\text{bulk}} g R^3 l}{EA} \int_{2\pi/3}^{\pi} \sin \left(\varphi + \frac{\pi}{3} \right) \cos \varphi \int_{2\theta}^{\varphi} [\Phi_{NQ}^{\text{h}}(\theta, \alpha) + \tan \lambda \Phi_{NQ\lambda}^{\text{h}}(\theta, \alpha)] d\alpha d\varphi + \\
 &+ \frac{C^K k \rho_{\text{bulk}} g R^3 l}{GA} \int_{2\pi/3}^{\pi} \sin \varphi \cos \left(\varphi + \frac{\pi}{3} \right) \int_{2\theta}^{\varphi} [\Phi_{NQ}^{\text{h}}(\theta, \alpha) + \tan \lambda \Phi_{NQ\lambda}^{\text{h}}(\theta, \alpha)] d\alpha d\varphi
 \end{aligned} \tag{B.9}$$

$$\begin{aligned}
 \delta_{4\text{bulk}}^h &= \int_L \frac{M_{14} M_{\text{bulk}}^h}{EI} ds + \int_L \frac{N_{14} N_{\text{bulk}}^h}{EA} ds + \int_L \frac{k Q_{14} Q_{\text{bulk}}^h}{GA} ds = \\
 &= \frac{C^K \rho_{\text{bulk}} g R^5 l}{EI} \int_{2\theta}^{\pi} (\cos \varphi - 1) \int_{2\theta}^{\varphi} [\Phi_M^h(\theta, \varphi, \alpha) + \tan \lambda \Phi_{M\lambda}^h(\theta, \varphi, \alpha)] d\alpha d\varphi + \\
 &+ \frac{C^K \rho_{\text{bulk}} g R^3 l}{EA} \int_{2\theta}^{\pi} \cos^2 \varphi \int_{2\theta}^{\varphi} [\Phi_{NQ}^h(\theta, \alpha) + \tan \lambda \Phi_{NQ\lambda}^h(\theta, \alpha)] d\alpha d\varphi + \\
 &+ \frac{C^K k \rho_{\text{bulk}} g R^3 l}{GA} \int_{2\theta}^{\pi} \sin^2 \varphi \int_{2\theta}^{\varphi} [\Phi_{NQ}^h(\theta, \alpha) + \tan \lambda \Phi_{NQ\lambda}^h(\theta, \alpha)] d\alpha d\varphi.
 \end{aligned} \tag{B.10}$$

4). For the cross-sectional filling degree characterized by the angle $\frac{2\pi}{3} \leq 2\theta \leq \pi$, or $\frac{\pi}{3} \leq \theta \leq \frac{\pi}{2}$ (see illustration in Fig. B.4), the resultant displacements $\delta_{1\text{bulk}}^h$, $\delta_{2\text{bulk}}^h$, and $\delta_{4\text{bulk}}^h$ are the same as the corresponding expressions given in Eqs. B.7, B.8, and B.10, respectively. The only difference appears for the displacement $\delta_{3\text{bulk}}^h$, which equals the following:

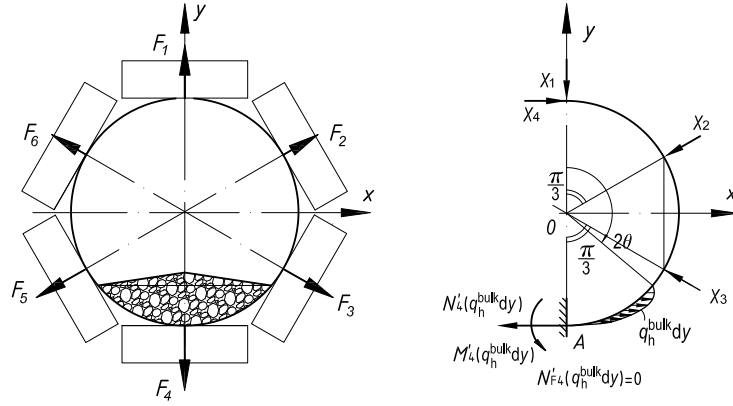


Figure B.4: The statically determinate system, subjected to the redundant forces X_1 , X_2 , X_3 , X_4 , and the horizontal load component from the bulk material $q_h^{\text{bulk}} dy$, distributed along the contour with angular position $2\theta \leq \varphi \leq \pi$, where $\frac{2\pi}{3} \leq 2\theta \leq \pi$.

$$\begin{aligned}
 \delta_{3\text{bulk}}^h &= \int_L \frac{M_{13} M_{\text{bulk}}^h}{EI} ds + \int_L \frac{N_{13} N_{\text{bulk}}^h}{EA} ds + \int_L \frac{k Q_{13} Q_{\text{bulk}}^h}{GA} ds = \\
 &= -\frac{C^K \rho_{\text{bulk}} g R^5 l}{EI} \int_{2\theta}^{\pi} \sin \left(\varphi + \frac{\pi}{3} \right) \int_{2\theta}^{\varphi} [\Phi_M^h(\theta, \varphi, \alpha) + \tan \lambda \Phi_{M\lambda}^h(\theta, \varphi, \alpha)] d\alpha d\varphi - \\
 &- \frac{C^K \rho_{\text{bulk}} g R^3 l}{EA} \int_{2\theta}^{\pi} \sin \left(\varphi + \frac{\pi}{3} \right) \cos \varphi \int_{2\theta}^{\varphi} [\Phi_{NQ}^h(\theta, \alpha) + \tan \lambda \Phi_{NQ\lambda}^h(\theta, \alpha)] d\alpha d\varphi + \\
 &+ \frac{C^K k \rho_{\text{bulk}} g R^3 l}{GA} \int_{2\theta}^{\pi} \sin \varphi \cos \left(\varphi + \frac{\pi}{3} \right) \int_{2\theta}^{\varphi} [\Phi_{NQ}^h(\theta, \alpha) + \tan \lambda \Phi_{NQ\lambda}^h(\theta, \alpha)] d\alpha d\varphi;
 \end{aligned} \tag{B.11}$$

Appendix C

Development of FEM models

The simulation procedures of the FEM models elaborated to determine PBC CFs are presented here. Following these procedures, it becomes possible to replicate the results, described in Chapter 6. The models are developed in ANSYS software using APDL for programming language and are organized here based on the principal from simple to complex.

C.1 Beam Simplified Model

Creating the model

The Beam Simplified Model is the simplest 2D beam model that closely replicates the assumptions used in the analytical approach, developed in Chapter 5.

For this model, the two-node Beam 188 element type was selected in ANSYS. This element has six degrees of freedom at each node with 16 integration points through the thickness. This element type supports the Timoshenko beam theory and includes bending, stretching, and shear effects. As a result, it is suitable for thick and thin structures.

Similar to the analytical model, developed in Chapter 5, the Beam Simplified Model represents a belt as an isotropic beam already formed in a pipe shape without overlap. As initial boundary conditions, the model has six fixed nodes with one radial restraint each. At the edges, the structure inherits additional restraints imitating the pinned supports (as illustrated in Fig. 5.21a in Chapter 5). Balancing between the precision from the sufficient fine mesh and the time of the solution convergence, the model of a pipe-shaped belt is meshed at every 0.5° with respect to the pipe origin. This constitutes 720 structural elements in total. The selection of physical parameters for modeling belt properties and external loads is described in Section 6.4.

Loads and load steps

The solution is obtained within one load step, i.e., all the loads are applied to the structure together. The belt model is subjected to gravity, load from the belt bending stiffness, and, if needed, to load from bulk material.

Similar to the analytical approach in Chapter 5, load from the belt bending stiffness is simulated using three alternative methods: 1) either by applying the expansion concentrated

moments M_{bst} at the edges, determined from Eq. 5.10 (see discussion in Section 5.3.1; 2) or by using a distributed radial load q_{bst} , calculated from Eq. 5.3 where the presence of the Poisson ratios is neglected as for a beam model (see Section 5.3.2); 3) or by incorporating a combination of distributed radial load q_{bst} and concentrated forces Q_{1bst} , Q_{2bst} , oriented at the belt cross-sectional contour at angle β (see Section 5.3.3). The loads q_{bst} , Q_{1bst} , Q_{2bst} and angle β are determined from the system of Eq. 5.26 and transcendental Eq. 5.25, respectively.

As it is discussed in Section 6.4, the length of a belt model can be the same as the length of the sample used for the case study in the experiment within the six-point stiffness device. The model can be also expanded by extending the longitudinal length of a belt section equal to conveyor pitch $l = l_c$. In this case, the load from the bulk material can also be taken into account.

For this purpose, two distributed loads are applied to the belt in addition to a gravity load and load from belt bending stiffness. Using the APDL program created, the distributed load consisted of two vertical and horizontal force-components, determined with respect to the angular $\varphi \in [0; \pi]$ position on the pipe contour and the filling degree k_Q (see Fig. 5.9). The

vertical and horizontal distributed forces were calculated as $\int_{\varphi}^{\varphi+\Delta\varphi} q_{bulk}^v dx$ and $\int_{\varphi}^{\varphi+\Delta\varphi} q_{bulk}^h dy$, respectively, and were automatically assigned to each corresponding element of the FEM model. The vertical and horizontal load components from the bulk material $q_{bulk}^v dx$ and $q_{bulk}^h dy$ are described in Section 5.4.3 and Section 5.4.4, respectively.

In order to prescribe a correct distribution of those load components onto the contour in the numerical model, a special program written in APDL was integrated in the modeling procedure. That program calculates and assigns the vertical and horizontal loads for each element with respect to its angular position φ . The more elements are used in the numerical model, the smoother the load distribution is simulated in the problem and more accurate results can be obtained.

Compared to the approach of Kulagin [126–129], Dmitriev and Kulagin [56], Dmitriev and Sergeeva [58], Sergeeva [208, 210] that divides the belt lateral contour into 24 sections (see Fig. 6.5), the Beam Simplified Model incorporates the vertical and horizontal load-components applied over 720 elements along the pipe contour. As a result, the Beam Simplified Model exhibits significantly smoother load distribution caused by the bulk material.

Noteworthy to mention is that using a beam model, both distributed loads from the bulk material are constant along the longitudinal length of each element, representing a sum of the pressure distributed on the element in longitudinal direction. For the horizontal load component, the results are obtained using different values of the coefficient C^K , characterizing the longitudinal development of the active and passive stress states of the bulk solids. In particular, the approaches of Krause and Hettler, Gushchin, Wheeler-Mulani, and the constant active stress state (see Eqs. 5.47) were exemplified.

Obtaining the solution

After creating the model and assigning all the external loads, the solution can be obtained using: 1) linear analysis, imitating the analytical linearized model, described in Chapter 5; 2) by means of finite strain nonlinear analysis. The solution control was carried out using

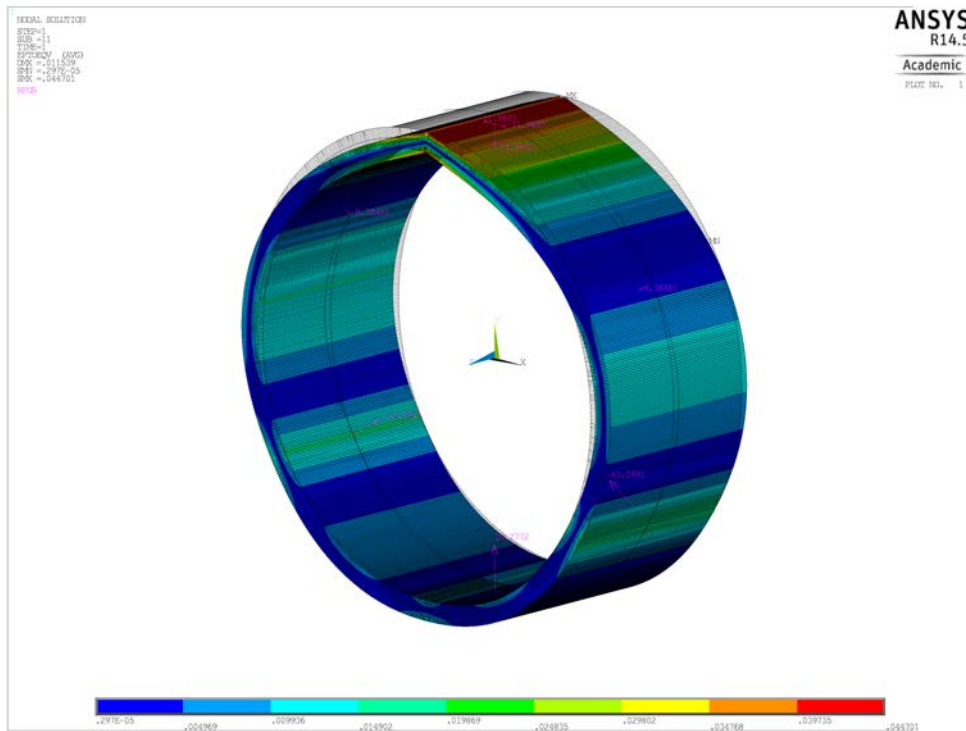


Figure C.1: Von Mises total mechanical strain, obtained from the Beam Simplified Model in ANSYS.

a Newton-Raphson scheme. Figure C.1 illustrates the Von Mises total mechanical strain solution for one of the cases, determined from the Simplified Beam Model.

The reaction forces determined at the structural constraints are the aim of the numerical solution. The reaction forces correspond to the CFs, as shown in Fig. 5.20. Similar to the analytical model, their correct positive directions of the forces are assumed as illustrated in Fig. 5.21. For the opposite case, there is a contact loss, and the restraint that corresponds to the maximal opposite force is removed from the model. The problem with the reduced number of constraints is solved again. This procedure should be repeated until the directions of all the reaction forces remained coincide with the ones accepted in Fig. 5.21.

C.2 Beam Step Model

Creating the model

This is a 2D nonlinear beam model with a more complex simulation procedure. It includes the belt model and also the hexagon supporting plates, similarly as it was used in the experiment with the six-point stiffness device. The model incorporates the contact interaction between the belt and plates and also the contact between the belt edges. The model is solved in steps, and at the first load step, the belt is folded from a stress-free flat shape into a pipe shape.

That is why this model can be solved only using nonlinear analysis.

A Beam Step Model was created using the same two-node element type (Beam 188) for modeling both belt and plates, as it was selected in the previous model. The element type used implies the Timoshenko beam theory and supports all the functional capabilities needed in the analysis. The belt was initially in a flat shape and was divided into 600 equal elements, whereas the hexagon beam plates were meshed into 50 elements each. This number of the division into elements was selected balancing between the precision from the sufficient fine mesh and the time of the problem convergence.

The physical parameters accepted for the model are described in Section 6.4. With respect to which model the present Beam Step Model is being compared, the plates can be simulated with extended length, as shown in Fig C.3a that copies the experiment test, or with reduced length, illustrated in Fig. C.3b as a step towards the analytical model.

Modeling the contact

The contact between the belt and plates was prescribed creating a 3D beam-to-beam contact pair, where the belt is selected as a contact body, and the plates as a target body [4]. The contact body (belt) was simulated using an additional two-node element type Conta 176 that accounts for the sliding contact between 3D segments [4]. As for the target body in contact pair, (supporting plates), the element Targe 170 is selected. The contact algorithm is performed using the Augmented Lagrange Method. The contact pair inherits Coulomb friction and shear stress friction.

For simulating the experiment case study, the sliding friction coefficient between the plates and the belt is assumed to be consistently minimal. This assumption was made, as in the physical experiment the impact of friction was minimized by inserting paper sheets with small friction coefficient in between the belt and plates (see Chapter 4). For the Beam Step Model, the contact between the belt and the plates was activated and deactivated with respect to load step by means of “birth” and “death” function, supported by BEAM 188 element. The effect of the beam thickness is included in the contact.

The contact between the belt edges is prescribed using the node-to-node contact element type CONTA 178 [4]. The contact is always active throughout all the solution steps. The contact implies compression in normal direction and Coulomb friction in tangential direction of contacting elements. This element type supports no separation contact, i.e., the nodes of belt edges are tied, even if they are situated with large gap in between. This is important during the solution step, when the belt is formed from a flat shape into a pipe shape. As soon as tied elements become physically in contact, sliding friction and compression are activated. If the belt belt’s pipe opens up and the belt edges do not touch each other, the contact pair again is deactivated.

Noteworthy to mention that, for the numerical modeling of a contact problem in ANSYS, two parameters FKN and FTOLN should be carefully selected, as the resultant CFs exhibit quite a sensitivity to these two parameters. FKN and FTOLN are assigned for each of the contact pair in command for the real constants.

FKN represents the stiffness of springs between two contacting bodies (see Fig. C.2). The reaction force calculated is proportional to this contact stiffness. The software developers [4] recommend to assume FKN= 1 for bulky solids in contact, and FKN= 0.01...0.1 for more flexible bending-dominated bodies. The higher the stiffness of the strings, the more accurate

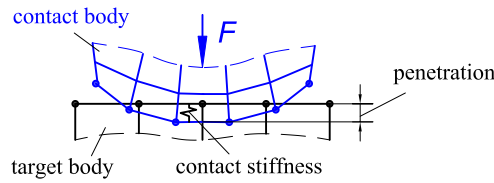


Figure C.2: Modeling behavior of two contacting bodies in normal direction (modified figure from ANSYS manual [4]).

results can be achieved. However, the significant value of FKN increases the number of iterations in each solution step and can affect an ability of the model to converge [4].

FTOLN defines the penetration tolerance, i.e., how much the belt is allowed to penetrate into the plates. The lower the value of this parameter, the better the accuracy of the results are obtained. This is due to the fact that in practice, physical contacting bodies do not interpenetrate. At the same time, too small value of FTOLN in the numerical model can significantly affect the ability of the problem to converge. So it is important to find a correct equilibrium between FKN and FTOLN as well as time of problem convergence and precision of the results.

After running a number of the test cases, tightening the requirements for FKN and FTOLN, it was found out that the Beam Step Model generates a stable convergence with the reasonable time by using rather strict precision requirement of FKN=1 and FTOLN = 0.001.

Now all the element features have been described, it is possible to present an actual modeling and solution procedure. The Beam Step Model is solved in three steps, using a special restart function.

Loads and load steps

Belt was folded from a flat shape into a pipe shape in order to capture the load from the belt bending stiffness. In addition, belt gravity was activated. The presence of a bulk material was not accounted for the Beam Step Model due to the reduced length of a belt geometry. All the participating loads are applied to the model in steps.

The first step represents a nonlinear process of folding the flat belt sample into a pipe shape by applying the concentrated closing moments M_{bst} at the edges of the structure. The absolute values of those moments can be calculated from Eq. 5.10. At this stage, the central node of the belt is fixed for all DOF. The contact between the belt and plates is disabled, using the “death” function of the elements. The bonded self-contact at the belt edges is active during all three load steps.

At the second step, in addition to the self-contact, the contact pairs between the belt and the plates are activated using the special “birth” function. The belt folded into a pipe shape, and supported by the plates, is released by assigning the moments $M_{bst} = 0$ at both edges. In addition, the constraints at the bottom node of a belt are also removed.

At the third load step, the gravity is activated. The belt is supported by the contact between the plate and the plates, and the belt’s self-contact at the edges is also active. In addition, the constraints at the bottom node of a belt are also removed. Figure C.3 illustrates the ultimate results obtained for the Beam Step Model with extended and reduced lengths of

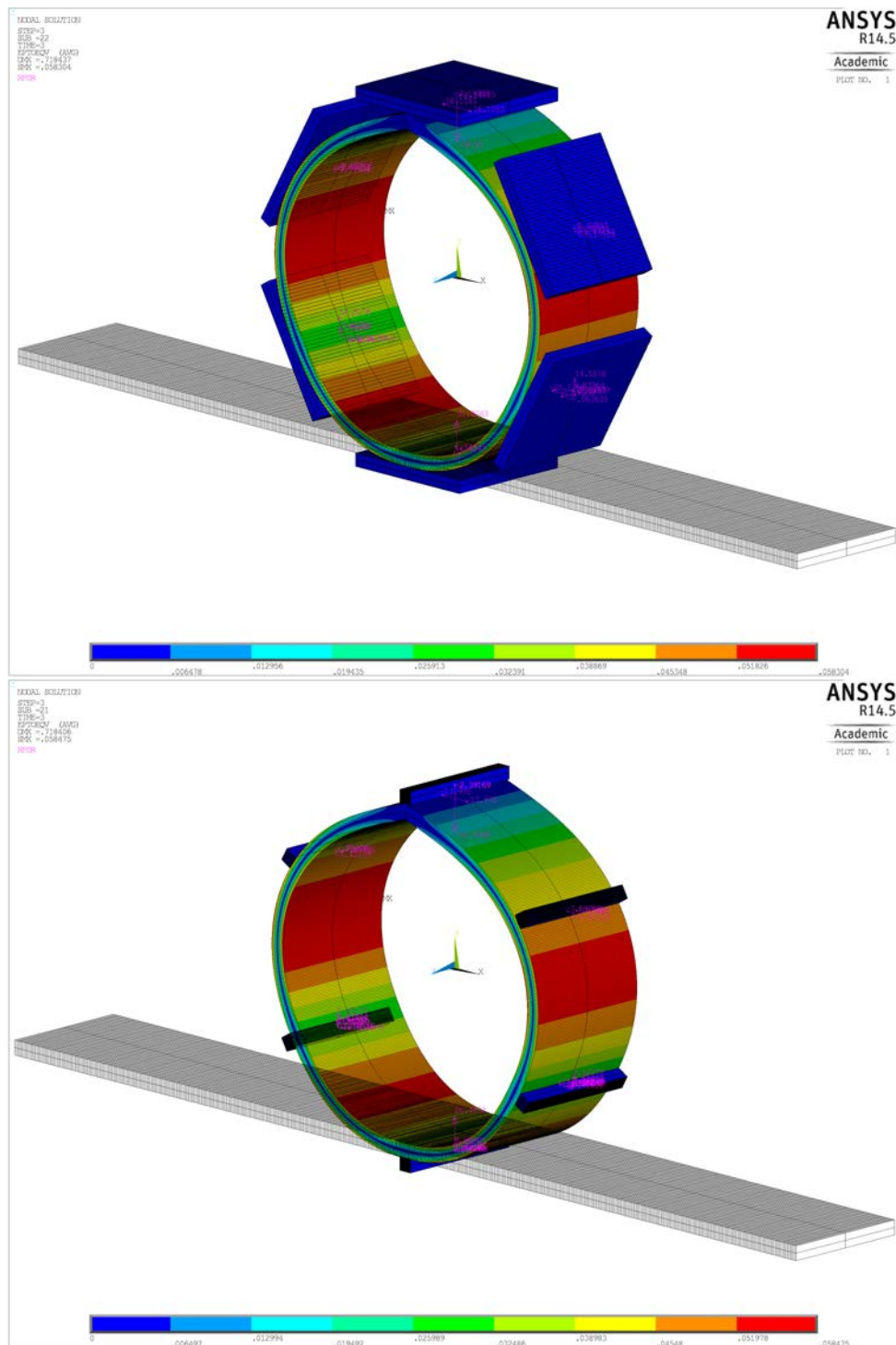


Figure C.3: Von Mises total mechanical strain, obtained from the Beam Step Model in ANSYS using hexagon supporting plates with: a) extended length, similar as in the experiment (see top figure); b) with reduced length as a step towards the analytical model (see bottom figure).

plates after performing the third final solution step.

Obtaining the solution

The solution is obtained performing a finite strain nonlinear analysis for each of the load step using Newton-Raphson scheme for the solution control. The analysis restarts from the results, obtained from the previous step. The resultant reaction forces are determined collecting all the loads distributed at each plate. The sum of those loads constitutes the reaction force from the corresponding plate. In addition, the reaction forces at the belt edges are determined from the contact model, similar as N_1' and N_1'' in Fig. 5.21. If there is a contact loss, the loads at the corresponding plate becomes equal to zero.

All the beam models (the Beam Simplified Model and the Beam Step Model) account only 2D shear effect, ignoring the impact of shear in additional third longitudinal direction of a belt. To accommodate 3D shear effects, the analysis is performed using the Shell Step Model.

C.3 Shell Step Model

Creating the model

This model has a similar modeling procedure, as the Beam Step Model. The Shell Step Model also includes the contact between the plates, the belt's self-contact at the edges. In addition, the belt is also folded from a flat shape into a pipe shape at the first load step. The only difference with the Beam Step Model is that the Shell Step Model uses shell element types. For the belt, the curvilinear 8-node Shell 281 element type is used, whereas the plates are constituted with a more simple 4-node Shell 181. Each node in both element types has six degrees of freedom. The elements follow the Mindlin-Reissner first-order shear deformation theory. This means that both Shell 281 and Shell 181 are suitable for large range of structures with slenderness varied from very thin (membrane type) to moderately thick shells with a more dominant shear effects. In addition, both element types are suitable for modeling isotropic and orthotropic material of the shell.

The belt structure in initial flat shape was meshed into 9600 equivalent quadratic elements, whereas the plates are divided into 600 elements each. The decision made for such mesh is made by balancing between the precision of the results achieved with the fine enough mesh and the convergence time. The physical parameters assigned for belt and plates are described in Section 6.4.

Modeling the contact

The contact between the belt and supporting plates is described in the model as a 3D surface-to-surface rigid-flexible contact. The contact pair is made of the element segments Targe 170 overlaying the plates' surface as a target body and with 8-node Conta 174 element type for a more flexible belt as a contact body [4]. This 3D sliding contact between two surfaces inherits Coulumb and shear stress friction. Similar to the previous model, the impact of sliding friction between belt and plates is assumed to be minimal. The contact models supports Augmented Lagrange algorithm. Similar to the previous model, the contact

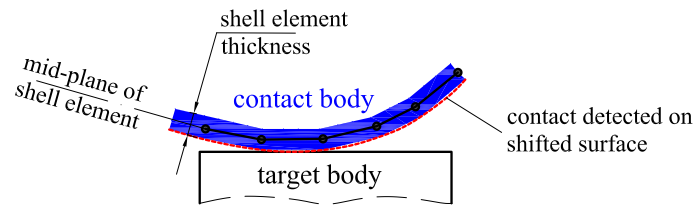


Figure C.4: Modeling the thickness effect by shifting the mid-plane surface of the contacting shell in ANSYS (figure modified from [4]).

surface situated in mid plane of shell is shifted to constitute thickness effect, as shown in Fig. C.4. The contact pair can be activated using “birth” function, and deactivated using “death” function of elements.

For describing the contact, the selection of normal contact stiffness (FKN) and penetration tolerance (FTOLN) is made by achieving the equilibrium between the precision of the results and the convergence time. After running several cases with various combinations of FKN and FTOLN, it was determined that the Shell Step Model can be converged at FKN= 0.1 and FTOLN= 0.005. As it can be seen, compared to the Beam Step Model, the Shell Step Model cannot be converged with the tighter requirements of FKN and FTOLN due to its complexity.

As for the belt’s self-contact at the edges, a special contact is created using 3D Conta 177 for contact elements and Targe 170 for target segments with mid-side nodes. Since for such contact, it is not clear, which body is more rigid and should be selected as a target and which one is more flexible and should be recognized as a contact body. As a result, a 3D line-to-line contact between shell edges is prescribed to be symmetrical. For modeling a symmetric contact, two contact pairs need to be created. The first contact pair contains one edge as a contact body and the other belt edge as a target body, whereas the second contact pair is constituted by the same edges but with the reverse order of contact-target designation [4].

In addition, both contact pairs between the belt edges are bonded and include an initial gap. This allows one to model the belt in its initial flat shape, and then fold it from a flat shape into a pipe shape. The bonded self-contact is active throughout all the load steps, despite the initial significant gap at the beginning. As soon as the belt edges start to penetrate each other, the sliding and compression between them become active.

Loads and load steps

The load from the belt bending stiffness is accounted as a correct belt stress state achieved after folding the belt from a flat shape into a pipe shape. In addition, the gravity is also taken into account. The Shell Step Model is used only for the case study comparison due to its complexity and extensive convergence time. As a results, the model does not account the bulk material load. The solution is divided into three load steps.

At the first load step, the belt in an initial flat shape is fixed at the central line of nodes for all DOF. The belt is folded using moments M_{bst} , applied at both belt edges. For each of the belt edges, the degrees of freedom are coupled. This allows one to apply the concentrated folding moment M_{bst} at one node of each edge, and DOF of that node are translated along

the corresponding edge. The absolute value of M_{bst} is provided in Eq. 5.11, accounting shear effect. Since the value of corresponds to the shell in plane strain state, the additional constraints are prescribed to the belt. In particular, if the belt is situated with lateral cross section in xy -plane (see e.g. Fig. 5.20), the displacements of the belt in longitudinal z -direction are forbidden. In addition, rotations around x - and y -axes are also restricted for all nodes of the belt model. At the first load step, the contact between the belt and plates is deactivated using contact “death” option. As for the bonded contact between the belt edges, it is active throughout all the load steps of the analysis.

The second step is devoted to activating the contact between the belt and the plates by using the “birth” function. The plates are constrained for all DOF. The fixation of belt central line of nodes is removed, so the belt can be supported only by the contact with plates and self-contact at the belt edges. At the same time, all the plane strain DOF restrictions (z -displacements, and rotation around x and y) of belt are preserved the same as for the previous load step. The belt is released by assigning the folding moments at both edges equal to zero $M_{bst} = 0$.

At the third load step, the belt is subjected to gravity. In addition, the constraints modeling the belt in a plane strain state are removed. The coupling along each of the belt edge is also deleted. In this case, the belt structure incorporates the self-contact at the edges, and is supported by the hexagon plates, similar as it is observed in the experiment.

The finite results after solving the third load step for the Shell Step Model are shown in Fig. C.5a. The figure clearly illustrates how the belt sags under the action of all the loads involved. The Shell Step Model also includes an anticlastic curvature effect that reasons to an uneven load distributed at each plate, causing higher loads close to the belt edges in longitudinal z -direction.

Obtaining the solution

Similar to previous models, the solution is achieved performing nonlinear analysis for finite strain following Newton-Raphson scheme. Analysis is performed using a restart frame, i.e. the next load step starts from the previous load step solution. The reaction force from the supporting plates are determined by collecting all the corresponding loads and summing them up. As for N_1' and N_1'' forces, they are determined summing the reaction forces distributed along the contacting belt edges.

The Shell Step Model has a quite extensive time for the convergence. That is why it is used here only for the case study, comparing the numerical results with CFs, measured in the experiment. However, this model can be used in further research as a more complex and precise model.

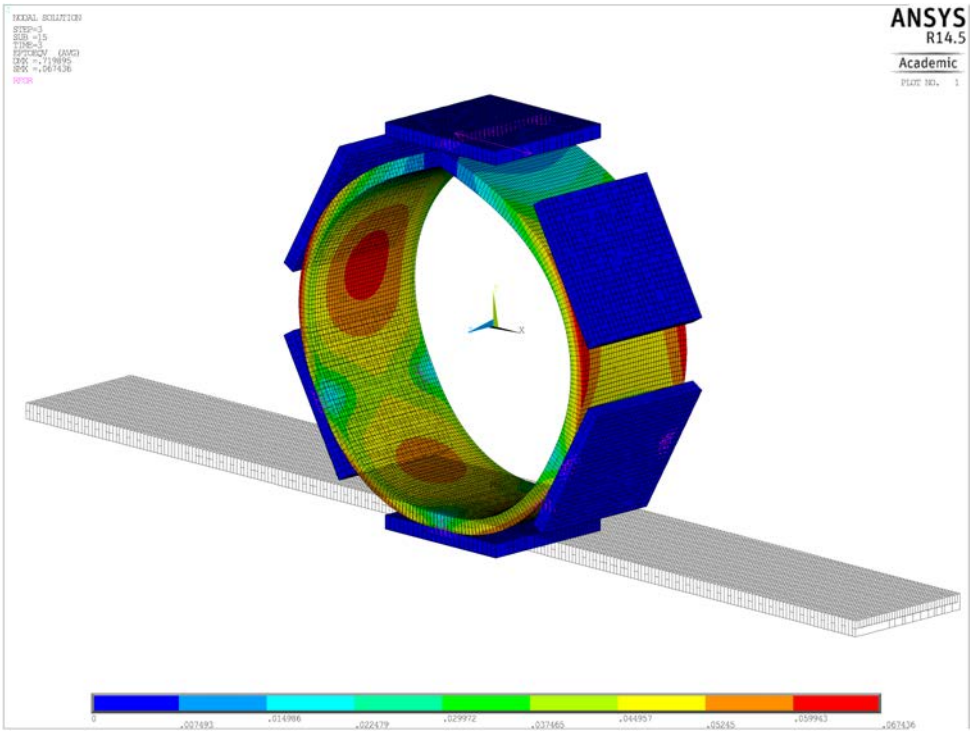


Figure C.5: Von Mises total mechanical strain, obtained for the Shell Step Model in ANSYS.

Bibliography

- [1] Aleksandrov, M. P., *Carrying and lifting machines*, (Подъемно-транспортные машины), 6th ed., 520 pp., Vysshaya Shkola, Moscow, (in Russian), 1985.
- [2] Alfutov, N. A., Bases for calculations on stability of elastic systems, The library of a technical specialist (Основы расчета на устойчивость упругих систем, Библиотека расчетчика), pp. 312, (in Russian), Moscow, Mashinostroenie, 1978.
- [3] Alles, R., W. Ernst, W. S. W. Lubrich, G. Bottcher, H. Simonsen, and H. Zintarra, *Conveyor Belt System Design, CONTI Conveyor Belt Service Manual*, ContiTech Transportbandsysteme GmbH, Hannover, Germany, 1994.
- [4] ANSYS®, Academic Teaching Advanced, Release 14.5, Help system Manual, ANSYS, Inc.
- [5] Arts, K., Case study: Aramid reinforced conveyor belt in Maritsa Istok 2 power plant, in *BELT-CON 15: International Materials Handling Conference (IMHC)*, South Africa, Johannesburg, 2-3 September, <http://www.beltcon.org.za/docs/b1504.pdf>, 2009.
- [6] Ashwell, D. G., The anticlastic curvature of rectangular beams and plates, *Journal of the Royal Aeronautical Society*, 54, 708–715, 1950.
- [7] ASTM D378, Standard Test Methods for Rubber (Elastomeric) Conveyor Belting, Flat Type, 2010.
- [8] Bahke, T., Calculation criteria and application of "Rollgurt" - conveyor (tube conveyor), in *BELTCON 6: International Materials Handling Conference (IMHC)*, South Africa, Johannesburg, 17-19 September, 1991, <http://www.saimh.co.za/beltcon/beltcon6/paper64.html>.
- [9] Baratta, F. I., When is a Beam a Plate?, *JACE Journal of the American Ceramic Society*, 64(5), 86, 1981.
- [10] Barburiski, M., Analysis of the pipe conveyor belt pressure on the rollers on its circuit, *Journal of Industrial Textiles*, 45(6), 1619–1634, 2014.
- [11] Bauman, J. T., *Fatigue, stress, and strain of rubber components: a guide for design engineers*, Hanser Publishers, Munich, Cincinnati (Ohio), 2008.
- [12] Bazhanov, P. A., Justification and choice of rational design parameters for pipe belt conveyor at straight route sections in mining (Обоснование и выбор рациональных конструктивных параметров линейной части ленточного трубчатого конвейера для горной промышленности), Ph.D. Thesis Synopsis, Moscow State Mining University, (in Russian), 2012.

- [13] Beck, A. T., and C. R. A. da Silva Jr, Timoshenko versus Euler beam theory: Pitfalls of a deterministic approach, *Structural Safety*, 33(1), 19–25, doi:<http://dx.doi.org/10.1016/j.strusafe.2010.04.006>, 2011.
- [14] Bellow, D., G. Ford, and J. Kennedy, Anticlastic behavior of flat plates, *Experimental Mechanics*, 5(10), 227–232, 1965.
- [15] Betz, E., Use of Kevlar aramid fibres in conveyor belts. Part I: Pull-out problem and splice design, *Bulk Solids Handling*, 6(2), 355–367, 1986.
- [16] Birger, I. A., and R. R. Mavlyutov, *Mechanics of materials*, (Сопротивление материалов), Nauka, Moscow, 1986.
- [17] Bisshopp, K. E., and D. C. Drucker, Large deflections of cantilever beams, *Quarterly of Applied Mathematics*, 3, 272–275, 1945.
- [18] BMH Technology, Tubular Conveyors, Product Specification Brochure, Finland, http://www.optieng.pt/media/representadas/bmh_energy.tubular_conveyors.pt.pdf, accessed 01. 04. 2014, 2008.
- [19] Boresi, A. P., and O. M. Sidebottom, *Advanced mechanics of materials*, Wiley, New York, 1985.
- [20] Boyarshinov, S. V., *Fundamentals of structural mechanics of machines*, 488 pp., Engineering, Moscow, (in Russian), 1973.
- [21] Brouwers, S., Playing with fire? A guide to fire-retardant conveyor belts, *Dry Cargo International*, pp. 119–122, 2014.
- [22] Brown, R., *Handbook of polymer testing: physical methods*, Dekker, New York, 1999.
- [23] Brown, R., *Physical testing of rubber*, Springer, New York, 2006.
- [24] Buchanan, C., Japan pipe belt conveyor system, in *BELTCON 3: International Materials Handling Conference (IMHC), South Africa, Johannesburg, 9-11 September, 1985*, <http://www.beltcon.org.za/docs/B3>
- [25] Buchanan, C., Japan pipe belt conveyor system, *South African mechanical engineer*, 36(2), 31,33–35, 1986.
- [26] Chadwick, J., Conveying the message, *International Mining Magazine*, pp. 29–34, 2005.
- [27] Chernenko, V. D., Development of the calculation methods for steep inclined belt conveyors, (Разработка методов расчета крутонаклонных конвейеров), PhD Thesis Synopsis, Bauman Moscow State Technical University, (in Russian), 1992.
- [28] Chernenko, V. D., *Calculation of the continuous transport systems* (Расчет средств непрерывного транспорта), 386 pp., Politekhnik, Saint-Petersburg, Russia, (in Russian), 2008.
- [29] CKIT, CKIT - The Bulk Materials Handling Knowledge Base.
- [30] Colijn, H., *Mechanical conveyors for bulk solids*, 512 pp., Elsevier, Amsterdam, 1985.
- [31] ContiTech Conveyor Belt Group, Rollgurtförderer, Closed-Trough Conveyor, Product Specification Brochure No. WT 4060 D/E 08, 2000(P1), 2000.

- [32] ContiTech Group of Continental AG, ContiTech Conveyor Belt Group, Tube Conveyor, Product Specification Brochure No. GB_CB 2 E 5/2002, 2002.
- [33] ContiTech Group of Continental AG, Conveyor Belt Group, Conti® MegaPipe, New Dimension in Technology of Pipe Belt Conveyors (Новое измерение в технологии трубчатых ленточных конвейеров), Product Specification Brochure No. WT 8589 RU 06, (in Russian), 2013.
- [34] Conveyor Belt Guide, <http://www.conveyorbeltguide.com>, Knowledge online database, accessed 07.11.2014.
- [35] Conveyor Equipment Manufacturers Association (CEMA), *Belt conveyors for bulk materials*, Florida, USA, 6 ed., Florida, USA, 2005.
- [36] Conveyor Equipment Manufacturers Association (CEMA), ANSI/CEMA Standard 550, Classification and definitions of bulk materials, 2009.
- [37] Conveyor Knowledge and Information Technology (CKIT) Conveyor Engineers, Pipe conveyors and their application in the cement industry, <http://www.pipeconveyor.com/Papers/Applications/Applications.htm>, accessed 02.10.2015.
- [38] Conway, H. D., The large deflection of simply supported beams, *Philosophical Magazine*, 38, Ser. 7, 905–911, 1947.
- [39] Craig, R. F., *Craig's soil mechanics*, 7th ed., Spon Press, London, New York, 2004.
- [40] Czaplicka, K., Analysis of stress relaxation processes in conveyor belts, *Mechanics of Composite Materials*, 30(4), 411–415, 1995.
- [41] Day, I. W., Pipe Conveyor Installations in the United Kingdom's North East Coalfield, in *BELT-CON 7: International Materials Handling Conference (IMHC)*, South Africa, Johannesburg, 26-28 October, 1993, <http://www.saimh.co.za/beltcon/beltcon6/paper64.html>.
- [42] de Graaf, R. M. T., and Y. Pang, Troughability testing on troughed and pipe conveyor belts. Report № 2012.TEL.7695, *Tech. rep.*, Delft University of Technology, 2012.
- [43] del Coz Díaz, J. J., P. J. García Nieto, J. A. Vilán Vilán, A. Martín Rodríguez, J. R. Prado Tamargo, and A. Lozano Martínez-Luengas, Non-linear analysis and warping of tubular pipe conveyors by the finite element method, *Mathematical and Computer Modelling*, 46(1-2), 95–108, 2007.
- [44] DIN 22100-1, Articles and materials from synthetics for use in underground mines - Part 1: Conveyor belts - Hygienic requirements, testing, marking, 2009.
- [45] DIN 22101, Continuous conveyors: Belt conveyors for loose bulk materials - Basis for calculation and dimensioning, 2011.
- [46] DIN 22102-1, Conveyor belts with textile plies for bulk goods - Part 1: Dimensions, specifications, marking, 2014.
- [47] DIN 22102-2, Conveyor belts with textile plies for bulk goods; testing, 1991.
- [48] DIN 22121, Conveyor belts with textile plies for coal mining - Permanent joints for belts with one or two plies; dimensions, requirements, marking, 2007.

- [49] DIN 22129, Steel cord conveyor belts for underground coalmining; dimensions, requirements, 1988.
- [50] DIN 53504, Testing of rubber - Determination of tensile strength at break, tensile stress at yield, elongation at break and stress values in a tensile test, 2009.
- [51] DIN-ISO 3435, Continuous mechanical handling equipment - Classification and symbolization of bulk materials, 1977.
- [52] Dmitriev, S. N., Analytical solution of the Hertzian contact problem of elastic deformations of a thin plate, positioned in a cylindrical chamber (Аналитическое решение контактной задачи об упругих деформациях тонкой пластины, помещенной в цилиндрическую полость), *Science and Education, Bauman Moscow State Technical University*, (1), 1—12, (in Russian), 2013.
- [53] Dmitriev, S. N., and S. I. Solodovnikova, Contact problem of the equilibrium of the plate, formed into a cylinder (Аналитическое решение контактной задачи об упругих деформациях тонкой пластины, помещенной в цилиндрическую полость), in *Aerospace technologies, 2004-2007: The collection of works*, pp. 348—351, (in Russian), Bauman Moscow State Technical University, 2008.
- [54] Dmitriev, V. G., The equation of twisting motion of pipe conveyor belt (Уравнение вращательного движения ленты трубчатого конвейера), *GIAB: Mining Informational and Analytical Bulletin (Scientific and Technical Journal)*, *Moscow State Mining University*, (9), 266–271 (in Russian), 2005.
- [55] Dmitriev, V. G., and M. S. Efimov, Assessment of angular misalignment of pipe conveyor belt and a way of its reducing during its rotational motion (Оценка и способ снижения угловых отклонений ленты трубчатого конвейера при вращательном движении), *GIAB: Mining Informational and Analytical Bulletin (Scientific and Technical Journal)*, *Moscow State Mining University*, 16(12), 31–52 (in Russian), 2009.
- [56] Dmitriev, V. G., and D. S. Kulagin, Modeling of the stress state of pipe conveyor belt (Моделирование напряженного состояния конвейерной ленты трубчатого конвейера), *GIAB: Mining Informational and Analytical Bulletin (Scientific and Technical Journal)*, *Moscow State Mining University*, (7), 283–286, (in Russian), 2004.
- [57] Dmitriev, V. G., and N. V. Sergeeva, Determination of the distributed rolling resistances of belt on straight route sections of pipe belt conveyor (Определение распределенных сопротивлений движению ленты на прямолинейных участках трассы ленточного трубчатого конвейера), *GIAB: Mining Informational and Analytical Bulletin (Scientific and Technical Journal)*, *Moscow State Mining University*, (9), 245–249 (in Russian), 2008.
- [58] Dmitriev, V. G., and N. V. Sergeeva, Tension calculation of pipe belt conveyors (Тяговый расчет ленточных трубчатых конвейеров), *GIAB: Mining Informational and Analytical Bulletin (Scientific and Technical Journal)*, *Moscow State Mining University*, (16), 144–170 (in Russian), 2009.
- [59] Dunlop Conveyor Belting, *Technical Manual, Version 2.3*, 41 pp., www.dunlopconveyorbelting.com/uploads/media/Dunlop_Technical_Manual.pdf, accessed 14.07.2014, 2011.

- [60] Dyachenko, A. V., Experimental studies of a bulk material stress state at increased compression of an overlapping conveyor belt, (Экспериментальные исследования напряженного состояния сыпучего груза при повышенной степени обжатия конвейерной ленты), *GIAB: Mining Informational and Analytical Bulletin (Scientific and Technical Journal)*, Moscow State Mining University, (8), 274–276, (in Russian), 2005.
- [61] Efimov, M. S., Justification of the method of decreasing the angular misalignments of the pipe conveyor belt in rotation mode for mining (Обоснование способа снижения угловых отклонений при вращательном движении ленты трубчатого конвейера для горных предприятий), Ph.D. Thesis Synopsis, Moscow State Mining University, (in Russian), 2008.
- [62] Efimov, M. S., Evaluation of uneven load distribution in lateral direction of pipe conveyor belt (Оценка неравномерности нагружения в поперечном направлении ленты трубчатого конвейера), *GIAB, Moscow State Mining University, GIAB: Mini*(6), 24–27 (in Russian), 2008.
- [63] Elvers, K.-H., W. Schnell, and H. Tonn, Universal, highly effective cross reinforcement system for conveyor belts, *Bulk Solids Handling*, 9(4), 393–398, 1989.
- [64] E&MJ, German industrial groups join to develop tubular belt conveyors, *Engineering and mining journal*, 216(6), 128–131, 2015.
- [65] Enshu, H., Conveyor belt and pipe conveyor, Patent No US 20130334013 A1, pp. 1-13, 2013.
- [66] Fedorko, G., and V. Molnár, The simulation model of experimental equipment for the research of pipe conveyor belts using ABAQUS software, 2014.
- [67] Fedorko, G., V. Ivanco, V. Molnár, and N. Husáková, Simulation of Interaction of a Pipe Conveyor Belt with Moulding Rolls, *Procedia Engineering*, 48, 129–134, 2012.
- [68] Fedorko, G., V. Molnár, and M. Kopas, Application of FEM Analysis for Development of a Pipe Conveyor Test Stand, *Bulk Solids Handling*, 2, 46–50, 2015.
- [69] FEM 2581, Schüttguteigenschaften, The European Materials Handling Federation (Fédération Européenne de la Manutention), 1991.
- [70] FEM 2582, Allgemeine Schüttguteigenschaften und ihre Darstellung in Kurzform, The European Materials Handling Federation (Fédération Européenne de la Manutention), 1991.
- [71] Feodosyev, V. I., *Selected problems and questions of Mechanics of Materials* (Избранные задачи и вопросы по сопротивлению материалов), 3 ed., 376 pp., Nauka, (in Russian), Moscow, 1967.
- [72] Ferry, J. D., *Viscoelastic properties of polymers*, Wiley, New York, 1980.
- [73] Fertis, D. G., *Nonlinear mechanics*, CRC Press, Boca Raton, 1999.
- [74] Fertis, D. G., *Nonlinear structural engineering with unique theories and methods to solve effectively complex nonlinear problems*, Springer-Verlag, Berlin; New York, 2006.
- [75] Fertis, D. G., and A. O. Afonta, Equivalent systems for large deformation of beams of any stiffness variation, *European Journal of Mechanics, A/Solids*, 10(3), 265–293, 1991.
- [76] Fertis, D. G., and M. E. Keene, Elastic and inelastic analysis of nonprismatic members, *Journal of structural engineering*, 116(2), 475–489, 1990.

- [77] Fertis, D. G., and C. T. Lee, Inelastic analysis of flexible bars using simplified nonlinear equivalent systems, *Computers and Structures*, 41(5), 947–958, 1991.
- [78] Finney, R. H., Finite Element Analysis, in *Engineering with rubber: How to design rubber components*, edited by A. N. Gent, 2 ed., chap. 9, pp. 306–355, Hanser; HanserGardner Publications, Inc., Munich; Cincinnati, 2000.
- [79] Fletcher, A. E. W., and E. L. du Toit, Environmentally Friendly Enclosed Conveyor Systems, in *BELTCON 10: International Materials Handling Conference (IMHC), South Africa, Johannesburg, 19-21 October, 1999*, <http://www.saimh.co.za/beltcon/beltcon10/paper1011.html>.
- [80] Galkin, V. I., V. G. Dmitriev, V. P. Dyachenko, I. V. Zapenin, and Y. Y. Sheshko, *The modern theory of belt conveyor systems for mining companies* (Современная теория ленточных конвейеров горных предприятий), 543 pp., Moscow State Mining University, (in Russian), Moscow, 2005.
- [81] Gent, A. N., *Engineering with rubber. How to design rubber components*, 2 ed., Hanser; HanserGardner Publications, Inc., Munich; Cincinnati, 2000.
- [82] Gere, J. M., and S. P. Timoshenko, *Mechanics of materials*, 4 ed., 913 pp., Stanly Thornes (Publishers) Ltd, United Kingdom, 1999.
- [83] Goodyear® Engineered Products, Veyance Technologies, Inc., Introducing Confine™ Pipe Conveyor Belt, A well-rounded solution for securing materials over the long haul, Product Specification Brochure No. 09GCON011-02/09, <http://www.goodyear.com/WorkArea/DownloadAsset.aspx?id=16734>, accessed 17.02.2014, 2009.
- [84] GOST 2085, Rubber conveyor belts: Specifications, (Ленты конвейерные резиноканевые: Технические условия), Russian State Standard, 2004.
- [85] Gratama, R., G. Lodewijks, and P. Staples, Test results from the pipe conveyor test rig. Report № 2005.TL.6930, Ckit, Johannesburg, Rep. of South Africa, *Tech. rep.*, Delft University of Technology, 2005.
- [86] Grimmer, K. J., and K. Grabner, Untersuchungen über die Normalkräfte zwischen Gurt und Tragrollen an kritischen Stellen des Gurtverlaufes bei bandförderanlagen, *Heft, 6*(BHM 138), 212–220, 1993.
- [87] Guo, Y., S. Wang, K. Hu, and D. Li, Optimizing the pipe diameter of the pipe belt conveyor based on discrete element method, *3D Research*, 7(1), 1–9, 2016.
- [88] Gushchin, V. M., *Research on a steep inclined deep trough belt conveyor in conditions of open cast mining*, (Исследование крутонаклонного конвейера с лентой глубокой желобчатости применительно к условиям открытых горных разработок), Moscow State Institute, Ph.D. Thesis Synopsis, (in Russian), Moscow, 1972.
- [89] Gushchin, V. M., Parameters determination of the load-carrying surface for the steep inclined conveyors with the deep troughed belt (Определение параметров грузонесущего полотна крутонаклонного конвейера с лентой глубокой желобчатости), *Mine and quarry transport, Nedra, 1*, 164–166, (in Russian), 1974.

- [90] Gushchin, V. M., Experimental study of the pressure of the loaded material on the deep troughed belt conveyors (Экспериментальные исследования давлений насыпного груза на ленту глубокой желобчатости), *Mine and quarry transport, Nedra*, 2, 116–118, (in Russian), 1975.
- [91] Gładysiewicz, L., *Belt conveyors: theory and calculation, (Przenośniki taśmowe: teoria i obliczenia)*, 315 pp., Oficyna Wydawnicza Politechniki Wrocławskiej, Warsaw, Poland, (in Polish), 2003.
- [92] Hager, M., and A. Hintz, The Energy-Saving Design of Belts for Long Conveyor Systems, *Bulk Solids Handling*, 13(4), 749, 1993.
- [93] Harrison, A., Dynamics measurement and analysis of steel cord conveyor belts, Ph.D. thesis, The University of Newcastle, Australia, 1984.
- [94] Harrison, A., A redefinition of troughability standards for conveyor belting, *Bulk Solids Handling*, 6(1), 33–35, 1986.
- [95] Harrison, A., Troughability measurement of fabric reinforced belting for powder and bulk handling industry, *Bulk Solids Handling*, 7(3), 381–384, 1987.
- [96] Hashimoto, K., Pipe conveyor, Patent No. US 3338383 A, pp. 1-9, 1967.
- [97] Hashimoto, K., and H. Okazaki, Tubular belt conveyor, Patent No. US 4762221 A, pp. 1-8, 1988.
- [98] Hashimoto, K., and H. Okazaki, Belt conveyor, Patent No. US 4778046 A, pp. 1-9, 1988.
- [99] Hashimoto, K., and H. Okazaki, Tubular belt conveyor, Patent No. US 4809844 A, pp. 1-9, 1989.
- [100] Hinkelmann, R., and U. Sander, FLEXOPIPE - From Conveyor Belt to Conveyor Pipe, *Bulk Solids Handling*, 13(3), 581–588, 1993.
- [101] Hinkelmann, R., U. Sander, and H. Begemann, Conveyor belt for pipe conveyor, Patent No US 5328023 A, pp. 1-4, 1994.
- [102] Hinterholzer, S., F. Kessler, and K. Grabner, Belt Conveyor Technology - Research on a Pipe Conveyor with a Completely New Belt Guidance, *Bulk Solids Handling*, 21(6), 614, 2001.
- [103] Hoffman, E. B., Polyamide and aromatic polyamide fibers of the 1990s, *Bulk Solids Handling*, 10(3), 1990.
- [104] Holden, J. T., On the finite deflections of thin beams, *International Journal of Solids and Structures*, 8(8), 1051–1055, 1972.
- [105] Horak, R. M., A new technology for pipe or tube conveyors, *Bulk Solids Handling*, 23, 174–181, 2003.
- [106] Horn, G., New Principles in the Transport of Bulk Materials, *Metallurgist*, 48(7-8), 7–8, 2004.
- [107] Hötte, S., Experimentelle Untersuchungen zu den Normalkräften bei Schlauchgurten, Ph.D. thesis, TEWISS-Technik und Wissen GmbH, Garbsen, Germany, 2014.
- [108] Hötte, S., L. Overmeyer, and T. Wennekamp, Form force behaviour of pipe conveyors in different curve radii, *Bulk Solids Handling*, 31(3), 164–169, 2011.

- [109] Hsieh, K.-T., Modeling of cord-reinforced rubber laminates, Ph.D. thesis, 1985.
- [110] Huffington, N. J., Theoretical determination of rigidity properties of orthogonally stiffened plates, Ph.D. thesis, 1954.
- [111] Hunter, S. C., The rolling contact of a rigid cylinder with a viscoelastic half space, *Journal of Applied Mechanics*, 28, 611–617, 1961.
- [112] Imai, A., Pipe Conveyor Development, Benchmark and Future Trend, *Whitepaper Bulk Solids Handling*, pp. 1–9, 2012.
- [113] ISO 10247, Conveyor belts - Characteristics of covers - Classification, 1990.
- [114] ISO 14890, Conveyor belts - Specification for rubber- or plastics-covered conveyor belts of textile construction for general use, 2013.
- [115] ISO 18573, Conveyor belts - Test atmospheres and conditioning periods, 2012.
- [116] Ivannikov, V., C. Tiago, and P. Pimenta, On the boundary conditions of the geometrically nonlinear Kirchhoff–Love shell theory, *International Journal of Solids and Structures*, 51(18), 3101–3112., 2014.
- [117] Jaky, J., Pressure in silos, in *2nd International Conference on Soil Mechanics and Foundation Engineering*, pp. 103–107, Rotterdam, the Netherlands, 1948.
- [118] Johns, S. H., Tubular belt conveyor, Patent No. US 2199935 A, pp. 1-4, 1940.
- [119] Jonkers, C. O., The indentation rolling resistance of belt conveyors, *Fordern und Heben*, 30, 312–316, 1980.
- [120] Kalidien, S., The design of an automatic maintained pipe conveyor, MSc Thesis, Delft University of Technology, 2006.
- [121] Karnovsky, I. A., *Theory of arched structures strength, stability, vibration*, Springer, New York, 2012.
- [122] Karnovsky, I. A., and O. Lebed, *Advanced methods of structural analysis*, Springer, New York; London, 2010.
- [123] Keller, M., Zur Optimierung hochfester Stahlseilgurtverbindungen, Ph.D. thesis, Dem Fachbereich Maschinenbau der Universität Hannover, Germany, 2001.
- [124] Kessler, F., Pipe conveyor with a completely new belt guidance, in *BELTCON 12: International Materials Handling Conference (IMHC), South Africa, Johannesburg, 23-24 July, 2003*, <http://www.beltcon.org.za/docs/b1210.pdf>.
- [125] Krause, F., and W. Hettler, Die Belastung der Tragrollen Gurtbandförderern mit dreiteiligen Tragrollenstationen infolge Fördergut unter Beachtung des Fördervorganges und der Schüttguteigenschaften, *Wissenschaftliche Zeitschrift der Technischen Hochschule Otto von Guericke Magdeburg*, 18(6/7), 667–674, 1974.
- [126] Kulagin, D. S., Influence of some design parameters of pipe belt conveyor on its allowable route curves radii in horizontal plane (Влияние некоторых конструктивных параметров ленточного трубч. конвейера на допустимые радиусы изгиба его трассы в горизонт. плоск.), *GIAB: Mining Informational and Analytical Bulletin (Scientific and Technical Journal), Moscow State Mining University*, (7), 271–274 (in Russian), 2005.

- [127] Kulagin, D. S., Influence of physical and mechanical properties of a conveyor belt on its ability to keep enclosed cross section in straight route of pipe conveyor (Влияние физико-механич. свойств конвейерной ленты на герметичность линейной части лент.трубч. конв.), *GIAB: Mining Informational and Analytical Bulletin (Scientific and Technical Journal)*, Moscow State Mining University, (8), 271–273 (in Russian), 2005.
- [128] Kulagin, D. S., Justification of the allowable curves radii of the route of pipe belt conveyors in horizontal plane (Обоснование допустимых радиусов изгиба трасс ленточных трубчатых конвейеров в горизонтальной плоскости), Ph.D. Thesis Synopsis, Moscow State Mining University, (in Russian), 2007.
- [129] Kulagin, D. S., Establishing the bending radii curves of pipe belt conveyor in horizontal plane by computer simulation (Установление радиусов изгиба трубчатого конвейера в горизонтальной плоскости путем моделирования на ЭВМ), *GIAB: Mining Informational and Analytical Bulletin (Scientific and Technical Journal)*, Moscow State Mining University, 16(12), 114–129 (in Russian), 2009.
- [130] Kusel, B., K. H. Elvers, C. Heidelmann, and H. Tonn, Tubular conveyor belt, Patent No US 5460261 A, pp. 1-10, 1995.
- [131] Lau, J. H., Large deflections of beams with combined loads, *ASCE Journal Engineering Mechanics Division*, 108(1), 180–185, 1982.
- [132] Lee, H.-C., A. J. Durelli, and V. J. Parks, Stresses in Largely Deflected Cantilever Beams Subjected to Gravity, *J Appl Mech*, 36(2), 323–325, doi:10.1115/1.3564633, 1969.
- [133] Lekhnitskii, S. G., *Anisotropic plates*, English translation of original work in Russian, Gordon and Breach, New York, 1968.
- [134] Levinson, M., On higher order beam and plate theories, *Mechanics Research Communications*, 14, 421–424, 1987.
- [135] Liu, X., Y. Pang, and G. Lodewijks, Theoretical and experimental determination of the pressure distribution on a loaded conveyor belt, *Measurement: Journal of the International Measurement Confederation*, 77, 307–316, 2016.
- [136] Lodewijks, G., Rolling resistance of conveyor belts, *Bulk Solids Handling*, 15(1), 15–22, 1995.
- [137] Lodewijks, G., Dynamics of belt systems, Ph.D. thesis, Delft University of Technology, the Netherlands, pp. 256, 1996.
- [138] Lodewijks, G., Modern Belt Conveyor Systems, in *7th International Conference on Bulk Material Storage, Handling and Transportation, Newcastle, Australia*, pp. 27–37, The Institution of Engineers, Australia Conference Preprints, 2001.
- [139] Lodewijks, G., Closed Belt Conveyor Systems - the State-of-the-Art, *Bulk Solids Handling*, 21, 592–601, 2001.
- [140] Lodewijks, G., Determination of Rolling Resistance of Belt Conveyors Using Rubber Data: Fact or Fiction?, *Bulk Solids Handling*, 23, 384–391, 2003.
- [141] Lodewijks, G., The design of conveyor belting for pipe conveyors, *Proceedings of the 9th International Conference Bulk Material Storage, Handling and Transportation, Newcastle, Australia*, pp. 1–10, 2007.

- [142] Lodewijks, G., Introduction to transport engineering and logistics: Belt conveyors, Lecture notes to course (WB3420-03), 2011.
- [143] Lodewijks, G., The next generation low loss conveyor belts, *Bulk Solids Handling*, 32(1), 52–56, 2012.
- [144] Lodewijks, G., and Y. Pang, Energy saving options for continuous transport systems, an exploration, in *11th International Congress on Bulk Materials Storage, Handling and Transportation (ICBMH 2013)*, The University of Newcastle, Australia, 2013.
- [145] Lodewijks, G., K. F. Drenth, and P. S. van der Mel, Belt Conveyor Technology - Rotation of Pipe Conveyors, *Bulk Solids Handling*, 30(3), 144–148, 2010.
- [146] Loeffler, F. J., Pipe/tube conveyors - a modern method of bulk materials transport, *Bulk Solids Handling*, 20(4), 431–435, 2000.
- [147] Look, B. G., *Handbook of geotechnical investigation and design table*, 356 pp., Taylor & Francis e-Library, London, UK, 2007.
- [148] Malkin, A. J., and A. I. Isayev, *Rheology concepts, methods, and applications*, 2012.
- [149] Maton, A. E., Tubular Pipe Conveyor Design Using a Standard Fabric Belt, *Bulk Solids Handling*, 20, 39–44, 2000.
- [150] Maton, A. E., Tubular pipe conveyor design: A review of cross section and belt selection, *Bulk Solids Handling*, 21(2), 179–182, 2001.
- [151] May, W. D., E. L. Morris, and D. Atack, Rolling friction of a hard cylinder over a viscoelastic material, *Journal of Applied Physics*, 30(11), 1713–1724, 1960.
- [152] Mazurkiewicz, D., Problems of numerical simulation of stress and strain in the area of the adhesive-bonded joint of a conveyor belt, *Archives of Civil and Mechanical Engineering*, 9(2), 75–91, doi:10.1016/S1644-9665(12)60061-2, 2009.
- [153] McGlinchey, D., *Characterisation of Bulk Solids*, 280 pp., Wiley-Blackwell, Oxford, 2009.
- [154] MetsoMinerals, Trellex FLEXOPIPE®... flexible, unique, ecological!, Product Specification Brochure No. 2412-05-10-MBL/Trelleborg-English, [http://www.metso.com/miningandconstruction/MaTobox7.nsf/DocsByID/5263A2CB2EDEB5C9C225770A0040C11F/\\$File/2412-Trellex%20Flexopipe_EN.pdf](http://www.metso.com/miningandconstruction/MaTobox7.nsf/DocsByID/5263A2CB2EDEB5C9C225770A0040C11F/$File/2412-Trellex%20Flexopipe_EN.pdf), accessed 01.04.2014, 2010.
- [155] Michalik, P., and J. Zajac, Using of computer integrated system for static tests of pipe conveyor belts, in *13th International Carpathian Control Conference (ICCC)*, pp. 480–485, doi:10.1109/CarpathianCC.2012.6228691, 2012.
- [156] Michalik, P., V. Molnár, G. Fedorko, and M. Weiszer, An experimental test rig: For measuring the strength of pipe conveyor belts, *Bulk Solids Handling*, 33(5), 52–55, 2013.
- [157] Minkin, A., A. Jungk, and T. Hontscha, Belt replacement at a long distance pipe conveyor: Belt design, installation and power measurements, *Bulk Solids Handling*, 32(6), 16–21, 2012.
- [158] Molnár, V., and G. Fedorko, Contact forces in hexagonal idler housing of pipe conveyor, *Bulk Solids Handling*, 34(2), 52–56, 2014.

- [159] Molnár, V., G. Fedorko, B. Stehlíková, L. Kudelás, and N. Husáková, Statistical approach for evaluation of pipe conveyor's belt contact forces on guide idlers, *Measurement: Journal of the International Measurement Confederation*, 46(9), 3127–3135, 2013.
- [160] Molnár, V., G. Fedorko, B. Stehlíková, P. Michalik, and M. Weiszer, A regression model for prediction of pipe conveyor belt contact forces on idler rolls, *Measurement: Journal of the International Measurement Confederation*, 46(10), 3910–3917, 2013.
- [161] Molnár, V., G. Fedorko, and B. Stehlíková, Regression model design for the prediction of pipe conveyor belt contact forces on idler rollers by experimental tests, 2014.
- [162] Molnár, V., G. Fedorko, B. Stehlíková, P. Michalik, and M. Kopas, Mathematical models for indirect measurement of contact forces in hexagonal idler housing of pipe conveyor, *Measurement: Journal of the International Measurement Confederation*, 47(1), 794–803, 2014.
- [163] Molnár, V., G. Fedorko, B. Stehlíková, M. Tomašková, and Z. Hulínová, Analysis of asymmetrical effect of tension forces in conveyor belt on the idler roll contact forces in the idler housing, *Measurement: Journal of the International Measurement Confederation*, 52(0), 22–32, doi: <http://dx.doi.org/10.1016/j.measurement.2014.02.035>, 2014.
- [164] Molnár, V., G. Fedorko, M. Andrejiová, A. Grinčová, and M. Kopas, Monitoring of dependences and ratios of normal contact forces on hexagonal idler housings of the pipe conveyor, *Measurement*, 64(0), 168–176, doi: <http://dx.doi.org/10.1016/j.measurement.2014.12.055>, 2015.
- [165] Molnár, V., G. Fedorko, M. Andrejiová, A. Grinčová, and M. Tomašková, Analysis of influence of conveyor belt overhang and cranking on pipe conveyor operational characteristics, *Measurement: Journal of the International Measurement Confederation*, 63, 168–175, 2015.
- [166] Molnar, V., G. Fedorko, B. Stehlikova, and A. Paulikova, Influence of tension force asymmetry on distribution of contact forces among the conveyor belt and idler rolls in pipe conveyor during transport of particulate solids, *Measurement: Journal of the International Measurement Confederation*, 63, 120–127, 2015.
- [167] Moore, B. A., Flow properties and design procedures for coal storage bins, Ph.D. thesis, Department of Mechanical Engineering, University of Wollongong, Australia, 1988.
- [168] Mulani, I. G., *Engineering science and application design for belt conveyors*, Saurabh Creation, Pune, India, 2001.
- [169] NEN-EN-ISO 14125, Fibre-reinforced plastic composites - Determination of flexural properties, 1998.
- [170] NEN-EN-ISO 15236, Steel cord conveyor belts - Part 1: Design, dimensions and mechanical requirements for conveyor belts for general use , 2005.
- [171] NEN-EN-ISO 178, Plastics - Determination of flexural properties, 2010.
- [172] NEN-EN-ISO 283, Textile conveyor belts - Full thickness tensile strength, elongation at break and elongation at the reference load -Test method, 2007.
- [173] NEN-EN-ISO 583, Conveyor belts with a textile carcass - Total belt thickness and thickness of constitutive elements - Test methods, 2007.
- [174] NEN-EN-ISO 703 (E), Conveyor belts - Transverse flexibility (troughability) - Test method, 2007.

- [175] NEN-EN-ISO 7590, Steel cord conveyor belts - Methods for the determination of total thickness and cover thickness, 2009.
- [176] NEN-EN-ISO 7622-1, Steel cord conveyor belts - Longitudinal traction test - Part 1: Measurement of elongation, 2013.
- [177] NEN-EN-ISO 9856, Conveyor belts - Determination of the elastic and permanent elongation and calculation of elastic modulus, 2004.
- [178] NEN-ISO 1209, Rigid cellular plastics - Determination of flexural properties - Part 1: Basic bending test; Part 2: Determination of flexural strength and apparent flexural modulus of elasticity, 2007.
- [179] NEN-ISO 5893, Rubber and plastics test equipment - Tensile, flexural and compression types (constant rate of traverse) - Specification, 2002.
- [180] NEN-ISO 703, Conveyor belts - Troughability - Transverse flexibility - Characteristics and test method, 1988.
- [181] Neubecker, I., An Overland Pipe Conveyor with 22 Horizontal and 45 Vertical Curves Connecting Coal Mine with Rail Load Out, *Bulk Solids Handling*, 18(3), 457–462, 1998.
- [182] Neumann, T., and A. Minkin, Conti® MegaPipe – A New Dimension in Closed-Trough Belt Technology, in *Proceedings of the 12th International Symposium Continuous Surface Mining - Aachen 2014*, edited by C. Niemann-Delius, pp. 1–10, Springer International Publishing, 2014.
- [183] Noels, L., and R. Radovitzky, A new discontinuous Galerkin method for Kirchhoff–Love shells, *Computer Methods in Applied Mechanics and Engineering*, 197(33-40), 2901–2929, 2008.
- [184] Nordell, L., X. Qiu, and V. Sethi, Belt conveyor steel cord splice analysis using finite element methods, *Bulk Solids Handling*, 11(4), 863–868, 1991.
- [185] Nuttall, A., Design Aspects of Multiple Driven Belt Conveyors, Ph.D. thesis, Delft University of Technology, 2007.
- [186] Nuttall, A. J. G., G. Lodewijks, and A. J. Klein Breteler, Modelling rolling contact phenomena in a pouch belt conveyor system, *Wear*, 260(9–10), 1081–1089, doi:10.1016/j.wear.2005.07.015, 2006.
- [187] Oehmen, H. H., 1.500 km of stahlcord belting, *Bulk Solids Handling*, 11(4), 881–891, 1991.
- [188] Pang, Y., and G. Lodewijks, Pipe belt conveyor statics - Comparison of simulation results and measurements, *Bulk Solids Handling*, 33(2), 52–56, 2013.
- [189] Petrikova, I., B. Marvalova, T. H. S., and P. Bocko, Experimental evaluation of mechanical properties of belt conveyor with textile reinforcement and numerical simulation of its behaviour, in *Constitutive Models for Rubber VIII*, pp. 641–644, CRC Press, doi:10.1201/b14964-116, 2013.
- [190] Phoenix conveyor belt systems GmbH, *Phoenix Conveyor Belts Design Fundamentals*, Brochure No. 513-102-0804, Hamburg, 2004.
- [191] Phoenix conveyor belt systems GmbH, World records: Highest efficiency conveyor belts, Brochure No. PH 1001 E 12.12 (BL), 2012.

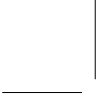
- [192] Qiu, X., Full Two-Dimensional Model for Rolling Resistance: Hard Cylinder on Viscoelastic Foundation of Finite Thickness, *J. Eng. Mech.*, 132(11), 1241–1251, 2006.
- [193] Raaz, V., Conveyor belt system, Patent No US 20140190798 A1, pp. 1-7, 2014.
- [194] Ramjee, S., and P. Staples, Pipe Conveyors for Infrastructure Projects - Innovative solutions for Conveyor Systems, *Bulk Solids Handling*, 23(3), 186–192, 2015.
- [195] Ramos, C. M., Coal transportation and belt conveyors, *Bulk Solids Handling*, 8(3), 297–305, 1988.
- [196] Reddy, J. N., *Theory and Analysis of Elastic Plates and Shells*, 568 pp., CRC Press, 2006.
- [197] Reddy, J. N., and I. R. Singh, Large deflections and large-amplitude free vibrations of straight and curved beams, *International Journal for Numerical Methods in Engineering*, 17(6), 829–852, doi:10.1002/nme.1620170603, 1981.
- [198] Rohde, F. V., Large Deflections of a Cantilever Beam with Uniformly Distributed Load, *Quarterly of Applied Mathematics*, 11, 337–338, 1953.
- [199] Rudolphi, T. J., Applied rubber belt cover loss prediction from indentation, pp. 25–33, 2008.
- [200] Rudolphi, T. J., and A. V. Reicks, Viscoelastic indentation and resistance to motion of conveyor belts using a generalized maxwell model of the backing material, *Rubber Chemistry and Technology*, 79(2), 307–319, 2006.
- [201] Rulmeca Group, Pipe conveyor, product catalogue on idler rolls, http://download.rulmeca.it/catalogo/serie_eng/Pipe.pdf, accessed 18.11.2015.
- [202] Sargasyan, A. E., *Mechanics of materials, theory of elasticity and plasticity: Fundamentals of the theory with examples of calculations* (Сопротивление материалов, теории упругости и пластичности: Основы теории с примерами расчетов), Vysshaya Shkola, Moscow, (in Russian), 2000.
- [203] Schilling, O., M. Westerwald, and J. Wiedenroth, ABAQUS FE Analysis of a Pipe Conveyor Using Solids with Embedded Truss Elements and Shells with Rebar Layers.
- [204] Schulte, A., Foerderanlage mit einem Schlauchband, Patent No. DE 913395 C, 1954.
- [205] Schulze, D., *Powders and bulk solids: behavior, characterization, storage and flow*, 511 pp., Springer-Verlag Berlin Heidelberg, 2008.
- [206] Seames, E., and H. D. Conway, A numerical procedure for calculating the large deflections of straight and curved beams, *J Appl Mech*, 24, 289–294, 1957.
- [207] Senturia, S. D., *Microsystem design*, Kluwer Academic, Boston, 2002.
- [208] Sergeeva, N. V., Determination of rolling resistance force from the indentation of idler rolls into the pipe conveyor belt (Определение силы сопротивления движению от вдавливания роликов в ленту ленточного трубчатого конвейера), *GIAB: Mining Informational and Analytical Bulletin (Scientific and Technical Journal)*, Moscow State Mining University, (12), 321–325, (in Russian), 2007.

- [209] Sergeeva, N. V., Determination of rolling resistance force from deformation of bulk material on pipe conveyor belt (Определение силы сопротивления от деформирования груза на ленте трубчатого конвейера), *GIAB: Mining Informational and Analytical Bulletin (Scientific and Technical Journal)*, Moscow State Mining University, (8), 35–38, (in Russian), 2008.
- [210] Sergeeva, N. V., Justification of the method for determining distributed rolling resistance of straight sections of pipe conveyor belt for mining (Обоснование метода расчета распредел. сил сопротивл. движению ленты на линейной части трубч.конв. для горных предприят.), Ph.D. Thesis Synopsis, Moscow State Mining University, (in Russian), Moscow, 2009.
- [211] Shaeffer, W., Gehaengefoerderer mit einem Schlauchband, Patent No. DE 942972 C, 1956.
- [212] Sisselaar, K. J. A., No Title, *Tech. rep.*, 1990.
- [213] Smirnov, V. I., *A Course of High Mathematics* (Курс высшей математики), vol. 1, 23 ed., 517 pp., Science, Moscow, Russia, 1974.
- [214] Sommer, J. G., and O. H. Yeoh, Tests and Specifications, in *Engineering with rubber: How to design rubber components*, edited by A. N. Gent, 2 ed., chap. 10, pp. 306–355, Hanser; HanserGardner Publications, Inc., Munich; Cincinnati, 2000.
- [215] Spaans, C., Calculation of the main resistance of belt conveyors, *Bulk Solids Handling*, 11(4), 809–820, 1991.
- [216] Staples, P., The history of pipe conveyors, *Bulk Solids Handling*, 22(3), 210–213, 253, 2002.
- [217] Staples, P., Effects of support structures on belt conveyor systems: a case for the triangular gantry, *Bulk Solids Handling*, 23(3), 186–192, 2003.
- [218] Staples, P., and A. K. Metha, Belt Conveyor Technology - Indo Gulf Copper Smelter Pipe Conveyor, *Bulk Solids Handling*, 21(5), 510, 2001.
- [219] Steele, C. R., and C. D. Balch, Introduction to the theory of plates, Lecture Notes, Stanford University, Department of Mechanical Engineering, Division of Mechanics and Computation, pp. 1–41, <http://web.stanford.edu/~chast/Course%20Notes/Introduction%20to%20the%20Theory%20of%20Plates.pdf>, accessed 10.11.2014, 2009.
- [220] Stehlíková, B., V. Molnár, and G. Fedorko, Possibilities of experiments and of using experimental results obtained from the test equipment for measuring properties of conveyor belts pipe conveyor, 2014.
- [221] Steven, R., L. K. Nordell, and Y. Zhang, Tubular Conveyor Belt, Patent No US 20100018841 A1, pp. 1-3, 2010.
- [222] Sumino, S., and M. Fujita, Conveyor belt, Patent No EP 0050962 A1, pp. 1-13, 1982.
- [223] Teijin Aramid B.V., Sustainable performance for conveyor belts, Product Brochure No 36-06-05/2012, <http://www.tejinaramid.com/wp-content/uploads/2012/08/Leaflet-Conveyor-Belts.pdf>, accessed 17.11.2015, 2012.
- [224] Teijin Aramid B.V., Aramids in conveyor belts: a strong, energy-saving alternative, Product Brochure, <http://www.tejinaramid.com/wp-content/uploads/2014/04/Case-study-Conveyor-Belts-Travelling-light.pdf>, accessed 17.11.2015, 2014.

- [225] The KOCH Pipe Conveyor®, Product Specification Brochure No. 2005/9, E5, 2005.
- [226] ThyssenKrupp Fördertechnik GmbH, Reference Pipe Conveyors: Pipe Conveyors by ThyssenKrupp Fördertechnik, Catalog No. 1021-REPLY from 2005-REF_PipeCon as per 0702, [http://www.thyssenkruppobins.com/References/Conveyors/1021-TKF%20from%202005-REF_%20PipeCon.pdf](http://www.thyssenkrupprobins.com/References/Conveyors/1021-TKF%20from%202005-REF_%20PipeCon.pdf), accessed 24.03.2014, 2006.
- [227] Timoshenko, S., and S. Woinowsky-Krieger, *Theory of Plates and Shells*, McGraw-Hill, New York, 1959.
- [228] Tolstov, G. P., *Elements of mathematical analysis* (Элементы математического анализа), vol. 1, 2 ed., Science, Moscow, Russia, 1974.
- [229] Treloar, L. R. G., *The physics of rubber elasticity*, 3 ed., Clarendon, Oxford, 2005.
- [230] Vaka, G. A., Pipe Conveyors - Development and Advantages, *Bulk Solids Handling*, 18(3), 451–456, 1998.
- [231] van den Berg, L., Kilometers kolentransport, *Maintenance Benelux*, pp. 22–24, 2008.
- [232] Ventsel, E., and T. Krauthammer, *Thin plates and shells: theory, analysis, and applications*, Marcel Dekker, New York, 2001.
- [233] Verruijt, A., *Grondmechanica*, Delft University Press, Delft, 1999.
- [234] Wang, J. F., R. H. Wagoner, D. K. Matlock, and F. Barlat, Anticlastic curvature in draw-bend springback, *International Journal of Solids and Structures*, 42(5-6), 1287–1307, 2005.
- [235] Wang, T. M., Non-linear bending of beams with uniformly distributed loads, *International Journal of Non-Linear Mechanics*, 4(4), 389–395, doi:[http://dx.doi.org/10.1016/0020-7462\(69\)90034-1](http://dx.doi.org/10.1016/0020-7462(69)90034-1), 1969.
- [236] Wang, Z. X., J. H. Jiang, and N. L. Chen, Nonlinear rate-dependent stress-strain behavior of light-weight textile conveyor belt, in *7th International Forum on Advanced Material Science and Technology, IFAMST-7*, vol. 675 - 677, pp. 453–456, Dalian; China, Materials Science Forum, Code 84039, 2011.
- [237] Weiss, M., An integrated approach to conveying technology, *Bulk Solids Handling*, 13(3), 571–578, 1993.
- [238] Wesemeier, M., Theoretische Untersuchungen zur Schlauchformkraft am Schlauchgurtsteilförderer, *Schüttgut*, 3(1), 29–33, 1997.
- [239] Wesemeier, M., Untersuchungen zum Bewegungswiderstand infolge der Schlauchformkraft bei Schlauchgurtförderung, in *Kolloquium Stetige Förderung von Schüttgütern*, Otto-von-Guericke-Universität Magdeburg, 16 September, 1997.
- [240] Wesemeier, M., Dimensionierung der Antriebsleistung eines Schlauchgurtförderers, in *Fachtagung Schüttgutfördertechnik '98*, pp. 1–20, Otto-von-Guericke-Universität Magdeburg, 24 September, 1998.
- [241] Wesemeier, M., Dimensionierung der Antriebsleistung von Schlauchgurtförderanlagen, *Schüttgut*, 5(2), 151–159, 1999.

- [242] Wesemeier, M., Projektierung von Schlauchgurt Senkrecht förderanlagen, in *Fachtagung Schüttgutförderertechnik '99*, pp. 1–17, Otto-von-Guericke-Universität Magdeburg, 23-24 September, 1999.
- [243] Wheeler, C., and P. Munzenberger, A pseudo 3D analysis of the indentation rolling resistance problem, in *BELTCON 15: International Materials Handling Conference (IMHC)*, South Africa, Johannesburg.
- [244] Wheeler, C., and P. Munzenberger, Indentation rolling resistance of steel cord conveyor belts: a pseudo 3D viscoelastic finite element analysis, in *Current developments in bulk solids handling, Belt Conveying*, edited by G. Lodewijks, 1 ed., pp. 37–47, Vogel Business Media GmbH & C. KG, 2010.
- [245] Wheeler, C. A., Predicting the main resistance of belt conveyors, in *BELTCON 12: International Materials Handling Conference (IMHC)*, South Africa, Johannesburg, 23-24 July, 2003.
- [246] Wheeler, C. A., Analysis of the main resistances of belt conveyors, Ph.D. thesis, The University of Newcastle, Australia, 2003.
- [247] Wiedenroth, J., Untersuchungen zum Betriebsverhalten unbeladener Schlauchgurtförderer, Ph.D. thesis, Universität Hannover, 1995.
- [248] Wiedenroth, J., The longest pipe conveyor of the world with double load transport at cementos Lima in Peru, in *Society of Mining, Metallurgy and Exploration 2010 Annual Meeting*, Phoenix, Arizona, USA, 2010.
- [249] Wiedenroth, J., and J. Staribacher, Pipe conveyor applications for double load transport, *Bulk Solids Handling*, 26(7), 494–497, 2006.
- [250] Williams, M., R. Landel, and J. Ferry, The Temperature Dependence of Relaxation Mechanisms in Amorphous Polymers and Other Glass-forming Liquids, *Journal of the American Chemical Society*, 77(14), 3701–3707, 1955.
- [251] Wu, M.-R., A large-scale biomass bulk terminal, Delft University of Technology, Ph.D. thesis, Delft, the Netherlands, 2012.
- [252] Xiaoxia, S., M. Wenjun, Z. Hui, Y. Yuan, and Y. Zhengmao, Analysis on the bending stiffness and the form force of the pipe conveyor belt, *Sensors and Transducers*, 161(12), 655–660, 2013.
- [253] Yan, Y., Finite Element Method in Pipe Conveyor Design and Analyses. Report № 2011.TEL.7560, *Tech. rep.*, Delft University of Technology, 2011.
- [254] Yokoyama, T., Fluidity of powder, in *Powder Technology Handbook*, edited by H. Masuda, K. Higashitani, and H. Yoshida, p. 920, CRC Press, USA, 2006.
- [255] Zaimi, Z., Z. Fang, and J. Jianheng, Parameters calculation and structure design of pipe belt conveyer, in *CAID/CD 2008. 9th International Conference on Computer-Aided Industrial Design and Conceptual Design*, pp. 614–617, doi:10.1109/CAIDCD.2008.4730642, 2008.
- [256] Zamiralova, M. E., and G. Lodewijks, Energy consumption of pipe belt conveyors: Indentation rolling resistance, *FME Transactions*, 40(4), 171–176, 2012.
- [257] Zamiralova, M. E., and G. Lodewijks, The shear center effect in the twisting of pipe conveyors, in *Proceedings for Bulk Solids Europe 2012, Wurzburg: Vogel Business media*, pp. 1–12, 2012.

- [258] Zamiralova, M. E., and G. Lodewijks, The indentation rolling resistance of pipe belt conveyors, in *Proceedings of the XX Triennial International Conference of Material Handling, Constructions and Logistics*, edited by S. Bosnjak, G. Kartnig, and N. Zrnic, pp. 65–70, University of Belgrade, Serbia, 2012.
- [259] Zamiralova, M. E., and G. Lodewijks, Pipe conveyor test rigs: Design, application and test results - Part A, *Bulk Solids Handling*, 34(5), 40–45, 2014.
- [260] Zamiralova, M. E., and G. Lodewijks, Pipe conveyor test rigs: Design, application and test results - Part B, *Bulk Solids Handling*, 34(6), 38–46, 2014.
- [261] Zamiralova, M. E., and G. Lodewijks, Pipe conveyor test rigs: Design, application and test results - Part C, *Bulk Solids Handling*, 35(1), 42–49, 2015.
- [262] Zamiralova, M. E., and G. Lodewijks, Measurement of a pipe belt conveyor contact forces and cross section deformation by means of the six-point pipe belt stiffness testing device, *Measurement: Journal of the International Measurement Confederation*, 70, 232–246, doi: 10.1016/j.measurement.2015.03.045, 2015.
- [263] Zamiralova, M. E., and G. Lodewijks, A new approach to determine pipe conveyor belt ability to form a stable pipe shape based on its troughability performance, in *Proceedings of the XXI International Conference on Material Handling, Constructions and Logistics, Vienna, Austria*, edited by G. K. N Zrnic, S Bosnjak, pp. 51–58, Fac. Mechanical Engineering, University of Belgrade, 2015.
- [264] Zamiralova, M. E., and G. Lodewijks, Shape stability of pipe belt conveyors: From troughability to a pipe-ability, *FME Transactions*, 44(3), 263–271, 2016.
- [265] Zamiralova, M. E., and G. Lodewijks, Review of the troughability test ISO 703 for quantifying a uniform transverse bending stiffness for conveyor belts, *Archives of Civil and Mechanical Engineering*, 17(2), 249–270, doi:http://dx.doi.org/10.1016/j.acme.2016.10.007, 2017.
- [266] Zamiralova, M. E., K. M. B. Jansen, and G. Lodewijks, Indentation rolling resistance of pipe belt conveyors using three-dimensional generalized Maxwell viscoelastic model, in *11th International Congress on Bulk Materials Storage, Handling and Transportation (ICBMH 2013)*, edited by M. Jones, pp. 1–11, The University of Newcastle, Australia, 2013.
- [267] Zamiralova, M. E., F. van Keulen, and G. Lodewijks, A new analytical approach to calculate the idler roll load distribution of a pipe conveyor, in *Proceedings of the 11th International Congress on Bulk Materials Storage, Handling and Transportation (ICBMH 2013)*, edited by M. Jones, pp. 1–12, The University of Newcastle, Australia, 2013.
- [268] Zenkov, R. L., *Mechanics of bulk solids* (Механика насыпных грузов), 214 pp., Nedra, (in Russian), Moscow, 1964.
- [269] Zhang, Y., Extended reach: Overland pipe conveyor with low rolling resistance belt, *Bulk Solids Handling*, 33(4), 16–21, 2013.
- [270] Zhang, Y., and R. Steven, Pipe conveyor and belt: Belt construction, low rolling resistance and dynamic analysis, in *Society of Mining, Metallurgy and Exploration 2012 Annual Meeting*, pp. 616–619, Washington, Seattle, 2012.
- [271] Zur, T. W., Viscoelastic properties of conveyor belts: properties of aramid belts, *Bulk Solids Handling*, 6(6), 1163–1168, 1986.



Glossary

List of symbols and notations

A list of the symbols and notations used in this thesis follows below.

Capitals

A	cross sectional area of a belt	[m ²]
A_C, A_L	areas of a bulk material lateral cross section, occupied over the central and lateral bottom rolls	[m ²]
A_Q	cross sectional area of a bulk material	[m ²]
B	belt width	[m]
C, C_3	constants of integration in Chapter 3	[-]
C_1	constant of integration in Chapter 3	[m ⁻²]
C_2	constant of integration in Chapter 3	[m ⁻¹]
C_{1T}	constant for a shift factor in WLF equation	[-]
C_{2T}	constant for a shift factor in WLF equation	[°C]
C^K	coefficient, characterizing a longitudinal development of a bulk solids active/ passive stress states along PBC pitch	[-]
$C_{n1}, C_{n2}, \dots, C_{n13}$	constants used to express functions of CFs parametrized	[-]
C_{nbst}	constant used to express a function of displacements from the load from belt bending stiffness	[-]
$C_{nbulk1}^v, C_{nbulk2}^v, C_{nbulk3}^v$	constants used to express a function of displacements from the vertical component of a bulk material load	[-]
C_{nbw1}, C_{nbw2}	constants used to express a function of displacements from the belt weight	[-]
$C_{nm1}, C_{nm2}, C_{nm3}, C_{nm1}^*, C_{nm2}^*, C_{nm3}^*$	constants used to express unit displacements as a function of input parameters	[-]
C_{w1}, C_{w2}	constants of integration in Chapter 5	[m]
D	pipe diameter	[m]
D_{bend}	a structural bending stiffness	[Nm ²]
D_{nom}	nominal diameter of a pipe, characterizing the hexagon dimension of idler rolls installation	[m]

D_{roll}	diameter of an idler roll	[m]
E	effective Young's modulus of elasticity of a belt, assumed as an isotropic body	[Pa]
E', E''	storage and loss moduli of a viscoelastic material	[Pa]
E_1, E_2	Young's elastic moduli of an orthotropic belt in its longitudinal and lateral direction, respectively	[Pa]
$E_M, E_{M0}, E_{M1}, \dots, E_{M1i}$	moduli of elasticity of the generalized Maxwell model	[Pa]
E_{FEM}	Young's modulus of a belt, determined using FEM	[Pa]
$E_{\text{Wang or Fertis}}$	Young's modulus of a belt, determined using Wang or Fertis approach	[Pa]
F_1, F_2, \dots, F_n	CFs at the idler rolls of a PBC	[N]
$F_{1\text{bst}}, F_{2\text{bst}}, \dots, F_{n\text{bst}}$	PBC CFs from the belt bending stiffness load	[N]
$F_{1\text{bulk}}, F_{2\text{bulk}}, \dots, F_{n\text{bulk}}$	PBC CFs from the bulk material load	[N]
$F_{1\text{bw}}, F_{2\text{bw}}, \dots, F_{n\text{bw}}$	PBC CFs from the belt weight	[N]
F_{bst}	total form force from the belt bending stiffness	[N]
$F_{\text{bulk}}^v, F_{\text{bulk}}^h$	vertical and horizontal scalar projections of a total vector-force from bulk material load	[N]
F_{bw}	concentrated force from the belt weight load	[N]
F_C, F_L	CFs, acting at the central and lateral bottom rolls	[N]
$F_{\text{ind}n}$	indentation resistance force for n -th idler roll	[N]
F_n^{calc}	the normal CFs in indentation contact model	[N]
F_n^{top}	scalar sum of the PBC CFs at the top rolls	[N]
$F_{n\text{bulk}}^v, F_{n\text{bulk}}^h$	PBC CFs from the vertical and horizontal components from the bulk material load	[N]
F_v	vertical scalar projection of a total vector-force from all PBC loads	[N]
F_x, F_y	scalar projections on x - and y - axis of a total vector-forces from all loads, respectively	[N]
G	shear modulus	[Pa]
I	moment of inertia of a belt structure	[m ⁴]
K	lateral stress ratio of a bulk material	[-]
K_0	lateral stress ratio of a bulk material, characterizing a switch between the active and passive stress states	[-]
K_a, K_p	lateral stress ratios of a bulk material in active and passive stress states, respectively	[-]
$K_{\text{min}}, K_{\text{max}}$	critical minimal and maximal lateral stress ratios of a bulk material, respectively	[-]
K_s	static belt sag ratio of a trough conveyor	[-]
L	half-length of a beam span (in Chapter 3); total length of a symmetrical half of a PBC cross-sectional contour (in Chapter 5)	[m]
M	bending moment	[Nm]

$M_{11}, M_{12}, \dots, M_{1n}, M_{1m}$	unit bending moments, caused by the unit loads	[m]
M'_4, M''_4	reaction bending moments at the bottom roll of the symmetrical right and left halves of a PBC cross section	[Nm]
M_A	resultant moment at point A	[Nm]
M_{bst}	bending moment from the load from belt bending stiffness	[Nm]
M_{bulk}	bending moment from the bulk material load	[Nm]
M_{bulk}^v, M_{bulk}^h	bending moments from the vertical and horizontal components of a bulk material load, respectively	[Nm]
M_{bw}	bending moment from the belt weight	[Nm]
M_P	bending moment from external load	[Nm]
M_{smp}	mass of a belt sample	[kg]
M_y	the torque in xz -plane	[Nm]
N	axial force	[N]
$N_{11}, N_{12}, \dots, N_{1n}, N_{1m}$	axial forces, caused by the unit loads	[-]
N'_1, N''_1	repulsion forces at the PBC belt edges	[N]
N_{bst}	axial force from the load from belt bending stiffness	[N]
N_{bulk}	axial force from the bulk material load	[N]
N_{bulk}^v, N_{bulk}^h	axial forces from the vertical and horizontal components of a bulk material load	[Nm]
N_{bw}	axial force from the belt weight	[N]
$N_{F1}, N_{F2}, \dots, N_{F6}$	reaction forces from the PBC idler rolls	[N]
N'_{F1}, N''_{F1}	reaction forces at the symmetrical right and left halves of a PBC cross section at the top roll, respectively	[N]
N'_{F4}, N''_{F4}	reaction forces at the symmetrical right and left halves of a PBC cross section at the bottom roll, respectively	[N]
N_P	axial force from external load	[Nm]
P, P_n	external load	[N]
\bar{P}_n	unit external load	[-]
Q	shear force	[N]
$Q_{11}, Q_{12}, \dots, Q_{1n}, Q_{1m}$	shear forces, caused by the unit loads	[-]
Q_{1bst}, Q_{2bst}	concentrated expansion forces for modeling the load from belt bending stiffness	[N]
Q_{bst}	shear force from the load from belt bending stiffness	[N]
Q_{bulk}	shear force from the bulk material load	[N]
Q_{bulk}^v, Q_{bulk}^h	shear forces from the vertical and horizontal components of a bulk material load	[Nm]
Q_{bw}	shear force from the belt weight	[N]
Q_c	conveyor capacity	[tph]
Q_P	shear force from external load	[Nm]
R	radius of a belt pipe	[m]
R_1, R_2	radii of a rigid cylinder and viscoelastic curved surface in an indentation contact model	[m]
S	arc length of a belt in the troughability test	[m]

T	temperature	[°C]
T_{ref}	reference temperature	[°C]
X_1, X_2, \dots, X_m	redundant forces	[N]
$\bar{X}_1, \bar{X}_2, \dots, \bar{X}_m$	unit forces equivalent the redundant forces	[-]
Y_{max}	maximal deflection of a belt, measured in the troughability test	[m]

Non capitals

a, a_1, a_2, \dots, a_p	center distance to a leading edge	[m]
a_T	temperature-frequency shift factor in WLF equation	[-]
b	longitudinal length of a belt sample (as for the troughability test); center distance to a trailing edge (Chapter 7)	[m]
b_1, b_2, \dots, b_p	center distance to a trailing edge	[m]
c	center distance to a contact edges	[m]
c_K	coefficient of a bulk material passive stress state K_p development	[-]
f_{ind}	IRR friction factor for a BBC system	[-]
$f_{\text{ind}}^{\text{DIN}}$	IRR friction factor of a PBC following recommendations of a DIN-standard	[-]
$f_{\text{ind}n}$	IRR friction factor for one n -idler roll	[-]
f_n^{bst}	function used to parametrize the CFs from the load from belt bending stiffness	[-]
$f_{n\text{bulk}}$	function used to parameterize the CFs from the bulk material load	[-]
$f_{n\text{bulk}}^v, f_{n\text{bulk}}^h$	functions used to parameterize the CFs from the vertical and horizontal components of a bulk material load	[-]
f_n^{bw}	function used to parametrize the CFs from the belt weight	[-]
$f_n^{*\text{empt}}, f_n^{\text{empt}}$	functions used to parameterize the CFs for an empty PBC	[-]
f_n^{loaded}	function used to parameterize the CFs for a loaded PBC	[-]
f_{n1}^v, f_{n2}^v	functions of a PBC filling degree used for the displacements from the vertical component of a bulk material load	[-]
f_r	friction factor	[-]
f_T^{beam}	troughability function of a belt sample, assumed as a beam	[-]
f_T^{shell}	troughability function of a belt sample, assumed as a shell	[-]
g	gravity acceleration	[m/s ²]
h	belt thickness	[m]
$h_{\text{bot}}, h_{\text{top}}$	bottom and top thicknesses of a belt rubber covers, respectively	[m]
h_{bulk}	height of a bulk material column, dividing bulk material cross section into layers	[m]

h_{carc}	thickness of a belt carcass	[m]
k	coefficient of a rectangular cross section ($k = 1.2$)	[-]
k_{Mi}	parameter introduced in the indentation generalized Maxwell model	[m]
k_Q	filling degree of a pipe conveyor cross section	[-]
l	longitudinal length of a belt section	[m]
l_c, l_r	carry spacing at the loaded and empty return strand, respectively	[m]
l_{pl}	length of supporting hexagon plates	[m]
l_{roll}	length of an idler roll	[m]
l_x	half-distance between the belt edges after deformation in the troughability test	[m]
m_y	distributed bending moment, applied with respect to y -axis	[N]
m'_{belt}	line mass of a belt per longitudinal unit length l	[kg/m]
m''_{belt}	area related ($B \times l$) distributed mass of a belt	[kg/m ²]
m'_{bulk}	line mass of a bulk material per longitudinal unit length l	[kg/m]
n	number of Simpson intervals in Chapter 3; a number of an idler roll in Chapters 5-7	[-]
q	transversally distributed load along belt width B	[N/m]
q_{bst}	distributed radial load from belt bending stiffness	[N/m]
$q_{\text{bulk}}^v, q_{\text{bulk}}^h$	vertical and horizontal components of a distributed bulk material load	[N/m]
q_{bw}	weight of a conveyor belt, distributed along its width B	[N/m]
q_x, q_z	axial and radial loads along x - and z - axis, respectively	[N/m]
r	radius of a structural curvature of bending in Chapter 3	[m]
s	length of an arc on a PBC cross-sectional contour	[m]
t	time	[s]
u	axial displacement of a belt structure	[m]
v	belt speed	[m/s]
w	transverse or radial displacement of a belt structure; the deformation of the contact viscoelastic plane with Winkler foundation (Chapter 7)	[m]
w^0	a transverse displacement of a mid-surface in Chapter 3	[m]
x	Cartesian coordinate	[m]
x_0	initial x -coordinate before structural deformation	[m]
x'	dummy variable of a Cartesian x -coordinate	[m]
y	Cartesian coordinate	[m]
z	Cartesian coordinate	[m]
z_0	initial z -coordinate before structural deformation; indentation depth (Chapter 7)	[m]

Greek capitals

Δ	the horizontal displacement of a belt sample after its deformation in the troughability test	[m]
Δ_{ov}	length of an overlap of a pipe conveyor belt	[m]
Λ	a function of an x -coordinate, introduced into Euler-Bernoulli Equation	[m]
Υ_{May}	function of Maxwell parameters and the x -coordinates of the leading and trailing edges for May approach	$[N^{-\frac{1}{3}}m^{-\frac{1}{3}}]$
Υ_{PBC}	function of Maxwell parameters and the x -coordinates of the leading and trailing edges for a PBC	$[N^{-\frac{1}{4}}m^{\frac{1}{2}}]$
$\Phi_M^h, \Phi_{M\lambda}^h$	functions from the bending moment, introduced for the simplicity of the displacements, caused by a horizontal component of a bulk material load	[-]
$\Phi_M^v, \Phi_{M\lambda}^v$	functions from the bending moment, introduced for the simplicity of the displacements, caused by a vertical component of a bulk material load	[-]
$\Phi_{NQ}^h, \Phi_{NQ\lambda}^h$	functions from the axial and shear forces, introduced for the simplicity of the displacements, caused by a horizontal component of a bulk material load	[-]
$\Phi_{NQ}^v, \Phi_{NQ\lambda}^v$	functions from the axial and shear forces, introduced for the simplicity of the displacements, caused by a vertical component of a bulk material load	[-]
Ψ	function of a belt slenderness B/h , introduced for CFs functions	[-]

Greek non capitals

α	angular coordinate on a PBC lateral cross-sectional contour or a dummy-variable of φ -coordinate	[rad]
α_1, α_2	angular coordinates, used for integration limits of a PBC CFs from bulk material load	[rad]
β	angle, characterizing position of Q_{1bst}, Q_{2bst} in a PBC lateral cross section	[rad]
β_{idl}	troughing angle of installation of the lateral idler rolls	[°]
γ_{xz}	structural strain in xz -plane	[-]
δ	loss factor	[-]
$\delta_1, \delta_2, \dots, \delta_n$	displacements, caused by the redundant forces	[m]
$\bar{\delta}_{11}, \bar{\delta}_{12}, \dots, \bar{\delta}_{nm}$	unit displacements at point n or displacements per unit load $\bar{X}_m = 1$	[m/N]
$\bar{\delta}_{1bst}, \bar{\delta}_{2bst}, \dots, \bar{\delta}_{nbst}$	displacements from the load from belt bending stiffness	[m]

$\delta_{1\text{bulk}}^h, \delta_{2\text{bulk}}^h, \dots, \delta_{n\text{bulk}}^h$	displacements from the horizontal component of a bulk material load	[m]
$\delta_{1\text{bulk}}^v, \delta_{2\text{bulk}}^v, \dots, \delta_{n\text{bulk}}^v$	displacements from the vertical component of a bulk material load	[m]
$\delta_{1\text{bw}}, \delta_{2\text{bw}}, \dots, \delta_{n\text{bw}}$	displacements from the belt weight	[m]
$\delta_{n\text{bulk}}$	displacement from bulk material load	[m]
$\delta_{1\text{P}}, \delta_{2\text{P}}, \dots, \delta_{n\text{P}}$	displacements from the external loads at position n	[m]
ε	axial strain of a belt structure	[-]
ε_0	initial strain	[-]
ε_{0x}	initial axial strain of a belt structure along x -axis	[-]
$\varepsilon_x, \varepsilon_z$	axial structural strains along x - and z - axis, respectively	[-]
ζ	ratio, characterizing an anticlastic curvature effect	[-]
$\eta_M, \eta_{M1}, \dots, \eta_{Mi}$	damping factors of the generalized Maxwell model	[Ns/m ²]
θ	angle, characterizing filling degree of a conveyor cross section (in Chapters 2, 5-6); curvature slope of a belt in the troughability test (in Chapter 3)	[rad]
$\theta_0, \theta_1, \dots, \theta_n, \theta_j$	curvature slopes of a belt in the troughability test, obtained for Simpson intervals	[rad]
θ_x, θ_y	angular displacements around x - and y -coordinate, respectively	[rad]
ϑ	angle, characterizing a curvature κ_y change of a structure deformed	[rad]
κ_y	curvature of a structural deformation in xz -plane	[m ⁻¹]
λ, λ_0	dynamic and static angles of repose of a bulk material, respectively	[rad]
μ	Poisson ratio of a belt, assumed as for an isotropic body	[-]
μ_1, μ_2	Poisson ratios of an orthotropic belt in its longitudinal and lateral direction, respectively	[-]
ω	angular frequency	[Hz]
ρ_{bulk}	density of a bulk material	[kg/m ³]
ρ_{carc}	density of a belt uniform carcass	[kg/m ³]
ρ_{rub}	density of a belt constituting rubber	[kg/m ³]
σ	structural stress	[N/m ²]
σ_0	initial stress	[N/m ²]
σ_v, σ_h	vertical and horizontal stress components of a bulk material load, respectively	[N/m ²]
σ_x, σ_z	structural stresses along x - and z - axis, respectively	[N/m ²]
σ_φ	radial stress component of a bulk material load	[N/m ²]
$\tau, \tau_1, \dots, \tau_i$	relaxation times of the generalized Maxwell parameters	[s]
τ_{xz}	structural shear stress in xz -plane	[N/m ²]
τ_φ	shear stress component of a bulk material load	[N/m ²]
φ	angular coordinate on a PBC cross-sectional contour	[rad]
φ_e	effective angle of internal friction of a bulk material	[rad]

List of abbreviations

The following abbreviations are used in this thesis:

APDL	Advanced Parametric Design Language
CEMA	Conveyor Equipment Manufacturers Association
CF	Contact Force
DEM	Discrete Element Method/ (Model)
DMA	Dynamic Mechanical Analysis /(Analyzer)
DOF	Degrees of Freedom
FDM	Finite Difference Method/ (Model)
FEM	Finite Element Method/ (Model)
IRR	Indentation Rolling Resistance
LRR	Low Rolling Resistance
PBC	Pipe Belt Conveyor
WLF	Williams-Landel-Ferry

Acknowledgments

I. S. Turgenev wrote once that “The virtue and gratitude are rarely acquainted”. However, when I look at my life objectively, I would allow myself to disagree to this statement of a famous Russian writer. Perhaps, a law of good energy preservation works in my life. I am really happy to have this opportunity to express my sincere and deepest gratitude to all those people who helped and supported me in this long way towards my PhD and to say thank you to those who contributed intentionally or unintentionally into shaping my personality into the person I am now. I would not say my path towards a PhD degree was full of flowers and butterflies all long. However, if it will be easy to get a PhD degree for everyone, it will not be that valuable.

At first, I would like to thank my promotor and supervisor Prof.dr.ir. Gabriel Lodewijks. Without you, this milestone of my achievement in life will never been reached. Thank you, Gabriel, for believing in me. When I, as a master student sent you an open (and perhaps rather bold) application to express my interest in doing a PhD under your supervision, you gave me such an opportunity. Thank you for guiding me through this project and always finding time for me. Having you as a promotor is like having a large umbrella protecting me and my project from any outside difficulty. I will always remember the significant role you played in this achievement of my life.

I would like also to express my gratitude to Prof. dr.ir. Fred van Keulen, who taught me to ask right questions in research, to simplify the problem and to have faith in my ideas and theories. Thank you, Fred, for being able to squeeze time (sometimes 10-15 minutes) for our discussions in your busy schedule. Even these short meetings were always useful and fully-packed. As for me, you emanated helpful ideas like an Indian god who emanated the world. Thank you for always finding kind supportive words. I appreciate your contribution in my PhD project.

I would like to thank Dr.-ing. Tobias Wennkamp and Dr.-ing. Stephan Hötte from Phoenix Conveyor Belt Systems GmbH for allowing me to use their test facilities and helping to perform experiment testing. Without physical observation of a belt behavior, I would not be able to find the correct boundary conditions for my analytical model. Thank you for your support, and for warm hosting in Bad Blankenburg. I am very grateful to Stephan Hötte for sharing his opinion on pipe conveyor test rigs and assisting in experiment tests with German precision and actual physical strength of a gentleman. I remember, I could not pull the belt to form a pipe shape and place it inside the test rig, because the belt was too stiff for me. That was actually the first time (and so far the only time) when I thought that perhaps the mechanical engineering is not for girls.

I am also grateful to Frans Podbevsek and Garry Vandeberg from Infinite B.V. support.

Your suggestions and tips were very helpful in achieving such a complex step FEM analysis in ANSYS. I would also say thank Sytze Brouwers and Jeroen Kattouw from Dunlop Conveyor Belting B.V. for providing me the belt samples for experiment. My gratitude goes to Ron de Bruin for allowing me to visit EBS terminal and having an opportunity to discuss the practical benefits and difficulties faced in PBC operation. I would also like to thank Dr.ir. Ashley Nuttall for his insightful comments and clarification of his indentation contact model.

I find it important to express my gratitude and appreciation to all my professors and teachers from my Alma mater (Moscow State Mining University) who contributed in my success. I will never forget where roots of my knowledge that deserved to a PhD title originate.

My special gratitude goes to Prof.dr. Valeriy Grigoryevich Dmitriev from MSMU, the person who taught me how to do research, who introduced me to pipe belt conveyors, whom I always admire because he combines majority of best human virtues. Perhaps, it sounds idealistic, but that is how I remember my perception of you back then when I was a young student-idealist that will always carry these views. Thank you, Valeriy Grigoryevich, for supervising my MSc thesis, for giving me a foundation of my knowledge. Thank you for your infinite care, your kindness and support. I never experienced such a father-like mentorship before and after.

I am also grateful to Prof.dr. E. E. Sheshko, Prof.dr. V. P. Dyachenko, and all the teaching staff members of Department of Mining Mechanics and Transport from MSMU, who taught me my profession, who introduced me to a world of belt conveyors and to bulk handling transport. Thank you for being so caring and kind to your students. It always felt like a family there. I would also like to thank Prof. dr. Y. A. Alyushin (theoretical mechanics), Prof. Dr. I. N. Falk (machines and mechanisms), Assoc. prof. O. L. Derbenyova (engineering graphics), Assist. prof. I. E. Zhuravlyova (mathematical analysis) from MSMU for not only conveying the knowledge to your students but also stimulating an interest in profession. I would also like to thank a vice-dean of my alma mater Prof.dr. V. L. Petrov who supported me in the fulfillment of my ideas.

Speaking about the origins, I would also like to pay my credits to my school teachers from Gymnasium 4 in Aktau, especially to director V. A. Malyih, teachers A. N. Gorbunova (mathematics), E.A. Maksimova (physics). Perhaps, it sounds a bit strange that I am mentioning my school teachers from that very past. However, I think, I should be very grateful to my school for creating a social lift for ambitious students who could rely only on themselves by giving a unique education in that difficult after 90s time. My school was my first springboard to persuade my ambitious dreams in the future.

During my PhD at TU Delft, it was disclosed to me that there are so many open and talented people working here, to whom I could address when I needed some help or advice. With the time, I find out that in most of the cases, a talent in those people is usually accompanied with sympathy and kindness. I felt so natural to communicate with all of you and to build relationships, as if the human frequencies coincide.

In this context, my special gratitude is always reserved to Joan Rijsenbrij and to Wouter van den Bos, who played significant role in my success at the very final stage. Thank you, Joan, thank you, Wouter, for giving me a real hand of help when I faced some difficulties in my life. I will always remember your kindness to me. Thank you, Wouter, also for your advices in my FEM analysis in ANSYS and for introducing me how to program within APDL.

I would like to say thank you to Banafsheh Sajadi, who spent time apart from her own project on our discussions on mechanics of materials and who also was a good person and a friend. Thank you, Erik Ulijn, for the assistance in image processing for a belt geometry and also for your sympathy that always cheered me up. My gratitude goes to Dick Mensch for translating my Summary into Dutch and always caring about my progress in life. Thank you, Giancarlo Mangone, for proofreading of some of my early publications and being next to me at certain stage of my life.

My gratitude also goes to my officemates Teus van Vianen, Erik Rotteveel, Kimberly Wu, Guangming Chen, Anca Mutu, Jialun Liu, Wenhua Qu, Javad Mohajeri, Hamid Gilvari. That was really nice to work next to you. Dear Erik, thank you for being always available to answer my questions especially about life in the Netherlands. Thank you, Teus, for our always tolerant political discussions and your help when those heavy belt samples had to be transported from our lab.

I would like to give my appreciation to Dingena Schott (especially thank you for warm supporting email last summer), Jaap Ottjes, Hans Veeke (btw you are a cool drummer), Dineke Heersma, Yusong Pang, Rudy Negenborn, Mark Duinkerken, Patty Bokop-van der Stap, Ed Stok, Freek Brakel, Anouk de Goede-Oosterhoff, Monique Gazendam, and all the staff members from our department. Please, forgive me if I did not mention you all by names, as my appreciation to you all is always preserved in my heart. Special gratitude goes to Jozephina Spoek-Schouten and also Marianne Stolker who were especially kind and caring to me.

I would like to say thank you to those friends who remained by my side during the most difficult times of my life, finding time for a warm word of support, giving me a real hand of help to pull me back up standing. I am very grateful to life that I have them in my life. You are the most precious ones. "You will never truly know yourself, or the strength of your relationships, until both have been tested by adversity," J.K. Rowling said in her Oxford speech. In this context, I would like to mention you, Anna Kirillova, Irina Korosteleva, Emil Gallyamov, Katsiaryna Ushakova, Natalia Vtyurina, Gleb Fedoseev. I would also like to thank for support and help Stef Lommen, Gleb Polevoy, Alexey Ilyushkin, Victoria Hancock, "modest" Ali Haseltalab.

Additional gratitude goes to you, Anna Kirillova, for our trips to the beach, for your advice on the carrier development and being a live example of a super girl. Thank you, Irina Korosteleva and Emil Gallyamov, for your jokes, warmth, for our dinners together and visits to classical music concerts. Thank you, Katsiaryna Ushakova, for your hand of help and support, discussions about art, and great hosting in Switzerland. Thank you, Natalia Vtyurina for so many helpful advices you gave and for being my voice of conscious in complex situations. Thank you, Stef, for our "combat" cycling trips that long and that far that I thought before was possible only for Dutch people. Thank you, Gleb Fedoseev, for your help when I just arrived in the Netherlands and also for your discussions about Mayakovsky poetry, slavophiles, and astro-chemistry. I am so grateful to life for meeting such good and interesting people as you, my truly friends, who lit my life with some sunshine.

I would like also to mention those friends I met who highlighted my life with jokes, sympathy and interesting conversations, such as Tatiana Kozlova, Maria Rudneva, Mikhail Belonosov, Oleg Guziy, Nikita Lenchenkov, Maia Khassina, Ilya Markov, Ilya Popov, Jianbin Xin, Francesco Corman, Antonio Jarquin Laguna, Selma Čaušević, Wasif, Patricio Torres, Edgar Rios Soltero, and also the friends whom I know since my Master studies - Nadezhda

Gvozdeva (Cherkashina), Anna Buzina, Evgeniya Semenova (Pantyukhina), and from the time when I studied Chinese and lived in Beijing – to Asya Kozlova, Vera Prelovskaya (Bukina), and Katerina Hopfgartner.

Finally, I would like to express my deepest gratitude to my beloved family, who supported me the most in my path to this achievement. I am deeply in debts to you. I am so grateful to my beloved mother for her infinite altruistic love and care, for teaching me to be a better person, more kind, responsible, modest, work hard and have a courage to go against the system, if that is for fare justice and help to other people. At the end, that is what makes a person to be a good moral person. Спасибо, мама!

I would also like to thank my father, who encouraged me to become an engineer, who always supported me in my perhaps adventurous ideas and dreams, such as to study Chinese, live in Beijing for a year or persuade a PhD degree in the Netherlands. Thank you, dad, for your wisdom, humor, courage, and your altruistic ability to care of our family more than to care of your own life. Dear father, I cannot even describe how strong bonds and deep level of understanding we are having together. You said that every young generation had to have a higher education than their parents in order the family and country could succeed. Well, so far I feel honored being a first PhD representative in our family. Спасибо, папа!

I would like to say thank you to my dear sister Anna Boykova (Zamiralova) who always remains my best and closest friend. Anyuta, without your love, friendship, and care, I would not be able to go that far. I truly believe that part of my PhD title belongs to you for the enormous support you gave to me. I would also like to thank Pavel Boykov for help and kindness to our family, being a truly member of it. I would also like to say my gratitude to little Maria (Boykova). For her, perhaps this thesis will be abracadabra for a long time, but the gratitude goes to her ability to lit the life of our family with a sunny joy that is so naturally carried in all children's hearts.

Maria E. Zamiralova
Delft, June 2017

Curriculum vitae

Maria Eduardovna Zamiralova was born in Shevchenko in Kazakh SSR (now Aktau, Kazakhstan). After completing her secondary education from Gymnasium 4 in Aktau in 2005, she entered Moscow State Mining University, Department of Mining Mechanics and Transport. The major focus of her studies goes to conceptual design development of machines and mechanisms involved in mining, transport, and bulk solids handling. In 2011, she received her MSc degree (summa cum laude) by defending her Master project, accomplished under the supervision of Prof. dr. V. G. Dmitriev. The project was focused on design development of a transport system, used in a construction of a new Moscow Subway section within shield tunneling machine.

Apart from her major education, from 2006 till 2011, she studied Chinese language at Moscow State University, Institute of Asian and African Countries at Intercollegiate Faculty of Chinese language. This activity resulted in the language internship to Beijing in 2008, where Maria lived for one academic year.

In 2011, she joined Delft University of Technology (the Netherlands), Department of Transport Engineering and Logistics, where she started her PhD project under supervision of Prof. dr. ir. Gabriel Lodewijks. Her PhD project, completed in 2017, is focused on development of an effective pipe belt conveyor design. During her PhD she supervised MSc project on a belt conveyor-related subject, presented her research in international conferences and published in scientific journals, industrial magazines, conference proceedings.

Currently, Maria is employed as a consultant in Royal Haskoning DHV (Rotterdam).

Publications

1. M. Zamiralova, G. Lodewijks, Review of the Troughability test ISO 703 for quantifying a uniform transverse bending stiffness for conveyor belts, Archives of Civil and Mechanical Engineering, Vol. 17, Iss. 2, DOI: 10.1016/j.acme.2016.10.007, pp. 249-270, 2017.
2. G. Lodewijks, M. Zamiralova, Design aspects of pipe conveyors, Proceedings of 12th International Conference on Bulk Materials Storage, Handling, and Transportation (ICBMH 2016), publisher Society of Engineers, pp. 448-464, Darwin, Australia, 2016.
3. M. Zamiralova, G. Lodewijks, Shape stability of pipe belt conveyors: From troughability to a pipe-ability, FME Transactions, Vol. 44, Iss. 3, DOI: 10.5937/fmet1603263Z, pp. 263-271, 2016.

4. M. Zamiralova, G. Lodewijks, A new approach to determine pipe conveyor belt ability to from a stable pipe shape based on its troughability performance, Proceedings of XXI International Conference on Material Handling, Constructions and Logistics (MHCL 2015), publisher Univ. of Belgrade, pp. 51-58, Viena, Austria, 2015.
5. M. Zamiralova, G. Lodewijks, Measurement of a pipe belt conveyor contact forces and cross section deformation by means of the six-point pipe belt stiffness testing device, Measurement: Journal of the International Measurement Confederation, Vol. 70, DOI:10.1016/j.measurement.2015.03.045, pp. 232-246, 2015.
- 6-8. M. Zamiralova, G. Lodewijks, Pipe Conveyor Test Rigs: Design, Application and Test Results, Bulk Solids Handling, publisher Vogel Verlag und Druck GmbH and Co.KG:
Part C - Vol. 35, Iss. 1, pp. 42-49, 2015;
Part B - Vol. 34, Iss. 6, pp. 38-46, 2014;
Part A - Vol. 34, Iss. 5, pp. 40-45, 2014.
9. M. Zamiralova, F. van Keulen, G. Lodewijks, A new analytical approach to calculate the idler roll load distribution of a pipe conveyor, Proceedings of 11th International Conference on Bulk Materials Storage, Handling and Transportation (ICBMH 2013), pp. 1-12, Newcastle, Asutralia, 2013.
10. M. Zamiralova, K.M.B. Jansen, G. Lodewijks, Indentation rolling resistance of pipe belt conveyors using three-dimensional generalized Maxwell viscoelastic model Proceedings of 11th International Conference on Bulk Materials Storage, Handling and Transportation (ICBMH 2013), pp. 1-11, Newcastle, Asutralia, 2013.
11. M. Zamiralova, G. Lodewijks, Energy consumption of pipe belt conveyors: indentation rolling resistance, FME Transactions, Vol. 40, Iss. 4, pp. 171-176, 2012.
12. M. Zamiralova, G. Lodewijks, The shear center effect in the twisting of pipe conveyors, Proceedings of Bulk Solids Europe 2012, published by Wurzburg: Vogel Business media, pp. 1-12, Berlin, Germany, 2012.
13. M. Zamiralova, G. Lodewijks, The indentation rolling resistance of pipe belt conveyors, Proceedings of XXI International Conference on Material Handling, Constructions and Logistics (MHCL 2015), published by University of Belgrade, pp. 65-70, Belgrade, Serbia, 2012.